Springer Series in Materials Science 203

Jai Singh
Richard T. Williams *Editors*

Excitonic and Photonic Processes in Materials

Springer

Springer Series in Materials Science

Volume 203

Series editors

Robert Hull, Charlottesville, USA
Chennupati Jagadish, Canberra, Australia
Richard M. Osgood, New York, USA
Jürgen Parisi, Oldenburg, Germany
Tae-Yeon Seong, Seoul, Korea, Republic of (South Korea)
Shin-ichi Uchida, Tokyo, Japan
Zhiming M. Wang, Chengdu, China

For further volumes:
http://www.springer.com/series/856

The Springer Series in Materials Science covers the complete spectrum of materials physics, including fundamental principles, physical properties, materials theory and design. Recognizing the increasing importance of materials science in future device technologies, the book titles in this series reflect the state-of-the-art in understanding and controlling the structure and properties of all important classes of materials.

Jai Singh · Richard T. Williams
Editors

Excitonic and Photonic Processes in Materials

Editors
Jai Singh
Faculty of Engineering, Health, Science and the Environment, School of Engineering and Information Technology
Charles Darwin University
Darwin, NT
Australia

Richard T. Williams
Department of Physics
Wake Forest University
Winston-Salem, NC
USA

ISSN 0933-033X ISSN 2196-2812 (electronic)
ISBN 978-981-287-130-5 ISBN 978-981-287-131-2 (eBook)
DOI 10.1007/978-981-287-131-2
Springer Singapore Heidelberg New York Dordrecht London

Library of Congress Control Number: 2014945464

© Springer Science+Business Media Singapore 2015
This work is subject to copyright. All rights are reserved by the Publisher, whether the whole or part of the material is concerned, specifically the rights of translation, reprinting, reuse of illustrations, recitation, broadcasting, reproduction on microfilms or in any other physical way, and transmission or information storage and retrieval, electronic adaptation, computer software, or by similar or dissimilar methodology now known or hereafter developed. Exempted from this legal reservation are brief excerpts in connection with reviews or scholarly analysis or material supplied specifically for the purpose of being entered and executed on a computer system, for exclusive use by the purchaser of the work. Duplication of this publication or parts thereof is permitted only under the provisions of the Copyright Law of the Publisher's location, in its current version, and permission for use must always be obtained from Springer. Permissions for use may be obtained through RightsLink at the Copyright Clearance Center. Violations are liable to prosecution under the respective Copyright Law.
The use of general descriptive names, registered names, trademarks, service marks, etc. in this publication does not imply, even in the absence of a specific statement, that such names are exempt from the relevant protective laws and regulations and therefore free for general use.
While the advice and information in this book are believed to be true and accurate at the date of publication, neither the authors nor the editors nor the publisher can accept any legal responsibility for any errors or omissions that may be made. The publisher makes no warranty, express or implied, with respect to the material contained herein.

Printed on acid-free paper

Springer is part of Springer Science+Business Media (www.springer.com)

Preface

Excitonic and photonic processes are responsible for the operation of many optoelectronic devices including solar cells, electroluminescent devices such as LEDs and OLEDs, quantum well and quantum dot lasers, detectors, scintillators, carbon nanotube-based devices and hybrid nanostructures. This book presents state-of-the-art understanding of a selection of excitonic and photonic processes in useful materials from semiconductors to insulators to metal/insulator nanocomposites, both inorganic and organic. Excitonic properties are particularly important in organic photovoltaics and light-emitting devices, as also in questions of the ultimate resolution and efficiency of new-generation scintillators for medical diagnostics, border security, and nuclear nonproliferation. Novel photonic and optoelectronic applications benefit from new material combinations and structures as discussed in this volume. The contents of this volume are expected to benefit all researchers in the field of photovoltaic, electroluminescent devices, light-emitting devices, nanostructure lasers, noncrystalline semiconductors and scintillators, including senior undergraduate and postgraduate students and industry researchers.

Chapter 1 describes the optical properties and carrier recombination dynamics in $SrTiO_3$ bulk crystals. $SrTiO_3$ is regarded to be a key material in oxide electronics because of its unique electrical and optical properties as thoroughly covered in this chapter. In Chap. 2, starting from a historical trace of key developments in the science and engineering of photovoltaics, an overview of photovoltaics and allied photonic architectures is presented. A review of selected recent research results on the integration of wave-optic coupling nanostructures in silicon photovoltaics is given with an emphasis on the use of photonic crystal constructs. In Chap. 3, the relationship between the optical properties of Polyfluorene and the polymer conformation is discussed within the framework of the simple effective conjugation length model. Polyfluorene is well known as an efficient blue emitter for polymer-based light-emitting diodes and is very attractive from a physical point of view because randomly twisted, regularly twisted, or planar conformations can be realized in its solid state. The electronic structure of polyfluorene is discussed based on the electroabsorption (EA) spectra of the three conformations. Chapter 4 presents a comprehensive study of bulk heterojunction organic solar cells (OSCs), which are an attractive alternative to silicon-based solar cells due to low-cost solution fabrication processes. After a brief overview of basics of OSCs, the charge transport properties and different approaches including

incorporating metal nanoparticles and surface plasmonic structures to enhance the absorption in OSCs are discussed. A comprehensive study on the degradation mechanisms of OSCs is also presented in this chapter. In Chap. 5 is presented the study of exciton-plasmon interaction in metal-semiconductor nanostructures, which offer a wide range of opportunities to control light-matter interactions and electromagnetic energy flows on nanometer length scales. The chapter emphasizes applications of nanocomposites in biophotonics and in sensing and switching applications. Strong exciton-surface plasmon coupling in metallic nanocomposites can lead to efficient transmission of quantum information between qubits for applications in quantum computing and communication.

In Chap. 6, following a phenomenological approach, the light yield of a scintillator is derived as a function of the rates of both radiative and nonradiative (quenching) excitonic processes to study the nonproportionality occurring in the yield of inorganic scintillators. The results are analyzed with a view to present a recipe for achieving an inorganic scintillator with optimal proportionality in its yield and hence optimal energy resolution. The theory presented here forms the fundamental background desired for understanding the nonproportionality observed in scintillators. Chapter 7 reviews the electronic properties of inorganic noncrystalline semiconductors using the effective mass approach in the real coordinate space. It is shown that many of the properties that can be studied through the effective mass approximation applied in the reciprocal lattice vector **k**-space in crystalline semiconductors can be studied in noncrystalline semiconductors in the real coordinate **r**-space. This includes the derivation of effective masses of charge carriers, mechanism of the double sign reversal leading to the anomalous Hall effect in hydrogenated amorphous silicon (a-Si:H), and the formation of excitons in noncrystalline semiconductors. In Chap. 8 are described the excitonic processes in organic semiconductors and their applications in organic photovoltaic and light-emitting devices. The mechanisms of excitonic absorption, diffusion, and dissociation of excitons at the donor–acceptor interface and their influences on the photovoltaic performance of bulk heterojunction organic solar cells are presented. Chapter 9 presents the important optical and electronic processes which influence the properties of semiconductor photonic devices used for light-emitting applications (lasers and LEDs) operating in a wide spectral range from visible to mid-infrared. The main carrier recombination mechanisms in semiconductor devices are discussed and experimental methodologies for measuring and analyzing these mechanisms are introduced. Finally, Chap. 10 discusses the electron-hole recombination processes that occur in the high excitation densities and strong radial gradients of particle tracks in scintillator detectors of radiation. In energy-resolving radiation detectors, intrinsic proportionality of light yield to gamma ray energy or electron energy is an important concern. This chapter gives special emphasis to understanding the physical basis for nonproportionality, while reviewing recent results on fundamental physics of nonlinear quenching, cooling and capture of hot electrons, co-evolving free-carrier and exciton populations, and diffusion in the dense and highly structured excitation landscape of electron tracks. The readers may find it useful to note that the theory

presented in Chap. 6 and discussions in Chap. 10 are expected to provide complementary information on scintillators.

We would like to express our gratitude to Dr. Loyola D'Silva at Springer Publishing for inviting us to bring a volume on this research topic to a wider audience, and to all our distinguished contributors for their efforts.

Darwin, Australia Jai Singh
Winston-Salem, USA Richard T. Williams

Contents

1 Photocarrier Recombination Dynamics in Perovskite Semiconductor $SrTiO_3$ 1
Yasuhiro Yamada and Yoshihiko Kanemitsu
1.1 Introduction 1
1.2 Photoluminescence Spectra 4
1.3 Band-to-Band Luminescence and Optical Absorption Spectra 6
1.4 Photocarrier Recombination Dynamics: Importance of Nonradiative Auger Recombination. 11
1.4.1 Undoped Crystals 12
1.4.2 Electron-Doped Crystals 16
1.4.3 Temperature Dependence 18
1.5 Surface Oxygen Deficient Layer: Bulk Crystals and Nanoparticles 21
1.6 Other Perovskite Semiconductors 28
1.7 Summary 32
References 33

2 Nano Architectures in Silicon Photovoltaics 37
Nazir P. Kherani
2.1 Introduction 37
2.2 Photovoltaics and Photonic Architectures: A Historical Perspective. 40
2.2.1 Photovoltaics 40
2.3 Nano Architectures in Silicon Photovoltaics: Recent Advances 47
2.3.1 Introduction 47
2.4 Future Outlook 58
References 58

3 Electronic Structures of Planar and Nonplanar Polyfluorene 63
Takashi Kobayashi, Takashi Nagase and Hiroyoshi Naito
3.1 Introduction 63
3.2 Fundamental Optical Properties 65

3.2.1 Conformation of F8 65
3.2.2 Effective Conjugation Length Model 67
3.2.3 Photoluminescence (PL) Properties 67
3.3 Electronic Structure 69
3.3.1 Electroabsorption(EA) Measurements 69
3.3.2 Essential-State Model 70
3.3.3 EA Spectrum of Glassy F8 70
3.3.4 Transition from Glassy to β-phase 72
3.3.5 Oscillatory Feature in Crystalline Thin Films 75
3.3.6 Discussions 76
3.4 Conclusions 78
References 79

4 Organic and Excitonic Solar Cells 81
Furong Zhu
4.1 Introduction 81
4.2 Basics of Organic Solar Cells 83
4.3 Electrode Modification and Interfacial Engineering 88
4.3.1 Plasma-Polymerized Fluorocarbon-Modified Ag Nanoparticles 89
4.3.2 Effect of ITO Surface Electronic Properties on OSC Performance 90
4.3.3 Ag Nanoparticles-Modified ITO/Plastic Substrate for Flexible OSCs 96
4.4 Charge Transport Properties in Bulk-Heterojunction OSCs 99
4.4.1 Charge Transport Properties in Polymer/Oxide Composites 99
4.4.2 Effect of Oxygen-Induced Traps on Charge Mobility and OSC Performance 105
4.5 Absorption Enhancementin OSCs 111
4.6 Stability of Bulk-Heterojunction OSCs 115
4.7 Conclusions 122
References 122

5 Exciton-Plasmon Coupling in Nanocomposites 127
Mahi R. Singh
5.1 Introduction 127
5.2 Surface Plasmon Polaritons 129
5.2.1 Quasi-Static Approximation 129
5.2.2 Metallic Heterostructures 130
5.2.3 Metallic Nanoparticles 132
5.3 MNP Polarization 135
5.4 Electric Field Enhancement 137

5.5 Exciton-Plasmon Interaction. 139
5.5.1 Dipole–Dipole Interaction 140
5.5.2 Interaction Hamiltonian. 142
5.6 Density Matrix Method 144
5.6.1 Two-Level Quantum Dot. 145
5.6.2 Decay Rate 146
5.6.3 Three-Level Quantum Dot. 148
5.7 Energy Exchange Rate 150
5.7.1 Spherical Nanoparticles. 151
5.8 Quantum Dot-Graphene Hybrid 152
5.9 Conclusion. 154
References 154

6 Influence of Excitonic Processes in the Energy Resolution of Scintillators 157
Jai Singh and Alex Koblov
6.1 Introduction 157
6.1.1 Non-proportionality in Scintillator Light Yield (Y). 159
6.2 Theory of Non-proportional Light Yield 160
6.2.1 Rate Equations. 161
6.2.2 Local Light Yield (Y_L) 163
6.2.3 Total ScintillatiorYield (Y). 166
6.3 Proportional Scintillator Yield 171
6.3.1 Excitonic Scintillators ($f_x = 1$) 171
6.3.2 Non-excitonic Scintillators ($f_x = 0$). 172
6.3.3 Dependence of Yield on Linear Rates (R_1, K_1) 173
6.3.4 Dependence of Yield on Bimolecular Quenching Rates (K_{2x}, K_{2eh}) 176
6.3.5 Dependence of Yield on Auger Quenching Rates (K_{3x}, K_{3eh}). 179
6.3.6 Dependence of Yield on Track Radius r 180
6.4 Discussions on Nonproportionality (NPR) in the Yield 183
6.4.1 Influence of R_{1x} on NPR 183
6.4.2 Influence of Ratio of Concentrations f_x 184
6.4.3 Influence of Bimolecular Quenching. 184
6.4.4 Influence of Auger Quenching 185
6.4.5 Influence of Track Radius 185
6.4.6 Influence of Evolution of Excitonic Concentration Within the Electron Track 187
6.5 Achieving Optimal Proportionality in a Scintillator. 190
6.6 Conclusions 191
References 191

7 Electronic Properties of Noncrystalline Semiconductors 193
Jai Singh
7.1 Introduction 193
7.2 Effective Mass of Charge Carriers in Inorganic Amorphous Semiconductors 198
7.2.1 Effective Mass of Electrons in the Conduction Band 198
7.2.2 Effective Mass of Holes in the Valence Band 202
7.3 Anomalous Hall Effect 203
7.4 Excitonic States in Noncrystalline Solids 206
7.4.1 Possibility (1): Creation of an Exciton by Exciting Both Electron and Hole in Extended States 209
7.4.2 Possibilities (2) and (3): Electron Excited in Extended and Hole in Tail, and Electron Excited in Tail and Hole in Extended States 210
7.4.3 Possibility (4): Both the Electron and Hole Are Excited in Their Respective Tail States 210
7.5 Excitonic Photoluminescence and Phosphorescence 211
7.5.1 Emission from Singlet Excitons (Photoluminescence) 211
7.5.2 Emission from Triplet Excitons (Phosphorescence) 213
7.6 Conclusions 226
References 226

8 Excitonic Processes in Organic Semiconductors and Their Applications in Organic Photovoltaic and Light Emitting Devices 229
Monishka Rita Narayan and Jai Singh
8.1 Introduction 230
8.2 Organic Solar Cells 230
8.2.1 Photon Absorption and Formation of Singlet Triplet Excitons in OSCs 232
8.2.2 Exciton Diffusion in Bulk-Heterojunction Organic Solar Cells 237
8.2.3 Diffusion Coefficient and Excitonic Diffusion Length 238
8.2.4 Exciton Dissociation in Bulk-Heterojunction Organic Solar Cells 240
8.3 Organic Light Emitting Devices 246
8.4 Conclusions 249
References 250

9 Optical and Electronic Processes in Semiconductor Materials for Device Applications 253
Igor P. Marko and Stephen J. Sweeney
9.1 Introduction: Optical and Electronic Processes in Semiconductor Optoelectronic Devices 253
9.1.1 Carrier Injection and Recombination. 254
9.1.2 Spontaneous Emission Analysis 257
9.1.3 High Pressure Analysis 259
9.2 Near-Infrared Quantum Well Lasers 263
9.2.1 The Temperature Dependence of 1.3- and 1.5-μm InGaAs(P)/InP Multi-quantum Well Semiconductor Lasers 264
9.2.2 Near-Infrared InGaAlAs/InP Based Lasers. 269
9.2.3 Analysis of Near-Infrared "Dilute Nitride" InGaAsN/GaAs Lasers 271
9.3 New Approaches in Development of the Near-Infrared Lasers 274
9.3.1 InAs-Based Quantum Dots. 274
9.3.2 Bismuth Containing III–V Material Systems 277
9.4 Semiconductor Emitters for Mid-Infrared Applications 280
9.4.1 Interband Structures for Longer Wavelength Lasers and LEDs 280
9.4.2 Short-Wavelength Quantum Cascade Lasers 283
9.4.3 Inter-Band Type II "W"-Cascade Lasers. 286
9.5 Physical Properties of Devices Emitting in Visible Range of the Spectrum 287
9.5.1 AlGaInP Lasers 287
9.5.2 Efficiency Droop Problem in InGaN Light Emitting Devices 289
9.6 Conclusions 293
References 293

10 Scintillation Detectors of Radiation: Excitations at High Densities and Strong Gradients. 299
R. T. Williams, J. Q. Grim, Qi Li, K. B. Ucer, G. A. Bizarri and A. Burger
10.1 Introduction 300
10.2 Measurements of Light Yield Functions 304
10.2.1 Gamma Photopeak Resolution 305
10.2.2 Gamma Energy Response 306
10.2.3 Electron Energy Response 306
10.2.4 X-ray Photon Energy Response 308
10.2.5 Ultraviolet Photon Density Response 309

10.3 Measuring Photon Density Response by the “Interband z Scan” Technique 310
10.3.1 Experiment 311
10.3.2 Pure 2nd Order Quenching in BGO Versus 3rd Order SrI_2 312
10.3.3 Mixed Kinetic Orders in CsI:Tl and NaI:Tl; Measuring the Free-Carrier Fraction η_{eh} 314
10.3.4 Experimental Determination of the Radius of the NLQ Zone at Track End in NaI:Tl and SrI_2. 318
10.4 Analysis of Photon Density Response 319
10.4.1 Second Order Quenching. 319
10.4.2 Third Order Quenching 321
10.5 Wings, Humps, Charge Separation, and Energy Storage 329
10.6 Tabulation of Results from Photon Density Response 332
10.7 Calculating Local Light Yield Versus Excitation Density in Electron Tracks 335
10.7.1 Dilution of e-h Density in the Track Core by Ambipolar Diffusion 336
10.7.2 Effects of Charge Separation 340
10.7.3 Recombination in the Field of a Cylinder of Self-Trapped Holes. 341
10.7.4 Effect of Charge Separation During Thermalized Diffusion on Light Yield 344
10.7.5 Effect on Light Yield of Charge Separation Due to Hot Electron Diffusion 346
10.8 Calculating Electron Energy Response 347
10.9 Toward a Design Rule: General Trends in Scintillator Proportionality and Light Yield Versus a Few Material Parameters 352
References 356

Contributors

G. A. Bizarri Lawrence Berkeley National Laboratory, Berkeley, CA, USA

A. Burger Department of Physics, Fisk University, Nashville, TN, USA

J. Q. Grim Department of Physics, Wake Forest University, Winston-Salem, NC, USA

Yoshihiko Kanemitsu Institute for Chemical Research, Kyoto University, Uji, Kyoto, Japan

Nazir P. Kherani Department of Electrical and Computer Engineering, University of Toronto, Toronto, ON, Canada; Department of Materials Science and Engineering, University of Toronto, Toronto, ON, Canada

Takashi Kobayashi Department of Physics and Electronics, Osaka Prefecture University, Sakai, Osaka, Japan

Alex Koblov Faculty of EHSE, School of Engineering and Information Technology, Charles Darwin University, Darwin, NT, Australia

Qi Li Department of Physics, Wake Forest University, Winston-Salem, NC, USA

Igor P. Marko Department of Physics and Advanced Technology Institute, University of Surrey, Guildford, Surrey, UK

Takashi Nagase Department of Physics and Electronics, Osaka Prefecture University, Sakai, Osaka, Japan

Hiroyoshi Naito Department of Physics and Electronics, Osaka Prefecture University, Sakai, Osaka, Japan

Monishka Rita Narayan Centre for Renewable Energy and Low Emission Technology, Charles Darwin University, Darwin, NT, Australia

Jai Singh Faculty of EHSE, School of Engineering and Information Technology, Charles Darwin University, Darwin, NT, Australia

Mahi R. Singh Department of Physics and Astronomy, The University of Western Ontario, London, Canada

Stephen J. Sweeney Department of Physics and Advanced Technology Institute, University of Surrey, Guildford, Surrey, UK

K. B. Ucer Department of Physics, Wake Forest University, Winston-Salem, NC, USA

R. T. Williams Department of Physics, Wake Forest University, Winston-Salem, NC, USA

Yasuhiro Yamada Institute for Chemical Research, Kyoto University, Uji, Kyoto, Japan

Furong Zhu Department of Physics, Hong Kong Baptist University, Hong Kong, China

Chapter 1
Photocarrier Recombination Dynamics in Perovskite Semiconductor $SrTiO_3$

Yasuhiro Yamada and Yoshihiko Kanemitsu

Abstract Perovskite oxide semiconductors have attracted a great deal of attention as new device materials because they show multifunctional properties beyond those of conventional semiconductors. With its unique electrical and optical properties, $SrTiO_3$ is a key material in oxide electronics. In this chapter, we discuss the optical properties and carrier recombination dynamics of $SrTiO_3$ bulk crystals. Electron-doped and strongly photoexcited $SrTiO_3$ crystals show photoluminescence (PL) consisting of three components: a 2.5-eV green PL, a 2.9-eV blue PL, and a 3.2-eV band-to-band PL. The blue PL dynamics in the presence of high-density carriers is determined by nonradiative three-carrier Auger recombination. The PL spectra and dynamics of undoped $SrTiO_3$ under strong photoexcitation are very similar to those of electron-doped $SrTiO_3$. From the PL decay dynamics, we evaluate the electron density in the near-surface oxygen-deficient region in $SrTiO_3$ bulk crystals and nanoparticles. PL spectra of other d^0-type perovskite semiconductors, $KTaO_3$, $BaTiO_3$, $LiNbO_3$, and $LiTaO_3$, are also discussed in comparison with $SrTiO_3$.

1.1 Introduction

Perovskite oxide semiconductors and their heterostructures have attracted a great deal of attention as new device materials because they show multifunctional and fascinating properties beyond those found in conventional semiconductors. The crystal structure of ABO_3-type *perovskite* oxides, where A and B denote two different cations, is illustrated in Fig. 1.1. These perovskite oxides show unique electronic properties such as superconductivity, colossal magnetoresistance, and metal-to-insulator transition. In addition, many of the perovskite oxides are semiconductors with wide band-gap energies, and show unique optical properties, which are used

Y. Yamada · Y. Kanemitsu (✉)
Institute for Chemical Research, Kyoto University, Uji, Kyoto 611-0011, Japan
e-mail: kanemitu@scl.kyoto-u.ac.jp

J. Singh and R. T. Williams (eds.), *Excitonic and Photonic Processes in Materials*, Springer Series in Materials Science 203, DOI: 10.1007/978-981-287-131-2_1,
© Springer Science+Business Media Singapore 2015

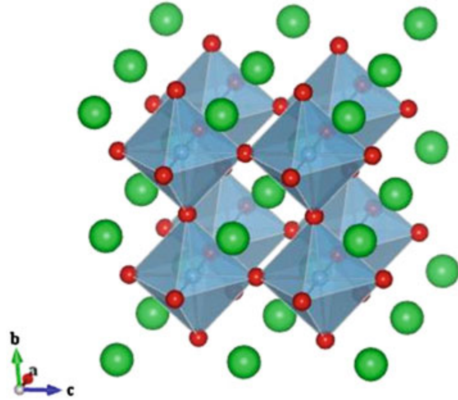

Fig. 1.1 Structure of ABO_3-type perovskite oxides

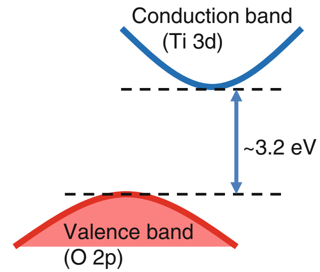

Fig. 1.2 Schematic band structure of $SrTiO_3$ crystals

for advanced optoelectronic devices such as nonlinear optics crystals [1, 2], scintillators [3], photoluminescence (PL) and electroluminescence materials [4, 5], and solar cells [6].

Strontium titanate ($SrTiO_3$) is one of the most promising perovskite oxides for applications in electronics and optoelectronics and is also a wide-gap semiconductor with a band-gap energy of about 3.2 eV. The electronic band structure of $SrTiO_3$ is illustrated in Fig. 1.2. $SrTiO_3$ is an indirect-gap semiconductor. According to [7], the conduction band minimum and valence band maximum are located at X and Γ points, respectively. The conduction and valence bands are mainly composed of empty Ti 3d levels and fully occupied O 2p levels, respectively.

Because $SrTiO_3$ as a single crystal is an excellent platform material for the epitaxial growth of oxide thin films [8, 9], oxide-based electronic devices can be integrated on $SrTiO_3$ crystals. In addition, $SrTiO_3$ itself shows unique electronic features. With the use of electron doping, the electronic properties of $SrTiO_3$ can be varied significantly from insulating to semiconducting, to metallic, and even to superconducting [10–13]. Doped or photogenerated carriers in $SrTiO_3$ show high mobility at low temperatures [14], which results in large conductivity and enhancement in the dielectric constant [15, 16]. Moreover, the recent discovery of two-dimensional electron gases (2DEGs) of the $LaAlO_3$/$SrTiO_3$ heterointerface has prompted further interests in $SrTiO_3$ [17–23]. Despite the insulating properties of $SrTiO_3$ and $LaAlO_3$,

a metallic 2DEG system is formed at the interface. Unique electronic and magnetic properties of the $LaAlO_3/SrTiO_3$ heterointerface, such as magnetoresistance and superconductivity, are observed at low temperatures [20–26]. Extensive studies on the electronic structures and electronic properties of $SrTiO_3$ bulk crystals and heterostructures have been made so far [3–26]. However, there have been no quantitative discussions on the intrinsic carrier recombination processes that determine their unique electronic and optical properties.

Recently, it has been discovered that strongly photoexcited, electron-doped, and Ar^+-irradiated $SrTiO_3$ crystals show blue photoluminescence (PL) at room temperature and band-edge PL at low temperatures [27–29]. To study optoelectronic properties of wide-gap semiconductors, PL spectroscopy is one of the most important and powerful tools. Observed these new PL bands provide an opportunity to deep understanding of the carrier recombination dynamics and electronic properties of perovskite oxide semiconductors and their heterointerfaces. As will be described below, the detailed studies of PL properties provide new insights of carrier transport mechanism in $SrTiO_3$.

The carrier transport mechanism in $SrTiO_3$ has been discussed in terms of a polaron, which is self-trapped electron (or hole) involving lattice distortions due to strong electron-phonon coupling [30, 31]. Electron-doped $SrTiO_3$ crystals such as $Sr_{1-x}La_xTiO_3$ and $SrTi_{1-y}Nb_yO_3$ show a broad absorption band below the band-gap energy ranging from the infrared to visible spectral region, quite different from the simple Drude-type absorption of free carriers [32–34]. This suggests the presence of localized carriers in $SrTiO_3$. In addition, at low temperatures, undoped $SrTiO_3$ crystals show a broad PL band with large Stokes shift [35–37], and no band-edge PL has been reported under weak photoexcitation. It is believed that these observations prove the stable polaronic states of charge carriers in $SrTiO_3$. However, since the polaron formation results in very large effective masses of carriers, the polaron description is considered to be inconsistent with the high carrier mobility of $SrTiO_3$. The discovery of band-edge PL in strongly photoexcited or electron-doped $SrTiO_3$ crystals evidences the non-localized free carriers at low temperatures [28, 38]. The detailed studies on the band-edge PL provides deeper understanding of the nature of band-edge states of charge carriers.

In this chapter, we summarize the optical properties of perovskite $SrTiO_3$ and discuss the nature of carriers and the recombination dynamics of $SrTiO_3$. The samples discussed in this chapter are undoped $SrTiO_3$, La-doped $SrTiO_3$, Nb-doped $SrTiO_3$, and Ar^+-irradiated $SrTiO_3$ single crystals. The substitution of La^{3+} for Sr^{2+} or Nb^{5+} for Ti^{4+} produces electron carriers and thus doped crystals become metallic. Ar^+ ion irradiation causes oxygen deficiencies in the surface region of $SrTiO_3$ [4, 39, 40], and an oxygen-deficient layer also shows metallic conduction. PL properties of $SrTiO_3$ nanoparticles are also discussed.

The PL decay dynamics are very sensitive to the carrier density. From the excitation-intensity dependence of the PL intensity, we have clarified that the broad blue PL at room temperature is caused by the radiative recombination of free electrons and holes and the PL decay dynamics is determined by the nonradiative Auger recombination. The photocarrier decay dynamics in photoexcited and electron-doped

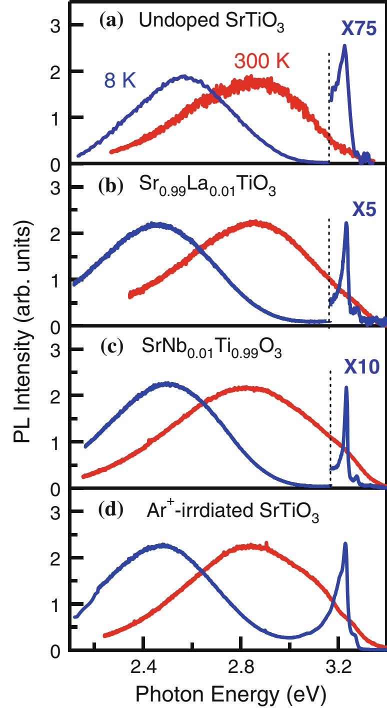

Fig. 1.3 Time-integrated PL spectra of **a** Strongly photoexcited undoped $SrTiO_3$, **b** $Sr_{0.99}La_{0.01}TiO_3$, **c** $SrNb_{0.01}Ti_{0.99}O_3$, and **d** Ar^+-irradiated $SrTiO_3$ under 3.49-eV photoexcitation at 8 and 300 K (After [41])

$SrTiO_3$ is described very well by a simple rate equation involving nonradiative single-carrier trapping, radiative electron-hole recombination, and nonradiative three-carrier Auger recombination processes. We discuss the PL properties and photocarrier recombination dynamics in $SrTiO_3$ and compare them with other perovskite semiconductors, e.g., $BaTiO_3$, $KTaO_3$, and $LiTaO_3$. The doping of electron carriers into perovskite semiconductors is essential for observation of efficient PL. Moreover, we demonstrate that the low-temperature PL spectrum of $SrTiO_3$ is quite different from that of other perovskite oxides: a band-edge PL is observed only in $SrTiO_3$. We present generic features of PL properties of perovskite oxide semiconductors.

1.2 Photoluminescence Spectra

Figure 1.3 shows the time-integrated PL spectra of (a) strongly photoexcited undoped $SrTiO_3$, (b) $Sr_{0.99}La_{0.01}TiO_3$, (c) $SrNb_{0.01}Ti_{0.99}O_3$, and (d) Ar^+-irradiated $SrTiO_3$ under 3.49-eV photoexcitation at 8 and 300 K. The PL intensities are normalized at their peaks. Note that the PL spectrum is similar to each other and that all PL spectra consist of three components: a 2.5-eV green PL, a 2.9-eV blue PL, and a 3.2-eV band-edge PL. Here, we briefly summarize the characteristics of the three PL bands.

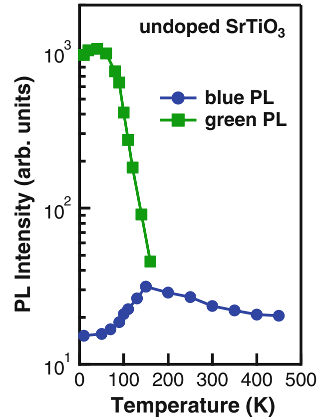

Fig. 1.4 Temperature dependence of *blue* and *green* PL intensity (After [43])

At low temperatures, a sharp band-edge PL peak and a broad green PL band appear at around 3.2 eV and 2.5 eV, respectively, in all $SrTiO_3$ samples. Two PL peaks appear at 3.22 and 3.27 eV in undoped and electron-doped samples. In the preceding Section, we showed that these two PL peaks coincide with the high- and low-temperature onsets of optical absorption and originate from band-to-band radiative recombination of free electrons and holes involving phonon-emission and phonon-absorption processes.

An efficient and broad green-PL band appears at around 2.5 eV in undoped $SrTiO_3$. Because of its long decay time of milliseconds at low temperatures, the origin of the green PL has been assigned to impurity centers or self-trapped excitons [35–37]. Although the spectral shape of the green PL in electron-doped $SrTiO_3$ is similar to that of undoped $SrTiO_3$, the PL efficiency and lifetime in electron-doped $SrTiO_3$ is quite different from those of undoped $SrTiO_3$: low PL quantum efficiency and short PL lifetime of electron-doped $SrTiO_3$. The reduction in the PL intensity and PL lifetime in electron-doped $SrTiO_3$ is attributed to the impurities and defects rather than to the intrinsic self-trapped excitons.

At room temperature, the PL spectra show a broad blue PL band at around 2.9 eV which is observed in strongly photoexcited $SrTiO_3$ and electron-doped $SrTiO_3$ [4, 27, 41–44]. In chemically doped $SrTiO_3$, the PL spectrum shape is independent of dopant species. With a decrease in temperature, the broad blue PL intensity increases. However, at low temperatures below 150 K, green PL intensity increases abruptly. There is an anti-correlation between the blue and green PL intensity, as shown in Fig. 1.4. The characteristics of the 2.9-eV PL will be discussed in the Sect. 1.4. We point out in this section that the undoped and electron-doped $SrTiO_3$ exhibit PL in the blue and green spectral region.

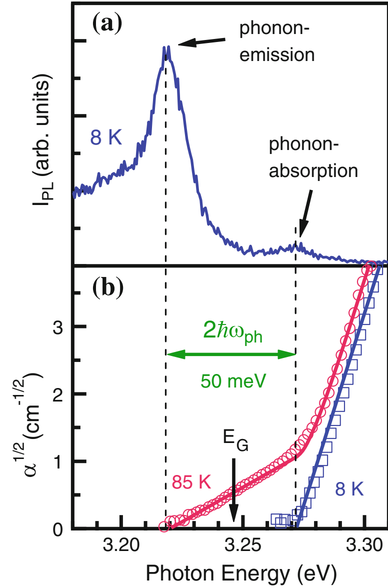

Fig. 1.5 **a** Time-gated (0–8 ns) PL spectrum near the band-gap energy in undoped $SrTiO_3$ crystals under strong 150-fs and 3.54-eV excitation at 8 K. **b** The square root of the optical absorption coefficient, α, at 8 and 85 K (After [28])

1.3 Band-to-Band Luminescence and Optical Absorption Spectra

In the previous section, we showed that two sharp peaks near the band-gap energy appear in strongly photoexcited and electron-doped $SrTiO_3$ crystals. Simultaneous measurement of PL and optical absorption spectra is powerful method for studying the band-edge electronic structure of materials. In this section, we discuss the origin of the two sharp PL peaks, observed in undoped $SrTiO_3$ crystals under strong photoexcitation and electron-doped $SrTiO_3$ crystals under weak photoexcitation. The PL peaks coincide with the low- and high-temperature onsets of the optical absorption spectra. The temperature-dependence of the PL and optical absorption spectra can be explained by the phonon-assisted band-to-band transition model. We clearly show that the two PL peaks correspond to phonon-assisted radiative recombination of photoexcited electrons and holes.

Figure 1.5a shows the time-gated (0–8 ns) PL spectrum near the band-gap energy in undoped $SrTiO_3$ crystals under strong 150-fs and 3.54-eV excitation at 8 K. Two PL peaks are clearly observed at approximately 3.22 and 3.27 eV. The band-edge PL peaks are asymmetric and have longer tails on the low energy side. The square root of the optical absorption coefficient, α, at 8 and 85 K are shown in Fig. 1.5b. The linear dependence of $\alpha^{1/2}$ on photon energy is an evidence that $SrTiO_3$ is an indirect-gap semiconductor and shows no exciton effects. Because of the large dielectric constant of $SrTiO_3$, the Coulomb interaction between electrons and holes gets screened and no excitons are formed. The energy separation between the low- and high-temperature

onsets in the optical absorption is approximately 50 meV. Since an optical transition in indirect-gap semiconductors should involve a wavenumber-conserving phonon, the low- and high-temperature onsets of the absorption spectra and two PL peaks correspond to band-to-band transitions involving phonon-absorption ($E_g + \omega_{ph}$) and phonon-emission ($E_g - \omega_{ph}$) processes, where E_g and ω_{ph} are the band-gap energy and the energy of wavenumber–conserving phonon at the X point, respectively. The involving phonon energy, 25 meV, is similar to TO_2 phonon energy at the zone boundary [45, 46]. Thus, we can conclude that the PL peaks at 3.220 and 3.271 eV are band-to-band optical transitions (i.e., radiative recombination of non-excitonic free electrons and holes) involving phonon absorption and emission. Note that the blue PL band and band-edge PL peaks are observed only under intense photoexcitation using a pulsed laser in undoped $SrTiO_3$ crystals.

Similar absorption spectra have been reported by Capizzi and Frova [47, 48]. They have argued that 3.220 eV-absorption edge originates from the band-to-band transition involving a 51-meV LO phonon emission and 3.270 eV absorption edge correspond to defect-mediated transition. However, no phonons with the energy of 51-meV are observed at the X point by Raman and neutron scattering studies [47]. On the other hand, we clearly show that the two PL peak energies coincide with the phonon-assisted optical transition energies. Then, we conclude that the band-gap energy is 3.246 eV at low temperatures.

Two band-to-band PL peaks are also observed in electron-doped $SrTiO_3$ crystals. Figure 1.6 shows PL spectra of (a) $SrNb_{0.01}Ti_{0.99}O_3$, (b) $Sr_{0.99}La_{0.01}TiO_3$, (c) Ar^+-irradiated $SrTiO_3$, and (d) strongly photoexcited undoped $SrTiO_3$ crystals at 8 K around the band-gap energy. Two PL peaks are observed in all electron-doped samples under weak continuous-wave (cw) laser excitation, while the undoped $SrTiO_3$ crystals exhibit band-to-band PL only under strong pulse laser excitation. Note that the band-edge PL is independent of the dopant species and high-density carrier doping is essential for observation of band-to-band PL.

The excitation intensity dependence of PL intensity also confirms that the origin of the two PL peaks is the band-to-band transition. Figure 1.7 shows the PL intensity monitored at 3.22 eV in (a) undoped $SrTiO_3$ and (b) $SrNb_{0.01}Ti_{0.99}O_3$ crystals as a function of excitation density. In the undoped $SrTiO_3$ crystal, the PL intensity shows quadratic dependence on the excitation density. This indicates that the band-edge PL originates from the two-carrier radiative recombination of photoexcited electrons in the conduction band and holes in the valence band. On the other hand, in the $SrNb_{0.01}Ti_{0.99}O_3$ crystal, the PL intensity linearly increases with an increase of excitation density under weak excitation condition where the chemically doped electron density is much higher than photoexcited electron density, indicating that the PL intensity is mainly determined by the recombination of photoexcited holes with doped electrons.

The spectral shape of the phonon-assisted PL spectra depends on the sample temperature. Figure 1.8 shows the PL spectra of $SrNb_{0.001}Ti_{0.999}O_3$ at 8, 20, 50, 75, and 100 K. The square root of the absorption coefficient is also shown in the same figure. The PL peak energies and spectral widths show the same temperature dependence. The PL peaks blue shift with increasing temperature and get broadened.

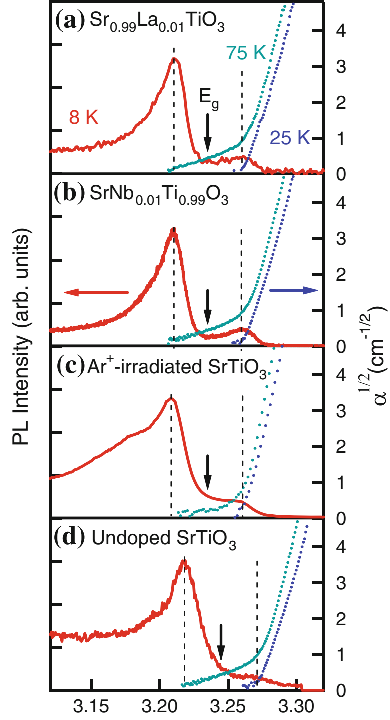

Fig. 1.6 PL spectra at 8 K and square roots of the optical absorption coefficient at 25 K and 75 K of **a** $SrNb_{0.01}Ti_{0.99}O_3$, **b** $Sr_{0.99}La_{0.01}TiO_3$, **c** Ar^+-irradiated $SrTiO_3$, and **d** Strongly photoexcited undoped $SrTiO_3$ crystals (After [38])

The broadening of the high-energy tail at higher temperatures suggests a thermal distribution of carriers. In contrast to the PL peak energy, the onset of the linear dependence of $\alpha^{1/2}$ on energy is almost independent of temperature, indicating that the band-gap remains constant below 100 K.

Here, we discuss the temperature dependence of the spectral shape of the band-to-band PL. According to [49], the spectral shape of band-to-band PL in indirect-gap semiconductors is described as,

$$I_{PL}(\hbar\omega) = \left(\hbar\omega - E_g \pm \hbar\omega_{ph}\right)^2 \exp\left(-\frac{\hbar\omega - E_g \pm \hbar\omega_{ph}}{k_B T}\right) \quad \left(for\ \hbar\omega > E_g \mp \hbar\omega_{ph}\right)$$
$$= 0 \quad (otherwise) \tag{1.1}$$

where the ± indicates (+) phonon emission and (−) phonon absorption. The solid curves in Fig. 1.8 are calculated results of band-to-band PL involving phonon emission process using (1.1) with E_g = 3.245 eV and ω_{ph} = 25 meV. We also include a linear background component, which results from the tail of the broad blue PL around 2.9 eV. This suggests that very shallow localized states exist near the band-edge. One possible origin of this localized state is a band-tail state caused by crystal disorder, which typically appears in mixed crystals, but could also be present in undoped crystals. In addition, because $SrTiO_3$ has an indirect-gap and complicated band structure,

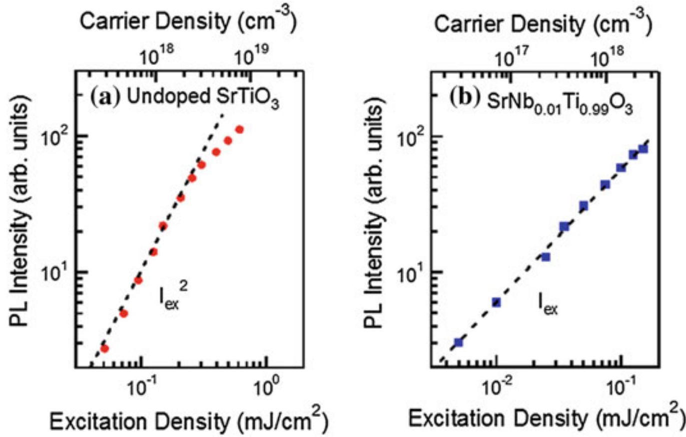

Fig. 1.7 PL intensity monitored at 3.22 eV in **a** Undoped $SrTiO_3$ and **b** $SrNb_{0.01}Ti_{0.99}O_3$ crystals (After [38])

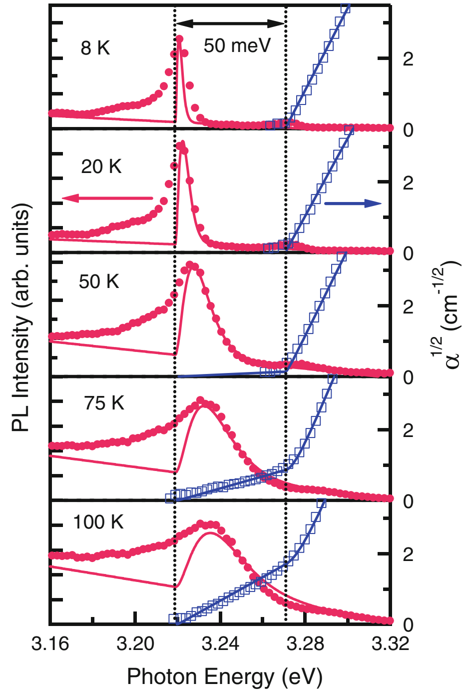

Fig. 1.8 PL spectra and square roots of optical absorption of $SrNb_{0.001}Ti_{0.999}O_3$ at 8, 20, 50, 75 and 100 K (After [28])

we need to consider optical transitions mediated by defects or impurities, as pointed out by Capizzi and Frova. Thus, we consider the spectrum broadening due to alloy disorders in doped semiconductors: the calculated spectrum shown in Fig. 1.8 is

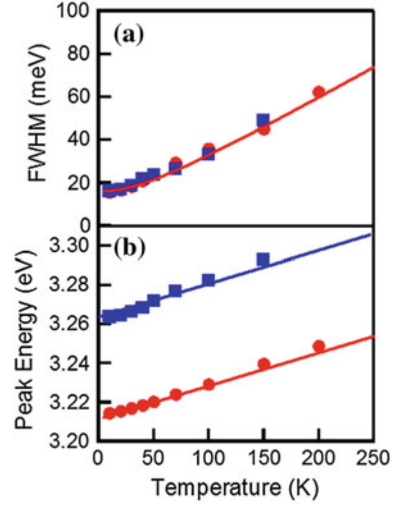

Fig. 1.9 **a** Spectrum widths and **b** Peak energies of two band-edge PL peaks in $SrNb_{0.01}Ti_{0.99}O_3$ as functions of temperature (After [38])

convoluted with a Gaussian function (width: 16 meV). To calculate the band-edge PL spectrum using (1.1), we use $E_g = 3.237$ eV and $\omega_{ph} = 25$ meV in heavily doped crystals. The solid curves are the calculated results, well reproducing the experimental data. Figure 1.9 illustrates (a) spectrum widths and (b) peak energies of two band-edge PL peaks in $SrNb_{0.01}Ti_{0.99}O_3$ as functions of temperature.

To further understand the band-edge states in doped $SrTiO_3$ crystals, we show the PL spectra of Nb-doped $SrTiO_3$ crystals with different dopant concentrations at 8 K under a weak cw photoexcitation. Note that the photocarrier density under cw excitation is much smaller than the chemically-doped electron density. The PL spectrum depends on the Nb concentration, as shown in Fig. 1.10. The band-edge PL in the electron-doped samples corresponds to the recombination of electrons that are present in the conduction band due to the doping and holes in the valence band due to photoexcitation. The PL energy shift shows that the band-gap shrinkage occurs owing to the high density of charge carriers. The spectral widths of the two PL peaks broaden with increasing carrier density. This broadening is attributed to alloy disorder in doped semiconductors [50, 51].

In this section, we have presented the band-to-band PL in various electron-doped $SrTiO_3$ crystals and strongly photoexcited $SrTiO_3$ crystals. Two PL peak energies coincide with the high- and low-temperature onsets of the optical absorption spectra, representing that the PL peaks correspond to the phonon-assisted band-to-band recombination of free electrons in the conduction band and free holes in the valence band. The band-edge PL intensity shows quadratic and linear dependences on excitation density in undoped and electron-doped samples, indicating that the PL comes from the radiative recombination of free electrons and free holes. The temperature dependence of the PL spectrum also confirms that the two PL peaks are due to the phonon-assisted band-to-band transition. The band-edge PL peaks redshift with

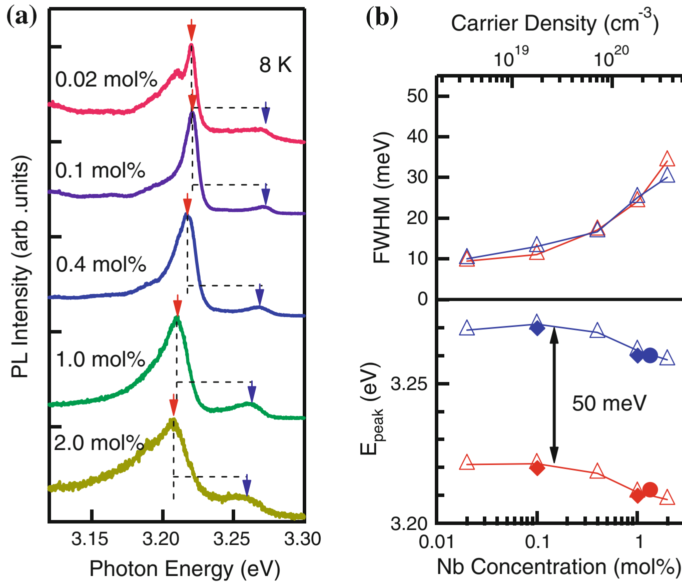

Fig. 1.10 **a** PL spectrum of $SrNb_xTi_{1-x}O_3$ with different Nb dopant concentrations. **b** Spectral width and PL peak energy as a function of Nb dopant concentrations (After [28])

increasing carrier density, reflecting the band-gap shrinkage due to the band-gap renormalization effect. The observation of a band-edge PL allows us an accurate determination of the band-gap of $SrTiO_3$, which is found to be 3.246 eV in undoped sample.

1.4 Photocarrier Recombination Dynamics: Importance of Nonradiative Auger Recombination

It has been reported in $SrTiO_3$ that an efficient green PL due to polarons or defects/impurities appears at low temperatures [35–37, 52]. Under intense pulse-laser photoexcitation, extrinsic defect and impurity PL usually saturate, and intrinsic blue PL bands appear at room temperature even in undoped $SrTiO_3$. Understanding of the blue PL dynamics provides a further insight into carrier recombination processes in $SrTiO_3$ bulk crystals and $SrTiO_3$-based heterostructures. In this section, we discuss the photocarrier recombination dynamics in undoped and electron-doped $SrTiO_3$ revealed by time-resolved PL spectroscopy and pump-probe transient absorption (TA) spectroscopy. A 2.9-eV PL is observed in undoped and electron-doped $SrTiO_3$ crystals over a wide range of temperature. PL dynamics are found to be sensitive to the photocarrier density and the doped electron density. The blue PL decay dynamics can be well explained by a simple rate-equation model,

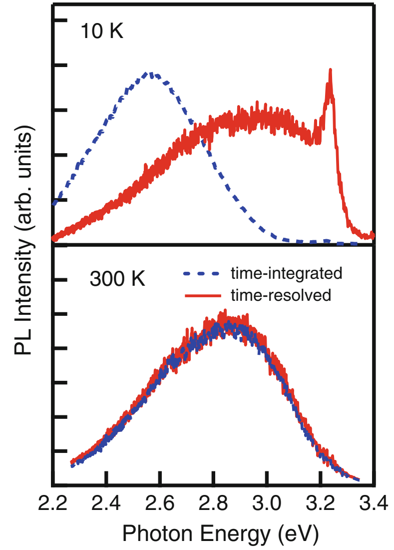

Fig. 1.11 Time-gated (0–8 ns) and time-integrated PL spectra of undoped $SrTiO_3$ at 10 and 300 K (After [43])

which includes single carrier trapping, two-carrier radiative recombination, and three-carrier nonradiative Auger recombination processes. Here, we stress the importance of nonradiative Auger recombination of carriers in $SrTiO_3$ crystals.

1.4.1 Undoped Crystals

Figure 1.11 shows the time-gated (0–8 ns) and time-integrated PL spectra of undoped $SrTiO_3$ typically under 8.9-mJ/cm^2, 150-fs, and 3.49-eV laser excitation at 10 and 300 K. The broad blue and green PL intensities are normalized by their peak intensities. At 10 K, three components are observed: the time-gated PL spectrum shows a sharp peak at 3.2 eV and a broad band at around 2.9 eV, and the time-integrated PL spectrum shows a green broad PL band at 2.5 eV. The green PL shows a long decay time of milliseconds, and its initial states are assigned to impurity centers or self-trapped excitons [35–37, 52]. In contrast, at 300 K, a broad blue PL band appears at around 2.9 eV in the time-gated PL spectrum, which agrees very well with the time-integrated PL spectrum. The broken curve shows the absorption spectrum, which rapidly increases above the band gap energy at 3.27 eV. The difference between the band gap energy and the emission peak energy (Stokes shift) is to be 0.3–0.4 eV. This suggests that the blue PL is not due to a simple radiative recombination between free electrons in the conduction band and free holes in the valence band, but it involves the formation of polarons, due to the strong electron-phonon coupling in $SrTiO_3$ [30, 31].

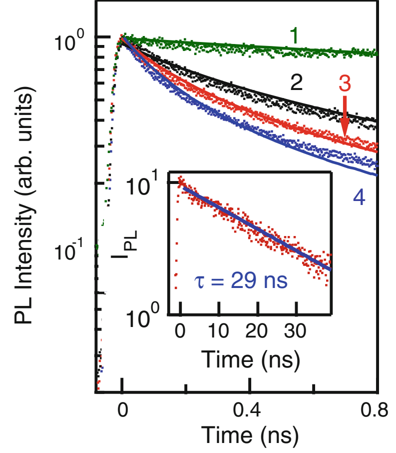

Fig. 1.12 PL decay curves of undoped $SrTiO_3$ under excitation density of (*1*) 1.5 mJ/cm^2, (*2*) 3.8 mJ/cm^2, (*3*) 5.2 mJ/cm^2, and (*4*) 5.9 mJ/cm^2. The *inset* shows the PL decay dynamics under excitation of 0.4 mJ/cm^2 in the longer time scale (After [44])

Figure 1.12 shows the PL decay curves of undoped $SrTiO_3$ at room temperature under different excitation density. Under a low excitation density, the PL dynamics shows slow decay. As shown in the inset of Fig. 1.12, the PL decay dynamics shows almost single exponential decay with the decay time of 29 ns under weak excitation density of 0.4 mJ/cm^2. As the excitation density increases, a fast and nonexponential decay component appears, and the PL decay time becomes shorter.

Here we discuss the carrier dynamics in strongly photoexcited $SrTiO_3$ using the rate equation of photocarriers. In semiconductors, the rate equation for the photocarriers can be written as follows [27, 43, 44, 53–55]:

$$\frac{\mathrm{d}n}{\mathrm{d}t} = -An - Bn^2 - Cn^3, \tag{1.2}$$
$$I_B \propto Bn^2$$

where n is the photocarrier density. An represents the single-carrier trapping and Bn^2 represents the two-carrier radiative recombination. Finally, C is the coefficient of Auger nonradiative recombination including three-particle, electron-hole-electron and electron-hole-hole, processes, where the nonradiative recombination energy of the electron-hole pairs is transferred to the kinetic energy of the other electron (hole). I_B denotes the blue PL intensity and is proportional to the square of the photocarrier density. The B coefficient is negligibly small because of the low PL efficiency observed in $SrTiO_3$ samples.

The solid curves in Fig. 1.12 are given by (1.2) and the experimental results are well described by the above simple rate equation. The fast and slow components are contributed by the Auger recombination (C coefficient) and single-carrier trapping (A coefficient), respectively.

We present the excitation intensity dependencies of the time-integrated PL intensity and the PL decay time at room temperature in Fig. 1.13. Here, the effective

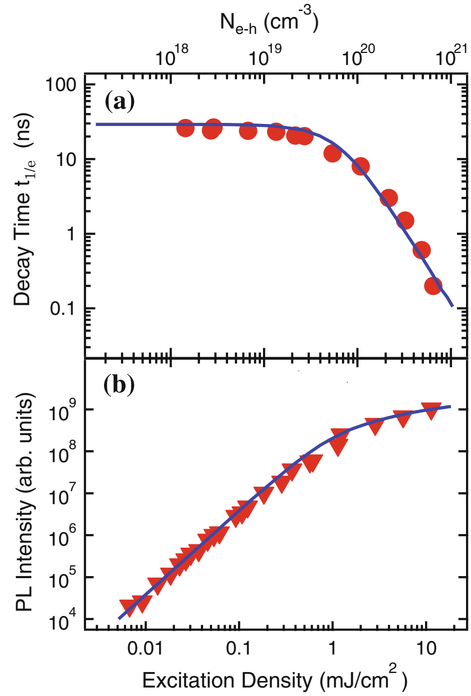

Fig. 1.13 Excitation intensity dependencies of **a** PL decay time and **b** Time-integrated PL intensity at room temperature (After [27])

decay time $t_{1/e}$ is defined as the time at the intensity of I_0/e, where I_0 is the PL intensity at zero delay time. The photogenerated electron-hole pair density (N_{e-h}) is estimated from the incident photon number and the optical absorption coefficient at the excitation energy. [21] Under weak excitation density below about 0.5 mJ/cm^2, the PL decay time is constant (about 30 ns) but the PL intensity increases as square of the excitation density. At high intensities, the shortening of the PL lifetime and the saturation of the PL intensity occur simultaneously. This behavior can be explained in terms of a nonradiative Auger recombination process. As the quantum efficiency at room temperature is very low (<0.01), the predominant mechanism of recombination is nonradiative. The temporal changes in the carrier density are determined by the single-carrier trapping and the Auger recombination processes. Excellent fits are found with $A = 1.7 \times 10^7$ s^{-1} and C = 1.2×10^{-32} cm^{-6}/s.

To gain a deeper insight into the photocarrier recombination dynamics, we have measured femtosecond TA spectra of undoped $SrTiO_3$ crystals under intense photoexcitation at room temperature. The carrier recombination dynamics evaluated from TA experiments can be well explained by (1.2).

Fig. 1.14a shows temporal changes in TA signals of undoped $SrTiO_3$ under 3.49-eV and 150-fs excitation at different intensities of 0.5, 4.4, 8.9, and 13.3 mJ/cm^2. The probe pulse energy was 1.55 eV. Under weak excitation of 0.5 mJ/cm^2, the TA signal shows a very slow decay and the decay time is much longer than 2 ns. As shown in

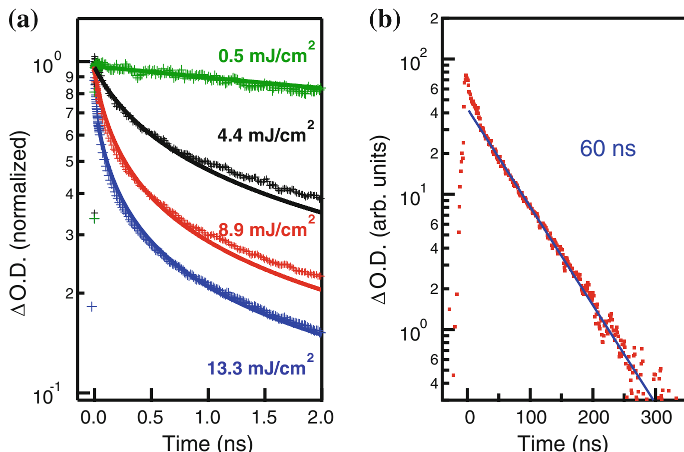

Fig. 1.14 **a** Temporal changes in TA signals of undoped $SrTiO_3$ under 3.49-eV and 150-fs excitation at different intensities of 0.5, 4.4, 8.9 and 13.3 mJ/cm^2. **b** Temporal evolution of optical density change (OD) at 0.8 mJ/cm^2 excitation density in the nanosecond time region (After [44])

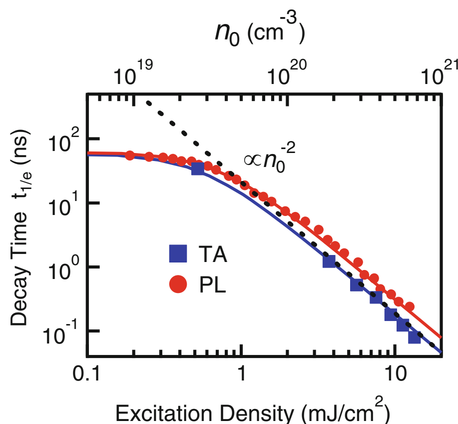

Fig. 1.15 Decay times derived from PL (denoted by *circle*) and TA (*square*) decay curves as a function of the excitation intensity (After [44])

Fig. 1.14b, the TA signal shows a single exponential decay with a decay time of 60 ns under the weak excitation condition of 0.8 mJ/cm^2. Under high excitation intensities above about 3 mJ/cm^2, the fast and nonexponential decay component clearly appears in the picosecond time region, and the TA decay time becomes faster as the excitation density increases. Under the same experimental conditions, the temporal behaviors of TA intensity are in very well agreement with those of PL intensity.

The excitation-intensity dependence of the TA and PL decay times is shown in Fig. 1.15. Here, we define the effective decay time $t_{1/e}$ as the time at the carrier

density of n_0/e. The initial photogenerated carrier density n_0 is estimated from the incident photon number and the optical absorption coefficient at the excitation photon energy in [53]. Note that $I_{PL}(t_{1/e}) = I_{PL}(0)/e^2$ and $\alpha_{TA}(t_{1/e}) = \alpha_{TA}(0)/e$ are used because of the relations $I_{PL} \propto n^2$ and $\alpha_{TA} \propto n$, where I_{PL} and α_{TA} are the PL and TA intensities. We have plotted $t_{1/e}$ derived from PL (denoted by circle) and TA (square) decay curves as a function of the excitation intensity in Fig. 1.15. The effective decay times $t_{1/e}$ of TA and PL signals show good agreement with each other. Below about 0.5 mJ/cm^2, $t_{1/e}$ is independent of the excitation intensity, while it decreases as the inverse square of the excitation intensity under high excitation intensities. This indicates that the carrier dynamics is dominated by three-carrier processes, as in the case of Auger recombination process, under high intensity excitation.

According to (1.2), the effective decay time $t_{1/e}$ can be approximated by

$$t_{1/e} = (A + Bn_0 + Cn_0^2)^{-1}. \tag{1.3}$$

We have fitted the decay times of TA and PL dynamics shown in Fig. 1.15 by using (1.3). The best fit-parameters are $A = 1.7\times10^7\,\mathrm{s}^{-1}$ and $C = 1.7\times10^{-32}\,\mathrm{cm^6s^{-1}}$ for TA dynamics, and $A = 1.7\times10^7\,\mathrm{s}^{-1}$ and $C = 1.2\times10^{-32}\,\mathrm{cm^6s^{-1}}$ for PL dynamics. Here, we confirm that Bn^2 is negligibly small compared to An and Cn^3 and therefore it is neglected. In fact, the calculated solid curves shown in Fig. 1.15 with $B = 0$ reproduce the experimental results very well. This result means that the recombination rate of two-body processes (i.e., the radiative two-carrier recombination) is very small in $SrTiO_3$. This result is in agreement with the low PL quantum efficiency (PL quantum efficiency <0.01). The calculated TA and PL decay curves using the above best-fit-parameters also reproduce the experimental decay curves very well. From the TA and PL measurements and the calculation using the same equation, we determine the coefficients, $A = 1.7\times10^7\,\mathrm{s}^{-1}$ and $C = (1.5\pm0.3)\times10^{-32}\,\mathrm{cm^6s^{-1}}$. Finding no significant difference between TA and PL decay times clearly shows that the intrinsic Auger recombination process determines the photocarrier decay dynamics under high excitation intensity.

Thus, we have shown that both TA and PL decay dynamics in strongly excited $SrTiO_3$ are well explained by the same rate equation model, which includes single carrier trapping, two-carrier radiative recombination, and three-carrier Auger recombination. The detailed microscopic carrier recombination mechanisms for determining A and C coefficients remain still an open question.

1.4.2 Electron-Doped Crystals

The PL spectra of highly photoexcited $SrTiO_3$ crystals are very similar to those of chemically electron-doped $SrTiO_3$ crystals. In undoped $SrTiO_3$ crystals, the PL decay dynamics at the high carrier density region are determined by the three-carrier Auger recombination process. As the Auger coefficient C is usually determined from

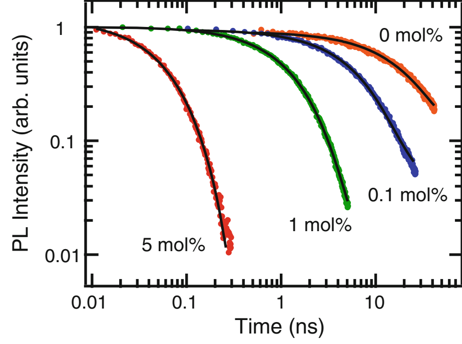

Fig. 1.16 PL decay curves in La- doped $SrTiO_3$ with different La concentrations (After [27])

carrier lifetimes measured in heavily doped samples, we have studied the photocarrier recombination dynamics in electron-doped samples. In chemically doped samples, the electron density is properly controlled by the dopant concentration. The electron density of $Sr_{1-x}La_xTiO_3$ and $SrTi_{1-y}Nb_yO_3$ samples can be estimated from the values reported previously [13, 56, 57], assuming a linear relationship between the carrier density and dopant concentration. In $Sr_{1-x}La_xTiO_3$, the electron density N_e is approximately given by $N_e = 1.80 \times 10^{22} \times x$ cm^{-3} and in $SrTi_{1-y}Nb_yO_3$ as $N_e = 1.78 \times 10^{22} \times y$ cm^{-3}. Using these samples, we have examined the PL decay dynamics as a function of the electron density. The PL decay curves in La-doped $SrTiO_3$ samples are plotted in Fig. 1.16, where the photogenerated carrier density (N_{e-h}) was about 3×10^{17} cm^{-3}, which is much lower than N_e. All decay curves are approximately described by a single-exponential function (solid curves in the figure). The rate of PL decay becomes faster with an increase in the dopant concentration or the chemically doped electron density.

In Fig. 1.17, the PL decay time and PL intensity in $Sr_{1-x}La_xTiO_3$ and $SrTi_{1-y}$ Nb_yO_3 samples are plotted as a function of the dopant concentration and doped electron density. In heavily electron-doped samples, the PL decay time τ_{PL} and the PL intensity in the two-carrier radiative recombination process are determined by the number of minority carrier holes $p(t)$ and given by:

$$\tau_{PL}^{-1} = 2A + C_1 N_e^2, \tag{1.4}$$

$$I \propto \int B N_e p(t) dt$$

where C_1 is the coefficient of electron-hole-electron Auger recombination. The numerical calculations using (1.4) are plotted as a solid curves. The constants A and C were obtained from the undoped $SrTiO_3$ measurement in Fig. 1.17, i.e., $A = 1.7 \times 10^7$ s^{-1}, $C = 1.3 \times 10^{-32}$ cm^{-6}/s, and we have assumed $C_1 \sim C$, because undoped $SrTiO_3$ is an n-type semiconductor. The model can explain quantitatively the enhancement of the PL intensity observed in an electron-doped $SrTiO_3$. These calculations agree quite well with experimental observations in doped samples,

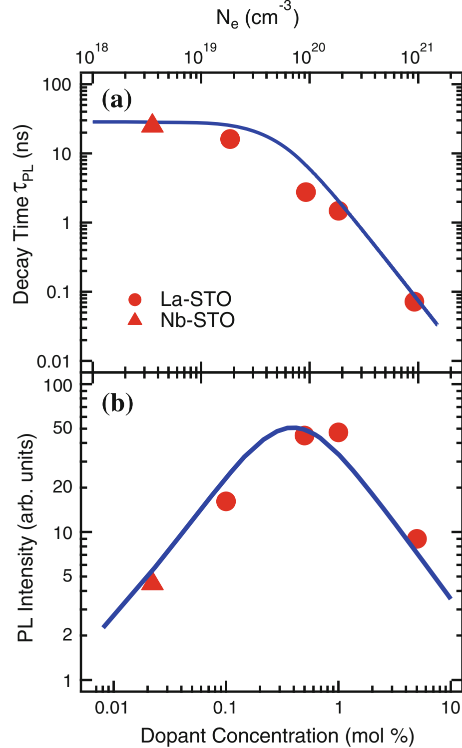

Fig. 1.17 **a** PL decay time and **b** PL intensity in $Sr_{1-x}La_xTiO_3$ and $SrTi_{1-y}Nb_yO_3$ as a function of dopant concentration and doped electron density (After [27])

clearly confirming that nonradiative Auger recombination determines the $SrTiO_3$ PL properties.

In electron-doped $SrTiO_3$, the PL lifetime decreases by increasing the doped electron density under weak excitation. These experimental data are well explained by a simple model including the two-carrier radiative recombination and the Auger nonradiative recombination processes. Our finding shows the importance of the three-carrier Auger recombination processes in undoped and electron-doped $SrTiO_3$.

1.4.3 Temperature Dependence

In the previous sections, we have described how the three-carrier Auger recombination plays a critical role in the PL decay dynamics and carrier recombination processes in $SrTiO_3$. In bulk crystals, the **k**-conservation rule plays an essential role in determining the three-carrier Auger decay rate, because the third carrier needs to gain both the energy and momentum of the recombined e-h pair. Owing to the **k**-conservation rule, the Auger decay rate in bulk crystals is very sensitive to temperature; no-phonon assisted Auger decay rate depends exponentially on the temperature

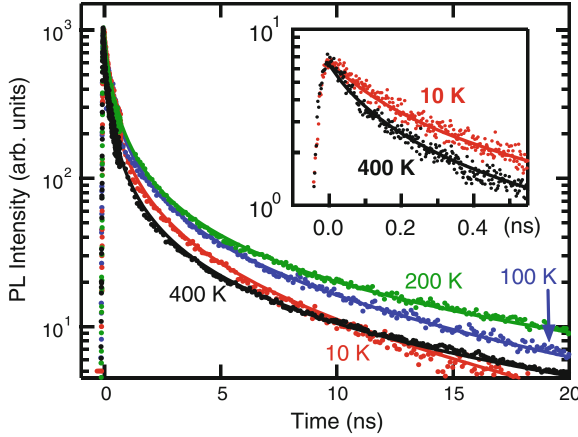

Fig. 1.18 Decay curves of *blue* PL in undoped $SrTiO_3$ at 10, 100, 200 and 400 K under an excitation density of 8.9 mJ/cm^2. The inset shows the PL dynamics at 10 and 400 K in subnanosecond time region (After [43])

and the phonon-assisted Auger decay rate is determined by the thermal distribution of phonons. The temperature dependence of the PL decay dynamics provides essential information of the Auger recombination mechanism in semiconductors.

Figure 1.18 shows the decay curves of blue PL in undoped $SrTiO_3$ at 10, 100, 200, and 400 K under an excitation density of 8.9 mJ/cm^2. The decay profiles have two decay components: a non-exponential fast decay with a sub-nanosecond time constant, and a single-exponential slow decay with a time constant of several nanoseconds. The PL dynamics shows a single-exponential decay in the low carrier density region and non-exponential decay in the high carrier density region depending on the excitation intensity.

The solid curves in Fig. 1.18 are given by (1.2) and the experimental results are well described by the above simple rate equation. The inset shows an enlarged view of the PL decay profiles in the sub-nanosecond region at 10 and 400 K. At 10 K, the PL intensity decays slower than at 400 K, reflecting the reduction in the Auger coefficient C with decreasing temperature.

We have measured the PL decay curves of undoped and electron-doped $SrTiO_3$ under 3.54-eV and 150-fs laser excitation over a wide range of temperature from 10 to 450 K. The PL decay curves at all temperatures are well reproduced by the same rate equation of (1.2), as shown in Fig. 1.18. The temperature dependences of A and C coefficients obtained by the best-fit are plotted as a function of temperature in Fig. 1.19. The A coefficient shows an abrupt increase in green PL below 150 K with increasing in the intensity and a decrease in the blue PL (see Fig. 1.4). This abrupt increase in single-carrier trapping is due to the rapid carrier relaxation into the deep states for the green PL band. In addition, the Hall measurement revealed that the electron mobility increases below 100 K [14, 17, 20]. Thus, we may conclude that the large mobility of the carriers enhances the carrier-trapping rate at low temperatures.

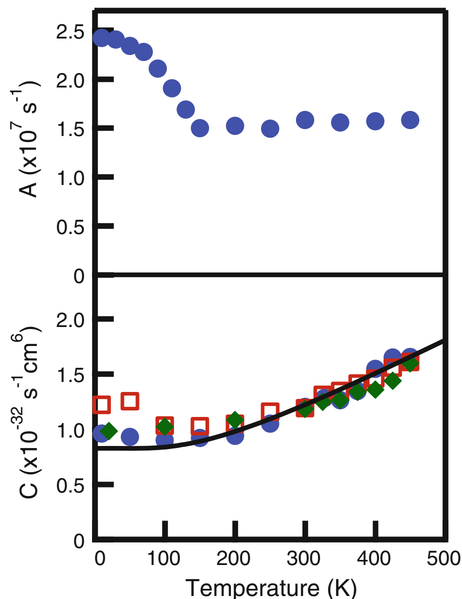

Fig. 1.19 Temperature dependence of the A and C coefficients obtained from the PL dynamics of undoped $SrTiO_3$ (*circles*), $SrTi_{0.99}Nb_{0.01}O_3$ (*squares*), and $SrTi_{0.98}Nb_{0.02}O_3$ (*diamonds*) (After [43])

In contrast to the A coefficient, the C coefficient shows no significant change by increasing the temperature up to 150 K, but it increases with increasing temperature at higher temperatures. This temperature dependence corresponds to the gradual decrease in the intensity of blue PL with increasing temperature above 150 K. The temperature dependence of the Auger coefficient of semiconductors is usually described by a phonon-assisted Auger recombination model [58], in which the Auger coefficient is proportional to the sum of phonon emission and absorption rates as:

$$C \propto 2N_{phonon} + 1 = \frac{\exp(\hbar\omega/kT) + 1}{\exp(\hbar\omega/kT) - 1}, \tag{1.5}$$

where $\hbar\omega$ is the energy of the phonon involved in the Auger recombination. This model is applicable in many bulk semiconductors (e.g., silicon [59]). We have fitted the Auger coefficient obtained by PL dynamics of undoped $SrTiO_3$ using (1.5). The solid curve in Fig. 1.19 shows the results of this fit. The value obtained for the best-fit parameter $\hbar\omega$ is 40 meV, which is very close to the energy 41 meV of the zone boundary of TO_3 phonon [45]. The intrinsic Auger recombination determines the PL decay dynamics over a wide temperature range.

We have also examined the temperature dependence of the PL decay in electron-doped $SrTiO_3$. Figure 1.20 shows the PL decay profiles in $SrTi_{0.99}Nb_{0.01}O_3$ at 50, 250, and 450 K, where the PL intensity is integrated over the spectrum. All curves show a single exponential decay with a time constant of a few nanoseconds and their decay rates are given by (1.4). The temperature dependence of the decay rate, τ^{-1}, is shown in the inset of Fig. 1.20. At high temperatures, the decay rate decreases

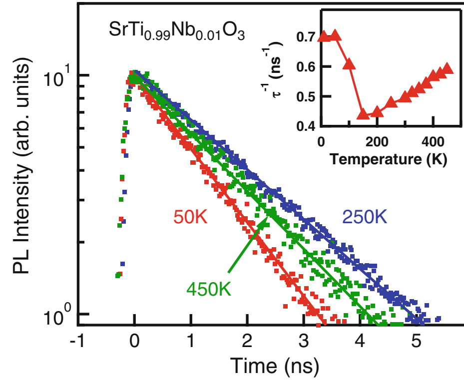

Fig. 1.20 PL decay profiles in $SrTi_{0.99}Nb_{0.01}O_3$ at 50, 250 and 450 K. The inset shows the temperature dependence of the PL decay time (After [43])

monotonically as the temperature decreases but it changes abruptly at 150 K. This temperature dependence suggests that at high temperatures the decay dynamics is determined by the Auger recombination, while at low temperatures below 150 K the single-carrier trapping dominates the decay dynamics. We have determined the C coefficient from the PL dynamics of electron-doped $SrTiO_3$ using (1.4) and shown in Fig. 1.19, where we have assumed that the carrier-trapping rate in electron-doped $SrTiO_3$ follows the same temperature dependence as undoped $SrTiO_3$. These observations indicate that our model described by (1.2) works well for both electron-doped and undoped $SrTiO_3$ over a wide temperature range.

In conclusion, we have studied the temperature dependence of carrier dynamics in undoped and electron-doped $SrTiO_3$ by means of time-resolved PL measurements. A simple model involving single-carrier trapping, two-carrier recombination, and Auger recombination describes the PL dynamics at all temperatures in both undoped and electron-doped $SrTiO_3$quite well. The phonon-assisted Auger recombination determines the temperature-dependent PL dynamics. At low temperatures, rapid energy transfer occurs from the near band-edge state of blue PL to the deep state.

1.5 Surface Oxygen Deficient Layer: Bulk Crystals and Nanoparticles

The blue PL decay dynamics of $SrTiO_3$ crystals are sensitive to the electron density. As we have quantitatively evaluated the Auger recombination rate, where the carrier dynamics depends on the carrier density, the analysis of the PL dynamics provides a quantitative evaluation method of the spatial carrier- and defect-density profiles. In addition, the optically monitored region of the sample surface can be controlled by changing the energy of the excitation light. Therefore, PL spectroscopy becomes a powerful experimental technique for studying the carrier-density profiles in $SrTiO_3$. In this section, we demonstrate that the PL-decay dynamics in undoped $SrTiO_3$

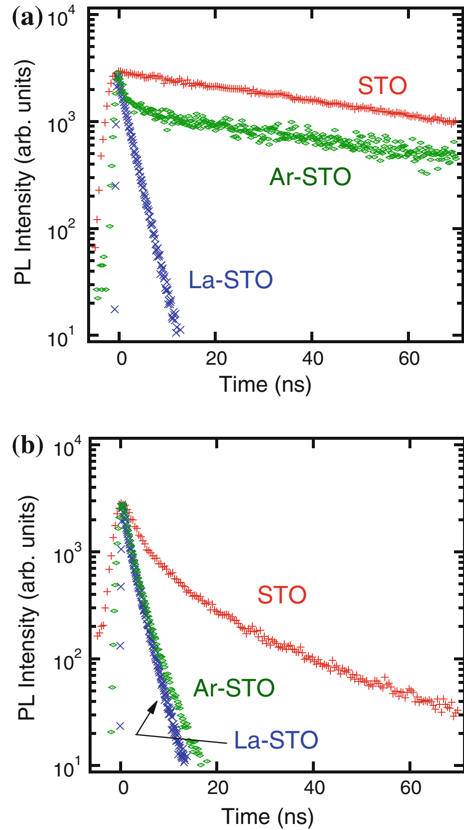

Fig. 1.21 **a** PL dynamics monitored at 2.9 eV for undoped, La-doped, and Ar^+-irradiated $SrTiO_3$ crystal (STO, La-STO, and Ar-STO) samples under 3.26 eV excitation at room temperature. **b** PL dynamics in three samples under an excitation of 3.87 eV (After [53])

and Ar^+-irradiated $SrTiO_3$ depends strongly on the excitation photon energy. With an increase in the photon energy, the PL-decay time decreases and the PL profile becomes nonexponential. This behavior can be explained by assuming that the Auger recombination of electrons originating from oxygen vacancies with photocarriers determines the PL lifetime and that the electron densities near the surface are much higher than those in the bulk crystal. On the basis of PL dynamics, we successfully demonstrate the optical measurements of the depth profile of carriers in the near-surface region of the $SrTiO_3$ samples.

Figure 1.21a shows the PL dynamics monitored at 2.9 eV for undoped, La-doped, and Ar^+-irradiated $SrTiO_3$ crystal (STO, La-STO, and Ar-STO) samples under 3.26 eV excitation at room temperature. The excitation energy is close to the band-gap energy of undoped $SrTiO_3$ of $\sim$3.2 eV, and the optical penetration depth at 3.26 eV is large and is about 10 μm [60]. The PL dynamics of undoped $SrTiO_3$ shows a single exponential decay profile with a lifetime of 50 ns. La-doped $SrTiO_3$ also shows a single exponential decay profile, but the lifetime (2 ns) is much shorter than that of undoped $SrTiO_3$. In Ar^+-irradiated $SrTiO_3$, two decay components are observed.

The first is a fast decay component with a decay time of a few nanoseconds, and the second is a slow decay with a decay profile that is quite similar to that of undoped $SrTiO_3$. The rapid PL decay is caused by the Auger recombination of electrons originating from oxygen vacancies with photocarriers.

In the chemically doped $Sr_{0.99}La_{0.01}TiO_3$ crystals, doped electrons are distributed homogeneously throughout the sample. In this case, the PL decay is a single exponential curve. In contrast, in Ar^+-irradiated $SrTiO_3$, we observe two distinct decay components. Ar^+ irradiation introduces oxygen vacancies only near the sample surface, and the electrons originating from oxygen vacancies are inhomogeneously distributed with respect to depth [4, 61]. We argue that the fast decay component comes from the near-surface metallic layer where Auger recombination of doped electrons with photocarriers is dominant. The slow component comes from the undoped $SrTiO_3$ substrate. Therefore, the two decay components in the Ar^+-irradiated $SrTiO_3$ crystal originate from two different electron-density regions: the oxygen-deficient metallic layer near the surface and the undoped insulating substrate. The fast PL-decay component provides a quantitative information about the density and spatial profile of carriers in the sample.

Figure 1.21b shows the PL dynamics in three samples under an excitation of 3.87 eV. The excitation energy is well above the band-gap energy of the undoped samples, and the penetration depth at 3.87 eV is very small and is about 40 nm. Thus, the photocarriers are generated in the near-surface region, and the PL dynamics is strongly affected by the oxygen vacancies in the near-surface region. Undoped $SrTiO_3$ shows a nonexponential decay that is faster than that under an excitation of 3.26 eV. Even in the nominally undoped sample, defects producing electron carriers are inevitably introduced, especially very close to the surface [62]. In contrast, in La-doped $SrTiO_3$, the absence of any significant dependence of the PL-decay time on the excitation energy also clearly supports the spatially homogeneous distribution of doped electrons. Moreover, Ar^+-irradiated $SrTiO_3$ shows only the fast decay component; the slow decay component disappears. This implies that the PL dynamics is determined by the near-surface oxygen-deficient metallic layer under high-energy excitation. Our findings show that the spatial distributions of electron carriers in $SrTiO_3$ crystals can be estimated from the photon-energy dependence of the PL dynamics.

We discuss the spatial distribution of electron carriers originating from oxygen vacancies in Ar^+-irradiated $SrTiO_3$ composed of the metallic near-surface layer and insulating undoped substrate. In Fig. 1.22a, we show the excitation photon energy dependence of the intensity ratio of the fast decay components. The optical penetration depth, estimated from the reflection spectra from [53], is also shown. Here, we approximately describe the PL-decay curves shown in Fig. 1.22a using two exponential functions and fix the decay time of the slow decay component to 50 ns. With an increase in the excitation energy, the optical penetration depth decreases and the photocarriers are generated in the near-surface region. Therefore, the PL from the near-surface metallic layer increases and that from the insulating substrate decreases.

To evaluate the electron-carrier distribution near the surface quantitatively, we focus on the fast PL dynamics. Figure 1.22b shows the PL-decay curves in

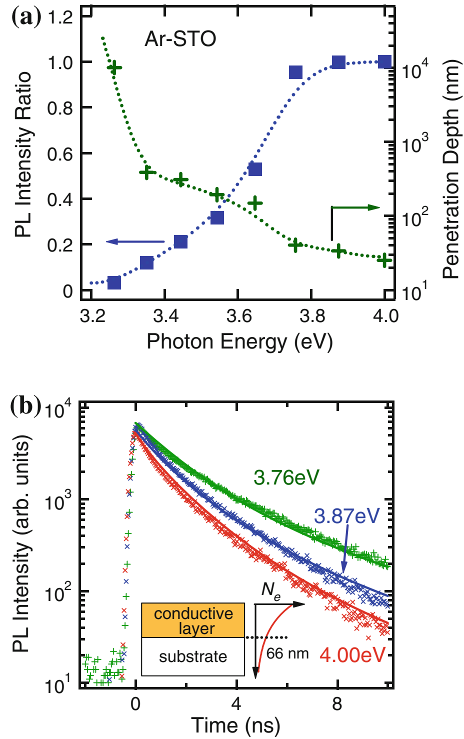

Fig. 1.22 **a** Excitation photon energy dependence of the intensity ratio of the fast decay components. **b** PL-decay curves in Ar^+-irradiated $SrTiO_3$ samples under excitation of 3.76, 3.87, and 4.00 eV (After [53])

Ar^+-irradiated $SrTiO_3$ samples under excitation of 3.76, 3.87, and 4.00 eV. To study the spatial distribution of the carrier density, we assume an exponential spatial profile trial function, $N_e(z) = N_0 \exp(-\beta z)$, where $1/\beta$ is the depth of the carrier distribution. The temporal variation of the luminescence is expressed as

$$I(t) \propto B \int_0^\infty N_e(z) n(z, t) dz, \quad (1.6)$$

where $n(z, t)$ is given by (1.4), and $n(z, 0) = n_0 \exp(-\alpha z)$ and $1/\alpha$ is the optical penetration depth.

Here we assume that the values of A, B, and C coefficients are independent of the densities of oxygen deficiencies and carriers. The results fitted to (1.6) are shown in Fig. 1.22b as solid lines, reproducing the experimental results rather well. The best-fit parameters are found to be $1/\alpha = 66$ nm and $N_0 = 2.4 \times 10^{20}$ cm^{-3}. These results are schematically illustrated in the inset of Fig. 1.22b. Therefore, we conclude that in Ar^+-irradiated $SrTiO_3$, the electron carriers doped by oxygen deficiencies are distributed in an exponential decay profile from the surface. In the present experiments and analyses, the spatial resolution is about 10 nm, which is determined by the penetration depth of the incident UV light. The metallic near-surface layer is

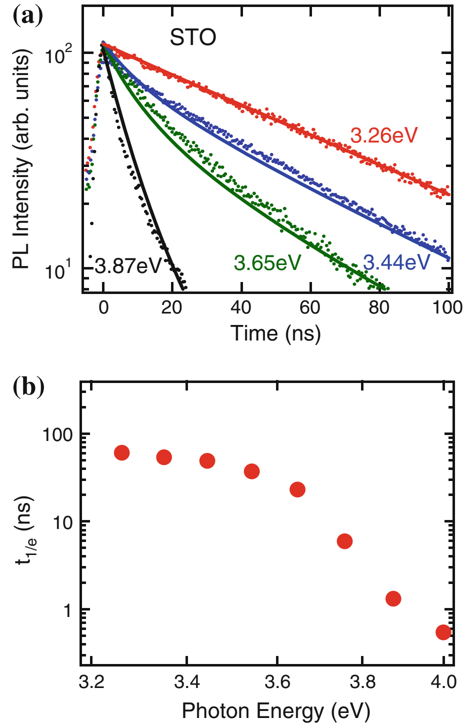

Fig. 1.23 **a** PL dynamics in undoped $SrTiO_3$ under excitation at 3.26, 3.44, 3.65 and 3.87 eV. **b** Decay time of PL intensity as a function of excitation photon energy (After [53])

estimated to be ∼60 nm deep, which is consistent with the transmission electron microscopy observations in [4].

We have also evaluated the spatial profile of electrons originating from oxygen vacancies in undoped $SrTiO_3$. Figure 1.23a shows the PL dynamics in undoped $SrTiO_3$ under excitation at 3.26, 3.44, 3.65, and 3.87 eV. The PL decay time is plotted in Fig. 1.23b, which demonstrates that the PL-decay dynamics strongly depends on the excitation photon energy. The PL dynamics under 3.26 eV excitation shows a single exponential decay profile with a lifetime of 50 ns. With an increase in the photon energy, the PL shows a nonexponential profile and the PL-decay time becomes shorter. This photon-energy dependence comes from the inhomogeneous distribution of electron carriers as a function of the depth and suggests the formation of an oxygen-deficient region near the surface, even in undoped $SrTiO_3$ samples.

The decay curves in Figs. 1.22b and 1.23a agree quite well if we assume that the electron-density profile is described by an exponential function, similar to that for Ar^+-irradiated $SrTiO_3$. Using (1.6), we obtain the exponential carrier profile, $N_e(z) = N_0\exp(-\beta z)$, where $N_0 = 8\times10^{19}\text{cm}^{-3}$ and $1/\beta = 16\,\text{nm}$. The fitting results reproduce the experimental results fairly well, as shown by the solid lines in Fig. 1.23. This means that very thin and electron-rich layers are formed near the surface, even in undoped $SrTiO_3$. The electron density is low and the thickness of

the layer is very thin compared to Ar^+-irradiated $SrTiO_3$. However, the estimated surface carrier density seems to be high for the undoped $SrTiO_3$, because it is known that the undoped $SrTiO_3$ substrate is an insulator.

In the above discussion, oxygen vacancies produce electron carriers and the Auger recombination of electrons originating from oxygen vacancies with photocarriers determines the PL-decay dynamics. We assumed that the value of A coefficient is independent of the densities of oxygen vacancies and carriers. However, highly dense oxygen vacancies will affect the carrier-trapping coefficient, A, in (1.2). In fact, in undoped $SrTiO_3$, the electron density obtained is close to the Auger-limit density, $(A/C)^{1/2}$, in which case an increase in the carrier-trapping coefficient will affect the PL-decay dynamics. In such cases, the excited-photon-energy dependence of the PL-decay dynamics means the spatial distribution of the carrier-trapping rate. We should point out that an increase in the A coefficient reduces the estimated carrier density in undoped samples, and speculates that the insulating behavior of undoped $SrTiO_3$ originates from the increase of the carrier trapping rate near the surface. In both cases of the carrier trapping and Auger recombination limits, the appearance of the photon-energy dependence of the PL dynamics reflects the depth profiles of the oxygen-vacancy density and clearly shows the existence of the oxygen-deficient surface layer.

The surface of $SrTiO_3$ crystals plays an important role in the optical properties: the oxygen-deficient surface layer exists in $SrTiO_3$ bulk crystals and causes efficient PL from the surface metallic layer [53]. Since their surface effects are more pronounced due to large surface-to-volume ratios, nanoparticles provide unique optical properties, which are not observed in bulk crystals: For example, oxidized surfaces of indirect-gap Si and Ge semiconductor nanoparticles show efficient room-temperature PL [64, 65]. Thus, it is anticipated that $SrTiO_3$ nanoparticles would show attractive PL properties, different from those of bulk crystals. However, the PL properties of $SrTiO_3$ nanoparticles are not yet understood. Therefore, here, we have studied the PL spectrum and dynamics of $SrTiO_3$ nanoparticles.

The $SrTiO_3$ nanoparticles were synthesized using the microemulsion method. The details are described in [66] and [67]. In Fig. 1.24, we have shown the excitation-density dependences of the PL intensity in the nanoparticle sample monitored at 2.9 eV and 1.7 eV under (a) cw and (b) pulse laser excitations. Under weak cw excitation, below 0.5 mW/cm^2, both the 2.9-eV and 1.7-eV PL intensities show a linear dependence on the excitation density. The blue PL intensity in electron-doped $SrTiO_3$ bulk crystals also increases linearly with the excitation density (see Fig. 1.7). We conclude that $SrTiO_3$ nanoparticles contain unintentionally excess electrons originating from oxygen-deficient surface and that the blue PL originates from the two-carrier (two-body) recombination of excess electrons and photoexcited holes. Above 0.5 mW/cm^2, the blue PL intensity shows quadratic dependence on the excitation density, suggesting that the blue PL originates from two-carrier recombination of photoexcited electrons and holes. It is believed that high-density surface states exist due to large surface-to-volume ratios. Thus, the trap-assisted Auger recombination process is significant in nanoparticles, while its rate is negligibly small in $SrTiO_3$ bulk crystals [43].

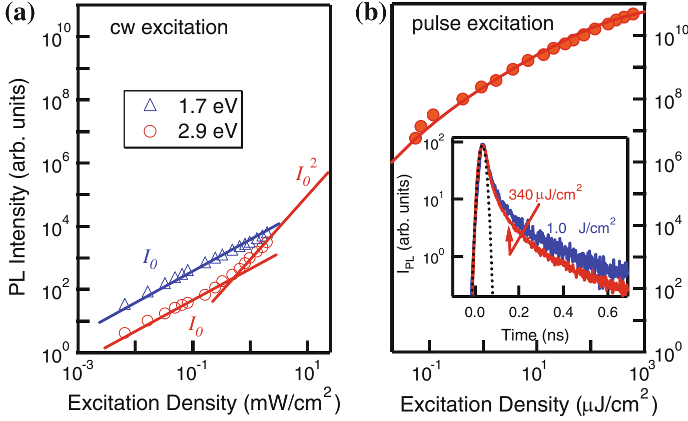

Fig. 1.24 Excitation-density dependences of the PL intensity in the $SrTiO_3$ nanoparticle under **a** cw and **b** pulse laser excitation (After [63])

To examine the Auger recombination process under strong photoexcitation, we have measured the PL decay dynamics. The inset of Fig. 1.24b shows the PL decay dynamics at 2.9 eV of the nanoparticle sample under 340 and 1.0 μJ/cm^2 excitation. We have also plotted the instrumental function in the same figure as a dotted curve. As the excitation density is increased, the PL decays faster, and the PL decay curve becomes non-exponential. The blue PL decay curves in the subnanosecond time region are approximately described by two exponential functions. The decay time of the fast component is several tens of picoseconds, corresponding to Auger recombination rate. The slow decay time is approximately 5 ns, insensitive to the laser excitation intensity, and we obtain $A = 1.0 \pm 0.1 \times 10^8$ s^{-1}.

We have estimated the $B$and$C$ coefficients for $SrTiO_3$ nanoparticles based on the excitation density dependence of the blue PL intensity. We fitted the PL intensity as a function of excitation density, where we fixed $A = 1 \times 10^8 \mathrm{s}^{-1}$. The results are plotted in Fig. 1.24b as a solid curve, where the best-fit values of the parameters are obtained as $B = 6.4 \pm 3.3 \times 10^{-10}$ s^{-1}cm^3, and $C = 1.8 \pm 0.2 \times 10^{-30} \mathrm{s}^{-1}\mathrm{cm}^6$. The calculated curve well reproduces the experimental results. The C coefficient of nanoparticles is found to be much larger than that of bulk crystals ($C = 1.3 \times 10^{-32}$ cm^{6}s^{-1}) [27, 43].

Here, we discuss the origin of the large Auger recombination coefficient of $SrTiO_3$ nanoparticles. Nanoparticles possess large surface-to-volume ratios and the surface plays a crucial role in the enhancement of intrinsic Auger recombination as well as trap-assisted Auger recombination [68–70]. We may point it out that possible enhancement effects are (i) increased final state density, and (ii) reduced dielectric constant. In nanoparticles, the final state density of Auger recombination process is anticipated to increase with the increase of surface state density [70, 71]. Moreover, the reduced dielectric constant of $SrTiO_3$ surface should also be considered. It has been reported that the dielectric constant of $SrTiO_3$ nanoparticles and thin films is much smaller than that of bulk crystals [72–74]. The reduction in dielectric constant

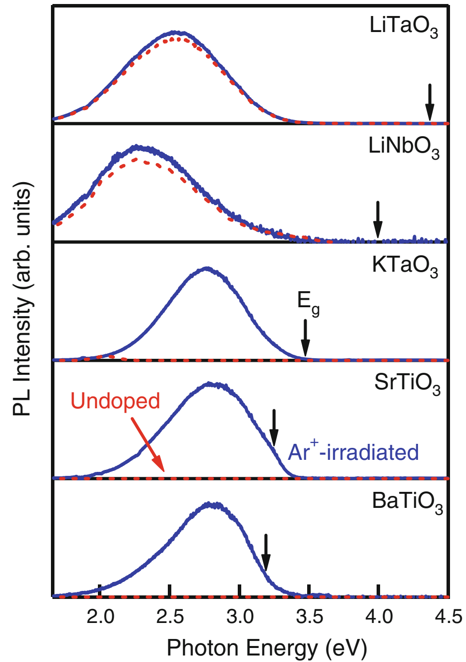

Fig. 1.25 PL spectra of the undoped and Ar^{+}-irradiated $LiTaO_3$, $LiNbO_3$, $KTaO_3$, $SrTiO_3$, and $BaTiO_3$ crystals at room temperature (After [80])

enhances the Coulomb interaction between electrons and holes, which results in the increase of Auger recombination rate. Therefore we may conclude that the surface effects enhance the Auger recombination rate of $SrTiO_3$ nanoparticles.

In conclusion, we have demonstrated that the Auger recombination of electrons originating from oxygen vacancies with photocarriers determines the PL lifetime in the near-surface region and that the electron densities near the surface are much higher than those in the bulk crystal. The Auger recombination coefficient of $SrTiO_3$ nanoparticles is much larger than that of bulk crystals. We have pointed out that the enhancement of the Auger recombination coefficient is related to the large surface-to-volume ratios of nanoparticles.

1.6 Other Perovskite Semiconductors

Figure 1.25 shows PL spectra of undoped and Ar^{+}-irradiated $LiTaO_3$, $LiNbO_3$, $KTaO_3$, $SrTiO_3$, and $BaTiO_3$ crystals at room temperature. These crystals are indirect-gap semiconductors, whose band-gap energies are indicated by the arrows [28, 47, 75–77]. The PL intensity is enhanced by Ar^{+} ion irradiation in all samples. The PL spectra in Fig. 1.25 are normalized at their peak intensities. Here, note that Ar^{+} ion irradiation causes oxygen deficiencies in the surface region of oxide semiconductors [4]. This oxygen-deficient layer shows metallic conduction and emits

the blue light at room temperature in Ar^+-irradiated $SrTiO_3$. The PL properties of Ar^+-irradiated $SrTiO_3$ are very similar to those of La-doped and Nb doped $SrTiO_3$ [27, 43], where the chemically substituted La ions for Sr ions or Nb ions for Ti ions produce electron carriers and these chemically doped samples are metallic [13, 57]. Thus, it is considered that the electron carriers doped by the oxygen deficiency play an important role in the enhancement of the blue PL band.

For $KTaO_3$, $SrTiO_3$, and $BaTiO_3$, the samples are excited at 3.82 eV using a cw He-Cd laser. Undoped samples (red broken curves) show no PL at room temperature, but a broad blue PL band appears in Ar^+-irradiated samples (blue solid curves). The broad PL bands show large Stokes shifts and broad spectrum widths, suggesting that the PL originates from "extrinsic" localized states of impurities and defects or "intrinsic" states through strong electron-phonon couplings (for example, polarons or self-trapped excitons). Note that the PL spectrum shape is independent of excitation density. In addition, similar broad PL bands are observed in undoped $KTaO_3$, $SrTiO_3$, and $BaTiO_3$ crystals under high-density pulse laser excitation (not shown here. For $SrTiO_3$, see [27] and [43]), indicating that carrier doping due to the formation of defects by Ar^+ irradiation causes the efficient PL. The strong photoexcitation and Ar^+ irradiation experiments indicate that high-density carriers by doping are essential for efficient PL from $KTaO_3$, $SrTiO_3$, and $BaTiO_3$.

For $LiTaO_3$ and $LiNbO_3$ crystals, excitation light source was a wavelength-tunable pulse laser under weak low excitation density (8 and 12 μJ/cm^2 for $LiTaO_3$ and $LiNbO_3$, respectively). Excitation photon energies were 4.59 and 4.28 eV for $LiTaO_3$ and $LiNbO_3$, respectively. In $LiTaO_3$ and $LiNbO_3$, no significant changes of PL intensity were observed by Ar^+ irradiation. The PL spectra in both undoped and Ar^+-irradiated samples are similar to each other. The PL peak energies of $LiTaO_3$ and $LiNbO_3$ are lower than those of $KTaO_3$, $SrTiO_3$, and $BaTiO_3$, while the band-gap energies of $LiTaO_3$ and $LiNbO_3$ are larger than those of $KTaO_3$, $SrTiO_3$, and $BaTiO_3$. The PL intensities of Ar^+-irradiated $LiTaO_3$ and $LiNbO_3$ samples are much lower than those of Ar^+-irradiated $KTaO_3$, $SrTiO_3$, and $BaTiO_3$ samples. All Ar^+-irradiated samples show single broad PL bands, but PL spectra are classed into two groups: (i) $KTaO_3$, $SrTiO_3$, and $BaTiO_3$ and (ii) $LiTaO_3$ and $LiNbO_3$.

For a better understanding of PL processes, we have studied the excitation-density dependence of the broad PL bands. Figure 1.26a shows the excitation-density dependence of the PL intensity of undoped $KTaO_3$ and $LiTaO_3$ crystals under pulse laser excitation. For undoped $KTaO_3$ crystals, the PL intensity shows a quadratic dependence on the excitation density under low excitation density, meaning that two-carrier recombination of photoexcited electrons and holes dominates the PL process. Under high-density excitation, above 300 μJ/cm^2, the PL intensity shows saturation behavior, which may probably be attributed to an increase of nonradiative three-carrier Auger recombination rate [27, 43, 55]. Undoped $SrTiO_3$ and $BaTiO_3$ crystals also display similar excitation-density dependence. In contrast to the case of $KTaO_3$, the PL intensity of undoped $LiTaO_3$ crystals is linearly dependent on the excitation density. Similar linear excitation-density dependences observed in undoped $LiNbO_3$ crystals as well. Perovskite oxides used in this work possess large dielectric constants [13, 57, 75, 78], and thus excitonic effects do not appear at room

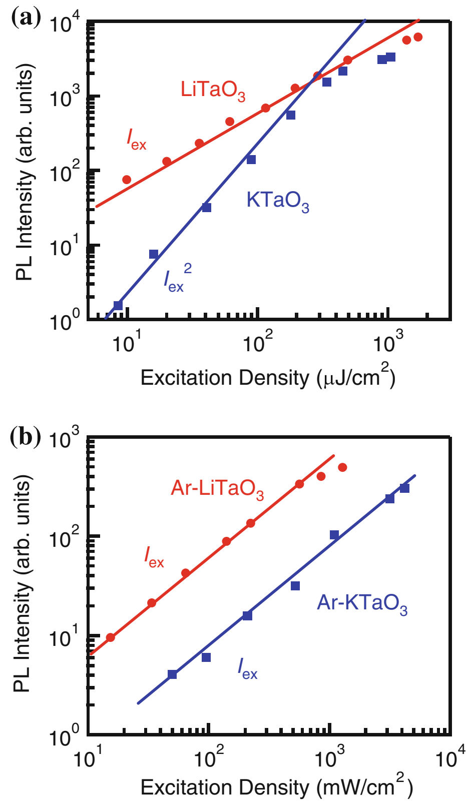

Fig. 1.26 **a** Excitation-density dependence of the PL intensity of undoped $KTaO_3$ and $LiTaO_3$ crystals under pulse laser excitation. **b** Excitation density dependence of PL intensity in Ar^+-irradiated $KTaO_3$ (under cw excitation) and $LiTaO_3$ (under pulse laser excitation) samples (After [80])

temperature. This linear dependence implies that carrier tapping determines the PL process. These results mean that the PL processes in $KTaO_3$, $SrTiO_3$ and $BaTiO_3$ are completely different from those in $LiTaO_3$ and $LiNbO_3$.

Figure 1.26b shows the excitation-density dependence of PL intensity in Ar^+-irradiated $KTaO_3$ (under cw excitation) and $LiTaO_3$(under pulse laser excitation) samples. Ar^+-irradiated $KTaO_3$ sample shows a broad blue PL under weak cw excitation, whose intensity shows linear increase with increasing excitation density. This indicates that the PL in Ar^+-irradiated $KTaO_3$ samples is determined by the radiative recombination of doped electrons and photoexcited holes. As discussed with respect to Fig. 1.26a and b, the PL behaviors of undoped and electron-doped samples are explained by a simple rate (1.2) including single-carrier trapping, radiative two-carrier recombination, and nonradiative three-carrier Auger recombination processes [27, 43].

We have also studied the low-temperature PL properties. Figure 1.27 shows the PL spectra of undoped and Ar^+-irradiated samples at 10 K. Note that PL measurement in undoped $BaTiO_3$ crystals was not performed at low temperatures because undoped $BaTiO_3$ single crystals can be broken to pieces due to rapid volume change at the

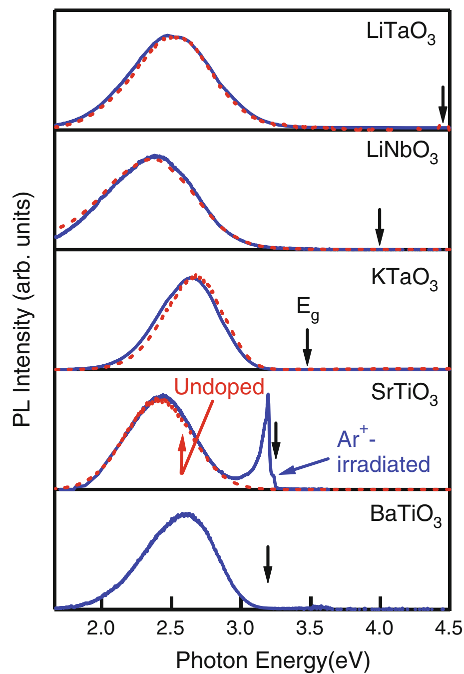

Fig. 1.27 PL spectra of undoped and Ar^+-irradiated samples at low temperature (After [80])

phase transition temperature. Here, the PL intensities are normalized at their peak intensities. Undoped samples show broad PL bands, similar to those of Ar^+-irradiated samples. In undoped and Ar^+-irradiated $LiTaO_3$ and $LiNbO_3$, no significant spectral changes are observed in a wide temperature range between 10 and 300 K, which implies that the origins of the broad PL bands at 10 K and room temperature are identical. On the other hand, in $KTaO_3$, $SrTiO_3$, and $BaTiO_3$, the broad PL band red-shifts at low temperatures. It is considered that the origins of efficient PLs at 10 K in these crystals are different from those at room temperature.

The temperature dependence of the PL intensity of (a) undoped samples and (b) Ar^+-irradiated samples is plotted in Fig. 1.28. The PL intensity is normalized at 10 K. All the undoped samples show Arrhenius-like temperature dependence. Undoped $LiTaO_3$ and $LiNbO_3$ show gradual decrease of PL intensity with increasing temperature resulting in a weak PL at room temperature. On the other hand, the PL intensity of undoped $SrTiO_3$ and $KTaO_3$ samples shows a thermal quenching below 100 K and the room temperature PL is not observed. In Ar^+-irradiated $KTaO_3$ and $SrTiO_3$ samples, the PL intensity is also reduced compared to undoped samples at low temperatures. However, their PL intensities remain almost constants above 150 K unlike the case of undoped samples. These results mean that the electron doping by Ar^+ irradiation enhances the broad PL intensity at high temperatures.

It is noteworthy that the low-temperature PL spectrum of Ar^+-irradiated $SrTiO_3$ samples show significant difference compared to other samples: band-edge PL is

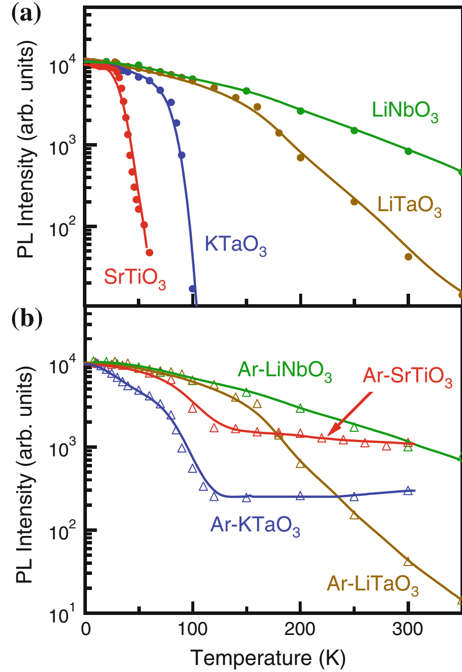

Fig. 1.28 PL intensity of **a** undoped samples and **b** Ar^+-irradiated samples as a function of temperature (After [80])

observed only in Ar^+-irradiated $SrTiO_3$ samples, as shown in Fig. 1.27. The band-edge PL peak is observed in chemically electron-doped $SrTiO_3$ and strongly photoexcited $SrTiO_3$ (see Sect. 1.3). The observation of band-edge PL indicates the existence of free electrons and holes in $SrTiO_3$. Although $LiTaO_3$, $LiNbO_3$, $KTaO_3$, and $BaTiO_3$ are indirect-gap semiconductors and show no excitonic effects similar to $SrTiO_3$, no band-edge PL is observed in perovskite semiconductors other than in $SrTiO_3$. At present stage, we believe that the band-edge PL of $SrTiO_3$ is related to the fact that $SrTiO_3$ shows significantly high carrier mobility compared to other oxide semiconductors [49, 79]. It is likely that in other perovskite semiconductors carriers would be localized and no band-edge PL is observed.

1.7 Summary

In conclusion, we have found the band-to-band PL peaks in strongly photoexcited $SrTiO_3$ and electron-doped $SrTiO_3$ at low temperatures. The two band-edge PL peaks correspond to radiative band-to-band recombination involving phonon emission and absorption processes. The band-edge PL peaks redshift with increasing carrier density, reflecting the band-gap shrinkage due to the band-gap renormalization effect. The observation of band-edge PL allows us an accurate determination of the band-gap of $SrTiO_3$, which was found to be 3.246 eV. Band-to-band PL provides a powerful

method for studying the electronic structure of bulk $SrTiO_3$ and $SrTiO_3$-based heterostructures.

We have examined the PL dynamics of undoped $SrTiO_3$ and electron-doped $SrTiO_3$ as a function of photo- and chemical-doped carrier density. In undoped $SrTiO_3$, fast-decay and non-exponential PL component was observed in the nanosecond time region under strong excitation. In electron-doped $SrTiO_3$, the PL lifetime decreases with an increase of the doped electron density under weak excitation. These experimental data are well explained by a simple model including the two-carrier radiative recombination and the Auger nonradiative recombination processes, which demonstrate the importance of the multi-particle recombination processes in $SrTiO_3$.

The temperature dependence of carrier dynamics is evaluated in undoped and electron-doped $SrTiO_3$ by means of time-resolved PL measurements. The carrier recombination model well describes the PL dynamics at all temperatures in both undoped and electron-doped $SrTiO_3$. The phonon-assisted Auger recombination determines the temperature-dependent PL dynamics. At low temperatures, rapid energy transfer occurs from the near band-edge state of blue PL to the deep state. The low-temperature PL dynamics is closely related to high mobility of carriers at low temperatures.

The PL dynamics under band-to-band excitation depends strongly on the excitation photon energy. The excitation-energy-dependent PL dynamics can be explained by the Auger recombination process of electrons originating from oxygen vacancies with photocarriers. We have clarified that in undoped $SrTiO_3$, an oxygen-deficient near-surface layer exists with a depth of a few tens of nanometers.

Further, we have shown the blue PL spectrum and dynamics of $SrTiO_3$ nanoparticle thin films under strong photoexcitation. The excitation-density dependence of the blue PL intensity and the rapid PL decay indicate Auger-dominated recombination process. The Auger recombination coefficient of $SrTiO_3$ nanoparticles is found to be much larger than that of bulk crystals. We have suggested that the enhancement of the Auger recombination coefficient is related to large surface-to-volume ratios of nanoparticles.

Acknowledgments The authors would like to thank H. Yasuda, T. Tayagaki, D. Kan, Y. Shimakawa, T. Terashima, and K. Suzuki for their help and discussions. Part of this work was supported by The Sumitomo Electric Industries Group CSR Foundation, KAKENHI (Nos. 20104006 and 25247052), and JST-CREST.

References

1. I.P. Kaminow, W.D. Johnston, Phys. Rev. **160**, 519 (1967)
2. S. Zhu, Y.Y. Zhu, N.B. Ming, Science **278**, 843 (1997)
3. A.J. Wojtowicz, W. Drozdowski, D. Wisniewski, J.L. Lefaucheur, Z. Galazka, Z.H. Gou, T. Lukasiewicz, J. Kisielewski, Opt. Mater. **28**, 85 (2006)
4. D. Kan, T. Terashima, R. Kanda, A. Masuno, K. Tanaka, S. Chu, H. Kan, A. Ishizumi, Y. Kanemitsu, Y. Shimakawa, M. Takano, Nat. Mater. **4**, 816 (2005)
5. H. Takashima, K. Shmimada, T. Katsumata, Y. Inaguma, K. Ueda, M. Itoh, Adv. Mater. **21**, 3699 (2009)

6. S.Y. Yang, J. Seidel, S.J. Byrnes, P. Shafer, C.-H. Yang, M.D. Rossell, P. Yu, Y.-H. Chu, J.F. Scott, J.W. Ager III, L.W. Martin, R. Ramesh, Nat. Nanotech. **5**, 143 (2010)
7. A.H. Kahn, A.J. Leyendecker, Phys. Rev. **135**, A1321 (1964)
8. D.A. Muller, N. Nakagawa, A. Ohtomo, J.L. Grazul, H.Y. Hwang, Nature (London) **430**, 657 (2004)
9. Y. Muraoka, T. Muramatsu, J. Yamaura, Z. Hiroi, Appl. Phys. Lett. **85**, 2950 (2004)
10. H.P.R. Frederikse, W.R. Thurber, W.R. Hosler, Phys. Rev. **134**, A442 (1964)
11. O.N. Tufte, P.W. Chapman, Phys. Rev. **155**, 796 (1967)
12. J.F. Schooley, W.R. Hosler, M.L. Cohen, Phys. Rev. Lett. **12**, 474 (1964)
13. H. Suzuki, H. Bando, Y. Ootuka, I.H. Inoue, T. Yamamoto, K. Takahashi, Y. Nishihara, J. Phys. Soc. Jpn. **65**, 1529 (1996)
14. T. Ishikawa, M. Kurita, H. Shimoda, Y. Sakano, S. Koshihara, M. Itoh, M. Takesada, J. Phys. Soc. Jpn. **73**, 1635 (2004)
15. M. Takesada, T. Yagi, M. Itoh, S. Koshihara, J. Phys. Soc. Jpn. **72**, 37 (2003)
16. T. Hasegawa, S. Mouri, Y. Yamada, K. Tanaka, J. Phys. Soc. Jpn. **72**, 41 (2003)
17. A. Ohtomo, H.Y. Hwang, Nature (London) **427**, 423 (2004)
18. N. Nakagawa, H.Y. Hwang, D.A. Müller, Nat. Mater. **5**, 204 (2006)
19. S. Thiel, G. Hammerl, A. Schmehl, C.W. Schneider, J. Mannhart, Science **313**, 1942 (2006)
20. N. Reyren, S. Thiel, A.D. Cavigla, L. Koukoutis, G. Hammerl, C. Richter, C.W. Schneider, T. Kopp, A.S. Rüetschi, D. Jaccard, M. Gabay, D.A. Muller, J.M. Triscone, J. Mannhart, Science **317**, 1196 (2007)
21. M. Basletic, J. -L. Maurice, C. Carrétéro, G. Herranz1, O. Copie, M. Bibes, É. Jacquet, K. Bouzehouane, S. Fusil, A. Barthélémy, Nat. Mat. **7**, 621 (2008)
22. K. Janicka, J.P. Velev, E.Y. Tsymbal, Phys. Rev. Lett. **102**, 106803 (2009)
23. A.D. Caviglia, S. Gariglio, C. Cancellieri, B. Sacépé, A. Fête, N. Reyren, M. Gabay, A.F. Morpurgo, J.-M. Triscone, Phys. Rev. Lett. **105**, 236802 (2010)
24. A. Brinkman, M. Huijben, M. van Zalk, J. Huijben, U. Zeitler, J.C. Maan, W.G. van der Wiel, G. Rijnders, D.H. Blank, H. Hilgenkamp, Nat. Mater. **6**, 493 (2007)
25. J.A. Bert, B. Kalisky, C. Bell, M. Kim, Y. Hikita, H.Y. Hwang, K.A. Moler, Nat. Phys. **7**, 767 (2011)
26. L. Li, C. Richter, J. Mannhart, R.C. Ashoori, Nat. Phys. **7**, 762 (2011)
27. H. Yasuda, Y. Kanemitsu, Phys. Rev. B **77**, 193202 (2008)
28. Y. Yamada, Y. Kanemitsu, Phys. Rev. B **82**, 121103(R) (2010)
29. Y. Kanemitsu, Y. Yamada, Phys. Stat. Sol. (B) **248**, 416 (2011)
30. D. Keroack, Y. Lepine, J.L. Brebner, J. Phys. C: Solid State Phys. **17**, 833 (1984)
31. C. Ang, Z. Yu, Z. Jing, Phys. Rev. B **61**, 3922 (2000)
32. W.S. Baer, Phys. Rev. **144**, 734 (1966)
33. H. Okamura, M. Matsubara, K. Tanaka, K. Fukui, M. Terakami, H. Nakagawa, Y. Ikemoto, T. Moriwaki, H. Kimura, T. Nanba, J. Phys. Soc. Jpn. **75**, 023703 (2006)
34. J.L.M. van Mechelen, D. van der Marel, C. Grimaldi, A.B. Kuzmenko, N.P. Armitage, N. Reyren, H. Hagemann, I.I. Mazin, Phys. Rev. Lett. **100**, 226403 (2008)
35. T. Feng, Phys. Rev. B **25**, 627 (1982)
36. R. Leonelli, J.L. Brebner, Phys. Rev. B **33**, 8649 (1986)
37. S. Mochizuki, F. Fujishiro, S. Minami, J. Phys. Condens. Matter **17**, 923 (2005)
38. Y. Yamada, Y. Kanemitsu, Thin Solid Films **520**, 3843 (2012)
39. D.W. Reagor, V.Y. Butko, Nat. Mater. **4**, 593 (2005)
40. V. F. Pichugin, A. A. Bulycheva, V. Yu. Yakovlev, I.W. Kim, Phys. Stat. Sol. (C) **2**, 208 (2005)
41. Y. Yamada, Y. Kanemitsu, J. Appl. Phys. **109**, 102410 (2010)
42. A. Rubano, D. Paparo, F. Miletto, U. Scotti di Uccio, L. Marrucci, Phys. Rev. B **76**, 125115 (2007)
43. Y. Yamada, H. Yasuda, T. Tayagaki, Y. Kanemitsu, Phys. Rev. Lett. **102**, 247401 (2009)
44. Y. Yamada, H. Yasuda, T. Tayagaki, Y. Kanemitsu, Appl. Phys. Lett. **95**, 121112 (2009)
45. C.H. Perry, J.H. Fertel, T.F. McNelly, J. Chem. Phys. **47**, 1619 (1967)
46. W.G. Nilsen, J.G. Skinner, J. Chem. Phys. **48**, 2240 (1968)

47. M. Capizzi, A. Frova, Phys. Rev. Lett. **25**, 1298 (1970)
48. A. Frova, Nuovo Cimento B **55**, 1 (1968)
49. P.Y. Yu, M. Cardona, Fundamentals of Semiconductors, 3d edn. (Springer, Berlin, 2005)
50. C.F. Klingshirn, *Semiconductor Optics*, 3rd edn. (Springer, Berlin, 2007)
51. R. Zimmermann, J. Cryst. Growth **101**, 346 (1990)
52. T. Hasegawa, M. Shirai, K. Tanaka, J. Lumin. **87–89**, 1217 (2000)
53. H. Yasuda, Y. Yamada, T. Tayagaki, Y. Kanemitsu, Phys. Rev. B **78**, 233202 (2008)
54. P.T. Landsberg, *Recombination in Semiconductors* (Cambridge University Press, Cambridge, 1991)
55. P.T. Landsberg, Appl. Phys. Lett. **50**, 745 (1987)
56. T. Okuda, K. Nakanishi, S. Miyasaka, Y. Tokura, Phys. Rev. B **63**, 113104 (2001)
57. S. Ohta, T. Nomura, H. Ohta, K. Koumoto, J. Appl. Phys. **97**, 034106 (2005)
58. A. Haug, Solid State Commun. **28**, 291 (1978)
59. K.G. Svantesson, N.G. Nilsson, J. Phys. C **12**, 5111 (1979)
60. M. Cardona, Phys. Rev. **140**, A651 (1965)
61. V.E. Henrich, G. Dresselhaus, H.J. Zeiger, Phys. Rev. B **17**, 4908 (1978)
62. K. Szot, W. Speier, R. Carius, U. Zastrow, W. Beyer, Phys. Rev. Lett. **88**, 075508 (2002)
63. Y. Yamada, K. Suzuki, Y. Kanemitsu, Appl. Phys. Lett. **99**, 093101 (2011)
64. Y. Kanemitsu, S. Okamoto, M. Otobe, S. Oda, Phys. Rev. B **55**, R7375 (1997)
65. S. Okamoto, Y. Kanemitsu, Phys. Rev. B **54**, 16421 (1996)
66. Y. Yamashita, H. Yamamoto, Y. Sakabe, Jpn. J. Appl. Phys. **43**, 6521 (2004)
67. M. Inoguchi, K. Suzuki, K. Kageyama, H. Takagi, Y. Sakabe, J. Am. Ceram. Soc. **91**, 3850 (2008)
68. A. Pandey, P. Guyot-Sionnest, J. Chem. Phys. **127**, 111104 (2007)
69. G.E. Cragg, A.L. Efros, Nano Lett. **10**, 313 (2010)
70. S. Taguchi, M. Saruyama, T. Teranishi, Y. Kanemitsu, Phys. Rev. B **83**, 155324 (2011)
71. A. Cretì, M. Anni, M. Zavelani-Ross, G. Lanzani, L. Manna, M. Lomascolo, Appl. Phys. Lett. **91**, 093106 (2007)
72. A.A. Sirenko, C. Bernhard, A. Golnik, A.M. Clark, J. Hao, W. Si, X.X. Xi, Nature (London) **404**, 373 (2000)
73. M. Stengel, N.A. Spaldin, Nature (London) **443**, 679 (2006)
74. M.C. Wang, F.Y. Hsiao, H.H. Huang, N.C. Wu, Jpn. J. Appl. Phys. **43**, 6323 (2004)
75. S. Çabuk, A. Mamedov, J. Opt. A: Pure Appl. Opt. **1**, 424 (1999)
76. I. Katayama, K. Tanaka, J. Phys. Soc. Jpn. **75**, 064713 (2006)
77. S.H. Wemple, M. Didomenico Jr, I. Camlibel, J. Phys. Chem. Sol. **29**, 1797 (1968)
78. G. Rupprecht, R.O. Bell, Phys. Rev. **135**, A748 (1964)
79. F. Gervais, J.-L. Servoin, A. Baratoff, J.G. Bednorz, G. Binnig, Phys. Rev. B **47**, 8187 (1993)
80. Y. Yamada, Y. Kanemitsu, J. Lumin. **133**, 30 (2013)

Chapter 2
Nano Architectures in Silicon Photovoltaics

Nazir P. Kherani

Abstract A historical trace of key developments in the science and engineering of photovoltaics introduces the reader to this important field of energy generation. An overview of photovoltaics and allied photonic architectures is presented including a synopsis of the relevant physics. A selected illustrative review of recent research results on the integration of wave-optic coupling nanostructures in silicon photovoltaics is given with an emphasis on the use of photonic crystal constructs. The chapter closes pondering the arc of development in silicon photovoltaics—the main stay of present day solar photovoltaics.

2.1 Introduction

Maxwell's equations, presented in 1864 to the Royal Society of London [1], remarkably remain to this day an adequate and elegant description of the underlying electromagnetic field for essentially all atomic and condensed matter phenomena [2]—notwithstanding the superseding comprehensive description of light–matter interactions provided by quantum electrodynamics [3, 4]. Within this framework, the physical structure or architecture[1] of systems have yielded extraordinary physical effects. Through the integrative effect of electromagnetic interactions in

[1] Structure is the arrangement and relationship among the constitutive parts of a given system; hence architecture is the physical structure of a system.

N. P. Kherani (✉)
Department of Electrical and Computer Engineering, University of Toronto,
10 King's College Road, Toronto, ON M5S 3G4, Canada
e-mail: nazir.kherani@gmail.com

N. P. Kherani
Department of Materials Science and Engineering, University of Toronto,
184 College Street, Toronto, ON M5S 3E4, Canada
e-mail: Kherani@ecf.utoronto.ca

J. Singh and R. T. Williams (eds.), *Excitonic and Photonic Processes in Materials*,
Springer Series in Materials Science 203, DOI: 10.1007/978-981-287-131-2_2,
© Springer Science+Business Media Singapore 2015

atomic or condensed matter systems, novel classes of materials have been produced which include metamaterials [5–7], photonic crystals [8–12] and plasmonic materials [13–15]. Further, the advent of advanced materials synthesis capabilities, particularly at the micrometer and nanometer length scales [16, 17], and the ready accessibility to powerful numerical computational tools, has ushered a cornucopia of research examining the practical applicability of these basic phenomena to information and communication technologies, medical diagnostics and therapies, and energy systems to name a few. The photovoltaic effect, generation of an electric potential between two electrodes upon exposure of the system to light, first observed by Edmond Becquerel and reported in 1839 [18] is the basis of direct conversion of light energy into electricity. Following a number of research advances in the intervening 100 plus years, in 1954 the first crystalline silicon photovoltaic device was developed at Bell Laboratories with an AM1.5[2] one sun photovoltaic energy conversion efficiency of 6 % [19]. This first silicon solar cell, a photodiode that operates in a passive externally-unbiased mode transducing light energy in to electrical energy, heralded a new technologically-viable globally-accessible renewable energy industry—solar photovoltaics or simply solar electricity. The enormous potential of this renewable energy source is self-evident in the solar irradiance map of the world, shown in Fig. 2.1.

Over the last six decades, crystalline silicon solar cells have experienced extensive scientific and technological advances that have led to record AM1.5 photovoltaic conversion efficiencies of 25 % for 400 micron thick silicon in the laboratory [20], recently to 24 %+ conversion efficiencies for less than 200 micron thick back-contact siliconsolar cells in industrial production,[3] and more recently 24.7 % for less than 100 micron thick low-temperature synthesized silicon solar cells [21] and even more recently 25.6 % for similar back-contact solar cells.[4] Concurrently, several other competing solar materials have developed into complementary commercial photovoltaic systems which include thin film cadmium telluride (CdTe), thin film copper indium gallium diselenide (CIGS), copper zinc tin sulphide (CZTS), thin film amorphous-microcrystalline silicon, and III–V crystalline semiconductor based concentrated photovoltaics [22–24].

Recently the field of photovoltaics has attracted much research attention spurred by a range of socioeconomic and environmental concerns and the resolve of a variety of stake holders to make solar electricity an economically inevitable reality. This has led to an exploration of a plethora of novel material systems for photovoltaic applications, some of which include dye sensitized solar cells [25–28], organic photovoltaics [29, 30], quantum dot solar cells [31, 32], and perovskites [33, 34], as well

---

[2] AM1.5 represents a standard solar spectrum with an integrated irradiance of 1,000 Wm^{-2} [ref], which corresponds on average to the irradiance level at mid-latitudes (corresponding to a solar zenith angle of $Z = 48.2°$)—where the rays of the sun traverse an air mass of 1.5 times the thickness of the atmosphere at the equator, at the zenith.

[3] http://www.renewableenergyworld.com/rea/news/article/2010/06/sunpower-sets-solar-cell-efficiency-record-at-24-2.

[4] http://www.panasonic.co.jp/corp/news/official.data/data.dir/2014/04/en140410-4/en140410-4.html.

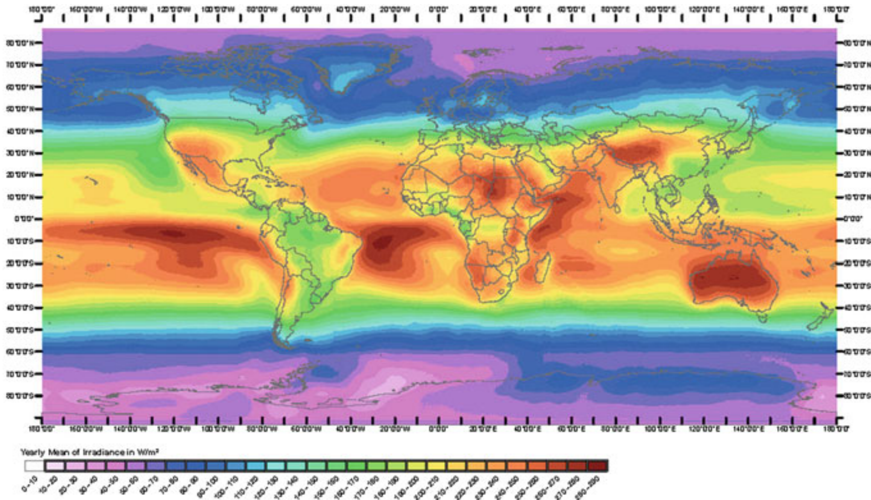

Fig. 2.1 Average solar irradiance map of the world illustrating the enormity of the distributed solar resource and that the variability/uniformity in the irradiance among most regions of the world lies within a factor of three. Copyright Mines Paristech/Armines 2006

as a further investigation of the incumbent photovoltaic material system of silicon. In this quest, the architecture of photovoltaic devices has played an increasingly important role, effecting changes in the optical and electrical properties of the systems. For example, quantum confinement effects are being considered in the pursuit of complete utilization of the solar spectrum and have led to the study of a range of quantum dot material systems including silicon [35–37]. In other cases, simply complete optical absorption of the supra-bandgap part of the solar spectrum have led to the study of a range of photonic constructs to effect the desired optical coupling [38, 39]. And yet in other instances, the need to effectively integrate new photonic constructs while addressing the device's electrical requirements of charge transport have been pursued [40–45].

With the advent of nanostructured material synthesis, the prospect of realizing novel optical and electrical effects in the entire gamut of solar materials including silicon has invigorated fundamental and applied research to new heights. In silicon, the expectation is that this terrestrially abundant, environmentally compatible, and industrially established material can be newly engineered to yield high optical to electrical conversion efficiency while requiring a minimal quantity of the material, and thus resulting in a ubiquitous energy converter at the lowest cost per watt [46, 47]. On the immediate horizon, the objectives are to explore existing crystalline silicon and thin film silicon platforms while in the longer term novel approaches such as nano-wire, nano-crystalline/particle and other nano-structures of silicon are being contemplated.

For crystalline silicon, the arc of progress is towards ultra-thin silicon which in the limit exacts light trapping at optical and infrared wavelengths, while for thin film amorphous-microcrystalline silicon the challenge is to not only harvest the light but to spectrally mold its flow in tandem device structures. Further, both platforms demand broad band absorption over broad angular incidence considering the outlook of stationary solar panels generating more energy without the need for solar trackers. Nanostructuring of dielectrics and semiconductors offering wave-optic coupling, light localization and light trapping indicate effective means of mitigating optical reflection at the incident interface, enhancing the path length of light within the absorber, and effectively back-reflecting the light at the far interface. The integration of such nano-architectures in silicon promises a path to the next generation of economically inescapable subsidy-free silicon photovoltaic solar cells.

In this chapter, we present an overview of photovoltaics and allied photonic architectures with an emphasis on approaches to enhance optical absorption, a synopsis of the physics pertaining to photovoltaics and photonic structures, and then provide a selected review of recent research results advancing the integration of wave-optic coupling in silicon photovoltaics and in particular highlighting the use of photonic crystal constructs.

2.2 Photovoltaics and Photonic Architectures: A Historical Perspective

2.2.1 Photovoltaics

In 1839 Edmond Becquerel while carrying out an electrolytic experiment observed an electrical response in the external circuit upon exposure of silver coated platinum electrodes to light, thus marking the beginning of the science of photovoltaics. In 1873 Willoughby Smith discovered the photoconductivity of selenium [48] which established the basis for the demonstration of the solid state photovoltaic effect by William Adams and Richard Day several years later in 1876 [49, 50]. Adams and Day, having made platinum contacts on a selenium rod, observed a change in the electrical characteristics of selenium upon light exposure and thus paved the way for the demonstration of the first solid state photocell.

In 1883 Charles Fritts fabricated the first solar cell by melting a 30 μm thin sheet of selenium onto an iron substrate followed by pressing down a 5 nm thin transparent leaf of gold on selenium, hence marking the beginning of the technology of photovoltaics [51]. Of the range of materials examined Fritts found that the photovoltaic action was most significant with brass, zinc and iron, reflective of the formation of different Schottky devices. The Schottky photovoltaic device was 30 cm^2 in area and operated at a conversion efficiency of approximately 1 % much lower than Fritts' expectations and his underlying hope of competing with Thomas Edison's coal-fired power plants.

In 1954 the celebrated report by Chapin, Pearson and Fuller of a silicon photovoltaic cell with a conversion efficiency of 6 % marked the beginning of the modern era of the science and technology of photovoltaics [19]. This extraordinary achievement was due to earlier research principally motivated by the development of silicon electronics. Notably, the development of point-contact diodes, also known as cat's whisker diodes, in the early part of the twentieth century led to the replacement of thermionic valves in most applications. These diodes which required the pressing of metal wires against polycrystalline silicon exhibited significant variability in performance owing to the substantial presence of impurities which resulted in so called "hot spots" in silicon. Russel Ohl at Bell Laboratories surmised the importance of growing purer silicon and thus led a series of experiments synthesizing the purest silicon ingots possible. These experiments led to the first observation of a photovoltage of approximately 0.5 V upon illuminating the diode with a flashlight. It is interesting to note that these early silicon devices were due to a fortuitous distribution of boron rich and phosphorus rich impurity regions that gave rise to contiguous *p*-type and *n*-type regions, respectively, during the growth of the silicon ingot. The first silicon photovoltaic devices were synthesized by slicing sections of the ingot that contained adjoining *p*-doped and *n*-doped regions followed by metallization of the doped surfaces. These first *pn* barrier or *pn* junction silicon devices, reported by Ohl in 1941, exhibited photovoltaic conversion efficiencies of a fraction of a percent [52]. Excerpts and figures taken from Russel S. Ohl's 1941 patent are shown in Fig. 2.2. With the recognition that controlled synthesis was critical in advancing device performance, major developments in the synthesis of single crystal silicon using the Czochlralski process and thermal diffusion of dopant impurities into the surface of silicon led to the remarkable performance of the first 6 % silicon solar cell.

These developments in the 1950s engendered enormous interest and ushered an expectation of remarkable progress in future silicon devices. Motivated by space applications, silicon solar cells with efficiencies of approximately 15 % under one sun conditions were developed by the 1960s [53]. Further, spurred by the oil embargo of the seventies, silicon photovoltaics experienced yet another surge of development leading to record one sun efficiency of 25 % [20] and concentrated[5] 100 suns efficiency of almost 28 % [54]. The principal developments making this possible include a series of materials and device configurational advances that have made complete optical absorption and photogeneration possible followed by effective separation of the photocarriers to yield maximal potential, current density and fill factor. At the materials level, the production of high quality single- and multi-crystalline silicon, surface preconditioning, and control over the diffusion processes have been key. Further, the importance of front and rear surface passivation through the reduction of interfacial defect densities (chemical passivation) and trapped surface charge (field passivation) have played a marked role in enhancing the open circuit potential of the devices as well as the current density; in this context, the passivation proper-

[5] Concentrated photovoltaics, attained using various optical field enhancement techniques, invariably yields a higher performance cell principally attributed to the increase in the open circuit voltage of the cell.

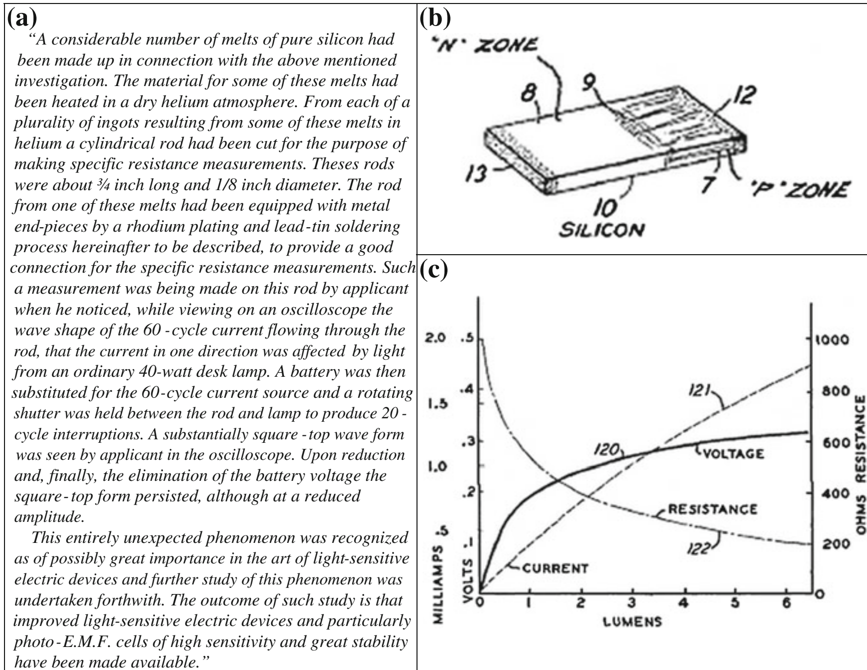
(a)

"A considerable number of melts of pure silicon had been made up in connection with the above mentioned investigation. The material for some of these melts had been heated in a dry helium atmosphere. From each of a plurality of ingots resulting from some of these melts in helium a cylindrical rod had been cut for the purpose of making specific resistance measurements. Theses rods were about ¾ inch long and 1/8 inch diameter. The rod from one of these melts had been equipped with metal end-pieces by a rhodium plating and lead-tin soldering process hereinafter to be described, to provide a good connection for the specific resistance measurements. Such a measurement was being made on this rod by applicant when he noticed, while viewing on an oscilloscope the wave shape of the 60 -cycle current flowing through the rod, that the current in one direction was affected by light from an ordinary 40-watt desk lamp. A battery was then substituted for the 60-cycle current source and a rotating shutter was held between the rod and lamp to produce 20 -cycle interruptions. A substantially square -top wave form was seen by applicant in the oscilloscope. Upon reduction and, finally, the elimination of the battery voltage the square-top form persisted, although at a reduced amplitude.

This entirely unexpected phenomenon was recognized as of possibly great importance in the art of light-sensitive electric devices and further study of this phenomenon was undertaken forthwith. The outcome of such study is that improved light-sensitive electric devices and particularly photo-E.M.F. cells of high sensitivity and great stability have been made available."

Fig. 2.2 Excerpts and figures from Russel S. Ohl's patent on *Light-Sensitive Electric Device* filed in 1941. **a** Excerpt recounting the manner of the discovery. **b** An illustration of the silicon *pn* junction highlighting the *p* (*7*) and *n* (*8*) regions, as well as the barrier region (*9*) which as described by Ohl is "apparently the seat of the photo-E.M.F. effect", and the contacts (*12* and *13*). **c** A plot of the cell's current, voltage and resistance as a function of the illumination [52]

ties of thermal oxide have been superlative. Incorporation of light trapping features have been principally addressed through patterning/texturing of front (light-facing) and rear surfaces, antireflective layers and back reflection coatings. Minimization of ohmic losses through reduction of contact and line (grid and bus bar) resistances, work function terracing, and reduction of shadowing losses have been key in the attainment of large area crystalline silicon solar cells. Today, the crystalline silicon photovoltaics industry has matured to a level where commercial solar cells are routinely produced at efficiencies typically ranging from 17 to 20+ % using silicon wafers as thin as 150–180 μm. Further, crystalline silicon photovoltaics over the last several decades has commanded 80–90 % of the market share and accordingly has contributed towards an estimated cumulative installed global PV capacity of 100 GWp[6] as of 2012 [55].

---

[6] GWp represents gigawatts of electricity generation under peak 1 sun (nominally 1,000 W/m^2) illumination. Photovoltaic generating capacity factors can vary from approximately 11–23 % corresponding to moderate to very high insolation (solar irradiation) sites.

Concurrent to the above described progress in crystalline silicon photovoltaics, a number of alternative approaches have been proposed [56–58]. We highlight two significant concepts the development of which have led to successful production and deployment in the field. The first is the archetype of thin film photovoltaics using silicon. In 1975 Spear and LeComber reported the successful enhancement in conductivity of hydrogenated amorphous silicon (aSi:H) using diborane and phosphine as precursor impurity doping gases in a silane plasma [59]. In 1976 David Carlson and Christopher Wronski successfully reported a thin film amorphous silicon solar cell with a conversion efficiency of 2.4 % [60]. Following several years of research the importance of hydrogen passivation of gap states in amorphous silicon was recognized as essential to the attainment of superior electronic properties. This advance led to single and multijunction hydrogenated amorphous silicon solar cells with stabilized efficiencies exceeding 10 % [61]. Further, the successful plasma-based growth of microcrystalline or nanocrystalline silicon thin films [62], wherein the films contain a large fraction of crystallites of silicon in a backdrop of hydrogenated amorphous silicon, led to the development of the all-silicon dual junction micromorph[7] solar cell—a cell concept that effectively dispenses with the use of germanium alloying in hydrogenated amorphous silicon used to narrow the bandgap of the absorber. Stabilized solar cell efficiencies of approximately 12–13 % for the micromorph cell have been demonstrated wherein the role of material quality, including film thickness and stability considerations, and light trapping features are evidently unavoidable characteristics [63, 64].

The second is a paradigm shift in the synthesis of crystalline silicon solar cells. The advent of amorphous silicon–crystalline silicon heterojunction has brought about the successful synthesis of record efficiency crystalline silicon cells fabricated at temperatures of less than 250 °C. In this approach nanometer thin films of intrinsic and doped hydrogenated amorphous silicon are deposited directly on silicon to attain high quality interfacial passivation and junction formation, respectively. The first silicon heterojunction cells reported by Tanaka et al. reported conversion efficiency exceeding 18 % using intrinsic a-Si:H [65]; more recently, an efficiency of 24.7 % using 98 μm thick c-Si has been reported by Panasonic. A host of similar heterojunction cell concepts have been investigated and reported by a number of other researchers [66]. Concurrently, much research has been underway examining alternative passivation materials, such as hydrogenated amorphous carbon, to overcome the unavoidable parasitic optical absorption losses of a-Si:H. Within this framework various cell concepts have been advanced including complete low temperature synthesis of back contact silicon solar cells [67, 68]. Further, alternative passivation techniques have been explored such as hydrogen plasma treatment of the amorphous silicon layer, the use of atomic layer deposited materials and various bilayer structures including the use offacile grown native oxideson crystalline silicon [69–72]. Moreover, the heterojunction paradigm is deemed to be a particularly viable approach to the synthesis of economic high-efficiency ultra-thin silicon solar cells.

---

[7] Consisting of a hydrogenated amorphous silicon *pin* solar cell ($E_g \sim 1.7$ eV) in tandem with an underlying microcrystalline silicon *pin* cell ($E_g \sim 1.1$ eV).

The foregoing synopsis illustrates the remarkable journey of silicon photovoltaics which has undoubtedly benefitted from the well-established silicon microelectronic industry. Notwithstanding the progress, silicon photovoltaics continues to be challenged economically and as a result much research has been underway to investigate new incremental enhancements that can be readily integrated in existing silicon solar cell concepts as well as explore novel approaches that may potentially leapfrog existing technologies. It is worth noting that while further economic gains can be made at the silicon cell level, parallel efforts in the effective vertical integration from cell to panel to deployment in the field is essential so as to ultimately break the economic barrier. Within this framework, there is a prevailing view that advances at the cell level along with effective vertical integration can make this possible. Accordingly, much attention has also been given to effectively harvest solar photons using advanced photonic constructs. We now provide a selected overview of light-matter interactions and the subsequent development of photonic structures for effective control over the flow of light from a photovoltaic perspective.

2.2.1.1 Photonic Architectures

Historically the science of optics originates with Euclid around 300 BC [73] and the subsequent Alexandrians Heron and Ptolemy [74] who followed him, providing the first narrative on the laws of reflection and indicating observations of optical aberration—notwithstanding archaeological discovery of the Nimrud rock crystal lens that suggests optical acumen may date as far back as 750 BC among the Assyrians. Almost 2 millennia later in 1621 Snell presented the law of refraction and in 1657 Fermat outlined the principle of least time that defined the path taken by a ray of light, a principle consistent with Snell's law[8] [75]. Fresnel whose work spanned from 1816 to 1821 helped definitively establish the validity of the wave theory of light, his crowning work showing that light is a transverse wave. Today, the Fresnel equations provide a detailed description of the reflection and transmission or refraction of light impinging a planar interface between media of different refractive indices—clearly accounting for the polarization of light. Optical effects such as complete transmission of p-polarized light at the Brewster angle and total internal reflection at angles exceeding the critical angle for light traversing from larger index to smaller index media emerge clearly from the Fresnel equations. Further, the Fresnel equations are the basis of studying a number of interference phenomena which include iridescence, antireflection coatings, optical filters, and interferometers.

The observation of a range of optical effects including the generation of structural colour has drawn the attention of many researchers and observers alike. For example, Hooke in 1665 noted that the remarkable pearly lustre of silverfish arises due to the manifold of reflecting surfaces of the transparent scales. Newton in his Opticks, published in 1704, described how the feathers of a bird exhibit a variety of

[8] It is noteworthy that recent historical research indicates that the law of refraction was known to Ibn Sahl prior to 984 and is accordingly credited with the discovery of the law of refraction.

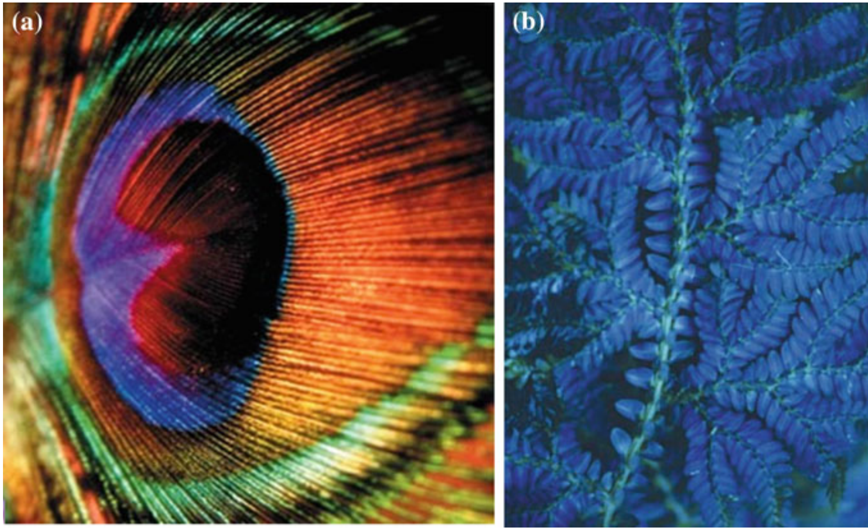

Fig. 2.3 Photonic crystals in nature. **a** The range of structural colours including browns in male peacock feathers [76]. *Image* Michael Shake/dreamtime.com. **b** Structural colour in flora illustrated by the *iridescent blue* in the fern-like tropical understory plants of the genus Selaginella [77]

colours when observed at different angles and attributed this to the transparency and slenderness of these very feathers. The physical basis of these natural examples of iridescence was clearly recognized as interference phenomena by Thomas Young who explained it about a century later in 1801—an important basis for the development of wave theory. Further, this is the basis of the phenomenon of diffraction—which is the resulting interference pattern of waves upon encountering obstacle(s)—first observed and characterized by Grimaldi in the seventeenth century followed by Fresnel's mathematical description in his 1815 publication. A few examples of photonic crystals occurring in nature are shown in Fig. 2.3.

The first observation of an antireflective film is attributed to Fraunhofer who discovered it by chance in 1817 as a result of tarnishing the surface of glass by nitric acid. Subsequently, upon observing the evaporation of a film of alcohol from a glass surface he noted that any transparent material being sufficiently thin will give rise to colour [78]. Similar observations were also made by Lord Rayleigh and further in his 1888 publication, *On the Remarkable Phenomenon of Crystalline Reflexion described by Prof. Stokes*, Lord Rayleigh proposes that bright colours of the chlorate of potash crystal are due to reflections at the twin planes of the crystal and that the fully formed colours are due to the presence of a number of alternating twin planes in the crystal [79]. These observations ultimately led Lord Rayleigh to conclude that the observed colours were a consequence of microscopic structure and hence coining the term structural colours. These basic studies have led to many studies examining multi-layered dielectric thin films including the Bragg mirror.

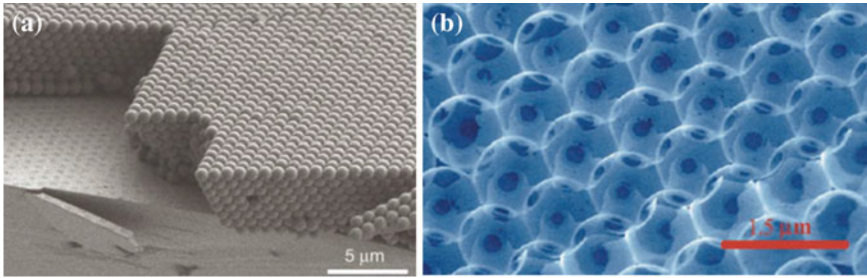

Fig. 2.4 Engineered photonic crystals. **a** Planar opal template using 855 nm spheres on a silicon wafer [80]. **b** Silicon inverse opal photonic crystal, [111] facet, with a complete three-dimensional bandgap near 1.5 μm [81]

A hundred years following the first observation of a 1 dimensional stop-band—a spectral range exhibiting large reflectivity—Yablonovitch and John published two independent papers that served to theoretically establish the possibility of an omni-directional stop-gap or a 3 dimensional photonic band gap [8, 9]. Similar to the periodic potential in semiconductor crystals that give rise to the electronic band structure, it was shown that periodic variation of the dielectric constant gives rise to a photonic band structure that exhibit allowed and disallowed modes of propagation for electromagnetic radiation—and hence the term photonic crystals which represents a class of periodic dielectrics or metallo-dielectrics wherein there are alternating regions of high and low dielectric media in one, two and/or three dimensions. Considering the diffractive basis of the physical effect, photonic crystals in the optical region are nanostructures with periodicity of the order of a fraction of the wavelength of light. Photonic crystals give rise to a whole host of fascinating phenomena which include suppression of spontaneous emission, light localization, photonic band gap, slow photons, the superprism effect, and low-loss waveguiding. A few examples of engineered photonic crystals are shown in Fig. 2.4.

The above outline highlights the foundational developments that have served to establish our understanding of optical and photonic phenomena which are critical for a multitude of optoelectronic applications. We now examine some of the early developments in silicon photovoltaics *vis-à-vis* optical coupling.

Paramount for the attainment of high efficiency operation in any photovoltaic device is complete optical absorption of the supra-bandgap portion of the solar spectrum. Complete optical absorption is challenged by thinning of the absorber material and exacerbated even further in indirect bandgap materials such as silicon. It is therefore clear that the employment of every possible technique that effectively serves to enhance the path length of the light and hence increase the probability of its absorption is essential.

St. John reported that through roughening of the silicon surface the number of internal reflections at the silicon-air interfaces can be increased and thus lead to light trapping and consequent intensity enhancement [82]. While such early studies were motivated by microelectronic applications, Redfield reported that maximizing the number of passes directly impacts the conversion efficiency of silicon solar cells and

accordingly multiple reflections are essential [83]. Yablonovitch and Cody using a statistical mechanical analysis showed that maximum possible enhancement in path length (relative to the thickness of the absorber) is $4n^2$ where n is the index of refraction of the weakly absorbing material such as silicon—having taken into account all oblique angle paths (factor of 2) and reflections from the rear interface (another factor of 2). These studies suggest that so long as the surface is sufficiently strongly textured, random or precisely grooved, an enhancement limit of $4n^2$ can be approached, which is approximately 50 for silicon [84]. Sheng, Bloch and Stepelman subsequently report that the use of 1-D or 2-D periodic patterning can render wavelength-selective absorption in thin film silicon [85]. Sheng et al. exemplify that analogous to the periodic potential in a crystal that gives rise to 'peaks' in the particle/electron density of states at a certain set of frequencies (otherwise referred to as van Hove singularities) and 'gaps' at others, the use of periodic gratings gives rise to a similar set of photon density of states. Through an appropriate selection of grating parameters the resonant photon density of states can be positioned within the optical gap of the material, effectively increasing the number of photon states above the absorption edge albeit at the expense of the states in the neighbouring non-absorbing region. Thus, in the absorbing region the density of states exceeds the n^2 limit and hence yielding further enhancement in light trapping.

The above described represent some of the first key studies that illustrated the enormous potential of modulating the flow of light in silicon solar cells through physical structuring of the absorbing material. A host of studies followed that investigated the use of patterned surfaces, gratings, inverted pyramids, tilted inverted pyramids, metallic back reflectors, introduction of dielectric interlayers between the metallic back reflector and the silicon absorber in an effort to maximize the absorption of the impinging solar radiation. These developments—together with advances in the electronic design of the devices as well as enhancements in device fabrication which have included the development of optimal passivation and effective carrier extraction techniques—have led to record photovoltaic conversion efficiencies in crystalline silicon albeit in relatively thick absorbers. Over the last couple of decades there has been much research to further develop novel photonic constructs at the wavelength and sub-wavelength scale so as to effectively tune spectral localization and thus attain complete optical absorption in both thin crystalline silicon and thin film silicon solar cells. We now examine some of these recent advances in the field.

2.3 Nano Architectures in Silicon Photovoltaics: Recent Advances

2.3.1 Introduction

Today, state-of-the-art commercial crystalline silicon solar cells with record photovoltaic efficiencies in the 22–24 % range have silicon wafer thicknesses in the range

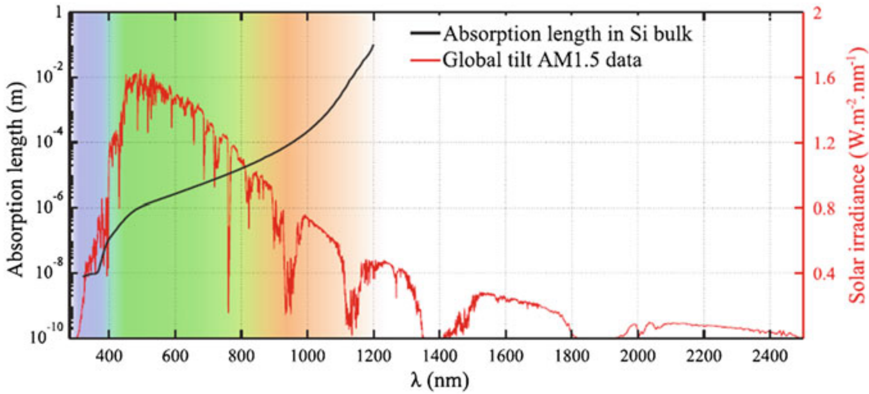

Fig. 2.5 The absorption length of crystalline silicon juxtaposed against the AM1.5G solar irradiance. The *blue*, *green*, and *red* coloured regions indicate the region with the highest optical absorption, the region with the highest solar irradiance, and the region with absorptions lengths in excess of 100 µm, respectively [86]

of 100–150 µm. While this is a remarkable achievement in relation to the foundational developments by Russel Ohl in 1941, recognition of the potential of developing silicon[9] solar cells with comparable efficiencies but some two orders of magnitude thinner has driven research towards the pursuit of a myriad of nano-photonic and plasmonic paradigms. An essential characteristic of this quest is efficacious light trapping and optical absorption so as to attain the ultimate photogenerated charge density and hence conversion efficiency; this is well illustrated in Fig. 2.5 which contrasts the absorption length in crystalline silicon against the AM1.5 solar spectrum.

Much of the research over the last decade has been optical in nature and hence independent of the electrical requirements of the device. Nonetheless, integrated designs have also been investigated and inevitably reveal the magnitude of the challenge. In the following sections we provide a selected overview of some of the recent advances in the field of crystalline silicon and amorphous silicon photonic crystal photovoltaics.

2.3.1.1 Photonic Crystals

The term 'photonic crystal' was coined to reflect the analogous behaviour of electromagnetic waves in three-dimensional periodic dielectric structures [8, 9] with that of electron waves in three-dimensional periodic potentials [87, 88]. Some of the earliest studies in photonic crystals were motivated by the objective of developing photonic bandgap materials that would permit control over radiative emission and light localization and thus usher an era of the three-dimensional all-optical micro-chip —the

[9] As well as other photovoltaic materials.

light computer [10, 89, 90]. These studies, in addition to the existing foundation of spectrally selective interference filters or Bragg stacks, spurred research into nano-structured silicon photonic crystal photovoltaics [91–94]. Within this framework, photonic crystals can be employed in photovoltaic cells in a variety of ways which can be principally divided into two categories. First, where the photonic crystal is outside the photoactive region and serves the function of omni-directional reflection and diffraction of quasi guided-modes into the unpatterned silicon absorber; examples of this application include back-reflector and intermediate reflectors. And second, the photoactive region is patterned into a photonic crystal itself so as to couple light into the quasi-guided modes within the absorber. Both approaches serve to enhance light intensity and hence photoabsorption [95].

2.3.1.2 Photonic Crystals in Crystalline Silicon PV

One of the early theoretical studies reporting on the use of photonic crystals in thin crystalline silicon (c-Si) solar cells by Bermel et al. [38] show that the use of nano-structured elements effect wave-optic light-trapping mechanisms which in contrast to geometric optics can be effectively tuned to enhance absorption in the near infrared part of the spectrum where the absorption coefficient in silicon is low owing to its indirect-gap band structure. Three cell concepts based on 2 μm thick c-Si are considered, as shown in Fig. 2.6. All cell structures consist of the silicon absorber and an anti-reflective coating on the front light-facing side, while the rear surfaces of the cells are structured with different back reflectors. In Fig. 2.6a the back reflector consists of a distributed Bragg reflector (DBR) comprising of ten thick bi-layers of c-Si and SiO_2 having indices of 3.5 and 1.5, respectively, with a period of 150 nm. The DBR parameters are chosen so as to reflect strongly in the near-IR. The overall cell efficiency is reported to be 12.44 % which is comparable to that with a plain aluminum back reflector of 12.72 %. In contrast, in the second design shown in Fig. 2.6b a 1D grating is introduced in the low-index SiO_2 layer immediately adjacent to the c-Si absorber. In addition to reflection, the grating serves to introduce diffractive modes into the absorber and hence extend the path length of the light. Optimization of the structure leads to an eight bilayer DBR having a period of 165 nm and a 1D grating with a period of 264 nm and etch depth of 67 nm for a 2 μm thick c-Si absorber, and hence a conversion efficiency of 15.42 %. The enhancement in absorption in c-Si absorbers ranging from 2 to 32 μm in thickness are shown in Fig. 2.6d. As expected, the enhancement is most significant for the thinnest absorber layer, attaining an almost 5-fold increase in the near-IR absorption. The third design, shown in Fig. 2.6c, replaces the back reflector with an inverse opal photonic crystal comprising the absorber material itself.[10] In this case not only are reflection

[10] An opaline structure consists of silica spheres appropriately close-packed to form a crystalline lattice, while an inverse opal architecture comprises the interstices of the opaline structure appropriately filled with a suitable dielectric material (wherein the spherical volume associated with the opal form the void with relative permittivity of 1).

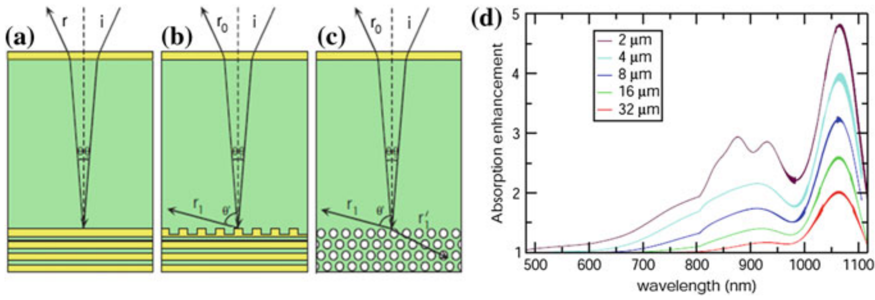

Fig. 2.6 Solar cell structures consisting of crystalline silicon absorber, an antireflective coating on the light facing side, and three different back reflectors. **a** Back reflector consisting of a distributed Bragg reflector. **b** Back reflector comprising a DBR and a 1D grating. **c** Back reflector comprising an inverse opal photonic crystal containing a triangular lattice of air holes. **d** Enhancement in the spectral absorption as a result of introducing a 1D grating into a DBR for c-Si absorber thicknesses ranging from 2 to 32 μm [38]

and diffractive modes contributing to photogeneration, but additional modes that penetrate into the photonic crystal absorber also contribute to the overall absorption. In this instance, the optimized efficiency is 15.73 % with 8 periods. It is worth noting that introduction of an optimized 2D grating however leads to an efficiency of 16.32 % with a 4 bilayer DBR; this structure is referred to as a textured photonic crystal back reflector where the DBR is a 1D photonic crystal. Zeng et al. fabricated a 5 mm thick c-Si photovoltaic device and showed a short circuit current density enhancement of 19 % compared to a 28 % scattering matrix method prediction [96].

In a similar vein, O'Brien et al. [40] demonstrated the use of an opaline photonic crystal (PC) as a back-reflector to enhance the photoabsorption in thin film amorphous silicon (Fig. 2.7a). Through variation of the diameter of silica spheres, ranging from 190 to 343 nm, the [111] stop-gap is tuned from its centered value of $\lambda = 410$ nm to $\lambda = 740$ nm; the opaline photonic crystal has a narrow stopgap of $\Delta\omega/\omega$ of 5.5 % in this direction between the second and third photonic bands. For a 250 nm thick amorphous silicon film an enhancement of 2.5 is observed compared to a scalar wave approximation (SWA) value of 3 (Fig. 2.7b). Further, it is shown that strong resonant modes exist within and outside of the stopgap which occur due to scattering at the photonic crystal surface and that these planar resonant modes propagate along the plane of the film and thus enhance absorption. In a subsequent study, O'Brien et al. [42] report on a similar opaline photonic crystal back reflector adjoining a 10 μm thick crystalline silicon wafer and show a 1.5 fold enhancement in absorption. In this study they also show that the introduction of an intervening electronic element, such as a transparent conducting oxide, in aid of creating a complete photovoltaic device very quickly diminishes the optical benefits of a contiguous photonic crystal back reflector (Fig. 2.7c), thus calling for the need of structuring the conducting back-contact itself in the form of a photonic crystal.

Chutinan et al. [97] investigated the prospect of configuring thin crystalline silicon solar cells such that the absorbing layer is a photonic crystal. The study considers

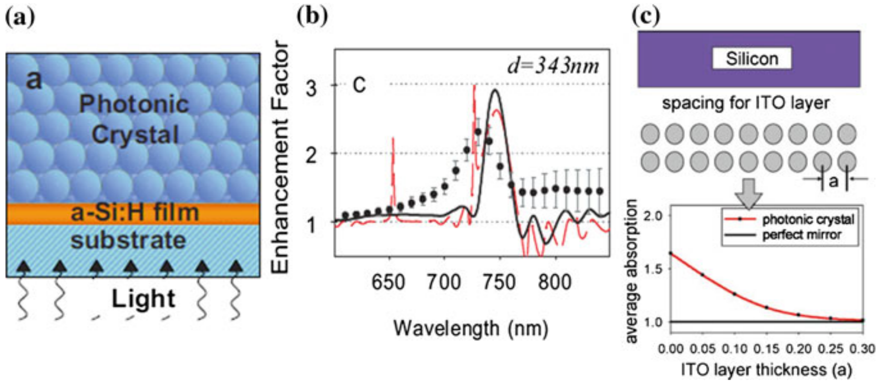

Fig. 2.7 Photonic crystal back reflectors on thin silicon absorbers. **a** Opaline photonic crystal on 250 nm thin a-Si:H film [40]. **b** Enhancement in the photoconductivity of the PC-a-Si:H construct (*d* is the opal diameter, *black curve* is the scalar wave approximation (SWA), and *red curve* is the finite-difference time-domain (FDTD) calculation) [40]. **c** An illustration of the loss in absorption enhancement due to the presence of an intervening indium tin oxide (ITO) layer between the c-Si absorber and PC back reflector [42]

crystalline silicon layers as thin as 2 μm such that the volume of silicon is maintained constant for each cell design for a given thickness. As a reference, optimal standard cell designs are evaluated where the cell comprises an antireflective coating on the light facing (front) side and a grating on the back side along with a perfect back reflector. The 2D photonic crystal cell architecture consists of a square lattice of square silicon rods in an air background (Fig. 2.8a); further, the light facing side has an appropriate light coupler (to couple the incoming light into the photonic crystal). In addition, as in the reference cell, the frontside has an antireflective coating and the backside has a grating and a perfect back reflector. The cell efficiencies of the photonic crystal designs are shown to exceed the standard designs with the greatest increase realized for the 2 μm case—the PC design showing an overall efficiency increase of 11 % over the standard design.

Mallick et al. [98] also investigated 2D silicon photonic crystal architectures albeit with an even thinner crystalline silicon thickness of 400 nm. The design consists of a double layer silicon photonic crystal architecture (Fig. 2.8b). The active double layer has an antireflection coating on the front side and a 400 nm thick SiO_2 layer on the back side, along with a metal layer that ensures double-pass reflection. A square lattice of cylindrical holes are introduced in the double layer 2D PC; the top layer has a set of holes which are smaller in diameter relative to those in the bottom layer, thus providing a greater degree of freedom in attaining an optimal design. The antireflective coating on the top along with the upper layer PC is also perforated. The optimal structure exhibits an average enhancement in absorption of approximately 2.5 compared to a standard flat cell with equivalent volume of c-Si when averaged over all angles; the maximum achievable photocurrent density increases 3.1 fold from 7.1 to 21.8 mA/cm^2 in comparison to the Yablonovitch limit of 26.5 mA/cm^2.

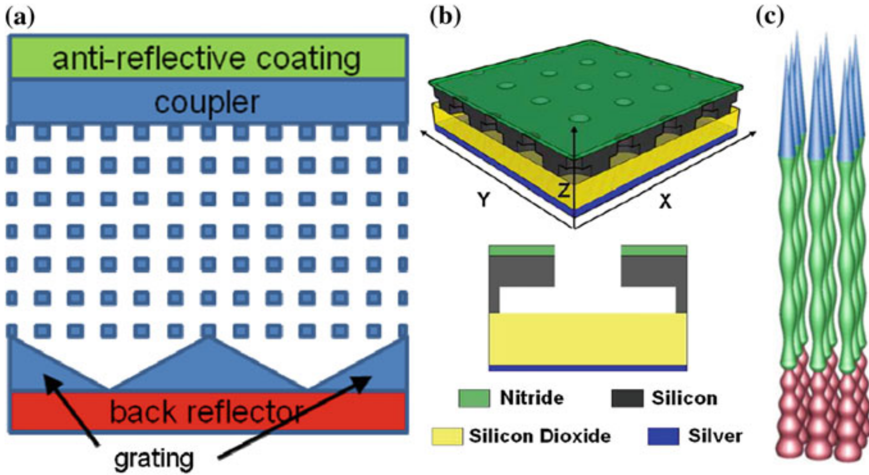

Fig. 2.8 Silicon photonic crystal absorbers. **a** 2D PC square lattice of square rods [97]. **b** 2D double layer photonic crystal lattice of holes [98]. **c** Radius-modulated nanowire integrating nanocones for antireflection, cubic photonic crystal for parallel interface refraction, and photonic back reflector [86]

Demesy et al. [86] have recently reported a silicon nanowire photonic crystal architecture that through nanostructuring integrates the optical effects of antireflection, light trapping and back reflection (Fig. 2.8c). Using a 1 μm thick crystalline silicon layer, the active region is shaped into a 3D simple-cubic photonic crystal consisting of radius-modulated silicon nanowires embedded within SiO_2 and placed on a quartz substrate. The top of the nanowires facing the incoming light are conical in shape with a linear change in radius wherein the nanocones provide effective broadband coupling of the incident light as well as good absorption at short wavelengths. The mid-section of the nanowire is a simple cubic photonic crystal that exhibits effective light trapping owing to parallel interface refraction resonances [99], deflecting light laterally into slow group velocity modes, thus leading to up to 150 fold enhancement in light intensity. The bottom section of the nanowire is shaped to create a 1D photonic back reflector. The modulated silicon nanowire photonic crystal structure is shown to trap and absorb approximately 75 % of the incident solar radiation in the 400–1,200 nm range. In a subsequent study, Deinega et al. [100] investigate this architecture for optimal junction and contact geometries, having solved Maxwell's equations and the continuity-transport equations, and show a 20 % enhancement in conversion efficiency compared to an equivalent volume of plain silicon.

In concluding this section it is important to note that while the above investigations highlight the salient aspects of integrating photonic crystals in silicon photovoltaics, there is an enormous body of recent allied research that is worthy of mention. We direct the interested readers to a selected set of publications in the open literature including some of the earliest research into coherent scattering of light in photovoltaics [101–105]. Moreover, we also point the readers to a body of research on

patterning of silicon surfaces including recent forays into nano-structuring where wave-optic light coupling techniques are being explored to effect light trapping in silicon PV [106–111].

2.3.1.3 Photonic Crystals in Thin Film Silicon PV

In contrast to crystalline silicon photovoltaics, which is a predominantly wafer based platform, thin film silicon photovoltaics is an essentially bottom-up low-temperature synthesis approach encompassing single and multiple junction hydrogenated amorphous silicon solar cells as well as the so-called dual-junction micromorph cell. Amicromorph cell consists of a hydrogenated amorphous silicon (a-Si:H) top-cell with a bandgap of ∼1.7 eV and a micro/nano-crystalline silicon (μc-Si:H) bottom-cell with a bandgap of ∼1.1 eV. The all-silicon micromorph thin film cell[11] has the potential of attaining the near-term target of a stabilized photovoltaic conversion efficiency exceeding 15 %, however, effective light harvesting and device engineering are required; it is noteworthy that theoretical efficiencies are predicted to be at least a factor of two higher [112].

The thin film micromorph device consists of the a-Si:H and μc-Si:H cells connected in series such that the output voltage of the micromorph is the sum of its two individual component cells. An essential requirement for optimal energy conversion in such multi-junction cells is matched cell current densities. The micromorph cells are top-limited, that is, their output is limited by the relatively lower current density generated in the top a-Si:H cell as compared to the higher current density generated by the bottom μc-Si:H based cell. While the top cell current density can be amplified by increasing its cell thickness, a thicker a-Si:H cell inevitably suffers from light induced degradation as a result of the Staebler-Wronski effect (SWE) and associated drop in the internal electric field intensity. Light trapping schemes have been implemented to increase photon absorption in the upper a-Si:H cell.

One commonly used strategy is to deposit a transparent conducting oxide (TCO) layer between the a-Si:H and μc-Si:H junctions. In this configuration the TCO layer acts as an intermediate reflector (IR), ideally causing Fabry-Perot oscillations that return incident photons of energy greater than ∼1.7 eV to the a-Si:H cell in order to enhance the current generated in the upper cell while transmitting photons of lesser energy to the underlying μc-Si:H cell.

A variety of materials and structures as possible alternatives for the fabrication of effective intermediate reflectors (IRs) have recently been investigated. Asymmetrically textured ZnO IRs, wherein the top surface has feature sizes of ∼300 nm to efficiently scatter blue-green light while the bottom surface has larger features to

[11] 'All-silicon' emphasizes the intrinsic hydrogenated amorphous silicon and intrinsic microcrystalline silicon absorber layers in the top and bottom cells, respectively, and the fact that there is typically no germanium alloying for bandgap engineering. The occlusion of germanium in amorphous silicon has been used to successfully fabricate triple-junction thin film amorphous Si cells; however this approach is fraught with a whole host of challenges and the micromorph is deemed to be a more promising alternative.

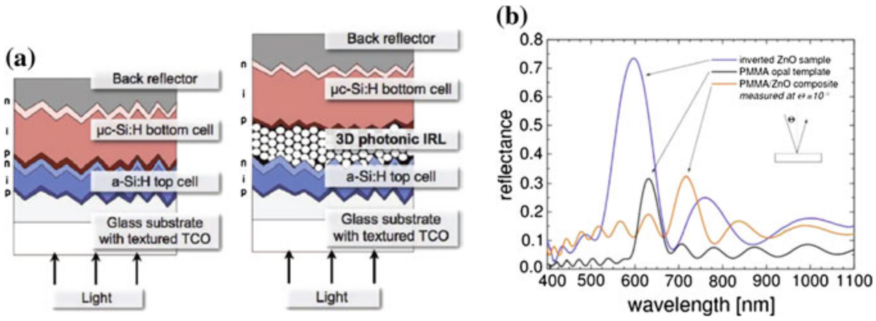

Fig. 2.9 Three dimensional photonic crystal intermediate reflector in the micromorph cell. **a** Schematic diagrams of the standard micromorph cell without an intermediate reflector and with an inverted opal photonic crystal intermediate reflector [44]. **b** Spectral reflectance profile of the inverted ZnO opal contrasted against the reflectance spectra of PMMA opaline PC and the PMMA composite wherein the interspaces are infiltrated with ZnO [41]

scatter red light, have been used to fabricate 11.2 % (initial) efficient micromorph cells on flexible plastic substrates [113]. Another approach has been to fabricate micromorph cells with doped silicon oxide IRs (SOIRs), motivated by the advantage of being able to deposit SOIRs in one and the same reactor as the micromorph cell itself; first cell with conversion efficiency of 12.2 % (initial) has been reported [114].

More recently, Bielawny et al. have proposed the utilization of three-dimensional photonic crystal IRs in the form of inverted aluminum doped zinc oxide (ZnO:Al) opals [41, 44, 93]. The 3D PC IR in a micromorph cell is illustrated in Fig. 2.9a. The top a-Si:H cell is grown conformally over the textured TCO on glass substrate followed by the synthesis of the inverted ZnO:Al opaline PC. The bottom µc-Si:H cell and a back contact which doubles as an optical reflector are deposited subsequently to complete the device fabrication. Typical measured spectral reflectance for the inverted ZnO:Al opal is shown in Fig. 2.9b, indicating the potential of high broadband enhancement in light trapping. The measured reflectance spectra for polymethyl-metacrylate (PMMA) and PMMA-ZnO:Al composite are also shown and suggest the PC synthesis process steps. Detailed analysis have shown that the PC provides photonic stop gap reflectance as well as diffractive modes, resulting in the overall enhancement of the photocurrent density in the top cell. Experimentally, an enhancement in the short circuit current density of the amorphous silicon top cell of 24.5 % has been reported which compares well with the theoretical prediction of 28 %.

In contrast, O'Brien et al. have carried out a comparative investigation of photonic crystal intermediate reflectors utilizing µc-Si/ZnO Bragg-reflector constructs and ZnO inverted opals in micromorph cells [115]. The cell configurations with the µc-Si/ZnO Bragg-reflector and ZnO inverted opal intermediate reflectors are shown in Fig. 2.10a, b, respectively. The top a-Si:H cell is 100 nm thick while the bottom microcrystalline cell is infinitely thick; use of a 2 µm thick µc-Si:H cell shows only a 1 % relative increase in the top cell current. The absorption/reflectance profiles for

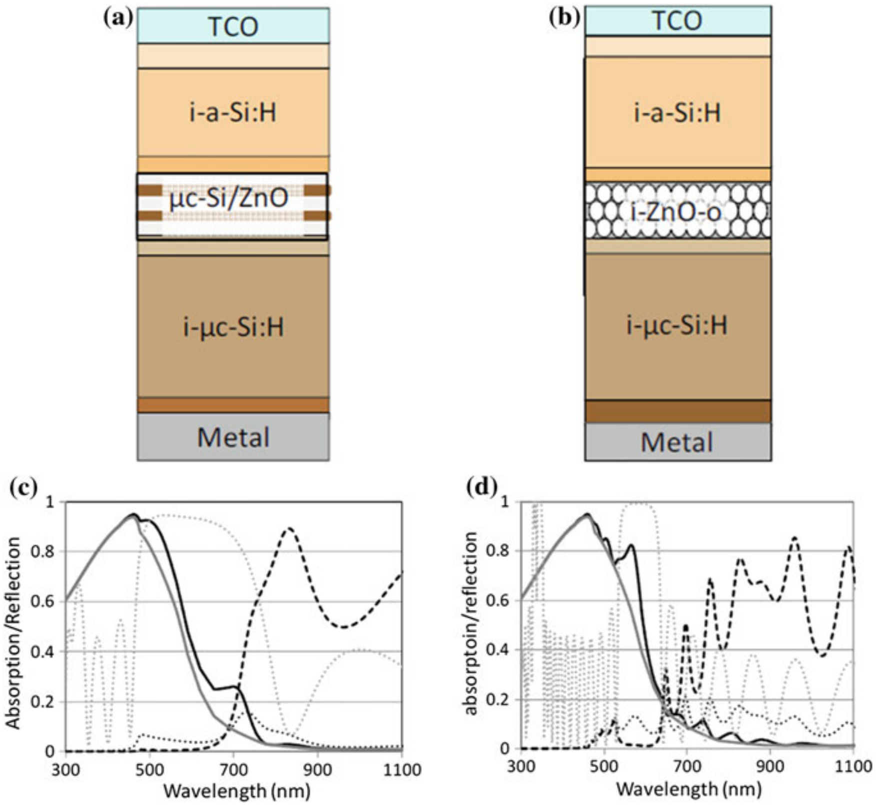

Fig. 2.10 Micromorph cells utilizing photonic crystals as intermediate reflectors. **a** Schematic diagrams of micromorph cells using a ZnO/μc-Si:H Bragg-reflector IR (**a**) and a ZnO inverted opal IR (**b**). Absorption and reflection profiles for the two cell configurations are shown in (**c**) and (**d**), respectively. The absorption spectrum for the top 100 nm thick a-Si:H cell in a reference micromorph tandem cell without an IR is shown as a *solid grey line* in (**c**) and (**d**). The absorption spectra for the top 100 nm thick a-Si:H in cells (**a**) and (**b**) are shown as *solid black lines* in (**c**) and (**d**), respectively. The absorption in the PCs and the underlying μc-Si:H cells are shown as the *dotted* and *dashed black lines*, respectively. The reflectance from a three and half bilayer ZnO/μc-Si:H Bragg-reflector and reflectance from a 13-layered ZnO inverted opal reflector, similar to configurations where the medium above and below the reflector is air and μc-Si:H, respectively, are plotted as *dotted grey lines*, respectively; absorption of the IRs in these reflectance spectra have been neglected in order to emphasize their reflectance peaks [115]

the μc-Si/ZnO Bragg-reflector and ZnO inverted opal IR based micromorph cells are shown in Fig. 2.10c, d, respectively. Both cell configurations indicate enhanced absorption in the top cell relative to that in a reference micromorph cell without an IR. The μc-Si/ZnO Bragg-reflector IR based micromorph cell indicates a 20 % increase in the top cell current while the ZnO inverted opal IR based micromorph cell shows a 13 % increase in its top cell current. The larger increase with the Bragg IR based cell is due to its larger stop-gap (evident by reflectance of the PC IRs represented by the

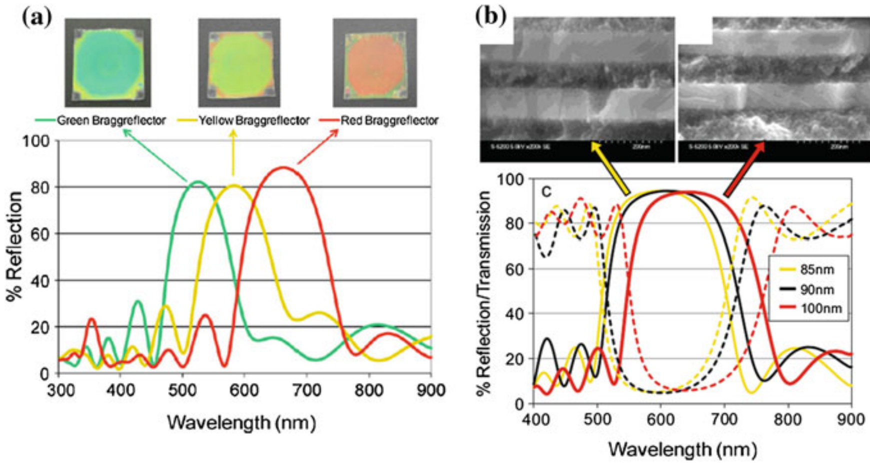

Fig. 2.11 Reflectance/transmittance spectra of 1D selectively transparent and conducting photonic crystals synthesized from bilayers of nanoparticle and transparent conducting oxide films. **a** Reflectance spectra, and corresponding photographs, of *red*, *yellow* and *green* STCPCs with Bragg peak's at approximately 670, 580 and 520 nm, respectively; these STCPCs were fabricated using antinomy tin oxide nanoparticles and indium tin oxide films. **b** Reflectance (*solid*) and transmittance (*dashed*) spectra of 5 bilayer STCPCs having equivalent ITO film thicknesses of 85, 90 and 100 nm; SEM cross-sectional viewgraphs of STCPS with 85 and 100 nm thicknesses are shown above the plot [43, 45]

grey dotted lines in Fig. 2.10c, d with $\Delta\omega/\omega$ of ~45 % for the Bragg and ~14 % for the opal IRs, respectively), the Bragg IR being optically thinner, and the opaline IR exhibiting greater absorption losses. Specifically, the Bragg IR micromorph shows a photogenerated current density of 13.8 mA/cm^2 in the top cell and 14.9 mA/cm^2 in the bottom cell.

More recently O'Brien et al. have reported the development of conducting photonic crystals, also known as selectively transparent and conducting photonic crystal (STCPC), amenable to a variety of optoelectronic devices including silicon micromorph solar cells [43]. The 1D STCPCs consist of bilayers of sub-wavelength nanoparticles and transparent conducting films each of the order of 100 nm in thickness which together provide the index contrast and an electrically continuous structure. In their first report, the STCPCs specifically consisted of 25 nm antimony tin oxide (ATO) nanoparticle films and sputtered indium tin oxide (ITO) films. The reflectance spectra of these STCPCs are shown in Fig. 2.11a, illustrating the wide band tunability of these conducting photonic crystals that have sheet resistances of less than 88 Ω/□ and 55 Ω/□ for 3.5 and 5.5 bilayers, respectively. In a subsequent development, the properties of the STCPCs are improved further through the utilization of 10 nm silica nanoparticles which serve to increase the index contrast as well as overcome the parasitic absorption losses in the ATO nanoparticles [45]. The reflectance spectra of these silica nanoparticle STCPCs, shown in Fig. 2.11b, indicate peak transmissivities of 95 % with significantly wider reflection bands that are easily

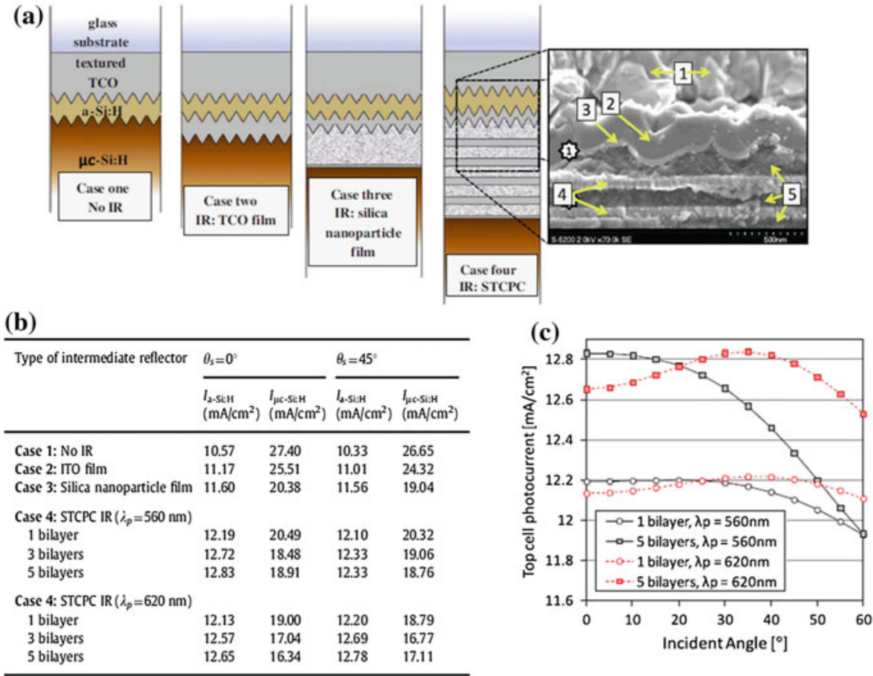

Type of intermediate reflector	$\theta_s=0°$		$\theta_s=45°$	
	$I_{a\text{-}Si:H}$ (mA/cm²)	$I_{\mu c\text{-}Si:H}$ (mA/cm²)	$I_{a\text{-}Si:H}$ (mA/cm²)	$I_{\mu c\text{-}Si:H}$ (mA/cm²)
Case 1: No IR	10.57	27.40	10.33	26.65
Case 2: ITO film	11.17	25.51	11.01	24.32
Case 3: Silica nanoparticle film	11.60	20.38	11.56	19.04
Case 4: STCPC IR (λ_p=560 nm)				
1 bilayer	12.19	20.49	12.10	20.32
3 bilayers	12.72	18.48	12.33	19.06
5 bilayers	12.83	18.91	12.33	18.76
Case 4: STCPC IR (λ_p=620 nm)				
1 bilayer	12.13	19.00	12.20	18.79
3 bilayers	12.57	17.04	12.69	16.77
5 bilayers	12.65	16.34	12.78	17.11

Fig. 2.12 **a** Schematic diagram of the micromorph cells with different intermediate reflectors examined using the scattering matrix method. The reference case has no IR while cases 2–4 consist of an ITO film IR, silica nanoparticle film IR, and STCPC IR, respectively. The SEM cross-sectional view corresponding to case 4 illustrates the planarizing effect of the silica nanoparticles; in this figure, *1* is the textured TCO, *2* is the 150 nm thick a-Si:H film, *3* is the conformal 50 nm thick ITO film, *4* points to the ITO films within the STCPC and *5* points to the silica nanoparticle films also within the STCPC. **b** Summary of the short-circuit current densities in the top a-Si:H cell and the bottom μc-Si:H cell for AM1.5 illumination at normal incidence and at 45° from the normal corresponding to the different cases illustrated in (**a**). **c** The top cell short circuit current densities as a function of the angle of incidence for micromorph cells with different STCPC IRs [45]

tuned. Further, contrary to conventional wisdom, the electrical conductivity of these films is even greater with sheet resistance of 15 Ω/□ for 5.5 bilayer structures; the development of a continuous electrical pathway is attributed to infiltration and percolation of ITO in the interstices of the essentially close-packed silica nanoparticle films and any shunts due to imperfections/holes in the nanoparticle films.

Integration of these STCPCs as intermediate reflectors in micromorph cells have been investigated using the scattering matrix method and compared against the reference cases of no intermediate reflector, an ITO thin film IR and a silica nanoparticle film IR. A schematic of the four cases is shown in Fig. 2.12a and a corresponding summary of the photogenerated current densities is shown in Fig. 2.12b. Incorporation of STCPC IRs leads to photocurrent density enhancements in top cell, relative to the case of no IR, of 15.3, 20.3 and 21.4 % for 1, 3 and 5 bilayer STCPCs, respectively,

where the Bragg peak is at 560 nm and the 1 sun illumination is at normal incidence. Photocurrent enhancements are also evident for off-normal incidence of 45° and in particular the enhancement is equally large for STCPCs tuned with a Bragg peak at 620 nm. The photocurrent densities in the top cell as a function of the incidence angle, for STCPCs with the two Bragg peaks, are shown in Fig. 2.12c; the curves indicate the ability to tune STCPCs to attain directionally-invariant enhancement. It is also interesting to observe the planarizing effect of the STCPC (see Fig. 2.12a, case 4); specifically, the silica nanoparticles fill the texture in the underlying TCO on the glass substrate and thus present a much smoother surface for the growth of microcrystalline silicon with potentially ameliorative implications.

The above presentation highlights some of the recent efforts to integrate photonic crystals in thin film silicon photovoltaics. As in the crystalline silicon case, significant research into various surface patterning constructs to effect light trapping have been carried out and we direct the interested reader to a selected set of articles in this body of literature [116–119]. We also point the interested reader toward allied integration of photonic crystals and nanostructures in other photovoltaic material systems [120–123].

2.4 Future Outlook

The remarkable surge of fundamental research activity in the field of nanostructured materials over the last decade coupled with the effort to apply these emerging basic insights to photovoltaics bodes favourably for the ultimate attainment of versatile and economic generation of solar electricity. Ground breaking research activities in plasmonic metamaterials, use of topology optimization techniques based on genetic algorithms, and the drive towards monolithic integration is expected to create an exciting future for a range of photovoltaic materials including silicon [124–126]. It is anticipated that silicon will continue to evolve in its applicability with new advances in science and technology considering its obvious advantages, mature manufacturing platform and its abundance.

Acknowledgments The author gratefully acknowledges copyright holders' granting permission to reproduce selective figures and tables (which have been clearly cited) in this chapter.

References

1. J.C. Maxwell, Proc. R. Soc. Lond. A **13**, 531 (1864)
2. J.C. Maxwell, Philos. Trans. R. Soc. B **155**, 459 (1865)
3. R.P. Feynman, *Quantum Electrodynamics* (W. A. Benjamin, New York, 1961)
4. C. Cohen-Tannoudji, J. Dupont-Roc, G. Grynberg, *Photons and Atoms: Introduction to Quantum Electrodynamics* (Wiley, New York, 1989)
5. V.G. Veselago, Sov. Phys. Uspekhi-Ussr **10**, 509 (1968)

6. D.R. Smith, J.B. Pendry, M.C.K. Wiltshire, Science **305**, 788 (2004)
7. M. Memarian, G.V. Eleftheriades, Light Sci. Appl. **2**, e114 (2013)
8. S. John, Phys. Rev. Lett. **58**, 2486 (1987)
9. E. Yablonovitch, Phys. Rev. Lett. **58**, 2059 (1987)
10. J.D. Joannopoulos, S.G. Johnson, J.N. Winn, R.D. Meade, *Photonic Crystals: Molding the Flow of Light*, 1st edn. (Princeton University Press, Princeton, 1995) (2nd edn, 2008)
11. D.W. Prather, S. Shi, A. Sharkawy, J. Murakowski, G.J. Schneider, *Photonic Crystals: Theory, Applications, and Fabrication* (Wiley, Hoboken, 2009)
12. V.M.N. Passaro, *Advances in Photonic Crystals* (InTech, Rijeka, 2013)
13. W.L. Barnes, A. Dereux, T.W. Ebbesen, Nature **424**, 824 (2003)
14. H.A. Atwater, Sci. Am. **296**, 56 (2007)
15. S.A.A. Maier, *Plasmonics: Fundamentals and Applications* (Springer, New York, 2007)
16. G. Cao, *Nanostructures and Nanomaterials: Synthesis, Properties and Applications* (Imperial College Press, London, 2004)
17. G.A. Ozin, A.C. Arsenault, L. Cademartiri, *Nanochemistry: A Chemical Approach to Nanomaterials* (Royal Society of Chemistry, Cambridge, 2009)
18. E. Becquerel, Comptes rendus de l'Académie des Sciences **9**, 561 (1839)
19. D.M. Chapin, C.S. Fuller, G.L. Pearson, J. Appl. Phys. **25**, 676 (1954)
20. M.A. Green, Prog. Photovoltaics **17**, 183 (2009)
21. M. Taguchi, A. Yano, S. Tohoda, K. Matsuyama, Y. Nakamura, T. Nishiwaki, K. Fujita, E. Maruyama, IEEE J. Photovoltaics **4**, 96 (2013)
22. A. Luque, S.E. Hedgedus, *Handbook of Photovoltaic Science and Technology* (Wiley, Chichester, 2011)
23. A. McEvoy, T. Markvart, L. Castañer, *Solar Cells: Materials, Manufacture and Operation* (Elsevier, Amsterdam, 2013)
24. M.A. Green, K. Emery, Y. Hishikawa, W. Warta, E.D. Dunlop, Prog. Photovoltaics **21**, 1 (2013)
25. K.E. Kalyanasundaram, *Dye-Sensitized Solar Cells* (EPFL Press, Lausanne, 2010)
26. A. Yella, H.W. Lee, H.N. Tsao, C.Y. Yi, A.K. Chandiran, M.K. Nazeeruddin, E.W.G. Diau, C.Y. Yeh, S.M. Zakeeruddin, M. Gratzel, Science **334**, 629 (2011)
27. L.Y. Han, A. Islam, H. Chen, C. Malapaka, B. Chiranjeevi, S.F. Zhang, X.D. Yang, M. Yanagida, Energy Environ. Sci. **5**, 6057 (2012)
28. N. Tétreault, M. Grätzel, Energy Environ. Sci. **5**, 8506 (2012)
29. C. Brabec, V. Dyakonov, U. Scherf, (eds.), *Organic Photovoltaics: Materials, Device Physics, and Manufacturing Technologies* (WILEY-VCH, Weinheim, 2008)
30. M. Wright, A. Uddin, Sol. Energy Mater. Sol. Cells **107**, 87 (2012)
31. A.G. Pattantyus-Abraham, I.J. Kramer, A.R. Barkhouse, X.H. Wang, G. Konstantatos, R. Debnath, L. Levina, I. Raabe, M.K. Nazeeruddin, M. Gratzel, E.H. Sargent, Acs Nano **4**, 3374 (2010)
32. O.E. Semonin, J.M. Luther, S. Choi, H.Y. Chen, J.B. Gao, A.J. Nozik, M.C. Beard, Science **334**, 1530 (2011)
33. J. Burschka, N. Pellet, S.J. Moon, R. Humphry-Baker, P. Gao, M.K. Nazeeruddin, M. Gratzel, Nature **499**, 316 (2013)
34. M.Z. Liu, M.B. Johnston, H.J. Snaith, Nature **501**, 395 (2013)
35. A.E. Al-Ahmadi, *Quantum Dots—A Variety of New Applications* (InTech, Rijeka, 2012)
36. L. Mangolini, E. Thimsen, U. Kortshagen, Nano Lett. **5**, 655 (2005)
37. M.L. Mastronardi, E.J. Henderson, D.P. Puzzo, Y.L. Chang, Z.B. Wang, M.G. Helander, J.H. Jeong, N.P. Kherani, Z.H. Lu, G.A. Ozin, Small **8**, 3647 (2012)
38. P. Bermel, C. Luo, L. Zeng, L.C. Kimerling, J.D. Joannopoulos, Opt. Express **15**, 16986 (2007)
39. A. Polman, H.A. Atwater, Nat. Mater. **11**, 174 (2012)
40. P.G. O'Brien, N.P. Kherani, S. Zukotynski, G.A. Ozin, E. Vekris, N. Tetreault, A. Chutinan, S. John, A. Mihi, H. Miguez, Adv. Mater. **19**, 4177 (2007)

41. A. Bielawny, J. Upping, P.T. Miclea, R.B. Wehrspohn, C. Rockstuhl, F. Lederer, M. Peters, L. Steidl, R. Zentel, S.M. Lee, M. Knez, A. Lambertz, R. Carius, Phys. Status Solidi A-Appl. Mater. Sci. **205**, 2796 (2008)
42. P.G. O'Brien, N.P. Kherani, A. Chutinan, G.A. Ozin, S. John, S. Zukotynski, Adv. Mater. **20**, 1577 (2008)
43. P.G. O'Brien, D.P. Puzzo, A. Chutinan, L.D. Bonifacio, G.A. Ozin, N.P. Kherani, Adv. Mater. **22**, 611 (2010)
44. J. Upping, A. Bielawny, R.B. Wehrspohn, T. Beckers, R. Carius, U. Rau, S. Fahr, C. Rockstuhl, F. Lederer, M. Kroll, T. Pertsch, L. Steidl, R. Zentel, Adv. Mater. **23**, 3896 (2011)
45. P.G. O'Brien, Y. Yang, A. Chutinan, P. Mahtani, K. Leong, D.P. Puzzo, L.D. Bonifacio, C.W. Lin, G.A. Ozin, N.P. Kherani, Sol. Energy Mater. Sol. Cells **102**, 173 (2012)
46. M. Fischer, A. Metz, S. Raithel, Semi international technology roadmap for photovoltaics (itrpv)—challenges in c-si technology for suppliers and manufacturers. Proceedings of 27th European photovoltaic solar energy conference, p. 527 (2012)
47. D.M. Powell, M.T. Winkler, H.J. Choi, C.B. Simmons, D.B. Needleman, T. Buonassisi, Energy Environ. Sci. **5**, 5874 (2012)
48. W. Smith, Nature **7**, 303 (1873)
49. W.G. Adams, R.E. Day, Proc. R. Soc. Lond. A **A25**, 113 (1877)
50. A. Mumtaz, G. Amaratunga, Solar energy: photovoltaic electricity generation. *Future Electricity Technologies and Systems* (Cambridge Univesity Press, Cambridge, 2006)
51. C.E. Fritts, Am. J. Sci. **26**, 465 (1883)
52. R.S. Ohl, US Patent 2402662 (1946)
53. M. Wolf, Historical development of solar cells, ed. by C.E. Backus. *Solar Cells* (IEEE Press, Piscatway, 1976)
54. R.A. Sinton, Y. Kwark, J.Y. Gan, R.M. Swanson, IEEE Electron Device Lett. **7**, 567 (1986)
55. IEA photovoltaic power systems programme annual report (2012)
56. M.A. Green, *Silicon Solar Cells: Advanced Principles & Practice* (University of New South Wales, Center for Photovoltaic Devices and Systems, 1995)
57. A. Goetzberger, J. Knobloch, B. Voss, Crystalline Silicon Solar Cells (Willey, New York, 1998)
58. T. Saga, NPG Asia Mater. **2**, 96 (2010)
59. W.E. Spear, P.G. Lecomber, Solid State Commun. **17**, 1193 (1975)
60. D.E. Carlson, C.R. Wronski, Appl. Phys. Lett. **28**, 671 (1976)
61. S. Guha, High-efficiency triple-junction amorphous silicon alloy photovoltaic technology, National Renewable Energy Laboratory, NREL/SR-520-26648 (1999)
62. S. Veprek, V. Marecek, Solid-State Electron. **11**, 683 (1968)
63. M. Yoshimi, T. Sasaki, T. Sawada, T. Suezaki, T. Meguro, T. Matsuda, K. Santo, K. Wadano, M. Ichikawa, A. Nakajima, K. Yamamoto, High efficiency thin film silicon hybrid solar cell module on 1 m2-class large area substrate, in *3rd World Conference on Photovoltaic Energy Conversion* (2003)
64. S.W. Ahn, S.E. Lee, H.M. Lee, Toward commercialization of triple-junction thin-film silicon solar panel with >12% efficiency, in *27th European Photovoltaic Solar Energy Conference* (2012)
65. M. Tanaka, M. Taguchi, T. Matsuyama, T. Sawada, S. Tsuda, S. Nakano, H. Hanafusa, Y. Kuwano, Jpn. J. Appl. Phys. Part 1-Regul. Pap. Short Notes Rev. Pap. **31**, 3518 (1992)
66. S. De Wolf, A. Descoeudres, Z.C. Holman, C. Ballif, Green **2**, 7 (2012)
67. K.S. Ji, H. Syn, J. Choi, H.M. Lee, D. Kim, in *Tech. Digest 21st International Photovoltaic Science and Engineering Conference*, Fukuoka, Japan (2011)
68. N. Mingirulli, J. Haschke, R. Gogolin, R. Ferre, T.F. Schulze, J. Dusterhoft, N.P. Harder, L. Korte, R. Brendel, B. Rech, Physica Status Solidi-RRL **5**, 159 (2011)
69. M. Mews, T.F. Schulze, N. Mingirulli, L. Korte, Appl. Phys. Lett. 102, 122106 (2013)
70. B. Hoex, J. Schmidt, P. Pohl, M.C.M. van de Sanden, W.M.M. Kessels, J. Appl. Phys. **104**, (2008)
71. D.S. Stepanov, N.P. Kherani, Appl. Phys. Lett. **101**, 171602 (2012)

72. Z.R. Chowdhury, K. Cho, N.P. Kherani, Appl. Phys. Lett. **101**, 221110 (2012)
73. E. Kheirandish, *The Arabic Version of Euclid's Optics* (Edited and translated with historical introduction and commentray) (Springer, New York, 1999)
74. J.B. Keller, Bull. Amer. Math. Soc. **84**, 727 (1978)
75. K.B. Wolf, G. Krötzsch, Eur. J. Phys. **16**, 14 (1995)
76. Y.Z. Li, Z.H. Lu, H.W. Yin, X.D. Yu, X.H. Liu, J. Zi, Phys. Rev. E **72**, 010902 (2005)
77. P. Vukusic, J.R. Sambles, Nature **424**, 852 (2003)
78. H.A. Macleod, *Thin-Film Optical Filters* (Institute of Physics Publishing, Bristol, 2001)
79. J.W. Strutt (Lord Rayleigh), Phil. Mag. S. 5, **26**, 256 (1888)
80. Y.A. Vlasov, X.Z. Bo, J.C. Sturm, D.J. Norris, Nature **414**, 289 (2001)
81. A. Blanco, E. Chomski, S. Grabtchak, M. Ibisate, S. John, S.W. Leonard, C. Lopez, F. Meseguer, H. Miguez, J.P. Mondia, G.A. Ozin, O. Toader, H.M. van Driel, Nature **405**, 437 (2000)
82. A.E. St. John, U.S. Patent 3 487 223 (1969)
83. D. Redfield, Appl. Phys. Lett. **25**, 647 (1974)
84. E. Yablonovitch, G.D. Cody, IEEE Trans. Electron Devices **29**, 300 (1982)
85. P. Sheng, A.N. Bloch, R.S. Stepleman, Appl. Phys. Lett. **43**, 579 (1983)
86. G. Demesy, S. John, J. Appl. Phys. **112**, 074326 (2012)
87. E. Yablonovitch, J. Mod. Opt. **41**, 173 (1994)
88. R.D. Meade, K.D. Brommer, A.M. Rappe, J.D. Joannopoulos, Phys. Rev. B **44**, 10961 (1991)
89. K.M. Ho, C.T. Chan, C.M. Soukoulis, Phys. Rev. Lett. **65**, 3152 (1990)
90. B.E. Chomski, S. Johh, C.L. Fernandez, J.F.M. Rico, G.A. Ozin, PCT Application: PCT/CA2001/000049 (2001)
91. L.C. Kimerling, N. Toyoda, W. Kazumi, PCT/US2002/020028 (2002)
92. X. Duan, L.C. Kimerling, Y. Yi, L. Zeng, PCT/US2005/027264 (2005)
93. R.B. Wehrspohn, Applications of silicon-based photonic crystals. Appl. Phys. Lett. **87**, 224106 (2005)
94. M. Peters, J.C. Goldschmidt, P. Loper, B. Gross, J. Upping, F. Dimroth, R.B. Wehrspohn, B. Blasi, Energies **3**, 171 (2010)
95. S.B. Mallick, N.P. Sergeant, M. Agrawal, J.Y. Lee, P. Peumans, MRS Bull. **36**, 453 (2011)
96. L. Zeng, P. Bermel, Y. Yi, B.A. Alamariu, K.A. Broderick, J. Liu, C. Hong, X. Duan, J. Joannopoulos, L.C. Kimerling, Appl. Phys. Lett. **93**, 221105 (2008)
97. A. Chutinan, N.P. Kherani, S. Zukotynski, Opt. Express **17**, 8871 (2009)
98. S.B. Mallick, M. Agrawal, P. Peumans, Opt. Express **18**, 5691 (2010)
99. A. Chutinan, S. John, Phys. Rev. A **78**, 023825 (2008)
100. A. Deinega, S. John, J. Appl. Phys. **112**, 074326 (2012)
101. S.E. Han, G. Chen, Nano Lett. **10**, 4692 (2010)
102. S.K. Karuturi, L.J. Liu, L.T. Su, A. Chutinan, N.P. Kherani, T.K. Chan, T. Osipowicz, A.I.Y. Tok, Nanoscale **3**, 4951 (2011)
103. A. Oskooi, P.A. Favuzzi, Y. Tanaka, H. Shigeta, Y. Kawakami, S. Noda, Appl. Phys. Lett. **100**, 181110 (2012)
104. S. Nishimura, N. Abrams, B.A. Lewis, L.I. Halaoui, T.E. Mallouk, K.D. Benkstein, J. van de Lagemaat, A.J. Frank, J. Am. Chem. Soc. **125**, 6306 (2003)
105. A. Mihi, H. Miguez, J. Phys. Chem. B **109**, 15968 (2005)
106. S.H. Zaidi, J.M. Gee, D.S. Ruby, S.R.J. Brueck, Characterization of si nanostructured surfaces, ed. by A. Lakhtakia, R.F. Messier (eds). Engineered Nanostructural Films and Materials, vol. 3790 (Spie-Int Soc Optical Engineering, Bellingham, 1999), p. 151
107. S.E. Han, G. Chen, Nano Lett. **10**, 1012 (2010)
108. X. Sheng, J.F. Liu, N. Coronel, A.M. Agarwal, J. Michel, L.C. Kimerling, IEEE Photonics Technol. Lett. **22**, 1394 (2010)
109. A. Mavrokefalos, S.E. Han, S. Yerci, M.S. Branham, G. Chen, Nano Lett. **12**, 2792 (2012)
110. K.X.Z. Wang, Z.F. Yu, V. Liu, Y. Cui, S.H. Fan, Nano Lett. **12**, 1616 (2012)
111. K. Kumar, K.K.C. Lee, P.R. Herman, J. Nogami, N.P. Kherani, Appl. Phys. Lett. **101**, 222106 (2012)

112. F. Meillaud, A. Shah, C. Droz, E. Vallat-Sauvain, C. Miazza, Sol. Energy Mater. Sol. Cells **90**, 2952 (2006)
113. T. Soderstrom, F.J. Haug, X. Niquille, V. Terrazzoni, C. Ballif, Appl. Phys. Lett. **94**, 063501 (2009)
114. P. Buehlmann, J. Bailat, D. Domine, A. Billet, F. Meillaud, A. Feltrin, C. Ballif, Appl. Phys. Lett. **91**, 143505 (2007)
115. P.G. O'Brien, A. Chutinan, K. Leong, N.P. Kherani, G.A. Ozin, S. Zukotynski, Opt. Express **18**, 4478 (2010)
116. C. Battaglia, C.M. Hsu, K. Soderstrom, J. Escarre, F.J. Haug, M. Charriere, M. Boccard, M. Despeisse, D.T.L. Alexander, M. Cantoni, Y. Cui, C. Ballif, Acs Nano **6**, 2790 (2012)
117. X. Sheng, S.G. Johnson, L.Z. Broderick, J. Michel, L.C. Kimerling, Appl. Phys. Lett. **100**, 111110 (2012)
118. X. Sheng, S.G. Johnson, J. Michel, L.C. Kimerling, Opt. Express **19**, A841 (2011)
119. Y.H. Kuang, K.H.M. van der Werf, Z.S. Houweling, R.E.I. Schropp, Appl. Phys. Lett. **98**, 151110 (2011)
120. R. Yu, Q. Lin, S.F. Leung, Z. Fan, Nano Energy **1**, 57 (2012)
121. S.Q. Yu, B. Witzigmann, Opt. Express **21**, A167 (2013)
122. P.G. O'Brien, L.-P. Heiniger, N. Soheilnia, Y. Yang, N.P. Kherani, M. Grätzel, G.A. Ozin, N. Tétreault, Adv. Mater. **25**, 5734–5741 (2013)
123. Y. Yang, P.G. O'Brien, G.A. Ozin, N.P. Kherani, Appl. Phys. Lett. **103**, 221109 (2013)
124. R.H. Fan, L.H. Zhu, R.W. Peng, X.R. Huang, D.X. Qi, X.P. Ren, Q. Hu, M. Wang, Phys. Rev. B **87**, 195444 (2013)
125. C. Wang, S.C. Yu, W. Chen, C. Sun, Sci. Rep. **3**, 3513 (2013)
126. M.D. Vece, Y. Kuang, J.K. Rath, L. van Dijk, R.E.I. Schropp, Rep. Prog. Phys. **76**, 106502 (2013)

Chapter 3
Electronic Structures of Planar and Nonplanar Polyfluorene

Takashi Kobayashi, Takashi Nagase and Hiroyoshi Naito

Abstract Polyfluorene is well known as an efficient blue emitter for polymer-based light-emitting diodes and is very attractive from a physical point of view because randomly twisted, regularly twisted, or planar conformations can be realized in its solid state. In this chapter, the relationship between its optical properties and the polymer conformation is discussed within the framework of the simple effective conjugation length model. The electronic structure of polyfluorene is also discussed based on the electroabsorption (EA) spectra of the three conformations. Different from other conjugated polymers, polyfluorene exhibits complicated EA spectra in its highly ordered thin films. From the analysis of these EA spectra, the similarities and differences in the electronic structure between polyfluorene and other conjugated polymers are clarified.

3.1 Introduction

Conjugated polymers have been extensively studied as semiconducting materials for light-emitting diodes, thin-film transistors, and photovoltaic cells because of their high photoluminescence (PL) quantum efficiency, high field-effect mobility, and large absorption coefficient [1–3]. An additional advantage of conjugated polymers is their excellent solution processability. Their continuous, homogeneous thin films can be more easily fabricated by solution processing, compared to other semiconducting materials. Conjugated polymers are, therefore, considered as key materials to realize low-cost, lightweight, and flexible electronic devices with the use of printing technology.

T. Kobayashi · T. Nagase · H. Naito (✉)
Department of Physics and Electronics, Osaka Prefecture University,
1-1 Gakuen-cho, Sakai, Osaka 599-8531, Japan
e-mail: naito@pe.osakafu-u.ac.jp

J. Singh and R. T. Williams (eds.), *Excitonic and Photonic Processes in Materials*,
Springer Series in Materials Science 203, DOI: 10.1007/978-981-287-131-2_3,
© Springer Science+Business Media Singapore 2015

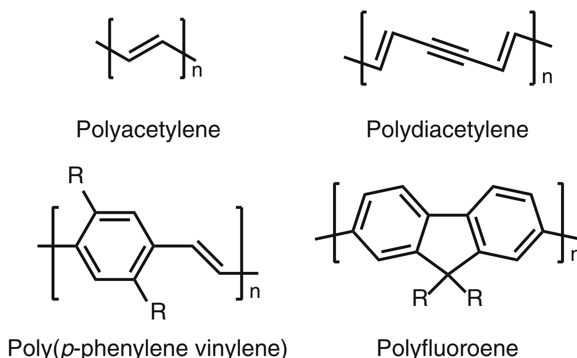

Fig. 3.1 Chemical structures of representative conjugated polymers

The optoelectronic properties of conjugated polymers are determined by π electrons, which are the electrons in connected π orbitals along the one-dimensional polymer backbone. Different from (σ) electrons in σ orbitals, which form the strong covalent bonds and define the backbone structure, π electrons can be excited with light in the visible range and added or subtracted by doping. To understand the optoelectronic properties of conjugated polymers, electron–lattice and electron–electron interactions also have to be taken into account. The former interaction is responsible for the slight deformation of the polymer backbone after electronic transition, and induces vibronic progressions in the absorption and PL spectra [4]. Electron-electron interaction is essential to explain the absence of PL in linear conjugated polymers (see top two examples in Fig. 3.1) [5–7]. In these linear conjugated polymers, an excited state with even inversion symmetry appears below the lowest excited state having odd inversion symmetry due to the electron-electron interaction. Since dipole transition between an even-parity state and the ground state is forbidden, all the excitations in such polymers have to decay nonradiatively. On the other hand, in conjugated polymers with ring structures (see last two examples in Fig. 3.1), electron-electron interaction is not as strong as in linear conjugated polymers [8]. As a result, a dipole-allowed excited state appears as the lowest excited state from where a moderate or intense PL originates. However, electron–electron interaction is still important in conjugated polymers with ring structures [8, 9]. Ring structures are known to improve chemical stability. Therefore, conjugated polymers with ring structures are predominantly used for optoelectronic applications.

If conjugated polymers adopt a fully planar conformation, π electrons delocalize over the whole polymer chain. Conjugated polymers, however, tend to twist around single bonds, in particular, in disordered thin films and in solution. The twists influence the electronic structure of the polymer through the decrease in the overlap of π orbitals of adjacent carbon atoms and the resultant increase in the energy of π electrons. Consequently, the optoelectronic properties depend on the polymer conformation. In some conjugated polymers, the conformation in thin films can be controlled. For instance, in the case of polythiophene derivatives (PTs), thin films

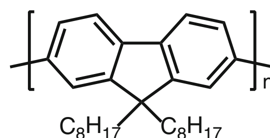

Fig. 3.2 Chemical structure of poly(9,9-dioctylfluorene) (F8)

containing planar and random coil conformations can be prepared from the polymers with high and low regioregularity, respectively [10, 11]. A more interesting example is poly(9,9-dioctylfluorene) (hereafter F8), which is well known as an efficient blue emitter for polymer-based light-emitting diodes [12, 13]. From the same F8 polymer, it is possible to prepare three different conformations, namely planar, regularly twisted, and random coil conformations, only by changing the fabrication conditions (the chemical structure of F8 is shown in Fig. 3.2). F8, therefore, provides the good opportunity to study the effect of the polymer conformation on the optical properties.

In this chapter, in addition to discussing the conformational dependence of the optical properties of F8, we compare the electronic structures of the three different conformations. For this purpose, we have carried out electroabsorption (EA) measurements, which had been performed for many other conjugated polymers. It is, thus, possible to not only discuss the conformational dependent on the electronic structures but also compare the electronic structures with other conjugated polymers.

3.2 Fundamental Optical Properties

3.2.1 Conformation of F8

In thin films prepared from a toluene solution by spincoating, F8 polymers adopt a random coil conformation. This can be confirmed from the fact that their featureless absorption spectrum is very similar to that in solution, as shown in Fig. 3.3a. These thin films are of what is called the glassy phase of F8.

F8 melts around 160–180 °C (depending on molecular weight), above which a liquid crystal state appears [14, 15]. By slow cooling from the melting point to room temperature, crystalline thin films are obtained. A characteristic feature of crystalline thin films is their clear intense X-ray diffraction pattern (see Fig. 3.4) [16–19]. Based on the results of X-ray and electron diffraction studies and molecular dynamics simulation, Chen et al. have determined the molecular packing structure in crystalline phase, in which neighboring repeating units are twisted to form dihedral angles ranging from 15° to 24° [17]. In the absorption spectrum of crystalline thin films, a shoulder appears at the lower side of the main band at 3.2 eV as shown in Fig. 3.3b.

Thin films containing planar conformation, which is called the β-phase, can be prepared in several ways, for instance, by exposing thin films to a vapor of a good solvent [16, 20, 21], by spincoating using particular solvents [22] and by dropcasting from a dilute solution [18]. In these methods, the solvent evaporates slowly so that

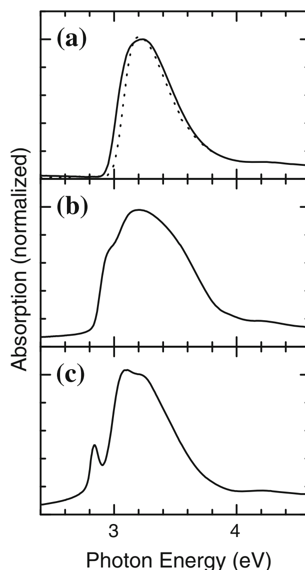

Fig. 3.3 Absorption spectra of **a** glassy, **b** crystalline, and **c** β-phase thin films of F8. The *dotted line* in (**a**) represents absorption spectrum of F8 in toluene

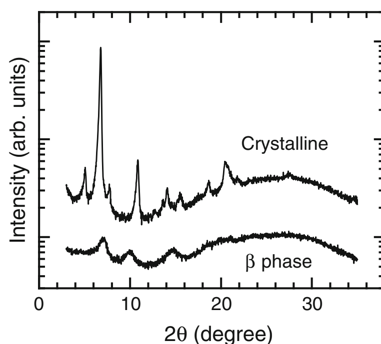

Fig. 3.4 X-ray diffraction patterns of (*upper*) crystalline and (*lower*) β-phase thin films of F8. The pattern for β-phase is shifted down by dividing it by 4 for clarity

the polymers have more time to form the stable conformation. The characteristic feature of β-phase thin films is an additional narrow absorption band around 2.8 eV (see Fig. 3.3c) [18, 20, 23, 24]. The position of the additional band indicates that π electrons are most stabilized in the β-phase thin films, and is regarded as one evidence indicating a planar conformation. X-ray and electron diffraction studies [16, 25] also suggest the planar conformation in the β-phase thin films although the diffraction intensity in these thin films is much weaker than that in crystalline thin films because of the poor interchain ordering (see Fig. 3.4).

It should be noted that properties of a conjugated polymer may change depending on the purity of the sample, the molecular weight of the polymer, and the used polymerization methods, and may even vary from batch to batch. For example, PL quantum efficiency of emitting polymers is largely dependent on the purity. We also have

found that some F8 polymers do not crystalize as well as those used in this work [19]. Thus, here we present only the data that were measured for samples of F8 provided by the Sumitomo Chemical Co. Ltd., and were obtained with a good reproducibility.

3.2.2 Effective Conjugation Length Model

The effect of the twists on the optical properties can be well explained by the effective conjugation length model, in which an actual polymer chain is regarded as an ensemble of segments with various effective conjugation lengths. In this model, the planar conformation is described by a longer average length of the effective conjugation. As mentioned in the previous subsection, F8 polymers adopt random coil, regularly twisted, and planar conformations in glassy, crystalline and β-phase thin films. The average effective conjugation length is considered to increase in the order of grassy phase < crystalline phase < β-phase. The relationship between the optical gap energy, E_g, of a segment and its effective conjugation length, N is given by:

$$E_g = A + \frac{B}{N}, \tag{3.1}$$

where A and B are constants determined by the polymer backbone structure [26–28]. The shift of the onset of the absorption spectrum in Fig. 3.3 is, of course, consistent with the 3.1 and the chain planarity. From 3.1, $|dE_g/dN| \propto N^{-2}$ is obtained. This means that as the average length increases, the energy distribution, i.e., the inhomogeneous broadening, is largely suppressed. This is the explanation for the very narrow shape of the additional absorption band in β-phase thin films.

3.2.3 Photoluminescence (PL) Properties

PL properties of F8 can also be explained using the effective conjugation length model. PL spectra of glassy, crystalline, and β-phase thin films are shown in Fig. 3.5. In thin films of conjugated polymers, photoexcitations tend to migrate into segments with longer effective conjugation lengths prior to emission [29]. In other words, PL preferentially originates from relatively longer segments contained in a sample. In the case of disordered thin films, such as glassy F8 thin films, the migration process significantly lowers the emitting level and leads to the large Stokes shift. This migration process is also the reason why the measured PL spectrum is narrower than the absorption spectrum. In ordered thin films, such as crystalline and β-phase thin films, PL originates from further longer segments so that a more redshifted and narrower PL appears. As the average length increases, the shift of the emitting level due to the migration process decreases. As a result, the extremely small Stokes shift is observed, in particular, in β-phase thin films.

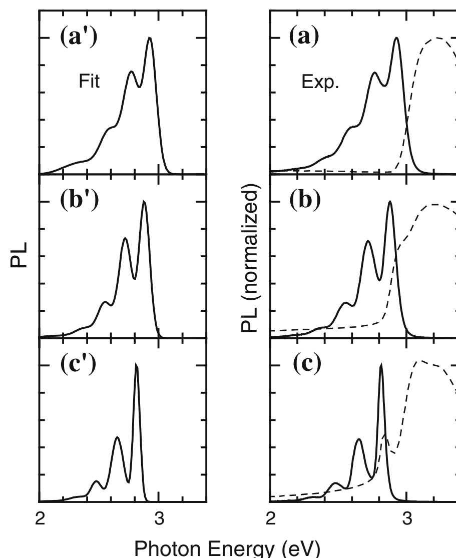

Fig. 3.5 (*Right*) PL spectra of **a** glassy, **b** crystalline, and **c** β-phase thin films of F8. *Dashed lines* are their absorption spectra. (*Left*) Fitted PL spectra using 3.2 and five Gaussian functions

In the PL spectra in Fig. 3.5, vibronic progressions are clearly seen. The associated phonon mode is assigned to a phenyl-ring stretching mode with a phonon energy of approximately 0.17 eV [23]. The relative intensities of 0–n transition, F_n, are given by the Franck–Condon factor, which becomes

$$F_n(s) = \frac{e^{-s}}{n!} S^n, \tag{3.2}$$

when harmonic potentials in the ground and excited states are assumed [4]. In 3.2, S is Huang–Rhys factor, which represents the strength of the electron–lattice interaction. In the left side of Fig. 3.5, we show the spectra simulated using 3.2 and five Gaussian functions for the inhomogeneous broadening. An excellent agreement between the experimental and simulated PL spectra is obtained. The S's determined from the simulations are listed in Table 3.1. It is known that as the delocalization of π electrons increases, the molecular deformation after an electronic transition is suppressed [30]. In the limit of an infinite chain, molecular deformation does not take place, and thus the electron-lattice interaction becomes zero. Therefore, it is naturally expected that S decreases with increasing the effective conjugation length, and such a tendency is indeed observed in Table 3.1.

As listed in Table 3.1, PL quantum efficiency of F8 is strongly dependent on the polymer conformation, and increases up to 70 % in the β-phase thin films. This increase in PL quantum efficiency is mainly caused by the enhancement of radiative decay rates. In an exciton system, the following relationship between the transition dipole moment, μ, and coherence length of exciton, L is found [31]:

$$|\mu|^2 \propto L. \tag{3.3}$$

Table 3.1 Huang-Rhys factor (S), PL quantum efficiency, PL lifetime, and radiative and nonradiative decay rates for F8 thin films [18]

Thin films	S	PL quantum efficiency (%)	PL lifetime (ps)	Radiative decay rate (10^9 s^{-1})	Non-radiative decay rate (10^9 s^{-1})
Glassy	0.70	37	380	0.97	1.7
Crystalline	0.63	46	400	1.2	1.4
β phase	0.43	70	280	2.5	1.1

Equation 3.3 suggests that longer segments will have the larger transition dipole moments and faster radiative decay rates, as observed in Table 3.1. Thus, the increase in PL quantum efficiency with increasing the effective conjugation length can also be understood within the framework of this model.

As mentioned in this and previous subsections, effective conjugation model can consistently explain the basic optical properties of F8, which are associated with the lowest excited state. However, there are some polymers whose PL properties cannot be explained with the effective conjugation length model. A well-known exception is the ordered thin films of PTs. Their PL quantum efficiency rather decreases as the order of molecular packing improves. Spano has proposed [32] that in ordered PTs thin films, H-aggregation is formed due to the weak interchain interaction. In H-aggregates, the lowest excited state is ideally dipole-forbidden but the residual structural disorder induces PL in actual samples. Spano has also theoretically demonstrated that such a system shows unique PL spectrum with an enormously large 0–1 transition, which has actually been observed [11, 33, 34] and provoked controversy because its shape cannot be reproduced with 3.2. However, in ordered thin films of F8, the chain distance is much longer [35] than that in PTs [36, 37]. Furthermore, ordered F8 thin films exhibit high PL quantum efficiency and show PL whose spectral shape can be explained by 3.2. Therefore, photoexcitations in F8 thin films can be safely treated as intrachain excitations.

3.3 Electronic Structure

3.3.1 Electroabsorption(EA) Measurements

The electronic structure of one-dimensional π conjugated polymers consists of dipole-allowed (B_u) and dipole forbidden (A_g) states. The latter states are absent from the absorption spectrum, but are active in nonlinear spectroscopy. Two-photon absorption and excitation measurements can be used to selectively find the A_g states. EA spectroscopy, which is one of the nonlinear spectroscopies, has been frequently used to determine the electronic structure of conjugated polymers [38–41]. EA spectroscopy can detect both B_u and A_g states, and allows the determination of the coupling strength between these states with the help of a sum-over-state calculation [42].

In EA measurements, the small absorption change due to the applied electric field is detected with a phase sensitive technique. Since a coherent light source is not needed, it is easier to obtain the spectral information by EA compared to other nonlinear spectroscopies, such as two-photon absorption and second harmonic generation measurements. In order to be able to apply a relatively high electric field, EA measurements are usually carried out at lower temperatures. For the details of our experimental setup see [43].

3.3.2 Essential-State Model

A measured EA spectrum is often compared with the first and second derivatives of the absorption spectrum to reveal the neutral and charge-transfer (CT) excitons, respectively. However, this simple method is not adequate to analyze EA spectrum of conjugated polymers. Guo et al. [44, 45] have performed calculations within an extended Peierls-Hubbard model and revealed that three characteristic excited states play a dominant role in nonlinear optical response of conjugated polymers. These excited states are called *essential states* and correspond to the lowest excited state ($1B_u$), the bottom of the continuum state (nB_u), and the dipole-forbidden state (mA_g) which is strongly coupled with both the $1B_u$ and nB_u states. Liess et al. [38] demonstrated that EA spectra of various conjugated polymers can be well reproduced by sum-over-state calculations [42] based on the essential-state model if inhomogeneous broadening is taken into account using an asymmetric Gaussian function. From the fit, the electronic structure, i.e., the positions of the essential states, can be determined [38, 39].

3.3.3 EA Spectrum of Glassy F8

We first determine the electronic structure of glassy F8 thin films [43]. EA spectrum of glassy F8 thin films is shown in Fig. 3.6, which is dominated by two oscillatory features with zero-level crossings at 3.12 and 4.03 eV. The low-energy feature matches well with the first-derivative of the absorption spectrum. Thus, the low-energy feature is attributed to the Stark shift of the $1B_u$ state. However, the high-energy feature cannot be reproduced by the first or even the second derivative of the broad absorption spectrum in the same spectral region (see Fig. 3.3a).

We have also carried out two-photon excitation (TPE) measurements for glassy F8 thin films and found the mA_g state around 3.9 eV (see Fig. 3.7b). Since the TPE peak appears at the same position as the high-energy EA feature, the EA signal can be attributed to the field-induced transition from the ground state to the mA_g state. Using the sum-over-state calculation, not only EA spectrum but also TPE spectrum can be fitted with a single set of physical constants. We basically follow the procedure that Liess et al. [38] developed to fit the EA and TPE spectra of glassy F8 thin films [43].The fitted EA and TPE spectra are shown in Fig. 3.7a, b, respectively and the

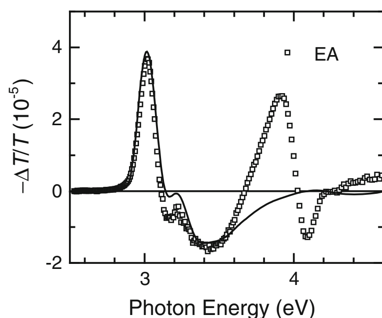

Fig. 3.6 (*Open squares*) EA spectrum of glassy F8 measured with an applied electric field of 71 kV/cm at 100 K. (*Solid line*) First derivative of the absorption spectrum

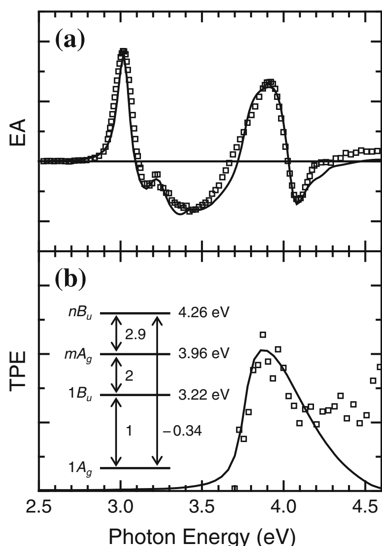

Fig. 3.7 **a** EA and **b** TPE spectra of glassy F8 thin films. In these figures, *open squares* indicate experimental results and *solid lines* are fitted results. *Inset* the electronic structure of glassy F8 thin films. Transition dipole moments and energy levels used for the fit are listed. The transition dipole moments are indicated in units of $\langle 1A_g|\mu|1B_u\rangle$

energy levels and the transition dipole moments used for the fits are presented in the inset of Fig. 3.7b. Both fitted spectra reproduce well the major features observed in the experimental spectra.

From a comparison with other conjugated polymers, it is found that the electronic structure of glassy F8 thin films has many common features. For instance, the resonance energy ratio between the $1B_u$ and mA_g states is found to be E_{1B_u} : $E_{mA_g} = 1 : 1.2{\sim}1.3$, which is almost the same as that in many conjugated polymers [38–40]. In addition, the ratios of $\langle 1A_g|\mu|1B_u\rangle : \langle 1B_u|\mu|mA_g\rangle \approx 1 : 2$ and $\langle 1A_g|\mu|1B_u\rangle : \langle mA_g|\mu|nB_u\rangle \approx 1 : 2.9$, where μ indicates the dipole moment operator, are similar to those of poly(p-phenylene vinylene) (PPV) [39]. The only remarkable difference is in the ratio of $\langle 1A_g|\mu|1B_u\rangle : \langle 1A_g|\mu|nB_u\rangle = 1 : -0.34$. This large absolute value of $\langle 1A_g|\mu|nB_u\rangle$ is needed to reproduce the high-energy feature with much larger amplitude than that in other conjugated polymers. This implies that the nB_u state in F8 has larger oscillator strength than that in other conjugated polymers.

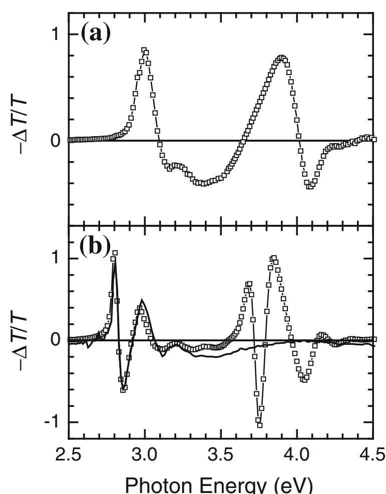

Fig. 3.8 EA spectra of **a** glassy and **b** β-phase F8 thin films measured with an applied electric field of 100 kV/cm at 10 K. The *solid line* in (**b**) represents the first derivative of the absorption spectrum

Thus, the nature of the nB_u state in F8 is considered to be different from that in other conjugated polymers. Before presenting a detailed discussion of the nature of the nB_u state, we show the data of β-phase and crystalline thin films in the next two subsections to see the effects of the chain planarity and inhomogeneous broadening.

3.3.4 Transition from Glassy to β-phase

In the reports on EA measurements of conjugated polymers, disordered thin films such as glassy F8 thin films were mainly used. In ordered thin films, inhomogeneous broadening can be suppressed but interchain interaction may influence the electronic structure. However, in the case of F8, interchain interaction can be negligible so that it is possible to directly compare the electronic structures of ordered and disordered thin films.

As shown in Fig. 3.3, an additional absorption band appears in the β-phase, but no other remarkable change can be seen. However, in EA spectrum, a dramatic change is observed as shown in Fig. 3.8b. As in glassy thin films, the low-energy EA feature of β-phase thin films can be interpreted simply in terms of the Stark shift of the $1B_u$ state. On the other hand, in the high-energy region, the broad positive peak around 3.9 eV in glassy F8 thin films splits into two in β-phase thin films, resulting in a complex oscillatory feature [46, 47]. In the following, we consider several possibilities as the origin of this oscillatory feature.

It is known that CT transitions could lead to an oscillatory feature in EA spectrum of polycrystalline thin films of small molecule [48, 49]. In the case of a CT transition, when an electric field is applied parallel to the transfer direction from one molecule to another, the amplitude of the EA signal associated with the CT transition becomes larger than when the field is perpendicular to the transfer direction [48].

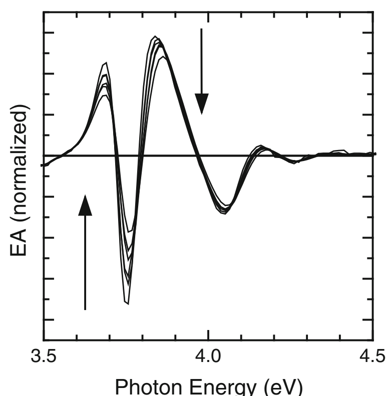

Fig. 3.9 Normalized EA spectra measured with the applied electric fields of 50, 75, 100, 125, 150, and 175 kV/cm. The spectra are normalized by dividing them by the square of the field strength. The *arrows* indicate the systematic variation from lower to higher field

In one-dimensional conjugated polymers, for a CT transition to occur the transfer direction must be perpendicular to the chain direction. In contrast, the EA signal due to the Stark shift is maximized when the field is parallel to the chain direction. Therefore, if the origin of the oscillatory feature was CT transitions, the oscillatory feature and the low-energy feature should show different directional dependences. To examine whether such directional dependences can be observed, we prepared oriented β-phase F8 thin films [21] and measured EA spectrum using a polarized light and applied the electric field parallel and perpendicular to the chain direction [47]. However, the measured EA spectral shape did not change at all. Therefore, we ruled out CT transitions as the origin of the oscillatory feature.

An oscillatory feature in EA spectrum may be reminiscent of the Franz-Keldysh (FK) oscillation (or the FK effect) observed near the band edge of inorganic semiconductors, which was extensively studied more than 40 years ago [50]. The FK effect has only been observed in the electroreflectance spectrum of polydiacetylene single crystals [51, 52] among conjugated polymers. We carefully examined the possibility of the FK effect but found many discrepancies between the experimental results and theoretical expectations [47, 53]. First of all, according to the FK theory, the period of oscillation increases with the electric field and its amplitude follows a 1/3 power law. This is also found to be true for a one-dimensional system with inhomogeneous broadening [54]. However, the oscillation in the F8 thin films are not broadened even if a relatively high electric field is applied (see Fig. 3.9). Second, in the case of the one-dimensional FK effect, the first negative peak of the oscillation is theoretically expected to appear at the band edge, but in F8 the onset of photoconductivity appears at a different position [47]. Finally, although the FK oscillation is expected to be observed only at low temperatures [52] the oscillation in F8 thin films can be observed even at room temperature. Therefore, we conclude that the oscillation is not due to the FK effect.

A recent molecular orbital calculation has revealed that, in addition to the essential states, there may exist some B_u and A_g states that contribute to the nonlinear optical properties as strong as the mA_g and nB_u states [55]. Thus, the oscillatory feature

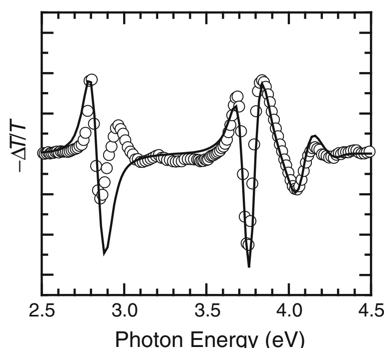

Fig. 3.10 (*Open circles*) experimental and (*solid line*) simulated EA spectra for β-phase F8 thin films

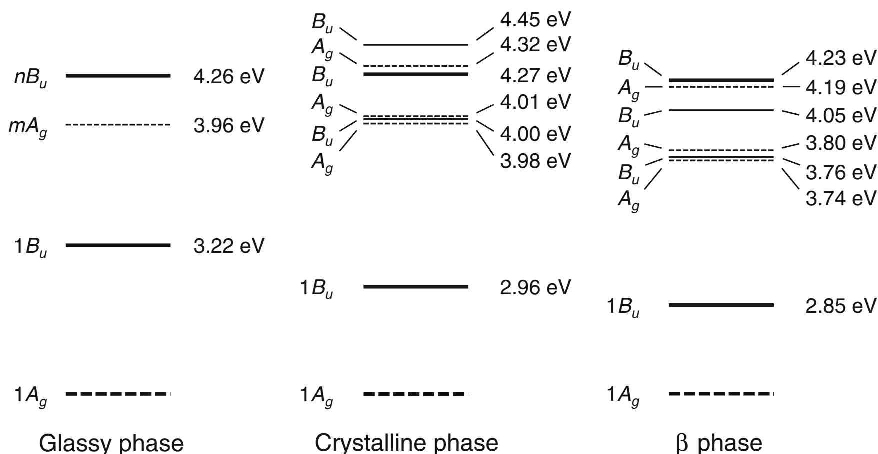

Fig. 3.11 Electronic structures used to reproduce the EA spectra of glassy, β-phase, and crystalline thin films. The *solid* and *dotted lines* indicate B_u and A_g states, respectively. The energy intervals between the $1B_u$ and $1A_g$ states are reduced to fit the figure within the scale

is considered to result from several excited states, some of which are not resolved in glassy thin films because of the inhomogeneous broadening. To reproduce the oscillatory feature in β-phase F8 thin films with the sum-over-state calculation, more than seven excited states are needed. Here, based on an eight-level model consisting of the ground state and the seven excited states, we have simulated EA spectrum. The best fit is shown in Fig. 3.10. In this simulation, we ignored the vibronic progressions and asymmetric inhomogeneous broadening because we focused only on the high-energy region. The agreement in the high-energy region is found to be satisfactory and the electronic structure used for this simulation is shown in Fig. 3.11.

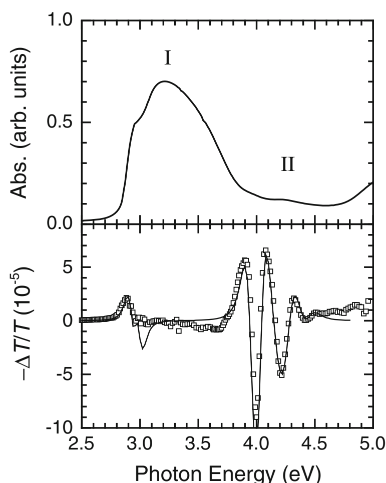

Fig. 3.12 Measured absorption (*Upper*) and EA spectrum (*lower*) of crystalline F8 thin films subjected to an applied electric field of 50 kV/cm at 10 K. The *solid line* in the lower panel is the best fit simulated with the sum-over-state calculation

3.3.5 Oscillatory Feature in Crystalline Thin Films

The oscillatory feature is also observed in crystalline thin films [53]. Moreover, the amplitude of the oscillation is largely magnified without any remarkable change observed in the absorption spectrum in the same region (see Fig. 3.12). In this figure, we show EA spectrum measured with a relatively weak electric field. When a field of the same strength is applied on crystalline thin films, the magnitude of the low-energy EA feature is almost the same as those in glassy and β-phase thin films.

The EA spectrum can be fitted with the sum-over-state calculation based on an eight-level model. The best fit is shown in Fig. 3.12 (lower panel), and the electronic structure used for the fit is depicted in Fig. 3.10. We do not consider that all of the seven excited states in Fig. 3.10 correctly represent the important excited states in β-phase and crystalline F8 thin films. However, the depicted electronic structures suggest the followings: (1) More than three excited states certainly contribute to the EA spectrum in β-phase and crystalline thin films; contributions from some of them may be masked by inhomogeneous broadening in the glassy thin films. (2) Not only $1B_u$ state but also some other excited states gradually redshift as the chain planarity improves. (3) In all of the three phases, the B_u state around 4.25 eV plays an important role; in other words, its energy level is independent of the chain planarity. This B_u state is the same excited state that we assigned to the nB_u state in glassy F8 thin films.

In the theoretical study by Guo et al. [44, 45], only the excited states associated with the lowest absorption band are considered, and the characteristic three excited states, i.e., the essential states, have been found. They have also revealed that the contributions from the excited states above the nB_u state (the bottom of the continuum state) to the EA spectrum cancel one another [45]. In fact, no remarkable EA features are observed above the nB_u state in many conjugated polymers [39]. In other conjugated polymers, EA features appear in a spectral range of about 1 eV from the

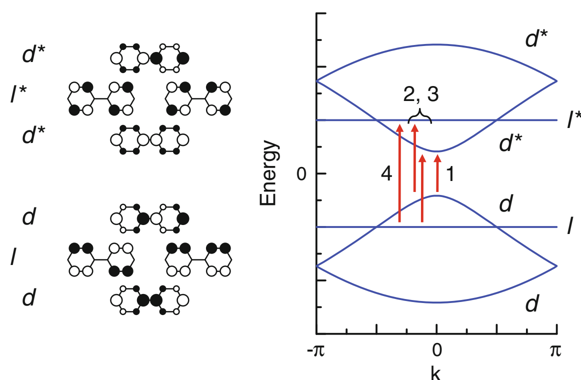

Fig. 3.13 (*Left*) Schematic representation of the molecular orbitals of biphenyl near the HOMO–LUMO gap. In this figure, *d* and *l* represent delocalized and localized orbitals, respectively, and * indicates unoccupied orbitals. *Open* and *closed circles* indicate positive and negative values, respectively. However, the radii of these circles do not represent correct amplitude of wavefunctions. (*Right*) The band structure of the model polymer calculated based on the tight-binding model. Note that under Hückel approximation, both of *l* and *l** are doubly degenerate. The low-lying electronic transitions are labeled 1–4

optical gap, and the nB_u state is always located within a spectral range of the lowest absorption band. Thus, the excited states associated with the second lowest absorption band do not need to be taken into account. On the other hand, in crystalline thin films, the oscillatory feature ranges from 2.8 eV up to 4.5 eV and it partly overlaps with the second lowest absorption band, which is labeled as II in Fig. 3.12. This suggests that some excited states associated with the absorption band II appear very close to or below the true nB_u state. Therefore, to correctly interpret the EA spectra of F8 thin films, it is necessary to understand the origin of the absorption band II.

3.3.6 Discussions

To understand the higher absorption bands in conjugated polymers with ring structures, the full chemical structure of the repeating unit has to be taken into account [8, 9, 56]. Here we consider biphenyl as a model repeating unit of F8; although the structure of π conjugation in biphenyl is not the exact same as that in fluorene, this simplification has little impact for qualitative discussion. Under the Hückel approximation, both the HOMO and LUMO levels in benzene are doubly degenerate. It is convenient to use these four molecular orbitals to construct some molecular orbitals in biphenyl. In the left side of Fig. 3.13, we show eight molecular orbitals near the HOMO–LUMO gap in biphenyl. Both of HOMO–1 and LUMO+1 levels are doubly degenerate. Molecular orbitals labeled as *l* and *l** in the figure have nodes at the carbon atoms that will link the neighboring repeating units if biphenyls are bonded to form a model polymer. This means that transfer integral between neighboring

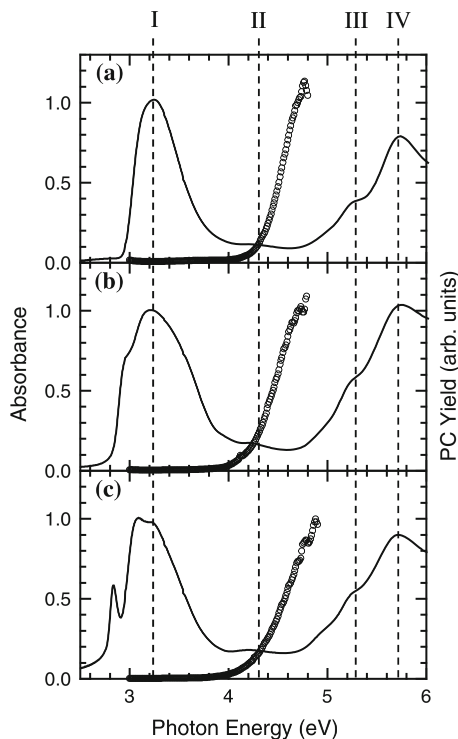

Fig. 3.14 Absorption spectra measured in wider spectral range for **a** glassy, **b** crystalline, and **c** β-phase F8 thin films. *Open circles* represent photocurrent (PC) yield, which are obtained by dividing the measured photocurrent spectrum by the corresponding absorption spectrum

repeating units is extremely small so that electrons are localized to their own unit. On the other hand, molecular orbitals labeled as d and d^* have large amplitude of wavefunction at those carbon atoms, which allow electrons to delocalize over the whole chain. In the right side of Fig. 3.13, we also show the band structure calculated based on the tight-binding model for the model polymer.

From the band structure, it is expected that absorption bands associated with d–d^*, d–l^*, l–d^*, and l–l^* transitions will appear near the optical gap. Under the Hückel approximation, d–l^* and l–d^* transitions are degenerate. However, Chandross et al. [9] demonstrated that two distinct absorption bands arise from d–l^* and l–d^* transitions if Coulomb interaction with an appropriate magnitude is considered. Although their theoretical work was done for PPV, which also has bands with localizing and delocalizing characters, the same conclusion must be obtained for F8. In fact, F8 shows four distinct absorption bands as shown in Fig. 3.14. The absorption bands indicated by I and IV can thus be attributed to d–d^* and l–l^* transitions, respectively, whereas the bands II and III are considered to be due to d–l^* and l–d^* transitions. Since d and d^* orbitals are delocalized over the whole chain, the absorption band I due to the d–d^* transition must be redshifted as the chain planarity improves. On the other hand, l and l^* orbitals are localized on the repeating units so that the absorption bands associated with l and l^* orbitals are virtually independent of the polymer

conformation. These features can be seen in Fig. 3.14, where the band II always appears at 4.25 eV, whereas the band I redshifts depending on the polymer conformation. The assignment of the absorption band at 4.25 eV to the band II is supported by their different optical anisotropy [43] and higher charge separation efficiency than the band I [57].

The understanding of the lowest two absorption bands provides us valuable clues to interpret the EA spectra of F8 thin films. It explains why the excited states having different dependences on the chain planarity exist in a spectral range between the absorption bands I and II. It is, thus, considered that the B_u state that we assigned to the nB_u state in glassy thin films does not represent the bottom of the continuum state (the true nB_u state) but it is the excited state associated with the absorption band II. Since the B_u state has relatively large oscillator strength and lies close to the excited states associated with the band I, such as the mA_g state, it largely contributes to the EA spectrum of F8. This interpretation also explains why the oscillation amplitude in β-phase thin films is smaller than that in crystalline thin films. In both phases, the inhomogeneous broadening is well suppressed, but in β-phase thin films, the excited states associated with the absorption band I is further redshifted. This redshift leads to relatively large separation between the excited states associated with the absorption bands I and II. Since contribution to the EA signal is inversely proportional to the energy gap between the associated two excited states, such a separation weakens their contribution to the EA signal.

As mentioned in the previous subsection, such a large oscillatory EA feature has not yet been reported in other conjugated polymers. In F8, the gap between the absorption bands I and II is similar to that of other conjugated polymers, for instance, PPV and its derivatives. However, the gap between the $1B_u$ and mA_g states is relatively large in F8 because this gap increases with increasing the optical gap (thus the ratio $E_{1B_u} : E_{mA_g}$ is a constant as mentioned in Sect. 3.3.3.). It should be noted that F8 has large optical gap so that it has been used as a blue emitter. Thus, the similar oscillatory EA feature may be found in other conjugated polymers with relatively large optical gap.

3.4 Conclusions

In F8, many optical properties that are associated with the lowest excited state can be consistently explained with the simple effective conjugation model. This is because in F8 interchain interaction is so weak that the nature of the lowest excited state does not change into a dipole-forbidden state. Our EA study reveals that the EA spectra of F8 cannot be understood only with the excited states associated with the lowest absorption band but others associated with the second lowest absorption band also need to be taken into account. We consider that the excited states associated with the first and second lowest absorption bands partly overlap which leads to a large complicated oscillatory EA feature. Although the amplitude is much smaller, a

similar oscillatory feature is observed in highly ordered PT thin films as well [58]. We believe that our findings will be helpful to fully understand the electronic structure of other conjugated polymers in highly ordered forms.

Acknowledgments We would like to thank Sumitomo Chemical Co. Ltd., for supplying the F8 polymer. This work was financially supported by a Grant-in-Aid for Scientific Research from Japan Society for the Promotion of Science, and by a Grant-in-Aid for Scientific Research on Innovative Areas "New Polymeric Materials Based on Element-Blocks (No.2401)" of the Ministry of Education, Culture, Sports, Science and Technology, Japan.

References

1. J.H. Burroughes, D.D.C. Bradley, A.R. Brown, R.N. Marks, K. Mackay, R.H. Friend, P.L. Burns, A.B. Holmes, Nature **347**, 539 (1990)
2. Z. Bao, A. Dodabalapur, A.J. Lovinger, Appl. Phys. Lett. **69**, 4108 (1996)
3. N.S. Sariciftci, L. Smilowitz, A.J. Heeger, F. Wudl, Science **258**, 1474 (1992)
4. B. Henderson, G.F. Imbusch, *Optical Spectroscopy of Inorganic Solids* (Clarendon Press, Oxford, 1989)
5. B. Lawrence, W.E. Torruellas, M. Cha, M.L. Sundheimer, G.I. Stegeman, J. Meth, S. Etemad, G. Baker, Phys. Rev. Lett. **73**, 597 (1994)
6. F. Kajzar, J. Messier, Thin Solid Films **132**, 11 (1985)
7. G. Orlandi, F. Zerbetto, M. Zgierski, Chem. Rev. **91**, 867 (1991)
8. W. Barford, *Electronic and Optical Properties of Conjugated Polymers* (Clarendon Press, Oxford, 2005)
9. M. Chandross, S. Mazumdar, S. Jeglinski, X. Wei, Z.V. Vardeny, E.W. Kwock, T.M. Miller, Phys. Rev. B **50**, 14702 (1994)
10. T. Kobayashi, J. Hamazaki, M. Arakawa, H. Kunugita, K. Ema, K. Ochiai, M. Rikukawa, K. Sanui, Phys. Rev. B **62**, 8580 (2000)
11. T. Kobayashi, J. Hamazaki, H. Kunugita, K. Ema, T. Endo, M. Rikukawa, K. Sanui, Phys. Rev. B **67**, 205214 (2003)
12. Y. Ohmori, M. Uchida, K. Muro, K. Yoshino, Jpn. J. Appl. Phys. **30**, L1941 (1991)
13. D. Neher, Macromol. Rapid Commun. **22**, 1365 (2001)
14. M. Grell, D.D.C. Bradley, M. Inbasekaran, E.P. Woo, Adv. Mater. **9**, 798 (1997)
15. S. Kawana, M. Durrell, J. Lu, J.E. Macdonald, M. Grell, D.D.C. Bradley, P.C. Jukes, R.A.L. Jones, S.L. Bennett, Polymer **43**, 1907 (2002)
16. M. Grell, D.D.C. Bradley, G. Ungar, J. Hill, K.S. Whitehead, Macromolecules **32**, 5810 (1999)
17. S.H. Chen, H.L. Chou, A.C. Su, S.A. Chen, Macromolecules **37**, 6833 (2004)
18. K. Asada, T. Kobayashi, H. Naito, Jpn. J. Appl. Phys. **45**, L247 (2006)
19. T. Kobayashi, H. Uda, T. Nagase, M. Watanabe, K. Matsukawa, H. Naito, Thin Solid Films **517**, 1340 (2008)
20. M. Ariu, D.G. Lidzey, M. Sims, A.J. Cadby, P.A. Lane, D.D.C. Bradley, J. Phys.: Condens. Matter **14**, 9975 (2002)
21. T. Endo, T. Kobayashi, T. Nagase, H. Naito, Jpn. J. Appl. Phys. **46**, L1093 (2007)
22. A.L.T. Khan, P. Sreearunothai, L.M. Herz, M.J. Banach, A. Köhler, Phys. Rev. **69**, 085201 (2004)
23. M. Ariu, M. Sims, M.D. Rahn, J. Hill, A.M. Fox, D.G. Lidzey, M. Oda, J. Cabanillas-Gonzalez, D.D.C. Bradley, Phys. Rev. B **67**, 195333 (2003)
24. A.J. Cadby, P.A. Lane, H. Mellor, S.J. Martine, M. Grell, C. Giebeler, D.D.C. Bradley, M. Wohlgenannt, C. An, Z.V. Vardeny, Phys. Rev. **62**, 15604 (2000)
25. T. Kawamura, M. Misaki, Y. Koshiba, S. Horie, K. Kinashi, K. Ishida, Y. Ueda, Thin Solid Films **519**, 2247 (2011)

26. R. Colditza, D. Grebnerb, M. Helbigb, S. Rentsch, Chem. Phys. **201**, 309 (1995)
27. G, Klaerner, R.D. Miller, Macromolecules **31**, 2007 (1998)
28. J. Gierschner, J. Cornil, H.-J. Egelhaaf, Adv. Mater. **19**, 173 (2007)
29. U. Rauscher, H. Bässler, Macromolecules **23**, 398 (1990)
30. T.W. Hagler, K. Pakbaz, K.F. Voss, A.J. Heeger, Phys. Rev. B **44**, 8652 (1991)
31. E. Hanamura, Phys. Rev. B **37**, 1273 (1988); ibid 38, 1228 (1988)
32. F.C. Spano, J. Chem. Phys. **122**, 234701 (2005)
33. K. Sakurai, H. Tachibana, N. Shiga, C. Terakura, M. Matsumoto, Y. Tokura, Phys. Rev. B **56**, 9552 (1997)
34. P.J. Brown, D.S. Thomas, A. Köhler, J.S. Wilson, J.-S. Kim, C.M. Ramsdale, H. Sirringhaus, R.H. Friend, Phys. Rev. B **67**, 064203 (2003)
35. M. Surin, E. Hennebicq, C. Ego, D. Marsitzky, A.C. Grimsdale, K. Müllen, J.-L. Brédas, R. Lazzaroni, P. Leclère, Chem. Mater. **16**, 994 (2004)
36. K. Tashiro, K. Ono, Y. Minagawa, M. Kobayashi, T. Kawai, K. Yoshino, J. Polym. Sci. B: Polym. Phys. **29**, 12232 (1991)
37. T.J. Prosa, M.J. Winokur, J. Moulton, P. Smith, A.J. Heeger, Macromolecules **25**, 4364 (1992)
38. M. Liess, S. Jeglinski, Z.V. Vardeny, M. Ozaki, K. Yoshino, Y. Ding, T. Barton, Phys. Rev. B **56**, 15712 (1997)
39. S.J. Martin, D.D.C. Bradley, P.A. Lane, H. Mellor, P.L. Burn, Phys. Rev. B **59**, 15133 (1999)
40. R.K. Meyer, R.E. Benner, M. Ozaki, M. Liess, Z.V. Vardeny, K. Yoshino, Y. Ding, T. Barton, Synth. Met. **84**, 549 (1997)
41. D. Beljonne, J. Cornil, Z. Shuai, J.L. Brédas, F. Rohlfing, D.D.C. Bradley, W.E. Torruellas, V. Ricci, G.I. Stegeman, Phys. Rev. B **55**, 1505 (1997)
42. B.J. Orr, J.F. Ward, Mol. Phys. **20**, 513 (1971)
43. S. Ikame, T. Kobayashi, S. Murakami, H. Naito, Phys. Rev. B **75**, 035209 (2007)
44. Y. Kawabe, F. Jarka, N. Peygambarian, D. Guo, S. Mazumdar, S.N. Dixit, F. Kajzar, Phys. Rev. B **44**, 6530 (1991)
45. D. Guo, S. Mazumdar, S.N. Dixit, F. Kajzar, F. Jarka, Y. Kawabe, N. Peyghambarian, Phys. Rev. B **48**, 1433 (1993)
46. T. Endo, S. Ikame, Y. Suzuki, T. Kobayashi, S. Murakami, H. Naito, Thin Solid Films **516**, 2537 (2008)
47. T. Endo, S. Ikame, T. Kobayashi, T. Nagase, S. Murakami, H. Naito, Phys. Rev. B **81**, 075203 (2010)
48. L. Sebastian, G. Weiser, H. Bässler, Chem. Phys. **61**, 125 (1981)
49. L.M. Blinov, S.P. Palto, G. Ruani, C. Taliani, A.A. Tevosov, S.G. Yudin, R. Zamboni, Chem. Phys. Lett. **232**, 401 (1995)
50. R.K. Willardson, A.C. Beer (ed.), *Semiconductors and Semimetals*, vol 9 (Academic, New York, 1972)
51. L. Sebastian, G. Weiser, Phys. Rev. Lett. **46**, 1156 (1981)
52. A. Horvath, G. Weiser, C. Lapersonne-Meyer, M. Schott, S. Spagnoli, Phys. Rev. B **53**, 13507 (1996)
53. T. Kobayashi, T. Endo, S. Ikame, T. Nagase, S. Murakami, H. Naito, J. Phys. Soc. Jpn. **80**, 034707 (2011)
54. T.G. Pedersen, T.B. Lynge, Phys. Rev. B **65**, 085201 (2002)
55. D. Beljonne, Z. Shuai, J. Cornil, D.A. dos Santos, J.L. Brédas, J. Chem. Phys. **111**, 2829 (1999)
56. J.D. Weibel, D. Yaron, J. Chem. Phys. **116**, 6846 (2002)
57. A. Köhler, D.A. dos Santos, D. Beljonne, Z. Shuai, J.-L. Brédas, A.B. Holmes, A. Kraus, K. Müllen, R.H. Friend, Science **392**, 903 (1998)
58. R. Österbacka, C.P. An, X.M. Jiang, Z.V. Vardeny, Science **287**, 839 (2000)

Chapter 4
Organic and Excitonic Solar Cells

Furong Zhu

Abstract Bulk heterojunction organic solar cells (OSCs) are an attractive alternative to silicon based solar cells due to low cost solution fabrication processes. The efficiencies and lifetimes of OSCs are not yet high enough for them to be commercially viable, but significant research effort has been devoted to improving the performance of OSCs through materials innovation and new device designs. It is known that the optical absorption in organic solar cells is limited due to the mismatch between the charge transport scale and optical absorption depth. There are two major research approaches aimed at improving the performance of OSCs. One approach is focused on the development of new organic compounds with tailored energy levels in order to increase the efficiency of OSCs through improved spectral response over the long wavelength region. The other is to realize broadband absorption enhancement in OSCs through light trapping effects. After a brief overview of basics of OSCs, the charge transport properties, different approaches including incorporating metal nanoparticles and surface plasmonic structures to enhancethe absorption in OSCs will be discussed. Apart from the encouraging results in achieving high efficiency for OSCs, realizing stabile OSC performance over a long operation lifetime also attracts a significant research effort. A comprehensive study on the degradation mechanisms of OSCs is also presented in the last part of the chapter.

4.1 Introduction

The direct conversion of solar energy into electricity by solar cells is considered as one of the lending contenders for renewable energy source and green power production as it generates no detrimental effects to the environment. However, the cost relating to power generation is one of the several challenges the photovoltaic (PV) technology faces today. The production of Si-based solar cells is approaching 3 GW/year with

F. Zhu (✉)
Department of Physics, Hong Kong Baptist University, Hong Kong, China
e-mail: frzhu@hkbu.edu.hk

J. Singh and R. T. Williams (eds.), *Excitonic and Photonic Processes in Materials*, Springer Series in Materials Science 203, DOI: 10.1007/978-981-287-131-2_4,

© Springer Science+Business Media Singapore 2015

billion dollars in worldwide revenue, but this figure is only representing a very small proportion of the total energy generated ($<1\,\%$) in the world [1]. Although, Si-based solar cells are still the dominant technology in the current market, other PV materials such as gallium arsenides and cadmium tellurides are also penetrating into the PV market, with a desire to reduce the manufacturing cost at the same time improving the cell efficiency [2].

The organic PV technology has attracted great interests due to its potential of low cost solution process capability. Bulk-heterojunction (BHJ) OSCs offer a potentially much cheaper alternative way to harness solar energy to generate electricity, and these can be made flexible and of large area. They can be also made semi-transparent and in different colors in building architecture. A broad range of distinct device technologies based on organic and organic/inorganic hybrid materials are being developed very rapidly, including polymer/fullerene blends, small molecule thin films and hybrid polymer/nanocrystal photovoltaic cells. Polymeric and organic semiconducting materials have been used for fabricating a variety of optoelectronic devices including organic light-emitting diodes (OLEDs) [3–5], organic thin film transistors [6], organic memory devices [7], organic photodetectors [8] and OSCs [9, 10]. In addition to the advantages of being lightweight, cost effective and compatible with flexible substrates, many of these organic and polymeric semiconducting materials possess broad absorption spectra, covering the entire visible spectrum as well as the ultraviolet and infrared spectral regions. The high absorption coefficients ($\sim 10^5\,\text{cm}^{-1}$) enable the use of thin films to achieve both efficient absorption of the incident light and fast response. The electronic and optoelectronic properties of these materials can be tailored through chemical structure modifications, to suit a particular application or spectral range. The low refractive indices of the organic materials and their corresponding transparent substrates (glass or plastics) also allow for efficient light coupling into devices, leading to potentially high quantum efficiencies.

The development of OSCs is still in its growing stage, particularly the design and optimization of their structure and the performance. The advantages such as low-cost due to possible solution processing technologies render OSC technology attractive for specialized or cost-sensitive applications. In particular, the flexibility and light weight make organic PV technology attractive for application in new markets such as flexible solar cells, power generating windows, smart sensors and outdoor lifestyle, etc. There is an increasing activity in this area, and the prospect for OSCs provides a realistic goal for eventual applications. The development of efficient and stable solar cells constitutes the next major step in this field.

After a brief overview of recent progresses of OSCs, device physics, organic/electrode interfacial engineering, realization of broadband absorption enhancement in nano-structured OSCs will be discussed. The device optimization of OSCs using optical admittance analysis and finite-difference time-domain (FDTD) simulation methods, light trapping and its effects on power conversion efficiency (PCE) and stability of BHJ OSCs will be discussed.

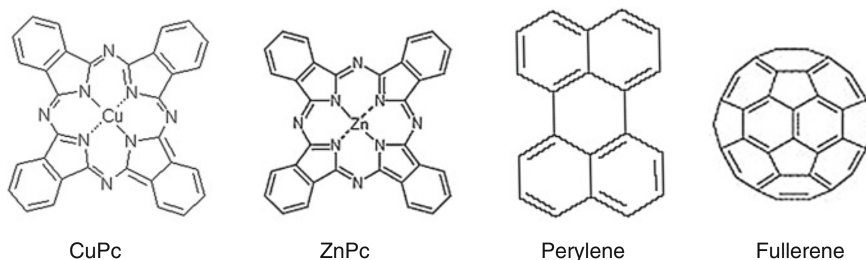

Fig. 4.1 Molecular structures of some organic photoactive materials of copper phthalocynine (CuPc), zinc phthalocyanine (ZnPc), perylene and fullerene (C_{60}) that are used for fabrication of small molecule OSCs

4.2 Basics of Organic Solar Cells

OSCs typically consist of a stack of organic functional layers, e.g., a blend layer of electron donor and electron acceptor materials, sandwiched between a front transparent electrode and a reflective counter electrode. The donor and acceptor can be small molecules, conjugated polymers, or a combination of both, which can be prepared using sublimation and solution processes. Organic photoactive materials, for example, phthalocyanine as donor and peryleneas acceptor and their derivatives are examples of small molecular materials that are commonly used for fabrication of OSCs. Figure 4.1 illustrates the molecular structures of phthalocyanine, perylene, bulkminster fullerene and their derivatives that can be fabricated through the sublimation method.

The optical bandgap of typical photoactive organic semiconducting materials is around 1.7–2.0 eV. The intrinsic carrier concentration in organic materials is very low at room temperature in the dark. The mobility of the carriers in organic semiconducting materials is relatively small as compared to the inorganic counterparts. Organic materials can be nearly regarded as insulators. However, there are a few ways to increase the charge carrier concentration through methods such as chemical, photochemical or electrochemical doping. These procedures introduce extrinsic charge carriers into the organic semiconductors. For making p-type, organic materials can be doped by exposing them to oxygen or other strong oxidizing agents. In this way, the doping effect is achieved by transferring an electron from the ground state of an organic semiconductor to the oxidizing agent, resulting in an increased holeconcentration in the organic semiconductor. Another common approach is to form a donor/acceptor blend. A mixture of CuPc and C_{60} or its derivatives is often used because C_{60} is reported as a strong electron acceptor. This mixture of CuPc:C_{60} system does not show an improved behavior in charge transport properties when it is in the dark, but it leads to an enhancement in photoconductivity under illumination due to the photoinduced charge transfer [11] or known as “photo-doping” [12].

Hole conducting polymers of MDMO-PPV and P3HT are examples of donor materials. The electron transporting materials include the derivatives of C_{60},

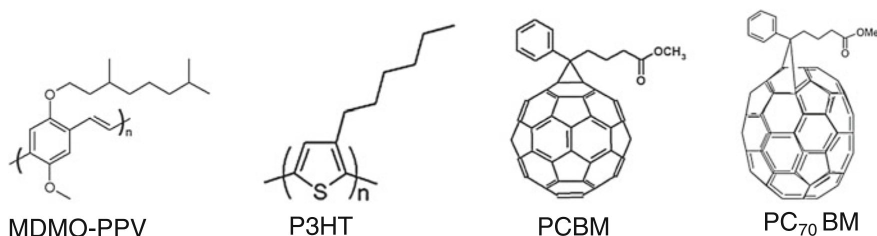

Fig. 4.2 Examples of solution processable conjugated polymers and fullerene derivatives used in OSCs as donors and acceptors, respectively

namely regio-regular poly(3-hexylthiophene):[6,6]-phenyl-C61-butyric acid methyl ester (PCBM, or $PC_{60}BM$) and 3′H-Cyclopropa[8,25] [5,6]fullerene-C70-D5h(6)-3′-butanoicacid, 3′-phenyl-, methyl ester ($PC_{70}BM$), are acceptors. The molecular structures of MDMO-PPV, P3HT, PCBM and $PC_{70}BM$ are shown in Fig. 4.2. These materials have side chains that enable them to be solution-processed [4, 13, 14].

The absorption coefficient of organic semiconductors, including conjugated polymers and small molecules, is very high ($>10^5\ cm^{-1}$), however, the absorption depth is usually greater than the diffusion range of the photo-generated excitons. Thus only a fraction of the excitons is able to find the donor/acceptor heterojunction interface at which exciton dissociation can take place. The possible performance enhancement may be realized in OSCs through use of blends of the donor and acceptor materials. Poorer utilization of photo-generated excitons and exciton dissociation by rapid and efficient charge transfer usually cause the lower photocurrent. Solutions for improving the conversion efficiency of OSCs includes (1) combining the double heterostructure with novel light trapping schemes, (2) using materials with extended exciton diffusion lengths, and (3) stacking of single heterojunction devices.

When donor and acceptor types of functional organic semiconducting materials are blended together, intimate donor-acceptor nanoscale morphology can be achieved. The energy levels of these materials will be meticulously controlled to facilitate charge transfer between the donor and acceptor at the interfaces of the thin films. Under the illumination, the organic photoactive materials, e.g., conjugated polymers or small molecules forming the electron donor region of OSCs, possess delocalized π electrons that result from carbon p orbital hybridization. These π electrons can be excited by light in or near the visible part of the solar spectrum from the highest occupied molecular orbital (HOMO) to the lowest unoccupied molecular orbital (LUMO) and holes on the HOMO of the molecules. As a result of the photo-excitation process, exitons are generated. The energy bandgap between LUMO and HOMO orbitals determines the absorption of light entering to the OSCs.

The performance of OSCs is determined primary by the following factors: (i) absorption efficiency of the materials for generating photo-induced excitons; (ii) the exciton diffusion length; (iii) the ratio of the exciton dissociation at the donor/acceptor interface; and (iv) the charge collection efficiency at the interfaces of anode/organic and organic/cathode. It has been recognized that the most efficient exciton dissociation in organic materials can occur at donor/acceptor interface

[15, 16]. Depending on the alignment of energy levels of the donor and acceptor, the dissociation of bound exciton can become generically favorable at the interface. The time scale for such a dissociation is of a few hundred femtoseconds, which is much shorter than any other competing process, thus the exciton dissociation (or charge transfer from the donor to the acceptor) efficiency can be made up to 100 %. Therefore, the device efficiency will be mainly determined by: exciton absorption, exciton diffusion to donor/acceptor interface and free charge transport to the opposite electrode. It has been reported that the exciton diffusion efficiency can be enhanced by establishing an intimate contact between the donor and acceptor by blending [15] and laminating [16] or co-depositing them [17, 18]. Thus controlling the film morphology to form percolating paths to enhance the exciton diffusion, charge transport and charge collection efficiency at anode/organic and organic/cathode interfaceare crucial for achieving high efficiency OSCs [19].

(i) Absorption efficiency of the materials for generating photo-induced excitons

Photoactive organic semiconducting materials have a relative high absorption coefficient ($\alpha \sim 10^5$ cm^{-1}). Although from a material point of view, an appreciate amount of incident light can be absorbed if the energy of incident photon, $E = h\upsilon$, is larger than or equal to the energy difference between the HOMO and the LUMO of the semiconducting materials. It is known that light absorption in OSCs is limited due to the presence of a mismatch between the charge transport scale and optical absorption depth. There are two major research approaches towards improving the performance of OSCs. One attention has been paid on the development of low band gap conjugated organic polymers whereby to increase PCE of OSCs through improved spectral response over the long wavelength region. The other is the device approach in which the enhanced absorption in OSCs is achieved using light trapping effects.

(ii) Exciton generation and diffusion

The primary photo-generated excitations in organic materials do not directly and quantitatively lead to free charge carriers but to form coulombically bound electron-hole pairs, or known as excitons. The binding energy of photo-generated excitons in organic materials, in a range of 200–500 meV [20, 21], is about 4–5 times larger than the ones in conventional inorganic semiconductors, e.g., Si, where photo-excitations typically lead to free carriers directly at room temperature. It is estimated that only 10 % of the photo-generated excitons will lead to free charge carriers in pure conjugated polymers [22]. Therefore, a strong electric field is required to break the excitons in organic semiconducting materials. At the interface, a strong electric field exists due to the presence of an abrupt potential energy difference at the donor/acceptor interface. Photo-generated excitons diffuse to the interface forming charge transfer exciton states if excitons reach the interface within their lifetime. The diffusion length of excitons in organic materials is an important parameter to be considered as it not only limits the thickness of a bilayer (donor-acceptor heterojunction configu-

ration), it also affects the PCE of the whole device. BHJ is widely adopted for application in OSCs, the exciton diffusion length should be of the same order of magnitude as the donor-acceptor phase separation length. Otherwise, excitonsmay decay via radiative or non-radiative recombinations before reaching the donor/acceptor interface. The diffusion length of photo-excited excitons in organic photoactive materials is typically in the order of 10–20 nm.

(iii) Interfacial exciton dissociation

It is reported that fullerene and its derivatives are strong electron acceptors [11]. The excitons can be dissociated effectively to form free carriers at donor/fullerene interface. Ultrafast photo-physics studies revealed that the photo-induced charge transfer in such blends occurs in a time scale of 45 fs. This is much faster than other relaxation processes such as photoluminescence (usually occurs at around 1 ns) [23]. The reverse electron transfer from fullerenes back to the polymer is extremely slow. The separated charges in such blends are metastable at low temperatures. They should be transferred away from the interface before getting recombined again.

(iv) Charge transport and collection

The free electrons and holes created by the dissociation of excitons in the process (iii), should be transported effectively towards the respective electrodes within their lifetime. These charge carriers are unable to do so unless a driving force is applied. A chemical potential gradient in electrons and holes is built up due to the difference in work functions of the two electrodes. This potential gradient is generally defined by the difference between the work functions $\Delta V = \phi_a - \phi_c$ between the anode (φ_a) and cathode (φ_c) electrodes. This internal electric field correlates closely with the open circuit voltage (V_{OC}) of OSCs and contributes to a field-induced drift of the charge carriers. Therefore, in order to enhance the charge transport, asymmetrical contacts are used, e.g., a cathode with a low work function for electron collection and an anode with a high work function for hole collection, to generate an external field in short circuit conditions according to a metal-insulator-metal configuration. In order to optimize the PCE and lifetime of OSCs, it is important to understand the charge transport properties under various operation conditions and to identify the loss (or degradation) mechanisms. The complexity of physics in understanding the operation of OSCs offers major challenging new research developments. In particular, the correlation between the charge transport/recombination and the device performance parameters (lifetime, efficiency) are not clearly understood and there are no known systematic reports on this topic. A better understanding on charge trapping behavior with respect to the quality of the materials and the process conditions is important for achieving high performance OSCs.

PCE is one of the critical parameters for OSCs, which is determined by the ratio of the maximum output power generated to the power of the incident light. The current

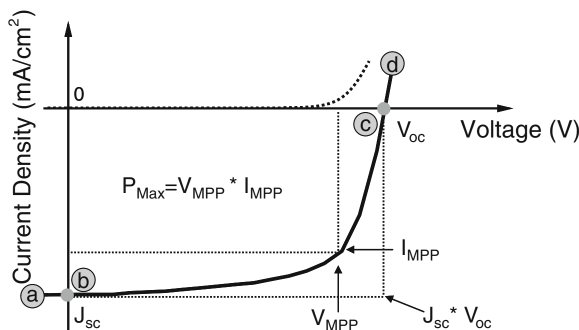

Fig. 4.3 Typical current density-voltage characteristics of a solar cell

density-voltage (*J–V*) characteristic of a solar cell is illustrated schematically in Fig. 4.3.

A conventional OSC can be considered as a photo diode. The dotted curve shown in Fig. 4.3 represents the *J–V* characteristics of an OSC measured in the dark. Under illumination, *J–V* curve (solid curve) is shifted under forward bias, representing the photo-generated current flows towards opposite direction of the external bias. For example, at point b in the *J–V* curve under illumination, there is no external voltage. The current density at point b is referred to the short circuit current density (J_{SC}). At point c on the same curve, the corresponding voltage at zero current density is defined as V_{OC}, where the flow of the injected current due to the external bias is the same as the photo-generated current but opposite in direction. The output power of an OSC is the product of its photocurrent density and the voltage. At a particular point in the solid curve in Fig. 4.3, for an OSC with a given active area, its maximum output power density, P_{out}, is determined by J_{MP}, where J_{MP} are the corresponding photo-generated current density and the photovoltage of the maximum output power of the cell under a given illumination with a power density of P_{in}. The PCE can be calculated using the following equation:

$$PCE = \frac{P_{out}}{P_{in}} = \frac{J_{MP} \times V_{MP}}{P_{in}}. \tag{4.1}$$

There is another way to estimate the PCE value using J_{SC} and V_{OC} that can be read directly from the *J–V* curve. In this approach, a fill factor (FF) of the solar cells is defined. This is the ratio of the maximum output power density $J_{MP} \times V_{MP}$ to $V_{OC} \times J_{SC}$. By replacing FF for $J_{MP} \times V_{MP}$ in (4.1), PCE is obtained as given in (4.2), which is often used to calculate PCE of the cell:

$$PCE = \frac{P_{out}}{P_{in}} = \frac{FF \times V_{OC} \times I_{SC}}{P_{in}}. \tag{4.2}$$

In parallel to the new materials development, detailed understanding of the charge or energy transfer processes and photo-generated exciton dynamics in OSCs is

another important area for developing high performance BHJ OSCs. Steady state photo-induced absorption (PA) using pump-probe technique has been used to study these excited states in the polymer film [24]. Vardeny and co-workers [25–28] have extensively studied the PA and stimulated emission related to singlet/triplet exciton, polaron and bipolarons in pristine polymer films and solutions. The exciton dynamics in OSCs has been focused to better understand the relaxation processes and dynamics of charge separation (from exciton) to weakly bound charge transfer (CT) state (i.e., CT exciton) at the donor-acceptor interface, and its subsequent dissociation to free charge carriers [29–34]. For investigation of relaxation dynamics, one uses time-resolved and transient PA techniques. Detailed transient PA measurements were carried out in the donor/acceptor blends to get a better understanding of the photo-generated carrier recombination dynamics in OSCs [29, 30, 33–35]. The results show that charge separation and recombination dynamics in polymer/fullerene interface are very complex with relaxation time scale from femtosecond to nanosecond and microsecond time scale [29]. PA experiment also indicates that significant amount of CT excitons get recombined at the donor/acceptor interface before they have a chance to completely separate forming mobile carriers [29, 32]. Various processes such as thermal annealing [31] or new synthesis routes [36] can alter the morphology of the bulk heterojunction mixture and consequently the relaxation dynamics and free carrier yields. For example, using thermal annealing, transient PA demonstrated slower decay and large PA signal from charge carriers [31]. The increase in the yield of dissociated charges by thermal annealing helps to produce solar cell with significantly high efficiency. Thus steady and transient PA is a very powerful tool to investigate the separation, relaxation and recombination dynamics of the photo-generated excitons.

4.3 Electrode Modification and Interfacial Engineering

The improvement in the PCE of OSCs relies on the thorough understanding as well as effective engineering of interfacial properties. The interfacial properties at cathode (metal)/organic and anode (ITO)/organic interfaces play a critical role in determining the device performance. Some electrode surface treatment methods, including UV-ozone exposure, argon and oxygen plasma treatments, have been used in organic electronic devices including OLEDs and OSCs. It is known that the interfacial energy level alignment at organic/electrode interface has a crucial impact on the device performance. The offset between LUMO of organic materials and the conduction band minimum of inorganic semiconductor electrode, e.g., ITO anode, is important for efficient charge collection and charge transport in OSCs. The knowledge on organic/electrode interfacial electronic structures, energy level alignment, interfacial charge transfer and emerging design concepts is a prerequisite for developing efficient OSCs. In order to optimize the performance of OSCs, it is also important to understand light distribution in the multilayer structure, charge transport properties and charge collection at organic/electrode to identify the loss (or degradation) mechanisms.

4.3.1 Plasma-Polymerized Fluorocarbon-Modified Ag Nanoparticles

It is known that light absorption in OSCs is limited due to the presence of a mismatch between optical absorption length and charge transport scale, caused by the low charge mobility in conjugated polymers. Therefore, the thickness of organic functional layer in OSCs is usually less than 300 nm. In order to enhance the absorption in such thin organic functional layer, light trapping is often used enabling thin photoactive layer in OSCs to absorb more light for high PCE. The feasibility of light trapping using textured surfaces and photonic crystal structures to couple and/or confine incident light more efficiently into OSCs has been demonstrated [37]. Another promising approach for light trapping in OSCs is through the use of plasmon resonance using noble metal structures. Under conditions of localized surface plasmon in metal nanoparticles or propagated surface plasmon resonance on metal surfaces, the conduction electrons in the metal are driven to oscillate and interact with the incident light [38, 39]. The energy of plasmon excitations is strongly localized at the interface of the metal/organic dielectric layer. Within the skin depth (usually 100–200 nm for organic thin films) of the electric field of plasmon excitation, the energy of plasmon excitation can be efficiently coupled to boost light absorption in the photoactive layer and thus to improve the performance of OSCs [40]. The excitation of plasmonic modes using Ag nanoparticles [41, 42], Ag nanoprisms [43] and metal gratings [44–46] has been experimentally proven to be viable approaches for absorption enhancement in OSCs.

The incorporation of metal nanoparticles in conventional solar cells [47, 48] has shown to enhance light absorption in the semiconductor layer, which is attributed to the plasmonic effect of metal nanoparticles and light absorption of the neighboring semiconductors close to the metal nanoparticles is greatly enhanced. An increase in PCE was also observed in organic solar cells with incorporation of metal nanoparticles in the active layers. It shows that the metal nanoparticles indeed have a notable effect on the improvement of light absorption resulting in overall device performance. In order to take the full advantage of absorption enhancement using plasmonic excitation, a better understanding of the performance enhancement in OSCs incorporating metal nano-scale features becomes a prerequisite. This would enable effective utilization of both low-dimensional semiconductor structures and thin films of functional organic photoactive semiconductors, which have poor charge transport properties, for high performance solar cells. The improvement in device efficiency with the incorporation of metal nanoparticles is discussed in this chapter.

In this section, we will discuss the plasmonic enhancement in OSCs made using Ag nanoparticles modified ITO front transparent electrode. ITO/Ag nano-particle contact can be prepared by controlled thermal evaporation of ultrathin Ag layer following a post-annealing to form a layer of nano-Ag particles on ITO surface or using solution-processed Ag nanoparticles that can be deposited with spin-coating method. The particle size, the coverage (or concentration) of Ag nanoparticles on ITO and the effect on the overall performance of OSCs, based on ZnPc:C_{60} system, can

be correlated to light absorption in the photoactive layer in the cells. Ag nanoparticles are modified by an ultra-thin plasma-polymerized fluorocarbon film (CF_X) to form a composite Ag nanoparticles/CF_X contact on an ITO surface to boost light absorption in ZnPc:C_{60}-based OSCs. The surface electronic properties of CF_X-modified Ag nanoparticles/ITO were studied using ultraviolet photoelectron spectroscopy (UPS) [49].

ZnPc:C_{60}-based OSCs have a layer configuration of glass/ITO(160 nm)/Ag (1.5 nm)/CF_X(~0.3 nm)/ZnPc:C_{60}(35 nm,1:1)/C_{60}(25 nm)/4,7-diphenyl-1,10-phenanthroline (BPhen) (7 nm)/Ag(100 nm), in which the CF_X-modified Ag nanoparticles/ITO forms a composite anode. The composite anode is formed by the thermal evaporation of an ultra-thin Ag layer on ITO/glass followed by the subsequent modification of Ag/ITO contact by an ultra-thin CF_X layer, deposited by a C_4F_8 plasma processing method [49]. After the formation of the composite electrode of CF_X-modified Ag nanoparticles/ITO, the active layer of ZnPc:C_{60}, electron transport layer of BPhen and cathode of Ag were then deposited through thermal evaporation. OSCs had an active area of 3.0 mm $\times$ 3.0 mm.

The *J–V* characteristics of the OSCs were measured under air mass 1.5 global (AM1.5G) irradiation (100 mW/cm^2), generated typically by a solar simulator. Light intensity of the solar simulator for OSC characterization in the laboratory can be determined by a monosilicon detector (with KG-5 visible color filter) calibrated by the National Renewable Energy Laboratory to minimize spectral mismatch. The surface work function of bare ITO and CF_X-modified Ag nanoparticles/ITO is examined using UPS with the Helium line (21.2 eV). UPS analysis reveals that the surface work function of the anode can be increased from ~4.4 eV for bare ITO to ~5.4 eV for CF_X-modified Ag nanoparticles/ITO, which is advantageous to charge collection at the anode/organic interface in organic photovoltaic cells. Hence, a CF_X-Ag nanoparticles/ITO anode has advantages of (i) improved charge collection efficiency at anode/organic interface, and (ii) enhanced light absorption in the active layer of ZnPc:C_{60}-based OSCs through broadband scattering of Ag nanoparticles.

4.3.2 Effect of ITO Surface Electronic Properties on OSC Performance

ITO has been widely used as anode for applications in OSCs. However, a device formed on a bare ITO surface usually shows imperfection in its performance. The mitigation of this problem has involved anode modification, e.g., oxygen/UV ozone plasma treatments or interposing an appropriate intermediate ultrathin interlayer between the organic and ITO anode. Ag/CFx has been demonstrated to be an effective anode for OLEDs [50]. The modification of ITO using an ultrathin Ag layer for application in OSC was investigated. It is found that CF_X-modified Ag nanoparticles/ITO forms an excellent anode for efficient OSCs. However, the performance of OSCs based on ultrathin Ag electrode deteriorates quite substantially as the Ag layer thickness increases, leading to a reduced absorbance in the active layer of the OSCs [49].

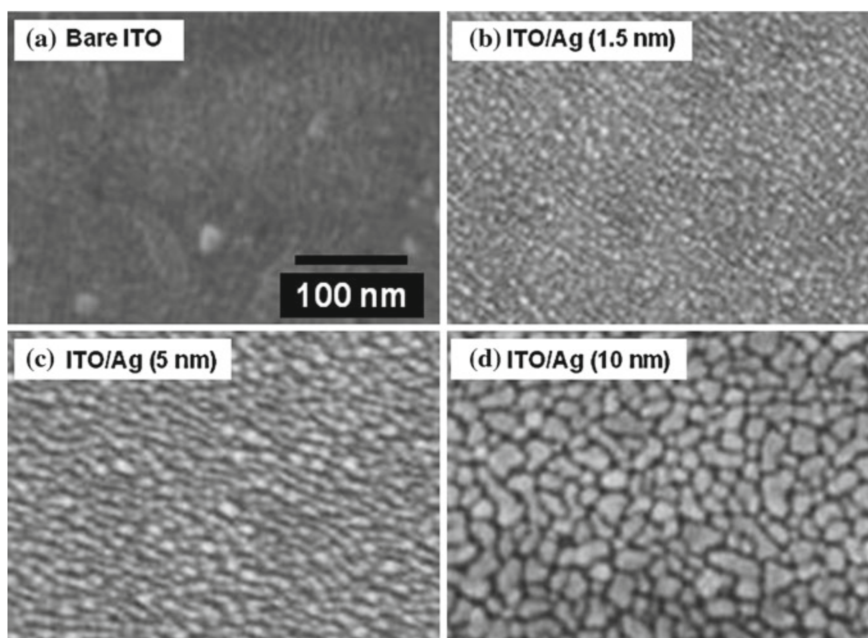

Fig. 4.4 SEM images of a bare ITO and Ag nanoparticles modified ITO surfaces: **a** ITO/glass, **b** 1.5 nm-thick Ag on ITO/glass, **c** 5 nm-thick Ag on ITO/glass, and **d** 10 nm-thick Ag on ITO/glass

Scanning electron microscopy (SEM) images for a bare ITO and the CF_X-modified Ag nanoparticles/ITO surfaces are shown in Fig. 4.4a–d. The average size of the Ag nanoparticles ranges from ∼10 to ∼20 nm as the thickness of the Ag film increases from 1.5 to 10 nm—a consequence of coalescence with increasing time of deposition. As a thick Ag layer is expected to increase the energy loss attributable to reflection or scattering from the metallic layer, a 1.5 nm thick ultra-thin Ag layer which is non-continuous as shown in Fig. 4.4b, was chosen such that the resulting anode retains a relatively high level of optical transparency and the beneficial contribution of plasmonic effect to enhance light absorption in the active layer of the OSCs.

In order to better understand the changes in surface work function of the ITO anode, the surface electronic properties of the modified ITO were studied using UPS measurement to determine the electronic structures on both bare ITO and CF_X-modified Ag nanoparticles/ITO surfaces. Figure 4.5 shows the secondary electron edge in the UPS spectra measured for bare ITO, Ag nanoparticles/ITO and CF_X-modified Ag nanoparticles/ITO surfaces, which can provide information on the work function of the ITO surface. The spectra show that the work function of ITO (∼4.4 eV) is reduced to ∼4.1 eV with the incorporation of a 1.5 nm-thick Ag layer in ITO/Ag, but the combinatory layer of ITO/Ag/CF_X significantly increased the anode work function to ∼5.4 eV. The work functions of ITO after UV-ozone and O_2 plasma treatments (not shown here) become about 5.1 and 5.4 eV, respectively.

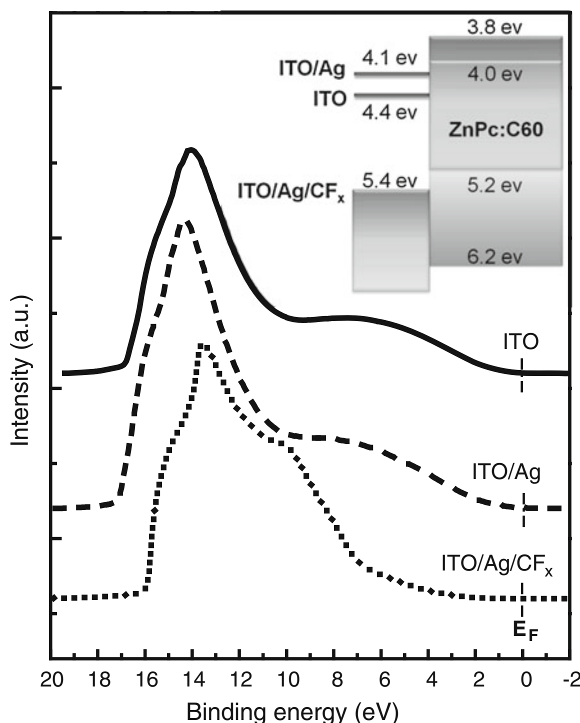

Fig. 4.5 Evolution of the secondary electron edge in UPS spectra measured for bare ITO, Ag nanoparticles/ITO, and CF_X-modified Ag nanoparticles/ITO surfaces (from *top* to *bottom*). The insert illustrates the schematic diagram of energy levels in ZnPc:C_{60}-based OSCs with different anode contacts of ITO, Ag nanoparticles/ITO and CF_X-modified Ag nanoparticles/ITO

A CF_X-modified Ag anode has been applied to improve carrier injection properties in organic light-emitting diodes [49]. It is found that CF_X-modified Ag nanoparticles/ITO also exhibits a higher surface work function. This clearly reveals that modification of ITO through Ag nanoparticles/CF_X confers superior high surface work function suited for application in OSCs. It is known that the interfacial energy level alignment at organic/electrode interface has a crucial impact on the device performance. The offset between the lowest-unoccupied-molecular-orbital of organic films and the Fermi level of an anode, e.g., ITO, is important for efficient charge collection in the devices. The inset in Fig. 4.5 illustrates the schematic energy diagram of a ZnPc:C_{60}-based OSC. As shown in the inset of Fig. 4.5, the difference in energy level between the work function of an ITO anode ($\sim$4.4 eV) and the highest occupied molecular orbital of ZnPc (5.17 eV [51]) at the ITO/ZnPc:C_{60} interface, can be reduced significantly after the ITO anode is modified with Ag nanoparticles/CF_X. The reduced electronic barrier at the ITO/CF_X-Ag nanoparticles /ZnPc:C_{60} interface is favorable for charge extraction in OSCs.

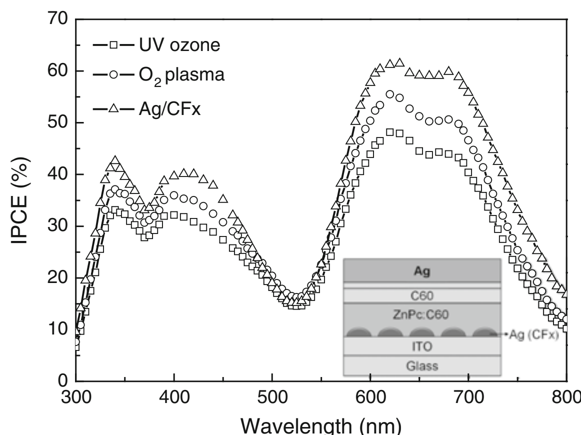

Fig. 4.6 Comparison of incident photon to current efficiency (IPCE) spectra measured for ZnPc:C_{60} based OSCs with different anode contacts: ITO with UV-ozone surface treatment (*open square* symbol), ITO with in situ O_2 plasma treatment (*open diamond* symbol) and CF_X-modified Ag nanoparticles/ITO anode (*open triangle* symbol)

OSCs of ITO/Ag/CF_X/ZnPC:C_{60}/C_{60}/BPhen/Ag were fabricated along with two other control devices of ITO/ZnPc:C_{60}/C_{60}/BPhen/Ag, each with different surface treatment of the ITO anode prior to thermal evaporation of the organic layers. Two control OSCs prepared for comparison studies are made with (i) an ITO anode treated with UV-ozone (control device-1) and (ii) an ITO anode treated with *in situ* O_2 plasma (control device-2). IPCE of the OSCs and the two control devices over the wavelength range from 300 to 800 nm were measured and the results are shown in Fig. 4.6. The general trend of the IPCE spectra of the OSCs made with UV-ozone treated, O_2 plasma treated and CF_X-modified Ag nanoparticles/ITO electrodes is similar, consisting of two broad peaks (each divided into 2 local peaks) and a trough at 480–580 nm. With the exception of the trough where the IPCE of all OSCs are similar, the IPCE of the OSCs is notably higher than that of the O_2 plasma processed device which is in turn greater than that of the UV-ozone case. The *J–V* characteristics of the OSCs are shown in Fig. 4.7. J_{SC}, V_{OC}, FF and PCE of the OSCs measured under AM1.5G irradiation are summarized in Table 4.1. It can be seen that the OSCs with CF_X-Ag nanoparticles/ ITO composite electrode has the best performance.

The work function measured for ITO treated with *in situ* O_2 plasma is about 5.4 eV, which is similar to that of a CF_X-modified Ag nanoparticles/ITO anode based on our UPS measurement (See schematic energy level diagram given as the inset of Fig. 4.5). This implies that the anode/organic interface in OSCs with *in situ* O_2 plasma (control device-2) and the modified-ITO (OSC) would have very similar charge collection efficiency. Hence, similar IPCE for both OSCs would be expected if this accounts for the main contribution to the improvement in device performance. Evidently, this has not been the case. For the same surface work function, the incorporation of the Ag metallic layer would, in all likelihood, reduce the admission of light into the device

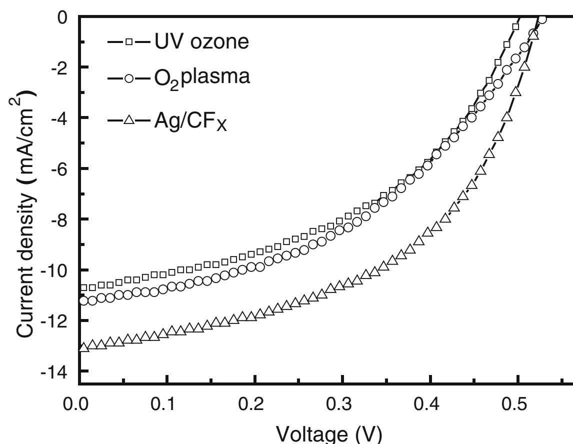

Fig. 4.7 *J–V* characteristics measured for ZnPc:C_{60}-based OSCs fabricated on ITO treated with: UV-ozone surface treatment (*open square*), in situ O_2 plasma treatment (*open circle* symbol) and CF_X-modified Ag nanoparticles/ITO anode (*open triangle* symbol)

Table 4.1 Photovoltaic characteristics of the ZnPc:C_{60}-based OSCs with ITO anode treated with UV ozone, O_2 plasma and modified with Ag nanoparticle/CF_X

Anode	UV ozone (Control device-1)	O_2 plasma (Control device-2)	Ag/CF_X
J_{SC} (mA/cm^2)	10.72 ± 0.50	11.13 ± 0.50	13.10 ± 0.50
V_{OC}(V)	0.50 ± 0.05	0.52 ± 0.05	0.52 ± 0.05
FF (%)	0.46 ± 0.05	0.47 ± 0.05	0.51 ± 0.05
PCE (%)	2.4 ± 0.1	2.7 ± 0.1	3.5 ± 0.1

and lower the IPCE. Therefore, an explanation involving only improved contact properties at anode/organic interface is not sufficient to account for the improved performance of the device concerned.

The increase in PCE of the OSCs with an CF_X-modified Ag nanoparticles/ITO anode can be attributed to combined effects of (1) improved charge collection properties at the modified ITO/organic interface, and (2) enhanced absorption in the active layer of OSCs through the advantages of broadband plasmonic enhancement effect [52, 53]. From the SEM image of the 1.5 nm-thick non-continuous Ag layer on ITO surface, as shown in Fig. 4.4b, it can be seen that the Ag nanoparticles have an average lateral dimension of ~5–10 nm. Localized plasmon resonance of Ag nanoparticles is known to be excited by incident light, the wavelength of plasmon resonance being dependent on the size and shape of the Ag nanoparticles and the permittivity of the surrounding dielectric background. Under conditions of plasmon resonance, the local electric field around the Ag nanoparticles (tens of nm) is strongly enhanced. The strong field aids the absorption of light in the organic photovoltaic devices, leading to enhanced device performance.

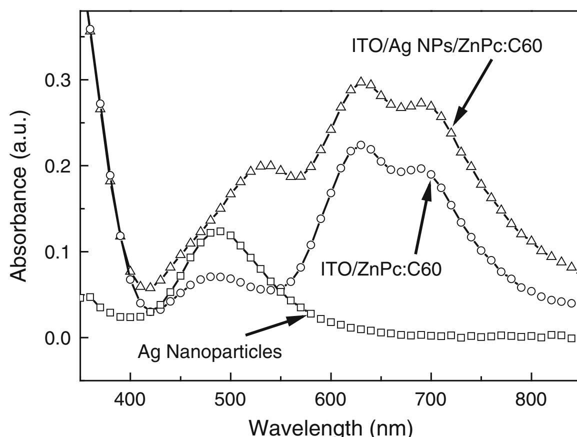

Fig. 4.8 Absorption spectra for Ag nanoparticles on ITO, 35 nm-thick ZnPc:C_{60} blend layer deposited on ITO and ITO/Ag nanoparticles

Optical absorption spectra measured for 1.5 nm-thick Ag nanoparticles on ITO are shown in Fig. 4.8. Deposition of Ag nanoparticles on ITO/glass evidently leads to higher absorption of the blend on glass/ITO/Ag (open trianglecurve. As the Ag nanoparticles have a range of lateral dimensions of ~5–10 nm, the absorption is relatively broad extending over a wavelength range below ~550 nm. The mean size of the Ag nanoparticles at ~10 nm accounts for the broad absorption peak at $\lambda \sim$ 480 nm. In comparison, the absorption peak is red shifted in the ZnPc:C_{60} blend layer deposited on CF_X-modified Ag nanoparticles/ITO. As shown in Fig. 4.8, it can be gleaned that the incorporation of the ultra-thin Ag layer significantly improves the absorption in an active ZnPc:C_{60} layer on the modified ITO anode over the wavelength range from ~420 to ~800 nm. The relative low absorption of ZnPc:C_{60} layer on CF_X/ITO over the wavelength range from ~420 to ~550 nm (open triangle curve) culminates to a local peak in the ZnPc:C_{60} layer on CF_X/Ag nanoparticles/ ITO, while the double peak over the wavelength range from ~580 to ~800 nm is further enhanced. The absorption spectra of ZnPc:C_{60} on Ag nanoparticle/ITO (open square curve) show a similar trend. Examining the absorption spectra of ZnPc:C_{60} in greater detail reveals that a slightly higher absorption is observed for the ZnPc:C_{60} blend layer on Ag nanoparticles/ITO (open square curve) than for the case with CF_X/Ag nanoparticles /ITO for wavelength >610 nm, implying that the former would induce a higher absorption in devices. However, the work function of a bare ITO/Ag anode (Fig. 4.5) is not favorable to an efficient charge extraction at ITO-Ag/organic interface.

Comparing the absorption spectra of the glass/ITO/CF_X/ZnPc:C_{60} and glass /ITO/Ag/CF_X/ ZnPc:C_{60} samples with the IPCE of the finished devices (glass/ITO /ZnPc:C_{60}/C_{60}/BPhen/Ag and glass/ITO/Ag/CF_X/ZnPc:C_{60}/C_{60}/BPhen/Ag), a good correspondence in the broad absorption peaks over the wavelength range from ~580 to ~800 nm can be observed. It is obvious that the enhanced absorption brought on by

the incorporation of the Ag nanoparticles layer translates into an improved spectral responsivity and hence the enhancement in the power conversion efficiency of the OSCs. It is clear that the IPCE of the OSCs with Ag nanoparticles/CF_X-modified anode remains higher than those with the bare ITO anode. This allows a notably higher J_{SC} of $13.10 \pm 0.50\,mA/cm^2$ to be achieved compared to $10.72 \pm 0.50\,mA/cm^2$ in control device-1 and $11.13 \pm 0.50\,mA/cm^2$ in control device-2, as summarized in Table 4.1. The results reveal that CF_X-modified Ag nanoparticles/ITO anode exhibits a superior surface work function of 5.4 eV suited for application in OSCs. The composite anode of Ag nanoparticles with inclusion of CF_X enhances the performance of OSCs through improved light harvesting in the OSCs, demonstrating a promising PCE of $3.5 \pm 0.1\,\%$, notably higher than that with a bare ITO anode ($2.7 \pm 0.1\,\%$).

4.3.3 Ag Nanoparticles-Modified ITO/Plastic Substrate for Flexible OSCs

OSCs have attracted a lot of attention due to their potential of low-cost and large area manufacturing capability. Research has been focused on developing flexible OSCs through materials innovation and device optimization. The potential for low-cost arises from the relatively simple processing steps, scalable processes, abundance of low cost materials and the fabrication flexibility [54–56]. The fabrication of OSCs on flexible substrates opens up avenues that are beyond the reach of rigid solar cells. For instance, through roll-to-roll processing techniques, gravure printing, doctor blading etc., really large-scale and low cost production of flexible OSC can be achieved [57]. ITO has been the most frequently used transparent conducting oxide (TCO) for many applications [58]. The unique bulk properties are generally described by a high optical transparency over the visible spectrum and a low electrical resistivity. However, deposition of ITO employs vacuum-coating steps and a high-temperature annealing step is required to develop the high conductivity—this is incompatible with plastic-based substrates. Another factor inhibiting higher PCE in OSCs, particularly large area modules, is resistive losses incurred within TCO anode network, resulting in inefficient charge collection. Although anode layout design can be optimized to minimize these losses, there is a lower limit to which this can be attained due to the intrinsic resistivity of the anode. There are other requisites for a high performance anode in OSCs such as high optical transmittance to minimize parasitic absorption by the anode, reasonably smooth surface to avoid shunting through the thin active layer, and high work function for efficient charge collection. A low-temperature process for depositing the TCO layer on the flexible substrate is also critical for low-cost OSCs and to avoid heat-induced damage to the plastic substrate.

High quality ITO films can be fabricated by radio frequency magnetron sputtering at a low processing temperature, involving the use of hydrogen species during the sputtering [59]. ITO film with a thickness of 130 nm and sheet resistance of $25 \pm 5\,\Omega/sq$ can be fabricated over the hydrogen partial pressure from about $1{-}3 \times 10^{-3}$ Pa. The average transmittance of over 85 % in the range of the visible

wavelength from 400–800 nm can be obtained on glass. A low-temperature (<60 °C) sputtering process of high quality ITO as a TCO was developed enabling the fabrication of a semitransparent solution-processed P3HT:PCBM [59] and ZnPc:C_{60} [60] based OSCs. ITO sputtering technology was also applied to the fabrication of an efficient semitransparent ZnPc:C_{60}-based OSCs with a transparent cathode of Ag/CF_X/ITO with a PCE of ∼3.0 % [60]. Bending tests of the low processing temperature ITO (LT-ITO) on flexible PET substrates for flexible top-emitting OLED applications have also been carried out. It was shown that good adhesion between the ITO-based anode and the substrate (no anode delamination) was achieved with the presence of an intermediate acrylic layer [61]. LT-ITO-coated PET flexible substrate, with an ITO layer thickness of ∼130 nm and a sheet resistance (25 ± 5 Ω/sq), was used for fabrication of flexible OSCs.

For comparison studies, BHJ OSCs based on ZnPc:C_{60} donor/acceptor system were fabricated using commercial ITO-coated glass (C-ITO) (thickness ∼120 nm, sheet resistance ∼8 Ω/square) and LT-ITO/PET substrate. The ITO substrates were cleaned using acetone, isopropanol and de-ionized water in an ultra-sonicator. This was followed by oxygen plasma treatment. A 35-nm-thick photoactive blend layer of ZnPc:C_{60} in a volume ratio of 1:1 was deposited via co-evaporation on the ITO substrate. Next, a 25-nm-thick C_{60} acceptor layer was deposited on the ZnPc:C_{60} blend followed with a 7-nm-thick (BPhen) exciton-blocking layer. A control OSC with an identical organic device structure but finished with a 100 nm thick Ag cathode was also fabricated for comparison studies. The ZnPc, C_{60}, BPhen and metal layers were thermally evaporated in a vacuum chamber with a base pressure of $\sim 10^{-5}$ Pa, with an active area of 3.0 mm × 3.0 mm.

The work function of LT-ITO films, fabricated at different processing conditions, can be deduced by the difference between the photon energy ($h\nu = 21.2$ eV) and the secondary electron cutoff in UPS spectra shown in Fig. 4.9a. It shows that the work function of LT-ITO films decreased with increasing hydrogen partial pressure leading to an increase in the carrier concentration in LT-ITO. A work function is defined as the energy difference between the Fermi energy and the vacuum level. The widening in the energy gap between the Fermi level and the vacuum level leads to an increase in the work function. This can be realized by either forming surface dipoles or changing surface band bending. If the shift in work function of ITO is due to change in its surface dipole, resulting a change in its electron affinity, but the Fermi level position relative to the energy band will not change. If the shift in work function is due to the variation in the surface band bending, the Fermi level position relative to the energy band will change [62]. In degenerated oxide semiconductors, e.g., ITO, the shift in the valance band maximum (VBM) can always be observed. In this case, the change in the work function is attributed to the variations in the surface band bending. This can be manifested by a shift in the VBM edge, which was observed from the spectra shown in Fig. 4.9a. The variation of ∼0.3 eV in the ITO work function can be attributed to the change of doping level, that is, the change of oxygen vacancies in ITO films. The addition of hydrogen into the sputtering gas mixture induced the variation in the stoichiometry of ITO films. The oxygen vacancies in the ITO films increased when the hydrogen partial pressure increased. This is converse to the effect

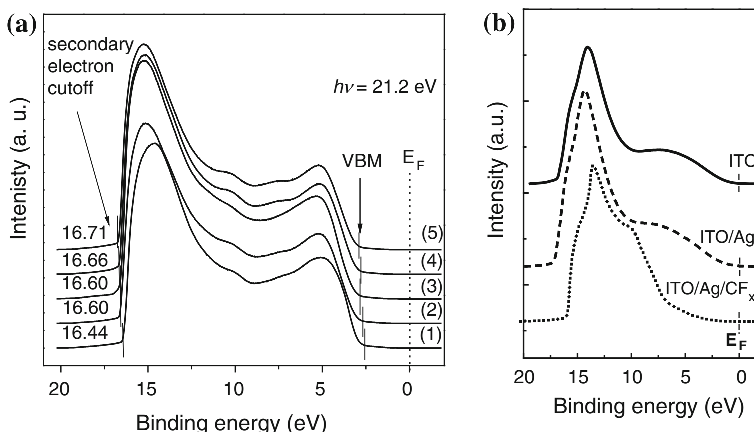

Fig. 4.9 **a** UPS valence band spectra measured for LT-ITO films prepared at different hydrogen partial pressures of (*1*) 0 Pa, (*2*) 1.1×10^{-3} Pa, (*3*) 2×10^{-3} Pa, (*4*) 2.6×10^{-3} Pa and (*5*) 3.2×10^{-3} Pa. **b** UPS spectra measured for LT-ITO, Ag/LT-ITO and Ag/CFx/LT-ITO on flexible substrate, The insert illustrates the schematic diagram of ZnPc:C_{60}-based OSCs fabricated with different anode contacts of LT-ITO, Ag nanoparticles/LT-ITO and CF_X-modified Ag nanoparticles/LT-ITO

of oxidizing treatment on the ITO surface. Oxidizing the ITO surface gives rise to an increment of the oxygen contents and is generally known to increase the work function [63]. The variation of work function in degenerated ITO films can be up to ~0.3 eV when the hydrogen partial pressure changed from $0-3.2 \times 10^{-3}$ Pa. The changes of the Fermi level position at the surface with respect to the band edges are related to the change of bulk doping in ITO films. For the LT-ITO on PET, the work function at 4.4 ± 0.1 eV with hydrogen partial pressure changed from 2.0×10^{-3} Pa. The inset in Fig. 4.9b illustrates the schematic energy diagram of a ZnPc:C_{60}-based OSCs. The difference in energy level between the work function of an ITO anode (~4.5 eV) and the highest occupied molecular orbital of ZnPc (5.17 eV) at the LT-ITO/ZnPc:C_{60} interface, can be reduced significantly after the ITO anode is modified with Ag nanoparticles/CF_X. The reduced electronic barrier at the LT-ITO/CF_X-Ag nanoparticles /ZnPc:C_{60} interface is favorable for charge extraction in OSCs.

J–V characteristics of the OSCs are shown in Fig. 4.10. Jsc, Voc, FF and PCE of the OSCs measured under AM1.5G irradiation are summarized in Table 4.2. Voc is similar for the control and flexible OSCs at ~0.55 ± 0.01 V and 0.53 ± 0.01 V. This is expected since OSCs have the same active materials and Voc is related closely with the energy offset between HOMO of the donor and LUMO of the acceptor. Jsc of the cells on the 100 W oxygen plasma treated flexible substrates, lower than the control device, is comparable at ~12.3 ± 0.1 mA/cm^2. FF of OSCs on flexible substrates with oxygen plasma (46 ± 2 %) treatment is considerably lower than that of the control device (53 ± 1 %). This may be attributed to the higher sheet resistance of the LT-ITO/flexible substrate (25 ± 5 Ω/sq) as compared to that of the ITO/glass substrate (8 Ω/sq). The higher ITO sheet resistance contributes to the series resistance

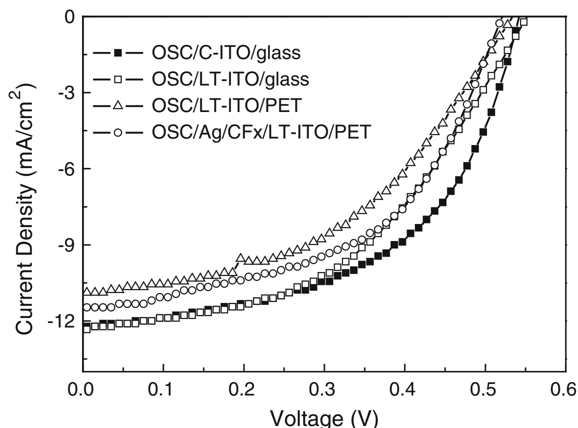

Fig. 4.10 *J–V* characteristics measured for OSCs made with different substrates of CFx-modified Ag nanoparticles /LT-ITO/PET, LT-ITO/PET, LT-ITO/glass and commercial C-ITO/glass

Table 4.2 A summary of the photovoltaic characteristics measured for the rigid and flexible OSCs

Device	V_{OC} (V)	FF (%)	J_{SC} (mA/cm^2)	PCE (%)
C-ITO/glass	0.54 ± 0.01	53 ± 1	12.3 ± 0.1	3.5 ± 0.1
LT-ITO/glass	0.55 ± 0.01	47 ± 1	12.3 ± 0.1	3.2 ± 0.1
LT-ITO/PET	0.53 ± 0.01	46 ± 2	10.9 ± 0.1	2.6 ± 0.2
CFx/AgNPs/LT-ITO/PET	0.53 ± 0.01	51 ± 1	11.5 ± 0.1	3.1 ± 0.1

of the device and is also reflected by the gentler slopes of the *J–V* curve under open circuit condition. The slopes of the flat portion of the *J–V* curves for both the control device and the OSC on the Ag/CFx treated flexible substrate are small and nearly coincident. This indicates that the Ag/CF_Xenhances the FF and Jsc in flexible OSCs. It can be seen that the OSCs with CF_X-modified Ag nanoparticles/ ITO plasmonic electrode has the best performance. It is expected that the process developed on the flexible substrate can easily be adapted for other higher performance polymer blends.

4.4 Charge Transport Properties in Bulk-Heterojunction OSCs

4.4.1 Charge Transport Properties in Polymer/Oxide Composites

Inorganic semiconductors nanoparticles and their composites with organic photoactive semiconductors have attracted significant research interest for application in OSCs. In particular, the combination of p-type conjugated polymer and n-type inorganic semiconductor nanoparticle is advantageous due to the solution processability of polymers and the high electron mobility of inorganic semiconductors. In recent years, various combinations of p-type conjugated polymers, such as MDMO-PPV

(poly[2-methoxy-5-(3′,7′-dimethyloctyloxy)-1,4-phenylene vinylene]), and regio-regular poly 3-hexylthiophene (P3HT), and n-type nanoparticles, such as PbSe, PbS CdS, CdSe, and ZnO have been utilised for the fabrication of BHJ OSCs [64–67]. Among these inorganic semiconductors, zinc oxide nano crystal particles (nc-ZnO) are attractive because of their less toxicity and inexpensive fabrication process. It has been reported that the solar cells with nc-ZnO/ MDMO-PPV composites show the efficiency of 1.6 % [68]. It is well known that the performance of OSCs depends on the efficiency of photo charge generation and their charge transport towards the electrodes. Therefore, the performance of OSCs can be improved through the understanding of charge transport in the composite films. Much research effort is focused on optimizing the performance of OSCs. Koster et al. [68] have studied the charge transport properties in PPV/ZnO composites using space charge limited current (SCLC) technique and found that the electron mobility is equal to 2.8×10^{-9} m^2/V·s, whereas the hole mobility is equal to 5.5×10^{-10} m^2/V·s. Beek et al. have reported that OSCs with P3HT/ZnO show PCE of 0.9 % and they attributed the low conversion efficiency to the coarse film morphology of P3HT/ZnO mixture [69]. Therefore, it is important to understand the charge transport mechanism in these mixtures for optimizing the performance of OSCs. It has been shown that the charge transport and recombination properties of BHJ OSCs can be studied simultaneously using photo-induced charge extraction by linearly increasing voltage (PhotoCELIV) technique [70, 71]. Mozer et al. [72, 73] have investigated the detailed charge transport and recombination properties in MDMO-PPV/PCBM composites using PhotoCELIV technique.

In the following discussion, the charge transport properties in P3HT/ZnO composites and the effect of ZnO nanoparticle size (50 and 12 nm) on charge transport properties in P3HT/ZnO composite film will be reviewed. The composition ratio used for this investigation is fixed to 85:15 % (P3HT:ZnO) weight ratio. The device fabrication process, film thickness and the PhotoCELIV measurement conditions were kept same so that the results can be compared. ZnO nanoparticles were synthesized by refluxing 0.4 mol/l KOH and 0.2 mol/l zinc acetate dihydrate in methanol at 65 °C for several hours. ZnO nanoparticles were then collected and washed with ethanol for several times and dried at 60 °C. P3HT and ZnO nanoparticles were dissolved in 1,2-dichlorobenzene in a weigh concentration of 50 and 5 mg/mL respectively. The two solutions were mixed together in a certain ratio and finally a uniform solution was formed. The mixture solution was filtered with 0.45 μm filter and spin-coated on ITO patterned glass. Finally, 100 nm Al cathode is deposited on the active layer, defining an active area of 3.0 mm × 3.0 mm. The composite films with the (P3HT:ZnO) composition ratio of 85:15 % is used for the charge transport studies.

In PhotoCELIV measurement, sample is illuminated from the ITO side of the device and the photocurrent under the influence of linearly increasing voltage pulse was monitored across a variable resistor using an oscilloscope. Upon application of a reverse bias linearly increasing voltage pulse with a voltage rise speed $A = dU/dt$, the typical electrical response is of a rectangular-shaped current transient with a plateau value corresponding to the capacitive displacement current $j(0) = \varepsilon\varepsilon_0 A/d$, where ε is the dielectric constant of the material, ε_0 is the permittivity of free space, and d is the thickness of the dielectric. The photocharge carriers can be generated

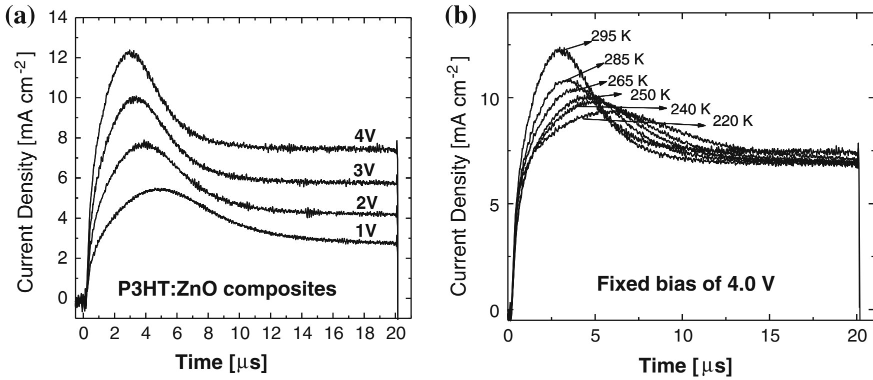

Fig. 4.11 **a** PhotoCELIV transients in P3HT/50 nm-ZnO (85:15 %) for various applied voltages at 295 K; **b** PhotoCELIV transients in P3HT/50 nm-ZnO (85:15 %) for various temperatures at a fixed bias of 4.0 V

throughout the film when the sample is excited with a suitable laser pulse. The photo-generated charge carriers can be extracted by adjusting the delay between the laser pulse and the voltage pulse. The time taken to reach the extraction current maximum ($t_{max.}$) and the maximum current due to photo-excitation (Δj) can be estimated from the PhotoCELIV transients. The charge mobility (μ) can be calculated using (4.3) as given below [70, 71]:

$$\mu = \frac{2d^2}{3At_{\max}^2\left[1 + 0.36\frac{\Delta j}{j(0)}\right]}. \tag{4.3}$$

Equation (4.3) is corrected for the electric field re-distribution during the charge extraction process. The PhotoCELIV transients can be recorded by varying the voltage rise speed (A), the sample temperature and the delay between the laser and voltage pulse in order to understand the complete transport and recombination properties in these composites.

The PhotoCELIV transients for various voltage rise speed A are recorded by fixing the time delay between the laser pulse and the voltage pulse ($t_{del.}$). Figure 4.11a shows the room temperature (T = 295 K) PhotoCELIV transients in P3HT/50 nm-ZnO (85:15 %) for various A and for fixed time delay ($t_{del} = 1\mu s$) between the laser pulse and the voltage pulse. The thickness of the film is around 215 nm. It is seen that the t_{max}. value decreases with the increase of A. This indicates that the charge mobility is dependent on the applied electric field. The charge mobility in P3HT/50 nm-ZnO (85:15 %) at 295 K is found to be 7.8×10^{-5} cm^2/Vs at an applied electric field of 2.5×10^4 V/cm, this varies linearly with the applied electric field. The charge mobility in P3HT/12 nm-ZnO (85:15 %) composite of similar film thickness was also calculated and found to be 1.7×10^{-4} cm^2/Vs at an applied electric field of 2.5×10^4 V/cm. It is found that the charge mobility in P3HT/12 nm-ZnO (85:15 %)

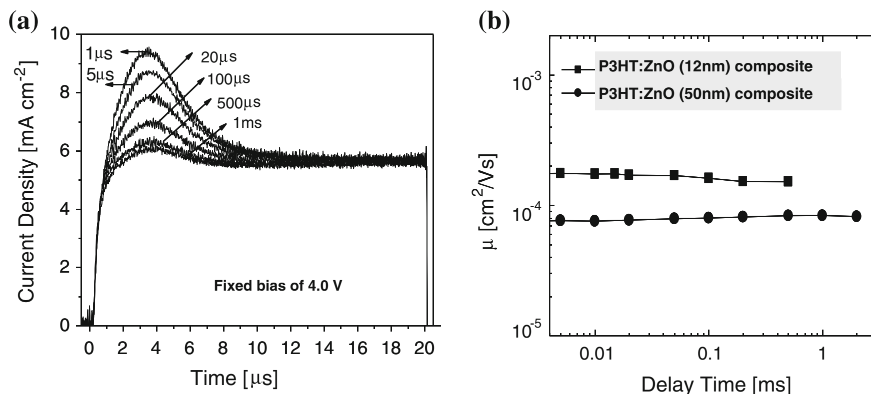

Fig. 4.12 **a** PhotoCELIV transients in P3HT/50 nm-ZnO (85:15 %) for various time delays between the laser pulse and voltage pulse at a fixed bias of 4 V, and **b** Variation of charge mobility with the time delay between the laser and voltage pulse

composite is almost three times higher than the charge mobility in P3HT/50 nm-ZnO (85:15 %) composite film.

In order to understand the temperature dependence of charge mobility, the PhotoCELIV transients were recorded for various temperatures from 295 to 220 K. The temperature dependence of PhotoCELIV transients in P3HT/50 nm-ZnO (85:15 %) composite for a fixed applied voltage (4 V) is shown in Fig. 4.11a. It is clearly seen that the t_{max}. value decreases with the increase of temperature. This indicates that the charge mobility in P3HT/ZnO composite is dependent on temperature.

The PhotoCELIV transients for different delay times between the voltage and laser pulse in a 215 nm thick P3HT/50 nm-ZnO (85:15 %) composite film is shown in Fig. 4.11b. The amplitude of the voltage ramp was fixed to 4V. It is observed that the position of the extraction maximum is independent of the delay between the laser pulse and voltage pulse. The area under the extraction curve, number of photogenerated charge carriers, decreases with the increase of the delay, which indicates that the charge recombination process takes place during the delay time. In addition, the observed carrier extraction without laser suggests that these P3HT/ZnO composite films have significant amount of equilibrium carriers at room temperature.

The charge mobility is calculated from the extraction current maximum and plotted as a function of time delay (shown in Fig. 4.12b). It is observed that the charge mobility in P3HT/50 nm-ZnO (85:15 %) is almost independent of the delay time between the laser and voltage pulse. The charge mobility in P3HT/12 nm-ZnO (85:15 %) is slightly decreasing with the increase of delay, which is attributed to the trapping effect. However, the charge mobility in P3HT/12 nm-ZnO (85:15 %) composite is almost two times higher than the charge mobility in P3HT/50 nm-ZnO (85:15 %) composite, indicates that the ZnO nano particle size has significant effect in determining the charge mobility in these composites.

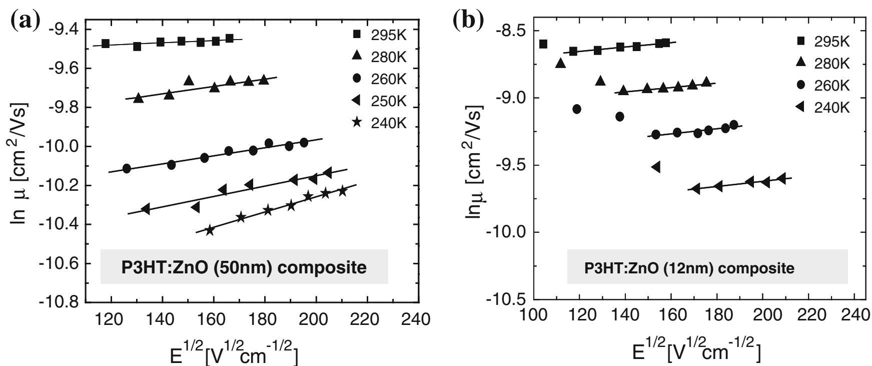

Fig. 4.13 Variation of PhotoCELIV mobility in **a** P3HT/50 nm-ZnO (85:15 %) and **b** P3HT/12 nm-ZnO (85:15 %) composites with applied electric field for various temperatures; the solid lines are the linear fits according to the (4.4)

The charge mobility was calculated for various temperatures (from 295 to 220 K) and for various applied voltages. The field dependence of charge mobility in P3HT/50 nm-ZnO (85:15 %) and in P3HT/12 nm-ZnO (85:15 %) composites for various temperatures from 295 to 220 K is shown in Fig. 4.13a, b. It was found that the electric field dependence of charge mobility in these composites follows the Pool-Frenkel (PF) form [74]:

$$\mu = \mu_0 \exp(\gamma \, E^{1/2}). \tag{4.4}$$

where μ_0 is the zero field mobility and γ is the slope of the field dependence of charge mobility. The parameters μ_0 and γ are extracted from the fit and plotted against temperature to further understand the charge transport mechanism in these composites composite. It was found that μ_0 increases with increasing temperature and the slope (γ) of the $ln\mu$ versus $E^{1/2}$ plot decreases with increasing temperature. This behavior is typical for hopping transport in disordered organic solids.

It is well known that charge transport in disordered organic materials can be described as hopping in an in-homogeneously broadened Gaussian density of localized states, where positional disorder between hopping sites lead to energy disorder. Using the simplest possible model (GDM) Bässler showed that the mobility can be expressed in a functional form as [75],

$$\mu_{GDM} = \mu_\infty \exp\left[-\left(\frac{2\sigma}{3kT}\right)^2\right] \exp\left[C\left\{\left(\frac{\sigma}{kT}\right)^2 - \sum^2\right\} E^{1/2}\right]. \tag{4.5}$$

where μ_∞ is the high temperature limit of the mobility, σ is the energetic disorder parameter, Σ is the positional disorder parameter, and C is an empirical constant which reflects the hopping distance that a charge carrier has to overcome to be transferred from one site to another. The energetic disorder parameter σ arises from

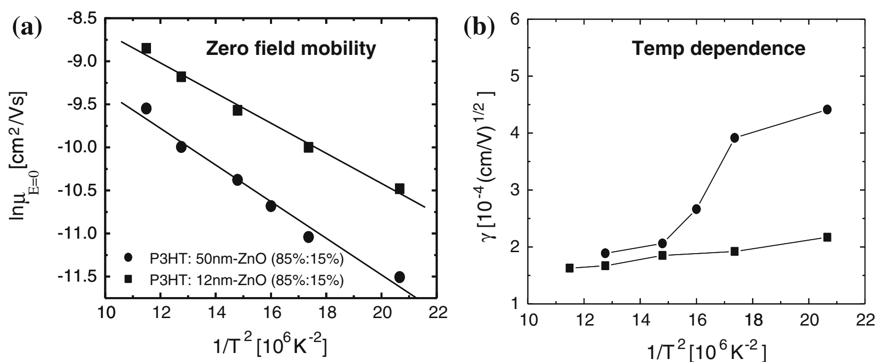

Fig. 4.14 **a** Variation of zero field mobility, the solid lines are the linear fits according to the (4.5), and **b** the correlation between the slope of the field dependence of charge mobility and temperature

the distribution of conjugation lengths, while the positional disorder parameter Σ arises from the fluctuations of intermolecular distances or morphological variations.

Figure 4.14 shows the variation of zero-field mobility in P3HT/50 nm-ZnO (85:15 %) and in P3HT/12 nm-ZnO (85:15 %) composites with temperature. It is clearly seen from the Fig. 4.14a that the zero-field mobility in P3HT/12 nm-ZnO (85:15 %) composite film is higher than the zero-field mobility in P3HT/50 nm-ZnO (85:15 %) composite film. The solid lines in Fig. 4.14a are the linear fits according to the (4.5).

The charge transport parameters obtained for P3HT/50 nm-ZnO (85:15 %) composite are: $\mu_\infty = 7.2 \times 10^{-4}$ cm^2/Vs, $\sigma_{GDM} = 60$ meV. The parameters obtained for P3HT/12 nm-ZnO (85:15 %) composite are: $\mu_\infty = 1 \times 10^{-3}$ cm^2/Vs, $\sigma_{GDM} = 54$ meV. The variation of γ with $(1/T)^2$ is shown in Fig. 4.14b, the parameters Σ and C obtained from the linear fit are found to be $\Sigma = 3.2$ and $C = 2.9 \times 10^{-4}$(cm/V)$^{1/2}$ for P3HT/50 nm-ZnO (85:15 %) composite, and $\Sigma = 1.4$ and $C = 9.5 \times 10^{-5}$(cm/V)$^{1/2}$ for P3HT/12 nm-ZnO (85:15 %) composite film. The temperature dependence of charge mobility is also analyzed based on the simple Arrhenius law ($\mu = \mu_o$ exp(-ΔE/kT) and is used to calculate the activation energy (ΔE) of charge mobility. The activation energy obtained are 0.15 and 0.12 eV for P3HT/50 nm-ZnO (85:15 %) and P3HT/12 nm-ZnO (85:15 %) composites respectively.

Two extraction peaks due to electrons and holes can be observed in PhotoCELIV measurements if both carriers are mobile and their motilities are significantly different. In the studied P3HT/ZnO composite films, only one peak was observed at all applied delay times and applied voltages. Even though the sign of the charge carriers investigated with PhotoCELIV measurements is under debate, the charge mobility values obtained for the P3HT/ZnO composite films in this work may be related to the electrons. We have also investigated the effect of charge mobility on the concentration of the ZnO in the P3HT/ZnO composite and observed that the charge mobility increases with the increase of ZnO concentration. It is accepted that the

electron mobility in ZnO/polymer blends strongly depends on the number of electrons per ZnO particle. This suggests that the charge mobility observed in P3HT/ZnO blends using the PhotoCELIV measurement could be due to electrons. In addition, the obtained mobility in P3HT/ZnO composite films is in good agreement with the electron mobility in PPV/ZnO blends reported by Koster et al. [10] using SCLC technique.

The PhotoCELIV mobility in P3HT/50 nm-ZnO at room temperature is found to be 7.8×10^{-5} cm^2/Vs at an applied electric field of 2.5×10^4 V/cm, which increases to 1.7×10^{-4} cm^2/Vs for P3HT/12 nm-ZnO composite. The mobility pre-factor obtained for P3HT/12 nm-ZnO mixture is higher than the value obtained for P3HT/50 nm-ZnO composite. The energy disorder parameter obtained for P3HT/12 nm-ZnO is smaller than the energy disorder parameter obtained for P3HT/50 nm-ZnO composite film. It is well known that the photo-induced electron transfer takes place from the polymer to ZnO-nanoparticles. The photo-induced charge separated state increases with the increase of the number of polymer-nanoparticle interfaces. It is also accepted that the film roughness increases with the increase of the size and the amount of ZnO nanoparticle. The systematic increase of charge mobility with the decrease of ZnO nanoparticle size indicates that the nanoscopic mixing of ZnO in the polymer matrix occurs in the studied composition ratio and hence the charge transport parameters can be controlled.

4.4.2 *Effect of Oxygen-Induced Traps on Charge Mobility and OSC Performance*

Recently, significant progresses in OSCs have been made using BHJ between an electron donating conjugated polymer and an electron accepting fullerene derivative [76, 77]. BHJ based on P3HT and PCBM is the most established system for application in OSCs [59]. The efficiency and operational stability of BHJ OSCs are strongly dependent on the charge transport properties in the active layer of the device. The charge mobility in conjugated polymer/fullerene composite film depends on the phase separation process, in which the thermal treatment or slow evaporation rate during film deposition significantly changes the nano-morphology of the composite film [78, 79]. In addition, the interfaces between the donor and acceptor nano-phases have significant influences on the charge trapping or charge recombination behavior, which in turn influences the device lifetime. Therefore the systematic investigation on the charge transport properties in the active photovoltaic materials is important to improve the device efficiency as well as to investigate the device lifetime issues. It has been shown in the literature that the charge transport properties in photovoltaic materials, especially in the electron donor and acceptor compositions, can be investigated using PhotoCELIV technique [72]. The PhotoCELIV technique can be used to study the mobility of both charge carriers simultaneously in the real OSC configuration. Mozer et al. have investigated the charge

transport and recombination properties in MDMO-PPV/PCBM based OSCs using the PhotoCELIV technique and found that the charge mobility increases by two orders of magnitude with increasing PCBM concentration [73]. The information about the lifetime of the charge carriers and the nature of charge transport (dispersive or nondispersive) was also obtained from the shape of the PhotoCELIV transients [80].

In order to realize efficient and durable OSCs, it is important to understand the charge transport properties under various operating conditions and to identify the loss (or degradation) mechanisms. Comprehensive analyses and studies of correlation between the charge transport/recombination and performance of OSCs are particularly important. It is necessary to improve the understanding of charge transport and stability of organic BHJ in order to design optimized device architectures and to identify suitable materials for better device efficiency and stability. The charge transport properties in BHJ OSCs can be studied using PhotoCELIV technique. PhotoCELIV is a powerful technique to study the charge transport and recombination properties of photovoltaic materials and devices, including the charge trapping behavior with respect to the quality of the materials and the process conditions. In the following discussion, we will apply PhotoCELIV technology to study the effect of oxygen-induced traps on charge mobility and device performance of typical BHJ OSCs based on P3HT/PCBM blend system. OSCs with types of ITO/ P3HT:PCBM (1:0.8) (200 nm)/Al (100 nm) and ITO/poly(3,4-ethylenedioxythiophene):polystyrenesulfonate (PEDOT:PSS)/P3HT:PCBM (1:0.8) (200 nm)/Al (100 nm) were fabricated, which were fabricated using the same fabrication processes. They were then exposed under different oxygen/air exposures in order to investigate the effect of oxygen-induced traps on charge mobility and its impact on the performance of the resulting OSCs.

P3HT (Sigma Aldrich) and PCBM (American Dye Source) were dissolved in 1,2-dichlorobenzene in a weight ratio of 1:0.8. The mixture solution was filtered with 0.45 μm filter and spin-coated on ITO patterned glass. The top layer of Al (100 nm) electrode was deposited in a vacuum chamber with a base pressure less than 10^{-5} mbar. Various oxygen exposures are carried in a vacuum chamber with a constant oxygen partial pressure of 0.01 mbar for 0.5, 1.0 and 4.0 h. An exposure of the OSCs in air for up to 20 h was also tested for comparison studies. PhotoCELIV transients measured for the control OSC without exposure to oxygen or air is shown in Fig. 4.15a. It is observed that the PhotoCELIV transients exhibit single peak for a control cell measured under different voltage ramps of 1, 2, 3 and 4 V. The time taken to reach the extraction current maxima was decreasing with the increase of A(the voltage rise speed), which indicates the electric field dependence of charge mobility. The charge mobility calculated from the PhotoCELIV transient is in the range of $2.0-3.5 \times 10^{-4}$ cm^2/Vs at an applied field from 7.1×10^3 V/cm to 1.4×10^4 V/cm, respectively. This charge mobility is consistent with the literature values on P3HT/PCBM composite film with similar device architecture [81]. The PhotoCELIV transients measured for OSC exposed to an oxygen partial pressure of 0.01 mbar for 30 min is shown in Fig. 4.15b. The charge mobility estimated was in the range of 1.9×10^{-4} cm^2/Vs, indicates that there is no significant change in the charge mobility

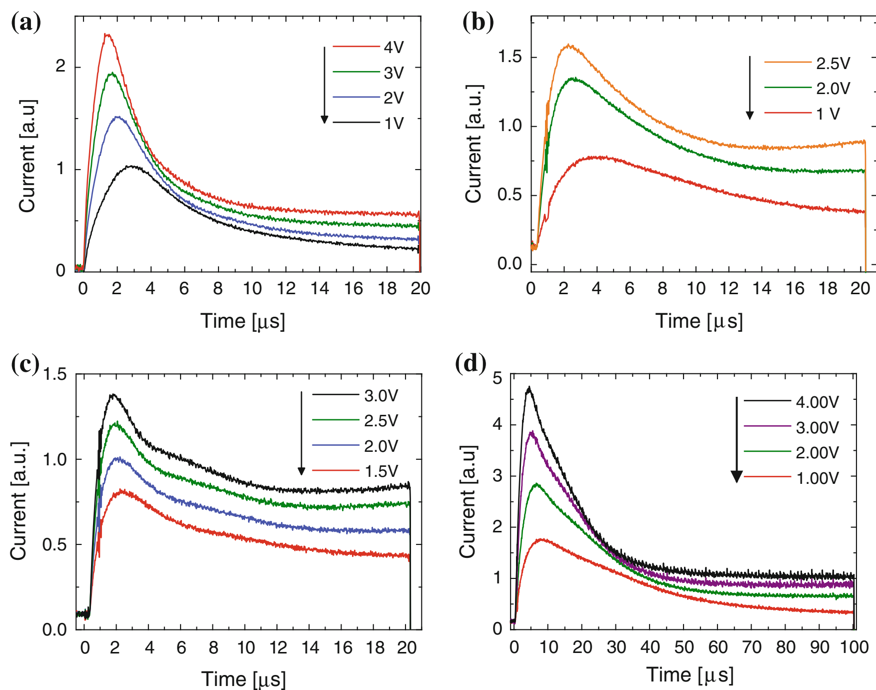

Fig. 4.15 PhotoCELIV transients for **a** the control device without oxygen/air treatment, **b** 30 min exposure to oxygen, **c** 1 h exposure to oxygen and **d** >20 h expose to air

in this device compared to the control device. However, it is clearly seen that the PhotoCELIV transients shown in Fig. 4.15b are broader than the transients observed for the control device, as shown in Fig. 4.15a. The broader PhotoCELIV transients compared to the control device indicate the charge dispersion in 30 min O_2 exposed device is higher than the charge dispersion in control device. It has already been demonstrated that oxygen and water diffuse through all the layers in the photovoltaic devices until the counter electrode (ITO) is reached where oxygen is exchanged onto the ITO surface in the interface [82]. There is no known report on the effect of diffused oxygen on the charge mobility characteristics in the photoactive layer. The PhotoCELIV transients recorded for the devices exposed to oxygen for 1 h and >20 h in air is shown in Fig. 4.15c, d, respectively. It was observed that the PhotoCELIV transients in Fig. 4.15c, d shows an additional shoulder at long time scale. It was also noted that the second peak shifts towards shorter time scale when the rate A is increased, which indicates the field dependence of charge extraction time.

The carrier transit times can be estimated from the PhotoCELIV maxima which can be used to and calculate the charge mobility for various voltage ramps. The variation of charge mobility with applied electric field for the devices with and without oxygen exposure is shown in Fig. 4.16. The charge mobility in the control device was in the range from 2×10^{-4} to 3.5×10^{-4} cm^2/Vs at an applied electric field

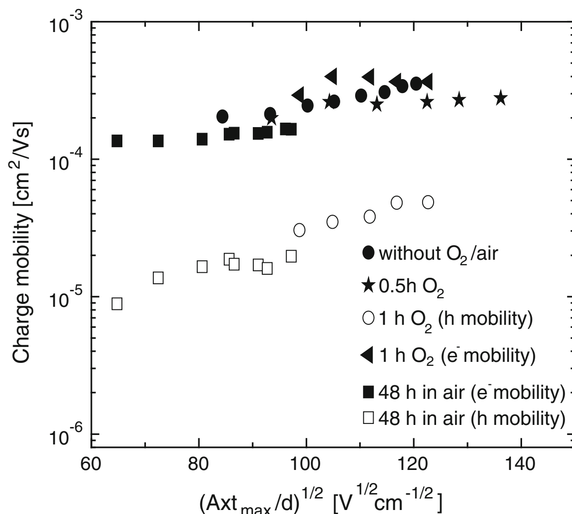

Fig. 4.16 Variation of charge mobility with applied electric field for OSCs with and without oxygen/air exposure

from 7.1×10^3 V/cm to 1.4×10^4 V/cm respectively. The charge mobility in 30 min exposed device was in the range from $1.9-2.6 \times 10^{-4}$ cm^2/Vs at an applied electric field from 8.7×10^3 V/cm to 1.8×10^4 V/cm respectively. The estimated charge mobility in 1 h O_2 exposed device was around 2.9×10^{-4} cm^2/Vs corresponding to the first PhotoCELIV peak and 3×10^{-5} cm^2/Vs due to the second maximum, whereas the charge mobility in 20 h air exposed devices was around 1.3×10^{-4} cm^2/Vs due to the first PhotoCELIV peak and 8.8×10^{-6} cm^2/Vs due to the second PhotoCELIV peak respectively. It was observed that the charge mobility estimated for the device exposed to air for 20 h is relatively slower for both electrons and holes compared to the other three devices.It has already been observed that the total trap density in pure P3HT film increased from 1×10^{16} to 1.7×10^{16} cm^{-3} after air exposure to 25 h which affects the performance of OSCs substantially [83].The obtained charge mobility results from the four devices with and without O_2/air treatment indicate that there is no significant changes in the charge mobility corresponding to the first PhotoCELIV peak position, however it is clearly seen that the second PhotoCELIV maximum starts appearing when the device is exposed to O_2/air for long time. It has already been shown in the literature that the PhotoCELIV measurement on conjugated polymer/fullerene blend system shows only one peak [72, 73] although it is experimentally possible to study the electron and hole mobility characteristics simultaneously using PhotoCELIV technique.The sign of the charge carriers extracted using PhotoCELIV was also under debate and most of the time it was related to the slowest carriers such as holes.

It has been reported that the extraction of electron and hole mobility using CELIV technique is possible with OSCs based on low band gap co-polymer (APFO-Green)/PCBM composite film [84]. The present study indicates that it is possible to observe dual PhotoCELIV transients when the photoactive film is exposed to oxygen or air which makes the electron and hole mobility differ significantly from

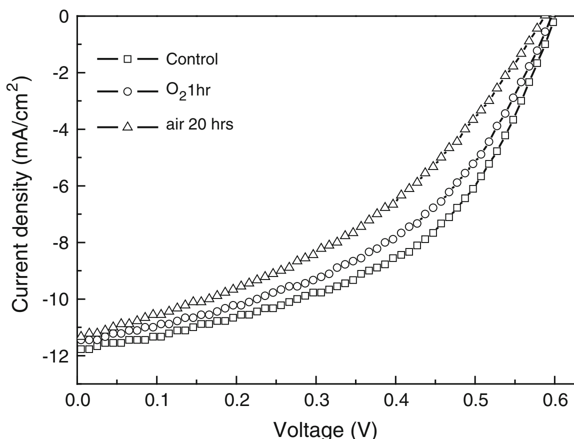

Fig. 4.17 *J–V* characteristics measured for the OSCs that were exposed under different oxygen/air exposures

each other. It is well known that the charge transport in P3HT is very sensitive to oxygen and moisture. It has already been reported that the charge mobility in pure P3HT decreases by one order of magnitude from 1.2×10^{-4} to 2.6×10^{-5} cm^2/Vs after 3 h exposure to oxygen [83]. The oxidation of P3HT and the subsequent degradation of thiophene rings breaks the macromolecular backbone configuration which affects the hole mobility in the system. The charge mobility estimated from the first PhotoCELIV peak observed in the present study is assigned to the extraction of electrons and the second PhotoCELIV maxima is assigned to holes based on the literature values. The observed results also indicates that the single PhotoCELIV transient reported for P3HT/PCBM composites in the literature were the superposition of electron and hole transients as the electron and hole mobility is in the same order of magnitude.

In order to study the effect of oxygen/air induced traps on the photovoltaic performance of OSCs, the evolution of *J–V* characteristics measured for OSCs as a function of the oxygen exposure were studied. *J–V* characteristics measured for OSCs exposed under different oxygen exposure time are plotted in Fig. 4.17. The corresponding OSC parameters including Voc, Jsc, FF and PCE are summarized in Table 4.3. The average PCE of OSCs that were not exposed to the oxygen (control cell) was around 3.5 %, and it decreased to 2.66 % after the cells were exposed to air for 20 h. The change in device performance due to different oxygen exposures was also studied by illuminating the cells continuously under AM1.5 illumination in an argon-purged glove box. The results are shown in Fig. 4.18. It can be seen that the changein PCE as a function of the operation time is much faster in the devices that were exposed previously to the oxygen/air as compared to the control device. The PCE of the control cells decreased to 80 % of its initial value after 20 h of continuous illumination, whereas the PCE of the cells that had pre-exposed to air for 20 h reduced to ~40 % of the its initial value after 20 h aging test. It is known that

Table 4.3 The parameters measured for OSCs exposed at different oxygen exposures

O_2 exposure (0.01 mbar) prior to cathode deposition	Voc (V)	Jsc (mA/cm^2)	FF (%)	PCE (%)
30 min	0.59	11.88	47.79	3.35
1.0 h	0.59	11.50	46.13	3.13
4.0 h	0.57	11.34	35.42	2.29
20 h (air)	0.59	10.44	43.18	2.66

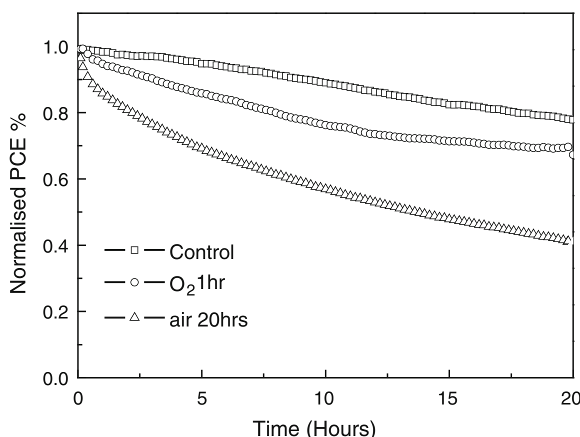

Fig. 4.18 The behavior of normalized PCE of as a function of operation time measured for a set of the identical OSCs that were exposed to different oxygen exposure conditions, the OSCs are characterized under simulated AM1.5 solar irradiation in an inert gas glove box

there are different types of degradation mechanisms taking place in OSCs. In order to improve the durability of the solar cells, it is important to identify various degradation pathways. It has been reported that atmospheric oxygen can easily diffuses through the pin holes of the aluminum electrode and reacts with the constituents of photoactive layer [82]. The results suggest that the oxygen-induced charge traps in active layer are one of the primary factors that are responsible for the imperfection in the charge transport properties and hence the performance of the OSCs.

The resulting deterioration in OSCs is attributed to the oxygen-induced charge traps within the active layer. The changes in *J–V* characteristics and the durability of the P3HT/PCBM-based OSCs due to the exposure to the oxygen also correlate with the observation seen in variation of the characteristics of charge mobility derived from the PhotoCELIV measurements. PCE of OSCs without oxygen/air exposure was around 3.5 % and reduced to 2.6 % after 20 h exposure in air. The change in PCE with time is much faster in the cells that were exposed to oxygen/air as compared to that of the control device. The charge mobility characteristics in P3HT:PCBM system reveal that the presence of oxygen in the operating environment of OSCs causes an oxygen-induced charge traps and hence leads to imbalanced charge mobility within BHJ photoactive layer, which is one of the major degradation pathways in OSCs.

4.5 Absorption Enhancementin OSCs

It is known that light absorption in OSCs is limited due to the presence of a mismatch between the charge transport scale and optical absorption depth. There are two major research approaches towards improving the performance of OSCs. One attention has been paid on the development of low band gap conjugated organic polymers whereby to increase PCE of OSCs through improved spectral response over the long wavelength region. The other is the device approach in which the enhanced absorption in OSCs is achieved using light trapping effects. The absorption depth in the organic photoactive layer is usually greater than the diffusion range of the photo-generated excitons. Thus a thinner thickness of the photoactive layer in OSCs is typically employed to reduce the exciton recombination losses and also to increase drift velocity of the carrier in higher electric field. The efficient use of the incident light and thus a high photocurrent generation in a thin OSC is a prerequisite for achieving high performance OSCs.

The use of light trapping is a capable approach to realize absorption enhancement in solar cells. In conventional Si solar cells, light trapping is typically achieved using a pyramidal surface texture that causes scattering of light into the solar cells over a large angular range, thereby increasing the effective optical path in the cell. Such large scale geometries are not suitable for thin film solar cells and OSCs. One of the promising schemes for light trapping in thin film solar cells is to utilize plasmon generated on the surface of metal nanoparticles or nanostructures. As discussed earlier, incorporation of metal nanoparticles in conventional solar cells [47, 48] helps to enhance light absorption in semiconductor layer through plasmonic effect of metal nanoparticles. The performance enhancement in OSCs using a CF_X-modified Ag nanoparticles/ITO anode is primary due to improved charge collection efficiency at anode/organic interface [50]. However, the enhanced light absorption due to plasmon excitations of metal nanoparticles is strongly localized in the vicinity of metal nanoparticle/organic interface. Realization of light trapping in OSCs without causing deterioration in the exciton dissociation and charge collection remains an open challenge.

Absorption enhancement in OSCs using nano-structures, e.g., buried nano-electrodes [85], microprism substrates [86], azopolymer based sub-micrometer topography substrate [87], and the periodic metallic gratings [88–92], has been reported. It has been demonstrated that the periodic metallic gratings, usually using Ag material, are promising approaches for application in OSCs. The metal gratings can be fabricated on the cathode side to reflect the incident light backwards [93] and also serve as the front anode layer to achieve a broadband optical absorption enhancement in OSCs. The incorporation of the metal grating in OSCs was shown to improve light absorption substantially due to the enhanced optical field by the surface plasmonic effect or the enhanced optical path in the photoactive layer due to the textured substrate morphologies [94]. The use of a transparent poly(methyl methacrylate) (PMMA)/ITO grating anode to improve absorption in OSCs has advantages for charge transport in OSCs. Both experiment and finite-difference time-domain

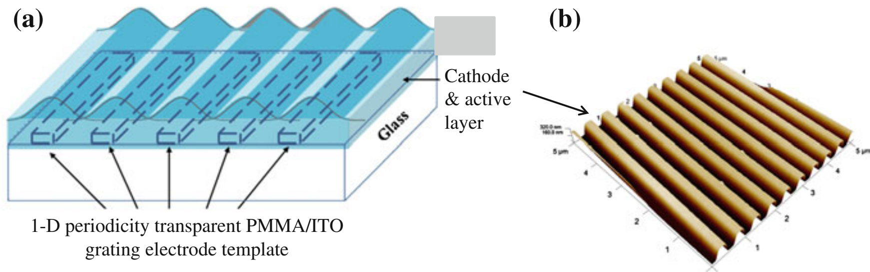

Fig. 4.19 **a** A schematic drawing of an OSC fabricated using a PMMA/ITO grating electrode. **b** AFM image measured form the cathode surface of a nano-structured OSC fabricated on a PMMA/ITO grating/glass

(FDTD) simulation reveal that ~60 % of enhancement in Jsc can be obtained in OSCs incorporating a front PMMA/ITO grating electrode.

A schematic diagram of a nano-structured OSC fabricated using a 1-dimensional (1-D) PMMA/ITO sub-mircometer grating electrode is shown in Fig. 4.19a. AFM image measured form the cathode surface of the nano-structured OSC with a configuration of glass/grating PMMA/ITO (150 nm)/ZnPc:C_{60} (40 nm)/C_{60} (30 nm)/BPhen (8 nm)/Ag (120 nm), is shown in Fig. 4.19b. The PMMA grating has a period of 500 nm with a width and a depth of a groove of 250 and 250 nm. AFM imaging reveals clearly that the nano-structured OSC also has a 1-D grating feature, with a peak to valley amplitude of ~110 nm.

PMMA is a transparent polymer with a large refractive index. PMMA/ITO grating electrode can serve as the scattering medium to scatter light resulting in absorption enhancement in OSCs. This phenomenon can be explained briefly using a grating model, as illustrated in Fig. 4.20. Let's consider the normal incident light with a wavelength (λ), the angle of the mth diffraction order can be evaluated by the (4.6):

$$m \cdot \vec{G} = n \cdot \vec{k} \cdot \sin\theta, \tag{4.6}$$

where $\vec{G}$ is the Bragg vector, $\vec{k}$ and $\vec{k}'$ are the wave vectors of incident and diffracted light, respectively, in OSCs, and n is the effective refractive index in the active layer. When the incident light is perpendicular to the substrate, the optical path length is the same as the thickness of the organic photoactive region. However, when light is incident on OSC at an angle θ, it is clear that the grating OSC diffracts the incident light and the optical path will be longer than the thickness of the organic media sandwiched between the rear cathode mirror and the front transparent grating anode. For example, at $\lambda = 650$ nm, the first order diffraction angle is ~43° (which is larger than the critical angle ~32°) for the grating period of 500 nm and effective refractive index ~1.9. Total internal reflection at the glass/air interface is attained. The rear metal cathode mirror and the high refractive index front grating ITO anode form an effective microcavity. The thickness of the organic medium sandwiched

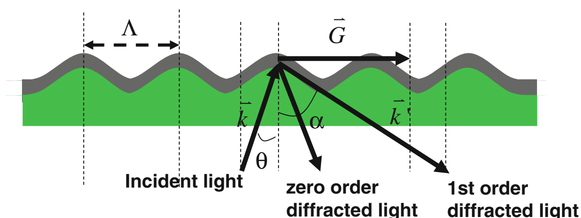

Fig. 4.20 Schematic diagram of light trapping in a grating OSC

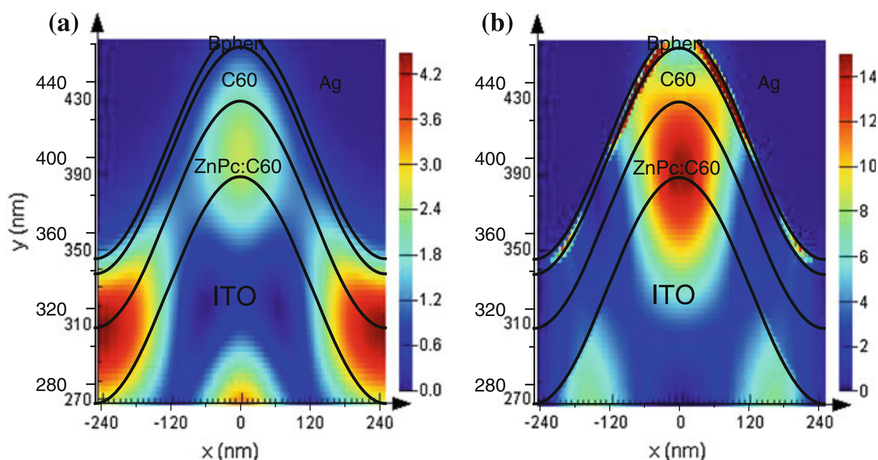

Fig. 4.21 Simulated E-field distribution in an OSC with a PMMA/ITO grating electrode, showing the strong localized field coupled into waveguide modes in the active layer at wavelength of 548 nm for TE polarization (**a**) and 762 nm for TM polarization (**b**)

between the electrodes is in the order of wavelength range. The cavity is then able to accommodate a series of waveguide modes. The photonic energy of these waveguide modes is dependent on the optical thickness of the organic layers. The waveguide modes inside OSCs can be modified by incorporating the periodic patterns or different nano-structures, e.g., a 1-D grating. In this case, the PMMA grating on glass substrate has a periodicity of 500 nm with a width and depth of the groove of 250 and 250 nm, respectively. The photons originally incident with a small angle away from normal to the cell surface are diffracted to oblique angles in the absorber layer, thereby increasing the path length and the dwell time of photons to realize broadband absorption enhancement in organic photoactive layers and thus the PCE of OSCs.

Figure 4.21 depicts a simulated E-field distribution inside a PMMA/ITO grating OSCs. Strong localized field for TE polarization at the incident wavelength of 548 nm and TM polarization at the incident wavelength of 762 nm inside the grating OSC is clearly seen, indicating light is coupled into waveguide modes in the OSCs

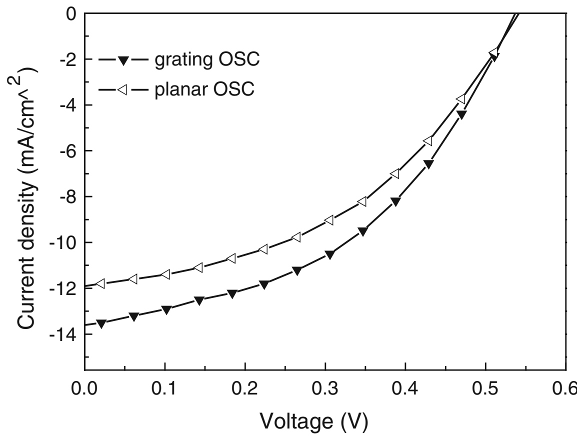

Fig. 4.22 *J–V* characteristics measured for a grating OSC and a planar control OSC under AM1.5G illumination of 100 mW/cm^2

by the PMMA/ITO grating electrode. The structure of nano-structured OSCs can be optimized to realize the desired absorption enhancement that matches with the absorption properties of the organic photoactive materials used in the OSCs.

J-V characteristics of the planar and grating OSCs, measured under simulated AM1.5G illumination of 100 mW/cm^2, are plotted in Fig. 4.22. Grating OSCs are of practical interest for achieving absorption enhancement in OSCs. The periodic nano-patterned PMMA grating structures can be prepared using nano-imprinting technique and cross beam lithography method. ITO layer is deposited on the patterned PMMA to form a transparent grating electrode. OSCs having a transparent PMMA/ITO grating electrode with sub-mircometer periodicity can then be fabricated. As shown in Fig. 4.23, the enhancement in performance of a grating OSC (PCE 3.29 %) over a planar control OSC (PCE 2.86 %) is mainly due to an increase in Jsc, e.g., from 11.93 mA/cm^2(planar control cell) to 13.57 mA/cm^2 (a grating incorporated OSC). OSCs with a grating electrode resulted in a 13 % increase in Jsc and 10 % improvement in PCE compared to a planar control OSC. The results reveal that over 60 % of enhancement in Jsc is due to an enhanced spectral responsivity via light scattering effect. Light coupled into the waveguide mode in the ZnPc:C_{60} active layer is primarily responsible for the absorption enhancement in OSCs. IPCE measured for the grating and planar OSCs using TE and TM polarizations are plotted in Fig. 4.23. Light trapping in grating OSCs is clearly demonstrated, an effective approach for realizing absorption enhancement in OSCs.

Light trapping in OSCs using large-area photonic structures has attracted a lot of attention recently. The propagation of light in photonic-structured OSCs is similar to the electron motion in the periodic potential in a semiconductor crystal. Light waves propagate in the photonic-structured OSCs depend on their wavelength. This gives rise to distinct optical phenomena and applications in broadband absorption enhancement in OSCs. It has been demonstrated that the incorporation of sub-wavelength

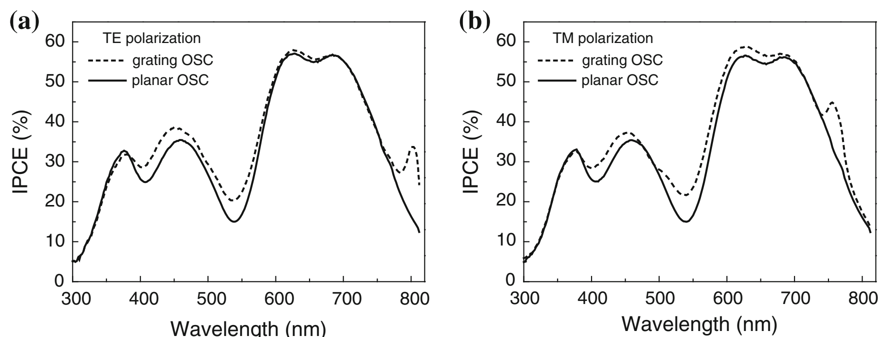

Fig. 4.23 External quantum efficiency of grating and planner OSCs measured under different polarized light: **a** TE polarization and **b** TM polarization

periodic structures, e.g., metal grating electrode and 2-D photonic structures [95, 96], enables to achieve effective light trapping in OSCs. However, the fabrication of large area 2-D and 3-D photonic structures that can be used in OSCs has yet to be developed. The reported nano-fabrication methods, e.g., nano-imprint, electron beam lithography, cannot be applied for large area OSCs due to processing bottlenecks [97, 98]. There are technical and engineering challenges, which, if solved, can have profound impact on the future of OSCs. One possible solution is through the generation of large area photonic structures using cross beam lithography method, a powerful technique for producing periodic nanostructures over a large area. Cross beam lithography technique, e.g., UV immersion lithography, has advantages of creating any desired nano-features over a wide area in a facile and inexpensive way. It can be one of the attractive nano-manufacturing techniques for application in photonic-structured OSCs.

4.6 Stability of Bulk-Heterojunction OSCs

Although OSC technology offers an attractive option for achieving alternative clean energy sources, considerable enhancement in overall performance of OSCs, including efficiency, durability and cost competitiveness, is needed if this technology is to become a viable option for sustainable energy. As discussed in the previous section of this chapter, the presence of oxygen and moisture in the operating environment of OSCs causes an oxygen-induced charge traps and hence leads to imbalanced charge mobility within the BHJ photoactive layer, which is one of the major degradation pathways in OSCs [99]. In addition to the charge traps formed in the organic photoactive layer, localized failure due to the water encroachment, oxidation occurring at the organic/cathode interface of OSCs [100] and UV-induced degradation processes [101] are also responsible for the instability of OSCs.

It is important to understand the degradation mechanisms so as to develop solutions for realizing stable OSC performance over a long period of operation. The stability of OSCs operated under different environment conditions, e.g., in humid air, at high temperature, and under UV exposure etc., the fundamental degradation mechanisms in organic semiconductors as well as its interface structure have only been partially understood. Polythiophenes are well investigated due to the ambient stability, and therefore current state-of-the-art polythiophene based OSCs employ morphologically stable BHJ P3HT:PCBM donor/acceptor system are studied. It shows that reactions of organic photoactive BHJ with oxygen and moisture occur not only in the volume [102] but also at the interfaces in OSCs [103, 104]. In the following discussion, the roles of moisture and the interfacial oxidation in the degradation process will be reviewed.

BHJ OSCs with a conventional cell structure of ITO/PEDOT:PSS/P3HT:PCBM/metal cathode are employed for stability studies. Metal cathode consisting of Ca/Al or Ca/Ag has been often used due to its improved electron collection ability at cathode/organic interface for high efficiency OSCs. OSCs were fabricated on the glass substrate and encapsulated with a glass lid in a glove box with both oxygen and moisture levels less than 0.1ppm. In some cases, a different amount of adhesive desiccants was also used in the device encapsulation. The use of the different amount of the desiccants is to control a substantial proportion of the residual moisture inside the OSCs, a useful approach helping us to evaluate the correlation between the OSC degradation process and the moisture level during the accelerated aging experiments. The encapsulated OSCs, with and without the adhesive desiccants, were then undergone the accelerated lifetime test at different aging conditions, e.g., under a high relativity humidity of 90 % and a low relative humidity of 5 % at 60 °C.

In order to obtain more reliable and meaningful experimental results for comparison studies, the *J*–*V* characteristics and the accelerated lifetime data measured for OSCs were represented by an average of 12 structurally identical devices fabricated using the same process conditions. The fluctuation in the *J*–*V* characteristics and the lifetime results thus measured for different sets of structurally identical OSCs is typically within an error range about 5–15 %. The accelerated aging tests for BHJ OSCs encapsulated with an area of 0.5 cm^2 desiccant were carried out in a humid chamber with a high relative humidity of 90 % at 60 °C. The performance of the device decayed over time and normalized OSC parameters, including FF, Jsc, Voc and PCE, are as shown in Fig. 4.24a. The shape of PCE curve indicates that degradation of OSCs undergoes treble steps. In the first 24 h, a decrease of about 20 % in PCE is observed; and then the device performs steadily in the next 240 h, followed by a dramatic decrease to a much lower level and the trend continues till the end. Moreover, compared with the degradation tendencies of Jsc, Voc and FF measured simultaneously, all three parameters play different roles in the decrease of PCE in various time ranges. Voc and FF decrease about 8 and 11 % in the first 24 h, while Jsc remains the same. None of them shows obvious changes up to 260 h. However, Jsc drops dramatically, causing a final decline in PCE, until the catastrophic failure after 400 h. The multiple stages of degradation observed in OSCs imply that there are at least two distinguishable degradation mechanisms.

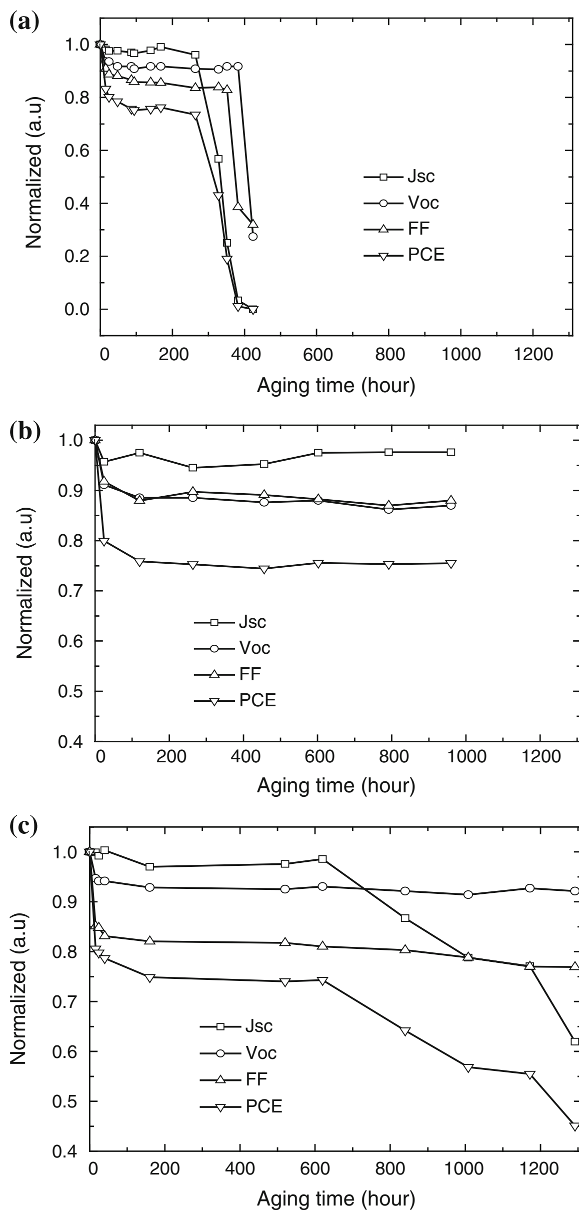

Fig. 4.24 **a** Jsc, Voc, FF and PCE versus aging time measured for encapsulated OSCs (devices encapsulated with the use of a 0.5 cm^2 sized adhesive desiccant, aged under a 90 % relative humidity at 60 °C). **b** Jsc, Voc, FF and PCE versus aging time measured for encapsulated OSCs (devices encapsulated without the use of adhesive desiccant, aged under $<$5 % relative humidity at 60 °C). **c** Jsc, Voc, FF and PCE versus aging time measured for encapsulated OSCs (encapsulated using a 1.0 cm^2 sized adhesive desiccant, aged under 90 % relative humidity at 60 °C)

In order to better understand the correlation between the initial degradation process in OSCs and the acceleration aging conditions, OSCs encapsulated with different amount of desiccant were aged at a relative low humidity of $<5\,\%$ at $60\,^{\circ}$C. It is found that by lowering the humidity level in the aging experiment, the OSCs exhibit only about 20 % of PCE deduction in the first 24 h as shown in Fig. 4.24b, which originates from the 10 % decrease in Voc and FF. And then all the operating parameters remain stable until the 1000 h mark. Comparing the degradation tendency of OSCs as illustrated in Figs. 4.24a, b, the decrease in the performance of OSCs within the first 24 h acceleration aging test seems less sensitive to the change in the moisture level, revealing that the initial degradation is likely associated with the deterioration occurred at organic/cathode contact, an inevitable interfacial passivation process due to the presence of residual oxygen at $60\,^{\circ}$C. The correlation between the initial degradation in OSCs with the possible residual oxygen in the accelerated aging test thus found also supports the results of our previous study of oxygen effect on the stability of P3HT:PCBM based OSCs in air. It is known that one of the degradation pathways in OSCs is related to an imbalanced charge mobility due to the formation of oxygen-induced charge traps within the P3HT:PCBM photoactive layer. The initial degradation of OSCs observed in the accelerated aging test correlates strongly with the interfacial passivation at organic/cathode interface, as illustrated in Fig. 4.24. It can also be seen from the time profile that the reaction finishes within the first 24 h, and thus the interface remains stable afterwards. The reduction in FF is related to the poor charge extraction due to the deterioration occurred at the organic/cathode interface, implying the quality of organic/cathode in the initial degradation of OSCs.

It can be seen that a more devastating degradation is the quick decrease after 260 h aging test, as shown in Fig. 4.24a, leading to the eventual device failure. J_{SC} is kept decreasing during this period, while little reduction in Voc and FF is observed. Therefore, the degradation of PCE in this stage is primary due to the drop in Jsc, which is different from that in OSCs as shown in Fig. 4.24b. More than one mechanism would be involved in the degradation processes. It has been reported that the degradation process of polymeric OSCs, water permeation often plays an important role [105]. In this accelerated aging test, OSCs encapsulated with a larger amount of desiccant were also used for the accelerated aging test, in order to investigate the possible change of the plateau in the degradation curve, in relation to the change of desiccant amount enclosed. As is expected, the plateau is extended from about 240 h in Fig. 4.24a to about 550 h in Fig. 4.24c, since the lager area desiccant absorbs more moisture. The extension of the plateau proves that the moisture diffusion in the packaging area is indeed the major cause of degradation. With the intention of understanding the impact of the cathode contact on device degradation during the accelerated aging test, a set of structurally identical OSCs with two different cathodes of Ca/Ag and Al were fabricated for the accelerated aging test under the same conditions. It shows that the rate of degradation in OSCs having Al contact was slower than the ones with Ca/Al cathode. This result implies that the OSCs with less reactive cathode materials also undergo a localized failure-related degradation process, due to the moisture encroaching in the active area of the OSCs.

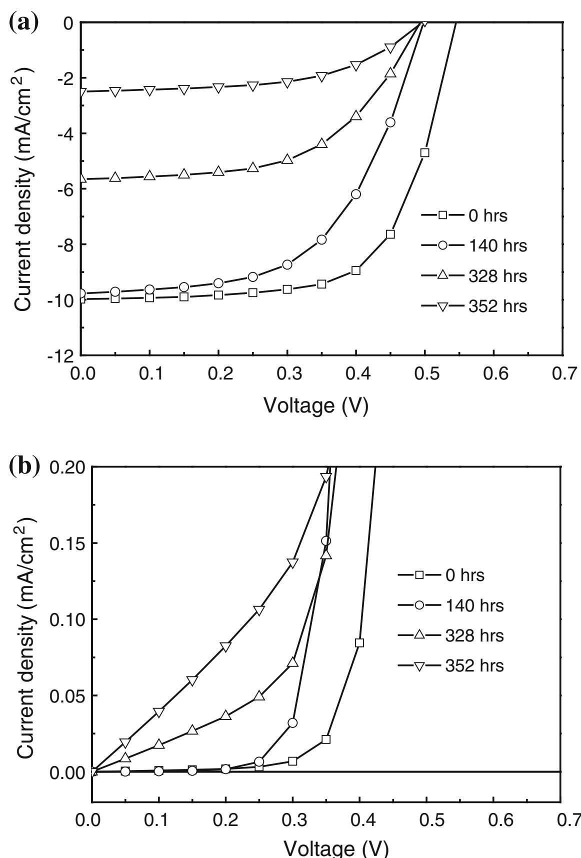

Fig. 4.25 Evolution of *J–V* characteristics of the OSCs, encapsulated using a 0.5 cm^2 sized adhesive desiccant and aged under a relative humidity of 90 % at 60 °C, measured under AM1.5 illumination (**a**) and dark (**b**)

The evolutions of the dark and the *J–V* characteristics of organic solar cells, encapsulated using a 0.5 cm^2 sized desiccant, measured under AM1.5 during the acceleration tests are shown in Fig. 4.25a, b, respectively. From Fig. 4.25, the reduction in Jsc, FF and Voc of the OSCs, aged under a high relative humidity of 90 % at 60 °C, was clearly observed. Comparing the *J–V* characteristics (Fig. 4.25) and the OSC lifetime plots shown in Fig. 4.25, there is one thing in common between Figs. 4.24a, c, both Voc and FF remain stable for a longer period of time than Jsc. This indicates that moisture-induced degradation act differently against the open circuit voltage from the short circuit current density. To answer the question of how they differ, two possible models are proposed; one is localized failure in functional area and the other a uniform degradation in the whole device.

IPCE characteristics of as-fabricated OSCs and the ones aged under different conditions were also measured. The decrease in IPCE was clearly observed in OSCs under different aging conditions. The measured IPCE characteristics provide the information of an average external quantum efficiency of the functional part in the aged OSCs. However, the information on the dead or much poorer performed part of the aged OSCs, e.g., the localized area around the sealing edge was not clearly reflected in the measured IPCE results. In order to reveal the deterioration of the cell performance including the less functional localized area in the aged OSCs, caused possibly due to the localized moisture encroachment, a photocurrent mapping was employed to analyze the localized and non-uniform degradation behavior in the aged OSCs. The photocurrent decrease is indicated by completely failed areas due to moisture encroachment, and in one cell some area is completely dead and central area still 100 % functioning. Further, the ratio of the dead area/the whole is calculated to be equal to the percentage of photocurrent decrease. The results exhibit that the moisture encroaches the charge generation area step by step until devouring the whole cell.

It shows that OSCs employing Ca containing cathode undergo treble degradation steps, relating to an initial degradation due to the presence of residual oxygen/moisture, a dawdling degradation process due to the localized moisture encroachment and a catastrophic failure. The deterioration of the organic/cathode contact is responsible for device degradation in a humid environment, e.g., under a high relative humidity of 90 % at 60 °C, resulting in the functional active area being reduced gradually during the accelerated aging test.

The commonly used BHJ OSCs discussed above, forming so called conventional OSC structure, have a donor/acceptor blend sandwiched between a transparent ITO anode and a reflective metal cathode. In conventional type of OSCs, a PEDOT:PSS hole-transporting buffer layer is often deposited on the surface of ITO anode to assist in the hole transport and carrier collection at ITO/organic interface. However, it is shown that the acidic nature of PEDOT:PSS in the conventional OSCs is not favorable for OSCs operating over a long period due to the deterioration in the contact property at ITO/PEDOT:PSS interface [106]. The upper metallic cathode in the conventional OSCs undergoes a gradual oxidation with the presence of residual oxygen in the cell environment. The interface of cathode/organic is thermally unstable, which is one of the reasons causing the deterioration in the cell performance [107].

Inverted OSCs avoid using the acidic PEDOT:PSS on ITO surface which is favorable for efficient operation of the cells. The surface of ITO anode is modified with a thin layer of a suitable low work function materials to form a front transparent cathode, e.g., solution-processable ZnO [101], TiO_2 [108] and Cs_2CO_3 [109], low work function metals of Ca [110] and Al [111]. Inverted OSCs with improved performance are demonstrated. For example, in a stability study, it is found that inverted OSCs fabricated with Al-modified ITO cathode are more stable as compared to the conventional OSCs. In this type of inverted OSCs, ITO surface is modified with $\sim$1.2 nm thick Al, forming an inverted OSC with a configuration of ITO/Al ($\sim$1.2 nm) /P3HT:PCBM (200 nm)/ MoO_3(5 nm)/Ag (100 nm). A control cell with

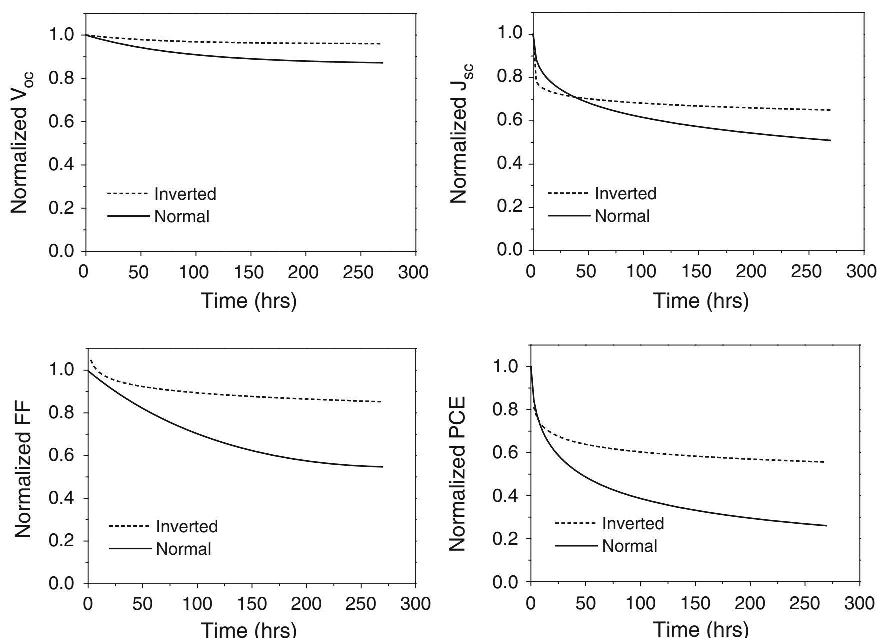

Fig. 4.26 Jsc, Voc, FF and PCE versus aging time measured for encapsulated inverted and conventional OSCs under ~100 mW/cm^2 (AM1.5G), 60 ± 5 °C

a conventional structure of ITO/PEDOT:PSS (40 nm)/P3HT: PCBM (200 nm)/Al (100 nm) was also made for comparison study.

The accelerated aging test of the inverted and conventional OSCs are conducted under the same conductions. In order to establish a comprehensive and reliable OSC lifetime data for durability studies, the lifetime results are averaged from a set of structurally identical OSCs for comparable studies. The normalized cell parameters of V_{OC}, FF, J_{SC} and PCE measured for inverted and conventional OSCs as a functional aging time are shown in Fig. 4.26. It can be seen that both types of OSCs undergo typically an initial fast degradation, followed by an extended period of slower decay. The initial fast degradation for inverted OSCs occurred within the first 10 h of aging, with a ~40 % loss in PCE by the 70 h mark. In comparison, the conventional control OSCs experienced a gradual and continuous decay in the first 70 h with ~60 % loss in PCE. It is clear that the inverted OSCs are more stable than the conventional OSCs aged under the same conditions over the aging period of $>$250 h.

It is found that there is very little change in FF and V_{OC}, while the degradation of the inverted OSCs is primary due to the gradual reduction in J_{SC} observed during the aging test. However, all cell parameters of the conventional OSCs decrease leading to much fast device degradation over the same aging test. The results suggest that the quality of the interfacial contacts in inverted, e.g., organic/MoO_3/Ag and organic/Al-ITO interfaces, function well for charge extraction during the aging,

implying the excellent stability of Al-ITO as a cathode layer. In contrast, an obvious reduction in V_{OC} of the conventional OSCs is observed due to the deterioration of the contact properties at ITO/PEDOT:PSS anode and upper organic/Al cathode interfaces. As a result that inverted P3HT:PCBM-based OSCs exhibited a PCE of 4.16 % compared to the conventional OSCs (3.67 %) and are more stable.

4.7 Conclusions

Compared to silicon-based solar cells that are rigid, organic-based solar cells that use solution-based processing deposition techniques are simpler and potentially less expensive to manufacture. Substantial progress has been made over the last five years by emergence of new organic photoactive materials with tailored energy levels, virtue of optimization of materials processing parameters and new fabrication methodologies. PCE of ∼9.0 % for single junction OSCs [112] and ∼10 % for tandem OSCs [113] have been demonstrated recently.The broadband absorption enhancement in nano-structured OSCs can be realized through theoretical simulation and integration of nanostructures. The success in the development of efficient OSCs with light trapping structures over a large area will lead to the creation of a wide spectrum of new materials and device process technologies with enormous commercial potential. The solution-processed and large printed fabrication techniques provide a cost-effective approach for mass production, contributing to the building of a sustainable knowledge-based economy.

OSCs can be made flexible, semitransparent and are light weight, offer an attractive option for achieving low-cost and clean energy sources. The unique flexibility and semi-transparency feature also add a decorative and aesthetic dimension to OSCs so that they can be used on curved and irregular surfaces, which cannot be done using traditional rigid silicon solar cells. The ubiquitous adoption of OSC technology as one of the primary energy sources, rendering the affordable next generation photovoltaic technology, will reduce greenhouse gas emissions, thus contributing to the preservation of our environment.

References

1. D.S. Ginley, M.A. Green, R.T. Collins, MRS Bull. **33**, 355 (2008)
2. A. Slaoui, R.T. Collins, MRS Bull. **32**, 211 (2007)
3. C.W. Tang, S.A. VanSlyke, Appl. Phys. Lett. **51**, 913 (1987)
4. J.H. Burroughs, D.D.C. Bradley, A.R. Brown, R.N. Marks, K. MacKay, R.H. Friend, P.L. Burn, A.B. Holmes, Nature **347**, 593 (1990)
5. Y.Q. Li, L.W. Tan, X.T. Hao, K.S. Ong, F.R. Zhu, Appl. Phys. Lett. **86**, 153508 (2005)
6. Z. Bao, A. Dodabalapur, A.J. Lovinger, Appl. Phys. Lett. **69**, 4108 (1996)
7. S. Moller, C. Perlov, W. Jackson, C. Taussig, S.R. Forrest, Nature **426**, 166 (2003)
8. P. Peumans, A. Yakimov, S.R. Forrest, J. Appl. Phys. **93**, 3693 (2003)
9. C.W. Tang, Appl. Phys. Lett. **48**, 183 (1986)
10. A. Shah, P. Torres, R. Tscharner, N. Wyrsch, H. Keppner, Science **285**, 692 (1999)

11. N.S. Sariciftci, L. Smilowitz, A.J. Heeger, F. Wudl, Science **258**, 1474 (1992)
12. H.S. Nalwa, *Handbook of Organic Conductive Molecules and Polymers*, vol. 1–4 (John Wiley & Sons Ltd, Chichester, 1997)
13. D. Braun, A.J. Heeger, Appl. Phys. Lett. **58**, 1982 (1991)
14. J. Shinar, *Organic Light-Emitting Devices: A Survey* (Springer, New York, 2004)
15. G. Yu, J. Gao, F. Wudl, A.J. Heeger, Science **270**, 1789 (1995)
16. J.J.M. Halls, C.A. Walsh, N.C. Greenham, R.H. Friend, A.B. Holmes, Nature **376**, 498 (1995)
17. T. Tsuzuki, Y. Shirota, D. Meissner, Sol. Energy Mater. Sol. Cells **61**, 1 (2000)
18. F. Zhang, M. Svensson, O. Inganas, Adv. Mater. **13**, 1871 (2001)
19. T. Kietzke, D. Neher, U. Scherf, Nat. Mater. **2**, 408 (2003)
20. R.N. Marks, J.J.M. Halls, D.D.C. Bradley, R.H. Friend, A.B. Holmes, J. Phys.: Condens. Matter **6**, 1379 (1994)
21. S. Barth, H. Bässler, H. Rost, H.H. Hörhold, Phys, Rev. Lett. **79**, 4445 (1997)
22. P.B. Miranda, D. Moses, A.J. Heeger, Phys. Rev. B **64**, 81201 (2001)
23. C.J. Brabec, G. Zerza, G. Cerullo, S. De Silvestri, S. Luzzati, J.C. Hummele, N.S. Sariciftci, Chem. Phys. Lett. **340**, 232 (2001)
24. J. Orenstein, in *Handbook on Conducting Polymers*, vol. 2, p. 1297 (Dekker, New York, 1986), ed. by T. Skotheim; or Springer Series in Solid State Sciences 76, Electronic Properties of Conjugated Polymers, vol. 107, ed. by H. Kuzmany, M. Mehring, S. Roth (1992)
25. Z. Vardeny, J. Tauc, Phys. Rev. Lett. **54**, 1844 (1985)
26. Z. Vardeny, E. Ehrenfreund, O. Brafman, M. Nowak, H. Schaffer, A.J. Heeger, F. Wudl, Phys. Rev. Lett. **56**, 671 (1986)
27. R. Österbacka, C.P. An, X.M. Jiang, Z.V. Vardeny, Science **287**, 839 (2000)
28. X.M. Jiang, R. Österbacka, O. Korovyanko, C.P. An, B. Horovitz, R.A.J. Janssen, Z.V. Vardeny, Adv. Funct. Mater. **12**, 587 (2002)
29. S. De, T. Pascher, M. Maiti, K.G. Jespersen, T. Kesti, F. Zhang, O. Inganä, A. Yartsev, V. Sundström, J. Am. Chem. Soc. **129**, 8466 (2007)
30. C.J. Brabec, G. Zerza, G. Cerullo, S. De Silvestri, S. Luzzati, J.C. Hummelen, S. Sariciftci, Chem. Phys. Lett. **340**, 232 (2001)
31. T. Clarke, A. Ballantyne, F. Jamieson, C. Brabec, J. Nelson, J. Durrant, Chem. Commun. **1**, 89 (2009)
32. I.W. Hwang, D. Moses, A.J. Heeger, J. Phys. Chem. C **112**, 4350 (2008)
33. I.W. Hwang, C. Soci, D. Moses, Z. Zhu, D. Waller, R. Gaudiana, C.J. Brabex, A.J. Heeger, Adv. Mater. **19**, 2307 (2007)
34. T.M. Clarke, A.M. Ballantyne, J. Nelson, D.D.C. Bradley, J. Durrant, Adv. Func. Mater. **18**, 4029 (2008)
35. N.S. Saricifci, L. Smilowitz, A.J. Heeger, F. Wudi, Science **258**, 1474 (1994)
36. J. Peet, J.Y. Kim, N.E. Coates, W.L. Ma, D. Moses, A.J. Heeger, G.C. Bazan, Nat. Mater. **6**, 497 (2007)
37. D.H. Ko, J.R. Tumbleston, L. Zhang, S. Williams, J.M. Desimone, R. Lopez, E.T. Samulski, Nano Lett. **9**, 2742–2746 (2009)
38. W.L. Barnes, A. Dereux, T.W. Ebbesen, Nature **424**, 824 (2003)
39. H.A. Atwater, A. Polman, Nat. Mater. **9**, 205 (2010)
40. H. Shen, P. Bienstman, B. Maes, J. Appl. Phys. **106**, 073109 (2009)
41. F.C. Chen, J.L. Wu, C.L. Lee, Y. Hong, C.H. Kuo, M.H. Huang, Appl. Phys. Lett. **95**, 013305 (2009)
42. S.S. Kim, S.I. Na, J. Jo, D.Y. Kim, Y.C. Nah, Appl. Phys. Lett. **93**, 073307 (2008)
43. A.P. Kulkarni, K.M. Noone, K. Munechika, S.R. Guyer, D.S. Ginger, Nano Lett. **10**, 1501 (2010)
44. K. Tvingstedt, N. Krister, O. Ingnas, A. Rahachou, I.V. Zozoulenko, Appl. Phys. Lett. **91**, 113514 (2007)
45. N.C. Lindquist, W.A. Luhman, S.H. Oh, R.J. Holmes, Appl. Phys. Lett. **93**, 123308 (2008)
46. R.A. Pala, J. White, E. Barnard, J. Liu, M.L. Brongersma, Adv. Mater. **21**, 3504–3509 (2009)

47. S. Pillai, K.R. Catchpole, T. Trupke, G. Zhang, J. Zhao, M.A. Green, Appl. Phys. Lett. **88**, 161102 (2006)
48. S. Nie, S.R. Emery, Science **275**, 1102 (1997)
49. X.Z. Wang, H.L. Tam, K.S. Yong, Z.K. Chen, F.R. Zhu, Org. Electron. **12**, 1429 (2011)
50. Y.Q. Li, L.W. Tan, X.T. Hao, K.S. Ong, F.R. Zhu, L.S. Hung, Appl. Phys. Lett. **86**, 153508 (2005)
51. F.T. Reisa, D. Mencaraglia, S. Oould Saad, I. Seguy, M. Oukachmih, P. Jolinat, P. Destruel, Synth. Met. **138**, 33 (2003)
52. J.R. Cole, N.J. Halas, Appl. Phys. Lett. **89**, 153120 (2006)
53. A. Aubry, D.Y. Lei, S.A. Maier, J.B. Pendry, Phys. Rev. B **82**, 125430 (2010)
54. M. Pagliaro, R. Ciriminna, G. Palmisano, Chem. Sus. Chem. **1**, 880 (2008)
55. C.J. Brabec, S.E. Shaheen, C. Winder, N.S. Sariciftci, P. Denk, Appl. Phys. Lett. **80**, 1288 (2002)
56. C.N. Hoth, S.A. Choulis, P. Schilinsky, C.J. Brabec, Adv. Mater. **19**, 3973 (2007)
57. S.R. Forrest, Nature **428**, 911 (2004)
58. H.L. Hatrnagel, A.L. Dawar, A.K. Jain, C. Jagadish, *Semiconducting Transparent Thin Films* (Institute of Physics Publishing, Bristol, 1995)
59. G.M. Ng, E.L. Kietzke, T. Kietzke, L.W. Tan, P.K. Liew, F.R. Zhu, Appl. Phys. Lett. **90**, 103505 (2007)
60. X.Z. Wang, G.M. Meng, J. Ho, H.L. Tam, F.R. Zhu, IEEE J. Sel. Top. Quantum Electron. **16**, 1685 (2010)
61. F.R. Zhu, X.T. Hao, K.S. Ong, Y.Q. Li, L.W. Tan, Proc. IEEE, **93**(8), 1440–1446 (2005)
62. A. Klein, Appl. Phys. Lett. **77**, 2009 (2000)
63. J.E.A.M. van den Meerakker, E.A. Meulenkamp, M. Scholten, J. Appl. Phys. **74**, 3282 (1993)
64. D.H. Cui, J. Xu, T. Zhu, G. Paradee, S. Ashok, M. Gerhold, Appl. Phy. Lett. **88**, 183111 (2006)
65. S.A. Mcdonald, G. Konstantatos, S.G. Zhang, P.W. Cyr, E.J.D. Klem, L. Levina, E.H. Sargent, Nat. Mater. **4**, 138 (2005)
66. N.C. Greenham, X.G. Peng, A.P. Alivisatos, Phys. Rev. B, **54**(17), 628 (1996)
67. W.J.E. Beek, M.M. Wienk, M. Kemerink, X.N. Yang, R.A.J. Janssen, J. Phys. Chem. B. **109**, 9505 (2005)
68. L.J.A. Koster, W.J. Strien, W.J.E. Beek, P.W.M. Blom, Adv. Funct. Mater. **17**, 1297 (2007)
69. W.J.E. Beek, M.M. Wienk, R.A.J. Janssen, Adv. Funct. Mater. **16**, 1112 (2006)
70. G. Juska, K. Arlauskas, M. Viliunas, J. Kocka, Phys. Rev. Lett. **84**, 4946 (2000)
71. G. Juska, K. Arlauskas, M. Viliunas, K. Genevicius, R. Osterbacka, H. Stubb, Phys. Rev. B **62**, R16235 (2000)
72. G. Dennler, A.J. Mozer, G. Juska, A. Pivrikas, R. Osterbacka, A. Fuchsbauer, N.S. Sariciftci, Org. Electron. **7**, 229 (2006)
73. A.J. Mozer, G. Dennler, N.S. Sariciftci, M. Westerling, A. Pivrikas, R. Österbacka, G. Juška, Phys. Rev. B **72**, 035217 (2005)
74. W.D. Gill, J. Appl. Phys. **43**, 5003 (1972)
75. H. Bässler, Phys. Status Solidi B **175**, 15 (1993)
76. C.J. Brabec, N.S. Sariciftci, J.C. Hummelen, Adv. Funct. Mater. **11**, 15 (2001)
77. I. Riedel, J. Parisi, V. Dyakonov, L. Lutsen, D. Vanderzande, J.C. Hummelen, Adv. Funct. Mater. **14**, 28 (2004)
78. Y.K. Kim, S. Cook, S.M. Tuladhar, S.A. Choulis, J. Nelson, J.R. Durrant, D.D.C. Bradley, M. Giles, I. Mcculloch, C.S. Ha, M. Ree, Nat. Mater. **5**, 197 (2006)
79. G. Li, V. Shrotriya, J.S. Huang, Y. Yao, T. Moriarty, K. Emery, Y. Yang, Nat. Mater. **4**, 864 (2005)
80. G. Juska, N. Nekrasas, K. Arlauskas, J. Stuchlik, A. Fejfar, J. Kocka, J. Non-Cryst. Solids **338–340**, 353 (2004)
81. G. Sliauzys, G. Juska, K. Arlauskas, A. Pivrikas, R. Osterbacka, M. Scharber, A. Mozer, N.S. Sariciftci, Thin Solid Films **511–512**, 224 (2006)
82. M. Jørgensen, K. Norrman, F.C. Krebs, Solar Energy Mater. Sol. Cells, **92**, 686 (2008)

83. J. Schafferhans, A. Baumann, C. Deibel, V. Dyakonov, Appl. Phys. Lett. **93**, 093303 (2008)
84. L.M. Andersson, F.L. Zhang, O. Inganas, Appl. Phys. Lett. **89**, 142111 (2006)
85. M. Niggemann, M. Glatthaar, A. Gombert, A. Hinsch, V. Wittwer, Thin Solid Films **619**, 451 (2004)
86. M. Niggemann, M. Glatthaar, P. Lewer, C. Muller, J. Wagner, A. Gombert, Thin Solid Films **628**, 511 (2006)
87. C. Cocoyer, L. Rocha, C.F. Debuisschert, L. Sicot, D. Vaufrey, C. Sentein, B. Geffroy, P. Raimond, Thin Solid Films **517**, 511 (2006)
88. S.I. Na, S.S. Kim, J. Jo, S.H. Oh, J.H. Kim, D.Y. Kim, Adv. Funct. Mater. **18**, 3956 (2008)
89. C.J. Min, J. Li, G. Veronis, J.Y. Lee, S.H. Fan, P. Peumans, Appl. Phys. Lett. **96**, 133302 (2010)
90. P.B. Catrysse, S. Fan, Nano Lett. **10**, 2944 (2010)
91. K.S. Nalwa, J.M. Park, K.M. Ho, S. Chaudhary, Adv. Mater. **23**, 112 (2011)
92. M.G. Kang, T. Xu, H.J. Park, X.G. Luo, L.J. Guo, Adv. Mater. **22**, 4378 (2010)
93. D.H. Ko, J.R. Tumbleston, L. Zhang, S. Williams, J.M. Desimone, R. Lopez, E.T. Samulski, Nano Lett. **9**, 2742 (2009)
94. K.S. Nalwa, S. Chaudhary, Opt. Express **18**, 5169 (2010)
95. S. Mokkapati, K.R. Catchpole, J. Appl. Phys. **112**, 101101 (2012)
96. P. Wang, R. Menon, Opt. Express **20**, 1849 (2012)
97. Z.N. Yu, P. Deshpande, W. Wu, J. Wang, S.Y. Chou, Appl. Phys. Lett. **77**, 927 (2000)
98. S.W. Ahn, K.D. Lee, J.S. Kim, S.H. Kim, J.D. Park, S.H. Lee, P.W. Yoon, Nanotechnology **16**, 1874 (2005)
99. C. Vijila, G.M. Ng, M.J. Tan, W.P. Goh, F.R. Zhu, Appl. Phys. Lett. **95**, 263305 (2009)
100. X.Z. Wang, X.X. Zhao, G. Xu, Z.K. Chen, F.R. Zhu, Sol. Energy Mater. Sol. Cells **104**, 1 (2012)
101. H.X. Liu, Z.H. Wu, J.Q. Hu, Q.L. Song, B. Wu, H.L. Tam, Q.Y. Yang, W.H. Choi, F.R. Zhu, Appl. Phys. Lett. **103**, 043309 (2013)
102. A. Seemann, H.-J. Egelhaaf, C.J. Brabec, J.A. Hauch, Org. Electron. **10**, 1424 (2009)
103. M.O. Reese, A.J. Morfa, M.S. White, N. Kopidakis, S.E. Shaheen, G. Rumbles, D.S. Ginley, Sol. Energy Mater. Sol. Cells **92**, 746 (2008)
104. X. Yang, J. Loos, S.C. Veenstra, W.J.H. Verhees, M.M. Wienk, J.M. Kroon, M.A.J. Michels, R.A.J. Janssen, Nano Lett. **5**, 579 (2005)
105. K. Norrman, S.A. Gevorgyan, F.C. Krebs, ACS Appl. Mater. Interfaces. **1**, 102 (2009)
106. M.P. deJong, L.J. van Jzendoorn, M.J.A. deVoigt, Appl. Phys. Lett. **77**, 2255 (2000)
107. M. Jørgensen, K. Norrman, F.C. Krebs, Sol. Energy Mater. Sol. Cells **92**, 686 (2008)
108. S.K. Hau, H.L. Yip, H. Ma, A.K.Y. Jen, Appl. Phys. Lett. **93**, 233304 (2008)
109. H.H. Liao, L.M. Chen, Z. Xu, G. Li, Y. Yang, Appl. Phys. Lett. **92**, 173303 (2008)
110. C.Y. Jiang, X.W. Sun, D.W. Zhao, A.K.K. Kyaw, Y.N. Li, Sol. Energy Mater. Sol. Cells **94**, 1618 (2010)
111. H.M. Zhang, J. Ouyang, Appl. Phys. Lett. **97**, 063509 (2010)
112. Z.C. He, C.M. Zhong, S.J. Su, M. Xu, H.B. Wu, Y. Cao, Nat. Photonics **6**, 591 (2012)
113. J.B. You, C.C. Chen, Z.R. Hong, K. Yoshimura, K. Ohya, R. Xu, S.L. Ye, J. Gao, G. Li, Y. Yang, Adv. Mater. **25**, 3973 (2013)

Chapter 5
Exciton-Plasmon Coupling in Nanocomposites

Mahi R. Singh

Abstract There has been growing interest in developing nanoscale optoelectronic devices by combining nanomaterials with complementary optical properties into composite (hybrid) structures. The number of possible nanocomposites that can be built from already existing nanostructures is simply enormous. A significant amount of research on nanocomposites has been devoted to the study of exciton-plasmon interactions in metal-semiconductor nanostructures, which offer a wide range of opportunities to control light-matter interactions and electromagnetic energy flows on nanometer length scales. Strong exciton-surface plasmon coupling in metallic nanocomposites could lead to efficient transmission of quantum information between qubits for applications in quantum computing and communication. These nanocomposites also have applications in biophotonics, sensing and switching applications.

5.1 Introduction

There is considerable interest in developing nanoscale **optoelectronic devices** by combining nanomaterials into **hybrid structures** (**nanocomposites**). The number of hybrid systems that can be built from existing nanostructures is simply enormous. For example, various types of hybrid nanostructures have been fabricated by combining semiconductor nanomaterials with noble metal nanomaterials. A significant amount of research on nanocomposites has been devoted to the study of exciton-plasmon interactions in these types of hybrid systems [1–11] because they offer a wide range of opportunities to control **light-matter interactions** and electromagnetic energy

M. R. Singh (✉)
Department of Physics and Astronomy, The University of Western Ontario,
London N6G 3K7, Canada
e-mail: msingh@uwo.ca

J. Singh and R. T. Williams (eds.), *Excitonic and Photonic Processes in Materials*,
Springer Series in Materials Science 203, DOI: 10.1007/978-981-287-131-2_5,

© Springer Science+Business Media Singapore 2015

flows on nanometer length scales. Strong **exciton-surface plasmon coupling** could lead to efficient transmission of quantum information between qubits for applications in quantum computing and communication. These nanocomposites also have applications in **biophotonics** and sensing, as nonradiative energy transfer between a **quantum dot** (QD) and a **metallic nanoparticle** (MNP) can also be used to detect biological molecules.

Recently **semiconductor nanostructures** and **graphene** nanocomposites have also been fabricated [12–14]. The effect of surface plasmons on the energy transfer between these structures has been investigated. **Surface plasmon polaritons** in graphene are created due to the collective oscillations of conduction band electrons, and are localized at the interface between graphene and the surrounding nonconductive environment. Surface plasmon polaritons can be used to develop plasmonic nanodevices for applications in ultrasensitive optical biosensing, photonic metamaterials, light harvesting, optical nanoantennas and quantum information processing. Noble metals are typically regarded as the best available plasmonic materials for the study of surface plasmon polaritons. However, surface plasmons in graphene have the advantage of being highly tunable via electrostatic gating. Compared to noble metals, graphene also has superior electronic and mechanical properties. Hence, the study of plasmonics in graphene has received significant attention experimentally and theoretically. Recently, graphene nanocomposites have been fabricated by several groups [12–14].

Here we consider nanocomposites made by combining dielectric nanoparticles and MNPs. The dielectric nanoparticles can be QDs, biological molecules (i.e. DNA) or chemical nanoparticles. The MNPs can be made from noble metals or graphene. In this chapter we consider QD-MNP and QD-graphene hybrid systems as examples. However, the theory developed in this chapter can be applied to any dielectric nanoparticle-MNP hybrid system. Energy transfer occurs in the QD-MNP hybrid system due to the interaction of optical excitations in the QD and MNP. These interactions are strong when the QD and MNP are in close proximity and their optical excitation frequencies are resonant. The optical excitations in the QD are excitons, which are electron-hole pairs bound by their Coulomb interaction. Optical excitations in the MNP are surface plasmon polaritons, which are created due to the collective oscillations of conduction band electrons. We consider that a probe laser field is applied to measure the power transfer spectra of the QD and MNP, while a secondary control laser field is applied to monitor and control the power transfer. These fields create excitons in the QD and surface plasmon polaritons in MNP. The excitons in the QD and surface plasmon polaritons in the MNP then interact via the **dipole–dipole interaction** (DDI). It is found that the **energy transfer** between the QD and MNP can be switched on and off by applying the control field. Therefore, these systems can be used as optical switching devices. It is also found that when the hybrid system is in contact with biological or chemical materials, the energy transfer between the QD and MNP is modified. Therefore, the present nanocomposite systems can be used to fabricate **nano-biosensors**, **all-optical nano-switche**s, energy transfer devices and **quantum tele-transportation devices**.

5.2 Surface Plasmon Polaritons

The metals used to make MNPs are considered to be plasmonic materials because they have an equal concentration of positive and negative charges, where one charge type is mobile. In graphene, it has been found experimentally and theoretically that the conduction and valence bands meet at the Dirac point in the absence of doping. This means that the graphene is a zero-band gap material and thus behaves as a metal. Therefore we also treat graphene as a plasmonic material.

The mobile charge carriers in metals are electrons which are located in the conduction band. In the presence of an external electromagnetic field the conduction band electrons oscillate. Let us consider a metal which has n_e electrons per unit volume. The mass and charge of an electron are denoted as m_e and e, respectively. In the effective mass approximation the interaction between the electrons and ions is included in the effective mass of the electron.

Surface plasmons in the classical picture are defined as collective oscillations in the electron density at the surface of a metal or MNP. In the quantum picture, surface plasmons are the quanta of surface-charge density oscillations in metallic materials. When an electromagnetic field is applied to a metallic material it couples to these surface charge density oscillations. In other words, photons and plasmons interact at the surface of the metal. The coupled photon-plasmon system creates new particles called surface plasmon polaritons, which are widely known by their acronym as SPPs.

SPPs are created at the interface between a dielectric material and a metallic material. The dielectric constant of the dielectric medium is considered to be frequency-independent a real quantity, whereas the dielectric constant for the metallic material is frequency-dependent and is a complex quantity. We have shown in the last section of this chapter that the dielectric constant of the metallic material becomes negative when the frequencies of external EM waves are less than the plasmon frequency. We will show in this section that when the dielectric constant of a metallic material is negative, SPPs are created at the surface of the metal and they are localized in the direction perpendicular to the interface between the metallic material and surrounding dielectric material.

5.2.1 Quasi-Static Approximation

Let us study the nature of SPPs in MNPs. Usually the size of MNPs is much smaller than the wavelength of an electromagnetic field in the optical regime. For example, the wavelength of light in the visible regime is on the order of 500 nm whereas the sizes of nanoparticles are on the order of 100 nm or less. In this situation one can consider that the amplitude of the external electric field is constant across the nanoparticle. In other words, the nanoparticles see a spatially invariant electric field amplitude. This condition is known as the quasi-static approximation [15–20]. In this approximation it is also considered that the electric field varies slowly with

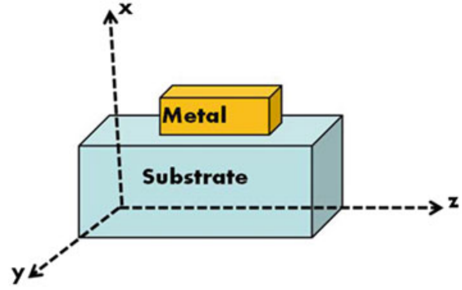

Fig. 5.1 Metallic and dielectric material hybrid heterostructure system

time so that the time dependence of the electric field is also neglected. Therefore, in the quasi-static approximation the Maxwell equations reduce to Laplace equations which are much easier to solve. We consider two Maxwell's equations as

$$\nabla \times \mathbf{E} = 0 \qquad (5.1)$$
$$\nabla \cdot \mathbf{D} = 0$$

where **E** is the electric field and **D** is the displacement vector. It is known that if the curl of the electric field is zero (i.e. $\nabla \times \mathbf{E} = 0$) then the electric field can be expressed as the gradient of a scalar electrical potential function V as follows

$$\mathbf{E} = -\nabla V \qquad (5.2)$$

where

$$\nabla = \mathbf{i}\frac{\partial}{\partial x} + \mathbf{j}\frac{\partial}{\partial y} + \mathbf{k}\frac{\partial}{\partial z}$$

Using $\mathbf{D} = \epsilon\mathbf{E}$ and the above expression in (5.1) we find

$$\nabla \cdot \nabla V = \nabla^2 V = 0 \qquad (5.3)$$

The above expression is called the Laplace equation.

5.2.2 Metallic Heterostructures

We consider here a metallic thin film or graphene layer deposited on a dielectric substrate. The dielectric constant for the substrate is denoted as ϵ_d and the dielectric constant for the metallic layer is denoted as ϵ_m. This structure is known as a **metallic heterostructure** (see Fig. 5.1). The interface between the metallic substance and the dielectric material lies in the y–z plane.

In Cartesian coordinates (x, y, z) the Laplace equation becomes

$$\left(\frac{\partial^2}{\partial x^2} + \frac{\partial^2}{\partial y^2} + \frac{\partial^2}{\partial z^2}\right) V(x, y, z) = 0 \tag{5.4}$$

Plasmon surface waves travel along the interface of both materials in the z-direction. These surface waves decay in both media in the x-direction. For simplicity we consider that $k_y = 0$. The solutions of the above equations in both media can then be written as

$$\begin{aligned} V_d &= A_d e^{-ik_z z} e^{i\kappa_d x} \quad \text{for } x < 0 \\ V_m &= A_m e^{-ik_z z} e^{-i\kappa_m x} \quad \text{for } x > 0 \end{aligned} \tag{5.5}$$

where

$$\begin{aligned} \kappa_d &= \sqrt{k_z^2 - \frac{\epsilon_d \omega^2}{c^2}} \\ \kappa_m &= \sqrt{k_z^2 - \frac{\epsilon_m \omega^2}{c^2}} \end{aligned} \tag{5.6}$$

We substitute the above equations into the Laplace equation and get

$$\begin{aligned} k_z^2 &= \kappa_d^2 \quad \text{for } x < 0 \\ k_z^2 &= \kappa_m^2 \quad \text{for } x > 0 \end{aligned} \tag{5.7}$$

At the interface of the heterostructure the electric potential and its derivative must be continuous. These two conditions give the following boundary conditions:

$$\begin{aligned} [V_d(x, y, z)]_{x=0} &= [V_m(x, y, z)]_{x=0} \\ \left[\epsilon_d \frac{\partial V_d(x, y, z)}{\partial x}\right]_{x=0} &= \left[\epsilon_m \frac{\partial V_m(x, y, z)}{\partial x}\right]_{x=0} \end{aligned} \tag{5.8}$$

The above boundary conditions lead to the following equations:

$$\begin{aligned} A_d &= A_m \\ \epsilon_d \kappa_d A_d &= -\epsilon_m \kappa_m A_m \end{aligned}$$

The above expressions give

$$\epsilon_d \kappa_d = \epsilon_m \kappa_m \tag{5.9}$$

Using (5.7) we get

$$\epsilon_d = \epsilon_m \tag{5.10}$$

Note that the refractive index of the metallic medium is negative for certain frequencies as illustrated in the Drude model. In this case we get

$$\epsilon_d = -\epsilon_m \tag{5.11}$$

From (5.6) the decaying wave vectors κ_d and κ_m along the x-direction are found as

$$\kappa_d = \sqrt{k_z^2 + \frac{\epsilon_d \omega^2}{c^2}} \tag{5.12}$$

$$\kappa_m = \sqrt{k_z^2 + \frac{\epsilon_m \omega^2}{c^2}}$$

Note that both wave vectors have positive values. This means that the waves are decaying along the x-direction in both media. However the wave propagates along the z-direction. These waves are surface plasmon waves. The dielectric constant in the Drude model is written as

$$\epsilon_m = 1 - \frac{\omega_p^2}{\omega^2} \tag{5.13}$$

Substituting this equation in (5.11) we obtain the expression for the surface plasmon frequency as

$$\omega_{sp} = \sqrt{\frac{\omega_p}{\epsilon_d + 1}} \tag{5.14}$$

5.2.3 Metallic Nanoparticles

Here we consider a **MNP** with dielectric function ϵ_m that is embedded in a dielectric material with dielectric constant ϵ_d. We consider that the nanoparticle has a spherical shape with radius R (see Fig. 5.2). The external electric field is applied along the x-direction, i.e. $\mathbf{E} = E_0 \mathbf{e}_x$. Because the nanoparticle has a spherical symmetry it is simpler mathematically to solve the Maxwell equations in spherical coordinates (r, θ, ϕ) in order to find surface plasmons rather than in Cartesian (x, y, z) coordinates. The spherical and Cartesian coordinate systems are related to each other via the following equations:

$$x = r \sin\theta \cos\phi, \quad y = r \sin\theta \sin\phi, \quad z = r \cos\theta \tag{5.15}$$

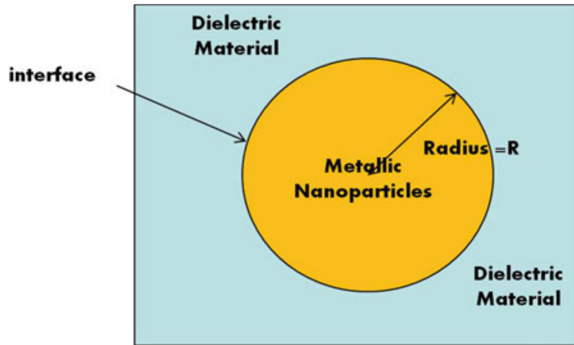

Fig. 5.2 Metallic nanoparticle and dielectric material hybrid system

The Laplace equation in spherical coordinates then becomes

$$\left[\frac{1}{r^2}\frac{\partial}{\partial r}\left(r^2\frac{\partial}{\partial r}\right)+\frac{1}{r^2\sin\theta}\frac{\partial}{\partial\theta}\left(\sin\theta\frac{\partial}{\partial\theta}\right)+\frac{1}{r^2\sin^2\theta}\frac{\partial^2}{\partial\varphi^2}\right]V(r,\phi,z)=0 \tag{5.16}$$

Solutions to the above expression within the nanoparticle and in the surrounding dielectric medium are obtained as [15, 16]

$$\begin{aligned} V_m &= \sum_{l=0}^{\infty} A_m^l r^l P_l(\cos\theta), & r < R \\ V_d &= \sum_{l=0}^{\infty}\left[A_{ext}^l r^l + A_d^l r^{-(l+1)}\right]P_l(\cos\theta), & r > R \end{aligned} \tag{5.17}$$

The expression for V_d contains two terms. The first term is the potential due to the external applied field and second term is the potential due to the electric field created by the nanoparticle. The above expressions reduce to a simpler forms for $l = 0$ as follows. We use $P_0(\cos\theta) = \cos\theta$ and obtain

$$\begin{aligned} V_m &= A_m r\cos\theta, & r < R \\ V_d &= \frac{A_d}{r^2}\cos\theta - E_0 r\cos\theta, & r > R \end{aligned} \tag{5.18}$$

We now use the boundary conditions which state that at the interface between the metallic sphere and the dielectric medium the tangential electric fields and the normal

components of the electric displacement should be continuous. These two conditions are expressed by the following two equations

$$\left[\frac{\partial V_d}{\partial \theta}\right]_{r=R} = \left[\frac{\partial V_m}{\partial \theta}\right]_{r=R}$$
$$\left[\epsilon_d \frac{\partial V_d}{\partial r}\right]_{r=R} = \left[\epsilon_m \frac{\partial V_m}{\partial r}\right]_{r=R} \quad (5.19)$$

Using (5.18) in the above expression we find

$$\frac{A_d}{R^2} - E_0 R = A_m R$$
$$-\epsilon_d \left(\frac{2A_d}{R^3} + E_0\right) = \epsilon_m A_m \quad (5.20)$$

Solving the above two equations gives

$$A_d = \left(\frac{\epsilon_m - \epsilon_d}{2\epsilon_d + \epsilon_m}\right) R^3 E_0$$
$$A_m = \left(\frac{-3\epsilon_d}{2\epsilon_d + \epsilon_m}\right) E_0 \quad (5.21)$$

Substituting the above two expressions in (5.18) gives the electric potential inside and outside the nanoparticle as

$$V_m = -\left(\frac{3\epsilon_d}{2\epsilon_d + \epsilon_m}\right) r \cos\theta E_0$$
$$V_d = \left(\frac{\epsilon_m - \epsilon_d}{2\epsilon_d + \epsilon_m}\right)\left(\frac{R^3}{r^3}\right) E_0 r \cos\theta - E_0 r \cos\theta \quad (5.22)$$

The electric fields inside and outside the nanoparticle can now be calculated from the electric potential by using the following identity

$$\mathbf{E}_m = -\nabla \cdot V \quad (5.23)$$

where the operator ∇ is written in cylindrical coordinates as

$$\nabla = \frac{\partial}{\partial r}\mathbf{e}_r + \frac{1}{r}\frac{\partial}{\partial \theta}\mathbf{e}_\theta + \frac{1}{r \sin\theta}\frac{\partial}{\partial z}\mathbf{e}_\phi \quad (5.24)$$

Here $\mathbf{e}_r$, $\mathbf{e}_\theta$ and $\mathbf{e}_\phi$ are the unit vectors in spherical coordinates. The electric field inside and outside the nanoparticle can be obtained by substituting (5.22) into (5.23) as

$$\mathbf{E}_m = \left(\frac{3\epsilon_d}{2\epsilon_d + \epsilon_m}\right) E_0 \left(\cos\phi \mathbf{e}_r - \sin\phi \mathbf{e}_\theta\right), \qquad r < R \tag{5.25}$$

$$\mathbf{E}_d = \frac{A_d}{r^3} E_0 \left(2\cos\phi \mathbf{e}_r + \sin\phi \mathbf{e}_\theta\right) + E_0 \left(\cos\phi \mathbf{e}_r - \sin\phi \mathbf{e}_\theta\right), \quad r > R$$

Note that $\mathbf{E}_m$ is the electric field inside the nanoparticle and $\mathbf{E}_d$ is the electric outside the nanoparticle. The unit vectors $\mathbf{e}_r$, $\mathbf{e}_\theta$ and $\mathbf{e}_\phi$ are related to the Cartesian unit vectors as follows

$$\mathbf{e}_r = \sin\theta\cos\phi \mathbf{e}_x + \sin\theta\sin\phi \mathbf{e}_y + \cos\theta \mathbf{e}_x$$
$$\mathbf{e}_\theta = \cos\theta\cos\phi \mathbf{e}_x + \cos\theta\sin\phi \mathbf{e}_y - \sin\theta \mathbf{e}_z$$
$$\mathbf{e}_\phi = -\sin\phi \mathbf{e}_x + \cos\phi \mathbf{e}_y$$

Using the above expressions, we can express the electric fields in terms of Cartesian unit vectors as

$$\mathbf{E}_m = \left(\frac{3\epsilon_d}{2\epsilon_d + \epsilon_m}\right) E_0 \mathbf{e}_x, \qquad r < R \tag{5.26}$$

$$\mathbf{E}_d = -\frac{A_d}{r^3}\left(\mathbf{e}_x - \frac{3x\mathbf{r}}{r^2}\right) + E_0 \mathbf{e}_x, \qquad r > R$$

Note that the electric field $\mathbf{E}_d$ has two contributions. The first term is simply the external electric field which is applied along the x-direction. The second term is the scattered electric field from the nanoparticle. In other words, the second term represents the electric field created by the nanoparticle due to the induced dipole moment created in the nanoparticle by the external field.

5.3 MNP Polarization

Before we discuss the electric field enhancement near metallic nanostructures let us briefly review the electric field produced by the dipole of a nanoparticle with a dipole moment $\mathbf{P}_{ns}$. The dipole electric field at a location $\mathbf{r}$ produced by this dipole is written as [17]

$$\mathbf{E}_d = \left[\frac{k^3 \left(\mathbf{n} \times \mathbf{P}_{ns}\right) \times \mathbf{n}}{4\pi\epsilon_0\epsilon_d (kr)} - \frac{ik^3 \left[3\mathbf{n}\left(\mathbf{n}.\mathbf{P}_{ns}\right) - \mathbf{P}_{ns}\right]}{4\pi\epsilon_0\epsilon_d (kr)^2} + \frac{k^3 \left(3\mathbf{n}\left(\mathbf{n}.\mathbf{P}_{ns}\right) - \mathbf{P}_{ns}\right)}{4\pi\epsilon_0\epsilon_d (kr)^3}\right] e^{ikr} \tag{5.27}$$

where $k = 2\pi/\lambda$ and $\mathbf{n}$ is the unit vector along the $\mathbf{r}$ direction and is defined as $\mathbf{n} = \mathbf{r}/r$, where $r = |\mathbf{r}|$. In the present study we consider that the size of the sample is much smaller than the wavelength of the light. This gives the condition $kr \ll 1$, which is known as the **near-field** condition in **nano-optics**. In this case the terms

proportional to $(kr)^{-1}$ and $(kr)^{-2}$ are negligible compared to the term proportional to $(kR)^{-3}$ and $e^{ikr} = 1$. With these considerations, the above expression reduces to

$$\mathbf{E}_d = \frac{3\mathbf{n}\left(\mathbf{n}.\mathbf{P}_{ns}\right) - \mathbf{P}_{ns}}{4\pi\epsilon_0\epsilon_d r^3} \tag{5.28}$$

In this chapter we have considered two special cases for the dipole electric field. In the first case we consider that the polarization is parallel to $\mathbf{r}$. In this case the above expression reduces to

$$\mathbf{E}_d = \frac{2\mathbf{P}_{ns}}{4\pi\epsilon_0\epsilon_d r^3}, \quad (\mathbf{P}_{ns} \parallel \mathbf{r}) \tag{5.29}$$

In the second case the polarization is perpendicular to $\mathbf{r}$ and we get

$$\mathbf{E}_d = -\frac{\mathbf{P}_{ns}}{4\pi\epsilon_0\epsilon_d r^3}, \quad (\mathbf{P}_{ns} \perp r) \tag{5.30}$$

The above two expressions can be combined into one as

$$E_d = \frac{g_{x,z} P_{ns}}{4\pi\epsilon_0\epsilon_d r^3} \tag{5.31}$$

Here $g_{x,z}$ is called the polarization parameter with $g_x = 2$ for $(\mathbf{P}_{ns} \parallel \mathbf{r})$ and $g_z = -1$ for $(\mathbf{P}_{ns} \perp r)$.

Let us look closely at the first term in (5.26), which is written as

$$E_d = -\frac{A_d}{r^3}$$

Note that this is the electric field created by the electric dipole at a distance r. Therefore, the amplitude A_d in this quantity is the dipole moment (p_{np}) of the nanoparticle i.e. $p_{np} = A_d$. The polarizability of the nanoparticle is related to the dipole moment p_{np} by the following expression

$$\alpha_{np} = \frac{4\pi\epsilon_0\epsilon_d p_{np}}{E_0}$$

Using the value of the amplitude $p_{np} = A_d$ from (5.21) in the above expression one can obtain

$$\alpha_{np} = 4\pi\epsilon_0\epsilon_d R^3\gamma_{np} \tag{5.32}$$

where

$$\gamma_{np} = \frac{(\epsilon_m - \epsilon_d)}{2\epsilon_d + \epsilon_m}$$

Note that the polarizability of the nanoparticle depends on its volume.

The polarizability for **metallic nanorods** and **metallic nanodiscs** have also been calculated [15–20]. In these cases (5.32) is slightly modified as

$$\alpha_{np} = 4\pi\epsilon_0\epsilon_d L_x L_y L_z \gamma_{np}$$
$$\gamma_{np} = \frac{(\epsilon_m - \epsilon_d)}{3\epsilon_b + 3\varsigma_{x,z}\left[\epsilon_m(\omega) - \epsilon_b\right]} \tag{5.33}$$

where L_x, L_y, L_z are length, width and height of the MNP, respectively and $\varsigma_{x,z}$ is the depolarization factor for the MNP. For an oblate spheroid where $L_x = L_y$ and $L_x > L_z$, the depolarization factors reduce to

$$\varsigma_z = \frac{1 - e_g^2}{e_g^2}\left[\frac{1}{2e_g}\log\left(\frac{1 + e_g}{1 - e_g}\right) - 1\right]$$
$$\varsigma_x = \varsigma_y = \frac{1}{2}(1 - \varsigma_z)$$

where the eccentricity of the nanodisk is defined as $e_g = \sqrt{1 - (L_x/L_z)^2}$. The above equation can be applied for both cases where $L_x > L_z$ and $L_x < L_z$. For a very flat and thin disk we take $L_x \gg L_z$ and the depolarization factors reduce to

$$\varsigma_x = \varsigma_y \cong \frac{\pi}{4}\frac{L_z}{L_x}$$
$$\varsigma_z \cong 1 - \frac{\pi}{2}\frac{L_z}{L_x}$$

The above method has been used to calculate the polarizability of a graphene nanoflake [15].

5.4 Electric Field Enhancement

Here we investigate the **electric field enhancement** near the MNP. We consider a spherical MNP embedded in a dielectric material. The dipole induced in the nanoparticle due to an external field E_0 has been calculated in the previous section and is written as

$$P_{np} = \left(\frac{\alpha_{np}}{4\pi\epsilon_0\epsilon_d}\right)E_0 \tag{5.34}$$
$$\alpha_{np} = \epsilon_0\epsilon_d\left(4\pi R^3\right)\gamma_{np}$$
$$\gamma_{np} = \frac{\epsilon_m - \epsilon_d}{2\epsilon_d + \epsilon_m}$$

where ϵ_d is the dielectric constant of the surrounding dielectric material Using the above expression for the dipole moment in (5.31) we obtain the electric field produced by the nanoparticle as

$$E_{np} = \frac{g_{x,z} R^3 \gamma_{np}}{r^3} E_0 \tag{5.35}$$

Let us calculate the electric field enhancement due to the electric field at the surface of the nanoparticle. If the radius of the nanoparticle is R, then the electric field at the surface of the nanoparticle is

$$E_{np} = g_{x,z} \left(\frac{2\epsilon_m - 2\epsilon_d}{2\epsilon_d + \epsilon_m} \right) E_0 \tag{5.36}$$

We know that for certain frequencies the dielectric constant of a MNP becomes negative. When this happens the denominator the above expression becomes small (i.e. $2\epsilon_d + \epsilon_m \approx 0$) and the electric field becomes large.

Now we calculate the magnitude of electric field enhancement. The dielectric constant of the metal in the MNP is a complex quantity and is expressed as

$$\epsilon_m = \epsilon_m^r + i\epsilon_m^i$$

where ϵ_m^r and ϵ_m^i are the real and imaginary parts of ϵ_m, respectively. The dipole electric field then becomes

$$E_{np} = g_{x,z} \left(\frac{2\epsilon_m^r + i2\epsilon_m^i - 2\epsilon_d}{2\epsilon_d + \epsilon_m^r + i\epsilon_m^i} \right) E_0 \tag{5.37}$$

Note that the real part of the metal dielectric constant can be a negative quantity. Therefore the term $\epsilon_m^r + 2\epsilon_d$ in the denominator can become zero for certain frequencies. This gives the following condition:

$$\begin{aligned} \epsilon_m^r + 2\epsilon_d &= 0 \\ \epsilon_d &= -\epsilon_m^r/2 \end{aligned} \tag{5.38}$$

In most noble metals $\epsilon_m^i \ll \epsilon_m^r$, and therefore we can neglect the ϵ_m^i term from the numerator of (5.37). Using the above condition in (5.9) we obtain

$$\left| \frac{E_{np}}{E_0} \right| = \left| \frac{3g_{x,\,z}\epsilon_m^r}{\epsilon_m^i} \right| \tag{5.39}$$

Note that the dipole electric field E_{np} is $3\epsilon_m^r/\epsilon_m^i$ times larger than the external electric field E_0. In case of gold this quantity is approximately 10.

In the Drude model for metals, the real (ϵ_m^r) and imaginary (ϵ_m^i) parts of ϵ_m have the following forms:

$$\epsilon_m^r = \frac{\omega^2 + \gamma_m^2 - \omega_p^2}{\omega^2 + \gamma_m^2}, \tag{5.40}$$
$$\epsilon_m^i = \frac{\gamma_m \omega_p^2}{\omega\left(\omega^2 + \gamma_m^2\right)}$$

This gives

$$\left|\frac{E_{np}}{E_0}\right| = \left|\frac{3g_{x,z}\omega\left[\omega^2 + \gamma_m^2 - \omega_p^2\right]}{\gamma_m \omega_p^2}\right| \tag{5.41}$$

It is also useful to calculate the intensity of the near-field produced by the metal nanoparticle. The intensity of dipole and external electric fields are written as

$$I_{np} = \epsilon_0 c\sqrt{\epsilon_d}\left|E_{np}\right|^2 \tag{5.42}$$
$$I_0 = \epsilon_0 c\left|E_0\right|^2$$

Therefore ratio of the intensity of the dipole to the external field can be expressed as

$$\frac{I_{np}}{I_0} = g_{x,z}^2\sqrt{\epsilon_d}\left|\frac{2\epsilon_m - 2\epsilon_d}{2\epsilon_d + \epsilon_m}\right|^2 \tag{5.43}$$

Note that at $\epsilon_m^r = -\epsilon_d/2$, the ratio has a very large value. This is known as electric field enhancement.

5.5 Exciton-Plasmon Interaction

Here we study the exciton-plasmon coupling in a QD and graphene hybrid system. We consider a **two-level QD** as an example. Both the QD and graphene are embedded in a host dielectric material such as silica. Optical excitations of the QD are excitons having sharp and discrete energies. The excitonic states are denoted as $|1\rangle$ and $|2\rangle$, where $|1\rangle$ is the ground state and $|2\rangle$ is the excited state. The energy difference between these two states is given by $\hbar\omega_{21}$. Here excitons in the QD act as quantum emitters. We consider a graphene sheet of a square shape of side L which lies in the x-y plane. The thickness of the graphene sheet is given by L_z and the center-to-center distance distance between the QD and the graphene is denoted as R. The surface plasmon frequency of the graphene sheet is denoted as ω_{sp}. A schematic diagram for this hybrid system is shown in Fig. 5.3.

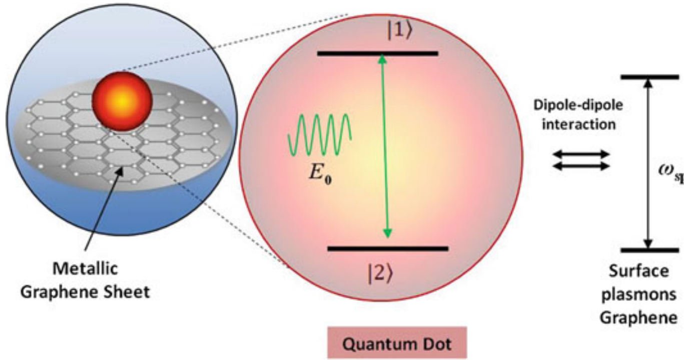

Fig. 5.3 The QD and graphene hybrid system

A probe field $E_p(t) = E_p \cos(\omega t)$ with frequency ω and amplitude E_p is applied between states $|1\rangle$ and $|2\rangle$ so that an exciton is created in state $|2\rangle$. We consider that the exciton transition frequency ω_{21} is resonant with the plasmon frequency ω_{sp}. In the presence of the probe field, dipoles are induced in the QD and graphene and they interact with each other via the dipole-dipole interaction (DDI). This interaction is very strong due to enhanced local dipole field in the vicinity of graphene, and leads to excitation (i.e. energy) transfer between the QD and graphene.

5.5.1 *Dipole–Dipole Interaction*

The electric field E_{qd} felt by the QD consists of two parts and is written as

$$E_{qd}(t) = \frac{1}{2}\left(E_p + E_{ddi}^{g}\right)e^{-i\omega t} + c.c. \tag{5.44}$$

where c.c. stands for the complex conjugate. The first term E_p in the above expression is the direct contribution from the probe field. The second term E_{ddi}^{G} is from the dipole field produced by graphene and is expressed as

$$E_{ddi}^{g} = \frac{g_r P_g}{4\pi\epsilon_b R^3} \tag{5.45}$$

Here ϵ_b is the dielectric constant of the host dielectric material in which the QD and graphene are embedded, and g_r is called the polarization parameter with $g_r = 2$ or $g_r = -1$. Similarly the electric field seen by graphene is written as

$$E_g(t) = \frac{1}{2}\left(E_p + E_{ddi}^{qd}\right)e^{-i\omega t} + c.c. \tag{5.46}$$

where

$$E_{ddi}^{qd} = \frac{g_r P_{qd}}{4\pi\epsilon_b R^3} \tag{5.47}$$

The electric field E_g creates a polarization P_g in graphene as

$$P_g = \alpha_g E_g \tag{5.48}$$

where α_g is the dipole polarizability and is written as

$$\alpha_g = 4\pi\epsilon_d R^3 \gamma_g \tag{5.49}$$
$$\gamma_g = \frac{\epsilon_m - \epsilon_b}{2\epsilon_b + \epsilon_m}$$

The polarization induced in the QD is obtained as [21]

$$P_{qd} = \mu_{12}\rho_{12} + c.c. \tag{5.50}$$

where μ_{12} and ρ_{12} are electric dipole moment and density matrix element due to the exciton transition between $|1\rangle$ and $|2\rangle$, respectively.

$$E_{ddi}^{g} = \frac{g_r \mu_{12}\rho_{12}}{4\pi\epsilon_b R^3} + c.c. \tag{5.51}$$

With the help of the above expression, the total field seen by graphene becomes

$$E_g = \frac{1}{2}\left(E_p + \frac{1}{4\pi\epsilon_B}\frac{g_r\mu_{12}\rho_{12}}{\epsilon_{dr} R^3}\right)e^{-i\omega t} + c.c. \tag{5.52}$$

Using (5.52) in (5.48), the graphene polarization is obtained as

$$P_g = 4\pi\epsilon_B R^3\left[\gamma_g\left(\frac{E_p}{2} + \frac{1}{4\pi\epsilon_b}\frac{g_r\mu_{12}\rho_{12}}{\epsilon_{dr} R^3}\right)e^{-i\omega_2 t}\right] + c.c. \tag{5.53}$$

The electric field seen by the QD can now be obtained by using the above expression for P_g in (5.44) and (5.45) as

$$E_{qd}(t) = \left(\frac{E_p}{2} + \frac{g_r R^3 \gamma_r E_p}{2R^3} + \frac{\mu_{12} g_r^2 R^3 \gamma_r \rho_{12}}{4\pi\epsilon_b R^6}\right)e^{-i\omega_2 t} + c.c. \tag{5.54}$$

The above expression for $E_{qd}(t)$ can be rewritten in a more compact form as

$$E_d = \frac{\hbar}{\mu_{12}}\left(\Omega_p + \Pi_{ddi} + \Lambda_{ddi}\right)e^{-i\omega t} + c.c. \tag{5.55}$$

where

$$\Omega_p = \frac{\mu_{12} E_p}{2\hbar\epsilon_{dr}}, \ \Pi = \left(\frac{l_m r_m^2 \gamma_{r,l} g_{r,l}}{R^3}\right)\Omega_p, \ \Lambda = \frac{\gamma_{r,l} l_m r_m^2 g_{r,l}^2 \mu_{12}^2 \rho_{21}}{4\pi\epsilon_b \hbar \epsilon_{dr}^2 R^6} \tag{5.56}$$

Note that the electric field felt by the QD contains three contributions Ω_p, Π and Λ. The term Ω_p represents the direct contribution from the probe field, while the term Π is the dipole field from graphene that is induced by the probe field. The Λ term arises when the probe field polarizes the QD, which in turn polarizes graphene. This means that the term Λ is nothing but the self-interaction of the QD because it depends on the polarization of the QD. We call the terms Π and Λ the dipole-dipole interaction (DDI) terms which depend on both the QD and graphene parameters.

5.5.2 Interaction Hamiltonian

Let us derive expressions which describe excitons in the QD and plasmons in graphene. Excitonic states in the QD $|1\rangle$ and $|2\rangle$ form as basis set and they satisfy the following orthogonality condition as

$$\langle i|j\rangle = \delta_{ij} \quad i, j = 1, 2 \tag{5.57}$$
$$\sum_i |i\rangle \langle i| = 1 \qquad i = 1, 2$$

The exciton creation operator σ_{21}^+ which excites an electron-hole pair between $|1\rangle$ and $|2\rangle$ is defined as:

$$\sigma_{21}^+ = |2\rangle \langle 1| \tag{5.58}$$

The Hamiltonian of the exciton in the QD is then written as

$$H_{ex} = \hbar\omega_{21}\sigma_{21}^+ \tag{5.59}$$

where ω_{21} is the exciton transition frequency between $|1\rangle \leftrightarrow |2\rangle$.

The electric field seen by the QD is $\mathbf{E}_{qd}$ and the induced the dipole moment is $\mathbf{P}_{qd}$. Therefore, the interaction Hamiltonian between the QD and graphene in the dipole approximation is written as follows

$$H_{int} = -\left(\mathbf{P}_{qd} \cdot \mathbf{E}_{qd}\right) + h.c. \tag{5.60}$$

where $h.c.$ stands for the Hermitian conjugate. Let us express the polarization operator in terms of the basis vectors and operators as

$$\mathbf{P}_{qd} = \sum_{i=1,2} \sum_{j=1,2} |j\rangle \langle j| \mathbf{P}_{qd} |i\rangle \langle i| \tag{5.61}$$

$$\mathbf{P}_{qd} = \sum_{i=1,2} \sum_{j=1,2} \langle j | \mathbf{P}_{qd} | i \rangle \sigma_{ji}^{+}$$

We know the matrix elements $\langle j | \mathbf{P}_{qd} | i \rangle$ for $i = j$ are zero but for $i \neq j$ are not zero. Therefore we get

$$\begin{aligned} \langle 1 | \mathbf{P}_{qd} | 1 \rangle &= \langle 2 | \mathbf{P}_{qd} | 2 \rangle = 0 \\ \langle 1 | \mathbf{P}_{qd} | 2 \rangle &= \langle 2 | \mathbf{P}_{qd} | 1 \rangle = \mu_{12} \end{aligned} \tag{5.62}$$

where μ_{12} is the matrix element of the dipole moment between states $|1\rangle$ and $|2\rangle$. The interaction Hamiltonian becomes

$$H_{int} = -\frac{1}{4} \left(\mu_{12} \cdot \mathbf{E}_{qd} \right) \sigma_{21}^{+} + h.c. \tag{5.63}$$

Note that in the above Hamiltonian we consider the electric field as a classical field and do not express it in operator form. This is known as the semi-classical model. Using the expression for the electric field from (5.55) in the above Hamiltonian gives

$$\begin{aligned} H_{int} &= H_{ep} + H_{ddi} \\ H_{ep} &= \Omega_p e^{-i\omega t} \sigma_{i1}^{+} + h.c. \\ H_{ddi} &= (\Pi_{ddi} + \Lambda_{ddi}) e^{-i\omega t} \sigma_{i1}^{+} + h.c. \end{aligned} \tag{5.64}$$

Now the interaction term consists of two terms. The first term H_{ep} is the interaction between the exciton and the external probe field. The second term H_{ddi} is the DDI which is due to the coupling between excitons and polaritons.

We consider that the exciton spontaneously decays from the excited state $|2\rangle$ to the ground state $|1\rangle$ due to the exciton coupling with the background radiation field. The Hamiltonian of the radiation field is written as

$$H_{ph} = \sum_k \hbar \omega_k a_k^{+} a_k + h.c. \tag{5.65}$$

where the terms ω_k and k are the frequency and the wave vector of background photons, respectively. Here a_k and a_k^{+} are the annihilation and creation operators for a photon with wave vector k, respectively. The interaction between the exciton and the background radiation field is written as

$$H_{eph} = -\sum_k g_k(\omega_k) a_k \sigma_{21}^{+} + h.c. \tag{5.66}$$

Here the parameter $g_k(\omega_k)$ is the coupling constant for the exciton-photon interaction and is written as

$$g_k(\omega_k) = \sqrt{\frac{\hbar \omega_k}{2\epsilon_b V}} \left(\mathbf{e}_k \cdot \mu_{i1} \right) \tag{5.67}$$

where $\mathbf{e}_k$ is the photon polarization and V is the volume of system. Finally the total Hamiltonian of the system is written as

$$H_0 = H_0 + H_{ddi} + H_{eph} \tag{5.68}$$

where H_0 is the non-interacting part of the Hamiltonian.

$$H_0 = H_{ex} + H_{ph} \tag{5.69}$$

We express the interacting part of the Hamiltonian in interaction representation, which is defined as

$$\begin{aligned} \overline{H}_{ddi} &= e^{iH_0 t} H_{ddi} e^{-iH_0 t} \\ \overline{H}_{eph} &= e^{iH_0 t} H_{eph} e^{-iH_0 t} \end{aligned} \tag{5.70}$$

In the interaction representation, the raising and lowering operators are transformed as

$$\begin{aligned} e^{iH_0 t} \sigma_{i1}^{+} e^{-iH_0 t} &= \sigma_{21}^{+} e^{i\omega_{21} t} \\ e^{iH_0 t} \sigma_{i1}^{-} e^{-iH_0 t} &= \sigma_{21}^{-} e^{-i\omega_{21} t} \\ e^{iH_0 t} a_k^{+} e^{-iH_0 t} &= \sigma_{21}^{+} e^{i\omega_k t} \\ e^{iH_0 t} a_k e^{-iH_0 t} &= a_k e^{-i\omega_k t} \end{aligned} \tag{5.71}$$

Using (5.70) and (5.71) in the interaction Hamiltonian terms we obtain

$$\begin{aligned} \overline{H}_{ddi} &= \left(\Omega_p + \Pi_{ddi} + \Lambda_{ddi}\right) \sigma_{i1}^{+} e^{i(\omega_{21}-\omega)t} + hc \\ \overline{H}_{eph} &= -\sum_k g_k\left(\omega_k\right) a_k \sigma_{21}^{+} e^{i(\omega_{21}-\omega_k)t} + hc \end{aligned} \tag{5.72}$$

5.6 Density Matrix Method

We use the **density matrix method** [21] to calculate the energy transfer between the QD and MNP. The equation of motion for the density matrix operator is written as [21]

$$\frac{\partial \rho(t)}{\partial t} = -\frac{i}{\hbar}\left[H, \rho(t)\right] \tag{5.73}$$

Here will use the notation $H = \overline{H}$ for the simplicity. Using the Hamiltonian obtained in (5.72) we write

$$\frac{\partial \rho(t)}{\partial t} = -\frac{i}{\hbar}\left[H_0 + H_{ddi} + H_{eph}, \rho(t)\right] \tag{5.74}$$

In the second-order Born approximation the above expression becomes

$$\frac{\partial \rho(t)}{\partial t} = -\frac{i}{\hbar}\left[H_0 + H_{ddi}, \rho(t)\right] + \frac{1}{\hbar^2}\int_0^t dt' \left[H_{eph}(t), \left[H_{eph}(t'), \rho(t)\right]\right] \quad (5.75)$$

Let us rewrite the above equation of motion as

$$\frac{\partial \rho(t)}{\partial t} = -\frac{i}{\hbar}\left[H_0 + H_p + H_{ddi}, \rho(t)\right] + \left[\frac{\partial \rho(t)}{\partial t}\right]_{int} \quad (5.76)$$

where

$$\left[\frac{\partial \rho(t)}{\partial t}\right]_{int} = \frac{1}{\hbar^2}\int_0^t dt' \left[H_{eph}(t), \left[H_{eph}(t'), \rho(t)\right]\right] \quad (5.77)$$

5.6.1 Two-Level Quantum Dot

To evaluate the second term we consider that the QD is in excited state $|2\rangle$ and the radiation field has n_k photons. The eigen ket of this state is denoted as $\left|\varepsilon_{2,n_k}\right\rangle = |2, n_k\rangle$. The exciton decays from $|2\rangle$ to ground state $|1\rangle$ by emitting one photon. Now the radiation field has $n_k + 1$ photons and QD is in the ground state. This state is denoted as $\left|\varepsilon_{1,n_k+1}\right\rangle = |1, n_k + 1\rangle$. The non-interacting Hamiltonian H_0 satisfies the following eigenvalue equation

$$\begin{aligned} H_0\left|\varepsilon_{2,n_k}\right\rangle &= \varepsilon_{2,n_k}\left|1, n_k\right\rangle \\ H_0\left|\varepsilon_{1,n_k+1}\right\rangle &= \varepsilon_{1,n_k+1}\left|1, n_k+1\right\rangle \end{aligned} \quad (5.78)$$

where the eigenvalues ε_{2,n_k} and ε_{1,n_k+1} are

$$\begin{aligned} \varepsilon_{2,n_k} &= \hbar\omega_2 + n_k\hbar\omega_{21} \\ \varepsilon_{1,n_k+1} &= \hbar\omega_1 + (n_k+1)\,\hbar\omega_k \end{aligned} \quad (5.79)$$

(5.72), (5.78) and (5.79) have been used to evaluate (5.77) for a two-level system, where it is found that [21]

$$\left[\frac{\partial \rho_{ij}(t)}{\partial t}\right]_{int} = -\Gamma\left[\left(\sigma_{21}^{+}\sigma_{21}^{-}\rho - \sigma_{21}^{-}\rho\sigma_{21}^{+}\right) + \left(\sigma_{21}^{+}\sigma_{21}^{-}\rho - \sigma_{21}^{-}\rho\sigma_{21}^{+}\right)^{*}\right] \quad (5.80)$$

where Γ is the decay rate of the exciton from the excited state $\left|\varepsilon_{2,n_k}\right\rangle$ to the ground states $\left|\varepsilon_{1,n_k+1}\right\rangle$ and is obtained as

$$\Gamma = \frac{2\pi}{\hbar}\sum_k \left|\left\langle\varepsilon_{1,n_k+1}\right| H_{int}\left|\varepsilon_{2,n_k}\right\rangle\right|^2 \delta(\varepsilon_{1,n_k}, -\varepsilon_{1,n_k+1}) \quad (5.81)$$

Using (5.80) in the density matrix equation of motion [(5.76)] gives

$$\frac{\partial \rho(t)}{\partial t} = -\frac{i}{\hbar}\left[H_0 + H_p + H_{ddi}, \rho(t)\right] \\ - \Gamma\left[\left(\sigma_{21}^{+}\sigma_{21}^{-}\rho - \sigma_{21}^{-}\rho\sigma_{21}^{+}\right) + \left(\sigma_{21}^{+}\sigma_{21}^{-}\rho - \sigma_{21}^{-}\rho\sigma_{21}^{+}\right)^{*}\right] \tag{5.82}$$

The above equation [(5.81)] can be expressed in matrix notation as

$$\frac{\partial \rho_{ij}(t)}{\partial t} = -\frac{i}{\hbar}\langle i|\left[H_0 + H_p + H_{ddi}, \rho(t)\right]|j\rangle \\ - \langle i|\,\Gamma\left[\left(\sigma_{21}^{+}\sigma_{21}^{-}\rho - \sigma_{21}^{-}\rho\sigma_{21}^{+}\right) + \left(\sigma_{21}^{+}\sigma_{21}^{-}\rho - \sigma_{21}^{-}\rho\sigma_{21}^{+}\right)^{*}\right]|j\rangle \tag{5.83}$$

where ρ_{ij} is the matrix element of the operator ρ between states $|i\rangle$ and $|j\rangle$ (i.e. $\rho_{ij} = \langle i|\,\rho\,|j\rangle$ where $i, j = 1, 2$). To evaluate (5.83) one must use the following identity:

$$\langle i|\,[H,\rho]\,|j\rangle = \sum_{k=1,2}\left[\begin{array}{c}\langle i|\left(H_0 + H_p + H_{ddi}\right)|k\rangle\,\langle k|\,\rho\,|j\rangle \\ -\langle i|\,\rho\,|k\rangle\,\langle k|\left(H_0 + H_p + H_{ddi}\right)|j\rangle\end{array}\right] \tag{5.84}$$

$$\langle i|\,[H,\rho]\,|j\rangle = \sum_{k=1,2}\left(H_0 + H_p + H_{ddi}\right)_{ik}\rho_{ki} - \rho_{ik}\left(H_0 + H_p + H_{ddi}\right)_{kj}$$

Using (5.64) and (5.78) the equations of motion for the density matrix elements become

$$\frac{d\rho_{21}}{d\tau} = -\left(\Gamma_{21} - i\delta_p\right)\rho_{21} - i\left(\Omega_p + \Pi_{ddi} + \Lambda_{ddi}\right)(\rho_{22} - \rho_{11}) \tag{5.85}$$

$$\frac{d\rho_{22}}{d\tau} = -\Gamma_2\rho_{22} + i\left(\Omega_p + \Pi_{ddi} + \Lambda_{ddi}\right)\rho_{21} - i\left(\Omega_p + \Pi_{ddi}^{*} + \Lambda_{ddi}^{*}\right)\rho_{12}$$

$$\frac{d\rho_{11}}{d\tau} = -\Gamma_1\rho_{11} - i\left(\Omega_p + \Pi_{ddi} + \Lambda_{ddi}\right)\rho_{12} + i\left(\Omega_p + \Pi_{ddi}^{*} + \Lambda_{ddi}^{*}\right)\rho_{21}$$

where $\rho_{21}^{*} = \rho_{12}$, $\Gamma_{21} = \left(\Gamma_2 + \Gamma_1\right)/2$ and $\delta_p = \omega - \omega_{12}$ is called the detuning parameter. The expression for the decay rates Γ_1 and Γ_2 are calculated as follows.

5.6.2 Decay Rate

The expression of the decay rate is given by (5.81) which is rewritten here

$$\Gamma = \frac{2\pi}{\hbar}\sum_{k}\left|\left\langle\varepsilon_{1,n_k+1}\right|H_{int}\left|\varepsilon_{2,n_k}\right\rangle\right|^2\delta(\varepsilon_{1,n_k}, -\varepsilon_{1,n_k+1})$$

The exciton is in the excited state $\left|\varepsilon_{2,n_k}\right\rangle$, and it decays to ground state $\left|\varepsilon_{2,n_k+1}\right\rangle$ by emitting one photon. In this case the matrix element $\left\langle\varepsilon_{1,n_k+1}\right| H_{int} \left|\varepsilon_{2,n_k}\right\rangle$ appearing in the above equation can be evaluated as

$$\left\langle\varepsilon_{1,n_k+1}\right| H_{eph} \left|\varepsilon_{2,n_k}\right\rangle = \left\langle\varepsilon_{1,n_k+1}\right| \sum_{k'} g_{k'} \left(a_{k'}\sigma_{21}^{+} + a_{k'}^{+}\sigma_{21}^{-}\right) \left|\varepsilon_{2,n_k}\right\rangle \tag{5.86}$$
$$\left\langle\varepsilon_{1,n_k+1}\right| H_{eph} \left|\varepsilon_{2,n_k}\right\rangle = \hbar g_k$$

For simplicity we have considered that $n_k = 0$. Using the above expression in the decay rate expression we find

$$\Gamma = 2\pi\hbar \sum_k g_k^2(\varepsilon_k)\delta(\varepsilon_{21} - \hbar\omega_k) \tag{5.87}$$

We now replace the summation over k by integration using the concept of the density of states as

$$\sum_k = \int D(\varepsilon_k)d\varepsilon_k \tag{5.88}$$

where $D(\varepsilon_k)$ is the density of states (DOS) for photons,

$$D(\varepsilon_k) = \frac{2V}{(2\pi)^3}\frac{4\pi}{3}k^2\frac{dk}{d\varepsilon_k} \tag{5.89}$$

Let us define a quantity called the form factor as

$$Z(\varepsilon_k) = \sqrt{(\hbar c)\,\frac{dk}{d\varepsilon_k}} \tag{5.90}$$

Using (5.90) in (5.89), DOS becomes:

$$D(\varepsilon_k) = \frac{\Omega}{3\pi^2}\frac{k^2}{(\hbar c)}Z^2(\varepsilon_k) \tag{5.91}$$

Using $\varepsilon_k = \hbar ck$ in (5.91) we obtain

$$D(\varepsilon_k) = \left(\frac{\Omega}{3\pi^2}\frac{\varepsilon_k^2}{(\hbar c)^3}\right)Z^2(\varepsilon_k) \tag{5.92}$$

Writing the DOS for photons in free space as

$$D_0(\varepsilon_k) = \frac{\Omega}{3\pi^2}\frac{\varepsilon_k^2}{(\hbar c)^3}, \tag{5.93}$$

the (5.91) for the DOS in terms of the form factor becomes

$$D(\varepsilon_k) = D_0(\varepsilon_k) Z^2(\varepsilon_k) \tag{5.94}$$

Substituting (5.91) into (5.87) we obtain the expression for the decay rate as

$$\begin{aligned}\Gamma &= 2\pi\hbar \int d\varepsilon_k D_0(\varepsilon_k) Z^2(\varepsilon_k) g_k^2(\varepsilon_k) \delta(\varepsilon_{21} - \hbar\omega_k) \\ &= 2\pi\hbar D_0(\varepsilon_{21}) g_k^2(\varepsilon_{21}) Z^2(\varepsilon_k)\end{aligned} \tag{5.95}$$

In (5.95) the expression in front of the form factor is simply the decay rate of the QD when it is located in free space and it is given by

$$\Gamma_0 = 2\pi\hbar D_0(\varepsilon_{21}) g_k^2(\varepsilon_{21}) \tag{5.96}$$

Substituting the values of $D_0(\varepsilon_{21})$ [(5.93)] and $g_k(\varepsilon_{21})$ in (5.96) one obtains

$$\Gamma_0 = \frac{\mu^2 \varepsilon_1^2}{\epsilon_0 \hbar^3 c^2} \tag{5.97}$$

Substituting (5.97) in (5.95), finally the decay rate for excitons in the QD can be obtained as

$$\Gamma = \Gamma_0 Z^2(\varepsilon_{21}), \tag{5.98}$$

which depends on the form factor.

5.6.3 Three-Level Quantum Dot

In this section we consider a **three-level QD** and graphene hybrid system [7]. The three excitonic states of the QD are denoted as $|1\rangle$, $|2\rangle$, and $|3\rangle$, where $|2\rangle$ and $|3\rangle$ are lower energy states which are each coupled to the ground state $|1\rangle$. The exciton transition frequencies for transitions $|1\rangle \leftrightarrow |2\rangle$ and $|1\rangle \leftrightarrow |3\rangle$ are denoted as ω_{21} and ω_{31}, respectively. A schematic diagram for the hybrid system is shown in Fig. 5.4. The plasmon frequency of graphene is denoted as ω_{sp}. A probe field $E_2 = E_2^0 \cos(\omega_2 t)$ with frequency ω_2 and amplitude E_2^0 is applied between states $|1\rangle$ and $|2\rangle$ so that an exciton is excited to state $|2\rangle$. Similarly an ultrafast control laser field $E_3 = E_3^0 \cos(\omega_3 t)$ with frequency ω_3 and amplitude E_3^0 is applied between states $|1\rangle$ and $|3\rangle$ and an exciton is excited to state $|3\rangle$. These excitons will decay spontaneously to the ground state when they couple with the background radiation field. This is known as radiative decay.

We assume that the exciton energies ω_{21} and ω_{31} are almost degenerate and lie near the plasmon frequency ω_{sp}. In the presence of the probe and control laser fields,

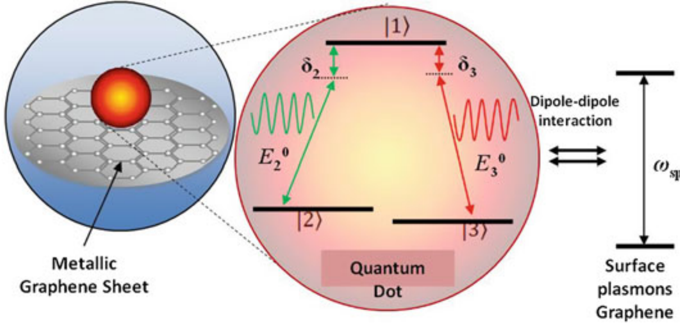

Fig. 5.4 Three-level QD and graphene hybrid system

induced dipoles are created in the QD and in graphene, which interact with each other via the DDI. This interaction leads to excitation transfer between the QD and the graphene. The hybrid system is embedded in a host dielectric material such as silica.

We use the density matrix method to evaluate the power loss in the QD and graphene. Using (5.77) we obtain the following equations of motion for the three-level density matrix elements [7]

$$
\begin{aligned}
\frac{d\rho_{22}}{d\tau} &= -2\left(\Gamma_{21}+\Gamma_2\right)\rho_{22} + i\left(\Omega_2+\Lambda_2\rho_{12}\right)\rho_{12} - i\left(\Omega_2^*+\Lambda_2^*\rho_{21}\right)\rho_{21} \\
\frac{d\rho_{33}}{d\tau} &= -2\left(\Gamma_{31}+\Gamma_3\right)\rho_{33} + i\left(\Omega_3+\Lambda_3\rho_{13}\right)\rho_{13} - i\left(\Omega_3^*+\Lambda_3^*\rho_{31}\right)\rho_{31} \\
\frac{d\rho_{32}}{d\tau} &= -\left(\Gamma_{32}-i\delta_p+i\delta_c\right)\rho_{23} - i\left(\Omega_2^*+\Lambda_2^*\rho_{21}\right)\rho_{31} + i\left(\Omega_3+\Lambda_3\rho_{13}\right)\rho_{12} \\
\frac{d\rho_{21}}{d\tau} &= -\left[\Gamma_{21}+\Gamma_2-i\left(\delta_p+\Delta_2\right)\right]\rho_{21} + i\Omega_2\left(\rho_{11}-\rho_{22}\right) - i\left(\Omega_3+\Lambda_3\rho_{13}\right)\rho_{23} \\
\frac{d\rho_{31}}{d\tau} &= -\left[\Gamma_{31}+\Gamma_3-i\left(\delta_c+\Delta_3\right)\right]\rho_{31} - i\left(\Omega_2+\Lambda_2\rho_{12}\right)\rho_{32} - i\Omega_3\left(\rho_{33}-\rho_{11}\right)
\end{aligned}
\tag{5.99}
$$

where

$$
\begin{aligned}
&\Gamma_{32} = \Gamma_{21}+\Gamma_{31}+\Gamma_2+\Gamma_3, \quad \delta_p = \omega_2-\omega_{21}\delta_c = \omega_3-\omega_{31} \\
&\Delta_2 = \mathrm{Re}\left[\Lambda_2\left(\rho_{11}-\rho_{22}\right)\right], \quad \Delta_3 = \mathrm{Re}\left[\Lambda_3\left(\rho_{11}-\rho_{33}\right)\right], \\
&\Gamma_2 = \mathrm{Im}\left[\Lambda_2\left(\rho_{11}-\rho_{22}\right)\right], \quad \Gamma_3 = \mathrm{Im}\left[\Lambda_3\left(\rho_{11}-\rho_{33}\right)\right]
\end{aligned}
\tag{5.100}
$$

In the above expression Δ_2 and Γ_2 are the nonradiative energy shift and decay rate due to the DDI term Λ_2, and similarly Δ_3 and Γ_3 are the energy shift and decay rate due to the DDI term Λ_3. Here Γ_{21} and Γ_{31} are the spontaneous decay rates of the excited states $|2\rangle$ and $|3\rangle$, respectively.

5.7 Energy Exchange Rate

In this section we discuss the energy exchange between constituent nanoparticles in hybrid systems. Energy exchange between light and nanoparticles is encountered in a variety of systems. One of the most important examples in nature is photosynthesis, a process in which photon energy is absorbed by chlorophyll molecules. These molecules channel the photon energy for long distances to proteins (reaction centers). The photon energy is used to perform a charge separation across the membrane surface. Recently there has been considerable interest in studying the photon energy transfer in hybrid systems made from semiconductor and metallic nanostructures.

Here we consider a hybrid system that is made of a QD and metallic nanostructure. Both are embedded in a dielectric material. An external EM field is applied to the hybrid system. This field induces dipoles in the QD and MNP. Therefore photon energy absorbed by the MNP is from the external electric field and also from the dipole electric field created by the QD.

Let us first calculate the energy transfer rate from the QD to the metallic nanostructure. The polarization of the MNP is written as

$$P_{ns}(t) = P_{ns} e^{i\omega t} + c.c. \tag{5.101}$$

where P_{ns} is related to the polarizability α_{ns} as

$$P_{ns} = \alpha_{ns} E_{ns} \tag{5.102}$$

The electric field seen by the MNP E_{ns} consists of two terms and is written as

$$E_{ns}(t) = E_0 e^{i\omega t} + E_{ddi}^{QD} e^{i\omega t} + c.c. \tag{5.103}$$

where the first term is the external electric field and the second term is the dipole electric field produced by the QD. The energy transfer rate can be calculated as [16]

$$W_{ns}(t) = -\int \left[j_{ns}^{*}(t) \cdot E_{ns}(t) \right] dV \tag{5.104}$$

where the volume integral is over the volume of the MNP V_{ns}. Here j_{ns} is the electric current density induced in the MNP, which is obtained from the polarization as

$$\begin{aligned} j_{ns}^{*} &= \frac{1}{V_{ns}} \left(\frac{dP_{ns}^{*}(t)}{dt} \right) \\ j_{ns}^{*} &= \frac{i\omega}{V_{ns}} P_{ns}^{*} e^{i\omega t} + c.c. \end{aligned} \tag{5.105}$$

Using (5.105) in the energy transfer rate equation [(5.104)] we find

$$W_{ns}(t) = -\frac{i\omega}{4} \left(P_{ns}^{*} E_{ns} + P_{ns} E_{ns}^{*} + P_{ns} E_{ns} e^{-i2\omega t} + P_{ns}^{*} E_{ns}^{*} e^{2i\omega t} \right) \tag{5.106}$$

Now we take the time average of $W_{ns}(t)$ over the period of the oscillating laser fields as

$$W_{ns} = \langle W_{ns}(t) \rangle = \frac{1}{T} \int_{-T/2}^{T/2} dt W_{ns}(t) \tag{5.107}$$

where $T = 2\pi/\omega$ is the period of oscillation for the external field. Using (5.106) into (5.107) we find

$$W_{ns} = -\frac{i\omega}{4} \left(P_{ns}^* E_{ns} - P_{ns} E_{ns}^* \right) \tag{5.108}$$
$$W_{ns} = \frac{\omega}{2} \, \mathrm{Im} \left(P_{ns}^* E_{ns} \right)$$

where we have used the following identity:

$$\frac{1}{T} \int_{-T/2}^{T/2} dt e^{-i(\omega_i - \omega_j)t} = \delta_{\omega_i, \omega_j}$$

Substituting (5.102) into (5.108) and after some simplification we can write the expression for the energy transfer rate as

$$W_{ns} = -\frac{\omega}{2} \, \mathrm{Im} \left(\alpha_{ns} \right) |E_{ns}|^2 \tag{5.109}$$

where we have used the identity $\mathrm{Im} \left(\alpha_{ns}^* \right) = -\mathrm{Im} \left(\alpha_{ns} \right)$ to obtain the above expression.

5.7.1 Spherical Nanoparticles

Let us calculate the ETR in a metallic **spherical nanoparticle**. The electric field E_{np} seen by a nanoparticle due to both external field and dipole field created by the QD is written as

$$E_{np} = E_0 + E_{ddi}^{qd} \tag{5.110}$$

where E_{ddi}^{qd} is the dipole field from the QD and is written as

$$E_{ddi}^{qd} = \frac{1}{4\pi\epsilon_B} \frac{g_r \mu_{12} \rho_{12}}{\epsilon_{dr} R^3}$$

Similarly the polarization in the spherical nanoparticle has been calculated in the previous section and is found as

$$\alpha_{np} = 4\pi\epsilon_d R^3 \gamma_{np} \qquad (5.111)$$
$$\gamma_{np} = \frac{\epsilon_m(\omega) - \epsilon_b}{\epsilon_b + 2\epsilon_m(\omega)}$$

Using (5.110) and (5.111) in (5.109) we obtain the expression for the energy transfer rate as

$$W_{ns} = 2\pi\epsilon_d R^3 \omega \,\mathrm{Im}\left(\gamma_{np}\right) \left| \left(E_0 + \frac{1}{4\pi\epsilon_B} \frac{g_r \mu_{12} \rho_{12}}{\epsilon_{dr} R^3} \right) \right|^2 \qquad (5.112)$$

Note that first term in the brackets is the energy transfer rate from the external field while the second term is due to the dipole field created by the QD. Therefore energy exchange between the QD and MNP can be written as

$$W_{ns} = 2\pi\epsilon_d R^3 \omega \,\mathrm{Im}\left(\gamma_{np}\right) \left| \frac{1}{4\pi\epsilon_B} \frac{g_r \mu_{12} \rho_{12}}{\epsilon_{dr} R^3} \right|^2 \qquad (5.113)$$

5.8 Quantum Dot-Graphene Hybrid

We consider a here a QD and graphene hybrid system [7]. The parameters used are $L_z = 0.35$ nm (i.e. a single graphene layer) and $L_x/L_z = 20$. The parameters for graphene are taken as $\epsilon_\infty = 1.964$, $\hbar\omega_p = 6.02$ eV and $\gamma_m = 5$ THz [11]. With these parameters, the SPP resonance frequencies are $\hbar\omega_{sp}^x = 0.8026$ eV and $\hbar\omega_{sp}^z = 4.1250$ eV for graphene. We consider a three-level self-assembled InAs QD with a lambda-type energy level configuration. The parameters for the QD are taken as $\epsilon_d = 12$ and $\mu_{12} = \mu_{13} = 0.1e \times$ nm. We consider that $\omega_{12} = \omega_{sp}^x + 2.0$ meV and $\omega_{13} = \omega_{sp}^x + 1.0$ meV, while the decay rates for the QD are taken as $\Gamma_{21} = 1.1370\,\mu$eV and $\Gamma_{31} = 1.1127\,\mu$eV. The background dielectric function is taken as $\epsilon_b = 2.081$.

It is found experimentally that the dipole moments μ_{12} and μ_{13} in the InAs QD are aligned perpendicularl to each other. Therefore, we first consider the case where μ_{13} and μ_{12} lie along z- and x-directions, respectively, and the probe and control fields are applied along the x- and z-directions, respectively. In this case, the probe laser field couples to the surface plasmons in graphene. This is because they are both aligned along the z-direction, for which ω_{12} is very close to ω_{sp}^x. On the other hand, the control laser field does not couple to the graphene because they are aligned along the z-direction, and ω_{13} is far away from ω_{sp}^z. In this case the the power absorbed by graphene can be written as

$$W_g = W_0 \left[\left(\frac{E_2^0}{2} + \frac{2g_{x,z}\mu_{12}\,\mathrm{Re}\,\rho_{12}}{(4\pi\epsilon_b)\,\epsilon_{dr} R^3} \right)^2 + \left(\frac{g_{x,z}\mu_{12}\,\mathrm{Im}\,\rho_{12}}{(4\pi\epsilon_b)\,\epsilon_{dr} R^3} \right)^2 \right] \qquad (5.114)$$

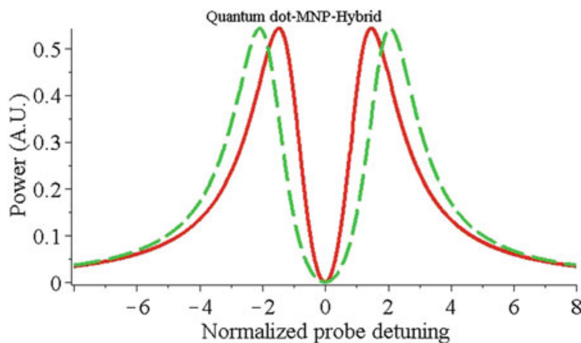

Fig. 5.5 Plot of power absorption (A.U.) in the graphene sheet as function of the normalized probe detuning. The intensity of the probe field is $I_2 = 1.0$ W/cm^2 and $R = 10$ nm. The soild and dotted curves are for $I_3 = 10.0$ W/cm^2 and $I_3 = 20.0$ W/cm^2, repsectively

$$W_0 = \frac{4i\epsilon_b l_g r_g^2 \,\mathrm{Im}\left(\gamma_{x,z}\right)\omega_2}{\epsilon_{bg}}$$

Let us derive an analytical expression of the density matrix ρ_{12} used in (5.114). When the intensity of the probe field is weak compared the control field (i.e. $\Omega_2 < \Omega_3$) one can obtain the following expression for ρ_{12}^0 by solving the density matrix equations in the steady state as

$$\rho_{12} = \frac{\rho_{12}^0(\Omega_2 + \Pi_2)}{1 - \rho_{12}^0\Lambda_2} \tag{5.115}$$

where

$$\rho_{12}^0 = \frac{i\delta_2}{\delta_2\left(\Gamma_2 + \Gamma_3 + i\delta_2\right) - i\Omega_3^2}$$

Using (5.115) we have plotted the power absorption in Fig. 5.5 as a function of the detuning parameter δ_2/Γ_{21}. We consider that the intensity of the probe field is $I_2 = 1.0$ W/cm^2 and $R = 10$ nm. The solid and dotted curves are for cases where $I_3 = 10.0$ W/cm^2 and $I_3 = 20.0$ W/cm^2, respectively. Note that the absorption spectrum has a minimum at zero detuning and that the energy splitting of the peaks depends on the Rabi frequency of the applied control field. In other words, as the intensity of the control field increases, the splitting in the peaks increases. This is a well-known phenomenon in quantum optics called electromagnetically indued transparency. We have also shown a three-dimensional plot of the power absorption in Fig. 5.6. Note that one peak splits into two peaks as the control field intensity increases. This means that the energy transfer between the QD and MNP can be switched on and off by applying the control field. Therefore, these systems can used as all-optical switching devices.

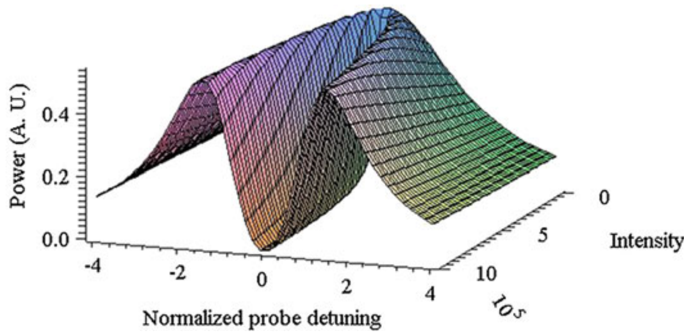

Fig. 5.6 Three dimensional plot of the power absorption in graphene (A.U.) as a function of normalized detuning and the control field intensity. The intensity of the probe field is taken as $I_2 = 1.0$ W/cm^2 and $R = 10$ nm

When the hybrid system is in contact with the biological or chemical materials the background dielectric constant ϵ_{bg} changes. Hence the height of the power absorption peak also changes (see 5.114). Thus the energy transfer between the QD and MNP is modified in the presence of biological and chemical materials. Therefore, the present nanocomposite systems can be used to fabricate nano-biosensors and nano-chemical-sensors.

5.9 Conclusion

The exciton-plasmon interactions in metal-semiconductor hybrid nanostructures offer a wide range of opportunities to control light-matter interaction on nanometer length scales. In this chapter we have studied the energy transfer rate in QD-metallic nanostructure nanocomposites. These nanocomposites also have applications in **bio-photonics** and **sensing**, as non-radiative energy transfer between a QD and MNP can be used to detect **biological molecules**.

Acknowledgments The author thanks Mr. Joel Cox for proofreading this chapter.

References

1. M.R. Singh, *Electronic, Photonic, Polaritonic and Plasmonic Materials* (Wiley Custom, Toronto, 2014)
2. R.D. Artuso, G.W. Bryant, Phys. Rev. B **82**, 195419 (2010)
3. S.M. Sadeghi, L. Deng, X. Li, W.-P. Huang, Nanotechnology **20**, 365401 (2009)
4. M.-T. Cheng, S.-D. Liu, H.-J. Zhou, Z.-H. Hao, Q.-Q. Wang, Opt. Lett. **32**, 2125 (2007)
5. A. Hatef, S. Sadeghi, M.R. Singh, Nanotechnology (at press) (2012)
6. M. Singh, D. Schindel, A. Hatef, Appl. Phys. Lett. **99**, 181106 (2012)

7. J. Cox, M. Singh, G. Gumbs, M. Anton, F. Carreno (2011), Phys. Rev. B86, 125452 (2012)
8. A. Hatef, S. Sadeghi, M.R. Singh, Nanotechnology **23**, 065701 (2012)
9. M. Singh, C. Racknor, D. Schindel, App. Phys. Lett. **101**, 051115 (2012)
10. M. Singh, C. Racknor, D. Schindel, Appl. Phys. Lett. **99**, 181106 (2011)
11. M.R. Singh, Phys. Rev. Lett (communicated, 2012)
12. F.H.L. Koppens, D.E. Chang, F.J.G. Abajo, Nano Lett. **11**, 3370 (2011)
13. Z. Chen et al., ACS Nano **4**, 2964 (2010)
14. H. Dong et al., Anal. Chem. **82**, 5511 (2010)
15. D. Sarid, W.A. Challener, *Modern Introduction to Surface Plasmons: Theory, Mathematica Modeling, and Applications* (Cambridge University Press, Cambridge; New York, 2010)
16. L. Novtny, B. Hecht, *Principle of Nano-Optics* (Cambridge University Press, Cambridge; New York, 2006)
17. M. Ohtsu, K. Kobayashi, *Optical Near Fields* (Springer, Heidelberg, 2004)
18. S. Gaponenko, *Introduction to Nanophotonics* (Cambridge University Press, Cambridge; New York, 2010)
19. U. Kribig, M. Vollmer, *Optical Properties of Metal Clusters* (Springer, Heidelberg, 2004)
20. H. Morgan, N.G. Green, *AC Electrokientics: Colloids and Nanoparticles* (Research Studies Press Ltd, Baldock, 2003)
21. M.O. Scully, M.S. Zubairy, *Quantum Optics* (Cambridge University Press, Cambridge, 1997)

Chapter 6
Influence of Excitonic Processes in the Energy Resolution of Scintillators

Jai Singh and Alex Koblov

Abstract A phenomenological approach is used to derive the light yield in a scintillator. Both absolute and relative yields are derived and then calculated for four scintillators, namely NaI:Tl, BaF_2, Gd_2SiO_5:Ce (GSO) and $LaCl_3$:Ce. The objective is to present a comprehensive theoretical study of the nonproportionality occurring in the yield of inorganic scintillators. This nonproportionality produces low energy resolution in most scintillators known to date. The dependences of absolute and relative yields on various rates of linear and nonlinear radiative and quenching processes are studied. The results are analysed with a view to present a recipe for achieving an inorganic scintillator with optimal proportionality in its yield and hence optimal energy resolution. The theory presented here forms the fundamental background desired for understanding the nonproportionality observed in scintillators.

6.1 Introduction

Inorganic scintillators are used as detectors in modern high energy physics accelerators, nuclear medical imaging systems of positron emission tomography (PET) [1] and single photon emission computed tomography (SPECT) [2], border and home security detection systems [3] and radiation detectors [4]. The nuclear medical imaging systems SPECT and PET are expected to be the most popular future diagnostic systems for human health in the world [5]. This is due to the fact that these systems have faster patient throughput, greater patient comfort, diagnostic certainty and staging accuracy which enable practitioners better treatment planning of diseases like cancers, tumours, heart diseases and Alzheimer's. As considerable cost savings can be obtained by reducing misdiagnosis and inappropriate treatments their use

J. Singh (✉) · A. Koblov
School of Engineering and Information Technology, B-purple-12, Faculty of EHSE,
Charles Darwin University, Darwin, NT 0909, Australia
e-mail: jai.singh@cdu.edu.au

J. Singh and R. T. Williams (eds.), *Excitonic and Photonic Processes in Materials*,
Springer Series in Materials Science 203, DOI: 10.1007/978-981-287-131-2_6,
© Springer Science+Business Media Singapore 2015

has also the potential to substantially improve the quality of health care and greatly reduce the cost. In addition there are more than 49,000 airports and 926 seaports at present in the world which require detectors of contraband nuclear materials at each of their entrances for their country's border and homeland security. Each of these detecting systems also requires, now more than ever, scintillators as detectors. Most existing scintillators suffer from poor energy resolution which limits the accuracy of their imaging capacity. Therefore it is very timely and desirable to either invent new scintillators which have superior energy resolution or improve the energy resolution of existing ones or both. To achieve this one has to understand very clearly why the existing scintillators have poor energy resolution and how to improve it.

It was found more than 50 years ago [6] that the amount of light emitted in the scintillation spark caused by absorption of an X-ray or a γ-photon in a crystal was not proportional to its energy. This non-proportional response of inorganic scintillators to ionizing radiation is one of the key problems that limits the development of new high energy resolution scintillation detectors [7–13]. To date no scintillators have either been designed or fabricated with proportional light yield in the full relevant energy range; typically 10 keV to 1 MeV. As a result they all have an energy resolution worse than the theoretical lower limit [13, 14] as explained below.

The energy resolution R of a scintillator, defined as the full width (ΔE) of the absorption peak at half the maximum intensity (FWHM) divided by the energy E, can be written as [15]:

$$\left(\frac{\Delta E}{E}\right)^2 = R^2 = R_{\mathrm{nPR}}^2 + R_{\mathrm{inh}}^2 + R_{\mathrm{p}}^2 + R_{\mathrm{M}}^2 \tag{6.1}$$

where R_{nPR} is the contribution of the non-proportional response of the scintillator to the energy resolution, R_{inh} is the contribution of inhomogenities in the crystal causing local fluctuations in the scintillation output, R_{p} is the transfer resolution contribution and R_{M} is the contribution of the photomultiplier tubes (PMT) and Poisson statistics in the number of detected photons to the resolution and is given by [13]:

$$R_{\mathrm{M}} = 2.35\sqrt{(1 + \mathrm{var}(M))/N_{\mathrm{phe}}^{\mathrm{PMT}}}, \tag{6.2}$$

where $\mathrm{var}(M) = 0.25$ is the variance in the PMT gain and N_{phe} is the total number of photoelectrons produced in the PMT. A high resolution requires R to be as low as possible. According to (6.1) and (6.2), for an absolutely homogeneous scintillatior crystal with perfect transfer efficiency, R_{inh} and R_{p} can be set to zero. Then the resolution is mainly dependent on R_{M} and R_{nPR}. According to (6.2), as R_{M} is fixed for a particular number of photoelectrons $N_{\mathrm{phe}}^{\mathrm{PMT}}$ produced in PMT, it becomes absolutely important to have R_{nPR} as low as possible for high energy resolution. The contribution of R_{nPR} is not negligible. For example, counting statistics limits the energy resolution, R_M, of two scintillators NaI:Tl and LSO:Ce to 3.8 and 4.2 % fwhm at 511 keV, but their measured energy resolutions are 7 and 9 %, yielding the non-proportionality contribution (R_{nPR}) of 5.9 and 7.9 %, respectively. That means the energy resolution can be nearly doubled by eliminating R_{nPR} in these scintillators.

6.1.1 Non-proportionality in Scintillator Light Yield (Y)

The scintillation yield (Y) is defined as the total energy of emitted photons (E_p) per unit energy (E) deposited by the incident particle, x-ray or gamma-ray photons in a scintillator material, i.e. $Y = E_p/E$ [16]. The experimentally observed scintillation yield is found not to be a constant but to vary with E, a phenomenon known as non-proportionality [17] in the scintillator response. A constant light yield implies that the scintillator is “proportional” and that means the amount of scintillation light generated is proportional to the amount of energy deposited into the scintillator. Although scintillators have been known for many decades, it is not clearly understood until recently [7, 18] what causes the non-proportionality. In fact, the issue has been addressed in so many ways that it has even created some confusion in the literature [5–16].

The emission of photons from a scintillator occurs when a γ photon absorbed in a scintillator first creates a very high energy electron which ionizes the medium of its track and high density excited electron (e) and hole (h) pairs are generated through this ionization in a cascade process eventually with energies close to the band gap; some of them recombine radiatively and some non-radiatively. The photons emitted due to the radiative recombination contribute to the light yield of a scintillator and is defined as the integrated light output per MeV of energy deposited in a scintillator. If the excited e–h pairs recombine only radiatively without going through any other processes of losing their energy, then one can expect a “proportional” scintillator response. However, the creation of high density excitations in scintillators involves various other types of radiative and non-radiative processes among the excitations and the light yield becomes a complicated function of the rates of all these processes. As the rates of these processes may be expected to vary from one material to another, different materials may exhibit different forms of non-proportionality, as indeed it has been observed [19].

The relative light output measured in several scintillators [20] and normalised to the total light yield (Y) at the highest electron energy in each case, is shown in Fig. 6.1a, b as a function of the initial energy (E) of the primary Compton-scattered electron responsible for the light pulse. A relative light yield is conventionally defined as the ratio of the light yield at an energy E (in keV) to that at an energy of 662 keV. Figure 6.1a shows the relative light yield in three classic scintillators of halide crystals doped with thallium (Tl) or sodium (Na) which are in use for some time. Figure 6.1b shows relative light yield in some newer scintillators. The light yields of halide scintillating crystals (Fig. 6.1a) show a hump in the lower energy range, i.e., it increases first and then starts decreasing and tails down in the higher energy range. In comparison, the yields presented in Fig. 6.1b show an increase going from lower to higher energy up to 100 keV and become constant (proportional) in the higher energy range. In an ideal proportional scintillator, the observed yield should be horizontal at a relative yield of 1, indicating no dependence on electron energy. Virtually none of the materials exhibit such an ideal shape. Only the scintillator light yield measured in YAP is observed to be proportional within a small incident energy span.

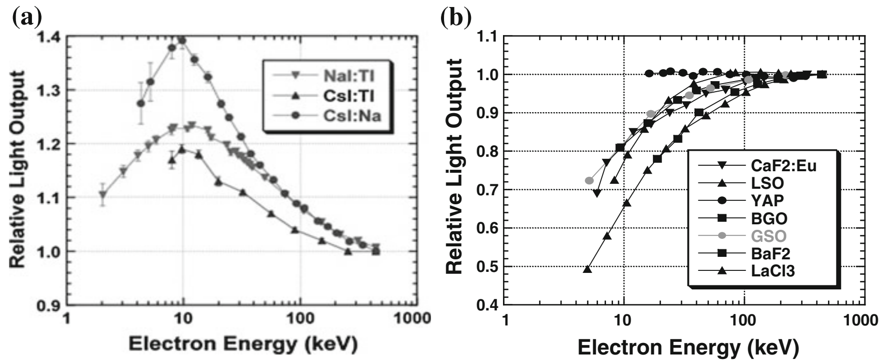

Fig. 6.1 The relative light output (light yield) versus incident energy measured by Mengesha et al. [16]. **a** For three materials, NaI:Tl, CsI:Tl and CsI:Na which show hump in the yield and **b** for seven materials, CaF_2:Eu, LSO, YAP,BGO, GSO, BaF_2, $LaCl_3$:Ce which show no hump in the yield

In addition there have been invented several new promising scintillating materials which include $LaCl_3$:Ce [20], $LaBr_3$:Ce [21], LuI_3:Ce [22], $CeBr_3$ [23], SrI_2:Eu [24], BaBrI:Eu_2 [25], Ba_2CsI_5:Eu [26], K_2LaCl_5:Ce^{3+}, $Lu_3Al_5O_{12}$:Pr^{3+}, $Lu_2Si_2O_7$:Ce^{3+} [13], CZT [27], etc. The non-proportionality is a common problem in all these materials, particularly in the low energy region $\leq$100 keV. A constant energy resolution between 3–5 % is considered to be optimal in most applications.

In order to understand the non-proportionality in scintillators it is therefore important to study various processes of interaction occurring in a high excitation density situation in a scintillating crystal when it is subjected to a high energy incident electron that can create high density excitations along its trajectory.

The objective of this chapter is to present the theory of calculating the light yield as a function of the rates of several radiative and non-radiative processes occurring within the electron track and analyse results to determine conditions under which the non-proportional yields can occur as shown in Fig. 6.1. The approach and results presented here form the fundamental understanding of the background of nonproportionality. More advanced and recent observations and their interpretations are presented in Chap. 10 by Williams et al.

6.2 Theory of Non-proportional Light Yield

In insulators and semiconductors, an incident energy larger than the band gap energy (but smaller than the threshold of multiplication of electronic excitations) excites an e–h pair, which loses the excess energy above the band gap non-radiatively to lattice vibrations, usually in the pico-second or even shorter time range. In such materials some of these relaxed e–h pairs, but not all, may recombine radiatively by emitting a photon, whose energy is equal to the band gap energy and some of the

free e–h pairs may form excitons due to their Coulomb interaction and the excess energy equal to the binding energy is again lost to the lattice non-radiatively. These excitons are called free excitons (FE) and can recombine radiatively by emitting a photon of energy less than the band gap energy, called FE photoluminescence (PL). Free exciton PL (FEPL) and direct radiative electron-hole recombination is usually observed in crystals with little to very small charge carrier-lattice interaction. Such crystals are usually known to be quite rigid in their structure. For scintillators, the crystals used are ionic and organic solids, which have strong charge carrier-lattice interaction and hence not as rigid. In such crystals, the excited e–h pairs can undergo further non-radiative relaxation due to the lattice interaction and form what are called self-trapped excitons (STE). STE can then recombine radiatively by emiting photons, called STE photoluminescence, which occurs at an energy less than FEPL. In some crystals, usually organics, both FE and STE have been observed to co-exist [28]. These three radiative processes and associated non-radiative processes are known to be linear and if these are the only processes that occur in a scintillator, which may be possible at a very low excitation density, then it may be expected to give a proportional response.

Here a phenomenological approach is presented to study the scintillator response of a scintillator by including the rates of linear, binary and ternary (Auger) processes in two rate equations. It is considered that initially one creates a number of excitations, some of which form excitons before their radiative recombination and some remain e–h pairs. The exchange between e–h pairs and excitons is also possible and considered. First the general theory is developed and approximate expressions for the local light yield (Y_L) and total light yield (Y) are derived as functions of different rates of recombination. Then the results are applied to calculate the scintillator response in four scintillating crystals, NaI:Tl, BaF_2, Gd_2SiO_5:Ce (GSO) and $LaCl_3$:Ce. As these four scintillators have been widely studied experimentally and used as scintillators, results obtained here can easily be compared with experiments. Rates of recombination are extracted from experiments where possible, and in other cases by estimation. The dependence of the light yield on different recombination rates and track radius is investigated. A qualitative agreement is found with the experimental yields. The theory is general and if the rates are known the light yield can be calculated for any scintillator.

6.2.1 Rate Equations

We include in the rate equations only excitons and pairs of electron and hole (e–h pairs) that are generated within the electron track. Phonons are also generated by the relaxation of energetic carriers and self-trapping of excitons. Following earlier works [7, 29], we consider a cylindrical track of average radius r with a stepwise dependence of exciton and carrier concentration in radial direction. The dynamical changes in exciton and e–h pair densities at any point, x, along the track can be expressed by the following two rate equations [7]:

$$-\frac{dn_{ex}(x)}{dt} = (R_{1x} + K_{1x})n_{ex}(x) + (R_{2x} + K_{2x})n_{ex}^2(x) - \gamma_{ex}n_{eh}(x) + \gamma_{xe}n_{ex}(x) + K_{3x}n_{ex}(x)^3 - f_x n(x)\delta(t), \quad (6.3)$$

$$-\frac{dn_{eh}(x)}{dt} = (R_{1eh} + K_{1eh})n_{eh}(x) + (R_{2eh} + K_{2eh})n_{eh}^2(x) - \gamma_{xe}n_{ex}(x) + \gamma_{ex}n_{eh}(x) + K_{3eh}n_{eh}^3(x) - (1 - f_x)n(x)\delta(t), \quad (6.4)$$

where $n_{ex}(x)$ is the excitonic concentration and $n_{eh}(x)$ is the concentration of excited e–h pairs not bound like excitons at any point x on the beam track. f_x is the fraction concentration of excitons, $(1 - f_x)$ is the fraction concentration of e–h pairs, and $n(x)\delta(t)$ represents the total number of excitations, $n(x) = n_{ex}(x) + n_{eh}(x)$, created by the incident energy at time $t = 0$ at any point x along the track. Accordingly, $n(x)$ (cm^{-3}) is defined as:

$$n(x) = \frac{\left(-\frac{\partial E}{\partial x}\right)}{\pi r^2 E_{eh}}, \quad (6.5)$$

where E is the total initial energy incident at any point x, πr^2 is the average area of cross section of the track and E_{eh} is the average energy required to create an excitation in a scintillator, and here it is assumed to be three times the band gap energy $(E_g) : E_{eh} = 3E_g$ [7]. It is to be noted that the use of x to denote excitons as well as the position in the track in (6.3)–(6.4) may appear to be confusing, which may be clarified like this: when x appears as a subscript it refers to excitons otherwise it denotes the position at any time t within the track.

In (6.3) and (6.4), R_{ix} and K_{ix} denote the rates of radiative and non-radiative (quenching) recombination of excitons, respectively, and $i = 1, 2$, denote through linear (1) and binary (2) processes. R_{2x}, the rate of *radiative* exciton decay promoted by exciton-exciton interaction is assumed to be zero because the bilinear interaction is regarded to be only non-radiative for the four scintillators under present consideration [7]. R_{ieh} and K_{ieh} $(i = 1, 2)$ are the corresponding rates of recombination for an e–h pair, and K_{3x} and K_{3eh} are rates of non-radiative Auger (ternary) recombination of excitons and an e–h pairs, respectively. Auger processes do not contribute to any radiative recombination. γ_{ex} and γ_{xe} are rates of converting an eh pair into an exciton and vice versa, respectively. This is important to consider both the possibilities for applying the theory at higher temperatures.

According to (6.3) and (6.4), we can classify scintillators in three categories: (i) excitonic with $f(x) = 1$, (ii) non-excitonic with $f(x) = 0$, and (iii) mixed case $0 < f(x) < 1$. It is important to note that the rate of any process in (6.3) and (6.4) represents the sum of all the rates in that process. For example, R_{1x} represents the sum of the first order excitonic rates of radiative recombination through all possible channels, including recombination through doped impurities. $R_{1x} = R_{1x}^{STE} + R_{1x}^{ad}$, where R_{1x}^{STE} and R_{1x}^{ad} are rates of recombination of an intrinsic self-trapped excitons (STE) and through an activator impurity atom, respectively. Both processes contribute to the scintillation light yield. The radiative and nonradiative processes considered in (6.3) and (6.4) are presented in Fig. 6.2 pictorially.

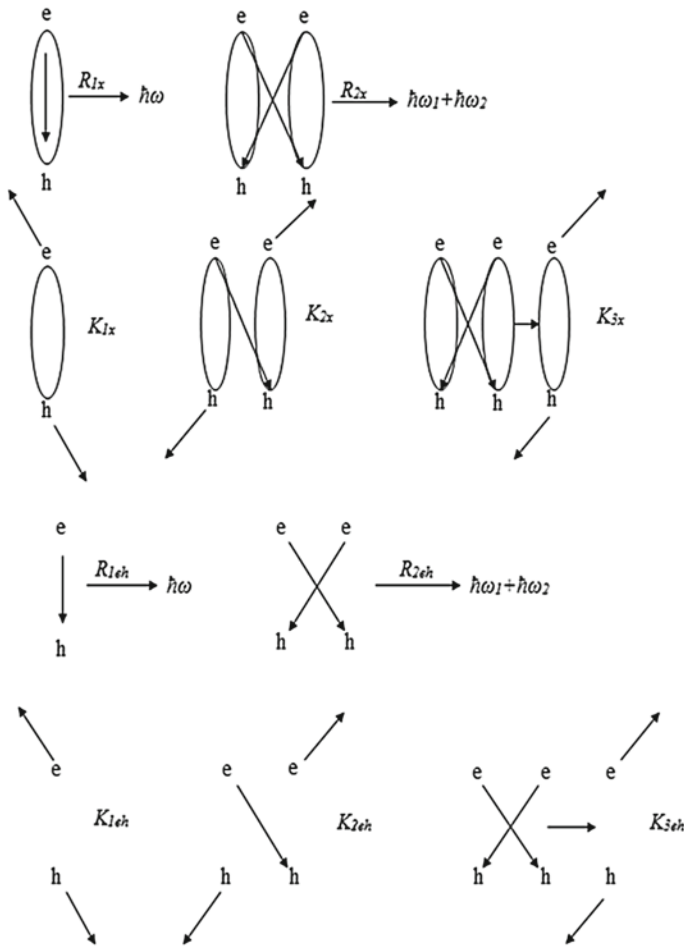

Fig. 6.2 Schematic representations of radiative and non-radiative (quenching) linear and nonlinear processes considered to be occurring within the track and their corresponding rates. *Ellipses with e* and *h* represent excitons and *e* and *h without ellipses* denote e–h pairs

6.2.2 Local Light Yield (Y_L)

Let us use (6.3) and (6.4) to calculate the light yield first at any point x within the track also known as the local light yield. For this we integrate (6.3) and (6.4) over time to get [7]:

$$0 = (R_{1x} + K_{1x}) < n_{ex}(x) > +(R_{2x} + K_{2x}) < n_{ex}^2(x) > -\gamma_{ex} < n_{eh}(x) >$$
$$+ \gamma_{xe} < n_{ex}(x) > +K_{3x} < n_{ex}^3(x) > - f_x n(x), \tag{6.6}$$
$$0 = (R_{1eh} + K_{1eh}) < n_{eh}(x) > +(R_{2eh} + K_{2eh}) < n_{eh}^2(x) > -\gamma_{xe} < n_{ex}(x) >$$
$$+ \gamma_{ex} < n_{eh}(x) > +K_{3eh} < n_{eh}^3(x) > -(1 - f_x)n(x), \tag{6.7}$$

where $< n(x) >$ represents the integrated value of $n(x)$ over time, and $\int_0^\infty \frac{dn(x)}{dt} dt = n(x)_{|\infty} - n(x)_{|0} = 0$ is used in arriving at (6.6) and (6.7). It is obvious that (6.6) and (6.7) have similar forms as (6.3) and (6.4) in the steady-state but with unintegrated concentrations.

Adding (6.6) and (6.7) we get:

$$\begin{aligned}(R_{1x} + K_{1x}) < n_{ex}(x) > +(R_{2x} + K_{2x}) < n_{ex}^2(x) > +(R_{1eh} + K_{1eh}) < n_{eh}(x) > \\ +(R_{2eh} + K_{2eh}) < n_{eh}^2(x) > +K_{3x} < n_{ex}^3 > +K_{3eh} < n_{eh}^3 >= n(x)\end{aligned} \tag{6.8}$$

In theory the yield is defined as the total integrated photons emitted divided by the total number of excitations created. Using (6.8), the local light yield (Y_L) at any point x along the track can be defined by:

$$Y_L = \frac{R_{1x} < n_{ex}(x) > +R_{2x} < n_{ex}^2(x) > +R_{1eh} < n_{eh}(x) > +R_{2eh} < n_{eh}^2(x) >}{n(x)}, \tag{6.9}$$

where the numerator consists of only terms of the radiative processes in (6.8). Y_L in (6.9) is called the local light yield, which means the instantaneous yield at any point x along the track and it can be calculated provided all the rates and $< n_{ex}(x) >$, $< n_{ex}^2(x) >$, $< n_{ex}^3(x) >$, $< n_{eh}(x) >$, $< n_{eh}^2(x) >$ and $< n_{eh}^3(x) >$ are known. Latter ones can probably be determined in more than one way, but here we have estimated these using the linear order approximation as given below:

As an approximation, we consider only the linear processes in (6.6) and (6.7) and solve it for $< n_{ex}(x) >$ and $< n_{eh}(x) >$, respectively, to get [7]:

$$< n_{ex}(x) >= An(x) \text{ and } < n_{eh}(x) >= Bn(x), \tag{6.10}$$

where

$$A = \frac{[\gamma_{ex} + (R_{1eh} + K_{1eh}) f_x]}{(R_{1x} + K_{1x})(R_{1eh} + K_{1eh}) + \gamma_{ex}(R_{1x} + K_{1x}) + \gamma_{xe}(R_{1eh} + K_{1eh})}, \tag{6.11}$$

and

$$B = \frac{[(1 - f_x)(R_{1x} + K_{1x}) + \gamma_{xe}]}{(R_{1x} + K_{1x})(R_{1eh} + K_{1eh}) + \gamma_{ex}(R_{1x} + K_{1x}) + \gamma_{xe}(R_{1eh} + K_{1eh})}. \tag{6.12}$$

We also need $< n_{ex}^2(x) >$, $< n_{eh}^2(x) >$ and $< n_{eh}^3(x) >$, which can also be determined from the linear order approximation, within which the concentration

can be assumed to have the following form [7]:

$$n_{ex}(x,t) = n^0_{ex}(x)e^{-t/\tau_{ex}}, \quad 1/\tau_{ex} = R_{1x} + K_{1x}, \tag{6.13}$$

and

$$n_{eh}(x,t) = n^0_{eh}(x)e^{-t/\tau_{eh}}, \quad 1/\tau_{eh} = R_{1eh} + K_{1eh}, \tag{6.14}$$

where τ_{ex} and τ_{eh} are lifetimes, and $n^0_{ex}(x)$ and $n^0_{eh}(x)$ are the initial concentrations at time t= 0 of an exciton and an e–h pair, respectively. The above forms of $n_{ex}(x,t)$ and $n_{eh}(x,t)$ assume that the initial population of excitons and e–h pairs created at any point x decays exponentially in time through the linear processes. The advantage of the assumptions of (6.13) and (6.14) is that these can be integrated on time easily and then we get:

$$< n_{ex}(x,t) > = n^0_{x}(x)\int_0^\infty e^{-t/\tau_{ex}}dt = n^0_{ex}(x)\tau_{ex}, \tag{6.15}$$

and

$$< n_{eh}(x,t) > = n^0_{eh}(x)\int_0^\infty e^{-t/\tau_{eh}}dt = n^0_{eh}(x)\tau_{eh}. \tag{6.16}$$

Within the linear approximation, we can also determine $< n^2_{ex}(x,t) >$, $< n^2_{eh}(x,t) >$, $< n^3_{ex}(x,t) >$ and $< n^3_{eh}(x,t) >$ as:

$$< n^2_{ex}(x,t) > = n^0_{ex}(x)^2\int_0^\infty e^{-2t/\tau_{ex}}dt = \frac{1}{2}n^0_{ex}(x)^2\tau_{ex}, \tag{6.17}$$

$$< n^2_{eh}(x,t) > = n^0_{eh}(x)^2\int_0^\infty e^{-2t/\tau_{eh}}dt = \frac{1}{2}n^0_{eh}(x)^2\tau_{eh}, \tag{6.18}$$

$$< n^3_{ex}(x,t) > = n^0_{ex}(x)^3\int_0^\infty e^{-3t/\tau_{ex}}dt = \frac{1}{3}n^0_{ex}(x)^3\tau_{ex}, \tag{6.19}$$

and

$$< n^3_{eh}(x,t) > = n^0_{eh}(x)^3\int_0^\infty e^{-3t/\tau_{eh}}dt = \frac{1}{3}n^0_{eh}(x)^3\tau_{eh}. \tag{6.20}$$

Using (6.15) and (6.16) in (6.10), we get:

$$n_{ex}^{0} = An(x)/\tau_{ex}, \text{ and } n_{eh}^{0} = Bn(x)/\tau_{eh}. \tag{6.21}$$

Using (5.15) to (6.20) in (6.9), the local light yield can be expressed as:

$$Y_L = \frac{(R_{1x}A + R_{1eh}B)n(x) + (\frac{1}{2\tau_{ex}}R_{2x}A^2 + \frac{1}{2\tau_{eh}}R_{2eh}B^2)n(x)^2}{[((R_{1x} + K_{1x})A + (R_{1eh} + K_{1eh})B)n(x) + (\frac{1}{2\tau_{ex}}(R_{2x} + K_{2x})A^2 + \frac{1}{2\tau_{eh}}(R_{2eh} + K_{2eh})B^2)n(x)^2 + (\frac{1}{3\tau_{ex}^2}K_{3x}A^3 + \frac{1}{3\tau_{eh}^2}K_{3eh}B^3)n(x)^3]} \tag{6.22}$$

Dividing the numerator and denominator of (6.21) by $(R_{1x} + K_{1x})An(x) + (R_{1eh} + K_{1eh})B$, we can write Y_L in the following form:

$$Y_L = \frac{a_1 n(x) + a_2 n^2(x)}{n(x) + a_3 n^2(x) + a_4 n^3(x)}, \tag{6.23}$$

where

$$a_1 = \frac{(R_{1x}A + R_{1eh}B)}{D}; \quad D = (R_{1x} + K_{1x})A + (R_{1eh} + K_{1eh})B, \tag{6.24}$$

$$a_2 = \frac{(R_{2x}A^2/\tau_x + R_{2eh}B^2/\tau_{eh})}{2D}, \tag{6.25}$$

$$a_3 = \frac{(R_{2x} + K_{2x})A^2/\tau_x + ((R_{2eh} + K_{2eh})B^2/\tau_{eh}}{2D}, \tag{6.26}$$

$$a_4 = \frac{1}{3D}(\frac{K_{3x}A^3}{\tau_x^2} + \frac{K_{3eh}B^3}{\tau_{eh}^2}). \tag{6.27}$$

Using (6.5) and (6.22), the local yield can be calculated as a function of $(-\frac{dE}{dx})$ (keV/cm) for any scintillating crystal. Such graphs of Y as a function of $(-\frac{dE}{dx})$ have been calculated theoretically [29] and compared with the experimental results [8]. However, recent experiments are carried out to measure the total scintillation light yield as a function of the total energy deposited as shown in Fig. 6.1. The derivation of the total scintillator yield is described below.

6.2.3 *Total ScintillatiorYield (Y)*

For calculating the total scintillator light yield, one needs to find the total number of photons generated divided by the total number of excitations generated within the whole track by the total incident energy. This can be achieved by integrating the

numerator and denominator of the local yield in (6.23) over the whole track length and then one gets the total yield, Y as [7]:

$$Y = \frac{a_1 n + a_2 \bar{n}^2}{n + a_3 \bar{n}^2 + a_4 \bar{n}^3} \tag{6.28}$$

Dividing the numerator and denominator of (6.28) by n, we can write Y as:

$$Y = \frac{a_1 + a_2(\bar{n}^2/n)}{1 + a_3(\bar{n}^2/n) + a_4(\bar{n}^3/n)}, \tag{6.29}$$

where $n = \frac{1}{L}\int_0^L n(x)dx$, $\bar{n}^2 = \frac{1}{L}\int_0^L n^2(x)dx$, $\bar{n}^3 = \frac{1}{L}\int_0^L n^3(x)dx$ and L denotes the total track length. It should be noted from above that the bar used on $\bar{n}^2$ and $\bar{n}^3$ is to distinguish that these are not the squared and cubed of n, respectively. However for evaluating these integrals we need to know $(-dE/dx)$ in (6.5) as a function of the local energy incident at each point. There are many approaches for determining (*–dE/dx*), including the calculation of energy loss function $\mathrm{Im}\left(-\varepsilon^{-1}(\omega, q)\right)$ in a number of approximations (see, e.g., [30–34]). In order to obtain analytical formulas for calculating the total yield here we have used an analytical form of (*–dE/dx*) derived from the Bethe-Bloch equation [35]. This form does not depend on the detailed description of energy loss function but on average ionization energy of the ions constituting the crystal and hence easy to use for analytical derivations, as described below.

Stopping power given by the modified (non-relativistic) Bethe equation [36] is:

$$-\frac{dE}{dx} = \frac{2\pi e^4 \kappa^2 \rho_e}{E} \ln\{(\frac{2.71}{2})^{1/2}[(E + 0.81I)/I]\}, \tag{6.30}$$

where $\kappa = (4\pi\varepsilon_0)^{-1} = 8.9877 \times 10^9$, E is the total initial incident energy of gamma rays at any point x along its track, I is the average ionization energy and ρ_e is the electron density given by:

$$\rho_e = \frac{N_A Z \rho}{A}, \tag{6.31}$$

where $N_A = 6.022 \times 10^{23}$ is the Avogadro number, Z and A are the atomic number and atomic weight number, respectively and ρ is the density of the material. The form of $(-dE/dx)$ in (4.30) is used here to calculate the excitation density and described below.

Substituting (6.30) in (6.5) and using $E_{eh} = 3E_g$ we get:

$$n(x) = \frac{2e^4\kappa^2\rho_e}{3r^2 E_g E} \ln\{1.164[E + 0.81I]/I\}. \tag{6.32}$$

Using (6.5), the first integral of $n(x)$ can easily be evaluated as:

$$n = \frac{1}{3\pi r^2 E_g}[\frac{1}{L}\int_0^L (-\frac{dE}{dx})dx] = \frac{1}{3\pi r^2 E_g}[\frac{1}{L}\int_0^E (-\frac{dE}{dx})(\frac{dx}{dE})dE] = \frac{1}{3\pi r^2 E_g}[\frac{E}{L}], \tag{6.33}$$

where E is the total incident energy of the γ-ray. It is interesting to note that the total concentration n in (6.33) does not depend on the mathematical form of $(-\frac{dE}{dx})$ but higher powers of n do. Using (6.5) and (6.32), we can also integrate $n(x)^2$ and $n(x)^3$ over the track length as:

$$\bar{n}^2 = \frac{1}{L}\int_0^L n^2(x)dx = \frac{1}{(3\pi r^2 E_g)^2}[\frac{1}{L}\int_0^E (-\frac{dE}{dx})^2(\frac{dx}{dE})dE] = \frac{\pi e^4\kappa^2\rho_e}{(3\pi r^2 E_g)^2 L}A, \tag{6.34}$$

where

$$A = \{\ln[1.164(E + 0.81I)/I]\}^2, \tag{6.35}$$

and

$$\bar{n}^3 = \frac{1}{L}\int_0^L n^3(x)dx = \frac{1}{(3\pi r^2 E_g)^3}[\frac{1}{L}\int_0^E (-\frac{dE}{dx})^3(\frac{dx}{dE})dE] \tag{6.36}$$

$$= \frac{1.164(2\pi e^4\kappa^2 n_e)^2}{L(3\pi r^2 E_g)^3 I A_t}[2A_t - (\ln(A_t))^2 - 2\ln(A_t) - 2]$$

where

$$A_t = \{1.164(E + 0.81I)/I]\}. \tag{6.37}$$

Using (6.33), (6.34) and (6.36) we get:

$$(\bar{n}^2/n) = \frac{e^4\kappa^2\rho_e}{(3r^2 E_g)E}A, \tag{6.38}$$

$$(\bar{n}^3/n) = \frac{1.164}{A_t I E}\left(\frac{2e^4\kappa^2\rho_e}{3r^2 E_g}\right)^2[2A_t - (\ln(A_t))^2 - 2\ln(A_t) - 2]. \tag{6.39}$$

Using (6.38) and (6.39) in (6.29) the total yield Y can be obtained as a function of the total incident energy E. The scintillator light yield thus obtained has been calculated under various conditions for four scintillators NaI:Tl, BaF_2, GSO:Ce and $LaCl_3$:Ce using rates listed in Table 6.1. These rates are deduced from independent measurements whereever possible as described in [7].

Table 6.1 Rate constants and other parameters used to calculate the scintillation light yield versus particle energy curves for four materials

Rate constants	NaI:Tl	BaF_2	GSO:Ce	$LaCl_3$:Ce
R_{1x}	$\mathbf{4.7 \times 10^6 s^{-1}}$	$\mathbf{1.6 \times 10^9 s^{-1}}$	$\mathbf{3 \times 10^7 s^{-1}}$	$\mathbf{3 \times 10^7 s^{-1}}$
K_{1x}	$\mathbf{1.2 \times 10^6 s^{-1}}$	$\mathbf{4 \times 10^8 s^{-1}}$	$\mathbf{3 \times 10^6 s^{-1}}$	$\mathbf{3 \times 10^6 s^{-1}}$
R_{1eh}	**0**	**0**	**0**	**0**
K_{1eh}	3×10^6 s^{-1}	3×10^6 s^{-1}	3×10^6 s^{-1}	3×10^6 s^{-1}
R_{2eh}	$\mathbf{3 \times 10^{-11} cm^3/s}$	3×10^{-11} cm^3/s	3×10^{-11} cm^3/s	3×10^{-11} cm^3/s
K_{2eh}	3×10^{-12} cm^3/s	3×10^{-12} cm^3/s	3×10^{-12} cm^3/s	3×10^{-12} cm^3/s
R_{2x}	**0**	**0**	**0**	**0**
K_{2x}	2×10^{-11} cm^3/s	2×10^{-11} cm^3/s	2×10^{-11} cm^3/s	2×10^{-11} cm^3/s
K_{3eh}	1×10^{-29} cm^6/s	1×10^{-29} cm^6/s	1×10^{-29} cm^6/s	1×10^{-29} cm^6/s
K_{3x}	1×10^{-29} cm^6/s	1×10^{-29} cm^6/s	1×10^{-29} cm^6/s	1×10^{-29} cm^6/s
γ_{eh-x}	0	0	0	0
γ_{x-eh}	0	0	0	0
f_x (ex fraction)	*0.1*	*1*	*1*	*0.6*
r (track rad.)	*6* nm	*2* nm	*4* nm	*4* nm

Values in bold type were determined from independent measurements and considerations [7]. Values in normal type were constrained as constants common to all four materials since they could only be roughly estimated. Values in italics are varied as fitting parameters among the four materials

Although the use of (6.32) in calculating the light yield Y in (6.29) is expected to give more accurate results under the linear approximation, (6.32) produces complicated expressions for $\bar{n}^2$ (6.34) and $\bar{n}^3$ (6.36). One can reduce such complications drastically by using an approximate expression for $n(x)$ suggested by Jaffe [37] as described below.

The dominant term in the expression of $-dE/dx$ in (6.30) dependent on energy is E^{-1}, the log factor which can be approximated by the value 5 in the energy range 10–100 keV [37]. Then we get:

$$-\frac{dE}{dx} \approx \frac{10\pi e^4 \kappa^2 \rho_e}{E}. \tag{6.40}$$

For photons of initial energy E, the length of a track can be defined as [37]:

$$L = \int_E^0 \left(-\frac{dE'}{dx}\right)^{-1} dE' \tag{6.41}$$

Substituting (6.40) in (6.41), we get the approximate track length as:

$$L \approx \frac{E^2}{20\pi e^4 \kappa^2 \rho_e}, \tag{6.42}$$

where $\rho_e \approx 10^{30}\ \mathrm{m}^{-3}$. And using this approximate track length in (6.33), we get the approximate average excitation concentration within the track length as:

$$n \approx [\frac{20e^4\kappa^2\rho_e}{3E_g r^2}]E^{-1} = QE^{-1}. \tag{6.43}$$

with $Q = \frac{20e^4\kappa^2\rho_e}{E_{eh}r^2}$; E_{eh}=$3E_g$. Approximating the log factor by 5, we get $A^2 \approx 25$ in (6.35). Substituting this and L from (6.42) in (6.34) we get [39]:

$$\bar{n}^2 \approx \frac{5}{4}Q^2E^{-2}. \tag{6.44}$$

In order to evaluate $\bar{n}^3$, it is better to evaluate the integral in (6.36) as follows:

$$\bar{n}^3 = \frac{1}{L}\int_0^L n^3(x)dx = \frac{1}{(3\pi r^2 E_g)^3}[\frac{1}{L}\int_E^0(-\frac{dE}{dx})^3(\frac{dx}{dE})dE] = \frac{1}{(3\pi r^2 E_g)^3 L}\int_E^0(-\frac{dE}{dx})^2 dE \tag{6.45}$$

Using (6.40) the integral in (6.45) can easily be evaluated and then substituting for L from (6.42) we get [39]:

$$\bar{n}^3 \approx \frac{1}{4}Q^3E^{-3}. \tag{6.46}$$

Using (6.43)–(6.46), the total yield in (6.29) is obtained as a function of the initial incident energy as [38, 39]:

$$Y_= \frac{a_1 + 1.25a_2QE^{-1}}{1 + 1.25a_3QE^{-1} + 0.25a_4Q^2E^{-2}}. \tag{6.47}$$

The yield in (6.47) is the absolute (total) yield of a scintillator. However, as a matter of convention, the yield measured experimentally is the relative yield which is relative to the yield obtained at energy of 662 keV. The relative yield can easily be obtained by dividing the absolute yield in (6.47) by that obtained at $E = 662$ keV. Thus, the relative yield (Y_R) is obtained as [38, 40]:

$$Y_R = \frac{(a_1 + 1.25a_2QE^{-1})(1 + 1.25a_3Q(662\,\mathrm{keV})^{-1} + 0.25a_4Q^2(662\,\mathrm{keV})^{-2})}{(a_1 + 1.25a_2Q(662\,\mathrm{keV})^{-1})(1 + 1.25a_3QE^{-1} + 0.25a_4Q^2E^{-2})}, \tag{6.48}$$

The influence of various radiative and non-radiative processes on the scintillator light yield and under what conditions the yields Y and Y_R can become proportional can be easily discussed through (6.47) and (6.48). This is done in the next few sections.

6.3 Proportional Scintillator Yield

It is obvious from the absolute yield that if $a_2 = a_3 = a_4 = 0$, then from (6.46) we get $Y = a_1$ which is a constant and does not depend on energy and under this condition the relative yield in (6.48) becomes unity, $\mathrm{Y}_R = 1$. That means in a proportional scintillator one should have $a_2 = a_3 = a_4 = 0$. According to (6.24)–(6.27), a_2 and a_3 depend on the bimolecular radiative and nonradiative rates and a_4 depends on the Auger quenching rates. That means in a scintillator, if the second (bimolecular) and third order (Auger) processes can be stopped from occurring within the electron track, it will be a proportional ideal scintillator. Do we also need to have the bimolecular radiative rates to be zero? Although in Table 6.1, R_{2x} is chosen to be zero for the reason explaned in [7], we only need the higher order quenching rates to be zero to get perfect proportionality. The expressions of a_2 and a_3 in (6.26) and (6.27), respectively, show that for vanishing bimolecular and Auger quenching rates, i.e., $K_{2x} = K_{2eh} = 0$ and $K_{3x} = K_{3eh} = 0$, $a_2 = a_3$ and $a_4 = 0$ and then the yield in (6.47) mainly depends on a_1, which depends on both R_1 and K_1. According to Table 6.1 as $R_1 > K_1$ for all the four scintillators the yield will be nearly proportional. The dependence of the yield on bimolecular and Auger quenching rates is presented below. However, before we study the conditions under which the higher order processes (beyond the linear or first order) can be eliminated or reduced, let us look at the dependence of yield in (6.47) for the four scintillators considered here on the nature of the excitation.

In the rate (6.3) and (6.4), we have considered two types of excitations: (1) excitonic and (2) e–h pairs. The fractional excitonic population is represented by f_x and the fractional e–h pairs by $1 - f_x$. Although the light yield for any value of the fraction excitonic concentration f_x can be calculated from (6.47) and (6.48), two cases of $f_x = 0$ and 1 are special because then the two rate equations (6.3) and (6.4) reduce into one equation. The value of f_x may vary from one scintillator material to another and from this point of view scintillator materials can be characterised into three groups: (i) excitonic with $f_x = 1$, (ii) non-excitonic with $f_x = 0$ and (iii) mixed with $0 \leq f_x \leq 1$. Let us discuss these three conditions below:

6.3.1 *Excitonic Scintillators* ($f_x = 1$)

In this case only one (6.3) of the rate equations is relevant, which for $f_x = 1$ reduces to:

$$-\frac{dn_{ex}(x)}{dt} = (R_{1x} + K_{1x})n_{ex}(x) + K_{2x}n_{ex}^2(x) + K_{3x}n_{ex}^3 - n(x)\delta(t). \quad (6.49)$$

(6.48) is derived by considering only the non-zero rates in Table 6.1. Following the steps in deriving (6.46), the light yield reduces to Y_{ex} as:

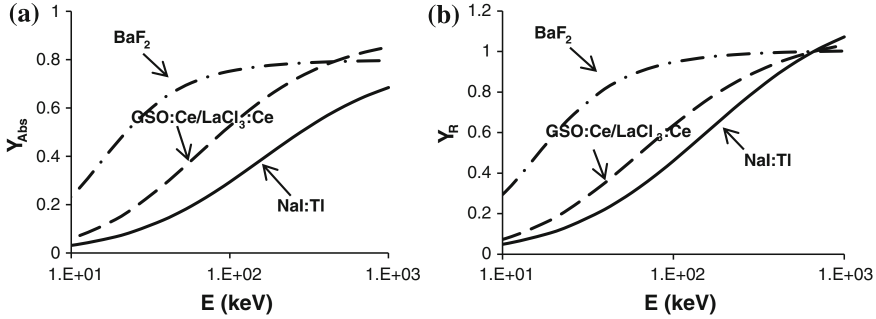

Fig. 6.3 **a** The absolute and **b** relative yields calculated as a function of energy from (6.47) and (6.48), respectively, for $f_x = 1$ for NaI:Tl, BaF_2, GSO and $LaCl_3$:Ce

$$Y_{ex} = \frac{a_1}{1 + 1.25 a_3 Q E^{-1} + 0.25 a_4 Q^2 E^{-2}}, \tag{6.50}$$

where $a_1 = \frac{R_{1x}}{(R_{1x}+K_{1x})}$, $a_3 = \frac{K_{2x}}{2(R_{1x}+K_{1x})}$ and $a_4 = \frac{K_{3x}}{3(R_{1x}+K_{1x})}$.

The light yield in (6.50) increases initially with energy in the lower energy range and then it approaches asymptotically to a_1 at higher energies after a certain intermediate energy. In other words, according to (6.43), light yield in (6.50) is a monotonically decreasing function of excitation density in the high excitation density range. Such a dependence of the yield on energy is experimentally observed in BaF_2, GSO and $LaCl_3$:Ce as shown in Fig. 6.1. In this case, the relative yield will become independent of the parameter a_1. It may be noted that it is not necessary to write a separate yield as in (6.50) for the excitonic case. One can get the same result by plotting the yield in (6.47) for $f_x = 1$. However one may not be able to compare it as clearly as from (6.50) without plotting it. In Fig. 6.3 are plotted the absolute and relative yields calculated from (6.47) and (6.48), respectively, for $f_x = 1$ as a function of the incident energy E(keV).

6.3.2 *Non-excitonic Scintillators ($f_x = 0$)*

This case is the other extreme and here also the two rate equations reduce to one equation (6.4) as:

$$-\frac{dn_{eh}(x)}{dt} = K_{1eh} n_{eh}(x) + R_{2eh} n_{eh}^2(x) + K_{3eh} n_{eh}^3(x) - n(x)\delta(t), \tag{6.51}$$

where again only the non-zero rates in Table 6.1 are considered. In this case the light yield in (6.47) becomes Y_{eh} as:

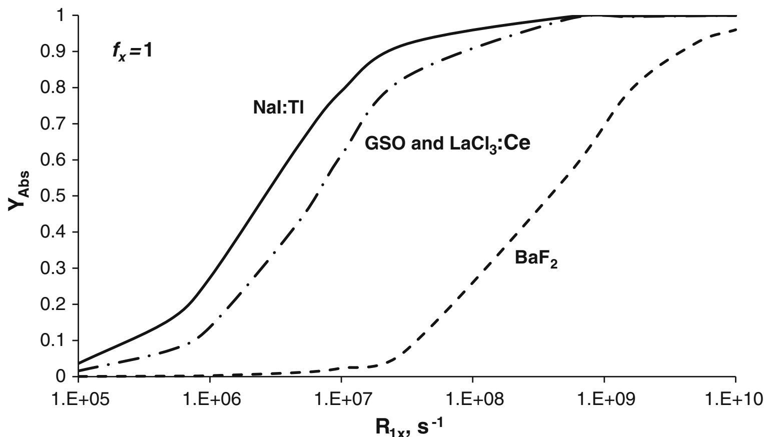

Fig. 6.4 Light yield of (6.47) is plotted for $f_x = 1$ at $E = 662\,\text{keV}$ as a function of linear excitonic rate of radiative emission R_{1x} (s^{-1}) for the four scintillators, NaI:TL, BaF_2, GSO:Ce and $LaCl_3$:Ce

$$Y_{eh} = \frac{1.25 a_2 Q E^{-1}}{1 + 1.25 a_3 Q E^{-1} + 0.25 a_4 Q^2 E^{-2}}, \tag{6.52}$$

where

$$a_2 = a_3 = \frac{R_{2eh}}{2K_{1eh}}, \text{ and } a_4 = \frac{K_{3eh}}{3K_{1eh}}. \tag{6.53}$$

Equation (6.52) produces scintillation light yield curves that rise initially in the lower energy range and then starts decreasing in the higher energy range. The experimental scintillation yield curves for NaI:Tl and other halide scintillators shown in Fig. 6.1 exhibit this character.

6.3.3 Dependence of Yield on Linear Rates (R_1, K_1)

The absolute yield Y_{abs} (6.47) is plotted in Fig. 6.4 as a function the linear excitonic rate of radiative emission R_{1x} (s^{-1}) at $E = 662\,\text{keV}$ for all the four scintillators, i.e., NaI:Tl, BaF_2, GSO:Ce and $CaCl_3$:Ce by keeping other rates and parameters constant at their values given in Table 6.1. The case presented in Fig. 6.4 is in which only for excitons (no free e–h pairs) are excited in the track, i.e., $f_x = 1$.

According to Fig. 6.4, the light yield reduces to zero if the rate R_{1x} reduces below $10^6\ \text{s}^{-1}$ but becomes constant at 1 if $R_{1x} \geq 10^{10}\ \text{s}^{-1}$. A constant yield means the yield becomes proportional and under this condition a scintillator will have no nonproportionality (NPR) and hence have optimal energy resolution [7, 38, 41, 42]. It may be noted that the input parameters used for GSO:Ce and $LaCl_3$:Ce are the same (see Table 6.1) so the calculated yield is the same for both of these scintillators.

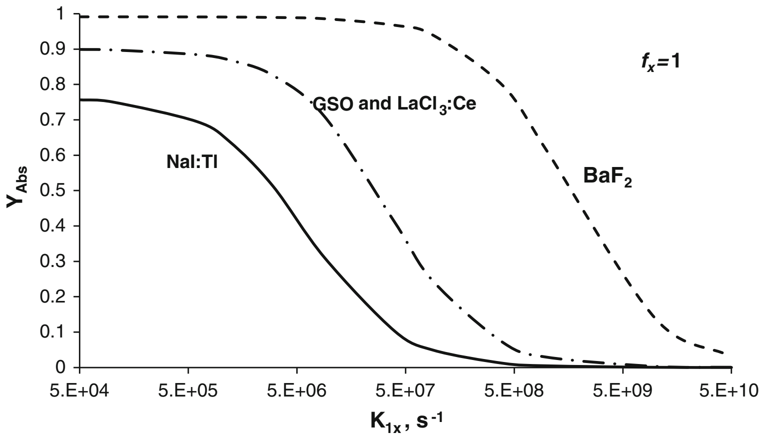

Fig. 6.5 Light yield of (6.47) is plotted for $f_x = 1$ at $E = 662\,\text{keV}$ as a function of linear exciton quenching rate K_{1x} (s^{-1}) for the four scintillators, NaI:TL, BaF_2, GSO:Ce and $LaCl_3$:Ce

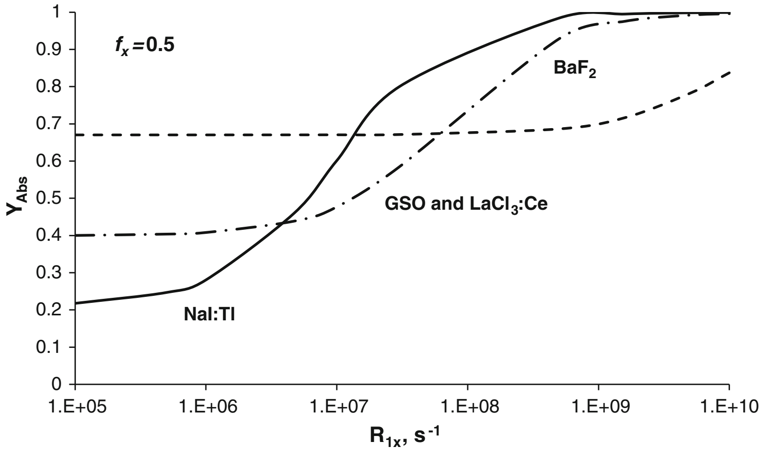

Fig. 6.6 Light yield of (6.46) is plotted for $f_x = 0.5$ at $E = 662\,\text{keV}$ as a function of linear excitonic rate of radiative emission R_{1x} (s^{-1}) for the four scintillators, NaI:TL, BaF_2, GSO:Ce and $LaCl_3$:Ce

The measured values of the radiative rate R_{1x} in the four scintillators are 4.7×10^6 s^{-1} in NaI:Tl, 1.6×10^9 s^{-1} in BaF_2, and $3 \times 10^7\text{s}^{-1}$ in GSO:Ce and $LaCl_3$:Ce [7].

In Fig. 6.5 is plotted the absolute yield (6.47) in all four scintillators for $f_x = 1$ at $E = 662\,\text{keV}$ as a function of the linear exciton quenching rate K_{1x} (s^{-1}) keeping other parameters constant.

According to Fig. 6.5, the yield remains proportional in BaF_2 if $K_{1x} \leq 10^7\text{s}^{-1}$, in GSO:Ce and $LaCl_3$:Ce if $K_{1x} < 10^6\text{s}^{-1}$ and in NaI:Tl no proportionality is apparent down to $K_{1x} < 5 \times 10^4\text{s}^{-1}$.

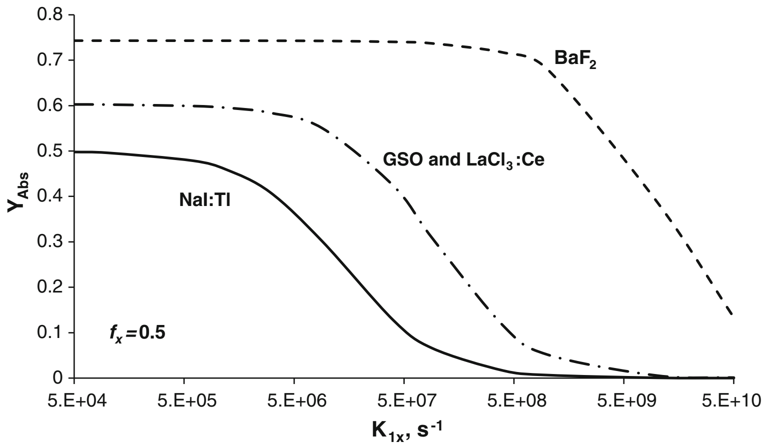

Fig. 6.7 Light yield of (6.46) is plotted for $f_x = 0.5$ at $E = 662$ keV as a function of linear exciton quenching rate K_{1x} (s^{-1}) for the four scintillators, NaI:TL, BaF_2, GSO:Ce and $LaCl_3$:Ce

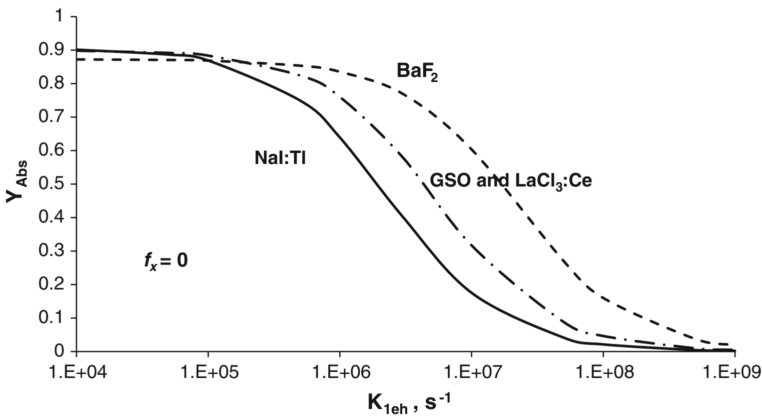

Fig. 6.8 Light yield of (6.46) is plotted for $f_x = 0$ at $E = 662$ keV as a function of linear e–h quenching rate K_{1eh} (s^{-1}) for the four scintillators, NaI:TL, BaF_2, GSO:Ce and $LaCl_3$:Ce

It should be noted here that for the excitonic case with $f_x = 1$, the linear e–h pair rates, R_{1eh} and K_{1eh}, do not contribute to the yield.

We now consider the case of an electron track with half the excited population being excitons ($f_x = 0.5$) and other half is e–h pairs. In Figs. 6.6 and 6.7 are plotted yields in (6.47) for all four scintillators as a function of R_{1x} and K_{1x}, respectively, at E = 662 keV and keeping other parameters constant. In Fig. 6.6, the yields become proportional for $R_{1x} > 10^9$ s^{-1} except in BaF_2 the yield apparently increases but it remains constant at lower rates. The yields in Fig. 6.7 are similar to those in Fig. 6.5 but slightly lower at lower quenching rates. The variation of yields with respect to the e–h pair linear radiative and quenching rates are found to be similar to those in Figs. 6.6 and 6.7, respectively, and hence not shown here.

The case of non-excitonic scintillators, where only e–h pairs are excited within the track, i.e., $f_x = 0$, the yields are plotted as a function of K_{1eh}, in Fig. 6.8 at $E = 662$ keV. It may be noted that in our choice of rates given in Table 6.1, the linear e–h radiative rate is chosen to be zero ($R_{1eh} = 0$). In this case the yield in BaF_2 remains proportional for $K_{1eh} < 10^6$ s^{-1}, for GSO:Ce and $LaCl_3$:Ce for 10^5 s^{-1} and for NaI:Tl for $<10^5$ s^{-1}. Within the choice of different rates and parameters considered here, the case of non-excitonic scintillators is found to have most NPR [7, 38, 41, 42]. The choice of $R_{1eh} = 0$, may be attributed to the presence of defects as traps, where the non excitonic e and h pairs get trapped, preventing their radiative recombination.

6.3.4 Dependence of Yield on Bimolecular Quenching Rates (K_{2x}, K_{2eh})

In this section the dependence of the absolute yield Y_{abs} (6.47) and relative yield (6.48) is plotted as a function of energy at different values of the bimolecular quenching rates, K_{2x} and K_{2eh} for the four scintillators under three conditions: (i) $f_x = 1$ excitonic, (ii) $f_x = 0.5$ mixed and (iii) $f_x = 0$ non-exciton.

(i) *Excitonic case* $f_x = 1$
In this category BaF_2, $LaCl_3$:Ce and GSO:Ce are considered to belong. In Fig. 6.9a, the absolute yield Y_{abs} (6.47) is plotted as a function of the incident energy in BaF_2 for four increasing values of the bimolecular excitonic quenching rate K_{2x} and in Fig. 6.9b is shown the corresponding relative yield $Y_{R.}$(6.48). The starting value of K_{2x} is 2×10^{-17} m^3/s taken from Table 6.1. The absolute yield Y_{abs} (Fig. 6.9a) illustrates very clearly that the nonproportionality becomes worse by increasing the quenching rate K_{2x} which is not so obvious from the relative yield plotted in Fig. 6.9b. The reason is that the absolute yield decreases as K_{2x} increases but not so clearly does the relative yield. As K_{2x} increases from 2×10^{-17} to 2×10^{-14} m^3/s the absolute yield reduces drastically for energy E $<10^4$ keV. As the relative yield is a ratio one finds that it becomes very high at $K_{2x} = 10^{-14}$ m^3/s because the absolute yield at 662 keV is nearly zero which appears in the denominator of Y_R. From this point of view, the relative yield may not show meaningful results in all ranges.

The influences of decreasing the bimolecular excitonic quenching rate K_{2x} on the absolute and relative yields for BaF_2 are shown in Fig. 6.10a, b, respectively. It is obvious from Fig. 6.10a, b that both the absolute and relative yields show no change by lowering K_{2x} for $E > 10^3$ keV. Although both yields are nonproprtional in the lower energy range E <100 keV they are only a little affected by decreasing the rate of bimolecular quenching. Therefore, the lower bimolecular quenching rate is good for getting the proportional light yield.

(ii) *Mixed* ($f_x = 0.5$) *and Non-Excitonic scintillators* ($f_x = 0$)
One of the most studied and used inorganic scintillators is NaI:Tl. Here two cases are presented for NaI:Tl with $f_x = 0$ and 0.5. The case of $f_x = 0.5$ means that

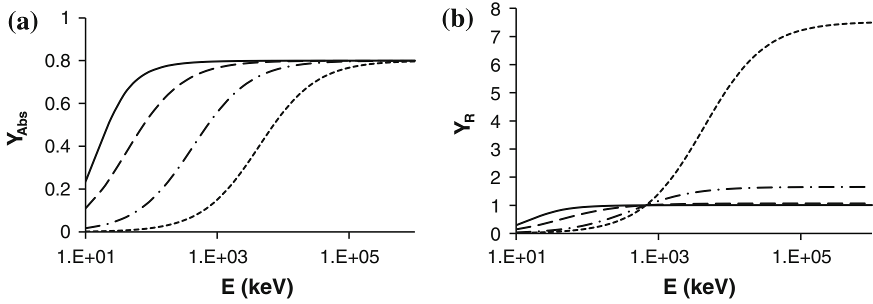

Fig. 6.9 **a** The absolute yield Y_{abs} (6.46) and **b** relative yield Y_R (6.47) plotted as a function of the incident energy for four increasing values of the bimolecular excitonic quenching rate K_{2x} at (——) 2×10^{-17} m^3/s, (– –) 2×10^{-16} m^3/s, (– · –) 2×10^{-15} m^3/s and (- - - -) 2×10^{-14} m^3/s

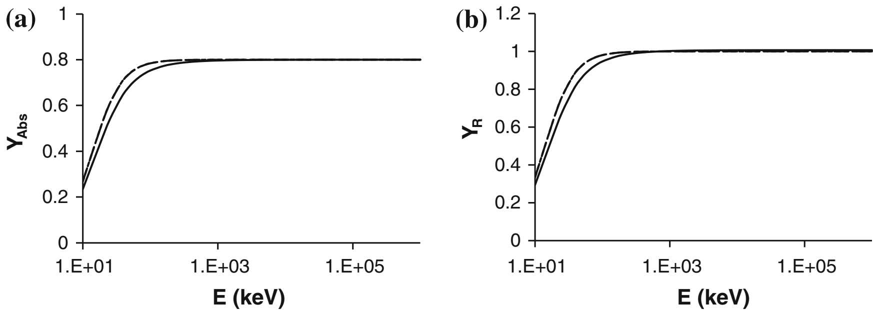

Fig. 6.10 **a** The absolute yield Y_{abs} (6.46) and **b** relative yield Y_R (6.47) are plotted as a function of energy for three decreasing values of the bimolecular excitonic quenching rate K_{2x} = (——) 2×10^{-17} m^3/s, (– –) 2×10^{-19} m^3/s and (- - - -) 2×10^{-23} m^3/s

half of the concentration of excitations in the track is excitons and the other half e–h pairs. The absolute and relative yields for NaI:Tl are shown as a function of Energy in Fig. 6.11a, b, respectively, for three decreasing values of K_{2x}, 2×10^{-17} m^3/s, 2×10^{-19} m^3/s and 2×10^{-23} m^3/s. According to Fig. 6.11a, b, both absolute and relative yields do change a little, particularly in the lower energy range $E < 10^3$ keV where the hump appears and the height of the hump increases when K_{2x} decreases from 2×10^{-17} to 2×10^{-19} m^3/s. However, no further change in the yields appears by lowering K_{2x} further down to 2×10^{-23} m^3/s. A little reduction in the relative yield appears also in the higher energy range. This is apparently due to the fact that the yield at 662 keV becomes slightly higher than that at higher E.

In Fig. 6.12 is shown the absolute yield in NaI:Tl at three increasing values of K_{2x}, 2×10^{-17} m^3/s, then 2×10^{-16} and 2×10^{-15}m^3/s. The relative yield is not shown here for the reason explained above. As the rate of bimolecular quenching increases from 2×10^{-17} to 2×10^{-15} m^3/s the absolute yield reduces nearly to zero in the lower energy range and nonproportionality also extends to energies up to 10^5 keV. These results are similar to those shown in Fig. 6.11a for the excitonic scintillators

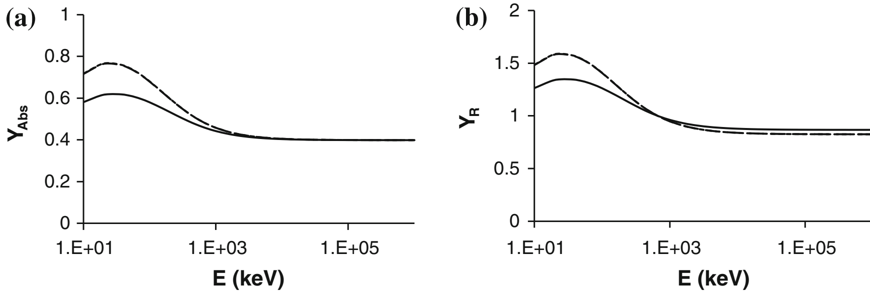

Fig. 6.11 **a** The absolute and **b** relative yields for NaI:Tl as a function of energy E (keV) plotted for three values of K_{2x}, (——)2×10^{-17} m^3/s, (– –) 2×10^{-19} m^3/s and (- - - -) 2×10^{-23} m^3/s

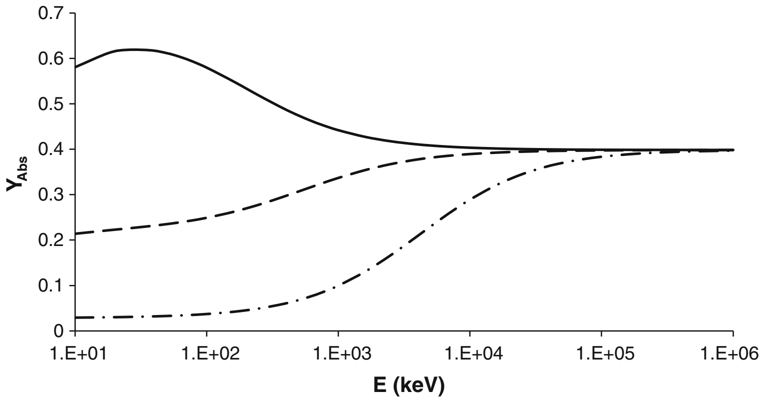

Fig. 6.12 The absolute yield as a function of energy is plotted in NaI:Tl for three values of K_{2x}: (——) 2×10^{-17} m^3/s, (– –) 2×10^{-16} m^3/s and (– · –) 2×10^{-15} m^3/s

except that the magnitude of the absolute yield is nearly half here and no hump is found in the lower energy range in the excitonic semiconductors.

The influence of the magnitude of the e–h pair bimolecular quenching rate K_{2eh} on the absolute and relative yields of NaI:Tl is found to be silimar to the results presented in Figs. 6.11 and 6.12. This is expected because at $f_x = 0.5$ the excitonic concentration is equal to the e–h pair concentration.

Now the results for NaI:Tl at $f_x = 0$ (nonexcitonic case) are presented in Fig. 6.13. The absolute light yield is plotted as a function of energy for increasing K_{2eh} values from 3×10^{-18} to 3×10^{-10} m^3/s. The interesting point to note is that as K_{2eh} increases to 3×10^{-10} m^3/s, the absolute yield reduces close to zero at all energies as a result the relative yield does not give meaningful result and hence not shown here. The effect of lowering K_{2eh} from 3×10^{-18} to 3×10^{-23} m^3/s (not shown here) raises only the peak of the hump from 0.65 to 0.7 in the absolute yield without much influence on the nonporoprtionality.

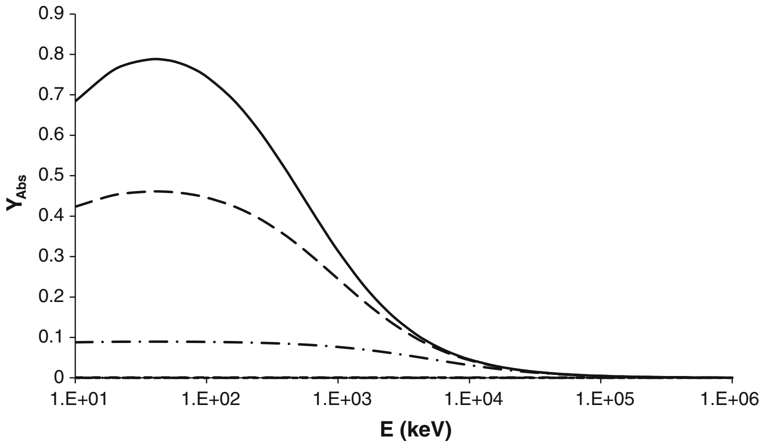

Fig. 6.13 The absolute yield in NaI:Tl at $f_x = 0$ plotted as a function of energy for six increasing values of K_{2eh}: (——) 3×10^{-18} m^3/s, (– –) 3×10^{-17} m^3/s, (– · –) 3×10^{-16} m^3/s, (- - -) 3×10^{-14} m^3/s, (– · · –) 3×10^{-13} m^3/s and (- - - -) 3×10^{-10} m^3/s

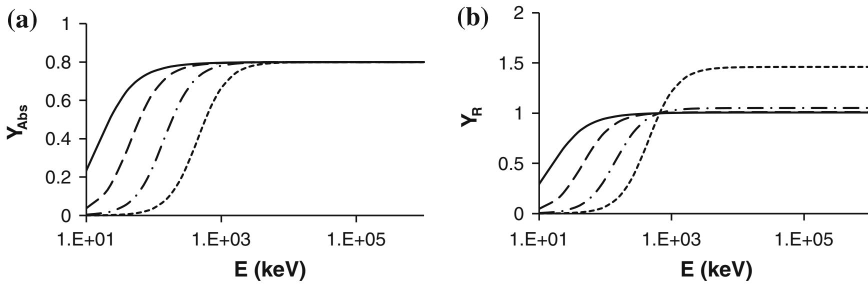

Fig. 6.14 **a** The absolute and **b** relative yields in BaF_2 plotted as a function of energy for four increasing values of the Auger rate of excitonic quenching at K_{3x} = (——) 1×10^{-41} m^6/s, (– –) 1×10^{-40} m^6/s, (– · –) 1×10^{-39} m^6/s and (- - - -) 1×10^{-38} m^6/s

6.3.5 Dependence of Yield on Auger Quenching Rates (K_{3x}, K_{3eh})

(i) *Excitonic scintillators* ($f_x = 1$)
In Fig. 6.14a, b are shown the absolute and relative yields, respectively, in BaF_2 as a function of energy for four increasing values of K_{3x} from 10^{-41} to 10^{-38} m^6/s. The absolute yield decreases nearly to zero at lower energies $E < 10^2$ keV as the Auger quenching rate increases which is not reflected so well in the relative yield because of the ratio as explained above. The nonproportionality in the absolute yield which occurs only in the lower energy range $E < 10^2$ keV at $K_{3x} = 1 \times 10^{-41}$ m^6/s stretches to higher energies $E < 10^4$ keV at $K_{3x} = 1 \times 10^{-38}$ m^6/s.

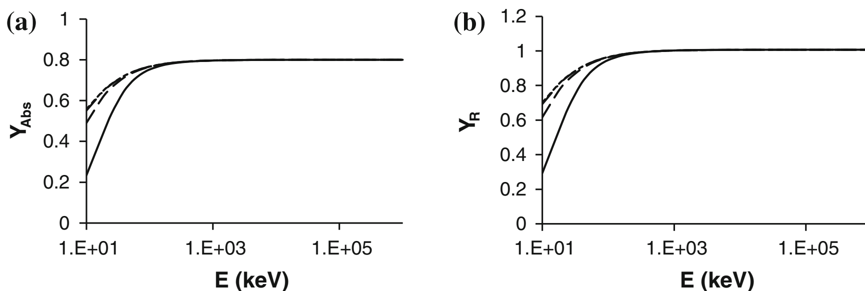

Fig. 6.15 **a** The absolute and **b** relative yields in BaF_2 plotted as a function of energy for four decreasing values of the excitonic Auger quenching rate K_{3x} at (——) 1×10^{-41} m^6/s, (– –) 1×10^{-42} m^6/s, (– · –) 1×10^{-43} m^6/s and (- - - -) 1×10^{-44} m^6/s

In Fig. 6.15a, b are presented the absolute and relative yields, respectively, for BaF_2 as a function of energy for four decreasing values of the excitonic Auger quenching rate from 1×10^{-41} to 1×10^{-44} m^6/s. Both the yields exhibit higher proportionality, stretching down to much lower energy range $E < 20$ keV as K_{3x} decreases. This is a clear illustration of the fact that materials with slower Auger quenching processes will exhibit higher proportionality. Similar results are obtained for GSO:Ce and $LaCl_3$:Ce as well.

(ii) *Mixed* ($f_x = 0.5$) *and Non-Excitonic scintillators* ($f_x = 0$)
The effect of the Auger quenching rate K_{3x} on the yields for $f_x = 0.5$ in NaI:Tl is similar to that in excitonic scintillators. The yield reduces and nonproportionality stretches to higher energy range if the magnitude of K_{3x} increases but the yield does not change much if it decreases.

The influence of the Auger quenching rate K_{3eh} on the yield for $f_x = 0$ in NaI:Tl is that the hump disappears when K_{3eh} decreases from 1×10^{-41} to 1×10^{-44} m^6/s and the absolute yield starts reducing slowly at very low energies and then reduces drastically starting at an energy of 10^2 keV to nearly zero at 10^4 keV. On the other hand if one increases K_{3eh} from 1×10^{-41} m^6/s the hump shifts to the higher energy and the absolute yield reduces to zero at 1×10^{-37} m^6/s.

6.3.6 Dependence of Yield on Track Radius r

The yield in (6.47) depends on Q, which has the dimensions of energy and it depends on the track radius as r^{-2}. Thus the yield is more sensitive to the track radius than to the rates of linear and non-linear excitonic processes presented above. In this section, we study the dependence of yields on the track radius in detail.

For the excitonic scintillators with $f_x = 1$, the influence of the track radius r on the absolute and relative yields in BaF_2 are shown in Figs. 6.16 and 6.17. In Fig. 6.16a, b, are shown absolute and relative yields, respectively, as a function of energy at four

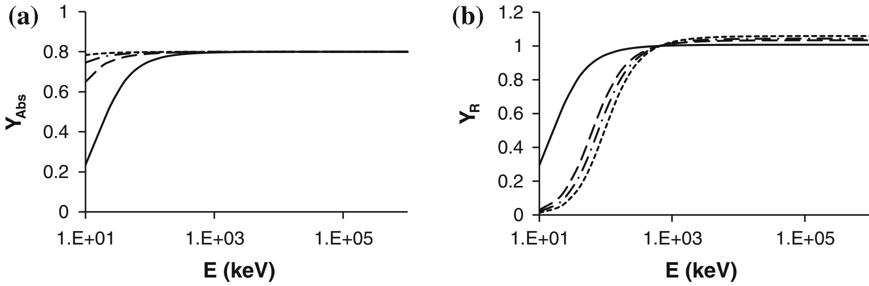

Fig. 6.16 **a** The absolute and **b** relative yields in BaF_2 plotted as a function of energy for four decreasing values of the track radius r = (——) 2 nm, (– –) 1.0 nm, (– · –) 0.9 nm and (- - - -) 0.8 nm

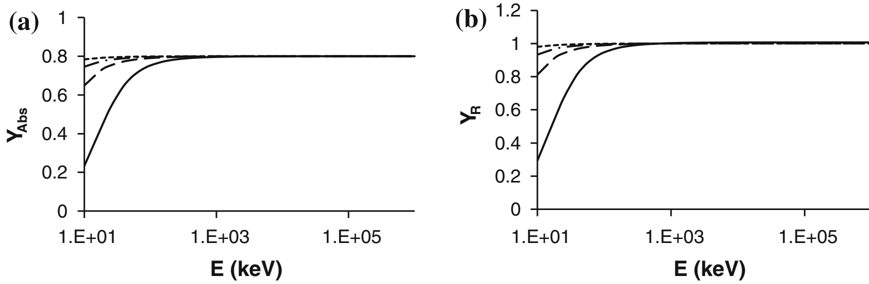

Fig. 6.17 **a** The absolute and **b** relative yields in BaF_2 as a function of energy plotted for four increasing values of r = (——) 2nm, (– –) 4nm, (– · –) 6 nm and (- - - -) 10 nm

different decreasing values of r starting from 2 nm (see Table 6.1) to 1 nm, 0.9 and 0.8 nm. At 2 nm the nonproportionality is confined to energies $E < 100$ keV, which becomes worse as the radius decreases and it stretches to higher $E < 10^3$ keV for $r = 0.8$ nm and also both the as well. This is the common behavior for all excitonic scintillators.

For the case of mixed and non-excitonic scintillator we will study here again NaI:Tl.

In Fig. 6.18, the yield is plotted for $f_x = 0.5$ as a function of the incident energy at different decreasing values of the track radius starting from 6 nm (the value given in Table 6.1) and decreasing down to 0.8 nm. The hump in the absolute yield that appears at $E = 10^2$ keV, $K_{2eh} = 3 \times 10^{-18}$ m^3/s and $r = 6$ nm, shifts to higher energy and appears at $E = 10^4$ keV when r reduces to 0.8 nm. The nonproportionality becomes worse by reducing the size of the track radius. The effect reverses, however, when the radius increases as shown in Fig. 6.19. The hump shifts to lower energy at 50 keV at $r = 10$ nm. The yield becomes nearly proportional after the hump and the hump nearly disappears and yield becomes proportional at all energies when track radius size expands to 80 nm. However, no apparent influence of increasing track radius appears in improving the nonproportionality in non-excitonic ($f_x = 0$) scintillators as shown in Fig. 6.20. At a track radius smaller than 6 nm, which is used for NaI:Tl

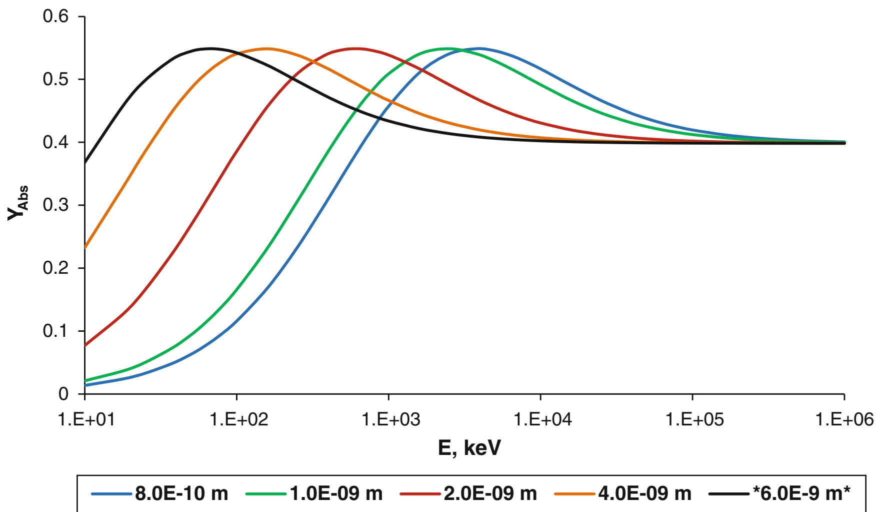

Fig. 6.18 The dependence of Y_{Abs} (6.46) on the incident energy at $f_x = 0.5$ (mixed case) and decreasing track radius *r* (m) from 6 nm (Table 6.1) for NaI:Tl

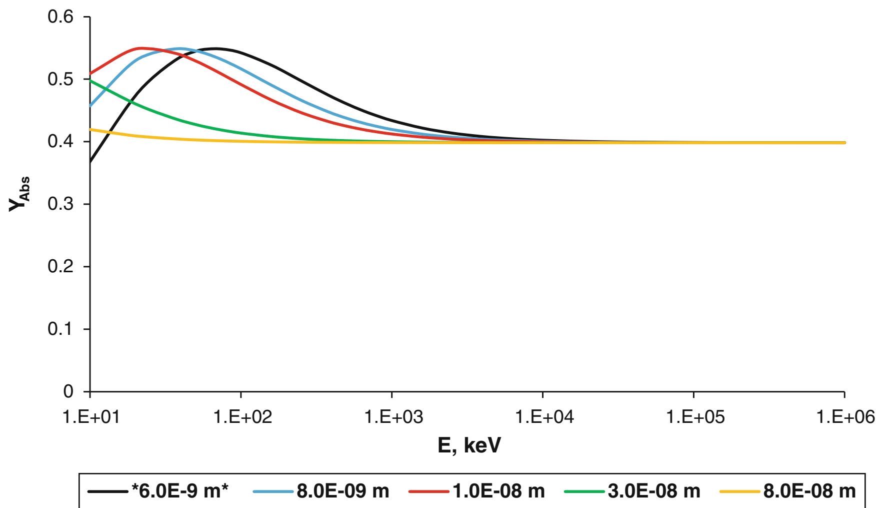

Fig. 6.19 The dependence of Y_{Abs} on the incident energy at $f(x) = 0.5$ and increasing value of the track radius from 6 nm (Table 6.1) for NaI:Tl

(see Table 6.1), a hump peak appears but as the radius becomes larger the absolute yield starts decreasing and reduces to zero. No sign of proportionality is apparent in this case at larger track radius (Fig. 6.20).

6.4 Discussions on Nonproportionality (NPR) in the Yield

In the previous section we have considered the dependence of scintillator light yield on various material parameters, which include the fractional excitonic concentration f_x within the track, linear radiative rates R_1, bimolecular quenching rates K_2, Auger quenching rates K_3 and the radius of the track. Let us analyze these results with a view to eliminate/reduce nonproportionality in the scintillator yield.

The electron track is formed when a γ-photon is absorbed in a scintillating crystal within a very short time frame; i.e. femtoseconds. The track contains very high density excitations, and if these excitations are not destroyed/quenched non radiatively, all of them recombine radiatively by emitting photons then there will be no energy loss. Such scintillators will not exhibit any nonproportionality in their yields. In a high excitation density situation, both excitons and e–h pairs (not bound as excitons) are excited in the track but non-radiatively they can recombine and excitons can be dissociated into e–h pairs to get quenched nonradiatively. These radiative and nonradiative processes occurring within the track have already been presented in Fig. 6.2.

6.4.1 *Influence of R_{1x} on NPR*

According to Fig. 6.4, the light yield reduces to zero if the rate R_{1x} reduces below 10^6 s^{-1} but becomes constant at 1 if $R_{1x} \geq 10^{10}$ s^{-1}. A constant yield means the yield becomes proportional and under this condition a scintillator will have no NPR and hence have optimal energy resolution [7, 38–42]. The measured values of the radiative rate R_{1x} in the four scintillators are 4.7×10^6 s^{-1} in NaI:Tl, 1.6×10^9 s^{-1} in BaF_2, and 3×10^7 s^{-1} in GSO:Ce and $LaCl_3$:Ce [7]. According to this BaF_2 is close to be a proportional scintillator. This, of course, neglects the influence of slow excitonic luminescence in the scintillation response [43].

In Fig. 6.5 is plotted the yield in all four scintillators for $f_x = 1$ at $E = 662$ keV as a function of the linear exciton quenching rate K_{1x} (s^{-1}) keeping other parameters constant. Accordingly, the yield remains proportional in BaF_2 if $K_{1x} \leq 10^7$ s^{-1}, in GSO:Ce and $CaCl_3$:Ce if $K_{1x} < 10^6$ s^{-1} and in NaI:Tl no proportionality is apparent down to $K_{1x} < 5 \times 10^4$ s^{-1}. It should be noted here that for the excitonic case with $f_x = 1$, the linear e–h pair rates, R_{1eh} and K_{1eh}, do not contribute to the yield. Accordingly, a proportional yield requires $R_{1x} > 3 \times 10^7$ s^{-1} and higher rate of radiatve recombination implies strong Coulomb interaction between the excited e–h pairs which also implies strong tendency to form excitons because the formation of excitons also depends on binding energy between the excited e–h pairs; stronger the binding energy more probability of forming excitons. Does this mean that if the electron track is occupied by more excitons than e–h pairs, will the yield be more proportional? This is examined below.

6.4.2 Influence of Ratio of Concentrations f_x

Considering the results of yields presented for $f_x = 1$, which means only excitons are excited within the track, in Figs. 6.4, 6.5, 6.9, 6.10, 6.14, 6.15, 6.16 and 6.17, the absolute yield starts at a very low value at the lowest energy, then rises to a maximum of about 80 % and remains proportional (constant) after that in the higher energy range. Thus, the nonproportionality occurs only in the lower energy range. Although a similar behavior in the absolute light yield is found when f_x reduces to 0.5, its proportional value in the higher energy range reduces to nearly half of that found at $f_x = 1$.

For $f_x = 0$, when only e–h pairs are created in the electron track initiated by a gamma ray, the proportionality in the absolute light yield disappears even from the higher energy range. The absolute light yield starts from a very low value and rises to a maximum and then reduces to zero in the higher energy range (see Fig. 6.13). This analysis concludes that scintillators which favour the formation of excitons can have more proportional light yield in comparison with those which do not [18, 38–42]. The formation of excitons in the beginning of the electron track within femto- to pico- seconds and continuing until the whole energy has been deposited depends on: (1) high density situation should be relieved so that nonlinear bimolecular and Auger quenching processes cannot be activated and (2) excitons should not dissociate which requires the excited e and h with an exciton should move together as an exciton. This requires that the electron and hole mobilities should nearly be the same to retain excitonic population as long as possible within the track. For relieving the high density situation from the track, one requires to move the excited e–h in the radial directions as soon as possible. This implies that both electron and hole mobilities is a scintillator should be very high [38–40]. More on the mobility of charge carriers in scintillators will be discussed below in analysing the influence of the track radius on NPR. Here, let us first summarise the influence bimolecular and Auger quenching processes.

6.4.3 Influence of Bimolecular Quenching

For excitonic scintillators, the nonproportionality in yield becomes worse if K_{2x} increases (Fig. 6.9) but it only makes a little difference in the behavior of the light yield (Fig. 6.10) if it decreases to 2×10^{-19} m^3/s. Firstly, this implies that this may be the maximum value of K_{2x} for BaF_2, GSO:Ce and $LaCl_3$:Ce scintillators to confine nonproportionality only in the low energy range E $<$100 keV. And secondly, any faster bimolecular quenching processes will reduce the number of excitations from the track much faster than the rate of recombination which contributes to the light yield and hence reduces it. It may be noted that K_{2eh} has no influence on the light yield of excitonic scintillators.

For mixed scintillators ($f_x = 0.5$), both K_{2x} and K_{2eh} influence the light yield in the same way. When they increase the light yield reduces and nonproportionality stretches to higher energy range (Fig. 6.12). However, as it can be seen in Fig. 6.11a, $K_{2x} = 2 \times 10^{-17}$ m^3/s is not the lowest value to give the highest yield particularly at the hump and 2×10^{-19} m^3/s will be a better choice. Whether the bimolecular rate constant can be altered through altering constituents of a scintillator is not yet understood at all.

In the case of non-excitonic scintillators with $f_x = 0$, as the absolute yield presented in Fig. 6.13 for NaI:Tl, it is found that it becomes worse when K_{2eh} increases above 3×10^{-18} m^3/s. Here again one gets slightly better yield at the hump if K_{2eh} decreases to 3×10^{-19} m^3/s (not shown here). K_{2x} does not play any role in the light yield of this class of scintillators.

6.4.4 Influence of Auger Quenching

Influence of the Auger quenching rate on the light yield is very similar to that of bimolecular quenching for excitonic scintillators (Fig. 6.14a). The absolute yield reduces as K_{3x} increases and the nonproportionality stretches to higher energies. In these scintillators apparently the maximum value of $K_{3x} = 3 \times 10^{-41}$ m^6/s confines the nonproportionality only to lower energies $E < 100$ keV. The nonproportionality becomes worse and stretches to higher energies if K_{3x} increases.

However, if the Auger excitonic quenching rate decreases to 10^{-44} m^6/s the yield becomes proportional down to much lower energies $E < 20$ keV (Fig. 6.15a). This is an interesting result to prove directly that the lower Auger exciton quenching rate in a scintillator produces better proportionality in the light yield.

In mixed scintillators with $f_x = 0.5$, e.g., the yield calculated for NaI:Tl, the hump disappears and the nonproportionality in the absolute yield stretches from an energy 10^3 keV to higher energies up to 10^4 keV as K_{3x} increases from 10^{-41} to 10^{-38} m^6/s. By decreasing K_{3x} from 10^{-41} to 10^{-44} m^6/s, although the nonproportionality remains unaffected a little rise in the yield of the hump appears. For $f_x = 0.5$, a very similar influence of the e–h pair Auger quenching rate K_{3eh} is found on the absolute yield. This is expected as both concentrations are equal in the track. However, how to alter the Auger quenching rate of a scintillator has not been attempted yet to the best of our knowledge.

6.4.5 Influence of Track Radius

As the excitation concentration n depends on the radius of the electron track as r^{-2} (6.43) it influences the light yield in a very sensitive way. For the excitonic scintillator ($f_x = 1$) BaF_2 both absolute and relative light yields (Fig. 6.17) become nearly perfectly proportional in all the energy range considered here as r increases

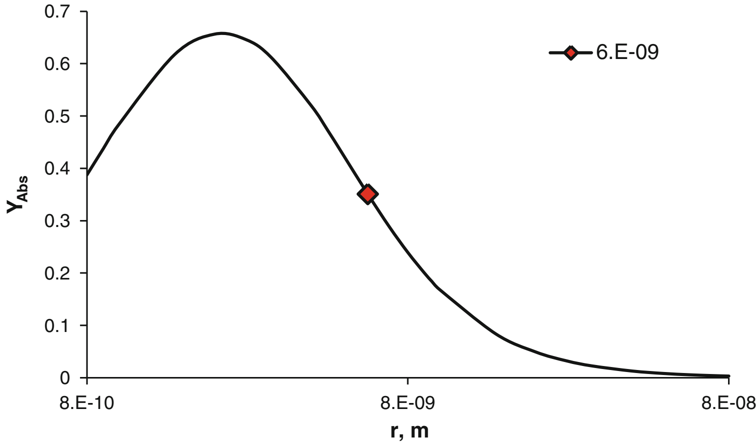

Fig. 6.20 Absolute yield calculated from (6.47) for NaI:Tl at $f_x = 0$ is plotted as function of the track radius at an energy 662 keV. Although the height of the hump increases with increasing track radius, the NPR does not seem to improve

from 2 to 10 nm. The similar behavior is found in the absolute light yield of mixed scintillators ($f_x = 0.5$), e.g., NaI.Tl which shows nearly perfect proportionality in the light yield when r increases from 6 to 80 nm. However, no apparent influence of increasing track radius appears in improving the nonproportionality in non-excitonic scintillators (see Fig. 6.20).

A bigger track radius may be interpreted as the faster diffusion of the excitations (excitons and e–h pairs) along the radial directions away from the central axis in a cylindrical electron track. As the mobility μ and diffusion coefficient D are related by the Einstein formula $\mu = eD/k_BT$, a faster diffusion means higher mobility of the excited charge carriers in the radial directions in such a way that the most concentration remains as excitons. As mentioned above, this means that e–h pairs must remain bound as excitons even if the track has expanded radially due to the faster lateral diffusion. This implies that the mobility of electrons and holes must be high as well as equal ($\mu_e \approx \mu_h$).The results of this analysis agree qualitatively but quite well with those by Williams and colleagues recently in a few publications [44, 45] and by Setyawan [46]. The nonproportionality becomes worse when the radius decreases. This means that the excitation density becomes very high in the track due to the squeeze in its radius and nonlinear quenching processes become very efficient.

For a quantitative estimate using (6.1) for $LaCl_3$:Ce from our calculation, we find $R_{npr} = 1.47\,\%$ at r= 10 nm at an energy $E = 662$ keV, and $R_M = 1.2\,\%$ [15]. The measured energy resolution at 662 keV in $LaCl_3$:Ce is reported to be 3.3 and 4.4 % [47]. Using these in (6.1) we get $R_{inh}^2 + R_p^2 \approx (2.7\,\%)^2$ and $(3.7\,\%)^2$ at $R = 3.3$ and 4.4 %, respectively. A value of 1.4 % is very reasonable considering the uncertainty

in the rates used and approximations involved. However, at $r = 4$ nm when we get $R_{npr} = 7.4\,\%$, we do not get any meaningful result for $R_{inh}^2 + R_p^2$ from (6.1).

The analysis of the yield presented here applies to the carrier diffusion in the thermal equilibrium relevant in the time scale of 20 ps to 1 femtosecond (fm). It may not be applicable to plasma excitations [48, 49] created in the track initially within fs time scale. However, Vasile'v has studied features of plasma excitations recently [7].

6.4.6 Influence of Evolution of Excitonic Concentration Within the Electron Track

The evolution of excitons and e–h pairs within the electron track created by 1 keV electron in the BaF_2 scintillator has been studied by Vasile'ev [50]. Accordingly, he has calculated the exciton population to be about 1.5 % at a time of 0.04 fs (initial $t = 0$) and then to 3 % after about 100 fs. This implies that initially excitations in the track consist of free pairs of charge carriers e and h, which relax to exciton states with time.

Recently, the influence of the rate of conversion of e–h pairs into excitons (γ_{ex}) on the scintillators yield has been studied in the four scintillators considered here [51]; how fast the conversion from free charge carriers to excitons should take place to minimize the nonproportionality.

In Table 6.1, the rates of conversion of e–h pairs into excitons (γ_{ex}) and vice versa (γ_{xe}) are assumed to be zero. Here we are going to study the influence of changing the e–h pair concentration into exciton concentration within the track with a non-zero rate after the initial time t = 0, when the excitonic concentration is assumed to be 50 % ($f_x = 0.5$). The absolute yield at γ_{ex}= 0 as a function of energy calculated from (6.47) for the rates given in Table 6.1 for the four scintillators is shown in Fig. 6.21. The yield Y_{abs} plotted in Fig. 6.21 first shows the part of a hump from 10 to 100 keV and then becomes nearly proportional at higher energies. However, it becomes less than 40 % over higher energies.

This is expected as the excitonic population is only 50 % and it is constant without any conversion from free e–h pairs to excitons. In Fig. 6.22 are shown the yields at three non-zero values of the rate of conversion from e–h pairs to excitons $\gamma_{ex} = 10^6$ s^{-1}, 10^7 s^{-1}, and 10^9 s^{-1}. For $\gamma_{ex} = 10^6$ s^{-1} (exciton formation time $\tau_F = \gamma_{ex}^{-1} = 1$ μs) the absolute yield (Fig. 6.22a) changes significantly in all energy ranges. At the lowest energy, 10 keV, the yield reduces and this reduction is significant for NaI:Tl from 60 to 46 % but for the other three scintillators the reduction is relatively small. In the higher energy range $\geq 10^3$ keV, the yield increases for all the scintillators. This effect is particularly significant for NaI:Tl, which become nearly proportional in the energy range 10–10^3 keV. However, when the exchange rate γ_{ex} is increased to 10^7 s^{-1}, as shown in Fig. 6.22b, the yield in all the scintillators, except BaF_2, decreases significantly at 10 keV but in the higher energy range it increases in all the scintillators. At an energy of 10^3 keV, the yield increases to 60 % for NaI:Tl,

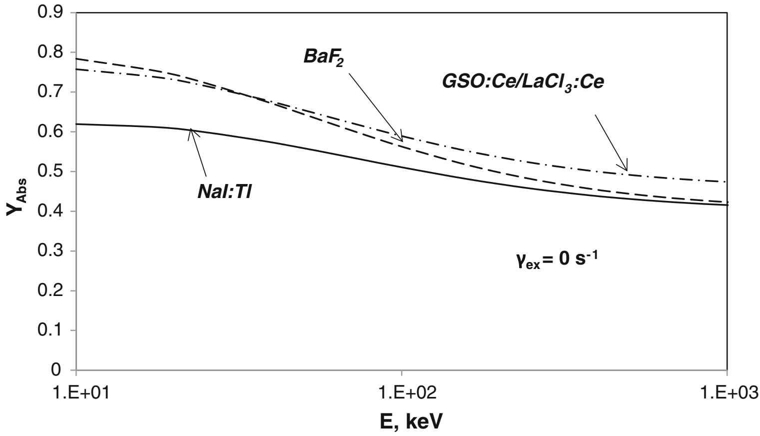

Fig. 6.21 The yield in (6.47) is plotted as a function of the incident energy for $f_{ex} = 0.5$ and $\gamma_{ex} = 0$ for the four scintillators: NaI:Tl (*solid line*), BaF_2 (*dashed line*) and GSO:CE and $LaCl_3$:Ce (*dashed-dotted line*)

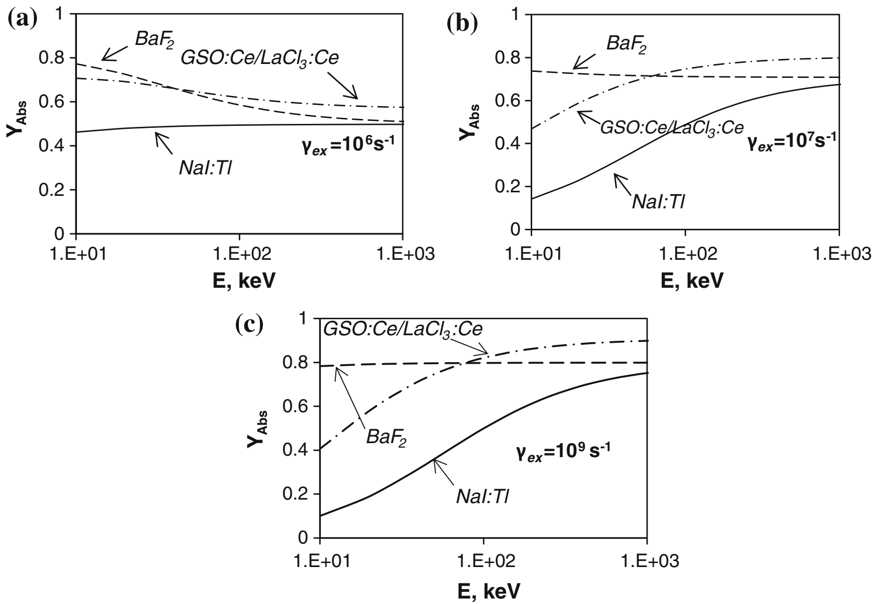

Fig. 6.22 The yield in (6.47) is plotted as a function of the incident energy for $f_{ex} = 0.5$ and **a** $\gamma_{ex} = 10^6$ s^{-1}, **b** $\gamma_{ex} = 10^7$ s^{-1}, **c** $\gamma_{ex} = 10^9$ s^{-1}for the four scintillators: NaI:Tl (*solid line*), BaF_2 (*dashed line*) and GSO:CE and $LaCl_3$:Ce (*dashed-dotted line*)

75 % to BaF_2 and 80 % to $LaCl_3$:Ce and GSO. At this value of the exchange rate BaF_2 becomes proportional in all the energy range but the other three scintillators become proportional only for energies $\geq 10^3$ keV. In Fig. 6.22c, the absolute yield is plotted at the exchange rate $\gamma_{ex} = 10^9$ s^{-1}. In this case, the yield of BaF_2 increases

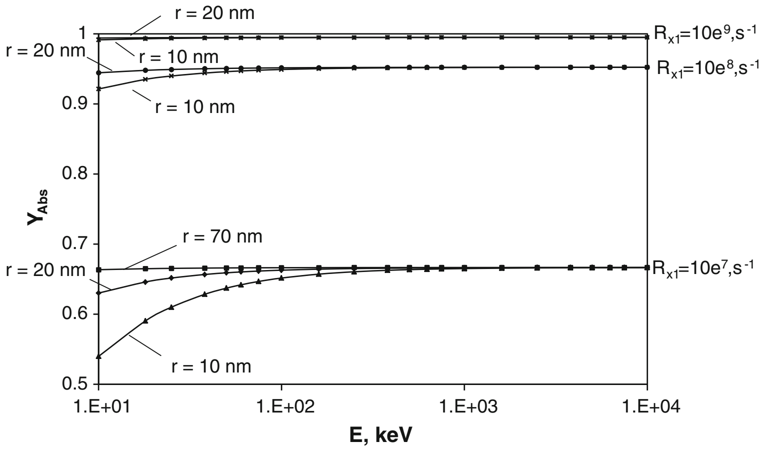

Fig. 6.23 Light yield of (6.47) is plotted for $f_x = 1$ as a function of energy E (keV) as a function of linear e–h quenching rate R_{1x} (s^{-1}) for the four scintillators, NaI:Tl, BaF_2, GSO:Ce and $LaCl_3$:Ce

nearly to 80 % at the lowest energy of 10 keV and remains proportional in the whole energy range. However, the yields of the other three scintillators reduce even further at energy 10 keV. In the higher energy range, the yields of other three scintillators increase a little and remain proportional. However, a conversion rate faster than 10^9 s^{-1}, e.g., 10^{10} s^{-1} shows little change in the absolute yield in the whole energy range and therefore not shown here. In a very short time range of 10–100 fs after the incidence of a photon, although most of the excitations consist of free e—h pairs in accordance with the simulation study on BaF_2 by Vasil'ev [50] after that how the excitation density evolves depends on the property of the material. If the exciton formation time is in the range of ns or less ($\gamma_{ex} \geq 10^9\ s^{-1}$), the yield gets enhanced and in BaF_2 it becomes proportional in the whole energy range. This outstanding behavior of BaF_2 is apparently due to the fact that the first order radiative rate of excitonic recombination $R_{1x} = 10^9$ s^{-1} in BaF_2, nearly two orders of magnitude higher than in $LaCl_3$:Ce and about three orders of magnitude higher than in NaI:Tl (see table). For a formation time slower than 10^{-7} s (Fig. 6.22a) the yield becomes nonproportional and a hump starts appearing in the lower energy range as it can be seen in Fig. 6.21 with $\gamma_{ex} = 0$.

In a scintillator where the exciton formation time is in the ns range or less, it will have enhanced proportionality in its yield [51, 52]. An exciton formation time in ps range involves relaxation of free e–h pairs to excitons by emission of optical phonons [52]. The exciton formation time in the ns range is usually due to emission of acoustic phonons as found in NaI:Tl. The present results suggest that an exciton formation time ps $\leq \tau_F \leq$ ns is expected to lead to more proportional scintillators. This also implies that for finding a scintillator with proportionality in its yield it is desirable to have dominantly excitonic concentration within the track, as discussed above.

Table 6.2 Required magnitude of various parameters for fabricating an optimally proportional inorganic scintillator with optimal energy resolution

Parameters	Required magnitude
Linear excitonic radiative emission	$R_{1ex} > 10^7\ \mathrm{s}^{-1}$
Linear exciton quenching	$K_{1ex} \leq 10^6\ \mathrm{s}^{-1}$
Exciton formation time τ_F	$\tau_F \leq$ ns
Excitation concentration in the track	Mostly excitonic $f_{ex} = 1$ [38, 42]
Excitonic bimolecular rate of quenching	$K_{2ex} \leq 2 \times 10^{-17} \mathrm{m}^3/\mathrm{s}$ [38, 42]
Electron-hole bimolecular rate of quenching	$K_{2eh} \leq 3 \times 10^{-18} \mathrm{m}^3/\mathrm{s}$ [38, 42]
Auger rate of quenching	K_{3ex} or $K_{3eh} \leq 10^{-41} \mathrm{m}^6/\mathrm{s}$ [38, 42]
Track radius	$r \geq 70$ nm (requires high mobility of charge carriers with condition $\mu_e \approx \mu_h$) [38, 42]

6.5 Achieving Optimal Proportionality in a Scintillator

On the basis of the results of various dependences on the scintillator yield presented in this chapter, it may be possible to predict under what conditions one can achieve a scintillator free from any nonproportionality.

Considering the yield as a function of nonlinear quenching rates and radius of the track, a scintillator with optimal proportionality or minimal nonproportionality (NPR) should have the properties as summarised in Table 6.2. For maintaining the excitation concentration dominantly excitonic, it is important that mobility of electrons and that of holes be equal otherwise excitons may dissociate into free e–h pairs. Why is the dominant excitonic concentration good for minimizing NPR? This may be explained rather easily because the formation of excitons depends on the Coulomb interaction between the excited free e and h.

That means a strong binding energy between e and h will form excitons faster and these excitons will not dissociate easily and hence will lead to dominant excitonic concentration within the track. At the same time, the radiative recombination of the excited e–h pairs also occurs due to the Coulomb interaction leading to a higher oscillator strength. Accordingly formation of excitons first makes a free e–h pair one step closer to the radiative recombination and hence it enhances it.

In Fig. 6.23, the yield in (6.47) is plotted as a function of energy using the recommended values of parameters in Table 6.2 for three sizes of track radius, $r = 10$ nm, 20 nm and 70 nm and three values of $R_{1x} = 10^7\ \mathrm{s}^{-1}$, $10^8\ \mathrm{s}^{-1}$ and $10^9\ \mathrm{s}^{-1}$. As it can be seen from Fig. 6.23, at $R_{1x} = 10^7\ \mathrm{s}^{-1}$ the yield becomes perfectly proportional only when the track radius is 70 nm wide. However, although the yield is proportional the yield intensity remains only about 65 %. If the radiative rate $R_{1x} = 10^8\ \mathrm{s}^{-1}$ then a scintillator becomes optimally proportional for the track radius size $r > 20$ nm and also for $R_{1x} = 10^9\ \mathrm{s}^{-1}$ a scintillator becomes perfectly proportional at $r \geq 20$ nm. However, the yield intensity remains 95 % at $R_{1x} = 10^8\ \mathrm{s}^{-1}$ which becomes 100 % at $R_{1x} \geq 10^9\ \mathrm{s}^{-1}$. Accordingly, for the highest proportional yield a scintillator should have $R_{1x} \geq 10^9\ \mathrm{s}^{-1}$ and $r \geq 20$ nm. It is interesting to note that at $R_{1x} > 10^9\ \mathrm{s}^{-1}$ the radiative emission is very fast and may eliminate

the occurrence of some of the nonlinear quenching processes as well. Thus, the nonproportionality can be minimised either by enhancing the emission rate R_{1x} or by reducing the quenching rates K_{1x}, K_{2x} and K_{3x}. The dependence of the nonlinear quenching rates K_{2x} and K_{3x} on the material parameters is not well understood yet however R_{1x} has been derived [41].

6.6 Conclusions

Our analysis of the dependence of light yield on the fractional excitonic concentration f_x present in the electron track initiated by a gamma ray in a scintillator, the bimolecular (K_{2x} and K_{2eh}) and Auger quenching (K_{3x} and K_{3eh}) rates and the size of the radius r the following conclusions can be drawn: The nonproportionality can be minimized if:

(i) The fractional excitonic conecentration can be maintained at $f_x \approx 1$.
(ii) Bimolecular and Auger rates of quenching should be as small as possible.
(iii) The radius of the track should expand at faster rate than the decay of excitations due to nonlinear quenching.
(iv) and (iii) can be achieved if the mobility of the charge carriers is high and equal, i.e., $\mu_e \approx \mu_h$.
(v) An exciton formation time $\tau_F \leq 1$ ns is required.

References

1. W.W. Moses, S.E. Derenzo, T.F. Budinger, Nucl. Instrum. Methods in Phys. Res. A **353**, 189 (1994)
2. W.W. Moses, V. Gayshan, A. Gektin, *In Radiation Detectors for Medical Applications*, ed. by S. Taverner, et al. (Springer, Berlin, 2006), pp. 37
3. E.R. Siciliano, J.H. Ely, R.T. Kouzes, B.D. Milbrath, J.E. Scheppe, M. Globus, Nucl. Instrum. Method. Phys. Res. A **550**, 647 (2005)
4. M. Globus, B. Grinyov, J.K. Kim, *Inorganic Scintillators for Modern and Traditional Applications* (Institute for single crystals, Kharkov, Ukraine, 2005)
5. P.J. Roach, D.L. Bailey, Int. Med. J. **35**, 577 (2005)
6. D. Engelkemeir, Rev. Sci. Instrum. **27**, 589 (1956)
7. G.E. Bizarri, W.W. Moses, J. Singh, A.N. Vasile'v, R.T. Williams, J. Appl. Phys. **105**, 044507 (2009)
8. R.B. Murray, A. Meyer, Phys. Rev. **122**, 815 (1961)
9. P.A. Rodnyi, P. Dorenbos, C.W.E. van Eijk, Phys. Stat. Solidi B **187**, 15 (1995)
10. P. Dorenbos, J.T.M. de Haas, C.W.E. van Eijk, IEEE Trans. Nucl. Sci. **42**, 219 (1995)
11. J.D. Valentine, B.D. Rooney, J. Li, IEEE Trans. Nucl. Sci. **45**, 512 (1998)
12. M. Moszynski, A. Nassalski, A. Syntfeld-Kazuch, L. Swiderski, T. Szcesniak, IEEE Trans. Nucl. Sci. **55**, 1062 (2008)
13. I.V. Khodyuk, J.T.M. de Haas, P. Dorenbos, IEEE Trans. Nucl. Sci. **57**, 1175 (2010)
14. W.W. Moses, Nucl. Instrum. Methods Phys. Res. A **487**, 123 (2002)
15. I.V. Khodyuk, P. Dorenbos, Phys. Cond. Matter. **22**, 485402 (2010)

16. J.D. Valentine, B.D. Rooney, P. Dorenbos, IEEE Trans. Nucl. Sci. **45**, 1750 (1998)
17. W.W. Moses, S.A. Payne, W.-S. Choong, G. Hull, B.W. Reutter, IEEE Trans. Nucl. Sci. **55**, 1049 (2008)
18. W.W. Moses, G.A. Bizarri, R.T. Williams, S.A. Payne, A.N. Vasil'ev, J. Singh, Q. Li, J.Q. Grim, W.-S. Choong, IEEE Trans. Ncl. Sci. **59**(5), 2038 (2012)
19. K.S. Shah, Y. Glodo, M. Klugerman, L. Cirignano, W.W. Moses, et al., Nucl. Instr. Meth. A **505**, 76(2003)
20. W. Mengesha, T. Taulbee, B. Rooney, J. Valentine, IEEE Trans. Nucl. Sci. **45**, 456 (1998)
21. K.S. Shah, J. Glodo, M. Klugerman, W.W. Moses, S.E. Derenzo, et al., IEEE Trans. Nucl. Sci. **NS- 50**, 2410 (2003)
22. K.S. Shah, J. Glodo, M. Klugerman, W. Higgins, T. Gupta, et al., IEEE Trans. Nucl. Sci. NS **51** (2004)
23. K.S. Shah, J. Glodo, W. Higgins, E.V.D. van Loef, W.W. Moses et al., IEEE Trans. Nucl. Sci. **52**, 3157 (2005)
24. N.J. Cherepy, G. Hull, A.D. Drobshoff, S.A. Payne, E. van Loef et al., Appl. Phys. Lett. **92**, 083508 (2008)
25. E.D. Bourret-Courchesne, G. Bizarri, S.M. Hanrahan, G. Gundiah, Z. Yan, S.E. Derenzo, Nucl. Instr. Meth. **A-613**, 95 (2010)
26. E.D. Bourret-Courchesne, G. Bizarri, R. Borade, Z. Yan, S.M. Hanrahan, G. Gundiah, A. Chaudhry, A. Canning, S.E. Derenzo, Nucl. Instr. Meth. A- **612**, 138 (2010)
27. P. Bloser, T. Narita, J. Grindlay, K. Shah, Proc. MRS **487**, 153 (1998)
28. J. Singh, *Excitation Energy Transfer Processes in Condensed Matter* (Plenum, N.Y., 1994)
29. G. Bizarri, W.W. Moses, J. Singh, A.N. Vasil'ev, R.T. Williams, Phys. Status. Solidi C **6**, 97 (2009)
30. M. Inokuti, Rev. Mod. Phys. **43**, 297 (1971)
31. R. Mayol, F. Salvat, J. Phys. B: At. Mol. Opt. Phys. **23**, 2117 (1990)
32. J.C. Ashley, J. Electron. Spectrosc. Relat. Phenom. **28**, 177 (1982)
33. J.C. Ashley, J. Electron. Spectrosc. Relat. Phenom. **46**, 199 (1988)
34. D.R. Penn, Phys. Rev. B **35**, 482 (1987)
35. H. Bethe, Ann. Physik. **5**, 325 (1930)
36. G.F. Knoll, *Radiation Detection and Measurement*, 3rd edn. (Wiley, New York, 2005)
37. J.E. Jaffe, Nucl. Instr. and Methods Phys. Res. A **580**, 1378 (2007)
38. J. Singh, A. Koblov, IEEE Trans. Nucl. Sci. **59**, 2045 (2012)
39. The yield has also been expressed as []: $Y_{abs} = \frac{a_1+1.25a_2QE^{-1}}{a_3+1.25a_4QE^{-1}+0.25a_5Q^2E^{-2}}$. Dividing the numerator and denominator by a_3 and then redefining $a_1 = a_1/a_3$, $a_2 = a_2/a_3$, $a_3 = a_4/a_3$ and $a_4 = a_5/a_3$ we get the yield in (6.46) and (6.47)
40. J. Singh, J. Appl. Phys. **110**, 024503 (2011)
41. J. Singh, A. Koblov, Eur. Phys. J. B **86**, 33 (2013). doi:10.1140/epjb/e2012-30693-9
42. J. Singh, A. Koblov, Nucl. Inst. Meth. Phys. Res. A **685**, 25 (2012)
43. P.A. Rodnyi, Rad. Meas. **38**, 343 (2004)
44. R.T. Williams, J.Q. Grim, Q. Li, K.B. Ucer, W.W. Moses, Phys. Stat. Solidi. B, **248**, 426 (2011)
45. Q. Li, J.Q. Grim, R.T. Williams, G. A. Bizarri, W.W. Moses. J. Appl. Phys. **109**, 123716 (2011)
46. W. Setyawan, R.M. Gaume, R.S. Feigelson, S. Curtarolo, IEEE Trans. Nucl. Sci **56**, 2989 (2009)
47. E.V.D. van Loef, W. Mengesha, J.D. Valentine, P. Dorenbos, C.W.E. Van Eijk, IEEE Tran. Nucl. Sci. **50**, 155 (2003)
48. K. Kimura, Nucl. Instrum. Methods Phys. Res. B **116**, 57 (1996)
49. K. Kimura, S. Sharma, A. Popov, Nucl. Instrum. Methods Phys. Res. B **191**, 48 (2002)
50. A.N. Vasil'ev, in *Proceedings of the 8th International Conference on Inorganic Scintillators and their Applications (SCINT 2005)*, ed. by A. Gektin, B. Grinyov (National Academy of Sciences of Ukraine, Kharkov, 2006) pp. 1–6
51. J. Singh, R.T. Williams, A. Koblov, D. Surovtseva, IEEE Trans. Nucl. Sci. **61**, 252 (2014)
52. Q. Li, J. Grim, N.A.W. Holzwarth, R.T. Williams, Presented at SCINT 2013, 15–19 April 2013, Shanghai, China

Chapter 7
Electronic Properties of Noncrystalline Semiconductors

Jai Singh

Abstract The electronic properties of inorganic noncrystalline semiconductors are reviewed in this chapter using the effective mass approach in the real coordinate space. It is shown that many properties that can be studied through the effective mass approximation applied in the reciprocal lattice vector **k**-space in crystalline semiconductors can be studied in noncrystalline semiconductors in the real coordinate **r**-space. The effective masses of electrons and holes are derived in their respective extended and tail states within the real coordinate space. The mechanism of the double sign reversal leading to the anomalous Hall effect observed in hydrogenated amorphous silicon (a-Si:H) has been successfully explained using the theory of effective mass. It is demonstrated that excitons can also be formed in noncrystalline semiconductors and the energy difference between the singlet and triplet exciton energies is larger than in crystalline semiconductors. The application of the new time-dependent exciton-spin-orbit-photon interaction derived recently by the author has been reviewed for harvesting the radiative emission from triplet excitons, where the traditional perturbation approach cannot be applied very successfully.

7.1 Introduction

Amorphous semiconductors, technically known as non-crystalline semiconductors, have become materials of enhanced research interest in the past few decades. Historically most semiconductor devices were fabricated from inorganic crystalline semiconductors like silicon (Si), germanium (Ge), etc. A crystalline material possesses a long range periodicity in the location of its atoms/molecules. For studying the electronic properties of such solids, the well known *Bloch* theorem can be applied

J. Singh (✉)
School of Engineering and Information Technology, B-purple-12, Faculty of EHSE,
Charles Darwin University, Darwin, NT 0909, Australia
e-mail: jai.singh@cdu.edu.au

J. Singh and R. T. Williams (eds.), *Excitonic and Photonic Processes in Materials*,
Springer Series in Materials Science 203, DOI: 10.1007/978-981-287-131-2_7,
© Springer Science+Business Media Singapore 2015

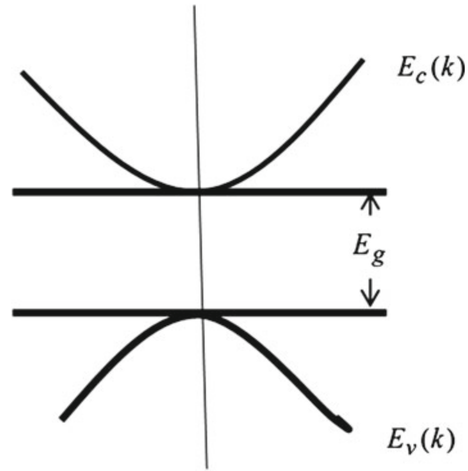

Fig. 7.1 The electron energy $E_c(k)$ of an electron in the conduction band (7.1) and hole energy $E_v(k)$ in the valence band (7.2) derived under the effective mass approximation and plotted as functions of the reciprocal lattice vector k in a crystalline material

which enables one to derive the electron energy as function of the reciprocal lattice vector **k**. By expanding this energy in a *Taylor* series at the minimum of the conduction band and maximum of the valence band and terminating the series at the second order terms, known as the effective mass approximation, one gets the parabolic energy bands [1]. Accordingly, the energy E_c of an electron in the conduction bandis obtained as:

$$E_c(\mathbf{k}) \approx E_g + \frac{\hbar^2 k^2}{2m_e^*}, \tag{7.1}$$

and that of a hole E_v in the valence band as:

$$E_v(\mathbf{k}) \approx -\frac{\hbar^2 k^2}{2m_h^*}, \tag{7.2}$$

where $m_e^* = [\frac{\partial^2 E_c(\mathbf{k})}{\partial \mathbf{k} \partial \mathbf{k}}]^{-1}$ and $m_h^* = [\frac{\partial^2 E_v(\mathbf{k})}{\partial \mathbf{k} \partial \mathbf{k}}]^{-1}$ are the effective masses of an electron in the conduction band and a hole in the valence band, respectively, and E_g is the energy band gap. It is not necessary that the minimum of the conduction band and maximum of the valence band occur at the same **k** value. Materials where they occur at the same **k** are called direct semiconductors or direct band gap materials and others are referred to as indirect gap materials. The effective masses are anisotropic and appear as tensors. The energies E_c and E_v are schematically plotted in Fig. 7.1 as a function of k.

It may be noted that for studying the hole-related electronic properties, we are dealing with the top of the valence band. As a result all the components of curvature are negative and hence the electronic properties of a hole are associated with the valence band which is an inverted parabola, as shown in Fig. 7.1. In this form the

energy of a hole becomes negative and it is associated with the positive effective mass and the real wavevector **k**, as has been discussed by Ziman [2] in detail about 50 years ago. Otherwise the negative energy of a hole in the valence band as shown in (7.2) can be associated either with a negative effective mass or with animaginary wavevector **k**. In this way the electronic properties of a hole can be described by associating it with a positive charge and either with a negative effective mass or imaginary wavevector. This concept is going to be very useful when considering a hole in noncrystalline semiconductors as described below.

Although Fig. 7.1 is well known and one would find it in every text book on condensed matter physics [3, 4], it is presented here for comparing it with the electronic properties of noncrystalline solids. The concept of parabolic bands was also adopted for organic crystalline materials and many organic semiconductor studies were carried out during the 1960s on crystalline materials like naphthalene, anthracene, etc. [5–7]. However, as the inter-molecular overlap of electronic wavefunctions is much smaller in organic solids the widths of the valence and conduction bands are very small. This leads to considering the highest occupied molecular orbital (HOMO) equivalent to the valence band and the lowest unoccupied molecular orbital (LUMO) as the conduction band in organic solids, for both crystalline and noncrystalline. However, the pure crystalline organic semiconductors, like naphthalene, anthracene, etc., could not be used in device fabrications as their inorganic counter parts because of very poor electronic properties. In addition, the organic polymers, commonly known as "plastics" were considered to be insulators and were employed mainly in various insulating applications, like coatings on electrical wires. Then the metallic conductivity was discovered in doped polyacetylene in the celebrated work of Heeger, MacDiarmid and Shirakawa in 1977 [8] for which they were awarded the Chemistry Nobel Prize in 2000. Afterward, the semiconducting properties were discovered in the intrinsic (undoped) conjugated polymers. As these polymers are not crystalline substances, subsequent developments in the field of organic photovoltaics, both on small molecule heterojunction [9] and polymer organic solar cells [10, 11] and organic light emitting devices [12, 13] have currently generated very intense research interests in noncrystalline organic small molecule materials and conjugated polymers.

Prior to the research development in organics, the research activities in inorganic noncrystalline semiconductors had already been far advanced, particularly in complex chalcogenide glasses [14, 15]. It was established [15] that in inorganic noncrystalline glasses the valence and conduction bands are not separated by a clean energy gap as shown in Fig. 7.1. Instead these bands split into two parts separated by a mobility edge. In the valence band this edge is called the hole mobility edge, at an energy E_v. Below this energy the hole states are delocalised and referred to as the valence extended states which collectively have the properties similar to those of a valence band in crystalline solids. In contrast to a crystalline solid which has no energy states within the gap,a noncrystalline solid has energy states above E_v as well. These states within the gap are localised and referred to as the valence tail states as shown in Fig. 7.2. Likewise the conduction band is split by an electron mobility edge at an energy E_c. Above E_c all energy states are referred to as the conduction extended

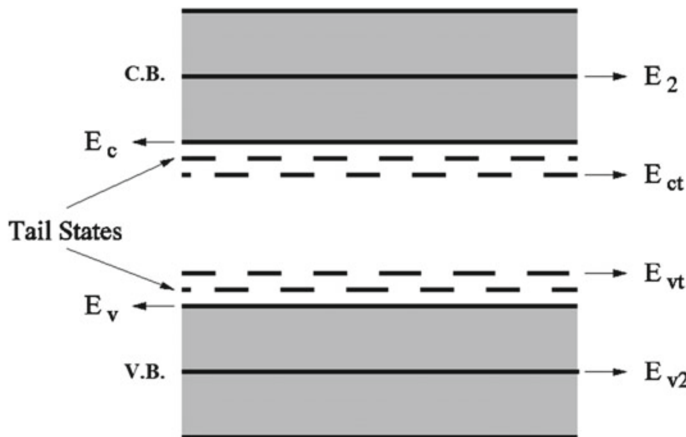

Fig. 7.2 Schematic illustration of electronic energy states, E_2, E_c, E_{ct}, E_{vt}, E_v and E_{v2}, in a-semiconductors. The *shaded region* represents the extended states

states which collectively have the property of a conduction band. The energy states below E_c are localised and referred to as the conduction tail states within the energy gap as shown in Fig. 7.2. Comparing Figs. 7.1 and 7.2, it becomes obvious that existence of valence and conduction tail states within the gap in noncrystalline inorganic solids is the key difference between crystalline and noncrystallinesolids. The other important difference is that energies of electrons and holes in nocrystalline solids cannot be associated with the reciprocal lattice vector **k**. The existence of both of these differences is attributed to the absence of long range periodicity in amorphous or noncrystalline solids [15, 16].

The absence of periodicity in noncrystalline semiconductors had puzzled theoreticians in condensed matter physics initially and many did not believe that these materials would be good for any applications. John Ziman [17] reasoned that, without periodicity in the atomic structure, amorphous materials could not have an electronic band structure and hence no gaps were possible. He said that, as a consequence, amorphous semiconductors could not exist. Even more interesting was his pronouncement that holes, being a concept derived from the negative curvature of an E-**k** curve, definitely could not occur in amorphous semiconductors.

Keeping in mind the results given in (7.1)–(7.2), one can see that in a way *Ziman* was correct although one can get the energy band gap within the tight-binding approximation [17] as well. Moreover, the theoretical developments along the line of (7.1)–(7.2), also questioned the concept and derivation of effective mass of charge carriers and existence of excitons in amorphous semiconductors. Therefore, until very recently,the free charge carrier mass was used in practice in noncrystalline materials wherever the effective mass was required and existence of excitons was not accepted until the early 1990s [18]. The theory of excitons in amorphous solids was not developed until 2002 [16, 19]. However, before discussing the concept of effective mass and excitons in amorphous semiconductors,we will first consider the development of

amorphous silicon, the most used and studied noncrystalline semiconductor to date. It was *Spear's* idea in the early 1970s to study elemental amorphous semiconductors, like amorphous silicon (a-Si), and see if the concept of extended and tail states as presented in Fig. 7.2 for complex glasses can also be used for a-Si [20, 21]. Prior to this, the technique of depositing the hydrogenated amorphous silicon (a-Si:H) thin films using electrode-less glow discharge, now known as the plasma enhanced chemical vapour deposition (PECVD), in silane gas (SiH_4) was pioneered by Stirling [22] in 1965 and the dark conductivity and photoconductivity of a-Si:H thus prepared were measured [23] with respect to the deposition temperature. It was found that the photoconductivity was negligible in the room temperature deposited samples but it was enhanced in samples deposited at 300 °C. They had also noted a smeared absorption edge between the wavelengths of 1.5 and 0.5 μm and attributed it to the new idea of localised states at the band edges. They observed the degradation of samples with age and had successfully deposited n-type a-Si:H by adding phosphine (PH_4) to silane. They observed that the electronic dark current in n-type samples increased by six orders of magnitude in comparison with that in intrinsic samples. However, these samples were prepared at high pressures due to their system's limitation and data obtained were affected by contaminations with impurities.

When *Spear's* group started working on amorphous silicon they found that samples of a-Si prepared by sputtering had so high percentage of structural defects that the effect of band tails could not be detected. However, then they prepared samples using PECVD and could successfully dope a-Si:H to n-type by adding phosphine to silane and p-type by adding diborane (B_2H_6) to silane. This pioneering work was published in 1975 [24] and gave birth to the development of a-Si:H thin film devices, like p–i–n solar cells.

Since then the science and technology of amorphous semiconductors have made tremendous progress. Many amorphous semiconductor based devices, both inorganic [25–28] and organic [9–13, 29], have been invented, including dye-sensitized solar cells [30, 31], hybrid devices based on crystalline-non-crystalline hybrid, inorganic-organic hybrid, amorphous-nano-structure hybrid [32–34], etc. The research on hybrid devices has become one of the most active areas in semiconductor technology. Although nanostructures like quantum dots, nanotubes, graphenes are crystalline single entities, their combinations and hybrid structures no longer have long-range translational symmetry and hence become amorphous in nature as a whole structure. The operation of most optical and opto-electronic devices is based on exciting or injecting electron-hole pairs which may form excitons followed by either dissociation of excitons and collection of electrons and holes at the opposite electrodes, e.g., solar cells or radiative recombination of excitons by emitting photons, e.g., light emitting devices.

The objective of this chapter is to present the excitonic processes which may occur in amorphous semiconductors and their importance in the operation of devices based on amorphous structures. In Sect. 7.2, it is described how one can model the energy bands, the effective mass of charge carriers and the formation of excitons in inorganic semiconductors.

7.2 Effective Mass of Charge Carriers in Inorganic Amorphous Semiconductors

For studying the electronic and optoelectronic properties of noncrystalline or amorphous semiconductors (a-semiconductors), there are four energy regions that need to be considered. As shown in Fig. 7.2, the valence band consists of the extended states below the hole mobility edge of energy E_v and tail states above E_v within the band gap. Likewise the conduction band consists of the extended states above the electron mobility edge at energy E_c and tail states below E_c within the band gap. Following the chemical bonding approach for the formation of electronic states in solids [16], it is established that the weakly bonded atoms contribute to the tail states and fully co-ordinated atoms to the extended states of a-semiconductors. With this approach the formation of energy bands in amorphous structures can be studied by deriving the electronic state energies in the real coordinate space (**r**-space) instead of the reciprocal lattice vector space (**k**-space) applicable for crystalline structures.The effective mass of charge carriers is then derived from this energy expression. Such approaches have also been applied for crystalline solids in the following examples: (1) in studying the problem of electron self-trapping, it was first shown by Toyozawa [35] that the effective mass of an electron interacting with acoustic phonons can be obtained in the real crystal space. (2) Kivelson and Gelatt [36] have developed a theory of calculating the effective mass of charge carriers in the real coordinate space. (3) In developing the theory of Frenkel excitons, Singh [37] has derived an expression for the effective mass of Frenkel excitons in the real crystal space. In this chapter, following our earlier work [16, 38] the theory of calculating the effective mass in inorganic amorphous solids is reviewed in the real coordinate space. As described above, according to Fig. 7.2, for inorganic amorphous solids the valence and conduction bands consist of extended and tail states. In the former, electronic states are delocalised which means the charge carriers are delocalised and can be associated with delocalised wavefunctions and in the latter, the charge carriers are localised and can be associated with localised wavefunctions. Accordingly the effective mass of a charge carrier is expected to be different in the extended and tail states, as described below:

7.2.1 Effective Mass of Electrons in the Conduction Band

Let us create an electron with energy E_e and spin σ_e in the conduction band of an amorphous solid. The eigenvector of such an electronic state in a noncrystalline solid can be written as:

$$|1, E_e, \sigma_e >= \sum_{\mathbf{l}} C_{1\mathbf{l}}(E_e) a_{1\mathbf{l}}{}^{+}(\sigma_e)|0>, \quad (7.3)$$

where $a_{j\mathbf{l}}^{+}(\sigma)$ is the creation operator of an electron with spin σ in the electronic state j ($j = 0$ for valence and $j = 1$ for conduction states) of an atom localized at $\mathbf{l}$. $C_{1\mathbf{l}}(E)$ are the probability amplitude coefficients. For crystalline solids, $C_{1\mathbf{l}}(E)$ can be written in the $\mathbf{k}$-space as $C_{1\mathbf{l}}(E) = N^{-1/2}\exp(i\mathbf{k}\cdot\mathbf{l})$, which is not applicable for a-solids. The vacuum state, denoted by |0>, is the one with completely filled valence band and totally empty conduction band, which include both extended and tail states for a-semiconductors. Therefore, a suitable form of the probability amplitude coefficient for a noncrystalline semiconductor is introduced here as [16, 38]:

$$C_{1\mathbf{l}}(E) = N^{-1/2}\exp(i\mathbf{t}_e\cdot\mathbf{l}), \tag{7.4}$$

where

$$|\mathbf{t}_e(E)| = \sqrt{\frac{2m_e^*(E - E_c)}{\hbar^2}}. \tag{7.5}$$

Here m_e^* is the effective mass of an electron in the conduction band, which is yet to be determined. The choice of $C_{1\mathbf{l}}(E)$ is based on the fact that for energy $E > E_c$ the electron will move as a free particle with an effective mass m_e^*, but for $E < E_c$, when the electron will be in the tail states, $t_e(E)$ becomes imaginary and the probability amplitude coefficient becomes an exponentially decreasing real function. In this case the electron will get localized at an atomic site corresponding to that energy state and the atomic site will act as the centre of localization. It may be noted that $t_e(E)$ has the dimensionality of the reciprocal of length, which the same as that of the reciprocal lattice vector $\mathbf{k}$, but the former is a function of energy. The choice of the above formalism helps determining the electron energy in the real coordinate space, not in $\mathbf{k}$-space, which is the advantage in dealing with non-crystalline solids.

Using the electronic Hamiltonian in the real coordinate space and the eigenvector in (7.3), we get the energy eigenvalue of an electron, W_{1e}, in the conduction band in the real coordinate space as [38]:

$$W_{1e} = W_0 + N^{-1}\sum_{\mathbf{l},\mathbf{m}}\exp[i\mathbf{t}_e.(\mathbf{m}-\mathbf{l})]E_{1\mathbf{lm}}. \tag{7.6}$$

where W_0 is the total energy of all valence electrons in the solid before an electron was excited to the extended conduction band, i.e., the Fermi energy at 0 K, N is the total number of atoms in the sample of noncrystalline material considered and $E_{1\mathbf{lm}}$ is the energy transfer matrix element of the electron in the conduction band, including its interaction with all the electrons in the valence band, given by:

$$E_{j\mathbf{lm}} =< j,\mathbf{l},\sigma\| -\frac{\hbar^2\nabla^2}{2m} + V(r)\|j,\mathbf{m},\sigma >. \tag{7.7}$$

It should be remembered that the energy matrix element, $E_{1\mathbf{lm}} < 0$, because it is the energy of interaction of an electron in a bound state j between two atoms/molecules at $\mathbf{l}$ and $\mathbf{m}$.

By expanding (7.6) in Taylor's series about $\mathbf{t}_e = \mathbf{0}$ up to the second order terms, the electron energy can be written within the effective mass approximation as [38]:

$$W_{1e} \approx W_0 + E_1 + \frac{\hbar^2 t_e^2}{2m_e^*}, \tag{7.8}$$

As stated above, the expansion is carried out about $\mathbf{t}_e = \mathbf{0}$, which in terms of energy means at an energy $E_1 = N^{-1} \sum_{\mathbf{l}} E_{1\mathbf{ll}} = E_c$, which is the energy of the electron mobility edge. The last term of (7.8) is written in the form of the kinetic energy to define the effective mass of the electron given by:

$$[m_e^*]^{-1} = -\hbar^{-2} N^{-1} \sum_{\mathbf{l} \neq \mathbf{m}} (\mathbf{m} - \mathbf{l})^2 E_{1\mathbf{lm}}. \tag{7.9}$$

Here the summation over **l** and **m** runs over all atomic/molecular sites some of which contribute to the extended states in the conduction band and some to its tail states. Assuming that the atoms/molecules located on deformed sites, which do not conform even to the short range order, contribute to the localised energies in the conduction tail states, (7.9) can be split in two terms. One term sums over all atoms/molecules contributing energies in the extended states and the other sums over all atoms contributing energies to the tail states. The energy interface of the extended and tail states lies at E_C, the energy of the electron mobility edge. Above E_C, all energy states are delocalised extended states and below E_C all energies are localised in the tail states (see Fig. 7.2). Equation (7.9) thus can be written as [38]:

$$[m_e^*]^{-1} = -\hbar^{-2} [a N_1^{-1} \sum_{\mathbf{l} \neq \mathbf{m}} (\mathbf{m} - \mathbf{l})^2 E_{1\mathbf{lm}} - b N_2^{-1} \sum_{\mathbf{l}' \neq \mathbf{m}'} (\mathbf{m}' - \mathbf{l}')^2 E_{1\mathbf{l}'\mathbf{m}'}], \tag{7.10}$$

where $a = \frac{N_1}{N} < 1$, N_1 is the number of atoms contributing to the extended states and $b = \frac{N_2}{N} < 1$, N_2 is the number of atoms contributing to the tail states, such that $a + b = 1$ $(N = N_1 + N_2)$. The first term gives the inverse of the effective mass of an electron in the extended states and second term gives that in the tail states as:

$$[m_e^*]^{-1} = [m_{ees}^*]^{-1} + [m_{ets}^*]^{-1}, \tag{7.11}$$

where m_{ees}^* is the effective mass of an electron in the extended states given by:

$$[m_{ees}^*]^{-1} = -\hbar^{-2} [a N_1^{-1} \sum_{\mathbf{l} \neq \mathbf{m}} (\mathbf{m} - \mathbf{l})^2 E_{1\mathbf{lm}}], \tag{7.12a}$$

and

$$[m_{ets}^*]^{-1} = -\hbar^{-2} [b N_2^{-1} \sum_{\mathbf{l}' \neq \mathbf{m}'} (\mathbf{m}' - \mathbf{l}')^2 E_{1\mathbf{l}'m'}]. \tag{7.12b}$$

It is interesting to note that according to (7.11), an electron in the conduction band of a non-crystalline solid has an effective mass which is the reduced effective mass of its mass in the extended and tail states. This is meaningful because during its motion an electron in the conduction band of a sample of non-crystalline solid will encounter both types of atoms, contributing to the extended and tail states. At the same time, as the tail states are localised, the effective mass m^*_{ets} is expected to be very large, according to (7.11) it will contribute little to the effective mass of an electron and hence the electron will have a kinetic energy only in the extended states.

The effective masses in the extended and tail states have already been derived [16, 38] within the nearest neighbour approximation as:

$$m^*_{ees} \approx \frac{E_L}{2(E_2 - E_c)a^{1/3}} m_e, \tag{7.13a}$$

and

$$m^*_{ets} \approx \frac{E_L}{(E_c - E_{ct})b^{1/3}} m_e. \tag{7.13b}$$

E_2 is the energy of the middle of the extended states where the imaginary part of the dielectric constant becomes maximum [39] and thus the half width of conduction extended states becomes $= E_2 - E_c$. The energy E_L is given by [16, 38]:

$$E_L = \frac{\hbar^2}{m_e L^2}, \tag{7.14}$$

where $L = \left[\frac{3}{4\pi n}\right]^{1/3}$ is the average bond length, $n = N/V$ is the atomic/molecular concentration (e.g., cm^{-3}) in a sample, E_{ct} is the energy of the end of the conduction tail states and m_e is the electronic mass. Using (7.10)–(7.13a), (7.13b) in (7.8), the energy of the electron in the conduction band can be written within the effective mass approximation as:

$$W_{1e} \approx W_0 + E_c + \frac{\hbar^2 t_e^2}{2m^*_{ees}} - \frac{\hbar^2 t_{ht}^2}{2m^*_{ets}}, \tag{7.15}$$

where

$$t_{ht}(E) = \sqrt{\frac{2m^*_{ets}(E_c - E)}{\hbar^2}}. \tag{7.16}$$

The last term representing the kinetic energy of an electron localised in the tail states with energy $E < E_c$. According to (7.5) its linear momentum $\hbar t_e = i\hbar t_t$ becomes imaginary (localised) and hence its kinetic energy becomes negative. Comparing (7.16) with (7.2), a negative kinetic energy represents an inverted parabola as in the valence band where holes become the mobile charge carriers. From this

point of view the energy of the electron in (7.15) can be interpreted as that in materials where the conduction band is split at the mobility edge E_c. The energy states above E_c behave like those in a conduction band with the electrons being the mobile carriers and states below E_c behave like a valence band with holes being the mobile carriers. Here of course the energy gap between the sub conduction and sub valence bands is zero.

7.2.2 Effective Mass of Holes in the Valence Band

A similar formalism can be adopted to apply the effective mass approximation to derive the energy of a hole in the valence band. The hole energy eigenvalue is thus obtained as [16, 38]:

$$W_{0h} \approx W_0 - E_v - \frac{\hbar^2 t_h^2}{2m_{hes}^*} + \frac{\hbar^2 t_{ht}^2}{2m_{hts}^*}, \tag{7.17}$$

where $E_v = N^{-1} \sum_{\mathbf{l}} E_{0\mathbf{ll}}$ is the energy of the hole mobility edge in the valence band.Below this energy all energy states represent the delocalised valence extended states and above this are energy states of the localised valence tail states. $\hbar \mathbf{t}_h$ and $\hbar \mathbf{t}_{ht}$ are linear momenta, and m_{hes}^* and m_{hts}^* are effective masses of hole in the valence extended and tail states, respectively, obtained as:

$$t_h(E_h) = \sqrt{\frac{2m_{hes}^*(E_v - E_h)}{\hbar^2}} \tag{7.18}$$

$$m_{hx}^* = \frac{E_L}{2(E_v - E_{v2})a^{1/3}} m_e, \tag{7.19}$$

and

$$t_{ht}(E_h) = \sqrt{\frac{2m_{hts}^*(E_h - E_v)}{\hbar^2}}, \tag{7.20}$$

$$m_{ht}^* = \frac{E_L}{(E_{vt} - E_v)b^{1/3}} m_e, \tag{7.21}$$

where E_{v2} and E_{vt} are energies corresponding to the half width of valence extended states and the end of the valence tail states, respectively. The energy eigenvalue of an electron in the conduction band as obtained in (7.15) and that of a hole, given in (7.17), are schematically plotted in Fig. 7.3.

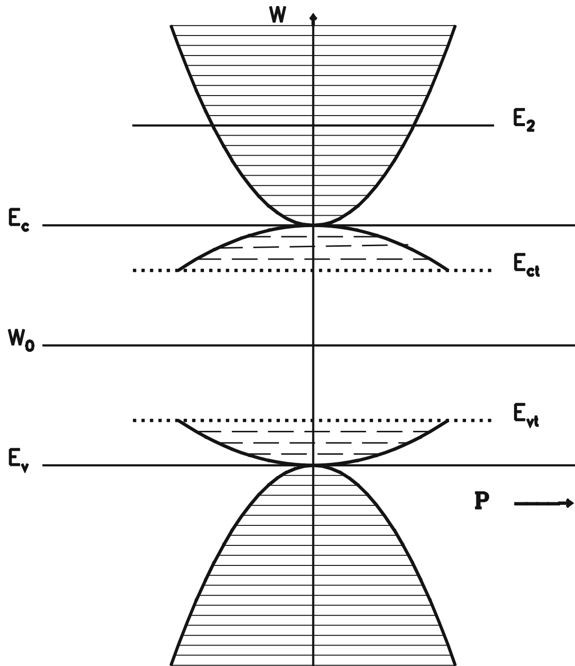

Fig. 7.3 Energy eigenvalues of an electron and a hole, derived using the effective mass approximation, are schematically plotted as a function of their linear momentum, to illustrate the sign reversal in the effective mass of charge carriers as they cross the mobility edges

7.3 Anomalous Hall Effect

In hydrogenated amorphous silicon (a-Si:H), it is observed near the mobility edge that when charge carriers are electrons the Hall coefficient becomes positive identifying them as holes and when charge carriers are holes the Hall coefficient becomes negative identifying them as electrons. This anomaly of the Hall coefficient observed in a-Si:H is also called as the double reversal of the Hall coefficient [15, 38, 40]. However, the double reversal is not observed in all noncrystalline semiconductors. The classical Hall coefficient given by $R_H = 1/nq$, n being the density of free carriers and q charge, appears to be valid in amorphous solids only in degenerate gases, for instance, in liquid metals. This expression is not valid for the conduction of electrons near the mobility edge. In some cases it is negative irrespective of the sign of charge carriers and in others its sign is opposite to that of the charge carriers. For instance, positive Hall coefficient has been observed in $CdGeAs_2$ [41, 42] and amorphous arsenic [43]. In the doped glow-discharge-deposited a-Si:H, LeComber et al. [44] have observed a positive Hall coefficient in n-type material and a negative Hall coefficient in p-type material. This is referred to as the double reversal stated above. A few theories have been put forward [38] on the anomaly of the Hall

coefficient in amorphous solids but it is difficult to evaluate if they lead to the same interpretation. For example, applying the concept of hopping polarons developed by Friedman and Holstein [45], Friedman [46] has put forward a theory for the Hall effect for carriers moving in a-solids near the mobility edge. It produces interference between two scattering paths involving three atomic sites A, B and C. One path is from A to B direct and the other from A to B via C. The Hall mobility deduced in this way is found to be independent of temperature and in qualitative agreement with the observations, but the Hall coefficient is always found to be negative whether the carriers are electrons or holes. This has been interpreted as *Friedman's* theory being correct only in predicting the n-type Hall coefficient for p-type material but not the p-type Hall coefficient for n-type material.

Emin has put forward another approach to the anomalous Hall coefficient in amorphous solids. For explaining the behaviour of n-type a-Si:H, Emin [47] has suggested a theory by considering that carriers form polarons located on Si–Si bonds. *Emin's* theory requires that the odd order close loops must be predominant in the structure, because the orbital on each bond is antibonding so that the wavefunction changes sign at each hop. Although polarons are not formed in crystalline silicon, *Emin* has suggested that they can be formed in amorphous silicon due to its softened structure. The observed activation energy in the mobility is then attributed to the polaron hopping. However, *Emin's* theory is not widely accepted, because it demands that the electron move from one bond to an adjacent bond, around an odd numbered ring, which is not always possible in any amorphous structure.

Then Mott [48] has suggested that the positive Hall coefficient for n-type silicon can be explained without any assumption of odd-numbered paths, if the centres which scatter electrons are considered to be the stretched Si–Si bonds. Such stretched bonds have electron energies different from the majority of the bonds. Extending then *Friedman's* theory to such stretched bonds as scattering centres, the interference between two paths, AB and ACB, can lead to a change in the sign of the electronic wavefunction.

Applying a perturbation renormalization-group procedure, Okamoto et al. [49] have studied the behaviour of weak field Hall conductivity near the mobility edge and found that the anomalous sign in the Hall coefficient can occur if the mean free path of carriers is shorter than a critical value. Accordingly, the microscopic Hall conductivity changes its sign near but above the mobility edge and hence the Hall coefficient also changes its sign.

As the concept of Hall effect is based on the free electron theory, the classical formula of R_H cannot be applied to charge carriers in amorphous semiconductors because they are not free charge carriers. It is applicable to crystalline solids because of the use of the effective mass, i.e., although a carrier is not free in a crystalline solid it is made so by associating it with an effective mass. The same concept should be applied to amorphous semiconductors as well and that means a charge carrier should be associated with an effective mass before the theory of Hall effect can be used. Now that we have derived the effective mass of electrons in the conduction extended and tail states and that of holes in the valence extended and tail states, we should consider the motion of charge carriers near the mobility edges of electrons in

the conduction band and holes in the valence band. According to Fig. 7.3, because of the presence of the localised tail states as stated above, the conduction and valence bands in a noncrystalline solid split at their mobility edges into a pair of conduction and valence bands with no energy gap. Use of this figure is the easiest way to explain the double reversal in the Hall effect as explained below:

The derived energy eigenvalues of an electron in the conduction band in (7.15), that of a hole in the valence band in (7.17), and the plot of both as a function of the linear momentum in Fig. 7.3 clearly illustrate that the effective mass of a free charge carrier changes its sign as the charge carrier crosses the mobility edge. This is analogous to (7.1) and (7.2) plotted in Fig. 7.1 for a crystalline solid with an energy gap E_g. For $E_g = 0$, the top of Fig. 7.3 will become like Fig. 7.1. That means, within the effective mass approximation, when a charge carrier crosses its respective mobility edge the sign of its effective mass changes resulting in the change in the sign of its kinetic energy. Thus the shape of the parabola reverses when the charge carrier crosses the mobility edge. Accordingly, an electron is a free carrier in the extended states of the conduction band with an effective mass m_{ees}^* (7.13a) but in the tail states of the conduction band a hole becomes the free carrier at the top of the tail states with an effective mass m_{eet}^*. Likewise, in the valence band a free charge carrier is a hole with an effective mass m_{hes}^* in the extended states and an electron in the tail states with an effective mass m_{het}^*. This dual behaviour of charge carriers within the same band, conduction or valence, is what gives the anomalous behaviour or double reversal in the Hall coefficient. For example, let us consider the case of a-Si:H. The n-a-Si:H will have most electrons below the mobility edge in the tail states, where only holes are the free carriers. Then the Hall coefficient will show the sign of holes. Likewise, in p-type a-Si:H the hole states overlap with the valence tail states above the mobility edge. The free charge carriers in these states are expected to be electrons and therefore one would observe the negative Hall coefficient. The change in the sign of charge of a charge carrier is associated with the change of sign it its effective mass as discussed in [38] in detail.

Spear et al. [50, 51] have measured the Hall coefficient in microcrystallites and found that the sign of the Hall coefficient reverts to normal for crystallite size greater than 20 Å. This has been used to conclude that the scattering length in amorphous material is expected to be less than 20 Å [48]. However, this also implies that in small microcrystallites as the number of atoms is small, the surface atoms contributing to the tail states are large in proportion. If the size is very small, all states would be localized like in the tail states. In this case, then mobile charge carriers will be holes and the Hall coefficient will have positive sign. The larger crystallites behave like crystals with no tail states and therefore exhibit the normal Hall effect. Thus, it is conclusive that the existence of the mobility edge and tail states is the cause for the anomalous behaviour of the Hall coefficient in noncrystalline solids.

To the best of the author's knowledge, there are no recent data available on the double reversal in the Hall coefficient, neither in a-Si:H nor in any other noncrystalline semiconductors. More experimental data may provide further insight in the problem.

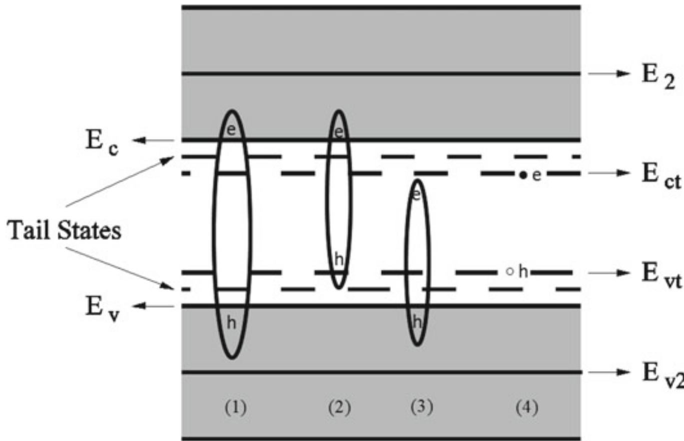

Fig. 7.4 Four possibilities of creating a photoexcitation in a noncrystalline inorganic semiconductor; (*1*) both electron (*e*) and hole (*h*) are excited in their respective extended states, (*2*) e in the extended and h in its tail states, (*3*) *e* in its tail and *h* in the extended states, and (*4*) both *e* and *h* are excited in their respective tail states and are hence localised (geminate pair type II, see Sect. 7.4.3)

7.4 Excitonic States in Noncrystalline Solids

A photon of energy $\hbar\omega \geq E_g$ incident on a crystalline semiconductor gets absorbed by exciting an electron from the valence band to the conduction band and leaving a hole behind in the valence band. Thus, an absorbed photon creates a pair of excited electron (e) and a hole (h). Although exactly the same process occurs when a photon is absorbed in a noncrystalline semiconductor, the band gap is not as well defined in such solids due to the existence of the tail states (see Fig. 7.2). In analogy with a crystalline solid (Fig. 7.1), it may be reasonable to assume that if a photon of energy $\hbar\omega \geq E_c - E_v$ is absorbed in a noncrystalline semiconductor, the excited e and h pair may behave like those in a crystalline semiconductor. However, this is not the only possibility of the photon absorption in a noncrystalline semiconductor. Depending on its energy a photon can be absorbed in four ways: (1) by exciting an electron from the valence extended states to the conduction extended states, which will occur when $\hbar\omega \geq E_c - E_v$, (2) by exciting an electron from the valence tail states to the extended conduction states, (3) by exciting an electron from the extended valence states to the localised conduction tail states and (4) by exciting an electron from the localised valence tail states to the localised conduction tail states. These four possibilities of excitations are illustrated in Fig. 7.4. The absorption of a photon in the processes (2)–(4) may occur for $(E_c - E_v)/2 \leq \hbar\omega < E_c - E_v$ but that in process (4) may also occur for $\hbar\omega \leq (E_c - E_v)/2$.

The other distinct property some noncrystalline semiconductors have is that separation between the singlet and triplet exciton energies, $\Delta E_{ST} = E_{xS} - E_{xT}$ is

relatively larger compared to that in crystalline semiconductors. Here E_{xS} and E_{xT} are energies of the singlet and triplet exciton states, respectively. For example, in crystalline silicon (c-Si) $\Delta E_{ST} \approx 0$ because of the nature of the large orbital radii Wannier excitons for which the exchange interaction becomes negligible leading to no energy separation between singlet and triplet excitons. However, in a-Si:H ΔE_{ST} is found to vary in the range of 3–40 meV [52, 53]. As a result, one does not observe the singlet and triplet states in c-Si separately but one does observe them distinctively in a-Si:H. The observed singlet–triplet exchange energy in a wide range may be understood due to the wide range of four excitation possibilities described above. In the crystalline silicon and other inorganic semiconductors where the concept of the large orbital excitons is applicable, the excitons are excited to what is called a mixed state. That means the singlet and triplet exciton energy states overlap with each other. In this case, to study the transition from a triplet to the ground state (emission), which is spin forbidden, first one uses the stationary spin-orbit interaction to remove the degeneracy of the triplet state and then uses the exciton-photon interaction operator as a perturbation to calculate the rate of transition from the triplet state, where the singlet components of the perturbed state contribute to the non-zero rate of triplet spontaneous emission [54–59]. In noncrystalline semiconductors this approach cannot be applied because the singlet and triplet exciton states are not mixed and are relatively widely spaced.

This difference between the crystalline and noncrystalline solids leads to further consequences in studying the electronic properties of the latter. In device applications where one requires conversion from singlet to triplet excitons through the intersystem crossing or vice versa, more energy is lost through the intersystem crossing or more energy is required for the up-conversion from triplet to singlet. This issue will be discussed further later in this chapter. Here we will first discuss the energy of singlet and triplet excitonic states and then present the rates of spontaneous emissions from these states.

Following the derivations of (7.8) and (7.17) and without yet worrying about the distinction between the extended and tail states, the Hamiltonian of an excited pair of electron and holein a noncrystalline solid can be written within the effective mass approximation as [16]:

$$H_{ex} = W_0 + E_{opt} + \frac{p_e^2}{2m_e^*} + \frac{p_h^2}{2m_h^*} - \frac{\kappa e^2}{\varepsilon'(S) r}, \tag{7.22}$$

where $E_{opt} = E_e - E_h$, which is the photon energy absorbed in exciting an electron from the valence band (E_v) to the conduction band (E_c), $p_e = \hbar t_e = -i\hbar\nabla_e$ and $p_h = \hbar t_h = -i\hbar\nabla_h$ are the linear momentum of the excited electron and hole, respectively. Further, $\kappa = (4\pi\varepsilon_0)^{-1} = 9 \times 10^9$, r is the relative coordinate between the excited electron and hole and $\varepsilon'(S) = \varepsilon[1 - \frac{(1-S)}{\alpha}]^{-1}$, where S is the exciton's spin ($S = 0$ for singlet and $= 1$ for triplet) and α is the ratio of the Coulomb to the exchange interactions between the excited e and h. It is expected to be different for different solids. For instance $\alpha = 1$ allows no binding between the excited pair of

charge carriers as the binding potential energy vanishes. For forming an exciton, it is necessary that α must be greater than unity ($\alpha > 1$). It may also be noted that for a very large value of $\alpha(\rightarrow \infty)$, the contribution of the exchange interaction becomes negligible and the binding energy reaches to the large radii orbital limit at which the energy difference between singlet and triplet states vanishes. This is usually the case in crystalline inorganic semiconductors. One way of determining α would be by evaluating the integrals in the Coulomb and exchange interactions numerically, which may depend on the sample size, kind of atomic wavefunctions chosen etc. Alternatively, α can be estimated from the experimental results as [16, 19]:

$$\alpha = \left[1 - \sqrt{1 - \frac{\Delta E_{xp}}{C_M}}\right]^{-1}, \tag{7.23}$$

where ΔE_{xp} is the difference between singlet and triplet exciton states energies measured experimentally and $C_M = \frac{\mu_x e^4 \kappa^2}{2\hbar^2 \varepsilon^2}$ with μ_x being the reduced mass of the excited electron hole pair given by: $\mu_x^{-1} = (m_e^*)^{-1} + (m_h^*)^{-1}$. It may however be noted that for a real value of α (7.23) requires that $\Delta E_{xp} \leq C_M$.

Replacing the linear momentum by the corresponding operator, $p \rightarrow -i\hbar\nabla$, and then transforming the co-ordinates into the centre of mass **R** and relative **r** coordinates, according to:

$$\mathbf{R} = \frac{m_e^* \mathbf{l}_e + m_h^* \mathbf{l}_h}{M}, \tag{7.24}$$

The Hamiltonian in (7.22) can be written as:

$$H_{ex} = W_0 + E_{opt} - \frac{\hbar \nabla_R^2}{2M} - \frac{\hbar^2 \nabla_r^2}{2\mu_x} - \frac{\kappa e^2}{\varepsilon'(S) r}, \tag{7.25}$$

where ∇_R and ∇_r are the differential operators associated with R and r, respectively, and $M = m_e^* + m_h^*$. The eigenfunction of the operator in (7.25) can be written as [37]:

$$\psi(r, R) = V^{-1} \exp(i \frac{\mathbf{P}.\mathbf{R}}{\hbar}) \phi_n(r), \tag{7.26}$$

where V is the volume of the solid, **P** linear momentum associated with the centre of mass motion of exciton, and $\phi_n(r)$ eigenfunctions corresponding to the principal quantum numbers n associated with the exciton energy operator given by:

$$[-\frac{\hbar^2 \nabla^2}{2\mu_x} - \frac{\kappa e^2}{\varepsilon'(S) r}] \phi_n(r) = E_n(S) \phi_n(r), \tag{7.27}$$

Using (7.25)–(7.27) in the Schrödinger equation $H_{ex}\psi(r, R) = W\psi(r, R)$, we get the exciton energy as:

$$W = W_0 + E_{opt} + \frac{P^2}{2m} + E_n, \tag{7.28}$$

where

$$E_n(S) = -\frac{\mu_x e^4 \kappa^2}{2\hbar^2 \varepsilon'(S)^2} \frac{1}{n^2}. \tag{7.29}$$

The wavefunction and energy of an exciton derived in (7.26) and (7.29), respectively, represent a general situation without distinguishing whether the exciton is created by exciting the electron and hole in the extended or tail states. Although the form of these expressions will not change but the associated physics is quite different as discussed below:

7.4.1 Possibility (1): Creation of an Exciton by Exciting Both Electron and Hole in Extended States

The theoretical formalism in this case is similar to that in crystalline semiconductors. According to (7.28), the centre of mass of an exciton thus created will move throughout the sample with a linear momentum $P = \hbar(t_e + t_h)$ and the electron and hole within the exciton will be bound in a hydrogenic energy state with energy $E_n(S)$ given by (7.29). It may however be noted that t_e (7.5) and t_h (7.18) depend on the energy of the electron and hole, respectively, and therefore the exciton will move through those atoms wich contribute to the extended energy states for both the electrons and holes. Therefore unlike crystalline solids not all atoms take part in this motion, which reduces the mobility of charge carriers in noncrystalline semiconductors.

In this case, as the charge carrier motion is more like the crystalline silicon, it is expected that the energy difference between singlet and triplet exciton states would be minimum. This energy difference in a-Si:H is observed to be in the range of 3–40 meV [52, 53] as stated above. We then assume that in this case the difference is 3 meV. The reduced effective exciton mass $\mu_x = 0.17m_e$ [17] and $\varepsilon = 12$. Using these in (7.23), we find $\alpha \approx 10$ with $C_M = 16.1$ meV. Using this in (7.29), we get the singlet and triplet exciton energies as: $E_1(S = 0) = -13.1$ meV and $E_1(S = 1) = -16.1$ meV. The corresponding binding energy $E_B(S) = -E_1(S)$ is then obtained as $E_B(S = 0) = 13.1$ meV and $E_B(S = 1) = 16.1$ meV. In this case the excitons will be delocalised like free waves with wave function given in (7.26) with the real linear momentum of the centre of their mass motion.

7.4.2 Possibilities (2) and (3): Electron Excited in Extended and Hole in Tail, and Electron Excited in Tail and Hole in Extended States

These two cases (Fig. 7.4) produce an excitonic reduced mas $\mu_x = 0.32m_e$ [16] and using the same value for $\alpha = 10$ as used in case (1) above, we get $C_M = 30.3$ meV. This leads to the singlet and triplet binding energies as $E_B(S = 0) = 24.5$ meV and $E_B(S = 1) = 30.3$ meV, respectively, which gives $\Delta E_{ST} = 5.8$ meV. This energy difference is larger than that in case 1. This is expected because one of the carriers is localised within the tail states, which has relatively lower energy. An exciton in this case will be a localised or bound exciton, where one carrier (e or h) is localised/trapped in the tail states and the other moves around it being excited in the extended states. An exciton created in this situation in a device like a solar cell may be more difficult to dissociate and hence will reduce the short circuit current.

7.4.3 Possibility (4): Both the Electron and Hole Are Excited in Their Respective Tail States

In this case, the linear momentum of both e (7.5) and h (7.18) becomes imaginary and the free particle wave function changes to an exponentially decaying wave function and hence both e and h get localised as shown in Fig. 7.4. There are two ways such localised excitations can be created in noncrystalline semiconductors, for example, in a-Si:H: (i) using a low energy photon and exciting directly from the valence tail to conduction tail states and (ii) creating excitons in the extended states and relaxing them to the tail states. In the process (i) as both e and h are localised they are not an exciton but a geminate pair. A geminate pair is defined to be a pair of electron and hole excited by the absorption of the same single photon but not bound in an excitonic state. This kind of excited e and h pairs are referred to as type I geminate pairs. However, another type II, geminate pairs can be created in noncrystalline semiconductors through the process (ii) when excitons formed in the extended states relax to the tail states [60–62]. They lose their excitonic character when they relax down to the localized tail states and become geminate pairs. The type II geminate pairs can be in singlet or triplet states depending on their original excitonic spin states and the average separation between the electron and hole is governed by the corresponding exciton Bohr radius. It is the type II geminate pairs that we consider here and it corresponds to creating an electron hole pair through the possibility (4), shown in Fig. 7.4.

In this case $\mu_x = 3.55m_e(m^*_{et} = m^*_{ht} = 7.1m_e)$[16], which gives $C_M = 0.34$ eV and $E_B(S = 1) = 0.34$ eV and $E_B(S = 0) = 0.28$ eV and the singlet-triplet exchange energy $\Delta E_{ST} = 60$ meV, which is in close agreement with the estimated

experimental value of 40 meV [52, 53]. However, as there are four possibilities of creating singlet and triplet exciton states, one may find different values of ΔE_{ST} from different possible choices of singlet and triplet exciton states. This kind of situation is not expected to occur in crystalline semiconductors.

7.5 Excitonic Photoluminescence and Phosphorescence

The emission from the radiative recombination of singlet excitons is called photoluminescence and that of triplet excitons is called phosphorescence. A transition from singlet excited state to singlet ground state is spin allowed through the exciton-photon interaction operator [60] as a perturbation and the rates of spontaneous emission [62] from these transitions are calculated.The case of spontaneous emission from singlet exciton has been reviewed in detail in [63] but some highlights are briefly presented in the Sect. 7.5.1. The transition from a triplet excited state to the singlet ground state is spin forbidden and it cannot occur without an available mechanism that can flip the spin to singlet configuaration. The case of radiative emission from triplet excitons (phosphorescence) is presented in Sect. 7.5.2.

7.5.1 Emission from Singlet Excitons (Photoluminescence)

The interaction operator between a pair of excited e and h or a singlet exciton and a photon can be written as [60, 63]:

$$\hat{H}_{xp} = -\frac{e}{\mu_x}\mathbf{A} \cdot \mathbf{p} \tag{7.30}$$

where **A** is the vector potential and within the dipole approximation it is given by:

$$\mathbf{A} = \sum_{\lambda} \left(\frac{\hbar}{2\varepsilon_0 n^2 V \omega_\lambda} \right)^{1/2} \left[e^{-i\omega_\lambda t} c_\lambda^+ \hat{\varepsilon}_\lambda + c.c. \right], \tag{7.31}$$

where n is the refractive index and V the volume of the material, ω_λ is the frequency and c_λ^+ is the creation operator of a photon in a mode λ, $\hat{\varepsilon}_\lambda$ is the unit polarization vector of photons and $c.c.$ denotes complex conjugate of the first term. $\mathbf{p} = -i\hbar\nabla_r$ is the linear momentum associated with the relative motion between e and h and μ_x is their reduced mass ($\mu_x^{-1} = m_e^{*-1} + m_h^{*-1}$). The operator in (7.30) does not depend on the centre of mass motion of e and h. Therefore, this operator is the same for the exciton-photon interaction and a pair of e and h and photon interaction.

Using the operator in (7.30) as a perturbation the rate of spontaneous emission from the transition from a singlet excited state to the ground state is calculated using

Fermi's golden rule. Within the two level approximation, which is commonly applied in most cases, the rate of spontaneous emission is obtained as [60, 63]:

$$R_{sp12} = \frac{4\kappa e^2 \sqrt{\varepsilon}\omega^3 |r_{e-h}|^2}{3\hbar c^3} s^{-1}, \tag{7.32}$$

where $\hbar\omega = E_2 - E_1$, the energy difference between the two levels and it is the same as the emission energy, $\varepsilon = n^2$ is the static dielectric constant, $|r_{e-h}|$ is the mean separation between the electron and hole and $\kappa = 1/(4\pi\varepsilon_0)$. For excitons, $|r_{e-h}|$ may be replaced by the corresponding excitonic *Bohr* radius a_{ex} described below.

For noncrystalline semiconductors, it is more appropriate to consider transitions under the four possibilities of the excited states energy locations as discussed in Sect. 7.4. Using the transition operator in (7.30), the rate of spontaneous emission from a singlet exciton for the transition possibilities (1)–(3) in Fig. 7.4 is obtained as [60–63]:

$$R_{spn} = \frac{\mu_x^3 e^2 a_{ex}^2}{2\pi^2 \varepsilon_0 n^2 \hbar^7 \nu \rho_A} \hbar\omega \left(\hbar\omega - E_0\right)^2 \Theta\left(\hbar\omega - E_0\right), \tag{7.33}$$

where $E_0 = E_c - E_v$ is the optical gap, $\Theta\left(\hbar\omega - E_0\right)$ is a step function used to indicate that there is no radiative recombination for $\hbar\omega < E_0$; $\hbar\omega$ being the emission energy, ν is the number of coordinating valence electrons per atom and ρ_A is the atomic density per unit volume. For the possibility (4), where both the excited carriers are localised in the tail states, the rate, R_{spnt}, of spontaneous emission is obtained as:

$$R_{spnt} = R_{spn} \exp(-2t'_e a_{ex}), \tag{7.34}$$

where the subscript *spnt* stands for the spontaneous emission from tail-to-tail states and $|\mathbf{t}'_e| = t'_e = \sqrt{2m_e^*(E_c - E_e)}/\hbar$; E_e being the electron's energy below the mobility edge energy E_c. In (7.33) and (7.34), a_{ex} is the excitonic *Bohr* radius of a singlet exciton given by [16, 19]:

$$a_{ex} = \frac{5\mu\varepsilon}{4\mu_x} a_0, \tag{7.35}$$

where μ is the reduced mass of an electron in the hydrogen atom and $a_0 = 0.529$ Å is the *Bohr* radius. As the reduced mass of the exciton μ_x is different for the four different possibilities (see Fig. 7.4), the excitonic *Bohr* radius is also different in accordance with (7.35).

The rate of spontaneous emission calculated in a-Si:H for the possibility (1) for singlet excitons with $\mu_x = 0.17\, m_e$, excitonic *Bohr* radius as $a_{ex} = 4.67$ nm, $n = 4$, atomic density $\rho_A = 5 \times 10^{28}\,\mathrm{m}^{-3}$ [64], $\nu = 4$ at an emission energy of 1.447 eV, the energy at which the rate is maximum, is obtained as $R_{spn} = 2 \times 10^8\,\mathrm{s}^{-1}$, which gives a radiative lifetime $\tau_r = R_{spn}^{-1} = 5$ ns. For the possibilities (2) and (3), with $\mu_x = 0.32\, m_e$, $a_{ex} = 2.5$ nm, one gets $R_{spn} = 3.45 \times 10^8\,\mathrm{s}^{-1}$ and $\tau_r = 2.9$ ns [63].

The shorter lifetime in this possibility in comparison with that of the possibility (1) may be attributed to the fact that one of the particles in the exciton is localised.

In the possibility (4) where both the carriers are localised but they are in singlet excitonic state, their recombination occurs through tunnelling a distance equal to the excitonic *Bohr* radius a_{ex}, as it can be seen from the exponential factor appearing in the rate given in (7.34). As a result the rate of emission decreases by nearly an order of magnitude to $R_{spnt} = 1.18 \times 10^{7}\,\mathrm{s}^{-1}$ and the radiative time gets prolonged to $\tau_r = 0.085\,\mu\mathrm{s}$. These results are obtained with $\mu_x = 3.5\,m_e$, $a_{ex} = 0.223\,\mathrm{nm}$ and $t_e' = 1.29\,\mathrm{m}^{-1}$. For details of calculations readers may like to refer to [63].

7.5.2 Emission from Triplet Excitons (Phosphorescence)

The photon emission due to the radiative recombination of triplet excitons is called phosphorescence. It is very well established that the radiative recombination of a triplet exciton to the singlet ground state is spin forbidden and hence no photon emission can occur due to the exciton-photon interaction given in (7.30) unless the triplet spin-conficuration can be flipped to singlet spin configuration. In crystalline inorganic semiconductors, the energy difference between a singlet and triplet exciton state is usually negligibly small because the exchange interaction between the excited electron and hole is of short range and it becomes negligible for large radii orbital Wannier excitons. In this case, singlet and triplet exciton states are considered to be a mixed state and can easily change from one to other through the thermal intersystem crossing and not much difference may be expected in the photoluminescence from singlet and phosphorescence from triplet excitons. However, in noncrystalline and organic semiconductors and polymers the energy difference between singlet and triplet states is relatively large. The phosphorescence from triplet excitons cannot occur unless some mechanism of flipping the spin of triplet to singlet configuration is available. Such a spin flip can be caused by the intersystem crossing for which it is required that the vibrational energy levels of singlet and triplet exciton states overlap. The singlet exciton state, usually being at a higher energy than triplet, relaxes down to the vibrationally overlapping triplet state such that the excess vibrational energy flips the spin and the exciton converts to a triplet state. In this case the photoluminescence from singlet excitons is quenched. However, if the sample is doped with elements/materials of a singlet state energy lower than the triplet state, the intersystem crossing can convert triplet excitons to singlet excitons and then the photon emission can occur through the transition operator in (7.30). This technique is used in the light emitting devices. However, if the energy difference between the singlet and triplet exciton states is large, the process of intersystem crossing will not be as efficient and there will be a loss of energy in the emission.

The triplet spin configuration can also be flipped into singlet configuration through the spin-orbit interaction as described below. The wellknown expression for an electron spin-orbit interaction in an atom is given by:

$$\hat{H}_{so} = \frac{Ze^2}{2m_e^2c^2r^3}\mathbf{s}_e.\mathbf{L}, \tag{7.36}$$

where Z is the atomic number, e and m_e are electronic charge and mass, respectively, c is the speed of light and r is the distance of an electron from the nucleus. $\mathbf{S}_e$ and $\mathbf{L}$ are the spin and orbital angular momentum of the electron, respectively. It is obvious that the spin-orbit interaction, $\hat{H}_{so}$ in (7.36) is zero for $\mathbf{s}_e = \mathbf{L} = \mathbf{0}$, i.e., for all s-state orbitals with $l = 0$ and also for singlet excitations ($\mathbf{s}= \mathbf{0}$). It is only non-zero for p- type or higher state orbitals. As such it cannot contribute to the radiative recombination of a triplet exciton in a semiconductor where both the singlet and triplet spin configurations arise from the first excited s-state with $n = 1$ and $l = 0$. However, the photoluminescence spectra from both singlet and triplet excitons in the first excited state have been observed in noncrystalline semiconductors [52, 53].

Furthermore, the spin-orbit interaction operator in (7.36) is a stationary operator and hence it cannot cause any transitions for which one needs a time-dependent perturbation operator. Therefore, it cannot be used as a transition operator, like the exciton-photon interaction operator in (7.30)–(7.31), to calculate a transition matrix element. Until recently [64], there has been no time-dependent spin-orbit interaction known in the literature to calculate the rate of transition directly. In the absence of such a time-dependent spin-orbit interaction operator, a traditional approach has been set up for decades to calculate the transition matrix element from a triplet state in two steps [54–58]. In the first step, applying the first order perturbation theory, the above stationary operator is used to calculate the energy splitting in a degenerate triplet state and the first order perturbed wave function of the triplet state is expanded as a linear combination of all singlet and triplet unperturbed wave functions. In the second step, then the time-dependent dipole transition operator is used to calculate the transition matrix element between the expanded first order perturbed triplet state and unperturbed singlet ground state wave functions. In this way one gets fractional non-zero matrix element contributed by the singlet components in the expansion of triplet wave function. This approach has been used for inorganic [58] as well as organic solids and molecules [54–57] although earlier attempts in some organic molecules and solids did not give good agreements with the experimentally observed lifetimes [54, 55]. Some recent works, however, have apparently applied this approach confidently on conjugated polymers [56] and non-planar aromatic heterocyclic molecules [57]. As it should be apparent, the traditional approach can only be applied to cases where singlet and triplet states are not separated very far apart and appear as a mixed state as the case is usually in the inorganic crystalline semiconductors, as explained below.

In inorganic crystalline semiconductors, like Si, Ge, GaAs, the valence band is typically of p-character and hence it is three-fold degenerate and the conduction

band is of s-character. The degeneracy in the valence band is removed by using the spin-orbit interaction operator (7.36) as a perturbation in the Hamiltonian. The first order perturbed energy eigenvalues and eigenfunctions of the triplet state are, respectively, obtained as [58, 65, 66]:

$$E_{ti}^1 = E_{ti}^0 + <^3 \psi_i \| H_{so} \|^3 \psi_i >, \quad i = 1, 2, 3 \tag{7.37}$$

$$\psi_{ti}^1 = \psi_{ti}^0 + \sum_{j \neq i} \frac{<^3 \psi_{ti}^0 \| H_{so} \|^3 \psi_{tj}^0 >}{E_{ti}^0 - E_{tj}^0} \psi_{tj}^0 + \sum_{j \neq i} \frac{<^3 \psi_{ti}^0 \| H_{so} \|^1 \psi_{sj}^0 >}{E_{ti}^0 - E_{sj}^0} \psi_{sj}^0, \tag{7.38}$$

where E_{ti}^0 and E_{ti}^1 are the unperturbed and first order perturbed triplet state energies, ψ_{si}^0 and ψ_{ti}^0 are unperturbed singlet and triplet state wave functions, respectively, and ψ_{ti}^1 is the first order perturbed triplet state wave function. Then the time-dependent electron-photon interaction dipole transition operator, $\hat{H}_{ep} = -\frac{e}{m_e^*}\mathbf{A} \cdot \mathbf{p}_e$, is used to calculate the transition matrix element μ_{T_1-G} between ψ_{ti}^1 (7.38) and the singlet ground state wave function ψ_{SG}^0. We thus obtain:

$$\mu_{T_1-G} =< \psi_{SG}^0 \| H_{ep} \| \psi_{ti}^1 > \sum_{j \neq i} \frac{<^3 \psi_{ti}^0 \| H_{so} \|^1 \psi_{sj}^0 >}{E_{ti}^0 - E_{sj}^0} < \psi_{sj}^0 \| \hat{H}_{ep} \| \psi_{sG}^0 >. \tag{7.39}$$

which is non-zero because of the mixed character (with contributions from both singlet and triplets) of the perturbed state with the wavefunction as obtained in (7.38). As the operator $\hat{H}_{ep}$ does not have any spin dependence it can cause transitions only between similar parity states, and hence the contribution of the singlet states (second term of (7.38)) becomes nonzero as it is obtained in (7.39). The rate of the spontaneous emission is then obtained using the transition matrix element in (7.39) with *Fermi's* golden rule. However, as stated above, the traditional approach cannot be applied in materials where the singlet and triplet exciton states appear far apart, as is the case of inorganic noncrystalline and organic semiconductors and polymers. What approach should one apply to calculate the transition rate from a triplet exciton to the ground state and vice versa? This problematic question prompted the invention of a new time-dependent exciton-spin-orbit-photon interaction operator in 2007 [64] as described below.

7.5.2.1 Time-Dependent Exciton-Spin-Orbit-Photon Interaction Operator

I. Atomic case

We first consider the spin-orbit interaction of an electron in an atom given by [67]:

$$\hat{H}_{so}^{at} = -\frac{eg}{2m_e^2c^2}\mathbf{s}_e \cdot \mathbf{p}_e \times \mathbf{E}, \tag{7.40}$$

where g is the gyromagnetic ratio ($g = 2$), $\mathbf{s}_e$ and $\mathbf{p}_e$ are the spin angular momentum and orbital momentum of the electron, respectively, and $\mathbf{E} = -\nabla V_n$ is the electric field on the electron generated by the electron- nuclear potential $V_n = \frac{Ze\kappa}{r_e}$, $\kappa = 1/4\pi\varepsilon_0$. Equation (7.40) is the starting expression for the spin-orbit interaction from which the spin-orbit interaction given in (7.36) is derived. The interaction operator in (7.40) is a stationary operator because it always exists in an atom. Now, if we shine light on the atom then the interaction in (7.40) will modify to:

$$\hat{H}_{so}^{at} = -\frac{eg}{2m_e^2c^2}\mathbf{s}_e \cdot (\mathbf{p}_e + \frac{e}{c}\mathbf{A}) \times (-\frac{1}{c}\frac{\partial \mathbf{A}}{\partial \mathbf{t}} - \nabla V_n) + \frac{eg}{m_e c}\mathbf{s}_e \cdot \mathbf{H}, \tag{7.41a}$$

where $\boldsymbol{A}$ is the vector potential of photons suitable for the electron-spin-orbit-photon interaction through the triplet excitation and it is given by:

$$\mathrm{A} = \sum_{\lambda} A_{ot}\left(\hat{\varepsilon}_\lambda c_\lambda^+ e^{-i\omega_\lambda^t} + \varepsilon_\lambda c_\lambda e^{i\omega_\lambda^t}\right) \tag{7.41b}$$

where $A_{ot} = [a\pi c^2\hbar/\varepsilon_0\varepsilon\omega_\lambda V]^{1/2}$, ε_λ is the polarization unit vector and $\mathbf{H} = \nabla \times \mathbf{A}$ is the magnetic field of the electromagnetic radiation. It may be noted that the second term of the vector potential in (7.41a) represents absorption of a photon so it will not be considered from here onwards. The modification in (7.41a) by shining light occurs due to the fact that an electromagnetic radiation field has got its own electric and magnetic fields which get added to the existing fields in (7.40). The effect of the electromagnetic radiation also modifies the electron orbital momentum, which has been completely ignored in earlier works [54] and this is what gives rise to the new time-dependent electron-spin-orbit interaction as shown below.

The interaction operator thus obtained in (7.41a), (7.41b) can be further simplified. Within the dipole approximation we get $\nabla \times \mathbf{A} = \mathbf{0}$, the magnetic contribution vanishes and also two other terms vanish because of the following:

$$\frac{e}{c^2}\mathbf{s}_e \cdot (\mathbf{A} \times \frac{\partial \mathbf{A}}{\partial t}) = 0, \tag{7.42a}$$

and

$$\frac{1}{c}\mathbf{s}_e \cdot \mathbf{p}_e \times \frac{\partial \mathbf{A}}{\partial \mathbf{t}} = -\frac{i\hbar}{c}\mathbf{s}_e \cdot \nabla \times \frac{\partial \mathbf{A}}{\partial \mathbf{t}} = -\frac{i\hbar}{c}\mathbf{s}_e \cdot \frac{\partial}{\partial t}(\nabla \times \mathbf{A}) = 0. \tag{7.42b}$$

Even otherwise, the contribution of the term in (7.42b) is expected to be small and therefore will not be considered here.

Substituting (7.42a), (7.42b) in (7.41a), (7.41b) the interaction operator reduces to [64]:

$$\hat{H}_{so}^{at} = -\frac{eg}{2m_e^2c^2}(-\frac{Ze\kappa\mathbf{s}_e \cdot \mathbf{L}}{r_e^3} - \frac{e}{c}\mathbf{s}_e \cdot (\mathbf{A} \times \nabla V)), \tag{7.43}$$

where $\mathbf{L} = \mathbf{r}_e \times \mathbf{p}$ is the orbital angular momentum of the electron. The first term of (7.43) is the usual spin-orbit interaction operator as given in (7.36) and it is obtained in the absence of any radiation. Its inclusion in the Hamiltonian as a perturbation can only split the degeneracy of a triplet state. As explained above, this term is a stationary operator and hence it cannot cause a transition. Only the last term, which depends on spin, radiation and time can be considered as the time-dependent perturbation operator and hence can cause transitions. Only this term is of interest from here onwards and denoting it by $\hat{H}_{so}^{at(t)}$ it can be written as:

$$\hat{H}_{so}^{at(t)} = -\frac{e^3 g Z\kappa}{2m_e^2 c^2 r_e^2} \sum_{\lambda} (\frac{2\pi\hbar}{\varepsilon_0 \omega_\lambda V})^{1/2} e^{-i\omega t} \mathbf{s} \cdot (\hat{\varepsilon}_\lambda \times \hat{\mathbf{r}}_e) c_\lambda^+, \tag{7.44}$$

where $\hat{\mathbf{r}}_e = \frac{\mathbf{r}_e}{r_e}$ is a unit vector. For evaluating the triple scalar product of three vectors, without the loss of any generality we may assume that vectors $\hat{\varepsilon}_\lambda$ and $\hat{\mathbf{r}}_e$ are in the xy-plane at an angle ϕ_λ. Then we get $\hat{\varepsilon}_\lambda \times \hat{\mathbf{r}}_e = \sin\phi_\lambda \hat{\eta}$, $\hat{\eta}$ being a unit vector perpendicular to the xy-plane. This gives $\mathbf{s} \cdot (\hat{\varepsilon}_\lambda \times \hat{\mathbf{r}}_e) = \mathbf{s} \cdot \hat{\eta} \sin\phi_\lambda = s_z \sin\phi_\lambda$, which simplifies (7.44) as:

$$\hat{H}_{so}^{(t)} = -\frac{e^3 g Z\kappa}{2m_e^2 c^2 r_e^2} \sum_{\lambda} (\frac{2\pi\hbar}{\varepsilon_0 \omega_\lambda V})^{1/2} e^{-i\omega t} \sin\phi_\lambda s_z c_\lambda^+. \tag{7.45}$$

Let us now consider that by shining light on the atom we have excited an electron from the ground state to the excited state and thereby creating a hole in the ground state. The field operator for an electron in the excited state and a hole in the ground state can be, respectively, written as:

$$\hat{\psi}_e(r_e) = \sum_{\sigma_e} \varphi_e(r_e, \sigma_e) a_e(\sigma_e), \tag{7.46a}$$

and

$$\hat{\psi}_h(r_e) = \sum_{\sigma_h} \varphi_g * (r_e, \sigma_h) d_g(\sigma_h); \quad d_g(\sigma) = a_g^+(-\sigma), \tag{7.46b}$$

where $\varphi(r_e, \sigma)$ is the electron or hole wave function as a product of orbital and spin functions corresponding to spin $\sigma = 1/2$ or $-1/2$, and $a_e(\sigma)$ and $d_g(\sigma)$ are the annihilation operators of an electron in the excited (e) state and hole in the ground (g) state, respectively. It may be noted that in an atom it is the same electron that is excited from the ground to the excited state therefore the same coordinate r_e is used for both the electron and hole in (7.46a), (7.46b). Using (7.46a), (7.46b) the interaction operator in (7.45) can be expressed in second quantization as:

$$\hat{H}_{so}^{at(t)} = -\frac{e^3 g Z\kappa}{2m_e^2 c^2 r_e^2} \sum_{\lambda} (\frac{2\pi\hbar}{\varepsilon_0 \omega_\lambda V})^{1/2} e^{-i\omega t} \sin\phi_\lambda < \varphi_h(r_e)|r^{-2}|\varphi_e(r_e) > \\ \times \sum_{\sigma_e, \sigma_h} \delta_{\sigma_e, -\sigma_h} s_z a_e(\sigma_e) d_g(\sigma_h) c_\lambda^+ \tag{7.47}$$

The sum over spins in (7.47) can be expressed for triplet configurations between an electron and a hole as:

$$a_e(+1/2)d_g(+1/2) = a_e(+1/2)a_g^+(-1/2)$$

$$\frac{1}{\sqrt{2}}[a_e(+1/2)d_g(-1/2) - a_e(-1/2)d_g(+1/2)] \tag{7.48a}$$

$$= \frac{1}{\sqrt{2}}[a_e(+1/2)a_g^+(+1/2) - a_e(-1/2)a_g^+(-1/2)] \tag{7.48b}$$

$$a_e(-1/2)d_g(-1/2) = a_e(-1/2)a_g^+(+1/2) \tag{7.48c}$$

Using the property of the spin operator $s_z a_e(\pm\frac{1}{2}) = \pm\frac{1}{2}\hbar a_e(\pm\frac{1}{2})$ we find that only the form of triplet configuration of (7.48b) gives the non-zero interaction operator in (7.47) and then (7.47) becomes:

$$\hat{H}_{so}^{at(t)} = -\frac{\hbar e^3 g Z\kappa}{4m_e^2c^2}\sum_{\lambda}(\frac{2\pi\hbar}{\varepsilon_0\omega_\lambda V})^{1/2}e^{-i\omega t}\sin\phi_\lambda[< \varphi_h(r_e)|r_e^{-2}|\varphi_e(r_e) >$$
$$\times [\frac{1}{\sqrt{2}}(a_e(+1/2)d_g(-1/2) + a_e(-1/2)d_g(+1/2))]c_\lambda^+ \tag{7.49}$$

It may be noted that the operator s_z has flipped the triplet spin configuration to a singlet configuration in (7.49). This is the key influence of the spin-orbit interaction which flips the spin from the triplet to singlet configuration and hence enables theradiative recombination to occur and to illustrate this point is the objective of presenting the atomic case here. In what follows we will consider the case of noncrystalline semiconductors.

II. Noncrystalline semiconductors case

Here we consider the effect of the spin-orbit interaction on an excited pair of electron and hole. Following (7.40), the spin-orbit interaction Hamiltonian for such an excited pair in a sample with N atoms can be written as [64]:

$$\hat{H}_{so}^{a-sem} = -\frac{eg}{2\mu_x^2c^2}\mathbf{s}_e\cdot(\mathbf{p}_e\times\sum_{n=1}^{N}\mathbf{E}_{ne}) + \frac{eg}{2\mu_x^2c^2}\mathbf{s}_h\cdot(\mathbf{p}_h\times\sum_{n=1}^{N}\mathbf{E}_{nh}), \tag{7.50}$$

where $\mu_x^{-1} = m_e^{*-1} + m_h^{*-1}$ is the reduced mass of the exciton, m_e^* and m_h^* are the effective masses of the electron in the conduction band and hole in the valence band, respectively. Other quantities with subscript e represent the electron and with subscript h represent the hole. According to (7.41a), (7.41b), in the presence of radiation, (7.50) becomes:

$$\begin{aligned}\hat{H}_{so}^{a-sem} &= -\tfrac{eg}{2\mu_x^2c^2}\mathbf{s}_e\cdot(\mathbf{p}_e + \tfrac{e}{c}\mathbf{A}_e)\times(-\tfrac{1}{c}\tfrac{\partial\mathbf{A}_e}{\partial t} - \textstyle\sum_{n=1}^{N}\nabla V_{ne})\\ &+\tfrac{eg}{2\mu_x^2c^2}\mathbf{s}_h\cdot(\mathbf{p}_h - \tfrac{e}{c}\mathbf{A}_h)\times(-\tfrac{1}{c}\tfrac{\partial\mathbf{A}_h}{\partial t} - \textstyle\sum_{n=1}^{N}\nabla V_{nh})\end{aligned}, \tag{7.51}$$

where the zero magnetic contribution is neglected. Applying the results of (7.42a), (7.42b), the Hamiltonian in (7.51) reduces to:

$$\hat{H}_{so}^{a-sem} = -\frac{eg}{2\mu_x^2 c^2}(-\sum_{n=1}^{N}\frac{Z_n e\kappa \mathbf{s}_e \cdot \mathbf{L}_{en}}{\varepsilon r_{en}^3} - \frac{e}{c}\mathbf{s}_e \cdot (\mathbf{A}_e \times \sum_{n=1}^{N}\nabla V_{ne})) + \frac{eg}{2\mu_x^2 c^2}(-\sum_{n=1}^{N}\frac{Z_n e\kappa \mathbf{s}_h \cdot \mathbf{L}_{hn}}{\varepsilon r_{en}^3} + \frac{e}{c}\mathbf{s}_h \cdot (\mathbf{A}_h \times \sum_{n=1}^{N}\nabla V_{nh})) \tag{7.52}$$

where ε is the static dielectric constant of the material. It may be pointed out here that the interaction operator as obtained in (7.52) is the same for a triplet exciton and an excited pair of electron and hole in a triplet spin configuration.

Here again, the first term in both electron and hole interactions represents the stationary spin orbit interaction and the second term in each represents the time-dependent electron- and hole- spin-orbit-photon interaction operator. We will consider only this last term in each which are responsible for the transition of triplet radiative recombination. Following the procedures applied above and using $A_0 = (\frac{2\pi\hbar}{\varepsilon_0\varepsilon\omega V})^{1/2}$ for a solid, the time-dependent part of the electron and hole-spin-orbit-photon interaction, denoted by $\hat{H}_{so}^{a-sem(t)}$ from (7.52), can written as:

$$\hat{H}_{so}^{a-sem(t)} = -\frac{e^3 g\kappa}{2\mu_x^2\varepsilon c^2}\sum_{\lambda,n}[\frac{Z_n}{r_{en}^2}(\frac{2\pi\hbar}{\varepsilon_0\varepsilon\omega_\lambda V})^{1/2}\sin\phi_{\lambda en}s_{ez} + \sum_{\lambda,n}\frac{Z_n}{r_{hn}^2}(\frac{2\pi\hbar}{\varepsilon_0\varepsilon\omega_\lambda V})^{1/2}\sin\phi_{\lambda hn}s_{hz}]e^{-i\omega_\lambda t}c_\lambda^+, \tag{7.53}$$

The field operator of an electron in the conduction band can be written as:

$$\hat{\psi}_c(r_e) = N^{-1/2}\sum_{l,\sigma_e}\exp(i\mathbf{t}_e \cdot \mathbf{R}_l^e)\varphi_l(r_e,\sigma_e)a_{cl}(\sigma_e), \tag{7.54}$$

where $\mathbf{R}_l^e$ is the position vector of an atomic site at which the electron is created, $\varphi_l(r_e)$ is the atomic wave function of an electron at the site l, r_e is the position coordinate of the electron with respect to site l and $\mathbf{t}_e$ is the same as given in (7.5). $a_{cl}(\sigma_e)$ is the annihilation operator of an electron with energy E_e and spin σ_e at a site l in the conduction c band. Likewise the field operator, $\hat{\psi}_v(r_h)$, of a hole excited with an energy E_h and spin σ_h in the valence band can be written as:

$$\hat{\psi}_v(r_h) = N^{-1/2}\sum_{l,\sigma_h}\exp(-i\mathbf{t}_h \cdot \mathbf{R}_l^h)\varphi_l^*(r_h,\sigma_h)d_{vl}(\sigma_h), d_{vl}(\sigma_h) = a_{vl}^+(-\sigma_h), \tag{7.55}$$

where $d_{vl}(\sigma_h)$ is the annihilation operator of a hole in the valence band v with energy E_h and spin σ_h.

Using (7.53), (7.5) and the triplet configurations of the electron and hole spins as given in (7.48a), (7.48b), (7.48c), the interaction operator in (7.54) can be written in the second quantisation as:

$$\begin{aligned}\hat{H}_{so}^{a-sem(3)} &= -\frac{\hbar e^3 g\kappa}{4\mu_x^2 \varepsilon c^2} N^{-1} \sum_{l,m} \exp[i\mathbf{t}_e \cdot \mathbf{R}_l^e] \exp[-i\mathbf{t}_h \cdot \mathbf{R}_m^h] \\ &\times \sum_{\lambda,n} Z_n (\frac{2\pi\hbar}{\varepsilon_0 \varepsilon \omega_\lambda \varepsilon V})^{1/2} [\sin\phi_{\lambda en} < \varphi_m(r_h)|r_{en}^{-2}|\varphi_l(r_e) > \\ &+ \sin\phi_{\lambda hn} < \varphi_m(r_h)|r_{hn}^{-2}|\varphi_l(r_e) >] e^{-i\omega_\lambda t} \\ &\times [\frac{1}{\sqrt{2}}(a_{cl}(+1/2)d_{vm}(-1/2) + a_{cl}(-1/2)d_{vm}(+1/2))] c_\lambda^+\end{aligned} \tag{7.56}$$

In deriving (7.56) all properties of spin operators used in deriving (7.49) have been applied.

We now consider a transition from an initial state with a triplet excitation whose spin has been flipped by the spin-orbit interaction but it has no photons, to a final state with no excitation (ground state) and one photon created in a mode λ. Within the occupation number representation, such initial $|i>$ and final $|f>$ states can be respectively written as:

$$|i> = |\frac{1}{\sqrt{2}}[a_{cl}^+(+1/2)d_{vm}^+(-1/2) + a_{cl}^+(-1/2)d_{vm}^+(+1/2)]|0> |0_p>, \tag{7.57}$$

$$|f> = c_\lambda^+|0> |0_p>, \tag{7.58}$$

where $|0>$ and $|0_p>$ represent the vacuum states of electrons (valence band completely filled and conduction band completely empty) and photons (no photons), respectively. Using (7.57) and (7.58), we get the transition matrix element as:

$$\begin{aligned}< f|\hat{H}_{so}^{a-sem(3)}|i> &= -\frac{\hbar e^3 g\kappa}{4\mu_x^2 \varepsilon c^2} N^{-1} \sum_{l,m} \exp[i\mathbf{t}_e \cdot \mathbf{R}_l^e] \exp[-i\mathbf{t}_h \cdot \mathbf{R}_m^h] \\ &\times \sum_{n} Z_n (\frac{2\pi\hbar}{\varepsilon_0 \varepsilon \omega_\lambda V})^{1/2} [\sin\phi_{\lambda en} < \varphi_m(r_h)|r_{en}^{-2}|\varphi_l(r_e) > \\ &+ \sin\phi_{\lambda hn} < \varphi_m(r_h)|r_{hn}^{-2}|\varphi_l(r_e) >] e^{-i\omega_\lambda t} \delta_{l,m},\end{aligned} \tag{7.59}$$

where $\delta_{l,m}$ ensures that at the time of recombination both particles are on the same site. The two integrals depend on the inverse squares of the electron and hole distances from a nucleus and therefore only the nearest nucleus is important and the influences of other nuclei can be neglected as an approximation. In a pure material, the atomic

number will be the same for all atoms and hence it is site independent. Incorporating these two points in (7.59), the transition matrix element for a pure material is obtained as:

$$< f|\hat{H}_{so}^{a-sem(3)}|i > \approx -\frac{\hbar e^3 g Z\kappa}{4\mu_x^2 \varepsilon c^2}(\frac{2\pi\hbar}{\varepsilon_0 \varepsilon \omega_\lambda V})^{1/2} N^{-1} \sum_{l,m} \exp[i\mathbf{t}_e \cdot \mathbf{R}_l^e] \exp[-i\mathbf{t}_h \cdot \mathbf{R}_m^h]$$
$$\times [\sin\phi_{\lambda em} < \varphi_m(r_h)|r_{em}^{-2}|\varphi_l(r_e) >$$
$$+ \sin\phi_{\lambda hm} < \varphi_m(r_h)|r_{hm}^{-2}|\varphi_l(r_e) >] e^{-i\omega_\lambda t} \delta_{l,m} \quad (7.60)$$

It is to be noted that in a doped material with heavier atoms only the atomic number of the heavy atoms is to be used. This is because the transition matrix element is proportional to the atomic number and inversely proportional to the inverse square of the distance from a nucleus. Equation (7.60) can be simplified further with the following two approximations. (1) Considering that the two integrals give the inverse squares of the distance between the electron and its nearest nucleus and the hole and its nearest nucleus, respectively, we may approximate them as:

$$< \varphi_m(r_h)|r_{em}^{-2}|\varphi_l(r_e) > = < \varphi_m(r_h)|r_{hm}^{-2}|\varphi_l(r_e) > \approx (r/2)^{-2}, \quad (7.61)$$

where r is the average separation between the pair of excited charge carriers, electron and hole, and (2) assume that $\sin\phi_{\lambda em} = \sin\phi_{\lambda hm} \approx \sin\phi_\lambda$. With these two approximations, (7.35) becomes:

$$< f|\hat{H}_{so}^{a-sem(3)}|i > \approx -\frac{2\hbar e^3 g Z\kappa}{\mu_x^2 c^2 \varepsilon r^2}(\frac{2\pi\hbar}{\varepsilon_0 \varepsilon \omega_\lambda V})^{1/2} \sin\phi_\lambda e^{-i\omega_\lambda t} p_{eh}, \quad (7.62)$$

where

$$p_{eh} = N^{-1} \sum_{l,m} \exp[i\mathbf{t}_e \cdot \mathbf{R}_l^e] \exp[-i\mathbf{t}_h \cdot \mathbf{R}_m^h] \delta_{l,m} \quad (7.63)$$

Although the above two approximations may not alter the magnitude of the transition matrix element, they have simplified the expression considerably. p_{eh} in (7.63) is expected to be different for the four different possibilities of transitions illustrated in Fig. 7.4. Accordingly it can be evaluated by considering the four possibilities of radiative recombination between the excited pair of electron and hole as shown below.

7.5.2.2 Possibility: Extended-to-Extended States Transitions

Here both e and h are excited in their respective extended states and the average separation between e and h can be taken as the excitonic Bohr radius a_{ex}. By rearranging then the exponent in (7.63), we get p_{eh} as [64]:

$$p_{eh} = \exp[i\mathbf{t}_e \cdot \mathbf{a}_{ex}]\delta_{\mathbf{t}_e,\mathbf{t}_h} \text{and} |p_{eh}|^2 = \delta_{\mathbf{t}_e,\mathbf{t}_h}. \quad (7.64)$$

Using $r = a_{ex}/\varepsilon$ and (7.64) in (7.62), we find the corresponding square of the transition matrix element as:

$$| < f|\hat{H}_{so}^{a-sem(3)}|i > |^2 \approx [-\frac{2\hbar e^3 g Z\kappa\sqrt{\varepsilon}}{\mu_x^2 c^2 a_{ex}^2}]^2 (\frac{2\pi\hbar}{\varepsilon_0 \omega_\lambda V}) \sin^2\phi_\lambda. \quad (7.65)$$

For a triplet exciton the excitonic Bohr radius is obtained as $a_{ex} = \frac{\mu\varepsilon}{\mu_x} a_0$ [16], where $a_0 = 0.529\,\text{Å}$ is the Bohr radius and μ is the reduced mass of electron in the hydrogen atom.

Using (7.65) and Fermi's golden rule, the rate $R_{sp}^{a-sem}(\text{s}^{-1})$ of spontaneous emission from a triplet exciton in amorphous semiconductors can be written as [64, 69]:

$$R_{sp} = \frac{16\pi^2\hbar^2 e^6 g^2 Z^2 k^2 \varepsilon}{\varepsilon_0 \mu_x^4 c^4 a_{ex}^4 \omega_\lambda V} \sin^2\phi_\lambda \sum_{E_c', E_v'} f_c f_v \delta(E_c' - E_v' - \hbar\omega_\lambda), \quad (7.66)$$

where f_c and f_v are the probabilities of occupation of an electron in the conduction and a hole in the valence bands, respectively. E_c' and E_v' are the energies in the conduction and balance bands to which an electron and hole can respectively be excited. Assuming that the excited charge carriers are in thermal equilibrium with the lattice, f_c and f_v can be given by the Maxwell-Boltzmann distribution functions and then their product is obtained as:

$$f_c f_v \approx \exp[-(\hbar\omega_\lambda - E_0)/\kappa_B T], \quad (7.67)$$

Using (7.67) in (7.66) and by converting the summation into integration over energy, we get the rate of spontaneous emission as:

$$R_{sp}^{a-sem} = \frac{16 e^6 g^2 Z^2 k^2 \varepsilon}{\varepsilon_0 \mu_x c^4 a_{ex}^4 (\hbar\omega_\lambda)\hbar^3 \nu\rho_A} (\hbar\omega - E_0)^2 \exp[-(\hbar\omega_\lambda - E_0)/\kappa_B T]\Theta(\hbar\omega - E_0), \quad (7.68)$$

where E_0 is the lowest energy state within the conduction band from where the radiative recombination occurs and it is given by [60, 63]:

$$E_0 = \frac{(1+\beta)E_{mx} - 2}{(1+\beta)}, \quad (7.69)$$

where $\beta = 1/\kappa_B T$ and E_{mx} is the energy at which the peak of the triplet PL is observed.

7.5.2.3 Possibilities: Transitions Involving Extended and Tail States

In the possibility (2) where the electron is in the extended state and hole is in the tail state, we can write p_{eh} as [60, 62]:

$$p_{eh} = N^{-1} \sum_{l} \sum_{m} \exp[i\mathbf{t}_e \cdot \mathbf{R}_l^e] \exp[-\mathbf{t}_{ht} \cdot \mathbf{R}_m^h] \delta_{l,m}, \tag{7.70}$$

By rearranging (7.70) and simplifying it, we get:

$$p_{eh} = \exp[i\mathbf{t}_e \cdot \mathbf{a}_{ex}] \delta_{\mathbf{t}_e, -i\mathbf{t}'_{ht}} \delta_{l,m}, \text{ and} |p_{eh}|^2 = \delta_{\mathbf{t}_e, -i\mathbf{t}'_{ht}} \delta_{l,m}. \tag{7.71}$$

Here $\delta_{\mathbf{t}_e, -i\mathbf{t}'_{ht}}$ preserves the momentum conservation.

Likewise for the possibility (3), where the electron is in the tail states and hole in the extended states, we get p_{eh} as:

$$p_{eh} = \exp[i\mathbf{t}_h \cdot \mathbf{a}_{ex}] \delta_{-i\mathbf{t}_{et}, \mathbf{t}_h} \delta_{l,m}, \text{ and } |p_{eh}|^2 = \delta_{-i\mathbf{t}_{et}, \mathbf{t}_h} \delta_{l,m} \tag{7.72}$$

Substituting (7.71) and (7.72) in (7.62), we get the same form of the rate of spontaneous emission as obtained in (7.68) for the possibility (1). However, one should remember that different reduced masses and excitonic Bohr radii need to be used for the possibilities (2) and (3).

7.5.2.4 Transitions from Tail-to-Tail States

In this case, an exciton loses its usual excitonic character and behaves like a geminate pair of type II [61]. This is because the localized form of wave functions of e and h does not give rise to an exciton. For this case, p_{eh} is obtained as:

$$p_{eh} = N^{-1} \sum_{l} \sum_{m} \exp[-\mathbf{t}_{et} \cdot \mathbf{R}_l^e] \exp[-\mathbf{t}_{ht} \cdot \mathbf{R}_m^h] \delta_{l,m}. \tag{7.73}$$

By rearranging the exponents and carrying out the sum we get [60, 62]:

$$p_{eh} = \exp[-\mathbf{t}_{et} \cdot \mathbf{a}_{ex}] \delta_{\mathbf{t}_{et}, -\mathbf{t}_{ht}} \delta_{l,m} \text{and} |p_{eh}|^2 = \exp[-2\mathbf{t}_e \cdot \mathbf{a}_{ex}] \delta_{\mathbf{t}_{et}, -\mathbf{t}_{ht}} \delta_{l,m}. \tag{7.74}$$

Using (7.74) in (7.62) and denoting the spontaneous rate in the tail-states by R_{spt}^{a-sem}, we get:

$$R_{spt}^{a-sem} = R_{sp}^{a-sem} \exp[-2t_{et} a_{ex}], \tag{7.75}$$

where the pre-exponential factor is the same as in (7.68). Here again one has to use the corresponding reduced mass and exciton Bohr radius.

Let us apply the above theory of spontaneous emission from triplet excitons to the case of a-Si:H. In a-Si:H the measured value of $E_{mx} = 1.320\,\text{eV}$ at a temperature of 3.7 K by Aoki et al. [68]. Using this in (7.69), we get $E_0 = 1.319\,\text{eV}$. The optical gap energy defined as the energy difference between the electron and hole mobility edges, $E_c - E_v = 1.8\,\text{eV}$ [26]. That means the triplet PL peak occurs with a *Stokes* shift of 0.48 eV, which is not possible solely due to the exciton binding energy.

It is well established that in a-Si:H the non-radiative relaxation of charge carriers is much faster, in the ps time range, than in crystalline Si. It is also known that holes relax to the tail states faster than the electrons [40]. Therefore, it is expected that PL occurs after at least holes have relaxed to the tail states, which means we should look at the rates of spontaneous emission only from the possibilities (2) to (4). The effective masses of electrons in the conduction band and holes in the valence band are found to be equal in sp^3 hybrid semiconductors like a-Si:H [16, 60, 63]. Thus, in the extended states the effective mass of charge carriers is $m_e^* = m_h^* = 0.34 m_e$ and in the tail states $m_{et}^* = m_{ht}^* = 7.1 m_e$. Using these values for the possibility (2) and (3) we get $\mu_x = 0.32 m_e$ and excitonic Bohr radius for a triplet exciton as $a_{ex} = 2.0\,\text{nm}$ [60]. For a-Si:H, $\varepsilon = 12$, $\nu = 4$ and $\rho_A = 5 \times 10^{28}\,\text{m}^{-3}$ [64]. Using these values and $\hbar\omega = E_{mx} = 1.32\,\text{eV}$ in (7.68), we get the rate of spontaneous emission for possibilities (2) and (3) at 3.7 K as $R_{sp}^{a-sem} = 13.94\,\text{s}^{-1}$, which gives a radiative lifetime, $\tau_R = 1/R_{sp}^{a-sem} = 71\,\text{ms}$.

For the possibility (4) when both charge carriers have relaxed in their respective tail states, they are not excitons. They are created when a triplet exciton has relaxed such that both of its carriers are localized in the tail states. This is an example of a geminate pair of type II as discussed above. In this case, although the excited charge carriers are localized, they maintain their excitonic Bohr radius, spin and internal binding energy. For the possibility (4), we have $\mu_x = 3.55 m_e$, $a_{ex} = 0.178\,\text{nm}$, $t_{et} = 1.29 \times 10^{10}\,\text{m}^{-1}$ [60] and use the same values of $\hbar\omega$ and E_0 as for possibilities (2) and (3) in (7.75) to get $R_{spt}^{a-sem} = 198.93\ \text{s}^{-1}$ and $\tau_{Rt} = 5\,\text{ms}$. This is shorter than the radiative lifetime calculated above (71 ms) for the possibility (2) and (3) but still in the ms time range, because of the shorter excitonic Bohr radius. This agrees quite well with the experimental radiative lifetime for a triplet exciton measured by Aoki [53] in the ms range at 3.7 K. It may therefore be concluded that the triplet phosphorescence observed at 3.7 K may be originating from possibilities (2)–(4).

Instead of using (7.68) and (7.65) for calculating the rate of spontaneous emission in a-Si:H, one may consider deriving it within the two level approximation (Like (7.32) for singlet excitons). The rate of phosphorescence thus obtained for a triplet exciton in amorphous solids is obtained as [64]:

$$R_{sp}^{2-level} = \frac{e^6 Z^2 \kappa^2 \varepsilon \hbar\omega_{12}}{2\mu_x^4 c^7 \varepsilon_0 a_{ex}^4}. \tag{7.76}$$

Using the above values for possibilities (2) and (3) with $\hbar\omega_{12} = 1.32\,\text{eV}$, we get $R_{sp}^{2-level} = 1.512\ \text{s}^{-1}$ and the corresponding radiative lifetime, $\tau_R = 0.661\,\text{s}$. For the

possibility (4), (7.76) gives $R_{sp}^{2-level} = 1.591\,\mathrm{s}^{-1}$ and $\tau_R = 0.628\,\mathrm{s}$. These are much longer than the observed radiative lifetime in the ms time range. This implies that the two level approximation may not be very suitable for noncrystalline semiconductors.

7.5.2.5 Discussions

Using the new time-dependent spin-orbit-photon interaction operator thus derived here as a perturbation and applying the first order time-dependent perturbation theory, the rates of spontaneous emission from a triplet excitoncreated under the four possibilities are derived in noncrystalline semiconductors with energy bands and localized tail states. The rate of spontaneous emission thus derived is found to be proportional to the square of the atomic number of an atom and inversely proportional to the fourth power of the distance between the excited pairs of charge carriers in noncrystalline semiconductors. Such sensitive dependences on Z^2 and r^{-4} are the main causes for the nearest heavy atom to contribute dominantly to the radiative recombination of triplet excitons. This explains very clearly why doping with heavy atoms increases the efficiency of triplet phosphorescence in polymers, which is described in Chap. 8 in detail. The present results also suggest that the efficiency of triplet phosphorescence can be used as a measure of the presence of heavy atom impurities in noncrystallinestructures, including organic materials.

The theory developed here for amorphous semiconductors has been applied to a-Si:H where the phosphorescence from triplet excitons has been measured using the quantum frequency-resolved spectroscopy (QFRS) technique [53, 68]. In noncrystallinematerials, due to the existence of tail states, there are four possibilities for creating excitons as described above: (1) both the excited carriers are in their extended states, (2) electron is in the extended and hole in the tail states, (3) electron is in the tail and hole in the extended states, and (4) both are in their respective tail states. The possibility (1) is not applicable in a-Si:H because the triplet PL occurs at a Stokes shift of 0.48 eV, which is much larger than the triplet exciton binding energy of about 60 meV in a-Si:H for the possibility (1).

About four decades ago a considerable research interest was devoted to studying the phosphorescence from triplet states in organic molecules and solids [54, 55, 70–72]. Hameka [54] has reviewed the theoretical attempts made then in calculating the rates of spontaneous emission from a triplet state in aromatic molecules. Following the traditional approach, described through (7.37)–(7.39), it was found that the contribution to the triplet state emission was very small even after the inclusion of terms beyond the dipole approximation. This is in agreement with the present result as well as derived in (7.43), where the interaction operator is obtained with two non-zero terms within the dipole-approximation. The first term is the usual stationary spin-orbit interaction operator and second term is the time-dependent spin-photon interaction operator that can cause radiative transitions, but it has been overlooked in earlier work [64]. The absence of any known time-dependent spin-orbit interaction operator is probably the reason for developing the traditional approach of first splitting the triplet state energy by the stationary spin-orbit interaction (the

first term in (7.43)) as a perturbation and then calculating the transition between the spin-allowed states within the usual dipole approximation. In fact, Hameka [54] does mention about a kind of confusion in the theoretical development in those days for calculating the radiative lifetime of triplet states in aromatic molecules. The case of organic semiconductors and polymers will be discussed in Chap. 8.

7.6 Conclusions

It is shown that the effective mass approximation developed in the real coordinate space can be successfully applied to study the electronic and optoelectronic properties of noncrystalline semiconductors, including the mechanism of occurrence of the double sign reversal leading to the anomalous Hall effect observed in a-Si:H. The application of the new time-dependent exciton-spin-orbit interaction operator in harvesting the radiative emission from triplet excitons is also reviewed.

References

1. C. Kittel, *Introduction to Solid State Physics*, 8th edn. (Wiley, Hoboken, 2004)
2. J. Ziman, *Principles of the Theory of Solids*, 2nd edn. (Cambridge University Press, Cambridge, 1972)
3. N.W. Ashcroft, N.D. Mermin, *Solid State Physics* (Saunders College, West Washington Square, 1976)
4. P.A. Taylor, *A Quantum Approach to Solid State Physics* (Prentice Hall, Englewood Cliffs, 1971)
5. L.E. Lyons, F. Gutman, *Organic Semiconductors* (Wiley, Sydney, 1967)
6. A.S. Davydov, *Theory of Molecular Excitons* (McGraw-Hill, New York, 1962)
7. D.P. Craig, S.H. Walmsley, *Excitons in Molecular Crystals* (Benjamin, New York, 1968)
8. C.K. Chang, C.R. Fincher Jr, Y.W. Park, A.J. Heeger, H. Shirakawa, E.J. Louis, S.C. Gau, A.G. MacDiarmid, Phys. Rev. Lett. **39**, 1098 (1977)
9. C.W. Tang, Appl. Phys. Lett. **48**, 183 (1986)
10. G. Yu, J. Gao, J.C. Hummelen, F. Wudl, A.J. Heeger, Science **270**, 1789 (1995)
11. Yong Cao, Ian D. Parker, Yu. Gang, Chi Zhang, Alan J. Heeger, Nature **397**, 414 (1999)
12. J.H. Burroughes, D.D.C. Bradley, A.R. Brown, R.N. Marks, K. Mackay, R.H. Friend, P.L. Burns, A.B. Holmes, Nature **347**, 539 (1990)
13. J.J.M. Halls, C.A. Walsh, N.C. Greenham, E.A. Marseglia, R.H. Friend, S.C. Moratti, A.B. Holmes, Nature **376**, 498 (1995); also see the review by A.C. Morteani, R.H. Friend, C. Siva, in *Organic Light Emitting Devices: mSynthesis, Properties and Applications*, ed. by K. Mullen, U. Scherf (Wiley-VCH, Weinheim, 2006) and references therein
14. N.F. Mott, E.A. Davis, R.A. Street, Philos. Mag. **32**, 961 (1975)
15. N.F. Mott, E.A. Davis, *Electronic Processes in Non-crystalline Materials*, 2nd edn. (Clarendon Press, Oxford, 1979) and references therein
16. J. Singh, K. Shimakawa, *Advances in Amorphous Semiconductors* (Taylor & Francis, London, 2003)
17. E.A. Davis, Personal communication, Prof.Davis presented a historical account of the conference " International Conference on Amorphous and Microcrystalline Semiconductors (ICAMS)" at ICAMS 20, held in Campos do Jordão, Brazil in 2003. The first conference

was held in 1965 in Prague, Czechoslovakia under the title, "International Conference on Amorphous and Liquid Semiconductors (ICALS 1)" and Professor John Ziman was an invited participant

18. S. Ambros, R. Carius, H. Wagner, J. Non, Cryst. Solids **137–138**, 555 (1991)
19. J. Singh, T. Aoki, K. Shimakawa, Philos. Mag. B **82**, 855 (2002)
20. A. Madan, J. Non-Cryst. Solids **352**, 881 (2006)
21. P.G. LeComber, W.E. Spear, Phys. Rev. Lett. **25**, 509 (1970)
22. H.F. Stirling, R.C.G. Swan, Solid-State Electron. **8**, 653 (1965)
23. R.C. Chittick, J.H. Alexander, H.F. Stirling, J. Electrochem. Soc. Solid State Sci. **116**, 77 (1969)
24. W.E. Spear, P.G. LeComber, Solid State Commun. **17**, 1193 (1975)
25. S. Hagedus, Prog. Photovoltaics **14**, 393 (2006)
26. A. Slaoui, R.T. Collins, MRS Bull. **32**, 211 (2007)
27. K. Ramanathan, M.A. Contreras, C.L. Perkins, S. Asher, F.S. Hasoon, J. Keane, D. Young, M. Romero, W. Metzger, R. Noufi, J. Ward, A. Duda, Prog. Photovoltaics **11**, 225 (2003)
28. T. Aramoto, S. Kumazawa, H. Higuchi, T. Arita, S. Shibutani, T. Nishio, J. Nakajima, M. Tsuji, A. Hanafusa, T. Hibino, K. Omura, H. Ohyama, M. Murozono, Jpn. J. Appl. Phys. **36**, 6304 (1997)
29. R.H. Friend, R.W. Gymer, A.B. Holmes, J.H. Burroughes, R.N. Marks, C. Taliani, D.D.C. Bradley, D.A. Dos Santos, J.L. Brédas, M. Lögdlund, W.R. Salaneck, Nature **397**, 121 (1999)
30. M. Grätzel, Nature **414**, 338 (2001)
31. M.K. Nazeeruddin, A. Kay, I. Rodicio, R. Humphry-Baker, E. Mueller, P. Liska, N. Vlachopoulos, M. Graetzel, J. Am. Chem. Soc. **115**, 6382 (1993)
32. W.U. Huynh, J.J. Dittmer, A.P. Alivisatos, Science **295**, 2425 (2007)
33. D.J. Milliron, I. Gur, A.P. Alivisatos, MRS Bull. **30**, 41 (2005)
34. B. Kippelen, J.-L.Bredas, Energy Env. Sci. **2**, 251 (**2**009) and ref therein
35. Y. Toyozawa, Prog. Theor. Phys. **26**, 29 (1959); in *Polarons and Excitons* ed. by C.G. Kuper, G.D. Whitfield (Oliver and Boyd, Edinburgh, 1963)
36. S. Kivelson, C.D. Gelatt Jr, Phys. Rev. B **19**, 5160 (1979)
37. J. Singh, *Excitation Energy Transfer Processes in Condensed Matter* (Plenum, New York, 1994)
38. J. Singh, J. Mater. Sci. Mater. Electron. **14**, 171 (2003)
39. S. Kivelson, C.D. Gelatt Jr, Phys. Rev. B **19**, 5160 (1979)
40. K. Morigaki, *Physics of Amorphous Semiconductors* (World-Scientific-Imperial College Press, London, 1999)
41. R. Callaerts, M. Denayer, F.H. Hashimi, P. Nagels, Discuss. Faraday Soc. **50**, 27 (1970)
42. P. Nagels, R. Callaerts, F.H. Hashimiand, M. Denayer, Phys. Status Solidi **41**, K39 (1970)
43. E. Mytilineou, E.A. Davis, Edinburgh, p. 632 (1977)
44. P.G. LeComber, D.J. Jones, W.E. Spear, Philos. Mag. **35**, 1173 (1977)
45. L. Friedman, T. Holstein, Ann. Phys. **21**, 494 (1963)
46. L. Friedman, J. Non-Cryst. Solids **6**, 329 (1971)
47. D. Emin, Philos. Mag. **35**, 1189 (1977) in *Proceedings of 7th International Conference on Amorphous and Liquid Semiconductors*, ed. by W.E. Spear (CICL, Edinburgh, 1977), p. 249
48. N.F. Mott, Philos. Mag. B **63**, 3 (1991)
49. H. Okamoto, K. Hattori, Y. Hamakawa, J. Non-Cryst. Solids **164–166**, 445 (1993)
50. W.E. Spear, G. Willeke, P.G. LeComber, Phys. B **117–118**, 909 (1983)
51. W.E. Spear, G. Willeke, P.G. LeComber, A.G. Fitzgerald, J. Phys. Paris **42**, C4–257 (1981)
52. T. Aoki, in *Materials for Information Technology in the New Millennium*, ed. by J.M. Marshall et al. Proceedings of International Summer School in Condensed Matter Physics, Varna (Bath, 2001), pp. 58–65
53. T. Aoki, in *Optical Properties of Condensed Matter and Applications*, Chapter 5, ed. by J. Singh (John Wiley, Chichester, 2006), p. 99
54. H.F. Hameka, *The Triplet State* (Cambridge University Press, Cambridge, 1967), pp. 1–30
55. J.B. Birks, *Photophysics of Aromatic Molecules* (Wiley, London, 1970)

56. D. Beljonne, Z. Shuai, G. Pourtois, J.L. Bredas, J. Phys. Chem. A **105**, 3899 (2001)
57. K. Schmidt, S. Brovelli, V. Coropceanu, D. Beljonne, J. Cornil, C. Bazzini, T. Caronna, R. Tubino, F. Meinardi, Z. Shuai, J.L. Bredas, J. Phys. Chem. A **111**, 10490 (2007)
58. R.S. Knox, *Theory of Excitons* (Academic, New York, 1965)
59. D.S. McClure, J. Chem. Phys. **17**, 905 (1949)
60. J. Singh, I.-K. Oh, J. Appl. Phys. **97**, 063516–063529 (2005)
61. J. Singh, J. Non-Cryst. Solids **352**, 1160–1162 (2006)
62. J. Singh, Phys. Status Solidi C **3**, 3378–3381 (2006)
63. J. Singh, in *Optical Properties of Condensed Matter and Applications*, Chapter 6, ed. by J. Singh (John Wiley, Chchester, 2006), p. 107
64. J. Singh, Phys. Rev. B **76**, 085205 (2007)
65. J. Singh, *Physics of Semiconductors and their Hetrostructures* (McGraw-Hill, Singapore, 1993)
66. B.R. Henry, W. Siebrand, J. Chem. Phys. **51**, 2396 (1969)
67. S. Gasiorowicz, *Quantum Physics*, 2nd edn. (Wiley, New York, 1996)
68. T. Aoki, T. Shimizu, S. Komedoori, S. Kobayashi, K. Shimakawa, J. Non-Cryst.Solids **338–340**, 456 (2004) and T. Aoki, J. Non-Cryst. Solids **352**, 1138 (2006)
69. J. Singh, J. Mater. Sci.: Mater. Electron. **20**, S81 (2009)
70. M. Klessinger, J. Michl, *Excited States and Photochemistry of Organic Molecules* (VCH Publishers, Winheim, 1995)
71. R. Farchioni, G. Grosso (eds.), *Organic Electronic Materials* (Springer, Berlin, Heidelberg, 2001), p. 394
72. D.S. McClure, J. Chem. Phys. **20**, 682 (1952)

Chapter 8
Excitonic Processes in Organic Semiconductors and Their Applications in Organic Photovoltaic and Light Emitting Devices

Monishka Rita Narayan and Jai Singh

Abstract This chapter discusses the excitonic processes in organic semiconductors and their applications in photovoltaic and light emitting devices fabricated from these materials. The mechanisms of excitonic absorption, diffusion and dissociation of excitons at the donor-acceptor interface are presented in bulk-heterojunction organic solar cells. After the formation of Frenkel excitons upon photon absorption, excitons must diffuse to the interface to dissociate into free charge carriers which are then collected at their respective electrodes. The interface must be in close proximity, of the order of the diffusion length, and for efficient dissociation the offset of the lowest unoccupied molecular orbital energy between the donor and acceptor must be at least equal to the exciton binding energy. The Förster and Dexter energy transfer mechanisms are used to calculate the exciton diffusion coefficients and exciton diffusion lengths for singlet and triplet excitons, respectively. The newly derived interaction operator between charge transfer exciton and molecular vibration energy is used to understand the mechanism and derive the rate of dissociation of excitons into free charge carriers. The exciton diffusion and dissociation in bulk-heterojunction organic solar cell are presented first followed by the radiative recombination of exciton in organic light emitting devices (OLEDs).

M. R. Narayan
Centre for Renewable Energy and Low Emission Technology,
Charles Darwin University, Darwin, NT 0909, Australia

J. Singh (✉)
Faculty of EHSE, School of Engineering and Information Technology,
Charles Darwin University, Darwin, NT 0909, Australia
e-mail: jai.singh@cdu.edu.au

J. Singh and R. T. Williams (eds.), *Excitonic and Photonic Processes in Materials*,
Springer Series in Materials Science 203, DOI: 10.1007/978-981-287-131-2_8,
© Springer Science+Business Media Singapore 2015

8.1 Introduction

The organic semiconductors consist of organic molecules, which are usually hydrocarbons. The inter-molecular separation in an organic solid is usually much larger than those in inorganic solids. As a result the overlap of inter-molecular electronic wavefunctions is relatively small which results in very narrow electronic energy bands, not much different from the electronic energy levels of the constituent organic molecules. This is the reason that organic solids like naphthalene, anthracene, etc. used to be referred as molecular solids [1–4] and the energy bands in organic solids correspond closely to energy levels of individual molecules. For example, the valence and conduction bands in organic solids are identified as the highest occupied molecular orbital (HOMO) and lowest unoccupied molecular orbital (LUMO) of individual molecules, respectively. The absorption of a photon occurs when the photon energy is larger than or equal to the energy separation between the LUMO and HOMO of individual molecules. An exciton is created when an electron (e) is excited from the HOMO to LUMO and thereby a hole (h) is created in the HOMO of a molecule, which means both e and h are excited on individual molecules. Therefore excitons created in organic semiconductors used to be known as molecular excitons [1–4]. The separation between the excited e and h is thus relatively small in comparison with that in inorganic semiconductors and hence these excitons are also referred to as small radii orbital excitons or Frenkel excitons as opposed to the large radii orbital excitons or Wannierexcitons observed in inorganic semiconductors, like Si and Ge.

Two types of devices made from organic semiconductors have attracted significant research attention recently. These are organic light emitting devices (OLEDs) and organic solar cells (OSCs). Easy formation of excitons in organic semiconductors, as discussed below, is favourable in the operation OLEDs but unfavourable in the operation of OSCs. Radiative recombination of excitons occurs due to Coulomb interaction and hence the exciton formation becomes an intermediate state prior to the emission of light by the radiative recombination of excitons. An OSC works on a principle that is the reverse of that of an OLED. In an OSC, solar photons excite excitons in organic semiconductors. The excitons need to be dissociated into free electrons and holes to be collected at their respective electrodes for generating current. The application of excitons in the operation of OSCs will be discussed first, followed by the operation of OLEDs.

8.2 Organic Solar Cells

Research interest in organic solar cells (OSCs) has escalated recently due to their cost effectiveness, flexibility, easy fabrication techniques and large scale production [5]. There are various types of OSCs, but the most efficient one at present is the bulk-heterojunction (BHJ) OSC [6]. As organic semiconductors cannot be doped in the same way as inorganic ones like Si, a p-n junction concept cannot be applied in

OSCs. The simplest OSC consists of a single layer organic material sandwiched between two electrodes. The top electrode, which is the anode, is a thin film of a transparent conducting oxide, e.g., indium tin oxide (ITO), and the bottom cathode is a thin film of a metal, like Ag, Al, Mg, etc. Solar photons incident on the top, excite excitons in the organic layer, with the electron excited to its LUMO and the hole in the HOMO. These excitons are dissociated into free electron (e) and hole (h) pairs and separated such that electrons are collected at the cathode and holes at the anode, by the potential energy available due to the difference between the work functions of the anode and cathode. This potential energy is usually not adequate to dissociate excitons as well as collect the charge carriers at their respective electrodes and hence such a simple OSC has very poor conversion efficiency of $<1\,\%$ [7]. The problem remained unsolved until the seminal work of Tang [8] replacing the single layer by a bilayer; the first layer is of a donor organic material and the second layer is of an acceptor organic material. Thus a donor-acceptor interface was introduced in the structure. A donor is an organic semiconductor with its LUMO located at a higher energy than that of the acceptor which is another organic semiconductor. In OSCs with the donor-acceptor interface, the difference between the energies of LUMO levels of the donor and acceptor materials provides additional excess energy available in the structure to dissociate excitons. Most OSCs fabricated currently are based on this concept. From this point of view, the operation of an OSC depends on the following four interdependent processes: (i) photon absorption and exciton generation, (ii) efficient transport of excitons to the interface before their quenching, (iii) dissociation into free e and h pairs at the interface and (iv) transport of e and h from the interface to the opposite electrodes. In a bilayer OSC, with the donor-acceptor interface being at a distance, the drawback is that the short exciton diffusion length in organic materials limits the thickness of the donor and acceptor layers [8, 9]. This problem was reduced by developing the bulk-heterojunction (BHJ) OSC.

In a BHJ OSC, the donor and acceptor organic materials are blended together to form an interface [10], which means that an interface can be found everywhere and hence the exciton dissociation becomes more efficient. However, in a bulk-heterojunction OSC also, the principal processes of operation remain the same as in a bilayer OSC and include: (1) Photon absorption and exciton formation [11, 12], (2) Exciton diffusion to the donor-acceptor interface [13], (3) Exciton dissociation at the interface [14] and (4) Transport of respective free charge carriers to opposite electrodes [15].

These four processes are interdependent and contribute to the conversion efficiency of bulk-heterojunction OSCs. If any of the above processes get hindered, the overall performance of an OSC is affected. This is one of the reasons why the conversion efficiency of OSCs prepared todate is relatively low (5–9.2 %) [16–19]. When photons are absorbed, the excited electron and hole pairs instantly form excitons due to the higher binding energy, E_B, in organic materials having low dielectric constant ($\varepsilon = 3$–4) [20–22]. After this process, excitons must be dissociated to create free electrons and holes in an OSC, a process as explained above that occurs at the donor-acceptor interface. Thus, after their creations, first the excited excitons are required to diffuse to the interface and then dissociate. Finally, free

charge carriers thus created need to be separated and transported to the opposite electrodes. Apparently only a few research efforts have been made in studying these processes in OSCs, systematically [8, 23–25]. The theory of the above four processes and their importance in the operation of bulk-heterojunction organic solar cells are represented here.

8.2.1 Photon Absorption and Formation of Singlet Triplet Excitons in OSCs

Photon absorption and exciton formation are primary processes in the operation of organic solar cells (OSCs) and hence play key roles in their conversion efficiency. Upon a photon absorption in the donor material of an OSC, an electron is excited to the LUMO, leaving a hole in the HOMO. The electron and hole instantly form a Frenkel exciton due to the low dielectric constant and weak intermolecular forces [26]. Rates of absorption of a photon to excite singlet and triplet excitons are described in this section. Absorption of a photon in any substance can excite an electron from the ground to the excited state. Such an excited state will usually be a singlet.

In organics, usually a triplet state lies at a lower energy, which can be populated from the singlet excited state through intersystem crossing. The excess singlet energy helps flipping the spin of a singlet excited electron which then relaxes to the triplet state. The triplet state can also be excited directly by photons of energy a little larger than that of the triplet state to flip the spin of the excited electron. The mechanism of absorption of a photon or excitation of an electron is well-known and is reviewed here first in Sect. 8.2.2 for completeness. Also, a triplet state can be excited directly due to the exciton-spin-orbit-photon interaction which is described in Sect. 8.2.3.

8.2.1.1 Excitation Due to Exciton-Photon Interaction

In this case, an electron is excited directly to a singlet state upon photon absorption. The interaction operator $\hat{H}_s$ between the exciton and photon is given by [27]:

$$\hat{H}_s = -\frac{e}{\mu_x}\mathbf{A} \cdot \mathbf{p} \tag{8.1}$$

where μ_x is the reduced mass of the exciton, **p** is the relative linear momentum of electron and hole inan exciton and **A** is the vector potential of the photon and is given by:

$$\mathbf{A} = \sum_{\lambda} A_o \hat{\varepsilon}_\lambda \left(c_\lambda e^{i\omega_\lambda t} + c_\lambda^+ e^{-i\omega_\lambda t} \right) \tag{8.2}$$

where $A_o = [2\pi c^2 \hbar / \varepsilon_o \omega_\lambda V]^{1/2}$, $\hat{\varepsilon}$ is the unit polarization vector, c_λ is the annihilation operator and c_λ^+ is the creation operator of a photon in mode λ,

respectively, e is electronic charge, ω_λ is the photon frequency, c is the speed of light, $\hbar$ is the reduced Planck's constant, ε_o is the vacuum permittivity and V is the illuminated volume.

The first term of (8.2) leads to photon absorption and the second term results in photon emission. Here only the first term will be considered for the absorption of a photon and the second term will be considered later for the emission of photons in organic light emitting devices. Incorporating field operators of electron in LUMO and hole in HOMO, the interaction operator for absorption in (8.1) can be written in second quantisation as:

$$\hat{H}_s = -\frac{e}{\mu_x}\sum_\lambda \left(\frac{\hbar}{2\varepsilon_o n^2 V w_\lambda}\right)^{1/2} Q_{LM} c_\lambda \quad (8.3)$$

where

$$Q_{LM} = N^{-1}\sum_l \sum_m \exp[-i\mathbf{t}_e \cdot \mathbf{R}_l^e]\exp[-i\mathbf{t}_h \cdot \mathbf{R}_m^h] Z_{lm\lambda} B_{LMlm}^{+} \quad (8.4)$$

where B_{LMlm}^{+} is the creation operator of an exciton by exciting an electron in the LUMO, L at site l and a hole in the HOMO, M at site m and rest of the symbols have their usual meaning as given in [27].

We consider excitation from HOMO to LUMO upon photon absorption as a transition from an initial state to final state. The initial state $|i\rangle$ consists of a photon and it can be expressed by the occupation number $|1\rangle\,|0\rangle$, with a photon and no exciton. The final state $|f\rangle$ has a singlet exciton and can be expressed as $|0\rangle\,|1\rangle$, with no photon and an exciton. Using these, the transition matrix element between the initial and final state is obtained as:

$$\left\langle f|\hat{H}_s\,|i\right\rangle = -\frac{e}{\mu_x}\sum_\lambda \left(\frac{\hbar}{2\varepsilon_o n^2 V w_\lambda}\right)^{1/2} p_{LM} \quad (8.5)$$

where

$$p_{LM} = N^{-1}\sum_l \sum_m \exp[-i\mathbf{t}_e \cdot \mathbf{R}_l^e]\exp[-i\mathbf{t}_h \cdot \mathbf{R}_m^h] Z_{lm\lambda}\delta_{l,m} \quad (8.6)$$

where $\delta_{l,m}$ represents the momentum conservation in the transition. Now applying Fermi's golden rule and the two-level approximation, the rate of singlet excitation, R_s is obtained as [11, 12, 27]:

$$R_s = \frac{4\kappa e^2 \omega^3 \sqrt{\varepsilon}\,|r|^2}{3\hbar c^3} \quad (8.7)$$

where r is the average separation between the electron and hole, $k = (4\pi\varepsilon_o)^{-1} = 9 \times 10^9$ and ε is the static dielectric constant of the material.

8.2.1.2 Excitation Due to Exciton-Spin-Orbit-Photon Interaction

The time-dependent exciton-spin-orbit-photon interaction operator derived in [28] can be expressed as

$$\hat{H}_t = -\frac{e^3 g\kappa}{2\mu_x^2 \varepsilon c^2} \sum_{\lambda,n} \left[\frac{Z_n}{r_{en}^2} \left(\frac{2\pi\hbar}{\varepsilon_0 \varepsilon \omega_\lambda V} \right)^{1/2} \sin\phi_{\lambda en} s_{ez} + \sum_{\lambda,n} \frac{Z_n}{r_{hn}^2} \left(\frac{2\pi\hbar}{\varepsilon_0 \varepsilon \omega_\lambda V} \right)^{1/2} \sin\phi_{\lambda hn} s_{hz} \right] \left[e^{i\omega_\lambda t} c_\lambda + e^{-i\omega_\lambda t} c_\lambda^+ \right] \quad (8.8)$$

where Z_n is the atomic number of an atom at the nth site, r_{en} and r_{hn} are the electron and hole distances from their nuclear site n, respectively and s_{ez} and s_{hz} are the spin projections along the z-axis of the electron and hole, respectively, in an exciton. Other symbols have their usual meanings [29]. Analogous to (8.2), the first term of (8.8), with the end factor, $e^{i\omega_\lambda t} c_\lambda$, corresponds to the photon absorption and the second, with the end factor $e^{-i\omega\lambda t} c_\lambda^+$, to photon emission. Only the first term will be used here to calculate the rate of absorption. The second term will be used in Sect. 8.3 for calculating the rate of spontaneous emission in organic light emitting devices.

In the donor layer of OSC, holes are created in HOMO and electrons in LUMO. Expressing such electron and hole states in second quantization, respectively, as [28]:

$$|\mathrm{LUMO}> = \sum_{\sigma_e} |\Psi_{\mathrm{LUMO}} > a_c^+(\sigma_e) \quad (8.9a)$$

$$|\mathrm{HOMO}> = \sum_{\sigma_h} |\Psi_{\mathrm{HOMO}} > d_g^+(\sigma_h) \quad (8.9b)$$

where $|\Psi_{\mathrm{LUMO}}>$ and $|\Psi_{\mathrm{HOMO}}>$ represent the molecular orbitals of LUMO and HOMO states and $a_e^+(\sigma_e)$ and $d_g^+(\sigma_h)$ are the creation operators of an electron in LUMO (e: excited) and hole in HOMO (g: ground) state with spins σ_e and σ_h, respectively. Using (8.8), the time-dependent operator of spin-orbit-exciton-photon interaction is obtained in second quantisation as [28]:

$$\hat{H}_t \approx -\frac{e^3 g Z\kappa}{\mu_x^2 c^2 \varepsilon r^2} \left(\frac{2\pi\hbar}{\varepsilon_0 \varepsilon V} \right)^{1/2} \sum_{\lambda} \sum_{\sigma_e,\sigma_h} \frac{\sin\lambda}{\sqrt{\omega_\lambda}} e^{i\omega t} \times (s_{ez} + s_{h_z}) a_e^+(\sigma_e) d_g^+(\sigma_h) \delta_{\sigma_e,\sigma_h} c_\lambda \quad (8.10)$$

The operator in (8.10) vanishes for singlet excitons. Considering the initial state of a photon and the final state of a triplet exciton and the transition operator in (8.10) as a perturbation, the rate of triplet excitation, R_t can be calculated from Fermi's golden rule. Applying the two-level approximation one obtains:

$$R_t = \frac{8e^6 g^2 Z^2 \kappa^2 (E_{LUMO} - E_{HOMO})}{\mu_x^4 c^7 \varepsilon_0 \varepsilon^3 r^4} \tag{8.11}$$

where g is the gyromagnetic ratio (g = 2) and $(E_{LUMO} - E_{HOMO})$ is the energy gap of the donor organic material, where the photons are absorbed. In deriving the rate in (8.11), the spin-orbit-photon interaction given in (8.8) is such that in the presence of photons an electron gets attracted to a nucleus and the attractive force is proportional to the atomic number and inverse square of the distance between the electron and nucleus. As terms within the summation sign depend on the inverse square of the distance of the electron from a nucleus, the nearest nucleus is expected to have the dominant influence and the presence of other nuclei may then be neglected [29]. Within this approximation, Z_n may be replaced by Z, an average site independent atomic number. However, this approximation is valid only for solids with atoms of not very different atomic numbers. In the case of hydrocarbons, only the atomic number of carbon is necessary to use. If a molecule contains heavier atoms, the atomic number of the heaviest atom should be used in the calculation. It may be noted that this approximation is not necessary for calculating the rates numerically. It is only used here to derive an approximate simple analytical expression for the rate of spontaneous emission.

The rates of formation of singlet and triplet excitatons can be calculated for organic solids using (8.7) and (8.11), respectively. In solids, one can replace the average separation between e and h in an exciton by the corresponding excitonic Bohr radius as $r = a_x/\varepsilon$, where a_x is the excitonic Bohr radius. Now substituting for r into (8.7) and (8.11), we get the rates of singlet and triplet excitation, respectively, as:

$$R_s = \frac{4\kappa e^2 (E_{LUMO} - E_{HOMO})^3 a_s^2}{3c^3 \varepsilon^{1.5} \hbar^4} \tag{8.12}$$

$$R_t = \frac{32 e^6 Z^2 \kappa^2 \varepsilon (E_{LUMO} - E_{HOMO})}{c^7 \varepsilon_o \mu_x^4 a_t^4} \tag{8.13}$$

where, $a_s = \frac{\alpha^2}{(\alpha-1)^2} \frac{\mu\varepsilon}{\mu_x} a_o$ and $a_t = \frac{\mu\varepsilon}{\mu_x} a_o$ are the excitonic Bohr radii of singlet and triplet excitons, respectively. Here, α is a material dependent constant representing the ratio of the magnitude of the Coulomb and exchange interactions between the electron and hole in an exciton, a_o is the Bohr radius and μ is the reduced mass of electron in a hydrogen atom. The singlet and triplet excitonic Bohr radii in organic materials have been calculated by Narayan and Singh [13].

The rate of absorption is calculated from (8.12) and (8.13) for various donor organic materials as a function of their energy gap. The inverse of the rate of absorption gives the time of formation of the respective exciton. Hence for various organic materials, the rate of absorption and excitonic formation time has been calculated as given in Table 8.1. Normally, organic materials consist of hydrocarbons, where Carbon, C, has the highest atomic number. The effect of light and heavy metals on the absorption rate of triplet exciton using (8.13) is also calculated using Z = 6 for C, and Z = 77 for Iridium (Ir).

Table 8.1 Rates of absorption and formation time of singlet excitons due to exciton-photon interaction and triplet excitons due to exciton-photon-spin-orbit interaction as a function of energy gap of the organic materials

Organic material	$E_{LUMO} - E_{HOMO}$ (eV)	R_t (C) 10^3 (s^{-1})	R_t (Ir) 10^5 (s^{-1})	τ_t (Ir) 10^{-6} (s)	R_s 10^{10} (s^{-1})	τ_s 10^{-11} (s)	References
P3OT	1.83	1.63	2.69	3.72	0.84	11.9	[30]
Pt(O-EP)	1.91	1.7	2.81	3.56	0.96	10.4	[31]
P3HT	2.1	1.87	3.09	3.24	1.27	7.85	[32]
PCBM	2.4	2.14	3.53	2.83	1.9	5.26	[33]
PPV	2.8	2.5	4.12	2.43	3.02	3.31	[34]
MEV-PPV	2.91	2.6	4.28	2.34	3.39	2.95	[35]
PFPy	2.94	2.62	4.32	2.31	3.49	2.86	[33]
α-NPD	3.1	2.77	4.56	2.19	4.1	2.44	[36]

According to Table 8.1, the rate of triplet excitation by incorporating Ir (Z = 77) increases by two orders of magnitude than without Ir i.e. with Z = 6. The rate of triplet absorption depends on the square of the atomic number and hence heavier atoms play the dominant role. It can be inferred from this that the incorporation of heavy metal atoms greatly enhances the rate of triplet excitations in OSCs.

Without the heavy metal, the spin-orbit interaction is negligible in organic solids and both singlet and triplet can be excited only through the exciton-photon interaction and subsequent intersystem crossing. A singlet can be easily dissociated to contribute to the conversion efficiency of an OSC. However, dissociation is difficult for triplet excitons because of their larger binding energy, leading to a low conversion efficiency. Further on dissociation of excitons is described in Sect. 8.2.4.

By incorporating heavy metal atoms, exciton-spin-orbit-photon interaction gets enhanced, leading to the enhanced rate of absorption in triplet excitations around such sites as given in (8.13). In organic solids each molecule can be incorporated with a heavy metal atom. However, this interaction simultaneously flips the spin to singlet configuration which becomes easier to dissociate and hence enhances the conversion efficiency. In case triplet excitons are created away from heavy metal atoms then they will move to such sites due to the attractive spin-orbit interaction and get the spin flipped. Such an enhancement of conversion efficiency has been observed experimentally [33, 34]. For all organic materials, the rate of singlet excitation is five orders of magnitude greater than that of triplet excitation. This is because R_s is proportional to the cube of the energy of photon absorbed, i.e., $\propto (E_{LUMO} - E_{HOMO})^3$, while R_t is only linearly dependent on $(E_{LUMO} - E_{HOMO})$. Hence, using organic materials with wide-band gap would greatly enhance both the rates in (8.12) and (8.13); however, the rate of singlet excitation would be much greater than that of triplet excitation.

8.2.2 *Exciton Diffusion in Bulk-Heterojunction Organic Solar Cells*

As described above, excitons in OSCs can be excited in singlet and triplet states which have different lifetimes (τ), diffusion coefficients (D) and diffusion lengths (L_D). For the efficient diffusion without decay, L_D should be larger than or equal to the donor layer thickness for efficient exciton transport to the donor-acceptor interface. The two common exciton transfer mechanisms between the donor and acceptor materials are obtained through the Förster and Dexter transfer theories. These theories describe the transfer processes of excitons as a function of the distance between the donor and acceptor materials [37]. The Förster and Dexter transfer processes are described below for the singlet and triplet exciton diffusions, respectively.

8.2.2.1 Förster Transfer

Försterresonance energy transfer (FRET) is a singlet to singlet energy transfer and is suitable for a long range process. It is a non-radiative, dipole-dipole interaction mechanism based on resonance theory of energy transfer. In this process, a singlet exciton on a molecule recombines radiatively by emitting a photon which then excites another singlet exciton on another identical molecule, and hence it is also known as the fluorescent resonance energy transfer. It is non-radiative in the sense that the exciton energy is not emitted out as a photon but gets transferred to excite another identical molecule, i.e., the energy is transferred from one exciton to create another exciton. The process is only applicable to singlet excitons because of the recombination involved which is only spin allowed for singlets. In OSCs if and when this transfer occurs at the donor-acceptor interface, it is not a resonance transfer because the donor and acceptor molecules are not identical and in this case some excess energy will be emitted as phonons or molecular vibrations and after the transfer a charge transfer exciton (CTE) will be created (see Sect. 8.2.4). A CTE has its electron transferred to the acceptor and hole in the donor but still be an exciton. The rate of Förster transfer, k_f, between donor and acceptor is given by [38]:

$$k_f = \frac{1}{\tau_S} \frac{R_f^6}{R_{da}^6} \tag{8.14}$$

where τ_S is the lifetime of singlet excitons, R_f is the Förster radius that scales the transfer rate to R_{da}, and R_{da} is the actual donor-acceptor separation distance. If $R_f = R_{da}$, one gets a transfer efficiency of 50 % for the Förster transfer. The transfer efficiency is given by:

$$\eta_{tr} = \frac{R_f^6}{R_f^6 + R_{da}^6}. \tag{8.15}$$

8.2.2.2 Dexter Transfer

The theory of resonance energy transfer was subsequently extended by Dexter to triplet excitons with electric dipole-forbidden transitions [39]. The nearest-neighbour diffusion of charge carriers is enabled through the electron exchange interaction between a triplet exciton and a neighboring molecule. As the recombination of triplet excitons is spin forbidden, the excited electron and hole in a triplet exciton get transferred to a nearby molecule due to the overlap of electronic wavefunctions and hence in the Dexter transfer the excited carriers get transferred instead of energy [40]. This is a very short range process since it requires the overlap of the electronic wavefunctions of two molecules. It is also a non-radiative energy transfer by exchange of the excited charge carriers and hence also known as the carrier transfer process. It is useful in OSCs when a resonant transfer can be obtained by transition of an excited electron in a triplet exciton on a molecule in the donor to another molecule in the acceptor at the interface by emitting the excess energy as phonons. The Dexter rate of transfer, k_d, is given by [38]:

$$k_d = \frac{1}{\tau_T} \exp\left[\frac{2R_d}{L}\left(1 - \frac{R_{da}}{R_d}\right)\right] \tag{8.16}$$

where τ_T is the lifetime of triplet excitons, L is the average length of a molecular orbital and R_d is the Dexter radius. Here also for $R_d = R_{da}$ the transfer efficiency becomes 50 % [37] according to (8.15) replacing R_f by R_d.

8.2.3 *Diffusion Coefficient and Excitonic Diffusion Length*

The diffusion coefficients *D(S)* and *D(T)* for singlet and triplet excitons, respectively, are obtained using the Förster and Dexter transfers as [40]:

$$D(S) = \frac{R_f^6}{6\tau_S R_{da}^4}, \tag{8.17}$$

$$D(T) = \frac{R_{da}^2}{6\tau_T} \exp\left[\frac{2R_d}{L}\left(1 - \frac{R_{da}}{R_d}\right)\right]. \tag{8.18}$$

Assuming that the lifetime of singlet and triplet excitons is the same, $\tau_S = \tau_T$, the relationship between $D(T)$ and $D(S)$ is obtained from (8.17) and (8.18) as:

$$D(T) = \frac{R_{da}^6}{R_f^6} \exp\left[\frac{2R_d}{L}\left(1 - \frac{R_{da}}{R_d}\right)\right] D(S) \tag{8.19}$$

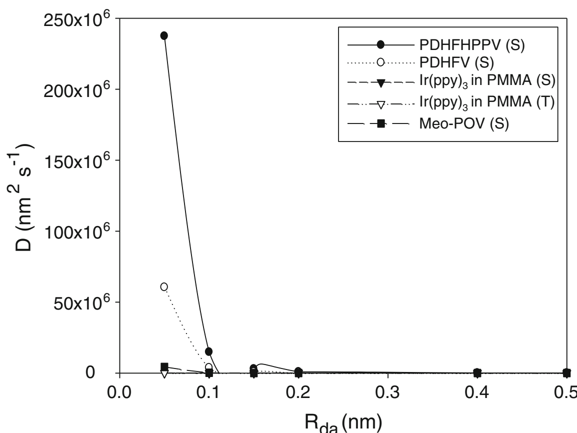

Fig. 8.1 Diffusion coefficient for singlet ($D(S)$) and triplet ($D(T)$) exciton states for some organic materials plotted as a function of R_{da} [13]

The above assumption is not strictly valid in general although it has been used as an approximation [13, 37]. Usually the triplet exciton lifetime is larger than that of singlet.

The diffusion length, $L_D = \sqrt{D\tau}$, for singlet and triplet excitons depends on the Förster and Dexter rates. Using (8.17) and (8.18), $L_D(S)$ and $L_D(T)$ for singlet and triplet states are obtained independent of their lifetimes as:

$$L_D(S) = \frac{1}{\sqrt{6}} \frac{R_f^3}{R_{da}^2} \tag{8.20}$$

$$L_D(T) = \frac{R_{da}}{\sqrt{6}} \exp\left[\frac{R_d}{L}\left(1 - \frac{R_{da}}{R_d}\right)\right] \tag{8.21}$$

Using (8.20) and (8.21), we get $L_D(T)$ as:

$$L_D(T) = \left(\frac{R_{da}}{R_f}\right)^3 \exp\left[\frac{R_d}{L}\left(1 - \frac{R_{da}}{R_d}\right)\right] L_D(S) \tag{8.22}$$

Using (8.17)–(8.22), the diffusion coefficients and lengths are calculated and plotted as a function of the donor-acceptor separation for few organic solids such as Poly(dihexylfluorenevinylene) (PDHFV) [41], fac-tris (2-phenylpyridine)iridium (III) Ir(ppy)^3 in poly(methyl methacrylate) (PMMA) [37], poly(dihexyl fluorenedihexoxyphenylenedivinylene) (PDHFHPPV) [42], and poly(tri phenyl methoxy triazinedietherdiethylhexyloxyphenylenedivinylene (Meo-POV) [43] in Figs. 8.1 and 8.2, respectively.

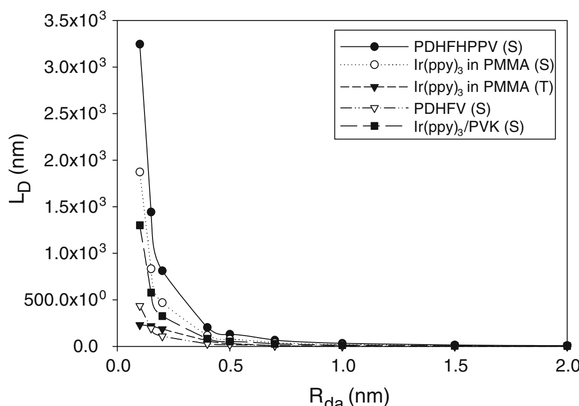

Fig. 8.2 Exciton diffusion lengths for singlet ($L_D(S)$) and triplet ($L_D(T)$) excitons in various organic materials versus R_{da} [13]

The highest value of $D = 2.37 \times 10^8\ \text{nm}^2\ \text{s}^{-1}$ for PDHFHPPV is found at a separation of 0.05 nm as shown in Fig. 8.1 and it reaches a minimum when $R_{da} > 0.15$ nm in most organic materials for both singlet and triplet excitons. Excitons in triplet states have a lower diffusion coefficient than in singlet states. However, the lifetime of excitons in the triplet state is always greater than that of singlet state. One mostly assumes that if τ is longer, then L_D would also be larger. However, this assumption ignores the role of D, which in this case has a substantial effect on L_D.

As shown in Fig. 8.2, the diffusion lengths L_D for all organic materials show similar decrease at larger R_{da} and it eventually becomes a minimum as $R_{da} > 1.5$ nm. The highest $L_D = 3.25 \times 10^3$ nm is found to be for PDHFHPPV because it has a higher diffusion coefficient. It can be concluded that $L_D(S) > L_D(T)$, for example, $Ir(ppy)_3$ has $L_D(S) = 8.32$ nm and $L_D(T)$ is only 1.02×10^{-2} nm at a separation of 1.5 nm. In this case, $L_D(S)$ is around two orders of magnitude larger than $L_D(T)$. Both diffusion lengths, singlet and triplets, have significant values for $R_{da} < 1.5$ nm but reduce to zero as the separation increases.

8.2.4 Exciton Dissociation in Bulk-Heterojunction Organic Solar Cells

After diffusion to the interface, a Frenkel exciton must dissociate efficiently into free charge carriers in an OSC. Here we propose that the mechanism of exciton dissociation may occur in two steps: (1) As the energy of acceptor's LUMO is lower than that of donor's LUMO, a Frenkel exciton relaxes to a charge transfer (CT) exciton state where electron gets transferred to the acceptor's LUMO [44] as shown in Fig. 8.3a. It is to be noted that the CT exciton is not yet dissociated because for dissociation it requires an external energy at least equal to its binding energy [25]. (2) This external energy comes from the excess vibrational energy released due to the formation of CT exciton. The excess vibrational energy thus released, if adequate,

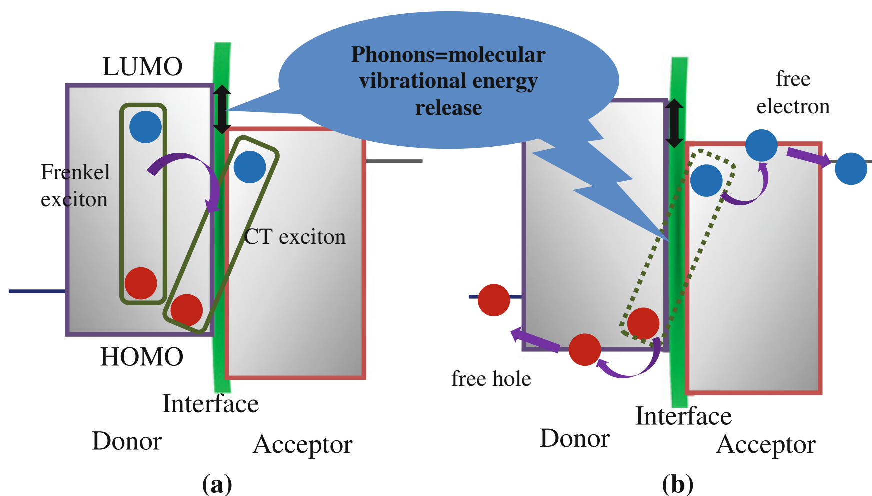

Fig. 8.3 **a** A Frenkel exciton in the donor relaxes to the CT exciton at the donor-acceptor interface whereby the electron moves to the acceptor's LUMO. Molecular vibrational energy in the form of phonons is released when the Frenkel exciton relaxes to the CT state. **b** The excess molecular vibrational energy, thus released, causes the CT exciton to dissociate into free charge carriers. Finally, the dissociated electrons move to the cathode and holes to the anode due to the potential energy difference provided by the difference in work functions of the two electrodes [44]

may impact back to the CT exciton causing it to dissociate into free charge carriers as shown in Fig. 8.3b. Free electrons, thus generated are drawn towards the cathode and holes towards the anode due to the potential energy difference generated by the difference in work functions of the two electrodes [10, 43] which will be discussed later in this chapter.

8.2.4.1 Rate of Exciton Dissociation

In organic solids, the intramolecular vibrations play a more significant role in the exciton dissociation than the intermolecular vibrations due to the larger intermolecular separation. Assuming that every Frenkel exciton will form a CT exciton once it reaches the interface, here we calculate the rate of dissociation of a CT exciton into a free electron-hole pair. The interaction operator, $\hat{H}_d$, between CT exciton and molecular vibrations (phonons) is given by [44, 45]:

$$\widehat{H}_d = \sum_{g,h,i,j,k,v_2} \sum_{\sigma_1,\sigma_2,\sigma_3,\sigma_4} \hbar\omega_{kv_2} G_{v_2} a^{+}_{gL_2}(\sigma_1) d^{+}_{hH_2}(\sigma_2) a^{+}_{iL_2}(\sigma_3) d^{+}_{jH_2}(\sigma_4)(b^{+}_{kv_2} + b_{kv_2}) \tag{8.23}$$

where $\hbar$ is the reduced Planck's constant, ω_{kv} is the phonon frequency, $b^{+}_{kv}(b_{kv})$ is the phonon creation (annihilation) operator in the vibrational mode, v, of molecule k.

G_ν is the exciton-phonon coupling constant, $a_{iL}^{+}(\sigma)(a_{iL}(\sigma))$ represents the creation (annihilation) operator of an electron of spin σ in the LUMOL of the ith molecule, $d_{jH}^{+}(\sigma)(d_{jH}(\sigma))$ represents the creation (annihilation) operator of a hole of spin σ in the HOMO H of the jth molecule. The rest of the symbols have their usual meaning as defined in our earlier work [44, 45].

For the process of dissociation, the initial state, $|i\rangle$, consists of a CT exciton and a phonon while the final state, $|f\rangle$, consists of dissociated pair of free electron-hole. The initial state can be represented as [44, 45]:

$$|i\rangle = N^{-3/2} \sum_{\ell,m,n} \sum_{\sigma_e,\sigma_h,\nu} a_{\ell L}^{+}(\sigma_e) d_{mH}^{+}(\sigma_h) b_{n\nu}^{+} |0;\nu\rangle \tag{8.24}$$

where the electron in CT exciton is created with spin σ_e at a site ℓ of the acceptor's LUMO, L and hole of spin σ_h at the site m of donor's HOMO, H and N is the number of molecules in the sample, $|0;\nu\rangle = |0\rangle|\nu\rangle$, where $|0\rangle$ represents the electronic vacuum state with the LUMO completely empty and HOMO completely full and $|\nu\rangle$ represents the occupation of the vibration state. The final state can be written as:

$$|f\rangle = N^{-3/2} \sum_{\ell_1,m_1} \sum_{\sigma_e',\sigma_h',\nu_1} a_{\ell_1 L_1}^{+}(\sigma_e') d_{m_1 H_1}^{+}(\sigma_h') \left|0;\nu_1\right\rangle \tag{8.25}$$

where a free electron is created with spin σ_e' at site ℓ_1 in LUMO, L_1 of acceptor and hole of spin σ_h' at site m_1 in HOMO, H_1 of donor.

Using (8.23)–(8.25), the transition matrix element is obtained as [44, 45]:

$$\langle f|H_d|i\rangle = N^{-1} \sum_n \hbar\omega_{n\nu} G_\nu n_\nu \tag{8.26}$$

where n_ν is the number of phonons required to dissociate a CT exciton.

Using Fermi's Golden Rule, the rate, R_d, of dissociation of a Frenkel exciton into a free e–h pair in bulk-heterojunction OSCs is obtained as [44, 45]:

$$R_d = \frac{8\pi^2}{3\hbar^3\varepsilon^2 E_B}\left[(E_{LUMO}^{D} - E_{LUMO}^{A}) - E_B\right]^2 (\hbar\omega_\nu)\mu_x a_x^2 \tag{8.27}$$

where E_{LUMO}^{D} and E_{LUMO}^{A} is the LUMO energy of donor and acceptor, respectively, μ_x is reduced excitonic mass, a_x is the excitonic Bohr radius and ε is the dielectric constant. The rate in (8.26) is valid only for $(E_{LUMO}^{D} - E_{LUMO}^{A}) \geq E_B$. The advantage of obtaining the rate of dissociation in the above form is that all quantities can be estimated from the known parameters of materials used as donor and acceptor in a bulk-heterojunction OSC.

From the expression derived in (8.27), the rate of dissociation of a Frenkel exciton into free charge carriers at the interface of any pair of donor and acceptor can be calculated in bulk-heterojunction OSCs. According to (8.27), the exciton dissociation

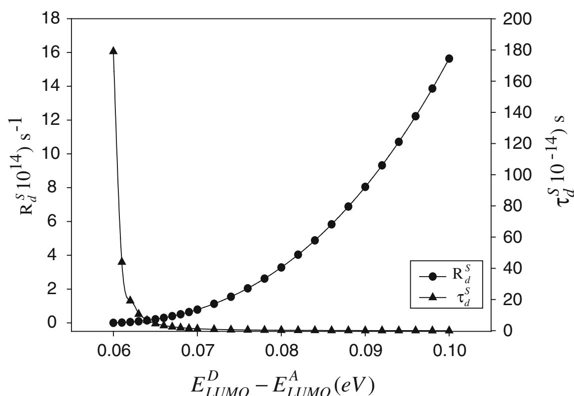

Fig. 8.4 The rate, R_d^S, (8.27) and time, τ_d^S, of dissociation of a singlet exciton as plotted as a function of LUMO offset between donor and acceptor, $(E_{LUMO}^D - E_{LUMO}^A)$ in a bulk-heterojunction OSC [44]

rate depends on the binding energy of an exciton, LUMO offset between donor and acceptor, molecular vibrational energy produced when the Frenkel exciton relaxes to a CT exciton, reduced excitonic mass, excitonic Bohr radius and the dielectric constant of the donor material. The inverse of the rate in (8.27) gives the time of dissociation of a Frenkel exciton into free charge carriers: $\tau_d = (R_d)^{-1}$. Thus the rate and time of dissociation of a Frenkel exciton can be calculated for any LUMO offset between the donor and acceptor provided $(E_{LUMO}^D - E_{LUMO}^A) > E_B$.

As singlet and triplet excitons have different binding energies and excitonic Bohr radius, different rates and times of dissociation are expected to be obtained. Using (8.27), the rate, R_d^S and time, τ_d^S (where the superscript S denotes singlet) of dissociation for singlet exciton, can be calculated if E_B^S, μ_x, a_x^S and ε are known. For organic semiconductors, R_d^S and time, τ_d^S are calculated using the following input parameters: $E_B^S = 0.059\,\text{eV}$, $\mu_x = 4.66\times 10^{-31}$ kg, $a_x^S = 4.352\,\text{nm}$ and $\varepsilon = 3$ [12]. These calculated rates and times of dissociation are plotted as a function of the LUMO offset in Fig. 8.4.

We have also calculated the triplet excitondissociation rate, R_d^T and time, τ_d^T (where the superscript T denotes triplet) in organic semiconductors, using $E_B^T = 0.759\,\text{eV}$ and $a_x^T = 0.317\,\text{nm}$ [13]. Other parameters remain the same as for the case of singlet excitons. These rates and times of dissociation for a triplet exciton are plotted as a function of the LUMO offset in Fig. 8.5.

According to Figs. 8.4 and 8.5, the time of dissociation of both singlet and triplet excitons decreases and the corresponding rate increases, with increasing LUMO offset between the donor and acceptor. This is because a higher LUMO offset means a higher excess energy is available to overcome the exciton binding energy and hence a quicker dissociation rate. The rate of dissociation of a singlet exciton is about three orders of magnitude faster than that of a triplet exciton. For example, at an offset of 0.10 eV, the rate of singlet exciton dissociation is $1.84\times 10^{15}\,\text{s}^{-1}$ and the corresponding dissociation time is 0.54×10^{-15} s (<1 fs). While for a triplet exciton, at 0.80 eV offset, the rate of dissociation is $6.08\times 10^{12}\,\text{s}^{-1}$ and the corresponding

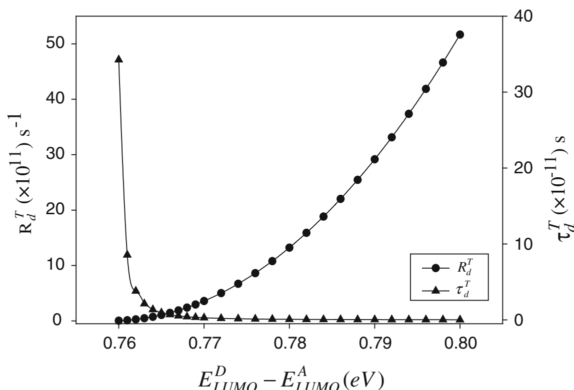

Fig. 8.5 The rate, R_d^T, (8.27) and time, τ_d^T, of dissociation of a triplet exciton as plotted as a function of LUMO offset between donor and acceptor, $(E_{LUMO}^D - E_{LUMO}^A)$ in a bulk-heterojunction OSC [44]

time is 0.16×10^{-12} s (<1 ps). The dissociation time of a singlet exciton agrees very well with experimental results [46, 47]. Conversely, the underlying question arises that if the rates of singlet and triplet exciton dissociations are so high, then why the conversion efficiencies of bulk-heterojunction OSCs obtained so far are limited to 5–9.2 %, experimentally [16, 19]? An attempt is made to answer this question below.

8.2.4.2 Loss Mechanisms

On the experimental side, the LUMO offset in bulk-heterojunction OSCs varies from 0.3–0.5 eV [48–50]. In the case of a triplet exciton, dissociation can only commence at an offset of ≥0.759 eV. Hence a triplet exciton cannot be dissociated at such an experimentally available offset and hence cannot contribute to the photovoltaic performance of bulk-heterojunction OSCs.

Comparing the formation of singlet and triplet excitons in OSCs with that in the organic light emitting devices (OLEDs), where electrons and holes are injected from the opposite electrodes, one may think that it is more probable to create triplet excitons than singlet excitons. This is because statistically, on average the formation of triplet excitons in OLEDs is three times more probable than singlet excitons [51, 52]. As the triplet exciton energies are lower, one may expect to excite more triplets than singlets. This implies that unless one can dissociate triplet excitons in OSCs, more than half of the absorbed energy may be lost through triplet excitons. It is to be noted that triplet excitons cannot also recombine radiatively due to spin restrictions and cannot dissociate due to insufficient LUMO offset. Hence they may lose their energy through non-radiative recombinations. One of the possibilities of such loss may be the creation of high density triplet excitons within a thin film to enable them to interact and dissociate each other non-radiatively. The net effect

of such non-radiative recombinations will be loss of photocurrent and hence low conversion efficiency in bulk-heterojunction OSCs. In our previous study [11, 12], it has been shown that the incorporation of heavy metal atom enhances the rate of absorption of triplet excitons due to the enhanced spin-orbit-interaction which flips the spin to a singlet form. This leads to a faster dissociation of triplet excitons and hence an overall enhancement in the conversion efficiency of organic solar cells. In addition, contributing to the loss of energy due to high density triplet excitons, there are other possibilities as well which need to be considered. These are due to three different inefficient processes: (1) transport of created excitons towards the interface, (2) transfer of vibrational energy back to CT for its dissociation and (3) transport of dissociated charge carriers to opposite electrodes. Impact of these three possibilities on the performance of an OSC is discussed below:

(i) **Inefficient transfer of excitons to the donor-acceptor interface**
An exciton created by the absorption of a solar photon is an electrically neutral entity as electron and hole are bound together through Coulomb interaction. An exciton created at a molecule can move in any direction of outward solid angle, Ω. Considering the fractional solid angle, $\mathrm{d}\Omega = \sin\theta \mathrm{d}\theta \mathrm{d}\phi$, we get the whole solid angle as $\int d\Omega = 4\pi$. This means that the probability of an exciton, created at a molecule to move to any one particular direction is $1/4\pi$. If this molecule is next to the interface then the transfer should be multiplied by $1/4\pi$. However, if this interface is a few molecules away from the excited molecule, the rate of transfer should be multiplied by $1/4\pi$ at each such molecular step. Thus, the probability that an exciton created n molecules away from the interface will reach the interface becomes $(1/4\pi)^n$. As $4\pi \sim 10$, the farther the exciton is from the interface, much less is the probability that it will reach the interface to form a CT exciton. This basically means that every single step away from the interface will reduce the probability by at least one order of magnitude. From this analysis, one may conclude that the only efficient way of ensuring that an exciton reaches the interface is that each donor molecule must be next to an acceptor molecule. If the fabrication is based on solution method, this implies that in a heterojunction OSC, donor-acceptor concentration should be equal (1:1).

(ii) **Inefficient transfer of vibrational energy back to CT exciton for dissociation**
When an exciton from a donor molecule converts itself to a CT exciton by transferring its electron to an acceptor molecule, the excess energy released will excite molecular vibrations. This vibrational energy can be dissipated in any direction from the excited molecule. The probability that it will be transferred back to the CT exciton to dissociate it is only one of the possible directions of a solid angle. Therefore, the transition matrix element of dissociation (8.13) of excitons must be multiplied by $1/4\pi$. This means that the rate of dissociation reduces by a factor of $(1/4\pi)^2$, which is nearly three orders of magnitude less than that obtained from (8.14) and hence the dissociation time will be longer by three orders of magnitude.

(iii) **Inefficient transport of free charge carriers to opposite electrodes**
After the dissociation of an exciton, free charge carriers are drawn to the opposite electrodes, solely by the difference between the ionisation potential of the anode and the electron affinity of the cathode, which are represented by their work functions. The difference in the work functions, Φ (in eV) between the anode and cathode is given as: $\Delta V = \Phi_a - \Phi_c$, where Φ_a and Φ_c are the work functions of the anode and cathode, respectively. The force, F, required for a charge carrier to be drawn towards the electrode is given as:

$$F = \frac{\Phi_a - \Phi_c}{r} \tag{8.28}$$

where r is the inter-electrode distance. In bulk heterojunction OSCs, normally ITO is used as the anode, $\Phi_{ITO} = 4.7$ eV [53] and Aluminium (Al) as the cathode, $\Phi_{Al} = 4.3$ eV [54] which provides $\Delta V = 0.4$ eV. The inter-electrode distance is around 100 nm [55] and using (8.28), the effective force for charge diffusion to the electrode is, $F = 0.64$ pN. According to (8.28), in order to enhance the force for charge diffusion to the electrodes, the potential difference should be larger and the inter-electrode distance should be smaller. Hence, Calcium (Ca), $\Phi_{Ca} = 2.9$ eV [56] and Caesium (Cs), $\Phi_{Cs} = 2.1$ eV may be employed as potential cathodes to enhance the potential difference to strengthen the force. The charge mobilities should also be high for efficient charge diffusion to the electrodes.

8.3 Organic Light Emitting Devices

The theoretical mechanism of operation of organic light emitting devices (OLEDs) is the reverse of that of OSCs. In the former a current is passed through the device, i.e., electrons and holes are injected in the device, electrons in the LUMO and holes in HOMO of an organic material layer sandwiched between the two electrodes. When these electrons in LUMO and holes in HOMO radiatively recombine, then emit light and such an emission is known as the electroluminescence (EL). However, in the organic layer, both of small molecules and polymers, which has a lower dielectric constant ($\varepsilon \approx 3$) and hence much larger binding energy between the injected electrons and holes enables them to form Frenkel excitons immediately after their injection from the opposite electrodes. On one hand, the formation of excitons due to their Coulomb interaction assists their radiative recombination leading to electroluminescence. On the other hand, excitons can be formed in two spin configurations, singlet and triplet and this complicates the mechanism of radiative recombination because the recombination of singlet excitons is spin allowed but that of triplet excitons is spin forbidden. The singlet and triplet exciton configurations are shown in Fig. 8.6 and accordingly the probability of forming singlet and triplet excitons may be in the ratio of one to three (1:3). If the triplet excitons cannot recombine due to forbidden spin configuration, then the light emission can occur only through singlet

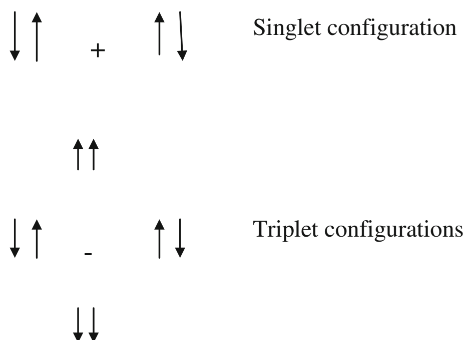

Fig. 8.6 Possible spin configurations of the injected electrons and holes in forming Frenkel excitons in OLEDs. Pairs of *arrows* represent pairs of electron and hole. The *upper* combination of spin configurations represents the single possibility for formation of a singlet exciton and *lower* three spin configurations represent the three possibilities for formation of a triplet exciton

excitons and that means internal quantum efficiency η_{int} can be only about 25 %, and 75 % of the injected electron-hole pairs will be lost through the non-radiative recombination due to the formation of triplet excitons [57].

A few attempts have been made for increasing the quantum efficiency to more than 25 %. For example, Cao et al. have reported that the quantum efficiency of emission in a substituted PPV-based LED can reach as high as 50 % [58]. This higher internal quantum efficiency is attributed to a larger cross section for an electron-hole pair to form a singlet exciton than that to form a triplet exciton [59] as explained below. If one denotes the cross section of the formation of a singlet exciton by σ_S and that of a triplet by σ_T then by assuming that all pairs of injected e and h form excitons, the internal quantum efficiency can be expressed in terms of cross sections as $\eta_{ex} = \frac{\sigma_S}{\sigma_S + 3\sigma_T}$. Thus, for $\sigma_S = \sigma_T$ one gets $\eta_{ex} = 0.25$ (or 25 %), for $\sigma_S = 3\sigma_T$, $\eta_{ex} = 0.5$ (50 %) and for $\sigma_T = 0$, $\eta_{ex} = 1(100\,\%)$. This suggests that if one can minimise the cross section of the formation of triplet excitons one can maximise the internal quantum efficiency in OLEDs. However, for modifying the cross sections one has to know the material parameters on which these cross sections depend on and then one has to manipulate those parameters to minimise the triplet cross section. This approach has not been applied yet probably because the dependence of cross sections on the material parameters has not been very well understood. The other approach of increasing the internal quantum efficiency to 100 % is by harvesting the radiative emissions from all triplet excitons as has been achieved by Adachi et al. [60]. The mechanism of this approach is presented here.

It is very desirable to capture the full emission from triplet excitons in OLEDs for two reasons: (1) one can gain 100 % internal quantum emission quantum efficiency without losing the injected charge carriers in triplet configurations which may recombine non-radiatively and disappear, and (2) triplet excitons have lower energy and hence by harvesting emission from both singlet and triplet excitons together the device can generate white light. The white light emission can be achieved by

incorporating fluorescent blue emitters (emission from singlet excitons) combined with phosphorescent green and red emitters (emission from triplet excitons) in the electroluminescent layer of OLEDs. Materials from which singlet emission can be harvested are called fluorescent or electro-fluorescent materials and those from which triplet emission is availed are called phosphorescent or electro-phosphorescent materials. An OLED that can emit white light is called white OLED (WOLED) actually it is an organic white light emitting device (OWLED). A successful cost effective technological development of WOLEDs is going to provide a huge socio economic benefit to mankind by providing brighter and cheaper lighting. WOLEDs show promise to have a major share in the future ambient lighting due to their very favourable properties such as homogenous large-area emission, good colour rendering, and potential realization on flexible substrates. This is expected to open new ways in lighting design such as light emitting ceilings, curtains or luminous objects of almost any shape [61, 62]. Therefore, much research efforts are continued in developing more cost effective and efficient white organic light emitting devices (WOLEDs) [61, 63, 64].

Here, the radiative recombination of both singlet and triplet excitons in organic solids/polymers is briefly reviewed. For details on the calculations of rates of spontaneous emission from singlet and triplet excitons readers may refer to our earlier works [27, 52, 57, 65, 66]. In Sect. 8.2.1, the rates of excitation by absorbing a photon to singlet and triplet excitonic states have been calculated using the absorption term of the vector potential (8.2) for singlet and (8.8) for triplet). As the emission term of the vector potential is just the complex conjugate of the absorption term, the rate of spontaneous emission is obtained the same as the corresponding rate of absorption derived in the Sect. 8.2.1. We thus obtain the rate of spontaneous emission from a singlet exciton, R_s^{SE}, analogous to (8.12) as [57]:

$$R_s^{SE} = \frac{4\kappa e^2 (E_{LUMO} - E_{HOMO})^3 a_s^2}{3c^3 \varepsilon^{1.5} \hbar^4}. \tag{8.29}$$

And the rate of spontaneous emission from a triplet exciton due to exciton-spin-orbit-photon interaction, R_t^{SE} analogous to (8.13) as:

$$R_t^{SE} = \frac{32 e^6 Z^2 \kappa^2 \varepsilon (E_{LUMO} - E_{HOMO})}{c^7 \varepsilon_o \mu_x^4 a_t^4}. \tag{8.30}$$

The right hand side of (8.29) and (8.30) are the same as those of (8.12) and (8.13), respectively. Accordingly the calculated rates of absorption and spontaneous emission are found to be the same in the same material as given in Table 8.1, if the emitted energy is the same as the absorption energy. The triplet spontaneous emission has also been calculated in several polymers and platinum porphyrin (PtOEP) and results agree very well with the experimental ones [58]. For example, in PtOEP the calculated rate of spontaneous emission from the triplet exciton is obtained as $R_t^{SE} = 4.9 \times 10^3\,\text{s}^{-1}$ with $Z = 78$, $\varepsilon = 3$, $E_{LUMO} - E_{HONMO} = 1.91\,\text{eV}$ [67], $\mu_x = 0.5 m_e$ and $a_t = 6a_0$. This gives a radiative lifetime $\tau_R = 1/R_t^{SE} = 2.03 \times 10^{-4}\,\text{s}$, which agrees with the experimental value of $7.0 \times 10^{-4}\,\text{s}$ [68] reasonably well.

For phosphorescent materials incorporated with iridium, like fac-tris (2-phenylpyridine) iridium (Ir(ppy)3) and iridium(III) bis(2-phenyl quinolyl-N,C20) acetylacetonate (PDIr), where Ir has the largest atomic number $Z = 77$, other atomic numbers can be neglected being mainly of carbon. The rate in (8.30) depends linearly on the emission energy and other quantities are the same for all iridium doped materials. Thus, for iridium complexes doped in organic polymers the rate is obtained as: $R = 1.5 \times 10^5\, \hbar\omega_{12}\, \mathrm{s}^{-1}$ (where $\hbar\omega_{12} = E_{LUMO} - E_{HONMO}$ is the emission energy in eV). For green phosphor,Ir(ppy) $_3$ has been doped for emission energy of 2.4 eV; for orange phosphor, Ir(MMQ) [69] and FIrpic [61] have been doped for emission at 2.00 eV. In all these films the rate of spontaneous emission would be of the same order of magnitude (3–$4 \times 10^5\, \mathrm{s}^{-1}$), which is in the same range as the rate of absorption in Ir-complexes listed in Table 8.1 and agrees quite well with the measured rate for Ir complexes [70].

8.4 Conclusions

The effects of diffusion coefficient and diffusion length of singlet and triplet states are investigated. The Förster and Dexter models are used to study the singlet and triplet diffusion coefficients and diffusion lengths, respectively. The singlet exciton diffusion length is larger than that of triplets at small separation between the donor and acceptor which is attributed to its large diffusion coefficient. A time-dependent interaction operator for the dissociation of an exciton into free charge carriers in bulk-heterojunction OSCs has been derived. It is proposed that at the donor-acceptor interface, the molecular vibrational energy generated when a Frenkel exciton relaxes to a charge transfer exciton provides the excess energy for the self-dissociation of the charge transfer exciton into free charge carriers. For such a mechanism of dissociation, the rate of dissociation of a Frenkel exciton into free charge carriers is derived, which depends on the LUMO offset between the donor and acceptor, molecular vibrational energy, reduced excitonic mass, binding energy, dielectric constant and the excitonic Bohr radius.

For a bulk-heterojunction OSC, increasing the LUMO offset between the donor and acceptor may lead to faster dissociation of both singlet and triplet excitons and hence may enhance the conversion efficiency. However, despite the dissociation rate being very fast, the conversion efficiency is still low. Possible reasons for this are inefficient transport of created excitons towards the interface, transfer of vibrational energy back to charge transfer for its dissociation, and transport of dissociated charge carriers to opposite electrodes. These studies provide greater insights into exciton diffusion and dissociation in bulk-heterojunction organic solar cells.

Rates of spontaneous emission from singlet and triplet excitons are derived for OLEDs using the time dependent exciton-photon and exciton-spin-orbit-photon interaction operators as perturbation. It is emphasized that the triplet exciton emission can be harvested by incorporating heavy metal complexes in the emitting layer.

References

1. L.E. Lyons, F. Gutman, *Organic Semiconductors* (Wiley, Sydney, 1967)
2. A.S. Davydov, *Theory of Molecular Excitons* (McGraw-Hill, New York, 1962)
3. D.P. Craig, S.H. Walmsley, *Excitons in Molecular Crystals* (Benjamin, New York, 1968)
4. J. Singh, *Excitation Energy Transfer Processes in Condensed Matter* (Plenum, New York, 1994)
5. N. Yeh, P. Yeh, Renew. Sustain. Energy Rev. **21**, 421 (2013)
6. M.T. Dang, L. Hirsch, G. Wantz, Adv. Mat. **23**, 3597 (2011)
7. A. Kitai (ed.), *Principles of Solar Cells, LEDs and Diodes: The Role of the PN Junction* (Wiley, Dewey, 2011)
8. C.W. Tang, Appl. Phys. Lett. **48**, 183 (1986)
9. W.C.H. Choy, *Organic Solar Cells: Materials and Device Physics* (Springer, Dewey, 2012)
10. I. Bruder, Thesis, Max-Planck-Institut für Festkörperforschung (2010)
11. M.R. Narayan, J. Singh, Eur. Phys. J. B **86**, 1 (2013)
12. M.R. Narayan, J. Singh, J. Appl. Phys. **114**, 154515 (2013)
13. M.R. Narayan, J. Singh, Phys. Status Solidi C **9**, 2386 (2012)
14. K. Tvingstedt, K. Vandewal, F. Zhang, O. Inganäs, J. Phys. Chem. C **114**, 21824 (2010)
15. C.-W. Chu, V. Shrotriya, G. Li, Y. Yang, Appl. Phys. Lett. **88**, 153504 (2006)
16. W. Cai, X. Gong, Y. Cao, Sol. Energy Mat. Sol. Cells **94**, 114 (2010)
17. G. Zhao, Y. He, Y. Li, Adv. Mat. **22**, 4355 (2010)
18. Y. Liang, D. Feng, Y. Wu, S.T. Tsai, G. Li, C. Ray, L. Yu, J. Am. Chem. Soc **131**, 7792 (2009)
19. Z. He, C. Zhong, S. Su, M. Xu, H. Wu, Y. Cao, Nat. Photonics **6**, 593 (2012)
20. J. Roncali, Acc. Chem. Res. **42**, 1719 (2009)
21. B. Kippelen, J.L. Brédas, Energy Environ. Sci. **2**, 251 (2009)
22. J.L. Brédas, J.E. Norton, J. Cornil, V. Coropceanu, Acc. Chem. Res. **42**, 1691 (2009)
23. Y. Liang, Z. Xu, J. Xia, S.T. Tsai, Y. Wu, G. Li, C. Ray, L. Yu, Adv. Mat. **22**, E135 (2010)
24. H. Ohkita, S. Ito, Polymer **52**, 4397 (2011)
25. M.C. Scharber, D. Mühlbacher, M. Koppe, P. Denk, C. Waldauf, A.J. Heeger, C.J. Brabec, Adv. Mat. **18**, 789 (2006)
26. M. Muntwiler, Q. Yang, W.A. Tisdale, X.-Y. Zhu, Phys. Rev. Lett. **101**, 196403 (2008)
27. J. Singh, I.K. Oh, J. Appl. Phys. **97**, 063516 (2005)
28. J. Singh, Phys. Status solidi A **208**, 1809 (2011). doi:10.1002/pssa.201084110
29. J. Singh, Phys. Rev. B **76**, 085205 (2007)
30. A. Shafiee, M.M. Salleh, M. Yahaya, Sains Malays. **40**, 173 (2011)
31. J. Singh, H. Baessler, S. Kugler, J. Chem. Phys. **129**, 41103 (2008)
32. C.M. Yang, C.-H. Wu, H.-H. Liao, K.-Y. Lai, H.-P. Cheng, S.-F. Horng, H.-F. Meng, J.-T. Shy, Appl. Phys. Lett. **90**, 133509 (2007)
33. G.L. Schulz, S. Holdcroft, Chem. Mater. **20**, 5351 (2008)
34. P.G. Da Costa, E. Conwell, Phys. Rev. B **48**, 1349 (1993)
35. Y.F. Li, Y. Cao, J. Gao, D.L. Wang, G. Yu, A.J. Heeger, Synth. Met. **99**, 243 (1999)
36. V.A. Dediu, L.E. Hueso, I. Bergenti, C. Taliani, Nat. Mater. **8**, 707 (2009)
37. F.S. Steinbacher, R. Krause, A. Hunze, A. Winnacker, Phys. Status Solidi A **209**, 340 (2012)
38. W.M. Yen, P.M. Selzer, *Laser Spectroscopy of Solids: Topics in Applied Physics*, vol. 49 (Springer, New York, 1986)
39. C.E. Swenberg, M. Pope, *Electronic Processes in Organic Crystals and Polymers* (Oxford University Press, Oxford 1999)
40. R.R. Lunt, N.C. Giebink, A.A. Belak, J.B. Benziger, S.R. Forrest, J. Appl. Phys. **105**, 053711 (2009)
41. J.-W. Yu, J.K. Kim, D.Y. Kim, C. Kim, N.W. Song, D. Kim, Curr. Appl. Phys **6**, 59 (2006)
42. X.-Y. Zhu, Q. Yang, M. Muntwiler, Acc. Chem. Res. **42**, 1779 (2009)
43. M.J. Kendrick, A. Neunzert, M.M. Payne, B. Purushothaman, B.D. Rose, J.E. Anthony, M.M. Haley, O. Ostroverkhova, J. Phys. Chem. C **116**, 18108 (2012)

44. M.R. Narayan, J. Singh, J. Appl. Phys. **114**, 073510 (2013)
45. M.R. Narayan, J. Singh, Can. J. Phys. (2013 in press)
46. R. Mauer, Thesis, Johannes Gutenberg-University Mainz (2012)
47. L. Koster, E. Smits, V. Mihailetchi, P. Blom, Phys. Rev. B **72**, 085205 (2005)
48. L. Koster, V. Mihailetchi, P. Blom, Appl. Phys. Lett. **88**, 093511 (2006)
49. M. Lenes, G.J.A. Wetzelaer, F.B. Kooistra, S.C. Veenstra, J.C. Hummelen, P.W. Blom, Adv. Mat. **20**, 2116 (2008)
50. J.D. Servaites, M.A. Ratner, T.J. Marks, App. Phys. Lett. **95**, 163302 (2009)
51. J. Singh, Phys. Status Solidi C **7**, 984 (2010)
52. J. Singh, Phys. Rev. B **76**, 085205 (2007)
53. J.S. Kim, J.H. Park, J.H. Lee, J. Jo, D.-Y. Kim, K. Cho, Appl. Phys. Lett. **91**, 112111 (2007)
54. S. Gunes, H. Neugebauer, N.S. Sariciftci, Chem. Rev. Columbus **107**, 1324 (2007)
55. A.J. Moulé, J.B. Bonekamp, K. Meerholz, J. Appl. Phys. **100**, 094503 (2006)
56. R. Friend, R. Gymer, A. Holmes, J. Burroughes, R. Marks, C. Taliani, D. Bradley, D. Dos Santos, J. Bredas, M. Lögdlund, Nature **397**, 121 (1999)
57. J. Singh, Harvesting emission in white organic light emitting devices in organic light emitting devices, Ch. 1, ed. by J. Singh (INTECH, Rijeka, 2012), pp. 1–20
58. Y. Cao, I.D. Parker, G. Yu, C. Zhang, A.J. Heeger, Nature **394**, 414 (1999)
59. Z. Shuai, D. Beljonne, R.J. Silbey, J.L. Bredas, Phys. Rev. Lett. **84**, 131 (2000)
60. C. Adachi, M.A. Baldo, M.E. Thompson, S.E Forrest, J. Appl. Phys. **90**, 5048 (2001)
61. G. Schwartz, S. Reineke, T.C. Rosenow, K. Walzer, K. Leo, Adv. Funct. Mat. **19**, 1319 (2009)
62. J. Singh, Phys. Status Solidi C **8**, 189 (2011)
63. J. Kido, K. Hongawa, K. Okuyama, K. Nagai, Appl. Phys. Lett. **64**, 815 (1994)
64. Y. Sun, N.C. Giebink, H. Kannao, B. Ma, M.E. Thompson, S.R. Forest, Nature **440**, 908 (2006)
65. J. Singh, *Optical Properties of Condensed Matter and Applications*, Ch. 6. ed. by J. Singh. Photoluminescence and photoinduced changes in noncrystalline condensed matter (Wiley, Chichester, 2006)
66. J. Singh, K. Shimakawa, *Advances in Amorphous Semiconductors* (Taylor & Francis, London, 2003)
67. F. Laquai, C. Im, A. Kadashchuk, H. Baessler, Chem. Phys. Lett. **375**, 286 (2003)
68. M.A. Baldo, D.F. O'Brien, Y. You, A. Shoustikov, S. Sibley, M.E. Thompson, S.R. Forrest, Nature **395**, 151 (1998)
69. S.-J. Su, E. Gonmori, H. Sasabe, J. Kido, Adv. Mater. **20**, 4189 (2008)
70. N.R. Evans, L.S. Devi, C.S.K. Mak, S.E. Watkins, S.I. Pascu, A. Köhler, R.H. Friend, C.K. Williams, A.B. Holmes, J. Am. Chem. Soc. **128**, 6647 (2006)

Chapter 9
Optical and Electronic Processes in Semiconductor Materials for Device Applications

Igor P. Marko and Stephen J. Sweeney

Abstract In this chapter we consider the important optical and electronic processes which influence the properties of semiconductor photonic devices. Focussing on a number of material systems, we describe semiconductor materials and structures used for light-emitting applications (lasers and LEDs) operating in a wide spectral range from visible to mid-infrared. The main carrier recombination mechanisms in semiconductor devices are discussed and experimental methodologies for measuring and analysing these mechanisms are introduced. Near infra-red (IR) quantum well (QW) lasers are discussed in depth considering several new approaches to overcome fundamental performance issues. Different approaches for the longer wavelength (mid-IR) semiconductor devices are reviewed showing the benefits of different approaches to material and device design where energy efficiency and high temperature operation are the principal concerns. Finally, semiconductor lasers and LEDs for the visible spectral range are briefly introduced in terms of the most important issues related to their performance.

9.1 Introduction: Optical and Electronic Processes in Semiconductor Optoelectronic Devices

The understanding of the optical and electronic physical processes in semiconductor materials is crucial for the development and optimization of semiconductor optoelectronic devices which are currently the main components of telecommunication, information, and many other modern technologies. For various reasons, including fundamental physical processes and device design, only a fraction of the energy injected into most optoelectronic devices is converted into a useful output.

I. P. Marko · S. J. Sweeney (✉)
Department of Physics and Advanced Technology Institute,
University of Surrey, Guildford, Surrey GU2 7XH, UK
e-mail: s.sweeney@surrey.ac.uk

J. Singh and R. T. Williams (eds.), *Excitonic and Photonic Processes in Materials*,
Springer Series in Materials Science 203, DOI: 10.1007/978-981-287-131-2_9,
© Springer Science+Business Media Singapore 2015

Similar reasons also impose limitations on device characteristics and their performance as a function of temperature. This leads to the requirement for temperature stabilisation circuitry which often consumes more energy than the devices themselves. Understanding the physical processes in different semiconductor material system sallows for the fabrication of semiconductor devices with desirable properties for specific applications. This has led to the development of new material systems to overcome performance limitations by suppressing unwanted processes. In this chapter, through the use of examples, we consider the optical and electronic properties in different semiconductor systems used in laser diodes (LDs) and light-emitting diodes (LEDs) which find use in various applications operating over a wide spectral range from visible to mid-infrared. In the section below we briefly review the main recombination and loss mechanisms in semiconductor devices and describe the experimental methodology for the measurement and analysis of these mechanisms which is necessary for effective device design and optimization. In Sect. 9.2 we apply this methodology to near infra-red (IR) quantum well (QW) lasers revealing fundamental operational issues. Section 9.3 considers new approaches to overcome these challenges. In Sect. 9.4, different approaches for the longer wavelength (mid-IR) semiconductor devices are reviewed showing specific examples of different semiconductor materials and engineering solutions to reach these long wavelengths while suppressing unwanted efficiency limiting processes. In Sect. 9.5 we briefly consider semiconductor lasers and LEDs for the visible spectral range and discuss the main issues related to device performance. Finally, we will summarize the main points in Sect. 9.6.

9.1.1 Carrier Injection and Recombination

The vast majority of semiconductor emitters are electrically operated and fabricated in the form of diodes. Electrically injected carriers (electrons and holes) either recombine (annihilate) radiatively, thereby transferring their energy to photons, or non-radiatively transferring their energy to other carriers or phonons causing heating of the device. The carriers which reach the other electrode without taking part in recombination process form a leakage current which reduces the device efficiency and causes additional energy loss. The total recombination rate, R, determined as the number of recombination acts per second in a unit volume, in most cases may be written as a sum of the following three main components: defect related non-radiative recombination, known as a Shockley-Read-Hall (SRH) process (a two-step electron transition via a defect state in the band gap) and is proportional to the carrier density, n, and negligible in devices with optimised growth and fabrication due to very low defect concentration; *spontaneous* radiative recombination, which is proportional to n^2 (we assume here that electron density, n, and hole density, p, are equal, i.e. $n = p$); and Auger recombination—a three-carrier process proportional to n^3, whereby energy of annihilated electron-hole pair is used to produce a third "hot" carrier, either an electron or a hole. Depending on location

of the carriers in the bands one can define different Auger processes such as the conduction-hole-conduction-conduction (CHCC) process, in which recombination energy of conduction band electron and valence band hole is used to excite another conduction band electron to a higher conduction band energy state; conduction-hole-spin-hole (CHSH) process with excitation of the second valence band hole into the spin-orbit split-off band; conduction-hole-heavy-hole (CHHH) and conduction-hole-light-hole (CHLH) processes, in which the second valence band hole is excited into heavy hole or light hole sub-band, respectively. There are also countless other examples of Auger processes involving defect states and phonon-assisted processes, however the processes described above are typically the most common. Combining the different recombination processes, the total recombination rate can therefore be written as:

$$R(n) = An + Bn^2 + Cn^3, \tag{9.1}$$

where A, B, and C are defect-related, radiative (spontaneous emission), and Auger recombination coefficients, respectively. Despite the recombination losses, there is also possible loss of injected carriers due to several types of carrier leakage when injected carriers thermally escape from the active region over hetero-interfaces or into indirect valleys of the conduction band. These processes tend to be very temperature sensitive and, if present, significantly limit device performance at room temperature and above. Taking into account the recombination processes and carrier loss due to leakage, which all together make up the total current passing through a device, the following equation can be written:

$$I = eVR + I_{leak} = eV(An + Bn^2 + Cn^3) + I_{leak}, \tag{9.2}$$

where e is the electronic charge, V is the active volume and I_{leak} is the leakage current.

Equation (9.2) one can use to analyse the internal quantum efficiency, η, of the spontaneous emission of a device which is determined by a ratio of the radiative part of the total current ($I_{rad} = eVBn^2$) to the total current described with (9.2). Therefore, assuming that all of injected carriers effectively reach the active region, the internal quantum efficiency can be written as follows:

$$\eta = \frac{Bn^2}{An + Bn^2 + Cn^3 + I_{leak}/eV}. \tag{9.3}$$

Figure 9.1 presents variation of the internal quantum efficiency with carrier density for several particular cases. In an ideal case, when there is no loss in the device ($A = C = 0$ and $I_{leak} = 0$), η is unity. If Auger recombination and carrier leakage are negligible ($C = 0$ and $I_{leak} = 0$), the efficiency will increase at low carrier densities and asymptotically approach a maximum level where the term "Bn^2" becomes much greater than "An". In the case when Auger recombination is important (e.g. long-wavelength emitters for near- and mid-infrared applications) the efficiency curve will have go through a peak decreasing at higher carrier densities due to the dominant

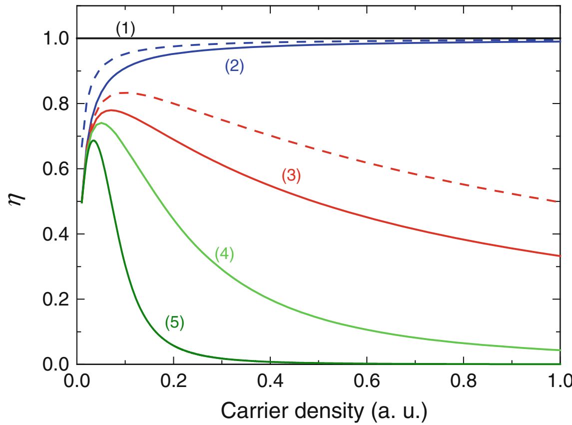

Fig. 9.1 The internal quantum efficiency versus carrier density according to a simple model given by (9.3): *(1)* an ideal case without any loss, *(2)* monomolecular defect related recombination present in addition to radiative recombination, *(3)* influence of Auger recombination is also taken into account, *(4, 5)* carrier leakage added assuming n^4 and n^5 power dependence, respectively, which is used to demonstrate a strong carrier density dependence of leakage current and its influence on the efficiency. *Dashed lines* are dependencies for 2 times smaller *A* and *C* coefficients compared to the corresponding *solid lines*

"Cn^3" term in (9.3) giving rise to so-called "efficiency droop". Carrier leakage has an approximately exponential dependence on n and can give rise to similar droop behaviour. In Fig. 9.1 carrier leakage demonstrated with curves (4) and (5) assuming n^4 and n^5 power dependence, respectively, which is used to demonstrate a strong carrier density dependence of leakage current and its influence on the efficiency. The extent to which this occurs depends on the material, wavelength and structure design.

In reality, most semiconductor emitters work in a regime above the efficiency peak which means that any increase in light output is accompanied by an overall decrease of the device efficiency. This efficiency droop is a very important issue in terms of optimal device performance and energy saving, something which is of particular concern in GaN-based LEDs for solid-state lighting [1].

Due to a large number of unknowns and fitting parameters corresponding to the different radiative and non-radiative processes (including carrier leakage) in real devices it is very important to develop experimental techniques to provide qualitative and, if possible, quantitative analysis of the different physical processes in semiconductor materials and devices. This allows for an unambiguous investigation of the dominant recombination processes limiting device efficiency.

The following two novel experimental approaches using directly measured pure spontaneous emission and high hydrostatic pressure dependence techniques have been developed and widely deployed by the authors of this chapter to gain fundamental information about recombination mechanisms in semiconductor lasers and light emitting diodes operating from the blue to the mid infra-red region of the electromagnetic spectrum. From these studies the physical processes responsible

for the operating characteristics of devices used in applications ranging from data storage (e.g. CD/DVDs), medical and gas sensing applications as well as optical fibre communications have been determined. Using the information derived from these experiments also provides valuable data which can be used as part of the design cycle for semiconductor devices. A brief summary of these techniques is given below in this section and more technical details can be found elsewhere [2].

9.1.2 Spontaneous Emission Analysis

The first method is based on measurements of the spontaneous emission emanating from semiconductor devices which can give quantitative information about recombination processes. On one hand, analysis of the spectral shape of the spontaneous emission can provide knowledge about the distribution of carriers in a structure under investigation. On the other hand, the integrated spontaneous emission is directly proportional to the radiative current ("n^2" term in 9.2). Thus, by measuring this emitted radiation one can characterise the behaviour of the current path due to radiative recombination. From (9.2), it can be seen that, in the absence of leakage current, the current flowing through the laser may consist of three n dependent terms. If one of these terms dominates over a given range of n, then (9.2) may be written as

$$I \propto n^z, \tag{9.4}$$

where Z is the power of carrier density dependence of the current, taking a value of 1, 2 or 3 depending on whether monomolecular, radiative or Auger recombination dominates [3]. The integrated spontaneous emission, L, is a direct measure of the radiative current and can be used to determine n for (9.4), thus, one may write that

$$I \propto Bn^z \to n \propto \sqrt{L} \to I \propto \left(\sqrt{L}\right)^z. \tag{9.5}$$

Therefore, by plotting a graph of *ln(I)* versus $ln(L^{1/2})$, one may determine Z, the carrier density power dependence of the current and identify the main recombination mechanism. The Z-analysis, however, should be used with caution in materials with the presence of localised states, internal fields and/or inhomogeneous carrier distribution (for example, self-assembled quantum dots, poorly alloying semiconductor materials, InGaN etc.) because in these cases the recombination coefficients may also be dependent on the carrier density making the analysis invalid. On the other hand, direct measurements of the spontaneous emission can always be used for direct study of behaviour of the radiative part of the total current and used as an indication of the presence of non-radiative process determined as the difference between the total injected current and its radiative component.

Figure 9.2 demonstrates experimental measurements of spontaneous emission using a standard near-infrared telecommunications laser diode. Below threshold, the light emanating from the laser facets is affected both by the gain and absorption.

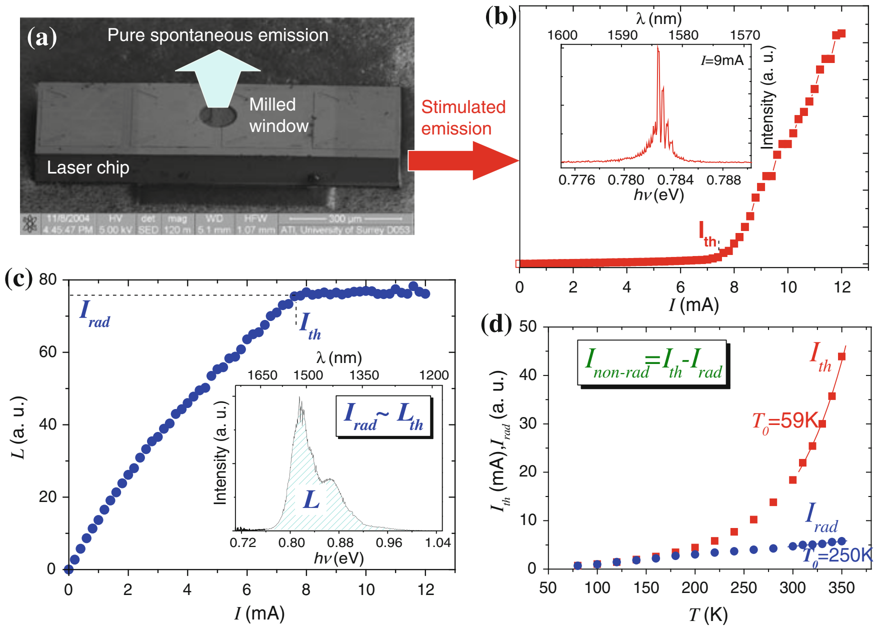

Fig. 9.2 Spontaneous emission technique: **a** laser chip with a milled window in the n-type substrate contact, both stimulated emission from the laser facet (**b**) and pure spontaneous emission from the milled window (**c**) are measured and analysed simultaneously. Comparison of measured temperature dependence of the threshold current, I_{th}, with its radiative component, I_{rad}, in (**d**) shows dominant presence of a non-radiativeprocess which can be quantified

In order to obtain pure unamplified spontaneous emission, the light needs to be collected before it undergoes either gain or absorption. To achieve this, the spontaneous emission is collected from a small window milled into the laser substrate contact (Fig. 9.2a). In this way, spontaneous emission randomly emitted in the active region may be collected in a direction perpendicular to the laser cavity. Transverse electric, TE, polarization without transverse magnetic, TM, mode can be measured in the vertical direction discussed here and both TE and TM polarizations are present in the in-plain emission from the device side (and can be accessed in buried heterostructure lasers or specially prepared devices). In these measurements, the maximum distance over which the spontaneous emission can be absorbed is equal to the total active region thickness (~10 nm) after which it passes through the wide band gap thick substrate (~100–300 μm thick). This makes absorption and gain effects negligible. The window can be formed in the substrate contact of the laser either during fabrication by including it on the mask set, or post-processed using an ion-beam milling technique. The windows produced by this process are typically circular with diameter of 100 μm or rectangular 50 μm wide and 100 μm long placed towards the centre of the contact, depending on the each device geometry. This is sufficiently small to avoid alteration of current flow in the device. As a matter of

routine, the threshold current is measured before and after the milling process to make sure that the device has not sustained any damage.

In order to collect spontaneous emission the laser is held in a spring clip with the window side pressed against a base plate. A multi-mode optical fibre is glued into the base plate in close contact with the window and the light from both the facet and window is analysed using an optical power meter and an optical spectrum analyser (see Fig. 9.2b, c). By integrating the spontaneous emission spectra from the window one can measure the value of L used in (9.5) in arbitrary units. In the example in Fig. 9.2, both light output from the facet and from the window show clearly the lasing threshold current at which, due to stimulated emission, a strong increase of the output from the facets starts and due to fast stimulated transitions the integrated spontaneous emissions pins due to pinning of Fermi levels. In an ideal case, above threshold each injected electron-hole pair produces a stimulated photon and all other recombination processes stay at the same level determined by the threshold conditions. Figure 9.2d shows how one can use this technique to analyse the temperature dependence of the threshold current, I_{th}, by measuring the integrated spontaneous emission at threshold, L_{th}. Providing that the light collection efficiency is constant with temperature, this allows one to determine the temperature dependence of the radiative component, I_{rad}, of the threshold current. In this particular example, due to negligible defect related recombination and Auger recombination at the lowest temperature, it was assumed that $I_{th} = I_{rad}$ at low temperatures. From Fig. 9.2d one can quantify the importance of the non-radiative process which becomes dominant at higher temperatures and causes a strong increase of I_{th}.

9.1.3 High Pressure Analysis

Hydrostatic pressure has long been used to study the properties of materials under extreme conditions. It is suitable for investigating many aspects of semiconductor physics including; electronic properties, lattice dynamics, defects and impurities, phase transitions, optical characteristics and the study of laser devices and photo-detectors [4]. The high hydrostatic pressure technique [2] provides additional unique information which allows for further understanding of the physical properties of semiconductor devices. The application of hydrostatic pressure to III–V semiconductors causes the direct band gap (E_g) to increase as shown in Fig. 9.3a for GaAs. Therefore, by applying pressure, one can investigate the effects of band gap change independent of the valence sub-band splitting and also eliminating influence of temperature (NB: the analysis of properties at different temperatures itself is quite challenging as temperature affects carrier distribution, carrier transport in some cases and other characteristic parameters). Pressure, in contrast, only affects the band structure. Furthermore, as pressure is applied to a III–V semiconductor, the conduction band Γ- and L-minima move towards higher energy with respect to the valence band maximum while the X-minima moves nearer to the valence band maximum as illustrated for GaAs in the figure [5]. The numbers show the movement of the

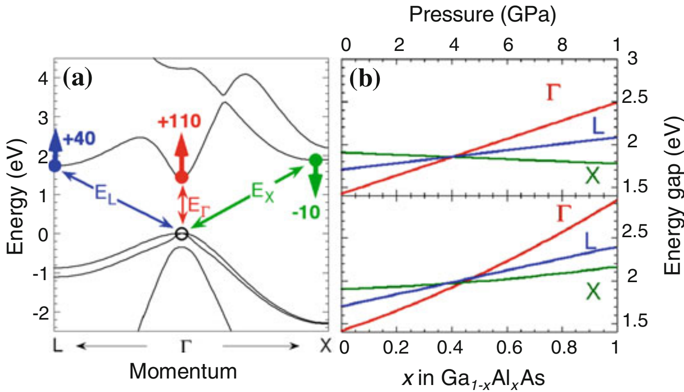

Fig. 9.3 Band structure alterations under high hydrostatic pressure: **a** shift of conduction band valleys is shown with the *arrows* and corresponding pressure coefficients are given in meV/GPa, **b** variation of direct and indirect bandgap by changing alloy composition and by application of high hydrostatic pressure

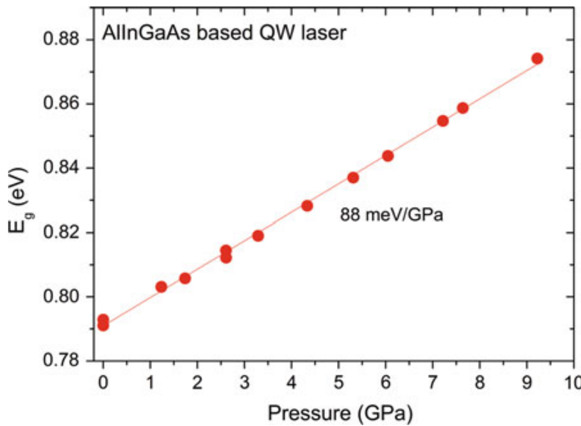

Fig. 9.4 The band gap measured using the emission peak as a function of pressure for an AlInGaAs/InP-based quantum well laser

corresponding valleys of the conduction band in meV/GPa with respect to the zone centre valence band maximum. These numbers are typical for most III–V compound semiconductors although exact values vary between different alloys [4, 6].

The different pressure dependencies of the conduction band minima can be effectively used to investigate inter-valley scattering processes and carrier leakage. Another unique use of the high pressure technique is presented in Fig. 9.3b where by applying pressure to a semiconductor, such as GaAs, one can mimic the effect of alloying. Figure 9.3b shows how the Γ, L and X conduction band minima of GaAs

vary as a function of pressure (top) compared with the variation of Γ, L and X in GaAlAs alloy moving from pure GaAs to pure AlAs. This clearly indicates that high pressure is indeed a valuable tool to investigate the effect of alloying and band structure on material and device properties. An example of effect of pressure on band gap can be seen in Fig. 9.4, where the band gap (determined from the emission peak) is measured as a function of pressure for an AlInGaAs/InP-based quantum well laser. From this it can be seen that the band gap increases linearly with pressure over this range.

In general, carrier recombination processes in semiconductor lasers are dependent on the band gap; therefore the application of hydrostatic pressure to semiconductor lasers provides a convenient method for investigating band gap dependent recombination mechanisms. For example, due to the fact that defect energy levels within the band gap are insensitive to the band edge position, the defect related recombination term in (9.2) will be pressure insensitive. In contrast, the pressure dependence of the radiative component of the threshold current in a quantum well laser is normally well described by the following expression [4]:

$$I_{th} \propto E_g^2, \tag{9.6}$$

where E_g is the band gap. This expression accounts for the fact that hydrostatic pressure increases the conduction band density of states and the optical mode density [4].

The pressure dependence of Auger recombination is determined by a strong dependence of the Auger coefficient, C, on the band gap. An expression for it is given in (9.7) considering the two most important Auger processes (known as CHSH (hot hole producing) and CHCC (hot electron producing)), where C_0 is approximately independent of pressure and temperature and E_a is the activation energy of the corresponding Auger process which is band gap and pressure dependent. Assuming parabolic and isotropic bands, the activation energies for CHSH and CHCC recombination are given by (9.8) and (9.9), respectively, where m_{so}, m_h and m_e are the spin-orbit, heavy-hole and electron effective masses, respectively, k is the Boltzmann constant, T is the temperature, and Δ_{so} is energy separation between the top of the valence band and the top of the spin-orbit split off sub-band.

$$C = C_0^{CHSH} \exp\left(-\frac{E_a^{CHSH}}{kT}\right) + C_0^{CHCC} \exp\left(-\frac{E_a^{CHCC}}{kT}\right), \tag{9.7}$$

$$E_a^{CHSH} = \frac{m_{so}}{2m_h + m_e - m_{so}}(E_g - \Delta_{so}), \tag{9.8}$$

$$E_a^{CHCC} = \frac{m_e}{m_h + m_e} E_g. \tag{9.9}$$

Under the condition that $E_g = \Delta_{so}$ CHSH Auger recombination becomes resonant, as evident from (9.7, 9.8) since $E_a \rightarrow 0$. In practical terms, if $\Delta_{so} > E_g$ then the CHSH process will be suppressed [7]. From (9.7–9.9) it can be seen that a decrease in the band gap (particularly, caused by application of high hydrostatic pressure) would significantly reduce the Auger recombination coefficient and corresponding loss processes in a device.

The carrier leakage current, I_{leak}, or inter-valley scattering can be strongly pressure dependent. It may be described by the following expression:

$$I_{leak} = I_0 \exp\left(-\frac{P}{kT}\frac{dE_a}{dP}\right), \tag{9.10}$$

where I_0 is a constant, P is the pressure and E_a is the activation energy of the leakage process. The value of dE_a/dP is determined by the difference in pressure coefficients for the band gap of adjacent layers or corresponding valleys of the conduction band, depending on a particular mechanism of the leakage process. Depending on the sign of dE_a/dP, current loss due to leakage may strongly increase or decrease with high pressure.

High pressure experiments are usually performed in a small cell containing either a liquid or gas pressure transmitting medium into which the sample is placed. There are many types and designs of high pressure systems. The high pressure measurements discussed here were performed using either a piston-in-cylinder apparatus capable of generating pressures up to 1.6 GPa (16 kbar) shown in Fig. 9.5 or using a Helium gas pressure cell capable of tuning pressure up to 1 GPa (10 kbar) presented in Fig. 9.6. The latter cell may be mounted inside a closed cycle cryostat for temperature and pressure dependence measurements. Further details of the experimental set-ups are discussed elsewhere [2, 8, 9]. Figure 9.5 illustrates the pressure cell with liquid used as a pressure transmitting medium. Sample holders may be designed in multiple ways to perform spectral measurements from the facet of a laser (Fig. 9.5b) as well as to carry out spontaneous emission measurements under pressure (Fig. 9.5c) [9]. The large sample volume also allows a special magnetic holder for carrier mobility measurements.

The advantages of the gas pressure cell presented in Fig. 9.6 are the following: use of a pure pressure medium with high thermal conductivity and low refractive index which does not affect optical losses of a laser sample, smaller size and possibility of changing temperature and the possibility of measurements with a large broadband transmission optical window make this system more attractive for mid-infrared devices.

In the following sections we consider the application of the above methodologies to study the physical properties of a wide range of different semiconductor light emitting devices and show how they have been used to elucidate an improved understanding of their fundamental behaviour and limitations. This is important for the optimisation of photonic devices.

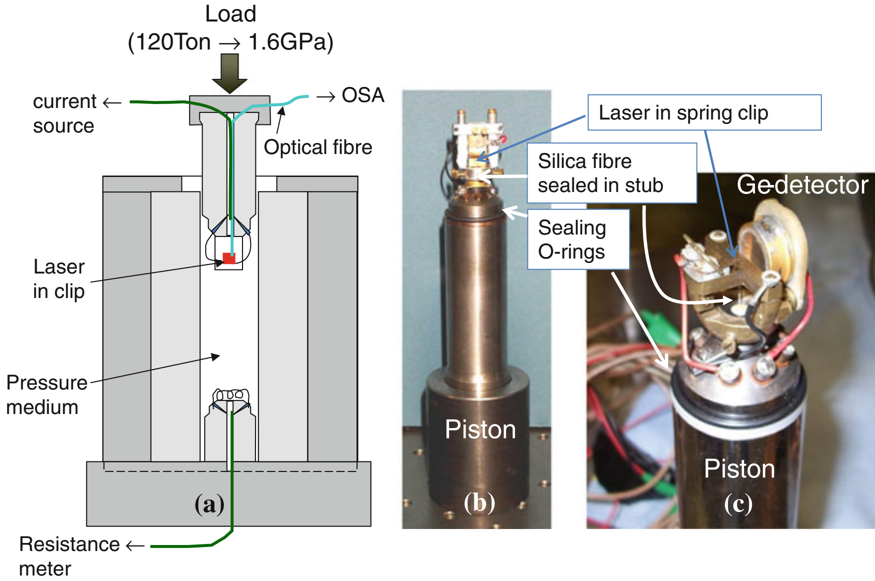

Fig. 9.5 High hydrostatic pressure setup with liquid pressure medium: **a** general diagram of the pressure cell, **b** piston with a fibre coupled sample holder for facet emission measurements, **c** piston with a holder for spontaneous emission measurements under high pressure

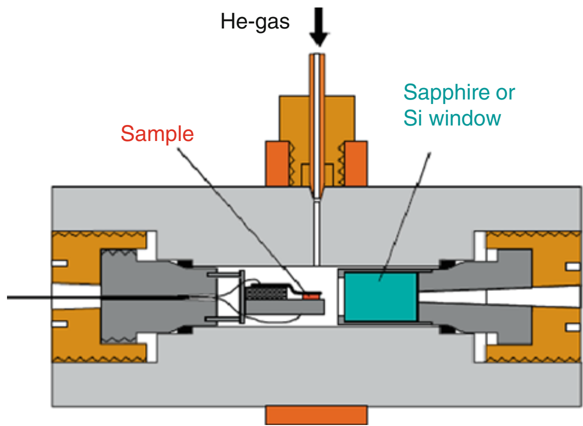

Fig. 9.6 High hydrostatic pressure setup with Helium gas as a pressure medium

9.2 Near-Infrared Quantum Well Lasers

A fast development of telecommunications and optical fibre broadband during recent decades only became possible due to development of near-infrared lasers [10] with emission wavelengthsof 1.31 and 1.55 μm where silica optical fibre has zero

dispersion and minimum loss, respectively. In this section we will consider several material systems used for telecom laser applications and how their properties may be analysed using spontaneous emission and high hydrostatic pressure techniques.

9.2.1 The Temperature Dependence of 1.3- and 1.5-μm InGaAs(P)/InP Multi-quantum Well Semiconductor Lasers

Historically, mainstream transmitting sources used in telecommunications systems have been based on InGaAs(P) semiconductor lasers operating close to 1.3 and 1.5 μm. Despite the well-established growth and fabrication technology, these lasers show quite strong temperature sensitivity which until around the turn of the century [3] had long been the subject of debate ascribed by various authors to a wide range of effects, including direct Auger recombination, phonon-assisted Auger recombination, inter-valence band absorption, temperature dependence of gain, recombination in the separate confinement hetero-structure region, and carrier leakage. The first step in rectifying this problem was to identify the dominant recombination mechanisms and to investigate their temperature dependence [3]. We will summarize the main results further in this section.

Considering the different terms in (9.2), An (defect-related recombination) is expected to be small in commercial high-quality devices and, it is indeed found to be negligible at the high carrier densities of concern. In order to determine how well the Bn^2 (radiative recombination) formalism holds at the high injection levels used in characterization, detailed calculations over the temperature range of 80–360 K were undertaken [3]. A six-band Hamiltonian was used in the calculation of the quantum-well (QW) band structure. Poisson's and Schrödinger's equations were solved self-consistently for both the conduction and valence band structures. A five-point finite-difference method was used which could take account of carrier spill-over into the barrier and separate confinement regions. The spontaneous emission rate, gain, and radiative current density were then calculated from these band structures for single QWs using the density matrix formulation including Lorentzian type broadening. The gain is calculated from the broadened spontaneous emission. The optical confinement factor and, hence, the threshold gain value required to overcome cavity and mirror losses also were calculated [3]. The theoretical results are shown in Fig. 9.7, where the current density due to radiative recombination, J_{Rad}, is plotted against carrier density on log scales for the 1.3-μm laser and the 1.5-μm laser and evaluated the gradient in the range corresponding to experimental measurements. One can see that for both 1.3- and 1.5-μm devices the Boltzmann approximation holds remarkably well with gradients of 1.85 and 1.87, respectively, close to the theoretically expected value of 2. From a combination of impedance-corrected carrier lifetime measurements together with spontaneous emission measurements, Flynn [11] experimentally demonstrated that B is independent of carrier density in 1.3 μm InGaAsP devices, in agreement with these theoretical calculations.

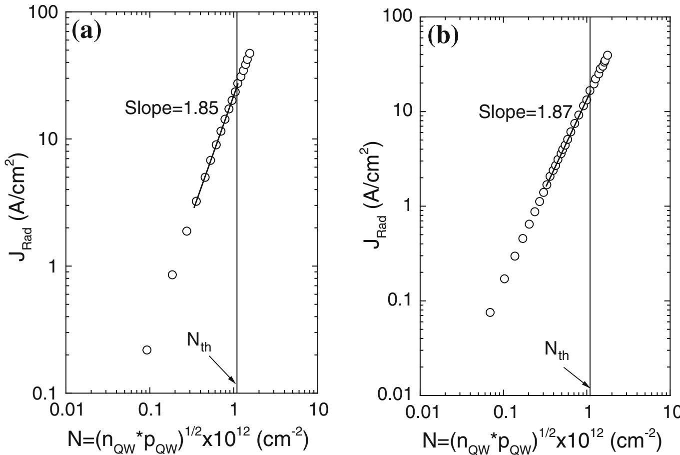

Fig. 9.7 Theoretical calculation of the radiative current density J_{Rad} as afunction of carrier density $N=(n_{QW*}p_{QW})^{1/2}$ for **a** 1.3-μm and **b** 1.5-μm lasers

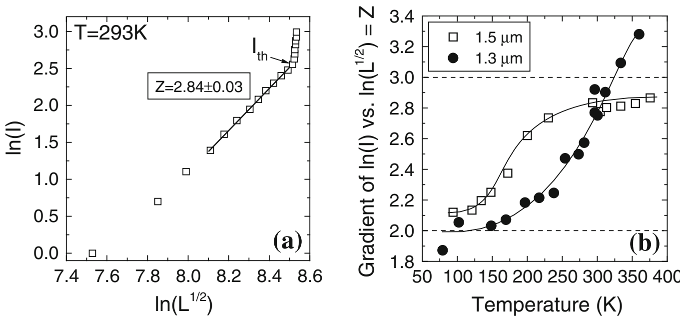

Fig. 9.8 **a** Example of determination of Z-value in a 1.5 μm laser at 293 K; **b** variation of Z from 80 K to above 350 K for the 1.5 μm (*open squares*) and the 1.3 μm (*closed circles*) lasers

Figure 9.8a shows experimentally measured dependence [3] of logarithm of injected current versus logarithm of the carrier density, determined according (9.5), i.e. $ln(L^{1/2})$. Data were collected from 80 to 350 K, and the values of evaluated from these data are shown in Fig. 9.8b for 1.5 and 1.3 μm InGaAs(P) lasers. It can be seen that, at both wavelengths, the value of Z is close to 2 for temperatures ∼100 K which means that $I \propto n^2$ and radiative recombination is dominant. As the temperature is increased, the Z value also increases, reaching a value of around 3 at room temperature, indicating that Auger recombination is the dominant current path at higher temperatures. The temperature at which the threshold current begins to deviate from purely radiative behaviour (the breakpoint temperature, T_B) is lower in the 1.5 μm laser, indicating the heightened importance of Auger recombination in the longer wavelength device. This is, in fact, expected, since the Auger recombination rate

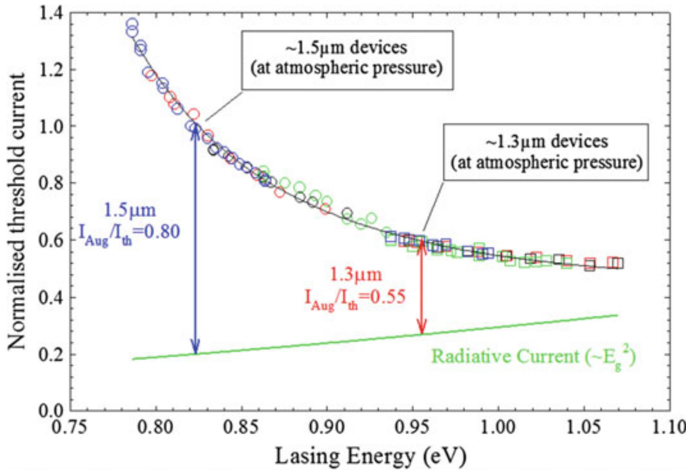

Fig. 9.9 Normalized threshold current as a function of lasing photon energy. The 1.3 μm data were normalized to the value of the 1.5 μm data at the point where the 1.5 μm device lased at 1.3 μm

increases as the bandgap decreases [4]. One can see that above room temperature, although for the 1.5 μm laser Z remains approximately constant, the value of Z for the 1.3 μm device continues to rise. This further increase in Z cannot be explained simply in terms of Auger recombination and strongly suggests that some other effect is becoming important at higher temperatures.

The application of hydrostatic pressure increases the bandgap at the Brillouin zone centre of InGaAs(P) and is, therefore, an ideal tool for the study of bandgap-dependent processes as discussed above. The measured lasing photon energy varies linearly with pressure over the pressure range 0–15 kbar in both devices. The values for dE_g/dP being 85 ± 1 and 86 ± 1 meV/GPa for the 1.3 and 1.5 μm devices, respectively, are only slightly above the value of 84 meV/GPa for the InP cladding showing that the band offsets remain roughly constant as pressure is increased, and so if the leakage current is dominant at room temperature, the threshold current is unlikely to change significantly with pressure.

Figure 9.9 shows the variation of threshold current with the pressure-induced energy shift. Close to 1.2 GPa, the 1.5 μm devices emit at 1.3 μm. We have, therefore, normalized I_{th} of the as-grown 1.3 μm lasers at atmospheric pressure to I_{th} of the 1.5 μm devices at 1.2 GPa (i.e., at the point where both devices emit at 1.3 μm). The solid line corresponds to the calculated band gap dependence of the *CHSH* Auger process, which forms a smooth curve through the measured data [12]. One can see a very good agreement between theory and experiment supporting the conclusion about the importance of Auger recombination in this band gap range. Since the Auger current is decreasing with pressure while the radiative current increases with pressure (shown in the Fig. 9.9 with a curve proportional to E_g^2), the results also demonstrate that there is a reduced amount of Auger recombination in the 1.3 μm

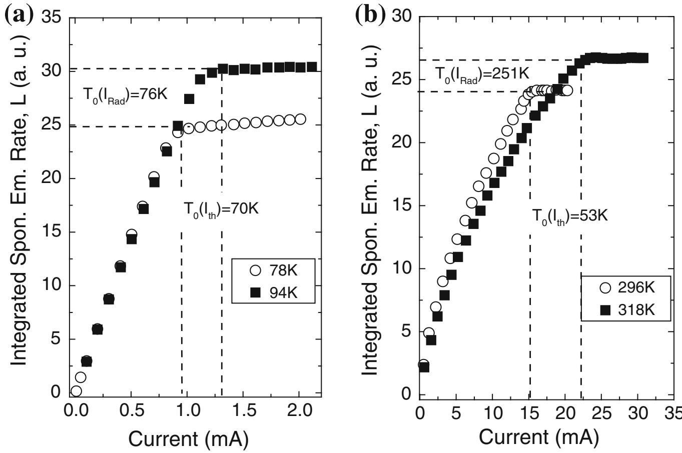

Fig. 9.10 Integrated spontaneous emission rate, L, measured from 1.5 μm laser at around 86 K (**a**) and 307 K (**b**)

as-grown devices. The spontaneous emission measurements discussed below allowed quantitative estimations of importance of Auger recombination.

To characterise the temperature dependence of a process an empirical term, the *characteristic temperature*, T_0, is used, which describes the rate of exponential increase/decrease of threshold current or other parameter with increasing temperature and is determined using the following equation:

$$T_0 = \left(\frac{1}{I_{th}} \frac{dI_{th}}{dT} \right)^{-1}. \tag{9.11}$$

Using (9.11) one may introduce experimentally a temperature sensitivity for the radiative component of the threshold current using spontaneous emission measurements. In a QW, the radiative recombination coefficient $B \propto 1/T$ and the threshold carrier density, n_{th}, is proportional to T^{1+x}, where x is a parameter taking into account non-idealities of the device such as carrier spill-over, inter-valence band absorption or the filling of higher subbands resulting in an increased temperature dependence [3]. Using (9.11) and the above assumptions for temperature dependencies of B and n_{th}, one can determine the characteristic temperature of the radiative current $T_0(I_{Rad})$ as:

$$T_0(I_{Rad}) = \frac{T}{1 + 2x}. \tag{9.12}$$

Similarly, assuming that the Auger coefficient $C = C_0 \exp(-E_a/kT)$, where C_0 is independent of temperature, a characteristic temperature of current fraction due to Auger recombination can be obtained as:

$$T_0(I_{Aug}) = \frac{T}{3 + 3x + E_a/_{kT}}. \tag{9.13}$$

Figure 9.10 shows examples of experimentally measured integrated spontaneous emission in the 1.5 μm laser. The carrier density and, thus, the pure spontaneous emission rate, pin at threshold allowing accurate determination of I_{th} and I_{rad} at each temperature. At an average temperature of 86 ± 8 K (Fig. 9.10a), a value for $T_0(I_{th})$ of 70 ± 5 K was found and a value for $T_0(I_{Rad})$ of 76 ± 15 K. Therefore, within experimental error $T_0(I_{th}) \approx T_0(I_{Rad}) \approx T$ as expected from (9.12) for $x = 0$ showing an excellent agreement between experiment and theory. In this temperature range, as has already been shown from the Z values, the threshold current of the laser is dominated by radiative current and the temperature sensitivity of the threshold current is governed by the temperature sensitivity of the radiative current at low temperatures. The same measurements around room temperature are shown in Fig. 9.10b, where from the Z values Auger recombination is expected to play a significant role. Indeed, one can find that, at an average temperature of 307 ± 11 K, $T_0(I_{Rad}) = 251 \pm 13$ K, whereas $T_0(I_{th}) = 53 \pm 3$ K [3]. Again, $T_0(I_{Rad}) \approx T$ (with some non-ideality associated with inter-valence band absorption), indicating that the variation of the radiative current with temperature is well behaved right up to room temperature. Since $T_0(I_{th})$ is significantly smaller than $T_0(I_{Rad})$ in this temperature range, one may conclude that the temperature dependence of the threshold current at room temperature cannot be explained in terms of the radiative current alone. It is also interesting to note the behaviour of the integrated spontaneous emission below threshold. On one hand, in the low temperature regime in Fig. 9.10a, for any fixed current below threshold, the integrated spontaneous emission rate at both temperatures is equal and depends only on the current as expected if the only current path is through radiative recombination. On the other hand, considering the high temperature data in Fig. 9.10b, for a fixed current below threshold, the integrated spontaneous emission rate is lower at the higher temperature, indicating that there is a non-radiative as well as radiative current path which increases faster with increasing temperature. The 1.3 μm showed similar behaviour of $T_0(I_{th})$ and $T_0(I_{Rad})$ corresponding to the Z measurements in Fig. 9.8b.

Having measured $I_{th}(T)$ in absolute units and $I_{rad}(T)$ in arbitrary units and knowing that $I_{th} = I_{rad}$ at the lowest temperature, one can plot the temperature dependencies of the radiative and non-radiative parts of the total threshold current. In [3] radiative current was plotted using $T_0(I_{Rad}) = T$ and x in (9.12) as a fitting parameter to match I_{rad} to I_{th} at low temperatures where the Z value was around 2. Figure 9.11 shows the experimentally measured I_{th} in 1.3 and 1.5 μm lasers and fitted curves for I_{Rad}, I_{Aug} and $I_{th} = I_{Rad} + I_{Aug}$. The current path due to Auger recombination was fitted using (9.13) for $T_0(I_{Aug})$ and E_a as a fitting parameter. A good fit was obtained in both cases up to around room temperature in the 1.5 μm devices with $E_a = 64$ meV and with $E_a = 140$ meV for the 1.3 μm devices.

From Fig. 9.11 it was found that at 300 K radiative recombination accounts for around 40–50 % of the total current in the 1.3 μm laser and 20 % of the total current in the 1.5 μm laser (see also Fig. 9.9). The rapid increase in I_{th} and decrease in

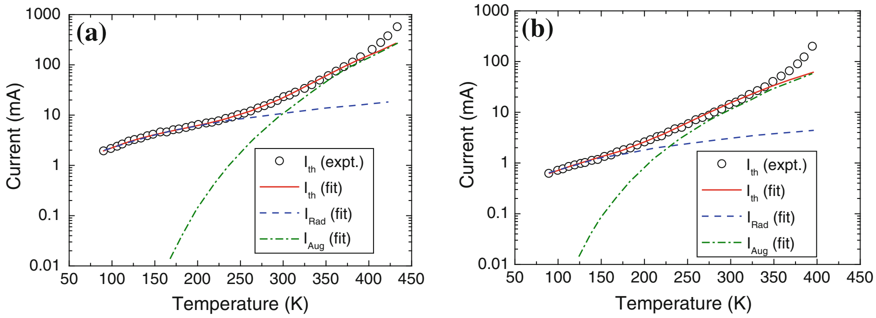

Fig. 9.11 Threshold current on a log scale as a function of temperature for **a** the 1.3 μm laser and **b** the 1.5 μm laser (*open circles*). The *solid*, *dashed*, and *dotted lines* are the fitted variations of the threshold current, radiative current, and Auger current, respectively

T_0 can be attributed largely to Auger recombination which however cannot explain strongly increasing I_{th} around 400 K. Measurements of the spontaneous emission and differential efficiency indicate that a combination of increased optical losses related to inter-valence band absorption and carrier overflow into the barrier and separate confinement heterostructure regions may further degrade $T_0(I_{th})$ above room temperature. A more detailed analysis and discussion can be found elsewhere [3].

9.2.2 Near-Infrared InGaAlAs/InP Based Lasers

It has been suggested that InGaAlAs/InP based semiconductor lasers would allow a better temperature performance and potentially uncooled operation compared to the standard InGaAsP/InP based near-infrared lasers for telecommunications applications [13, 14]. Due to the larger potential conduction band offset, ΔE_c, to the total band gap offset, ΔE_g, ratio of the InGaAlAs/InP material system of around $\Delta E_c = 0.7\Delta E_g$ compared to $\Delta E_c = 0.4\Delta E_g$ for the InGaAsP/InP heterostructures, InGaAlAs/InP has stronger electron confinement, reduced threshold current and therefore reduced Auger recombination. It has been shown using the results of temperature dependence measurements performed on 1.3 μm InGaAlAs and 1.5 μm InGaAlAs devices that the 1.3 μm devices show significantly smaller temperature sensitivity and reduced nonradiative current at threshold [13]. At room temperature, I_{rad} forms ~70 % of I_{th} compared with ~40 % for the 1.5 μm InGaAlAs lasers [13]. This is inconsistent with the threshold current being dominated by a simple carrier leakage into the barrier layers (since the 1.5 μm devices have a lower conduction band offset) and together with the pressure dependence data this suggests that the operating wavelength rather than the band offset is of most importance to the nonradiative current, which, as with the InGaAsP/InP materials system is consistent with the Auger recombination having a dominant effect [4].

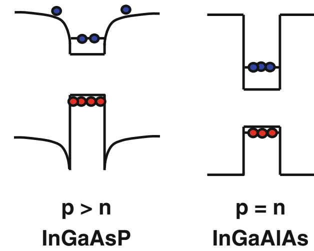

Fig. 9.12 A schematic band diagram for InGaAsP (p > n due to thermal escape of electrons) and InGaAlAs (p = n as there is no carrier leakage due to thermal escape) lasers emitting at 1.3 μm demonstrating how better electron confinement in the latter system allow reduction of hole concentration

It has been shown that InGaAlAs-based 1.3 μm lasers exhibit a reduced temperature sensitivity of the threshold current compared to conventional InGaAsP-based devices [15]. I_{th} is found to increase with increasing hydrostatic pressure in the InGaAlAs devices which is attributed to the dominance of radiative recombination. In contrast, a decrease of I_{th} with increasing pressure is observed in InGaAsP devices (as discussed earlier) and attributed to a large non-radiative Auger current, I_{Aug}, which decreases with increasing band gap. It is also shown that I_{Aug} accounts for ~50 % of I_{th} in 1.3 μm InGaAsP devices, but accounts for less than 30 % of I_{th} in the 1.3 μm InGaAlAs lasers leading to a lower temperature dependence of the threshold current [15]. Figure 9.12 illustrates a model showing how a larger conduction band offset in InGaAlAs leads to improved electron confinement and a reduced quantum well hole concentration at threshold, p, and hence a reduced CHSH Auger process ($I_{Aug} p^2 n$) as further discussed in [15].

High hydrostatic pressure studies of 1.5 μm InGaAlAs/InP based quantum well devices also demonstrate a superior temperature performance compared to InGaAsP/InP lasers with the same emission wavelength. It was shown that the use of InGaAlAs material allowed reduction of non-radiative Auger recombination from 80 % of I_{th} in InGaAsP based lasers [16] (see the previous section) to 60 % of I_{th} in InGaAlAs devices [13]. Figure 9.13 demonstrates direct measurements of the temperature dependencies of I_{th} and I_{Rad} using the integrated spontaneous emission technique in a 1.5 μm InGaAlAs based broad area laser. The threshold current has an improved T_0 of 70 K around room temperature and non-radiative recombination accounts for ~60 % of the threshold current. The temperature dependence of the Z value shows that the dominant radiative recombination at low temperature characterised with Z ≈ 2 is overcome by the Auger recombination at higher temperatures where Z value becomes close to 3. However, this has a relatively smaller effect than in the InGaAsP system making InGaAlAs more attractive for temperature stable telecommunications lasers.

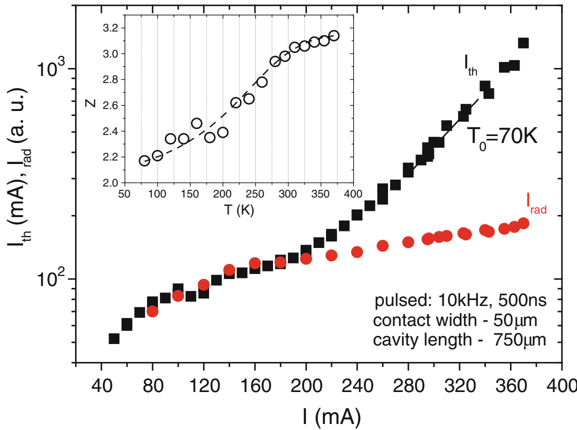

Fig. 9.13 Threshold current of InGaAlAs/InP 4 QW (1.5 % compressively strained) and its radiative component measured using the integrated spontaneous emission value at threshold as a function of temperature. No evidence of defect related recombination suggests that $I_{th} = I_{rad}$ at low temperatures. *Insert* temperature dependence of Z value determined from *ln(I)* versus $ln(L^{1/2})$ plot

9.2.3 Analysis of Near-Infrared "Dilute Nitride" InGaAsN/GaAs Lasers

Another approach to reach telecommunication wavelengths is based on using the InGaAsN/GaAs material system. The use of GaAs-based technology is very attractive due to possibility and relatively ease of fabrication of low cost vertical cavity surface emitting lasers (VCSELs). In this material system replacing a small amount of the group V element by nitrogen significantly reduces the energy gap. This reduction of about 0.1 eV per % of N (for up to 3 %) occurs because of a band anti-crossing (BAC) interaction between the conduction band edge and a higher-lying nitrogen resonant band [17] and dramatically changes the electronic structure [18], thereby offering a new route to band structure engineering and improved optoelectronic properties. In addition, the growth of strained InGaAsN/GaAs QW structures allows the benefits of compressive strain and the inclusion of N in the InGaAsN layers significantly increases the conduction band offset, leading to improved electron confinement and to decreased electron spill-over at room temperature and above, when compared with conventional InGaAsP 1.3 μm lasers. Edge-emitting and VCSEL laser structures with promising characteristics were reported by a number of groups, however, the influence of N on the electronic structure and laser characteristics remains of interest theoretically and experimentally [19–21]. One of the major challenges in producing InGaAsN based devices has been the material quality and the introduction of defects with increasing nitrogen fractions. Therefore in these lasers monomolecular (defect-related) recombination (*An* term in (9.2)) plays an important role [19, 21–23]. Figure 9.14 demonstrates a comparison of the *Z* value at lasing

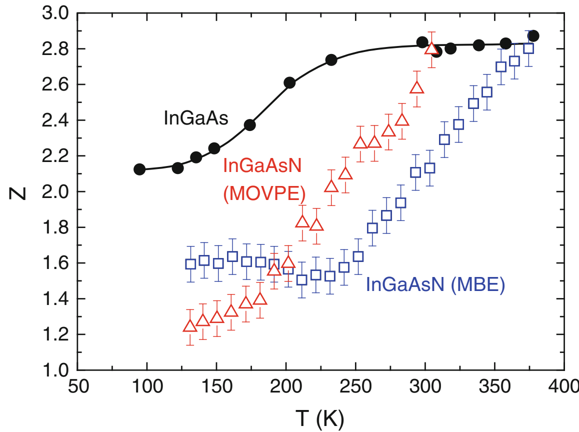

Fig. 9.14 Comparison of Z value just below lasing threshold of 1.3 μm GaInNAs/GaAs lasers with a standard 1.3 μm InGaAs/InP laser [22, 23]. Z values below 2 in the GaInAsN lasers indicate importance of defect related recombination described by "An" term in (9.2)

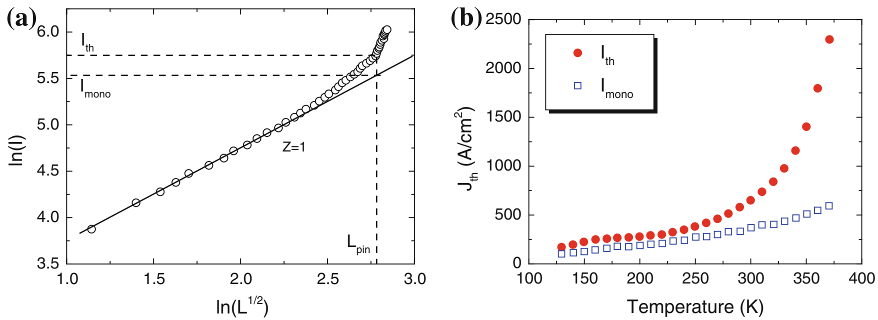

Fig. 9.15 **a** Method of determination of I_{mono} at lasing threshold using linear extrapolation of $\text{In}(I) \propto \text{In}(L^{1/2})$ plot until pinned level of integrated spontaneous emission, **b** resulting plot of I_{th} and I_{mono} as a function of temperature

threshold of 1.3 μm GaInNAs/GaAs lasers compared with a standard 1.3 μm InGaAsP/InP laser [22, 23]. Z values below 2 in the GaInAsN lasers clearly indicate presence and importance of defect related recombination corresponding to An term in (9.2) where for a device entirely dominated by defect-related recombination would yield a Z-value approaching 1.

To quantify the monomolecular current, I_{mono}, due to recombination via defect states spontaneous emission can again be used whereby the integrated spontaneous emission is measured with small current steps at very low currents where the defect-term is dominant and $Z = 1$. This $Z = 1$ behaviour on the dependence $\text{In}(I) \propto \text{In}(L^{1/2})$ graph may then be extrapolated to threshold where the integrated spontaneous emission starts to pin as shown in Fig. 9.15a. The value of current determined by the line at threshold therefore determines the contribution of

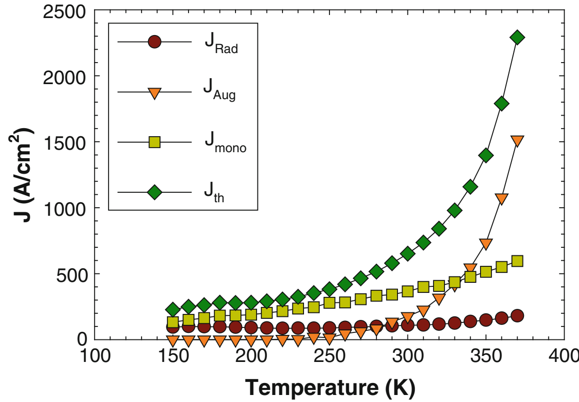

Fig. 9.16 Temperature dependence of current densities due to individual current paths: J_{mono}—defect related recombination, J_{Rad}—radiative recombination, and J_{Aug}—Auger recombination

the defect-related current to the total threshold current, I_{mono}. By repeating this at different temperatures one can plot the temperature dependence of the total threshold current and its part due to defect related non-radiative recombination in absolute units. Here it is assumed that coefficient A in (9.2) is independent of carrier density, n. Figure 9.15b demonstrates I_{th} and I_{mono} in absolute units over a wide temperature range 130–380 K [19, 22, 23]. One can see that the defect related recombination is very significant and accounts for up to 50–60 % of I_{th} around room temperature in these devices.

By subtracting I_{mono} from I_{th} and assuming negligible Auger recombination at the lowest temperatures one can plot the radiative current, I_{Rad} (measured directly using L_{th}) in absolute units. After that the current fraction due to Auger recombination can be determined as: $I_{Aug} = I_{th} - I_{mono} - I_{Rad}$. Thus, using the spontaneous emission technique the individual current paths can be quantitatively determined as shown in Fig. 9.16 [19, 22, 23].

High hydrostatic pressure studies of these devices and the development of the spontaneous emission technique in combination with high pressure has provided further insight into the physical properties of dilute nitride devices [21]. The pressure dependence of the current components of the recombination current at threshold in 1.3 μm InGaAsN lasers showed that an unusual rapid increase of the threshold current with increasing pressure above 6 kbar as presented in Fig. 9.17 is caused by an anomalous increase of the Auger-related recombination current, while the defect-related monomolecular recombination current is found almost independent of pressure. Theoretical calculations show that the increase of the Auger current can be attributed to a large increase in the threshold carrier density with pressure due to the increase in the electron effective mass arising from the enhanced level-anticrossing between the GaInAs host conduction band and the nitrogen level [21]. The dilute nitride lasers remain of high importance in the development of III–V based laser technology where developing high quality material becomes a key challenge.

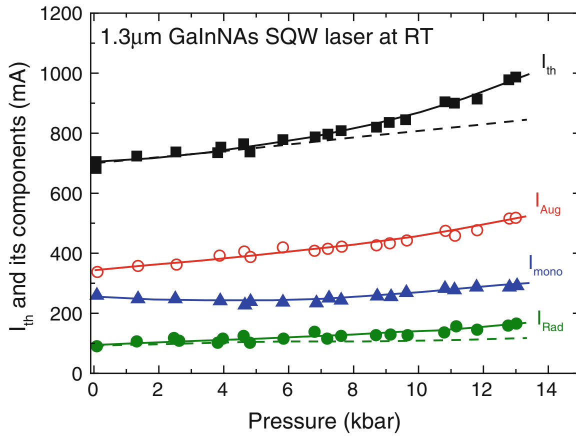

Fig. 9.17 High hydrostatic pressure dependencies of the total threshold current, I_{th}, and each recombination current component: the monomolecular nonradiative current, I_{mono}, radiative current, I_{Rad}, and Auger current, I_{Aug}, in GaInNAs SQW lasers at RT. The *dashed line* describes the variation of the ideal radiative current with pressure. The *solid lines* are guides to the eye

9.3 New Approaches in Development of the Near-Infrared Lasers

9.3.1 InAs-Based Quantum Dots

In 1982 Arakawa and Sakaki suggested an idea of using quantum dots (QDs) and three-dimensional confinement to improve the thermal stability of semiconductor lasers [24]. Theoretically it was predicted that in the absence of any loss process such lasers would be absolutely temperature stable. Experimentally, to fabricate these types of devices Stranski-Krastanow self-assembled growth technique [25] has been widely deployed. Despite the fact that very high quality QD lasers with extremely low threshold current densities can be grown, they still remain temperature sensitive [26, 27]. Although a proposal to use p-doping to improve the temperature characteristics of 1.3 μm QD lasers for telecommunications has been realized in practice, the high values of the characteristic temperature of the threshold current have only been achieved over a narrow temperature range and at the expense of an increased I_{th} compared to the intrinsic material [28]. Among more recent achievements, Ishida et al. reported temperature stable 25-Gbps direct modulation in 1.3-μm p-doped InAs/GaAs QD lasers [29]. The optimization of growth and device design has also allowed fabrication of 1.3-μm QD lasers with a high modal gain with continuous wave output powers of 2.5 W at room-temperature [30]. High gain 1.55-μm laser diodes with InAs quantum dot like active regions are described in detail in [31].

The trend reported in the literature for 1.3 μm InAs/GaAs QDs shows generally that a smaller threshold current density corresponds to a smaller value of character-

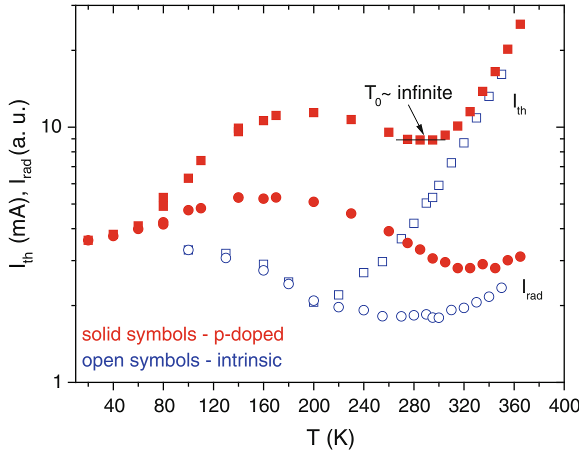

Fig. 9.18 Temperature dependence of the threshold current, I_{th}, and its radiative component, I_{Rad}, in p-doped (*solid symbols*) and intrinsic (*open symbols*) 1.3 μm QD lasers

istic temperature [26, 27]. It is also important to note that the nearly infinite T_0 in the p-doped lasers around room temperature reduces to ~60–70 K just above 60 °C similar to undoped devices as shown in Fig. 9.18 [28]. A decrease in the threshold current is very common in devices with significant inhomogeneous broadening of the carrier distribution due to variation of quantum dot sizes and localized energy states. It is related to carrier transport and redistribution effects and takes place in the temperature range up to 200 K in undoped QDs and may persist to much higher temperatures in p-doped devices [28] due to an improved carrier confinement induced by band distortion and Coulombic attraction of the conduction band electrons to the excess holes [28]. This effect therefore may be used to offset the strongly increasing non-radiative recombination which dominates the threshold current at room temperature [27, 28].

There have been a lot of discussions in the literature on the origin of non-radiative recombination in near-infrared quantum dots which is responsible for their temperature sensitivity [26, 32]. To explain the temperature sensitivity of the quantum dot lasers re-emission of carriers into the optical confinement layers (OCL) activated by increasing temperature and their subsequent radiative or nonradiative recombination in the OCL was proposed [33, 34]. Indeed, Matthews et al. [35] showed that the temperature sensitivity of short wavelength ($\lambda \sim 1$ μm) QD lasers is caused by gain saturation due to the presence of a high density of states in the wetting layer. Experimentally it was demonstrated that to decrease the temperature sensitivity of I_{th}, the shape of the QDs should be engineered to maximise the energy separation between the ground electron and hole states and their respective excited states [36].

Direct spontaneous emission measurements and analysis of temperature dependence of radiative current clearly show that temperature sensitivity of near-infrared quantum dot lasers is caused by a non-radiative process (see Fig. 9.18). In

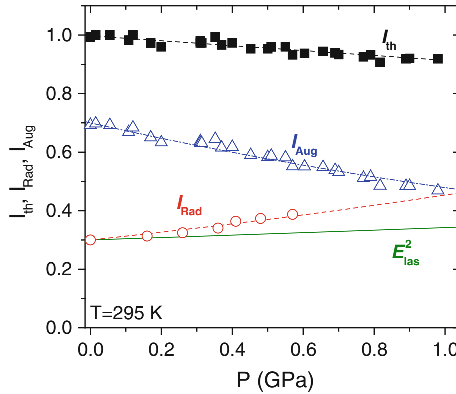

Fig. 9.19 Pressure dependencies of the normalised threshold current $I_{th}(P)/I_{th}(P = 0)$ (*squares*) and of its radiative, I_{Rad}, (*circles*) and nonradiative, I_{Aug}, (*triangles*) components. I_{Rad} was normalised to 30 % of I_{th} at atmospheric pressure as determined from the temperature dependent measurements and fitted as a function of the band gap over this pressure range ($I_{Rad} \sim E_g^6$). The *solid line* shows the pressure variation of I_{Rad} for an ideal QW laser with the same gradient dE_g/dP, where it is proportional to E_g^2. The *dashed-dotted* line is a fit of the difference ($I_{th} - I_{Rad}$) due to Auger recombination, where $I_{Aug} \sim E_g^{-5.5}$

addition, high hydrostatic pressure experiments showed that the thermal sensitivity of the threshold current in InAsquantum dots is due to non-radiative recombination processes, which depend on the band gap of the dots and their energy level distribution. The results showed the high probability of thermal carrier leakage and subsequent defect related recombination in shorter wavelength devices ($\lambda < 980$ nm) [32] and highlighted the likely importance that Auger recombination can have in 1.3 μm QD lasers [27, 28, 32]. Figure 9.19 shows pressure dependence of threshold current and its radiative component measured directly using the spontaneous emission technique under high pressure in a high quality 1.3 μm QD laser ($J_{th}(RT) \approx 40$ A/cm^2) [27]. From the temperature dependent measurements it was found that the radiative current in these high quality devices accounts for up to a maximum of 30 % of I_{th} and at least 70 % of I_{th} is lost due to Auger recombination [27, 28, 32]. Interestingly, from the pressure measurements it was found that the radiative current increases with the band gap much faster compared with the case of an ideal QW laser. From measurements on many different devices it was found that $I_{Rad} E_g^6$. While this power law has no theoretical basis, the strong super-linear dependence is likely to be the result of the gain saturation effect and could be even stronger in devices of shorter cavities or having a reduced QD density in the active region for which an increased mirror losses or a reduced maximum gain make the effect of gain saturation more important [27, 37].

To explain the importance of Auger recombination in near-infrared QD lasers a simple but realistic model was developed which takes into account the closely-spaced hole energy levels in such self-assembled quantum dots [38]. Radiative transitions

to these states from the lowest electron state are found to be suppressed and so do not make significant contribution into radiative recombination rate. However, non-radiative Auger recombination involving the holes from these excited states is expected to dominate at high carrier injection levels required for lasing. The proposed model is found to explain well both the very different temperature variations observed for the radiative and non-radiative components of the threshold current density, and also the temperature dependence of the different contributions to the total threshold radiative current density. The analysis highlights that in reality these self-assembled dot systems are quite different from the idealized structures originally envisaged by Arakawa and Sakaki [24]. It confirms that in such dots at room temperature and above, the total threshold current density is dominated by Auger recombination, as already shown through measurements of the variation of I_{th} and I_{Rad} with pressure [27] (also see Fig. 9.19).

These conclusions were also confirmed in studies of longer wavelength InAs based quantum dot [39, 40] and quantum dash lasers [41] emitting at 1.5 μm at RT grown on InP substrates. In these devices with a smaller band gap Auger recombination has been estimated to constitute 90 % or more of I_{th}[39, 40]. The high pressure characteristics of InAs/InP quantum dash lasers with emission wavelengths of 1.52 and 1.76 μm showed dramatically different behaviours of the threshold current which was interpreted assuming that in the 1.52 μm lasers, pressure independent defect related recombination outside the dashes due to thermal carrier spill-over dominates, while in the 1.76 μm quantum dash lasers at least 60 % of I_{th} is due to Auger recombination. Decreasing the band gap of quantum dashes and increasing the lasing wavelength improves carrier confinement and decreases carrier spill-over and consequent defect related recombination. However this causes a stronger Auger recombination at the longer wavelength [41]. In spite of the issues with Auger recombination in quantum dot lasers, the temperature stability that can be engineered with p-doping, coupled with their good modulation characteristics means that these are starting to become commercialised for use in data communications, primarily at 1.3 μm.

9.3.2 Bismuth Containing III–V Material Systems

The incorporation of bismuth into III–V semiconductors such as Ga(In)As causes a large band gap bowing which can be modeled using band-anti-crossing theory, albeit in the valence band for bismides (versus the conduction band for dilute nitrides) [42]. Moreover, due to the large size of bismuth atoms, the spin-orbit band moves down in energy, which coupled with the upward movement of the valence band edge produces a very large spin-orbit splitting [43]. This opens-up interesting new possibilities for efficient photonic devices, such as near- and mid-infrared lasers which are more thermally stable and less susceptible to losses compared to conventional InP-based devices. Substituting As with small amounts of Bi creates an energy level in the host valence band (VB) causing a VB anti-crossing (VBAC) interaction. This strongly reduces the bandgap, E_g, by ∼80 and ∼56 meV/Bi% in GaAsBi and

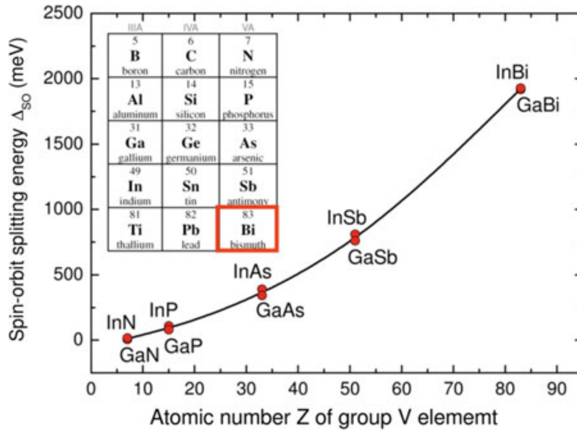

Fig. 9.20 Variation of the spin-orbit splitting energy as a function of group V atomic number for III–V binary compounds

InGaAsBi, respectively [44]. The VBAC interaction between the Bi level and the host III–V material system [45] is analogous to the conduction band (CB) anti-crossing for dilute nitride alloys [46]. As shown in Fig. 9.20 Bi enhances the SO splitting energy (Δ_{SO}). If Δ_{SO} can be made larger than E_g, fundamental loss processes such as Auger recombination and inter-valence-band absorption (IVBA)which dominate near-infrared emitters based on InGaAsP/InP can be reduced significantly or fully suppressed, as illustrated in Fig. 9.21 [3, 13, 15].

Moving into the mid-infrared, GaInAsSb/GaSb based lasers (also shown in Fig. 9.21 and discussed later in this chapter) operating at 2–3 μm have lower threshold current densities and a reduced sensitivity to temperature [47], which is due to the large spin-orbit splitting in antimonide-alloys such that Δ_{SO} is larger than E_g [48, 49]. This suppresses IVBA and CHSH-type Auger transitions via the spin-orbit band since energy and leads to improved laser performance in the mid-infrared. A similar effect is also observed in GaInAsSbP/InAs mid-infrared LEDs [50]. The unusual band structure properties of the bismide-alloys also provide a potential route to achieve the $\Delta_{SO} > E_g$ condition in the near-infrared range. Furthermore, it has been shown that by adding nitrogen to the bismide-alloys, lattice matched narrow band gap semiconductor heterostructures may be produced with the possibility of wide control of the conduction and valence band offsets [51].

There has been relatively little research to date on the carrier recombination and temperature dependent processes occurring in GaAsBi based devices. Using high hydrostatic pressure and low temperature techniques, the processes limiting device performance were probed in $GaAs_{1-x}Bi_x$/GaAs LEDs containing 1.8 % bismuth [52]. The results of this study also confirmed the type-I band alignment at the $GaAs_{1-x}Bi_x$/GaAs interface. A rapid decrease in the output efficiency was observed with increasing temperature in these devices indicating activation of loss mechanism(s) at higher temperature. The light-current characteristics showed a

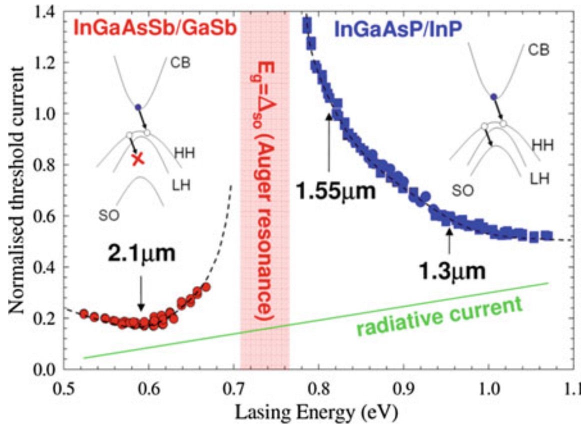

Fig. 9.21 Influence of Auger recombination on the threshold current of InP- and GaSb-based lasers in the near- and mid-infrared range (*dashed lines* are given as a guide to the eye). *Solid line* demonstrates variation of the radiative current versus lasing photon energy or bandgap

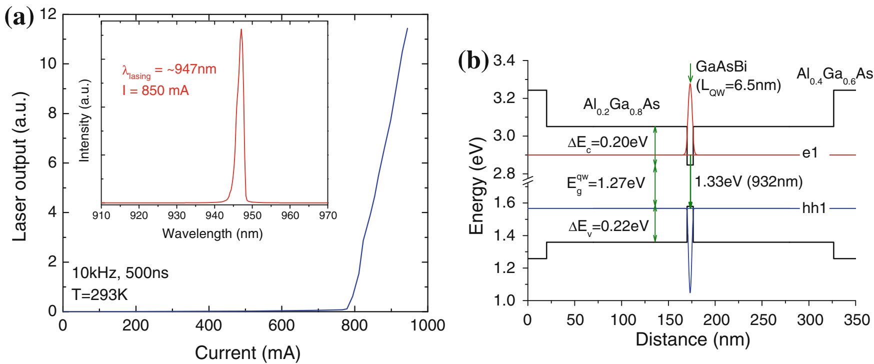

Fig. 9.22 **a** Light output—current characteristic and lasing spectrum at room temperature of the first GaAsBi/AlGaAs SQW laser. **b** Band structure of the laser with calculated wave functions for the ground electron and hole states

sub-linear behaviour even at temperatures as low as 80 K which indicates that the loss mechanism has a stronger carrier density (n) dependence than the radiative current [52]. Since the conduction band offset is very small and carrier leakage has an approximately exponential dependence on n, this may suggest that carrier leakage plays an important role in these devices, if, as expected, Auger recombination is negligible at these short wavelengths. The decrease in overall electroluminescence intensity with application of hydrostatic pressure together with a relatively increased emission from the GaAs barrier layers compared to the GaAsBi emission with increasing pressure suggests the presence of a carrier leakage path. The experimental data confirmed that carrier leakage into GaAs barriers is occurring in these devices since

dE_g/dP(GaAsBi) > dE_g/dP(GaAs) and the leakage activation energy decreases with increasing pressure [52].

The development of bismide based lasers recently experienced a breakthrough due to improvements in growth technology and demonstration of the first electrically pumped lasers operating at room temperature [53–55]. Figure 9.22a presents the light-output characteristic and a spectrum of such a laser based on a GaAsBi/AlGaAs single quantum well structure. It was grown by MOPVE and contains a single 6.5 nm QW with 2.3 % Bi [54, 55]. The laser showed room temperature operation at a wavelength of 947 nm in good agreement with theoretical predictions given in Fig. 9.22b. The room temperature threshold current density was measured to be 1.6 kA/cm^2, which is relatively high but promising for an SQW device in such a new materials system. Temperature and high pressure measurements are currently being carried out to identify the dominant losses in these lasers and will be discussed in details in [55]. This interesting new class of III–V materials, although in its infancy, shows great promise for the development of higher efficiency and temperature stable lasers and related devices operating in the near infrared.

9.4 Semiconductor Emitters for Mid-Infrared Applications

9.4.1 Interband Structures for Longer Wavelength Lasers and LEDs

Diode lasers emitting in the mid-infrared are important for the development of highly sensitive gas detection systems in various areas such as environmental pollution monitoring, medicine, industrial process control, etc. Many gases of interest have strong absorption lines in the 2–5 μm region. As shown in Fig. 9.21, InGaAsSb based structures can be effectively used for laser applications in the spectral range from around 1.85 μm (0.670 eV) up to 2.48 μm (0.500 eV). O'Brien et al. [56, 57] carried out investigations on InGaAsSb/AlGaAsSb quantum well lasers emitting at 2.11 and 2.37 μm at ambient conditions. High hydrostatic pressure measurements presented in Fig. 9.23 showed very different pressure dependencies of the threshold current in these devices. When plotted as a function of the band gap in Fig. 9.23b the data points show a minimum in the threshold current around 2.07 μm (0.600 eV). The use of spontaneous emission analysis showed that the threshold current of both the 2.11 and 2.37 μm lasers is dominated by non-radiative recombination, namely, Auger recombination [56, 57]. Interestingly, the high pressure results showed that Auger processes in the two devices are of different types. In the 2.37 μm devices, the CHSH Auger process is suppressed at ambient pressure as $\Delta_{SO} > E_g$ and the threshold current decreases with pressure due to reduction of the other Auger processes (CHCC—with excitation of a hot electron in the conduction band and CHLH—with excitation of a hot hole into the light-hole subband). However, at higher

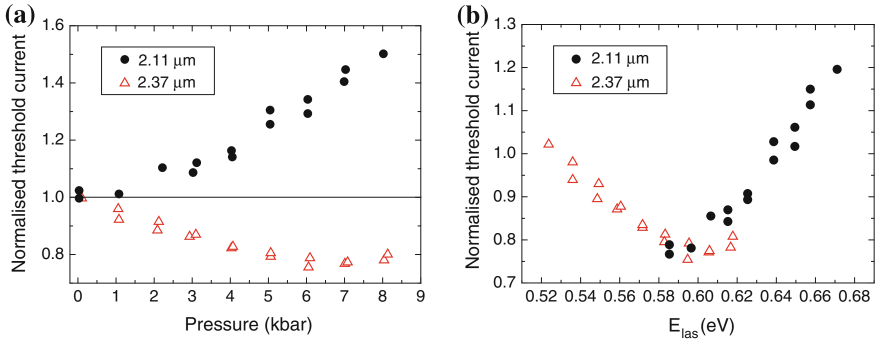

Fig. 9.23 Pressure dependence of the threshold current of two GaInAsSb lasers of different wavelengths (**a**) and variation of threshold current with lasing energy, E_{lase} (**b**). The observed minimum in threshold current value at a lasing energy of around 600 meV is because CHSH Auger recombination is not allowed and other Auger processes are also minimised

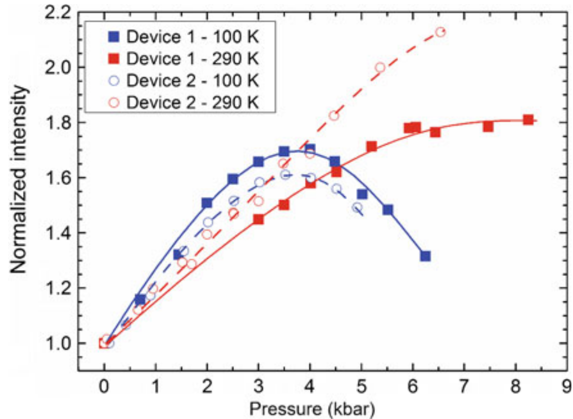

Fig. 9.24 Normalised light intensity versus hydrostatic pressure curves of two GaInAsSbP LEDs with different mesa sizes at 100 and 290 K (500 ns pulses at 10 kHz at 150 mA). *Solid lines* are fit as a guide to the eye

pressures E_g tends towards Δ_{SO} where the CHSH Auger recombination process is allowed and causes a strong increase in the threshold current (see points above 6 kbar in Fig. 9.23a or above 590 meV in Fig. 9.23b. In the 2.11 µm devices, where E_g is larger, the CHSH Auger process is already allowed at atmospheric pressure and increases in significance as pressure is applied. It is evident from Fig. 9.23 that there is a band gap range for which the CHCC or CHLH processes have been minimised and the CHSH process is suppressed. The energy at which this occurs will depend on the band gap and spin orbit splitting energy. For these devices the minimum occurs in the band gap range of 570–610 meV. It would appear that precise engineering of the strain and composition of lasers at these wavelengths, could keep them in this *minimal-Auger region* and help maximise device performance [56, 57].

Ikyo et al. [58] investigated the physical properties of GaInAsSb-based type-I quantum well edge emitting lasers emitting at 2.3 and 2.6 µm at ambient

conditions. At temperatures above 150 K both devices are dominated by non-radiative Auger recombination demonstrating T_0 values of 59 and 37 K, respectively. Despite a stronger Auger recombination at the longer wavelength, the temperature performance of the 2.6 μm devices is also affected by the hole hetero-junction leakage as hole confinement energy is smaller in these QW devices [58]. For effective mid-infrared device design, the effects of Auger recombination and carrier (primarily hole) leakage must be considered.

In addition to laser diodes, reliable and efficient mid-infrared light-emitting diodes (LEDs) are of increasing interest for a variety of technologically important applications including environmental gas monitoring, industrial process control, non-invasive medical diagnosis and infrared spectroscopy [59]. However, to overcome Auger recombination and inter-valence band absorption in III–V narrow band gap materials is a real challenge. K. J. Cheetham et al. developed an attractive alternative approach to use the pentanary alloy GaInAsSbP as the presence of the fifth element allows an additional degree of freedom for tailoring the band structure, while keeping the lattice parameter constant [60]. As discussed earlier, two of the primary Auger recombination mechanisms in narrow band gap semiconductors are recombination of a conduction band electron with a heavy-hole which produces a hole in the spin-orbit-split-off-band (CHSH) and conduction electron to heavy-hole where another conduction electron is excited to higher energy (CHCC). These are known to be strongly temperature dependent with a cubic dependence on the carrier concentration [see (9.2) and (9.7)–(9.9)]. Increasing the spin-orbit split-off energy (Δ_{SO}) to be larger than the bandgap (E_g) should help suppress CHSH non-radiative Auger recombination which becomes increasingly important near resonance when $E_g \approx \Delta_{SO}$. Under this condition CHSH Auger recombination becomes resonant, as evident from (9.7) and (9.8) since $E_a \rightarrow 0$. In practical terms, if $\Delta_{SO} > E_g$ then the CHSH process will be suppressed. It was measured that $\Delta_{SO} = 0.455 \pm 0.010$ eV for the pentanary alloy used in the LEDs and that this value is approximately independent of temperature. Hence, since $E_g = 0.319$ eV, CHSH Auger recombination is expected to be negligible under ambient conditions in these LEDs.

Figure 9.24 shows the integrated spontaneous emission (electroluminescence) as a function of high hydrostatic pressure at 290 and 100 K of these LEDs. Since the application of pressure causes an increase in the band gap while maintaining an approximately constant Δ_{SO}, it can be used to investigate the behaviour of the Auger processes without changing the device temperature, much as discussed previously in this section for the Sb-based lasers. The spontaneous emission rate increases monotonically with applied pressure, whereas for the CHCC Auger process, increasing pressure causes a decrease in the Auger coefficient, and hence the light output from the LEDs increases. For the CHSH process if Δ_{SO} is initially larger than E_g, as here, pressure can bring the CHSH process into resonance as E_g increases towards Δ_{so} therefore causing the light output to decrease. Thus, by measuring the output emission intensity of GaInAsSbP LEDs at a fixed current versus pressure, one may observe the competing effects of these two processes as one can see in Fig. 9.24. Two devices shown had the same structure and nominally the same composition. Device 1 had an emitting area 750 μm in diameter while device 2 had a smaller diameter

of 300 μm. At 290 K, an increase in integrated emission is observed with increasing pressure with a decrease in gradient at higher pressure tending towards a maximum at ∼7.4 kbar. The measured integrated emission increased by a factor of 1.75 from atmospheric pressure to 6 kbar (device 1,290 K). The initial increase in radiative output with applied pressure was smaller than that of previous type II InAs LEDs emitting at 3.3 μm [61], which exhibited a 4-times increase from 0 to 10 kbar, indicating that Auger recombination is less of a problem in the pentanary GaInAsSbP LEDs. At 100 K, a stronger increase in intensity is observed which reaches a maximum at ∼3.6 kbar at low temperature. The majority of the increase in electroluminescence originates from a reduction in Auger recombination with increasing pressure, due to the increase in the activation energy of the CHCC Auger process as the band gap increases [60].

The existence of the intensity maximum is consistent with the onset of the CHSH process as the band gap becomes equal to the spin-orbit splitting. The difference in pressure at the maxima (7.4–3.6 kbar) corresponds to a difference in band gap change of ≈41 meV (using a measured coefficient of $E_g/dP = 10.7$ meV/kbar). The band gap increases by 45 meV with cooling down from 290 to 100 K. This value is approximately equal to the observed difference in the band gap energies at the intensity maxima as shown in Fig. 9.24. At room temperature, with increasing pressure, the intensity initially increases due to the decrease in the CHCC Auger process. However, as E_g approaches Δ_{SO} the CHSH process becomes significant causing the intensity to decrease. This provides strong evidence that the CHSH Auger process has been suppressed at atmospheric pressure in pentanary LEDs. These findings highlight the possible advantages of GaInAsSbP alloys for band-structure engineering of higher efficiency mid-infrared emitters.

9.4.2 Short-Wavelength Quantum Cascade Lasers

A semiconductor quantum cascade laser (QCL) is a unipolar device where one type of carrier is utilized to create the population inversion and to generate stimulated emission. Normally, it is electrons and the laser structure requires a complicated and careful design of the conduction band profile to provide effective carrier injection and recombination in the active region. Due to the unipolar nature of QCLs they do not suffer from non-radiative loss due to Auger recombination. For inter-band lasers it is challenging to move to longer wavelength beyond 2.5 μm due to fundamental loss processes, such as Auger recombination, in narrow band gap semiconductors. In strong contrast, for QCLs photons are emitted due to electron transitions between sub-bands in a QW. This leads to the requirement of a large conduction band offset between the active QW and barriers. Hence it is more challenging to cover the shorter wavelength range below 3–3.5 μm [62]. Another important factor, which may affect the performance of these devices, is the position of the indirect X- and L-valleys of the conduction band. A quantum cascade laser should be carefully designed to maximise the separation between the top lasing level and X- or L-states to minimise

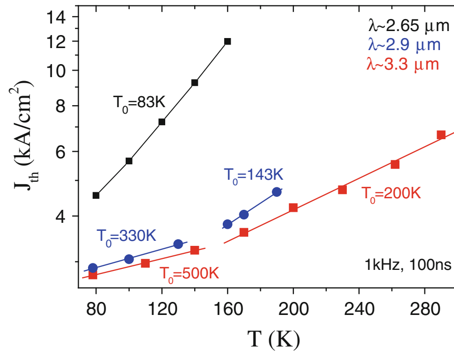

Fig. 9.25 Pulsed threshold current density (J_{th}) versus temperature in three different InAs/AlSb based QCLs emitting at 2.62, 2.9 and 3.3 μm

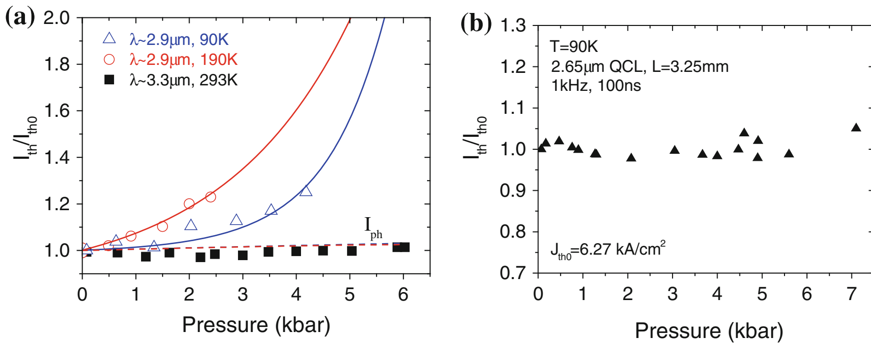

Fig. 9.26 Normalised pressure dependencies of the threshold current to its value at atmospheric pressure (I_{th0}) for three different InAs/AlSb QCLs: **a** 3.3 μm QCL at 293 K, 2.9 μm QCL at 90 and 190 K; **b** 2.65 μm QCL at 90 K

inter-valley carrier leakage, which is normally the main reason of limited performance of short-wavelength QCLs [62–65].

The InAs/AlSb material system is attractive for the development of short wavelength QCLs with lasing wavelength less than 3 μm due to the high conduction band offset of 2.1 eV and the large Γ-L separation of 0.73 eV in InAs. Studies of InAs-based QCLs under high hydrostatic pressure showed that their operation is not affected by carrier leakage into the L-valley in InAs in lasers emitting at wavelengths above 3 μm [64]. Figure 9.25 shows the temperature dependence of the threshold current density in three different InAs/AlSb based QCLs [66]. One can see that the threshold current density increases and the characteristic temperature decreases with decreasing emission wavelength. These observations indicate that a temperature sensitive loss process in these lasers is more important at shorter wavelengths, which is in agreement with the model of indirect carrier leakage into the L minimum of the conduction band, since the shorter wavelength devices have a smaller Γ-L separation [64, 66].

Figure 9.26 shows the pressure dependence of threshold current (I_{th}) at different temperatures for three such QC lasers with different lasing wavelengths. It is assumed that the total threshold current is formed by two components: the current due to inter-subband longitudinal optical phonon scattering (I_{ph}) and current loss due to the leakage into the L-valleys. The current component related to radiative transitions is very small in QCLs due to its longer lifetime and may be neglected in this analysis. The dashed line for I_{ph} in Fig. 9.26a shows that this current path is pressure insensitive [64]. The theoretical pressure variation of the leakage current can be derived using the temperature dependence of the leakage current at threshold which may be calculated from (9.14):

$$I^L_{leak}(T) = I_{0leak} \exp\left(-\frac{E_a}{kT}\right), \tag{9.14}$$

where I_{0leak} is a constant, k is the Boltzmann constant, and E_a is the activation energy of the leakage process, which is equal to the energy separation between the Fermi level (assumed to be at the upper lasing level) and L minimum of the InAs quantum well. Using (9.14) the following expression can be written:

$$I^L_{leak}(P) \propto \exp\left(-\left(\frac{dE_L}{dP} - \frac{dE_\Gamma}{dP}\right)\frac{P}{kT}\right), \tag{9.15}$$

where P is pressure value, dE_L/dP and dE_Γ/dP are pressure coefficients of the direct Γ and indirect L band gaps in the InAs quantum wells. We assume here that $\Delta E_a/kT = \frac{dE_a}{dP}\frac{P}{kT}$ (as $\Delta P \approx P$) and $dE_a = dE_L - dE_\Gamma$.

One can see from Fig. 9.26a that for the 3.3 μm QC laser, carrier leakage into the L-valleys is negligible even at RT. The threshold current in this case is dominated by phonon scattering intersubband relaxation with a very weak pressure dependence due to a small pressure dependence of the phonon energy. In contrast, the measured threshold current of the 2.9 μm device increases considerably with pressure indicating leakage into the L-valley. This effect becomes more pronounced with increasing temperature (see results for 90 and 190 K in Fig. 9.26a) in accordance with (9.15). To quantify values of the carrier leakage in 2.9 μm QCLs the experimental points in Fig. 9.26a were fitted taking into account that:

$$\frac{I_{th}}{I_0} = (1-x)\cdot\frac{I_{ph}}{I_{ph0}} + x\cdot\frac{I^L_{leak}}{I^L_{leak0}}, \tag{9.16}$$

where I_0, I_{ph0}, and I^L_{leak0} are the threshold current, phonon scattering current and leakage current at atmospheric pressure, respectively; x is a fraction of I_0 due to leakage into the L-minima at atmospheric pressure. The lines in Fig. 9.26a fit the experimental results well with x value of 0.006 and 0.130 at 90 and 190 K, respectively, showing that the loss of current due to L-leakage increases from 0.6 % of I_{th} at 90 K up to 13 % of I_{th} at 190 K. By applying pressure the leakage current increases

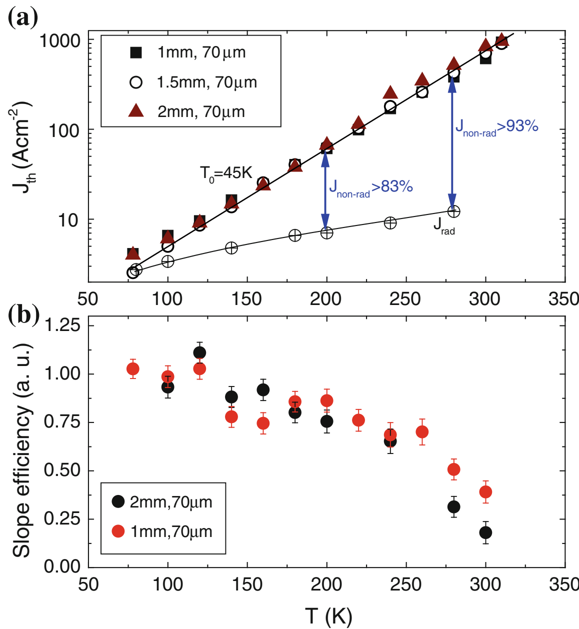

Fig. 9.27 Temperature dependence of J_{th} (**a**) with a $T_0 = 45$ K for three InAs/GaInSb "W"-lasers with the indicated cavity lengths. Radiative part J_{rad} of J_{th} of 1.5 mm device versus T is also plotted. Numbers show losses due to non-radiative recombination. Temperature dependence of the slope efficiency (**b**). All measurements carried out with 500 ns, 10 kHz pulses to avoid self-heating effects

up to 29 % of I_{th} at 2.4 kbar at 190 K and up to 20 % of I_{th} at 4.2 kbar at 90 K. Using absolute values of the leakage current determined for the 2.9 µm device from the fit at 90 and 190 K, together with (9.14) it was estimated that $E_a \approx 48$ meV, which is in reasonable agreement with the expected value [64].

Using these results, theoretically it was suggested that the L-valley leakage in InAs-based QCLs could be weakened by increasing the AlSb barrier thickness. This has the effect of reduced coupling the QWs thereby increasing the splitting to the L-minima [62]. The high pressure results presented in Fig. 9.26b are for devices with reduced QW overlap and show no evidence of L-valley leakage in shorter wavelength devices at 90 K (unlike the 2.9 µm QCLs). This is consistent with the expected lower overlap between Γ and L states in the active region.

9.4.3 Inter-Band Type II "W"-Cascade Lasers

Recently, mid-infrared lasers for 3–6 µm spectral range utilizing a mixed approach combining inter-band transitions for stimulated emission and cascade design for increased efficiency and output power have been developed [67]. The active region consists of pairs of InAs quantum wells with a GaInSb layer between them and

sandwiched with AlSb barriers, thus, forming a "W"-shaped type II band structure [67, 68]. Lasing operation around 3.7–3.9 μm has been achieved in continuous wave (CW) regime in a wide temperature range up to 380 K [67].

The temperature performance and physical properties of 5-stage "W" inter-band cascade casers (ICLs) emitting at 4.1 μm at room temperature were investigated by measuring the lasing and spontaneous emission properties as a function of temperature and high hydrostatic pressure [69]. The experimental results presented in Fig. 9.27a show that at room temperature more than 90 % of the threshold current in these devices is due to non-radiative loss process(es). While the measured threshold current density is extremely low at cryogenic temperatures, with a value of 4 A/cm^2 at 78 K, it increases exponentially to more than 700 A/cm^2 at room temperature. Even at the lowest temperatures the temperature dependence of J_{th} is strongly super-linear, unlike conventional inter-band quantum well lasers, due to contributions of non-radiative current paths to the threshold current, which are significant compared to the very small radiative current even at very low temperatures. The relatively high temperature sensitivity of these devices with a characteristic temperature, T_0, of 45 K is attributed to the large non-radiative current contribution [69]. The significant loss of current due to non-radiative recombination coupled with observed non-pinned carrier density above threshold [69] may be responsible for a strong temperature decrease of the external differential efficiency plotted in Fig. 9.27b which decreased by a factor of 3 with increasing temperature from 80 to 300 K. The lasing photon energy increased with pressure having the coefficient 8.7 meV/kbar [69]. Figure 9.28 shows that the threshold current density decreases as the band gap increases with application of pressure, which is related to a decrease of the Auger recombination rate [68, 69]. However, at 100 K the threshold current density initially decreases with increasing pressure reaching a minimum around 6 kbar and then increases at higher pressures ($E_g > 0.4$ eV).

Recent studies of ICLs lasers with improved design showed a significantly reduced non-radiative current contribution (60–65 % of J_{th} at 300 K) [70]. With the application of hydrostatic pressure the threshold current showed increasing behaviour even at 200 K. Theoretical modelling indicates that this may be caused by increased influence of the radiative component and a decreased overlap between electron and hole wave functions with increasing pressure [70].

9.5 Physical Properties of Devices Emitting in Visible Range of the Spectrum

9.5.1 AlGaInP Lasers

Unlike the fabrication of light-emitting devices in the blue-green spectral range which experience many difficulties with growth of wide-band gap semiconductor structures, AlGaInP lasers utilise the advantages of well-established InP-based growth

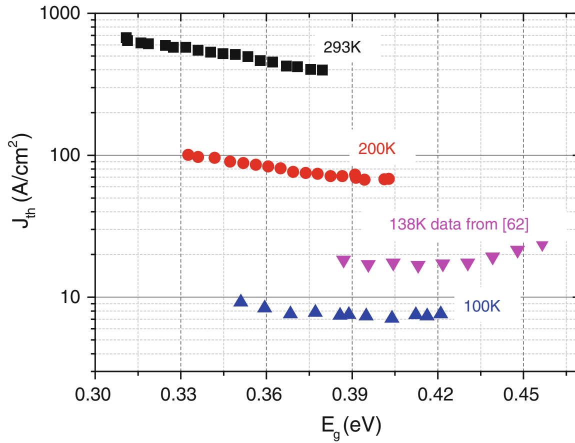

Fig. 9.28 Pressure-induced band gap dependence of J_{th} at 100, 200 and 293 K in InAs/GaInSb "W"-lasers measured in pulsed mode with 500 ns, 10 kHz pulses

and device fabrication technologies. These lasers are now widely used in different applications including CD/DVD drives, printers, computer mice, laser projection systems, etc. This material system can also be used in vertical cavity surface emitting lasers (VCSELs) for short haul communication networks using relatively inexpensive plastic optical fibre which have a minimum loss at 650 nm.

Temperature dependent studies of GaInP/AlGaInP/AlGaAs QW separate confinement heterostructure (SCH) lasers [71] showed an ideal behaviour at temperatures below 230 K where the threshold current consists mainly of radiative current as shown in Fig. 9.29a. Above 230 K electrons have sufficient energy to populate the higher lying indirect X states (around 300 meV above the QW Γ-minimum) and there is a rapid increase in I_{th} due to the onset of a leakage current (I_{Leak}) described with (9.14). There are parallels here with the short wavelength QCLs discussed in Sect. 9.4, however, in this case the leakage occurs via the X-valleys of the conduction band). For high quality material where non-radiative recombination through defects can be neglected, the total threshold current is equal to the sum of these two current paths:

$$I_{th} = I_{Rad} + I_{Leak}. \tag{9.17}$$

From the Fig. 9.29a, using (9.14) and (9.17), the activation energy of the leakage process was found to be 267 ± 21 meV. This is slightly lower than the Γ_{QW}–$X_{barrier/SCH}$ splitting of 300 meV because at lasing threshold the Fermi-level lies some energy above the electron QW confined state [71]. From the figure it is estimated that at room temperature I_{Rad} accounts for about 80 % of I_{th} with the remaining 20 % being due to I_{Leak}. With increasing temperature up to 350 K the I_{Leak}/I_{th} ratio ($K = I_{Leak}/I_{th}$) increases swiftly to $K > 70\,\%$ of I_{th} explaining the rapid

increase in I_{th} observed at elevated temperatures. These results were also confirmed using high hydrostatic measurements as shown in Fig. 9.30, which showed a strong increase of the threshold current with increasing pressure [71] (I_{th} increased more than 3 times with increasing pressure up to 6.5 kbar at room temperature). The analysis of the temperature variation of the characteristic temperature, T_0, (see (9.11)) is presented in Fig. 9.29b. Initially, T_0 follows the ideal $T_0^{red} = T$ line, in a similar way to the interband infrared devices discussed in Sect. 9.2. However, above approximately 200 K, it rapidly falls towards the $T_0^{Leak} = \frac{T}{(^{E_a}/_{kT})}$ curve.

Results from the pressure measurements strongly reinforce the findings from the temperature dependence experiments. Figure 9.30 shows the measured variation of I_{th} with pressure (normalised at atmospheric pressure). The relation in (9.6) for the radiative current and that in (9.10) for the leakage current were used to generate a set of theoretical curves representing different calculated values of K at ambient conditions. The value of dE_a/dP is equal to the rate at which the Γ and X minima of the conduction band approach each other, thus $dE_a/dP = -(dE_\Gamma/dP - dE_X/dP)$. It is assumed that $\mathrm{dE}_\Gamma/dP = dE_{las}/\mathrm{dP}$ and found to be 7.2 meV/kbar whereas $dE_X/dP = -2.1\mathrm{meV/kbar}$ [71]. From this, using (9.17), the relative importance of I_{Leak} at ambient conditions can be determined by taking the appropriate balance between $I_{Leak}(P)$ and $I_{Rad}(P)$. The experimental data increase sharply with pressure and fall close to the 20 % ($K = 0.2$) curve, in good agreement with the previous estimate obtained from the temperature dependence measurements. In the inset of Fig. 9.30 the extracted variation of K (expressed as a percentage) as a function of emission photon energy tuned by pressure is plotted. Interestingly, the contribution of carrier leakage to I_{th} rises from 20 % for $E_{las} = 1.846$ eV (672 nm) to ~70 % for $E_{las} = 1.892$ eV (655 nm) in these devices. Thus, in terms of the relative importance of carrier leakage, a 655 nm laser at RT is identical to a 672 nm device operating at 80 °C [71]. This illustrates the fundamental difficulty in producing temperature stable lasers at shorter wavelengths, where the close proximity of the indirect X minima results in carrier leakage becoming the dominant process limiting device performance.

Such analysis of non-radiative processes in more simple structures like Fabry-Perot lasers above is often very useful for analysis and optimization of more complicated devices. For example, the described data helped to understand the temperature performance of AlGaInP-based VCSELs where temperature induced detuning of the gain peak and cavity mode also has a significant impact on their performance, further details of which can be found in [72, 73].

9.5.2 Efficiency Droop Problem in InGaN Light Emitting Devices

Wide-bandgap GaN (also with added Al or/and In) based material systems are very interesting as they cover an important region of the electromagnetic spectrum from

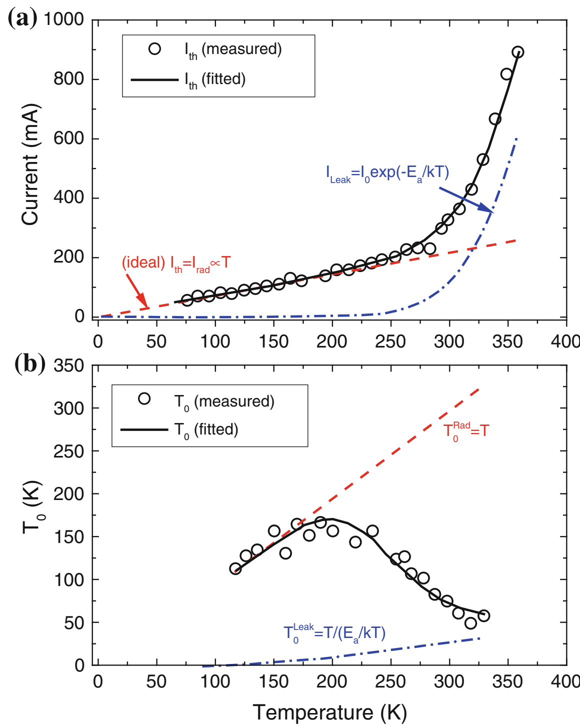

Fig. 9.29 **a** Temperature dependence of I_{th} (*open circles*). Up to T = 230 K ideal behaviour where $I_{th} = I_{Rad} \propto T$ was observed. Above this temperature I_{th} increases rapidly due to carrier leakage. **b** The corresponding variation of T_0 with temperature (*circles*). Initially, T_0 follows the ideal $T_0^{red} = T$ line until approximately 200 K, where it rapidly falls towards the T_0^{Leak} curve

the UV to the green. The many applications of such materials include energy efficient solid state lighting, large and portable displays, back lighting in different applications, traffic signal and auto-motive applications [74]. The improved performance of InGaN-based laser diodes over the recent years has led to commercially viable applications such as blu-ray players and pico-projection systems. However, continuing improvements in the performance of the InGaN emitters are required in order to achieve the market targets for InGaN-based light emitting devices. A phenomenon which limits the performance of the devices is the widely discussed issue of the efficiency droop [1, 75, 76] mentioned earlier in the introduction to this chapter in Fig. 9.1. It is observed that the efficiency peaks at alow current density and reduces as there is a further increase of injection. Despite intense investigations there is little agreement on the non-radiative recombination process which causes the efficiency droop. Auger recombination, carrier leakage and a defect-related loss mechanism are being under consideration and discussion [77]. In this section we briefly discuss the use of high hydrostatic pressure technique to understand the physical origin of

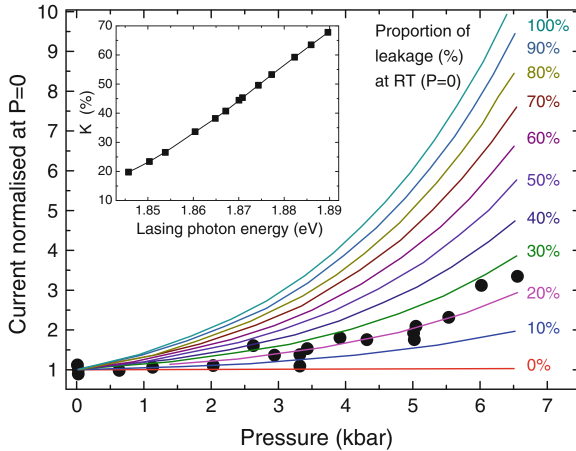

Fig. 9.30 The measured I_{th} (P) at RT (*closed circles*). The curves indicate the expected variation of I_{th} for different contributions of I_{Leak} to I_{th} (different K-values). The curve for which I_{Leak} forms ≈20 % of I_{th} at RT gives the best fit to experiment. The *inset* shows the extracted variation of $K = I_{Leak}/I_{th}$ as a function of lasing photon energy. K clearly increases strongly as the device moves towards shorter wavelengths (higher photon energies)

the observed efficiency limitations. More details can be found elsewhere [77, 78]. A recent review of different droop causing mechanisms in InGaN is given in [79].

The temperature and pressure dependencies of efficiency droop of commercially available InGaN multiple quantum well blue (∼460 nm) and green (∼515 nm) LEDs are presented in Fig. 9.31. Figure 9.31a shows a reduction in the efficiency over the entire current range with increasing temperature with an overall reduced rate of the efficiency drop at higher currents. Such behaviour is not consistent with a carrier leakage or Auger recombination being important as the carrier leakage and Auger recombination rates both increase with increasing temperature and current. If it was the case, the efficiency drop rate would increase with increasing temperature (a stronger droop effect). On the other hand, a defect-related cause of droop may explain these observations as in this case there will be a stronger influence of temperature on the efficiency at lower currents than at high current (see effect of An term in (9.3)).

The pressure coefficients of the band gap were found to be smaller in both InGaN LEDs (2.14 ± 0.01 meV/kbar for the blue LED and 1.21 ± 0.02 meV/kbar for the green LED) compared with the pressure coefficients of the band gap in binary materials GaN (4.0 meV/kbar) and InN (2.7 meV/kbar) [80], which is partly caused by increasing piezoelectric fields with increasing pressure [77]. Figure 9.31b shows that increasing pressure causes a reduced efficiency over the entire current range whilst there is little effect on the overall “droop” behaviour in both blue and green LEDs.

An increase in band gap as shown above reduces the direct Auger recombination rate (the same is true for the phonon-assisted Auger recombination rate). The increase

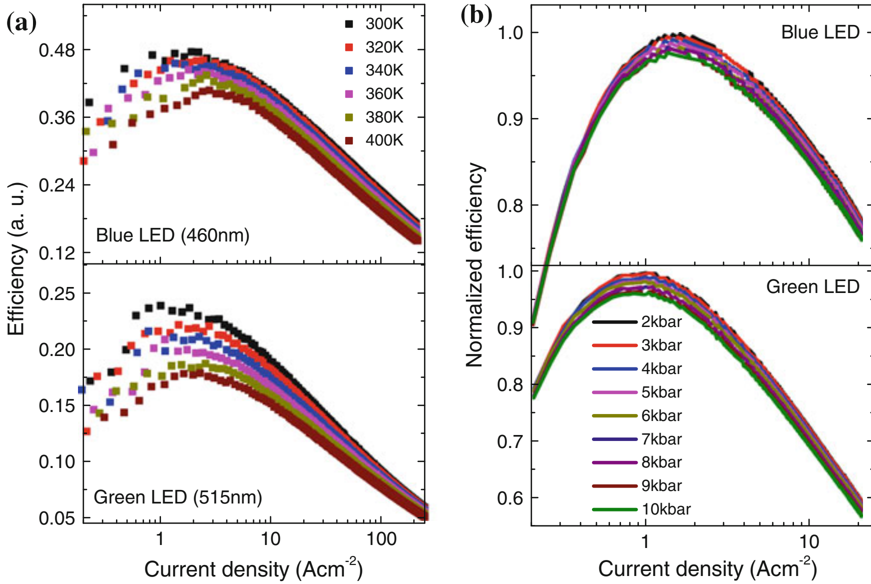

Fig. 9.31 **a** Dependence of the efficiency on the injection current density at different temperatures for *blue* and *green* LEDs. Pulsed measurements (2 μs with 2 % duty cycle) were used to minimize the Joule heating effects. **b** The normalized efficiency as a function of current at different pressure values for the same devices (CW measurements at low current <20 mA)

of the internal field strength is also expected to provide a further reduction in the Auger recombination rate due to reduced electron and hole wave function overlap. Thus, Auger recombination it unlikely to be the dominant droop-causing mechanism as the droop effect would be smaller with increasing pressure [77, 78]. Similarly, heterojunction carrier leakage cannot fully explain the observed data as it should be pressure dependent due to variation of piezoelectric fields in QWs with application of hydrostatic pressure.

The overall small reduction of the efficiency over the entire current range with increasing pressure may be explained by the reduced radiative recombination rate with increasing pressure caused by the reduction of overlap of the electron and hole wave function with increasing internal field [77, 78]. The relatively small effect of pressure on efficiency droop is also consistent with a defect-related efficiency loss mechanism as the defect recombination rate is approximately pressure insensitive because pressure has no significant impact on defect energy states. These remain preliminary results and this topic remains one of the most important areas of semiconductor optoelectronic device research where sophisticated experimental techniques, such as those discussed in these chapter, will play an important role in future device development.

9.6 Conclusions

The chapter considered optical and electronic properties in different semiconductor materials and structures used for light-emitting applications (lasers and LEDs) operating in a wide spectral range from visible to mid-infrared. The main recombination and loss mechanisms in semiconductor devices are discussed and experimental methodologies for measuring and analysis of these mechanisms are demonstrated. This provides an important step for effective device design and optimization. Near infra-red (IR) quantum well (QW) lasers are discussed considering several new approaches to overcome fundamental performance issues. Different approaches for the longer wavelength (mid-IR) semiconductor devices are reviewed showing specific of different materials and some interesting engineering solutions to reach these long wavelengths and at the same time to suppress unwanted efficiency loss processes. Semiconductor lasers and LEDs for the visible spectral range are demonstrated and most actual issues related to the device performance are discussed.

Acknowledgments The authors gratefully appreciate the input of various researchers at the University of Surrey over many years to this activity. In particular, we acknowledge Professor Alf Adams, FRS, for his pioneering activities in developing several of the characterisation techniques discussed here. We also gratefully appreciate the funding that has made this work possible, obtained principally from the Engineering and Physical Sciences Research Council (EPSRC), UK, the Technology Strategy Board (TSB), UK, the European Union Framework programmes and the large number of companies and university groups with whom it has been a pleasure to collaborate with.

References

1. J. Piprek, Unified model for the GaN LED efficiency droop. Proc. SPIE **7939**, 793916 (2011)
2. S.J. Sweeney, Novel experimental techniques for semiconductor laser characterisation and optimisation. Phys. Scr. 152 (2004). doi:10.1088/0031-8949/2004/T114/038
3. A.F. Phillips, S.J. Sweeney, A.R. Adams, P.J.A. Thijs, The temperature dependence of 1.3- and 1.5-μm compressively strained InGaAs(P) MQW semiconductor lasers. IEEE J. Sel. Top. Quantum Electron. **5**(3), 401 (1999)
4. A.R. Adams, M. Silver, J. Allam, *High Pressure in Semiconductor Physics II, Semiconductors and Semimetals*, vol. 55 (Academic Press, London, 1998)
5. A.R. Adams, *Properties of Gallium Arsenide*, 2nd edn. IEE EMIS. Datareviews Series No. 2 (INSPEC, London, 1990), p. 119
6. S.H. Wei, A. Zunger, Predicted band-gap pressure coefficients of all diamond and zinc-blende semiconductors: chemical trends. Phys. Rev. B **60**, 5404 (1999)
7. A. Rogalski, Z. Orman, Band-to-band recombination in InAs1-xSbx. Infrared Phys. **25**, 551–560 (1985)
8. B.J. Gunney et al., High pressure photoconductivity techniques and their application to semiconductor alloy systems. High Press. Res. Ind. **2**, 481 (1982)
9. S.R. Jin, S.J. Sweeney, S. Tomic', A.R. Adams, H. Riechert, Unusual increase of the Auger recombination current in 1.3 μm GaInNAs quantum-well lasers under high pressure. Appl. Phys. Lett. **82**, 2335 (2003)
10. A.R. Adams, Strained layer quantum well lasers. IEEE J. Sel. Top. Quantum Electron. **17**(5), 1364 (2011)

11. E.J. Flynn, Carrier-density-independent radiative constant in 1.3 μm buried heterostructure lasers. J. Appl. Phys. **78**, 4046 (1995)
12. S.J. Sweeney, A.R. Adams, M. Silver, E.P. O'Reilly, J.R. Watling, A.B. Walker, P.J.A. Thijs, Dependence of threshold current on QW position and on pressure in 1.5 μm InGaAs(P) lasers. Phys. Status Solidi B **211**, 525 (1999)
13. S.J. Sweeney, D. McConville, N.F. Masse, R.-X. Bouyssou, A.R. Adams, C.N. Ahmad, C. Hanke, Temperature and pressure dependence of recombination processes in 1.5 μm InGaAlAs/InP-based quantum well lasers. Phys. Status Solidi B **241**(14), 3391 (2004)
14. S.A. Sayid, I.P. Marko, P.J. Cannard, X. Chen, L.J. Rivers, I.F. Lealman, S.J. Sweeney, Thermal characteristics of 1.55-μm InGaAlAs quantum well buried heterostructure lasers. IEEE J. Quant. Electron **46**(5), 700 (2010)
15. S.J. Sweeney, T. Higashi, A. Andreev, A.R. Adams, T. Uchida, T. Fujii, Superior temperature performance of 1.3μm AlGaInAs-based semiconductor lasers investigated at high pressure and low temperature. Phys. Status Solidi B **223**, 573 (2001)
16. S.R. Jin, S.J. Sweeney, C.N. Ahmad, A.R. Adams, B.N. Murdin, Radiative and Auger recombination in 1.3μm InGaAsP and 1.5μm InGaAs quantum-well lasers measured under high pressure at low and room temperatures. Appl. Phys. Lett. **85**, 357 (2004). doi:10.1063/1.1772871
17. W. Shan, W. Walukiewicz, J.W. Ager, E.E. Haller, J.F. Geisz, D.J. Friedman, J.M. Olson, S.R. Kurtz, Band anticrossing in GaInNA's alloys. Phys. Rev. Lett. **82**, 1221–1224 (1999)
18. B.N. Murdin, A.R. Adams, P. Murzyn, C.R. Pidgeon, I.V. Bradley, J.-P.R. Wells, Y.H. Matsuda, N. Miura, T. Burke, A.D. Johnson, Band anticrossing in dilute InNSb. Appl. Phys. Lett. **81**, 256–258 (2002)
19. S. Tomic', E.P. O'Reilly, R. Fehse, S.J. Sweeney, A.R. Adams, A.D. Andreev, S.A. Choulis, T.J.C. Hosea, H. Riechert, Theoretical and experimental analysis of 1.3-μm InGaAsN/GaAs lasers. IEEE J. Sel. Top. Quantum Electron. **9**(5), 1228 (2003)
20. C.A. Broderick, M. Usman, S.J. Sweeney, E.P. O'Reilly, Band engineering in dilute nitride and bismide semiconductor lasers. Semicond. Sci. Technol. **27**, 094011 (2012)
21. S.R. Jin, S.J. Sweeney, S. Tomic', A.R. Adams, H. Riechert, High-pressure studies of recombination mechanisms in 1.3-μm GaInNAs quantum-well lasers. IEEE J. Sel. Top. Quantum Electron. **9**(5), 1196 (2003)
22. R. Fehse, S. Tomic, A.R. Adams, S.J. Sweeney, E.P. O'Reilly, A. Andreev, H. Riechert, A quantitative study of radiative, Auger, and defect related recombination processes in 1.3-μm GaInNAs-based quantum-well lasers. IEEE J. Sel. Top. Quantum Electron. **8**(4), 801 (2002)
23. R. Fehse, Recombination processes in GaInNAs/GaAs semiconductor quantum well lasers. Department of Physics, University of Surrey, June 2003
24. Y. Arakawa, H. Sakaki, Multidimensional quantum-well laser and temperature dependence of its threshold current. Appl. Phys. Lett, **40**(11), 939 (1982)
25. N.N. Ledentsov, V.A. Shchukin, M. Grundmann, N. Kirstaedter, J. Böhrer, O. Schmidt, D. Bimberg, V.M. Ustinov, A.Y. Egorov, A.E. Zhukov, P.S. Kop'ev, S.V. Zaitsev, N.Y. Gordeev, Direct formation of vertically coupled quantum dots in Stranski-Krastanow growth. Phys. Rev. B **54**, 8743 (1996)
26. R. Fehse, I. Marko, A.R. Adams, Long wavelength lasers on GaAs substrates. IEEE Proc. Circ. Devices Syst. **150**, 521 (2003)
27. I.P. Marko, A.R. Adams, S.J. Sweeney, I.R. Sellers, D.J. Mowbray, M.S. Skolnick, H.Y. Liu, K.M. Groom, Recombination and loss mechanism in low-threshold InAs/GaAs 1.3 μm quantum-dot lasers. IEEE J. Sel. Top. Quantum Electron. **11**(5), 1041 (2005)
28. I.P. Marko, N.F. Massé, S.J. Sweeney, A.D. Andreev, A.R. Adams, N. Hatori, M. Sugawara, Carrier transport and recombination in p-doped and intrinsic 1.3 μm InAs/GaAs quantum-dot lasers. Appl. Phys. Lett. **87**(21), 211114 (2005)
29. M. Ishida, M. Matsuda, Y. Tanaka, K. Takada, M. Ekawa, T. Yamamoto, T. Kageyama, M. Yamaguchi, K. Nishi, M. Sugawara, Y. Arakawa, Temperature-stable 25-Gbps direct-modulation in 1.3-μm InAs/GaAs quantum dot lasers. CLEO Technical Digest OSA 2012, CM1I.2
30. M.V. Maximov, V.M. Ustinov, A.E. Zhukov, N.V. Kryzhanovskaya, A.S. Payusov, I.I. Novikov, N.Y. Gordeev, Y.M. Shernyakov, I. Krestnikov, D. Livshits, S. Mikhrin, A. Kovsh, A 1.33 μm

InAs/GaAs quantum dot laser with a 46 cm? 1 modal gain. Semicond. Sci. Technol. **23**, 105004 (2008)
31. C. Gilfert, V. Ivanov, N. Oehl, M. Yacob, J.P. Reithmaier, High gain 1.55μm diode lasers based on InAs quantum dot like active regions. Appl. Phys. Lett. **98**, 201102 (2011). doi:10.1063/1.3590727
32. I.P. Marko, A.D. Andreev, A.R. Adams, R. Krebs, J.P. Reithmaier, A. Forchel, The role of Auger recombination in InAs 1.3 μm quantum dot lasers investigated using high hydrostatic pressure. IEEE J. Sel. Top. Quantum Electron. **9**(5), 1300 (2003)
33. L.V. Asryan, R.A. Suris, Temperature dependence of the threshold current density of a quantum dot laser. IEEE J. Quantum Electron **34**(5), 841 (1998)
34. M. Grundmann, O. Stier, S. Bognar, C. Ribbat, F. Heinrichsdorff, D. Bimberg, Optical properties of self-organized quantum dots: modeling and experiments. Phys. Status Solidi A **178**, 255 (2000)
35. D.R. Matthews, H.D. Summers, P.M. Smowton, M. Hopkinson, Experimental investigation of the effect of wetting-layer states on the gain-current characteristic of quantum-dot lasers. Appl. Phys. Lett. **81**(6), 4904 (2002)
36. O.B. Shchekin, G. Park, D.L. Huffaker, D.G. Deppe, Discrete energy level separation and the threshold temperature dependence of quantum dot lasers. Appl. Phys. Lett. **77**, 466 (2000)
37. I.P. Marko, A.R. Adams, S.J. Sweeney, N.F. Masse, R. Krebs, J.P. Reithmaier, A. Forchel, D.J. Mowbray, M.S. Skolnick, H.Y. Liu, K.M. Groom, N. Hatori, M. Sugawara, Band gap dependence of the recombination processes in InAs/GaAs quantum dots studied using hydrostatic pressure. Phys. Status Solidi B **244**(1), 82 (2007)
38. M.T. Crowley, I.P. Marko, N.F. Masse, A.D. Andreev, S. Tomic, S.J. Sweeney, E.P. O'Reilly, A.R. Adams, The importance of recombination via excited states in InAs/GaAs 1.3 μm quantum-dot lasers. IEEE J. Sel. Top. Quantum Electron. **15**(3), 799–807 (2009)
39. N.F. Masse, E. Homeyer, I.P. Marko, A.R. Adams, S.J. Sweeney, O. Dehaese, R. Piron, F. Grillot, S. Loualiche, Temperature and pressure dependence of the recombination processes in 1.5μm InAs/InP (311)B quantum dot lasers. Appl. Phys. Lett. **91**(13), 131113 (2007)
40. S.A. Sayid, I.P. Marko, S.J. Sweeney, P. Barrios, P.J. Poole, Efficiency limiting processes in 1.55μm InAs/InP-based quantum dots lasers. Appl. Phys. Lett. **97**, 161104 (2010). doi:10.1063/1.3504253
41. I.P. Marko, A.D. Andreev, S.J. Sweeney, A.R. Adams, R. Schwertberger, A. Somers, J.P. Reithmaier, A. Forchel, Recombination mechanisms in InAs/InP quantum dash lasers studied using high hydrostatic pressure. Phys. Status Solidi B **241**(14), 3427–3431 (2004)
42. K. Alberi, J. Wu, W. Walukiewicz, K.M. Yu, O.D. Dubon, S.P. Watkins, C.X. Wang, X. Liu, Y.-J. Cho, J. Furdyna, Valence-band anticrossing in mismatched III-V semiconductor alloys. Phys. Rev. B **75**, 045203 (2007)
43. Z. Batool, K. Hild, T.J.C. Hosea, X.F. Lu, T. Tiedje, S.J. Sweeney, The electronic band structure of GaBiAs/GaAs layers: Influence of strain and band anti-crossing. J. Appl. Phys. **111**, 113108 (2012)
44. J.P. Petropoulos, Y. Zhong, J.M.O. Zide, Optical and electrical characterization of InGaBiAs for use as a new mid-infrared optoelectronic material. Appl. Phys. Lett. **99**, 031110 (2011)
45. K. Alberi, O.D. Dubon, W. Walukiewicz, K.M. Yu, K. Bertulis, A. Krotkus, Valence band anticrossing in GaBixAs1–x. Appl. Phys. Lett. **91**, 051909 (2007)
46. Y. Zhang, A. Mascarenhas, L.W. Wang, Similar and dissimilar aspects of III-V semiconductors containing Bi versus N. Phys. Rev. B **71**, 155201 (2005)
47. K. O'Brien, S.J. Sweeney, A.R. Adams, B.N. Murdin, A. Salhi, Y. Rouillard, A. Joullie, Recombination processes in midinfrared InGaAsSb diode lasers emitting at 2.37 μm. Appl. Phys. Lett. **89**, 051104 (2006)
48. S.J. Sweeney, Patent WO 2010/149978 (2010)
49. S.J. Sweeney, SPIE Photonics West 2010, paper [7616-11] (2010)
50. K.J. Cheetham et al., Direct evidence for suppression of Auger recombination in GaInAsSbP/InAs mid-infrared light-emitting diodes. Appl. Phys. Lett. **99**, 141110 (2011)
51. S.J. Sweeney, S.R. Jin, J. Appl. Phys. **113**, 043110 (2013). doi:10.1063/1.4789624

52. N. Hossain, I.P. Marko, S.R. Jin, K. Hild, S.J. Sweeney, R.B. Lewis, D.A. Beaton, T. Tiedje, Recombination mechanisms and band alignment of GaAs1–xBix/GaAs light emitting diodes. Appl. Phys. Lett. **100**, 051105 (2012)
53. P. Ludewig, N. Knaub, W. Stolz, K. Volz, MOVPE growth of Ga(AsBi)/GaAs multi quantum well structures. J. Cryst. Growth **370**, 186 (2013)
54. P. Ludewig, N. Knaub, N. Hossain, S. Reinhard, L. Nattermann, I.P. Marko, S.R. Jin, K. Hild, S. Chatterjee, W. Stolz, S.J. Sweeney, K. Volz, Appl. Phys. Lett. **102**, 242115 (2013)
55. S. Sweeney et al., Appl. Phys. Lett. (2013) (Submitted)
56. K. O'Brien, S.J. Sweeney, A.R. Adams, S.R. Jin, C.N. Ahmad, B.N. Murdin, A. Salhi, Y. Rouillard, A. Joullié, Carrier recombination mechanisms in mid-infrared GaInAsSb quantum well lasers. Phys. Status Solidi B **244**(1), 203–207 (2007). doi:10.1002/pssb.200672573
57. K. O'Brien, S.J. Sweeney, A.R. Adams, B.N. Murdin, A. Salhi, Y. Rouillard, A. Joullié, Recombination processes in midinfraredInGaAsSb diode lasers emitting at 2.37 μm. Appl. Phys. Lett. **89**, 051104 (2006)
58. B.A. Ikyo, I.P. Marko, K. Hild, A.R. Adams, S. Arafin, M.-C.Amann, S.S. Sweeney, Effect of hole leakage and Auger recombination on the temperature sensitivity of GaInAsSb/GaSb mid-infrared lasers. CLEO/Europe-IQEC 2013, Munich, May 2013, CB-10.6 THU. J. Appl. Phys. (2013) (Submitted)
59. A. Krier, M. Yin, V. Smirnov, P. Batty, P.J. Carrington, V. Solovev, V. Sherstnev, The development of room temperature LEDs and lasers for the mid-infrared spectral range. Phys. Status Solidi A **205**, 129 (2008)
60. K.J. Cheetham, A. Krier, I.P. Marko, A. Aldukhayel, S.J. Sweeney, Direct evidence for suppression of Auger recombination in GaInAsSbP/InAs mid-infrared light-emitting diodes. Appl. Phys. Lett. **99**, 141110 (2011). doi:10.1063/1.3646910
61. S.A. Choulis, A. Andreev, M. Merrick, A.R. Adams, B.N. Murdin, A. Krier, V.V. Sherstnev, High-pressure measurements of mid-infrared electroluminescence from InAs light-emitting diodes at 3.3 μm. Appl. Phys. Lett. **82**, 1149 (2003)
62. O. Cathabard, R. Teissier, J. Devenson, J.C. Moreno, A.N. Baranov, Quantum cascade lasers emitting near 2.6 μm. Appl. Phys. Lett. **96**, 141110 (2010)
63. S.R. Jin, C.N. Ahmad, S.J. Sweeney, A.R. Adams, B.N. Murdin, H. Page, X. Marcadet, C. Sirtori, S. Tomić, Appl. Phys. Lett. **89**, 221105 (2006)
64. I.P. Marko, A.R. Adams, S.J. Sweeney, R. Teissier, A.N. Baranov, S. Tomić, Evidence of carrier leakage into the L-valley in InAs-based quantum cascade lasers under high hydrostatic pressure. Phys. Status Solidi B **246**(3), 512–515 (2009)
65. A. Aldukhayel, S.R. Jin, I.P. Marko, S.Y. Zhang, D.G. Revin, J.W. Cockburn, S.J. Sweeney, Investigations of carrier scattering into L-valley in λ=3.5 μm InGaAs/AlAs(Sb) quantum cascade lasers using high hydrostatic pressure. Phys. Status Solidi B **250**(4), 693–697 (2013)
66. I.P. Marko, A.M. Aldukhayel, A.R. Adams, S.J. Sweeney, R. Teissier, A.N. Baranov, S. Tomić, Physical properties of short wavelength 2.6μm InAs/AlSb-based quantum cascade lasers, in *IEEE Conference Digest—IEEE International Semiconductor Laser Conference*, pp. 95–96 (2010)
67. I. Vurgaftman, W.W. Bewley, C.L. Canedy, C.S. Kim, M. Kim, C.D. Merritt, J. Abell, J.R. Lindle, J.R. Meyer, Rebalancing of internally generated carriers for mid-infrared interband cascade lasers with very low power consumption. Nat. Commun. **2**, 585 (2011). doi:10.1038/ncomms1595
68. K. O'Brien, S.J. Sweeney, A.R. Adams, S.R. Jin, C.N. Ahmad, B.N. Murdin, C.L. Canedy, I. Vurgaftman, J.R. Meyer, High pressure studies of mid-infrared type-II "W" diode lasers at cryogenic temperatures. Phys. Status Solidi B **244**(1), 224–228 (2007)
69. B.A. Ikyo, I.P. Marko, A.R. Adams, S.J. Sweeney, C.L. Canedy, I. Vurgaftman, C.S. Kim, M. Kim, W.W. Bewley, J.R. Meyer, Temperature dependence of 4.1μm mid-infrared type II "w" interband cascade lasers. Appl. Phys. Lett. **99**, 021102 (2011)
70. Z.L. Bushell et al. (in preparation)
71. S.J. Sweeney, G. Knowles, T.E. Sale, A.R. Adams, Quantifying the effect of indirect carrier leakage on visible Al(GaInP) lasers using high pressures and low temperatures. Phys. Status Solidi B **223**(2), 567–572 (2001)

72. S.J. Sweeney, G. Knowles, T.E. Sale, Evaluating the continuous-wave performance of AlGaInP-based red (667nm) vertical-cavity surface-emitting lasers using low-temperature and highpressure techniques. Appl. Phys. Lett. **78**, 865 (2001). doi:10.1063/1.1342049
73. G. Knowles, S.J. Sweeney, T. Sale, Influence of leakage and gain-cavity alignment on the performance of AI(GalnP) visible vertical-cavity surface emitting lasers. IEE Proc-Optoelectron. **148**, 55–59 (2001)
74. J.K. Kim, E.F. Schubert, Transcending the replacement paradigm of solid-state lighting. Opt. Express **16**, 21835–21842 (2008)
75. H. Kim, M.F. Schubert, Q. Dai, J.K. Kim, E.F. Schubert, J. Piprek, Y. Park, Origin of efficiency droop in GaN-based light-emitting diodes. Appl. Phys. Lett. **91**, 183507 (2007)
76. J. Piprek, Efficiency droop in nitride-based light-emitting diodes. Phys. Status Solidi A **207**, 2217–2225 (2010)
77. B.G. Crutchley, I.P. Marko, J. Pal, M.A. Migliorato, S.J. Sweeney, Optical properties of InGaN-based LEDs investigated using high hydrostatic pressure dependent techniques. Phys. Status Solidi B **250**(4), 698–702 (2013). doi:10.1002/pssb.201200514
78. B.G. Crutchley et al. The temperature and pressure dependence of efficiency droop in blue-green InGaN LEDs (2013) (in preparation)
79. G. Verzellesi, D. Saguatti, M. Meneghini, F. Bertazzi, M. Goano, G. Meneghesso, E. Zanoni, Efficiency droop in InGaN/GaN blue light-emitting diodes: physical mechanisms and remedies. J. Appl. Phys. **114**, 071101 (2013). doi:10.1063/1.4816434
80. I. Gorczyca, T. Suski, A. Kamińska, G. Staszczak, H.P.D. Schenk, N.E. Christensen, A. Svane, In-clustering effects in InAlN and InGaN revealed by high pressure studies. Phys. Status Solidi A **207**, 1369–1371 (2010)

Chapter 10
Scintillation Detectors of Radiation: Excitations at High Densities and Strong Gradients

R. T. Williams, J. Q. Grim, Qi Li, K. B. Ucer, G. A. Bizarri and A. Burger

Abstract This chapter discusses the electron-hole recombination processes that occur in the high excitation densities and strong radial gradients of particle tracks in scintillator detectors of radiation. The particle tracks are commonly those of high-energy Compton- or photo-electrons produced in energy-resolving gamma-ray detectors, but could also include those of heavier charged particles such as those following interaction with neutrons. In energy-resolving radiation detectors, intrinsic proportionality of light yield to gamma ray energy or electron energy is an important concern. This chapter gives special emphasis to understanding the physical basis for nonproportionality, while reviewing recent results on fundamental physics of nonlinear quenching, cooling and capture of hot electrons, co-evolving free-carrier and exciton populations, and diffusion in the dense and highly structured excitation landscape of electron tracks. Particular attention is paid to short-pulse laser experiments at Wake Forest University giving data and insight on the above phenomena complementary to more traditional scintillator experiments using gamma-ray or electron excitation. Numerical modeling of diffusion, nonlinear quenching (NLQ), exciton formation, and linear capture processes serves to test and establish links between the laser excitation and particle excitation measurements.

R. T. Williams (✉) · J. Q. Grim · Q. Li · K. B. Ucer
Department of Physics, Wake Forest University, Winston-Salem, NC 27106, USA
e-mail: williams@wfu.edu

G. A. Bizarri
Lawrence Berkeley National Laboratory, Berkeley, CA 94720, USA

A. Burger
Department of Physics, Fisk University, Nashville, TN 37208, USA

J. Singh and R. T. Williams (eds.), *Excitonic and Photonic Processes in Materials*,
Springer Series in Materials Science 203, DOI: 10.1007/978-981-287-131-2_10,
© Springer Science+Business Media Singapore 2015

10.1 Introduction

Consistent with the common definition of "scintillate," a detector of radiation using scintillator materials should flash or sparkle when a charged particle passes through or is completely stopped within. The charged particles may themselves be incident or they may be launched within the material by Compton scattering or photoelectric absorption of gamma rays, for example, or by neutron reactions such as knock-on acceleration of protons or neutron capture followed by nuclear emissions. Properly chosen and prepared, a scintillator may be sensitive to particular types of radiation and capable of discriminating neutron from gamma events, for example. When pixelated and paired to determine line-of-flight and/or when fast enough to use time-of-flight, scintillators can reconstruct the location and shape of the emitting source. When chosen and prepared to have good *proportionality*, the scintillator will light up with a photon number proportional to the energy of a totally stopped gamma ray or particle. When combined with a photomultiplier or avalanche photodiode capable of registering the emitted number of photons, the proportional scintillator becomes an energy-resolving spectrometer. It may, for example, distinguish chemical elements and isotopes by neutron activation gamma spectroscopy in security scanning of shipping containers and logging of oil wells, identify bio-active radio-tracers in medical molecular imaging, perform "electromagnetic calorimetry" of particle collisions in high energy physics, or resolve gamma energies along with line of flight in astronomical gamma-ray telescopes. In all of these applications, better scintillator proportionality results in better spectrometer energy resolution. Intrinsic proportionality, what determines it, and how it can be improved by selecting or engineering scintillator materials, is the main focus of this chapter.

A perfect scintillator could be defined as a material in which every electron-hole pair excited by stopping of the incident particle recombines radiatively with creation of a photon collected by the detector. One would describe such a scintillator as perfectly proportional with unity light yield. In seeking the causes of less-than-perfect proportionality, we will be looking at losses that vary as a function of particle energy or that vary stochastically during stopping of particles of the same energy. Loss of a constant fraction of the excitations (a quenching loss rate that is linear in excitation density) would not in itself cause a lack of intrinsic proportionality between emitted photon number and particle energy, but rather a scaling of the proportional response. On the other hand, loss rate or radiative rate that varies as some nonlinear power of excitation density can be expected to result in nonproportionality, because excitation density varies both systematically and stochastically from beginning to end of an electron track. Therefore, we are prompted from the outset to look at coupled nonlinear rate equations governing the important populations of excited states on the relevant time scales to understand the origins of nonproportionality of light yield.

The most fundamental and earliest-appearing of the excited state populations produced by ionizing radiation are free carriers denoted by density n_e (electrons/cm^3) and n_h (holes/cm^3). Rate equations that contain the main terms governing the

densities of free electrons and holes on the tens of picoseconds timescale that we shall see is most relevant to NLQ can be written as

$$\frac{dn_e}{dt} = G + D_e \nabla^2 n_e - A_e n_e - B n_e n_h - K_{3ehe} n_e n_h n_e - K_{3ehh} n_e n_h n_h \tag{10.1a}$$

and

$$\frac{dn_h}{dt} = G + D_h \nabla^2 n_h - A_h n_h - B n_e n_h - K_{3ehe} n_e n_h n_e - K_{3ehh} n_e n_h n_h \tag{10.1b}$$

We will discuss below each of the terms contained within the above equations.

The generation rate G (cm^3/s) will be regarded in the following analyses as instantaneous, an approximation that simply establishes the starting densities of free electrons and holes. Although the time for electronic stopping of a 662 keV electron over its total trajectory of $\sim$1 mm takes about 5 ps, a main goal of this chapter is to calculate *local light yield* in small regions of dimension $\leq$100 nm along a track. The primary particle passes through such a region in $<$1 fs, and the individual electron scattering processes are even faster. For example, *Vasil'ev* calculated electron, hole, and exciton distributions indicating that the primary step in deposition of energy at a given location is nearly complete as early as 0.04 fs in BaF_2 [1]. Equations (10.1a) and (10.1b) will also be used to analyze laser experiments in the course of this chapter. The laser pulse width used was 500 fs, which may be reasonably treated as instantaneous for most of the phenomena analyzed. It will be noted that by the approximation of instantaneous G, we are excluding (re-)generation of free carriers by release from traps including ionization of excitons. Eventual recombination of de-trapped carriers is important for evolution of the full light pulse lasting nanoseconds, microseconds, or longer. However, our working hypothesis, supported by results of the experiments and analyses to be discussed, is that NLQ is already completed or at least pre-determined during an early stage of track evolution lasting approximately ten picoseconds. By the phrase "pre-determined", we mean that the spatial distribution of excitons and trapped charges that eventually emit light will have been established by diffusion, possible quenching recombination, and trapping of hot and thermalized carriers in roughly ten picoseconds. De-trapping, or tunneling leading to eventual radiative recombination proceeds from this starting distribution, governed by additional coupled rate equations operating on generally slower time scales. The slower processes have been treated in a number of publications dealing with pulse shape, afterglow, and scaling of the total light yield [2–4].

We believe that the data and analyses presented in this chapter show that nonlinearity and hence nonproportionality of scintillator response can be modeled and predicted in the main part by considering the free-carrier rate (10.1a) and (10.1b) and a coupled exciton equation to be introduced shortly. If this treatment is found to be deficient for analyzing experiments specifically on nonlinear light yield versus electron or photon excitation, then additional terms or coupled equations should be considered.

The tracks of energetic electrons represent strong radial concentration gradients of electron and hole densities. It will be shown in this chapter that near the end

of a track, electron and hole densities of the order of 10^{20} e-h/cm^3 are initially confined in a radius of about 3 nm. Thus, in electron tracks, diffusion represented by the second term in (10.1a) and (10.1b) can be a substantial contributor to the rate of change of carrier density. Diffusion out of the densely populated track core competes with NLQ in (10.1a) and (10.2), with consequence for the light yield and its proportionality. Furthermore, differences in the diffusion rates when $D_e \neq D_h$ can produce significant charge separation, which influences the outcomes of (10.1a) and (10.1b) through the 2nd and 3rd order terms. In materials with $D_e \gg D_h$ (and *vice versa*), the interaction of the separated charge distributions with the electric fields between them and with traps produces a rising light yield versus increasing excitation density proceeding from beginning to end of a track. Charge separation can protect against nonlinear dipole-dipole or free-carrier Auger quenching simply by disrupting the formation of dipoles and spatially separating the carriers. It will be shown that charge separation followed by recombination under influence of the collective electric field of a "line charge" of self-trapped holes is one of two distinct physical mechanisms that can produce the "halide hump" in electron energy response. The charge separation mechanism depends essentially on having a spatial gradient, unequal D_e and D_h, and competing linear quenching together. The other mechanism that can contribute to the hump in electron energy response is the phenomenon discussed previously by Murray and Meyer [5], as well as by Payne et al. in terms of *Onsager* radius [6]. In a discussion later in this chapter, it will be shown that the *Murray–Meyer/Payne-Onsager* mechanism is based on carrier density without regard to spatial gradient and relative electron and hole diffusion rates. The contributions of these two distinct mechanisms to trends producing humps (discussed in detail later) in various experiments can be experimentally distinguished in some cases and will be explored in Sects. 10.4 and 10.5 of the present chapter.

The coefficients A_e, A_h (s^{-1}) in (10.1a) and (10.1b) represent sums over linear rate constants for capture of electrons and holes on various traps. We will find it useful later on to divide the traps into deep ones (K_{1e}) and shallow ones (S_{1e}), so that $A_e = K_{1e} + S_{1e}$. The deep traps are those that will hold trapped carriers at room temperature longer than the time discriminator window. They may or may not ultimately contribute to afterglow, but in either case, such deep traps represent quenching of the useful scintillator light, with some aggregate capture rate constant that we designate K_{1e} for the case of electron trapping. Shallow traps are similarly defined as those that release their captured carriers within the timing discriminator window. The actual release and possible light emission with overall probability ρ occurs on a slower time scale than the dominant processes represented in (10.1a) and (10.1b). But at the time of initial capture with rate constant S_{1e}, it can already be specified that energy is being *stored* at the rate $\rho S_{1e} n$ and will appear eventually as useful scintillation light. The total electron capture rate constants for deep and shallow traps can be plugged into (10.1a) as $K_{1e} + S_{1e} = A_e$ (and similarly for holes).

The need to distinguish between quenching and storage capture rates arises from our stated choice to neglect explicit solution of the slow de-trapping equations in order to concentrate on a simpler set of (10.1a)–(10.2) operating on the time scale

of NLQ. This allows a reasonably simple framework for modeling nonlinearities, where the rates of quenching or storage on traps can be introduced by K_{1e}, S_{1e} and analogous linear rate constants for holes and excitons.

It will be shown in this chapter that A_e, A_h, and indeed *all* of the rate constants and diffusion coefficients in (10.1a) and (10.1b) should be regarded as time dependent functions of electron temperature. Energy deposition from stopping of high-energy electrons creates hot carriers that take a finite time to cool, depending on optical phonon frequency, ranging from a few tenths of a picosecond in oxides and fluorides up to several picoseconds in iodides and bromides [2]. We shall discuss experimental evidence indicating that the hot electron thermalization time is comparable to the main NLQ time in scintillators. The interplay between these two early phenomena is a strong determiner of scintillator proportionality and light yield. To be explicit, the diffusion coefficients and rate constants in (10.1a) and (10.1b) have the following dependences, where T_e is electron temperature as a function of time t: $D_e(T_e(t)), A_e(T_e(t)), B(T_e(t)), K_3(T_e(t))$, and similarly for holes. This dependence on electron temperature and time will be shown to have importance in governing spatial distributions achieved before the start of thermalized diffusion, commencement of electron trapping and exciton formation, and effective termination of Auger quenching.

The term that is second order in carrier density ($-Bn_en_h$) is the bimolecular carrier pairing rate or exciton formation rate. The identical term with a positive sign is the quadratic coupling term from the free-carrier rate equations into the exciton rate equation defined in (10.2) below. Light emission occurs via the exciton rate equation (10.2) and/or trapped-exciton equations not shown, rather than directly from the free-carrier equations (10.1a) and (10.1b). As alluded to earlier, both absolute carrier density and charge separation due to diffusion affect the bimolecular pairing term. Hot electron temperature controls capture probability including electron capture on holes, as noted above. This will be put in quantitative experimental and theoretical terms in the discussions of Sect. 10.4.

A coupled rate equation for the density N of excitons per unit volume can be written as

$$\frac{dN}{dt} = +Bn^2 + D_{exc}\nabla^2 n - C_1 N - K_2 N^2 \qquad (10.2)$$

The source term $+Bn^2$ couples excitons from the bimolecular pairing term of the free-carrier equation. Here, we use the approximation $n \approx n_e \approx n_h$ valid for strongly excited and/or intrinsic materials in which electron and hole mobilities are similar. The term $-C_1 N$ is the sum of linear radiative and nonradiative rates of exciton decay. Similar to the discussion of linear rates of carrier capture following (10.1a) and (10.1b), we represent $C_1 = R_1 + K_1$, where R_1 is the rate of radiative decay of intrinsic excitons, and K_1 is the total linear quenching rate due both to capture on defects and thermal quenching.

The last term, $-K_2 N^2$, is the dipole-dipole quenching term. Dipole-dipole annihilation is a case of Förster transfer from one excited dipole to another excited

dipole rather than to a ground-state dipole, resulting in annihilation of the first dipole and possibly ionization of the doubly-excited second one as well. The dipole-dipole transfer rate w_{dd} depends on the separation distance as

$$w_{dd}\left(r_{sep}\right) = \tau_R^{-1}\left(\frac{R_{dd}}{r_{sep}}\right)^6 \tag{10.3}$$

where τ_R is the radiative lifetime of the excited state and R_{dd} is the Förster transfer radius depending on the overlap of emission and absorption bands [7, 8]. The 2nd order rate constant K_2 appearing in (10.2) can be expressed in these terms for immobile species [7, 8] as

$$K_2(t) = \frac{2}{3}\pi^{3/2} R_{dd}^3 (t\tau_r)^{-1/2} \tag{10.4}$$

In summary of this introduction, predicting light yield versus excitation density or initial electron energy as a function of measured material parameters requires one to know at least the following:

(a) the rate constants from 1st through 3rd order in the applicable (10.1a)–(10.2)
(b) the fraction of the excitations that are free carriers (approximately the parameter η_{eh} introduced by Payne et al. [6, 9]) and the fraction that are excitons
(c) the initial value of the local track radius, and
(d) the subsequent time dependence of the track radius due to both hot and thermalized electronic diffusion.

In the next four sections of this chapter, we will describe a recent experiment that provides quantitative values for the parameters named in (*a*)–(*c*). We will discuss how to calculate (*d*) from available thermalized carrier diffusion data supplemented by calculated hot carrier diffusion parameters. Then, we will examine to what extent these parameters are sufficient for predicting the shape of the light yield curve versus initial excitation density and initial electron energy. That will suggest whether an effective design rule is within reach. In the final section of this chapter, the shape of such a rule will be outlined.

10.2 Measurements of Light Yield Functions

We have spoken of light yield as a function of initial electron energy and as a function of excitation density. To characterize nonproportionality and experimentally extract the values of some of the parameters needed to predict proportionality in a systematic way, measurements of normalized light yield as functions of several relevant parameters are important, as described below:

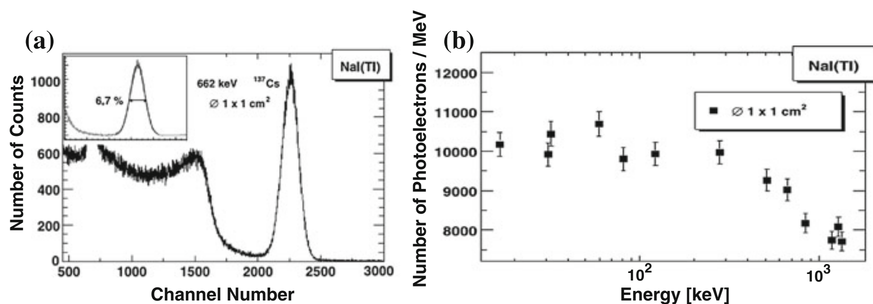

Fig. 10.1 **a** The pulse height spectrum of two NaI:Tl samples of different size excited by a Cs^{137} γ-source. The inset shows the width of the photopeak. Reprinted with permission [10]. **b** Gamma energy resolution of NaI:Tl. Reprinted with permission [10]

10.2.1 Gamma Photopeak Resolution

The energy resolution of a gamma scintillation detector is characterized by measuring the pulse height spectrum. In this method, the scintillator material is packaged with a photodetector such as a photomultiplier tube or a solid-state photodiode to form the detection unit. The detector is then exposed to gamma rays of a specified energy, such as the 662 keV emission of Cs^{137}. The amplitude of the resultant signal is a measure of the deposited gamma energy. A multichannel pulse height analyzer sorts these pulses into different channel numbers. Figure 10.1a shows the pulse height spectrum of NaI:Tl excited using a Cs^{137} source [10]. The rightmost peak is called the photopeak and corresponds to deposition of the full gamma ray energy in the detector. The photopeak is superimposed on a background extending to lower channel numbers due, e.g., to incomplete capture of the energy of Compton-scattered gamma rays or secondary X-rays from core hole decay. The ratio of the FWHM of the peak, ΔE, to the gamma energy, E, at which it occurs is defined as the resolution of the detector at that energy. NaI:Tl is capable of a 6.7 % resolution at 662 keV. One can repeat the same measurement using different gamma sources and plot the observed resolutions as a function of the exciting gamma energy.

The experimental resolution of a scintillator detector, $R = \Delta E/E$ defined above, is comprised of three contributions to the broadening, added as squares:

$$\left(\frac{\Delta E}{E}\right)^2 = R^2 = R_{stat}^2 + R_{intr}^2 + R_{det}^2 \qquad (10.5)$$

Here, R_{stat} is from the statistical broadening related to the number of photoelectrons. The transfer resolution, R_{det}, comes from spatial inhomogeneity in the detector and light collection assembly. Finally, R_{intr} is the intrinsic resolution of the scintillator crystal, related to its nonproportionality as well as inhomogeneity of the particular sample. Nonproportionality of response can be measured in several ways as seen in the sections below.

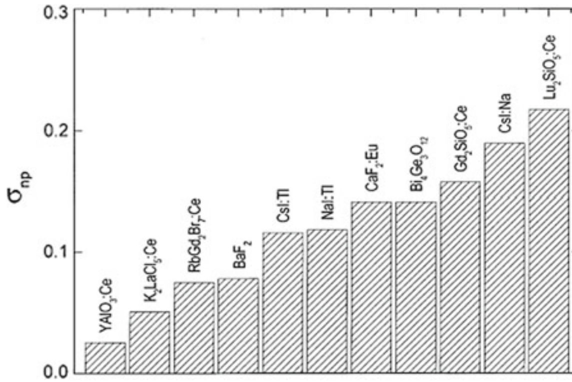

Fig. 10.2 Gamma response non-proportionality parameter σ_{NP} in various scintillator materials. Reprinted with permission [11]

10.2.2 Gamma Energy Response

One can characterize proportionality directly by measuring the light yield as a function of gamma energy using a series of gamma emitters such as Cs^{137}, Na^{22} and Am^{241}. The light yield may be plotted as a percentage of the light yield at a reference gamma energy, generally the 662 keV line of Cs^{137}. A proportional detector would have a flat response. Figure 10.1b shows the gamma energy response of NaI:Tl stated directly in photons/MeV rather than normalizing [10].

Dorenbos has defined a quantity σ_{NP} as a measure of non-proportionality [11].

$$\sigma_{NP} = \sqrt{\frac{1}{N}\sum_{i=1}^{N}\left(1 - \frac{Y_i}{Y_{662keV}}\right)^2} \tag{10.6}$$

where Y_i is the measured light yield at the ith sampled gamma energy. Figure 10.2 plots this nonproportionality parameter σ_{NP} forseveral scintillator materials [11].

This σ_{NP} parameter has been useful in classifying and modeling broad trends in scintillator nonproportionality versus material parameters such as effective mass ratio [12] and related ambipolar diffusion coefficient [13] discussed in Sect. 10.8.

10.2.3 Electron Energy Response

The first interaction of a gamma ray with matter (such as a scintillator) produces one or more high energy electron launched within the interior of the scintillator. Gamma interaction with valence electrons produces Compton electrons and scattered gamma rays. Gamma interaction with deeply bound electrons deposits energy in

core holes that can launch Auger electrons or X-rays upon relaxation. The balance of the absorbed gamma energy is deposited in a photoelectron directly excited to high kinetic energy. Each of these gamma or X-ray interaction channels provides an experimental means to measure "electron energy response," i.e., scintillation light yield as a function of the initial energy of a high energy electron.

10.2.3.1 Compton Coincidence Light Yield

The Compton coincidence technique, originally developed by Valentine and Rooney [14], consists of a scintillator crystal coupled to a PMT and irradiated by a collimated ^{137}Cs source. A high-purity germanium (HPGe) detector set at an e.g. angle θ relative to the incident gamma beam measured the energies of gamma rays scattered within its acceptance angle. From this information, the energy of the Compton electron launched within the sample could be determined. A high-throughput version of this technique called the Scintillation Light Yield Nonproportionality Characterization Instrument (SLYNCI) [15] uses five HPGe detectors arranged around the sample. Using a 662 keV ^{137}Cs source, Compton electron energies between 3.5 and 460 keV can be verified by detection angle and energies of the scattered gamma rays,thus defining the useful energy range of this technique [15]. Figure 10.3 shows electron energy response curves from the SLYNCI experiment for NaI:Tl, SrI_2:Eu, $LaBr_3$:Ce, and LSO:Ce. The vertical axis corresponds to the integrated light yield from the entire electron track starting from a given energy, and the horizontal axis is the initial kinetic energy of the Compton scattered electron. Ideal electron response of a scintillator would be a flat line, and deviations from that ideal are found to fall into two broad behaviors. The behavior common to all materials is a roll-off of light yield at the lowest electron energies.A second category of behavior is a rise in light yield going from the highest to lower initial energy, before ultimately giving way to the universal roll-off. This causes an apparent "hump" in response, seen in Fig. 10.3 for SrI_2 and NaI:Tl. The two categories of electron energy response were discussed in terms of an empirical model by Payne et al. [9, 16], and will be re-examined with respect to the roles of carrier mobilities, self-trapping of holes and hot electron thermalization rates in Sect. 10.8 of this chapter.

10.2.3.2 K-dip Analysis of Photon Energy Response

K-dip spectroscopy, a synchrotron radiation method developed by Khodyuk and Dorenbos et al. [17] extends the low-energy range of initial electron energy to as low as 80 eV for measuring electron energy response, compared with the $\sim$3.5 keV lower limit achievable by Compton coincidence. This *K*-dip technique analyzes the light yield resulting from *K*-shell excitation while tuning synchrotron radiation relative to the *K* edge energy. Scintillator response to an X-ray that has excited a *K*-shell electron is the sum of light produced by stopping of the *K*-shell photoelectron and by the relaxation of the hole in the *K*-shell, the latter of which is called the

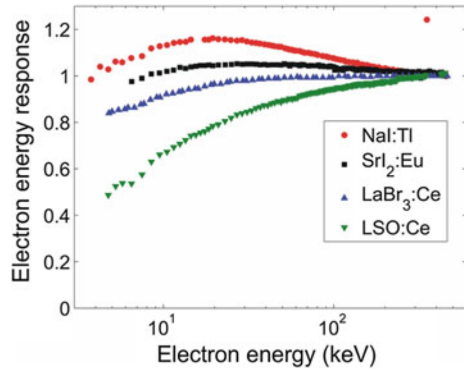

Fig. 10.3 Electron energy response curves from the SLYNCI experiment for NaI:Tl (*points*), SrI_2:Eu (*squares*), $LaBr_3$:Ce (*triangles*), and LSO:Ce (*inverted triangles*). Reprinted with permission

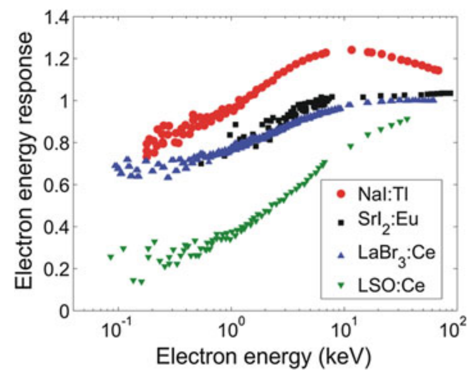

Fig. 10.4 Electron energy response curves from K-dip spectroscopy for NaI:Tl (*points*), SrI_2:Eu (*squares*), $LaBr_3$:Ce (*triangles*), and LSO:Ce (*invertedtriangles*). Reprinted with permission

K-cascade. The *K*-cascade is assumed to be independent of the initial X-ray energy. Therefore, subtracting the *K*-cascade response from the total X-ray response yields the *K*-shell photoelectron response as a function of starting electron energy. Figure 10.4 shows results from *K*-dip spectroscopy for the same four materials as shown in Fig. 10.3.

10.2.4 X-ray Photon Energy Response

In this technique, light yield is measured versus incident X-ray photon energy without performing the K-dip analysis. What we have called gamma energy response and X-ray photon energy response are formally the same, except discrete radioisotope gamma sources are typically used to measure the former while tunable synchrotron radiation is used to measure the latter. The light yield is customarily normalized to the yield for 662 keV gamma rays. *Khodyuk* and *Dorenbos* have measured photon energy response for 33 scintillators [18], four of which are shown in Fig. 10.5. Up to three signatures of nonproportionality may be exhibited by such data. There is a

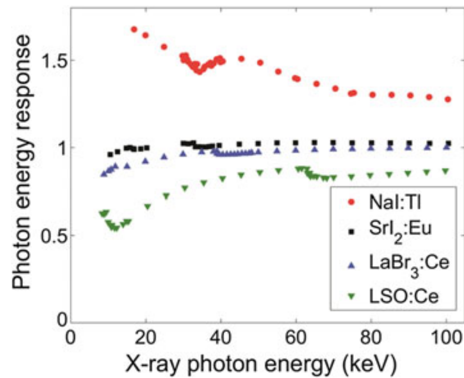

Fig. 10.5 X-ray photon energy response for NaI:Tl (*points*), SrI_2:Eu (*squares*), $LaBr_3$:Ce (*triangles*), and LSO:Ce (*inverted triangles*). Reprinted with permission

broad roll-off of light yield at low enough X-ray photon energy, suggestive of the trend seen in electron energy response (Fig. 10.4). The light yield of NaI:Tl rises before rolling off, producing an "alkali halide hump" similar to that seen in electron energy response. Superimposed on these broad trends are dips in light yield at the *K* and *L* edges of the constituent elements. These dips are associated with the low energy of the photoelectrons (and consequently the high densities of their secondary ionizations), as discussed under *K*-dip analysis immediately above. Similar to the electron energy response curves shown above, a flat photon energy response would correspond to a perfectly proportional material.

10.2.5 Ultraviolet Photon Density Response

Ultraviolet photons with energy somewhat above the band gap but still less than $2E_{gap}$ offer a certainty in determining excitation density because exactly one electron-hole pair is created per photon absorbed. In addition, the spatial distribution of absorption events is fairly uniform within the confines of the radial extent of the beam and the exponential absorption profile described by Beer's Law. Contrast this with the stochastic nature of carrier energies and densities produced in the tracks of high energy electrons, as well as the strong radial spatial gradients around a track. If we want to extract rate constants from experiments that are not themselves dominated by diffusion properties and wide mixtures of initial carrier energies, ultraviolet photons in the low interband range can be especially useful. In addition, by tuning the photon energy within the range $E_{gap} < h\nu < 2E_{gap}$, one can examine dependence of the quenching, recombination, and trapping processes on the initial carrier energies. Such measurements will be described in Sects. 10.3 and 10.4 and constitute the main body of new data that are used as input for the calculations and models to be discussed in this chapter. The data can be plotted as normalized light yield versus excitation density n_0, where n_0 is the absorbed photon density on the beam's central axis just under the entrance surface of the sample. The plots will be referenced by the photon

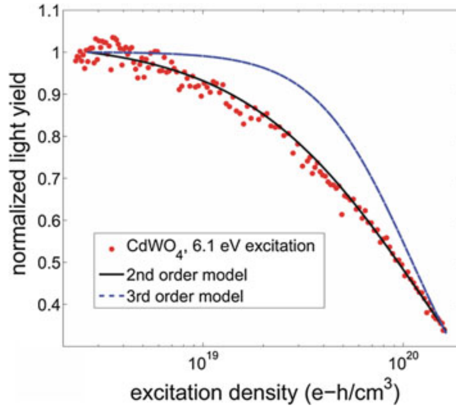

Fig. 10.6 Ultraviolet photon density response (PDR) of $CdWO_4$ for $h\nu - E_{gap}$ = 1.3 eV. Best attempts at fitting to 2nd and 3rd order quenching models, which yield values of the nonlinear rate constants K_2 or K_3 according to which fit is successful, are superimposed. In this case, the dependence is 2nd order with $K_2(t) = 3 \times 10^{-18}$ $t^{-1/2}$ cm^3 $s^{-1/2}$. The experimental method for measuring such data is described in the next section

energy used and by $h\nu - E_{gap}$, which is the excess kinetic energy shared by the two carriers created.

The example shown in Fig. 10.6 was measured in $CdWO_4$ with 6.1 eV laser photons. Best attempts at fitting to 2nd and 3rd order theories (described later), are superimposed, showing that only the 2nd order fit is successful in $CdWO_4$. The rate constant is measured to be $K_2(t) = 3 \times 10^{-18}$ $t^{-1/2}$ cm^3 $s^{-1/2}$. Carriers are excited up to 1.3 eV above the $CdWO_4$ band gap by 6.1 eV laser photons. The term *photon density response* (PDR) is short for "light yield versus absorbed photon density with photon number held constant", as shown in Fig. 10.6. We abbreviate to *photon density response* to maintain similarity to the shorthand names of the other light yield functional plots summarized above.

10.3 Measuring Photon Density Response by the "Interband z Scan" Technique

Nonlinear quenching rates in several wide gap materials useful for scintillator radiation detectors have previously been measured by time resolution of ultraviolet laser excited luminescence decay versus excitation density. Nikl et al. [19] studied dipole-dipole quenching kinetics of Ce^{3+} excited states in CeF_3 using gamma-ray and ultraviolet laser excitation. Kirm et al. [7], Nagirnyi et al. [20], and Lassner et al. [21] have studied the intrinsic excitonic scintillator $CdWO_4$, fitting decay time measurements versus excitation density to 2nd order quenching kinetics. We have conducted similar decay-time experiments on CsI, finding 2nd order quenching kinet-

ics in that case as well when exciting in the exciton spectrum or slightly above the band edge [22, 23]. The time-resolved measurements have also shown that in CsI:Tl, NaI:Tl [22], and LuAG:Ce [24], the NLQ occurs mainly in the population of host excitons, not among the Tl* or Ce* excited activators. Thus, determination of NLQ rate by decay time analysis may be applicable only to materials exhibiting reasonably bright luminescence of the host itself, whereas many scintillators depend on the activator ions for their bright emission. Therefore, we designed the experiments reported in this work to measure the variation of total light yield with excitation density, rather than having to resolve the decay time of the specific quenching population. Both methods are useful in complementary fashion where it is possible to apply them.

10.3.1 Experiment

The method we employ to measure PDR may be summarized as interband z-scan luminescence yield. Its similarity to z-scan measurements as commonly employed to study optical nonlinearities in materials transparent to the laser beam [25, 26] is that, in both cases, a Gaussian laser beam profile including the beam waist is translated longitudinally through the sample while acquiring data. Both applications make use of the fact that the total power of the laser beam remains constant throughout the scan. In absence of nonlinearities, the detected properties of transmitted (conventional z-scan) or absorbed and re-emitted (this work) optical signal should remain constant throughout the scan.

In the PDR experiments, the laser photon energy is above the fundamental absorption edge of the sample, so all incident energy after reflection is deposited and may then be re-emitted as luminescence unless quenched. The experimental setup is represented schematically in Fig. 10.7. The sample is placed in a highly reflective enclosure (integrating "sphere") formed by two parabolic mirrors with protected (300 nm SiO overcoated) aluminum films. The sample is oriented to reflect the ultraviolet laser beam back out through the entrance hole. Facing the sample at a 45° off-normal angle is a bi-alkali photomultiplier with a fused silica window. The 12-inch focal length S-1 silica lens is translated along the beam axis, thus moving the beam waist through the stationary sample surface, while the photomultiplier output is recorded with a boxcar averager. The luminescence signal is measured as a function of the distance of the beam waist behind ($z < 0$) and in front of ($z > 0$) the sample surface.

The optical beam is the 4th harmonic of an amplified femtosecond Ti:sapphire laser. The repetition rate is 10 Hz, and the duration of the amplified pulse is 0.5 ps. The 4th harmonic, generated in a BBO frequency doubler and re-doubler combination, is tunable in our experiment from 5.9 to 6.1 eV. Ultraviolet pulse energy is selectable in the range of 5–150 nJ with neutral density filters. Residual fundamental and 2nd harmonic wavelengths are removed before the experiment chamber by filters and a pair of fused quartz dispersing prisms in the incident beam. The beam

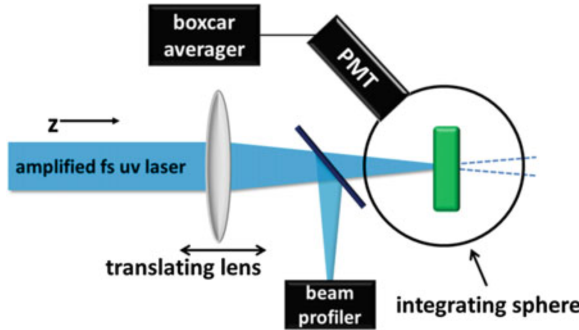

Fig. 10.7 Illustration of the experimental set-up used to measure photon density response, NLQ rate constants and kinetic order of quenching. A translating lens focuses a Gaussian beam that is absorbed by the sample. Luminescence photons are channeled into a photomultiplier

profile is measured with a Thorlabs BC106-UV CCD profiler with an integrated M^2 analysis system. M^2 is a beam quality factor modifying the Gaussian beam radius $w(z)$ expressed as the following function of distance z from the plane of the beam waist:

$$w(z) = w_{0M}\sqrt{1+\left(\frac{M^2\lambda z}{\pi w_{0M}^2}\right)^2}, \quad (10.7)$$

where w_{0M} is the beam waist radius, and λ is the wavelength.

From the on-axis laser fluence F_0, photon energy $h\nu$, and interband absorption coefficient α the initial excitation density distribution is expressed as

$$n\,(r, z, \zeta, t=0) = \frac{F_0\alpha}{h\nu}e^{-2r^2/w^2(z)-\alpha\zeta} = n_0e^{-2r^2/w^2(z)-\alpha\zeta}, \quad (10.8)$$

where r is the transverse radial coordinate on the sample surface and z is the position along the beam axis intersected by the sample surface, relative to $z = 0$ at the Gaussian beam waist. The $1/e^2$ radius of the irradiance profile on the sample surface at position z is $w(z)$ given in (10.7). Distance into the sample relative to the entrance face is represented by ζ. Measurement of the transverse and longitudinal beam profile allows converting z to a specific pulse fluence profile on the sample face. Knowledge of the optical absorption coefficient, α, at the excitation wavelength then allows plotting light yield versus on-axis excitation density, n_0.

10.3.2 *Pure 2nd Order Quenching in BGO Versus 3rd Order in SrI$_2$*

Figure 10.6 illustrated photon density response of $CdWO_4$ plotted as normalized Light Yield versus on-axis excitation density n_0 (eh/cm^3) on a semi-log scale. This

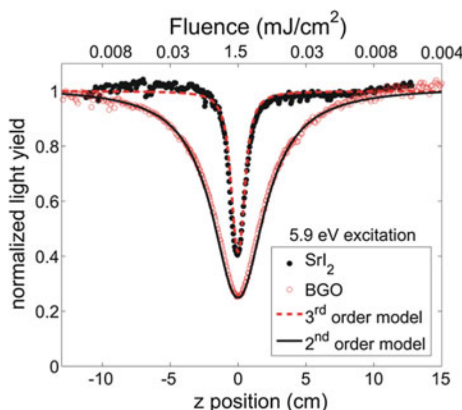

Fig. 10.8 Interband z scan light yield data for BGO (*red open circles*) and undoped SrI_2 (*black solid points*) acquired with 5.9 eV laser photon energy. The data for BGO can be fit by 2nd order quenching based on (10.2) with $K_2 = 1 \times 10^{-17}\ t^{-1/2}\ cm^3\ s^{-1/2}$ (*solid black line*). The data for SrI_2 can be fit by 3rd order quenching based on (10.1a), (10.1b) with $K_3 = 7 \times 10^{-30}\ cm^6/s$ (*red dashed curve*)

format of photon density response is most useful for interpreting and applying the data. It visually resembles local light yield model plots to be discussed later, but is not precisely the same because the local light yield model takes electron track geometry and excitation gradients into account while PDR does not. The general shape of a PDR plot also resembles the experimental electron energy response curves reviewed briefly above, but note that the horizontal axes are not the same—excitation density in one case and initial electron energy in the other.

Figure 10.8 displays the photon density response of BGO and SrI_2 in the raw form as it comes from experimental measurements of interband z scan luminescence yield. With reference to the experimental setup in Fig. 10.7, the horizontal axis of Fig. 10.8 is the z coordinate of the intersection of the sample surface with the Gaussian beam defined by the translating lens, where zero corresponds to the beam waist on the entrance surface of the sample.

Normalization is at the highest light yield, i,e. the left extreme of the z scan, for materials such as BGO and SrI_2 that exhibit net quenching over the entire fluence range. The BGO and SrI_2 data compared in Fig. 10.8 were acquired on the same day with the same 5.9-eV photon energy, beam profile, and externally incident beam power before reflectance corrections. Direct comparison makes the difference in kinetic orders very evident. The 3rd order curve that fits SrI_2 cannot be adjusted to fit BGO, and vice versa. The fitting functions for light yield quenched in 2nd and 3rd order will be discussed in Sect. 10.4.

Laser fluence can be calculated for each value of z using (10.8) if the laser beam power and reflectance losses have been measured. On-axis fluence is labeled across the top horizontal axis of Fig. 10.8 for BGO. The fluence scale for SrI_2 differs because of the reflectivity of sample and cell. Measuring absorption coefficient allows con-

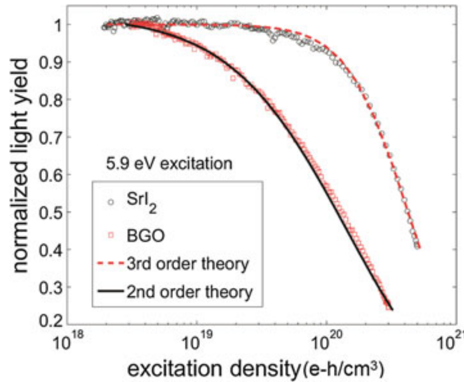

Fig. 10.9 The z scan data for BGO and SrI_2 are re-plotted here on a logarithmic scale of excitation density taking reflectance and absorption coefficient into account for comparison of light yield as a function of excitation density (photon density response). For making this comparison, the absorption coefficient for both crystals was assumed to be the same at $\alpha = 5.6 \times 10^5\ \mathrm{cm}^{-1}$

verting fluence to peak excitation density n_0. Figures 10.6 and 10.9 plot normalized light yield versus log n_0, the format we have termed photon density response.

Figure 10.9 compares the photon density response for BGO and SrI_2. The experimental light yield curves for both materials in Fig. 10.9 roll off at high excitation density as expected for NLQ. However, the SrI_2 light yield with dominant 3rd order quenching remains flat longer before finally falling off more steeply compared to BGO which exhibits dominant 2nd order quenching. This is a quite general, straightforward expectation of 3rd versus 2nd order kinetics. Light yield is flatter for a longer expanse of excitation density in the face of 3rd order quenching than for 2nd order quenching, all else being equal. This has practical significance for the proportionality and light yield of SrI_2 relative to BGO, and quite generally, for the performance of other scintillators when classified according to whether the dominant quenching kinetics are 2nd or 3rd order. Calculations of electron energy response combining Monte Carlo simulations of energy deposition with 2nd versus 3rd order quenching confirm that flatter electron energy response is predicted for 3rd order kinetics [27]. A second figure of merit for both sensitivity and resolution of scintillators is total light yield. Applying similar considerations to the areas under the light yield curves with 2nd order and 3rd order quenching suggests higher total light yield for 3rd order quenching, all else being equal.

10.3.3 *Mixed Kinetic Orders in CsI:Tl and NaI:Tl; Measuring the Free-Carrier Fraction* η_{eh}

Figure 10.10a, b shows photon density response for CsI:Tl(0.3 %) measured with laser photon energies of (*a*) hν = 6.1 eV and (*b*) $h\nu$ = 5.9 eV. For the room temper-

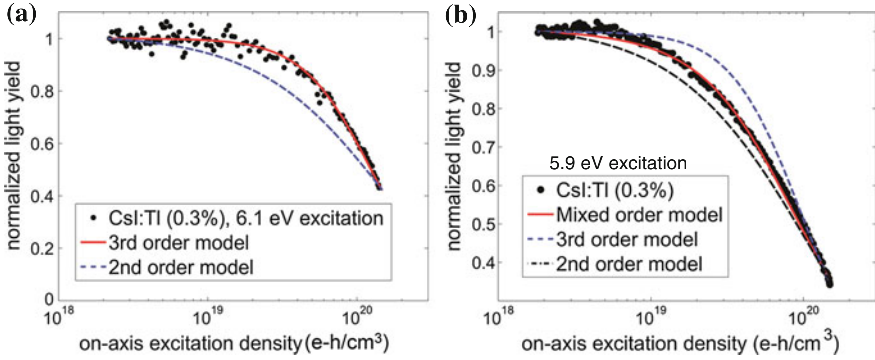

Fig. 10.10 Photon density response of CsI:Tl (0.3 %) excited by laser photon energies of **a** 6.1 eV and **b** 5.9 eV, producing carriers with energies approximately 0.3 eV and 0.1 eV above the band gap, respectively. Both figures show the best attempted fits with 2nd order and 3rd order quenching models. The fit in (**a**) is obtained with $\eta_{eh} = 1$. The *solid curve* in (**b**) is a mixed-order fit with $\eta_{eh} = 0.65$

ature band gap of CsI estimated as 5.8 eV [28], the shared kinetic energies of excited carriers in Fig. 10.10a and b are about 300 and 100 meV respectively. Both figures show the best attempted fits with 2nd order and 3rd order theories (see Sect. 10.4). In Fig. 10.10a, with initial carrier energies about 300 meV above the band minimum, the data can be seen to obey pure 3rd order quenching kinetics. In Fig. 10.10b, with excess carrier energy of roughly 100 meV, the photon density response data lie between the pure 2nd and 3rd order curves. A fit of the data by a mixture of 65 % free carriers (3rd order) and 35 % excitons (2nd order) is superimposed on the data. This establishes $\eta_{eh} = 0.65$ for the low initial carrier energy produced by this laser photon energy, in contrast to initial carrier energies encountered in actual use as a scintillator.

Similarly, Fig. 10.11a, b shows photon density response for NaI:Tl(0.1 %) measured with laser photon energies of (a) hν = 6.1 eV and (b) hν = 5.9 eV. For the room temperature band gap of NaI estimated as 5.7 eV, [28] the shared kinetic energies of excited carriers in Figs. 10.11a, b are about 400 meV and 200 meV respectively. Both figures show the best attempted fits with 2nd order and 3rd order theories (see Sect. 10.4). In Fig. 10.11a, with initial carrier energies about 400 meV above the band minimum, the data obey mixed-order kinetics that can be modeled as 65 % free carriers (3rd order) and 35 % excitons (2nd order), represented by the fit superimposed on the data. In Fig. 10.11b, with initial carrier energies about 200 meV above the band gap, the data can be seen to obey pure 2nd order kinetics in NaI:Tl.

In both CsI:Tl and NaI:Tl, the observed kinetics of nonlinear quenching shifts toward lower order (2nd) as the excess kinetic energy (h$\nu - E_g$) of initially excited carriers decreases. For a 200 meV lowering of excited carrier energy, CsI:Tl shifts from pure third order to mixed, and NaI shifts from mixed to pure 2nd order. The

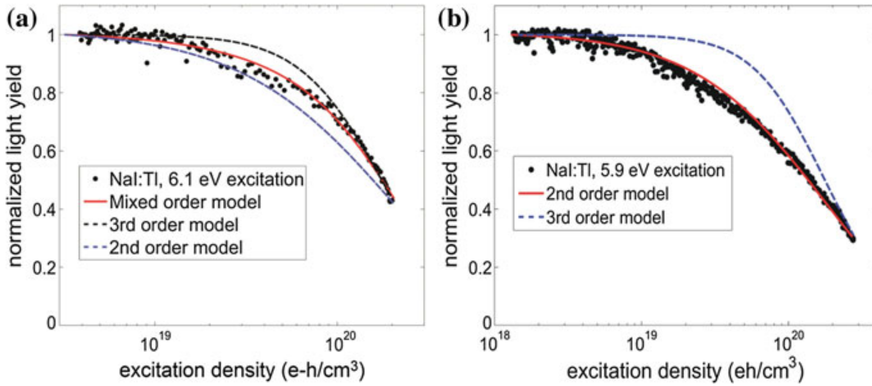

Fig. 10.11 Photon density response of NaI:Tl excited by laser photon energies of **a** 6.1 eV and **b** 5.9 eV, producing carriers with energies approximately 0.4 eV and 0.2 eV above the band gap, respectively. Both figures show the best attempted fits with 2nd order and 3rd order quenching models. The *solid curve* in **a** is a mixed-order fit with $\eta_{eh} = 0.65$. The fit in **b** is obtained with $\eta_{eh} = 0$

hot electron thermalization times starting from about 5 eV above the conduction band minimum have been evaluated as 7 ps in CsI and 2 ps in NaI [2]. The slower thermalization in CsI is accounted for mainly by its lower optical phonon frequency. The thermalization times starting from 300 meV above the cbm will be shorter, but the ratio between values in CsI and NaI could be expected to remain approximately 7/2. Consideration of the data in Figs. 10.10a, b and 10.11a, b is consistent with the hypothesis that excitons cannot form in these alkali iodides until the hot free carriers cool to within one exciton binding energy above the cbm. The binding of the electron in the Type I self-trapped exciton (STE) of NaI has been measured as about 0.2 eV [29]. The optical binding of the electron in the type I STE of CsI can be estimated from the 0.18 eV theoretical Type I STE relaxation energy [30] and picosecond absorption spectra of the room temperature equilibrated STE [31] to be very roughly 0.5 eV. Second order quenching kinetics is associated with formation of excitons upon carrier thermalization, and the data are indeed consistent with faster thermalization in NaI than in CsI.

If carrier thermalization and consequent electron-hole pairing occurs faster than the main part of NLQ, then the population consists of excitons during the time period that determines the kinetic order of NLQ. Then exciton dipole-dipole annihilation should produce the quenching, and 2nd order kinetics would be observed as in NaI:Tl at $h\nu - E_g \leq 0.2$ eV and BGO at $h\nu - E_g \leq 1.7$ eV. If carrier thermalization and consequent capture is slower than the main part of NLQ, then free carrier Auger recombination dominates, and 3rd order kinetics is observed as in SrI_2 and CsI:Tl. As we have just seen, if carrier thermalization and NLQ are competing directly on the same time scale, one can find a mixture of kinetic orders. What is changing is not the kinetic order of a single physical process, but the relative populations of free carriers and excitons in the total population of excited states undergoing relaxation

at any given time. If the above reasoning about determination of quenching kinetic order is correct, an important conclusion is implied: NLQ occurs approximately on the same time scale as carrier thermalization. Since thermalization is known to occur in a few picoseconds or less by calculation [2], the approximate time scale for the main part of NLQ is a few picoseconds according to this reasoning.

The hot electron energy relaxation rate given by [32]

$$\tau_{e,LO}^{-1}(E_e) = \frac{\hbar\Omega_{LO}\sqrt{m_e^*/m}}{\hbar\tilde{\varepsilon}\sqrt{RyE}}\ln\left(\frac{4E_e}{\hbar\Omega_{LO}}\right) \tag{10.9}$$

depends on the electron energy E_e. The hydrogen Rydberg is $R_y = e^2/(8\pi\varepsilon_0 a_B) = 13.6\,\text{eV}$, $\tilde{\varepsilon}$ is the effective dielectric permittivity, and m_e^*/m is the electron effective mass in terms of free electron mass. The thermalization time of carriers created with 300 meV of excess energy, such as in NaI and CsI which are excited by 6.1 eV photons in this experiment, will be somewhat shorter than the values calculated by Wang et al. for electrons with several eV energy [2, 33]. But the relative thermalization rates in different materials should scale approximately as ω_{LO} according to (10.9), and qualitative conclusions based on these relative thermalization rates can be drawn.

We pointed out earlier in the comparison of BGO and SrI_2 that the free carrier fraction is itself an important determiner of the electron energy response and proportionality. Payne et al. were early to point out the importance of the free-carrier fraction, which they labeled η_{eh} [6]. In terms of our labels for free-carrier and exciton densities, n and N respectively, the instantaneous free-carrier fraction is

$$\eta_{eh} = \frac{n}{n+N} \tag{10.10}$$

and correspondingly the exciton fraction is

$$1 - \eta_{eh} = \frac{N}{n+N} \tag{10.11}$$

if we classify carriers as either free or paired, whether trapped or not.

Since the free carrier and exciton densities n and N existing within the time of NLQ can be determined by kinetic order analysis of the laser PDR experiment, this affords a chance to characterize free carrier fraction η_{eh} by an experiment. The experiment does not give an instantaneous value of η_{eh} such as defined above, but rather an average η_{eh} that represents the evolving excitations over the time interval of the NLQ which is observed.

10.3.4 Experimental Determination of the Radius of the NLQ Zone at Track End in NaI:Tl and SrI_2

The radius of the ionization track produced by a high-energy electron is an important physical parameter governing nonlinear quenching and proportionality in scintillators because it is the link from linear energy deposition rate along the track, *dE/dx*, to excitation density, *n*, appearing in the rate equations. However, experimental measurements of the track radius have seemed difficult. The local electron-hole excitation density *n* can be expressed in terms of linear energy deposition rate, *dE/dx*, the energy to create an electron-hole pair, βE_{gap}, and the 1/e radius, r_{track}, of a Gaussian profile beam as:

$$n = \frac{dE/dx}{\beta E_{gap} \int_0^{2\pi} d\phi \int_0^{\infty} r \exp\left(-r^2/r_{track}^2\right) dr} = \frac{dE/dx}{\beta E_{gap} \pi r_{track}^2} \tag{10.12}$$

The laser fluence in a z-scan experiment can be adjusted to produce the same NLQ at the bottom of the dip as is seen in K-dip spectroscopy at a track-end value of electron energy (e.g. 80 eV) in NaI:Tl. Briefly, *K*-dip spectroscopy analyzes the light yield attributable to excitation by K-shell photoelectrons of specific energy selected by tuning synchrotron radiation relative to the K-edge [17] as discussed in Sect. 2.3.2. It is assumed that the same excitation density n_0 will produce the same amount of NLQ in each of the two experiments compared in Fig. 10.12. We equate the peak density of excitations produced by the laser pulse of fluence F_0 in a material of absorption coefficient α,

$$n_0 = \frac{F_0 \alpha}{h\nu} \tag{10.13}$$

to the excitation density near the track end described by (10.14) and solve for the effective radius in which nonlinear quenching occurs:

$$r_{NLQ}^2 = \frac{h\nu dE/dx}{F_0 \alpha \beta E_{gap} \pi} \tag{10.14}$$

The result in NaI:Tl with $\alpha = 4 \times 10^5$ eh/cm^3, [34] $F_0 = 0.4$ mJ/cm^2, $h\nu = 5.9$ eV, dE/dx (at 80 eV) = 64 eV/nm [35], $\beta = 2.5$ [11], and $E_{gap} = 5.8$ eV is $r_{NLQ} \approx 3$ nm near the track end. Using the NWEGRIM Monte Carlo code, Gao et al. have calculated the radius of the self-trapped hole distribution at track end in NaI to be 2.8 nm [36]. A similar analysis of SrI_2 K-dip and z-scan data, assuming $\alpha = 4 \times 10^5$ eh/cm^3 and dE/dx (at 80 eV) = 64 eV/nm, leads to $r_{NLQ} \approx 2.8$ nm in SrI_2 [37].

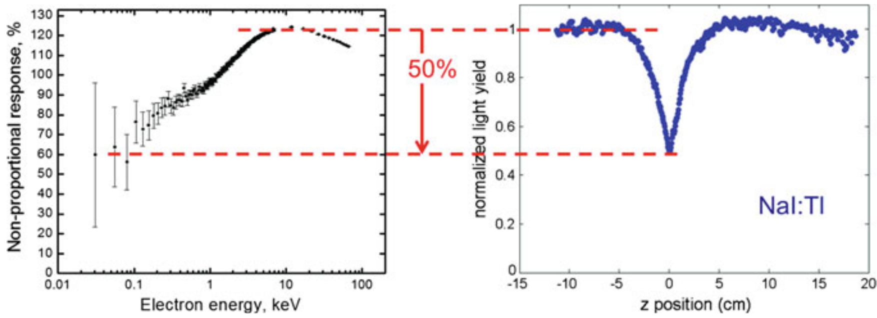

Fig. 10.12 K-dip spectroscopy for NaI:Tl (*left*) with 50 % quenching near the track end. On the *right* are the z-scan results for NaI:Tl with the uv laser fluence tuned to produce the same level of quenching [28]

10.4 Analysis of Photon Density Response

10.4.1 Second Order Quenching

The cases discussed above—in which we experimentally found 2nd order quenching to be dominant—are either oxides in which carrier thermalization is sub-picosecond followed by pairing to excitons, or alkali iodides photo-excited with minimal energy above the band gap. To begin analysis of data exhibiting 2nd order quenching, we consider the rate equation for exciton density N as given in (10.2), repeated below with neglect of the diffusion term. Neglect of diffusion is a reasonable approximation in the z-scan experiment applied to insulators:

$$\frac{dN}{dt} = Bn^2 - C_1 N - K_2 N^2 \tag{10.15}$$

When considering a pure exciton population, we will replace the bimolecular exciton source term Bn^2 by specification of a starting exciton density $N(t = 0)$. The linear rate $-C_1 N$ can be considered a sum of rates for 1st order radiative decay of excitons (rate constant R_1) and linear quenching to the ground state (rate constant K_1). With these two replacements, (10.15) becomes

$$\frac{dN}{dt} = -(R_1 + Q_1)N - K_2 N^2 \tag{10.16}$$

This is the rate equation to be solved for oxides and other cases of 2nd-order quenching. It was already used in published excitation-dependent decay-time analyses of $CdWO_4$ [7, 21] and undoped CsI excited in or slightly above the exciton bands [22]. For example, in undoped CsI, we found that the family of self-trapped exciton luminescence decay curves as functions of excitation density could be fit

with $(R_1 + K_1) = \tau_{obs}^{-1} = (1.4\,\text{ns})^{-1}$ and $K_2 = 2.4 \times 10^{-15}\,\text{cm}^3\,\text{s}^{-1/2}\,\text{t}^{-1/2}$. Since Nishimura et al. had independently determined $R_1 = (15\,\text{ns})^{-1}$ [38], we could deduce $K_1 = (1.5\,\text{ns})^{-1}$, which is attributed mainly to surface quenching since ultraviolet excitation was used [22].

Since every absorbed photon in the low interband spectrum results in the creation of one electron-hole pair, the initial carrier density distribution has the form shown in (10.8). This serves as the initial density distribution for the integration of the nonlinear differential equations given in (10.1a) and (10.2) to find $n(\vec{r}, t)$ of free carriers or $n(\vec{r}, t)$ of excitons, respectively.

The solution of (10.2)—describing decay of a population of immobile excitons created with the profile specified by (10.8)—can be written as

$$N\,(r, \zeta, z, t) = N_0(r, \zeta, z, t = 0)e^{-t/\tau}\left[1 + N_0(r, \zeta, z, t = 0)K_2\sqrt{\pi\tau}\,\text{erf}\left(\sqrt{t/\tau}\right)\right]^{-1} \tag{10.17}$$

where $\tau = (R_1 + K_1)^{-1}$ for undoped excitonic scintillators.

The qualification to immobile excitons refers to the result of bimolecular theory that the rate "constant" $K_2(t)$ is proportional to $t^{-1/2}$ when the interacting species are immobile, but is a constant when a well-mixed uniform distribution is maintained during bimolecular decay, e.g. by rapid diffusion [8, 22, 39, 40]. Kirm et al. [7] and Lassner et al. [21] used the immobile species solution presented in (10.4 and 10.17) when analyzing self-trapped exciton quenching in $CdWO_4$. We used it in decay time analysis of self-trapped exciton quenching in CsI [22, 23]. In the treatment of free carrier quenching in the next subsection, the carriers will be assumed mobile, and therefore constants K_3 and B will be used.

For 2nd order quenching of self-trapped exciton populations, the integrated light yield Y_{exc} as a function of lens position z can then be written

$$LY_{exc}(z) = \frac{\int_0^\infty R_1 N(r, \varsigma, z, t)d^2\vec{r}\,d\varsigma dt}{\int_0^\infty (R_1 + K_1)N(\vec{r}, t) + K_2 N^2(\vec{r}, t)d^3\vec{r}\,dt} = \frac{1}{\eta_{tot}}\int_0^\infty R_1 N(\vec{r}, t)d^3\vec{r}\,dt \tag{10.18}$$

where η_{tot} is the *total number* of excited states produced in the volume of integration, not to be confused with the population densities n and N. The full integration variables are shown only in the first numerator term on the right side, and are elsewhere represented by $N(\vec{r}, t)d^3\vec{r}\,dt$. The integration limits apply to both space and time variables.

In visualizing the time decay of a population under 1st through 3rd order processes, the illustration in Fig. 10.13 is a useful reminder. It plots on a log-log scale the decay of an initial population subject to decay rates of 1st through 3rd order in density of excited states, respectively. One often thinks of a first order decay process as slower than 2nd or 3rd order, which it certainly is initially. But the right-hand side of Fig. 10.13 reminds us that the first order solution (exponential decay) ultimately dives much faster than any single power law solution. Thus, the combined rate of

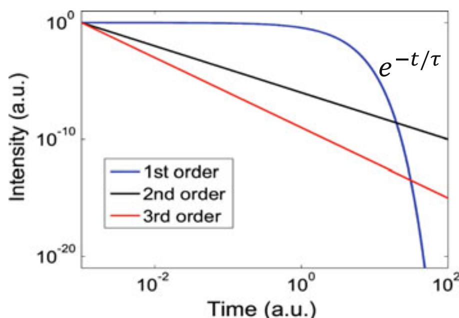

Fig. 10.13 The decay of an initial population subject to decay rates of 1st through 3rd order in density of excited states is plotted on a log–log scale

radiative decay and 1st order quenching effectively terminates the time integration interval in equations such as (10.18).

10.4.2 Third Order Quenching

The photon density response curves for alkali and alkaline earth iodides exhibit nearly pure 3rd order quenching when excited well above the band edge, and so will be analyzed in terms of the free-carrier rate equations given in (10.1a) and (10.1b). The exciton (10.2) will still be formally needed to address light emission after the free carriers ultimately pair to form excitons (free or trapped) but the exciton densities and associated 2nd order quenching should be much lower by then. If this were not the case, we would have seen mixed kinetic order rather than nearly pure 3rd order in the experiments on iodides discussed above.

The gradient of carrier density along z in the interband laser experiment is about 10 times smaller than the radial gradient around an electron track, while the laser radial gradient is negligible in comparison to both. Therefore, two simplifications of (10.1a) and (10.1b) are possible when analyzing PDR experiments for insulators with modest or low carrier mobilities, a category that includes most of the common scintillators. The first is to neglect the diffusion term in the laser experiment. However, when analyzing electron-excited light yield in Sects. 10.8 and 10.9 of this chapter, the full (10.1a) and (10.1b) have to be used to address diffusion and consequent charge separation in the radial gradient of electron tracks.

Since we are neglecting diffusion in laser experiments on most insulators, electrons and holes will not separate according to different mobilities, and a second important simplification for PDR analysis becomes possible. The pair of terms in (10.1a) and (10.1b) that are third order in carrier density represent the sum of the two channels of free carrier Auger decay labeled by the sign of the spectator carrier. We cannot, at this point, distinguish K_{3ehe} from K_{3ehh} by experiment. Having formally acknowledged the existence of $n_e n_h n_e$ and $n_e n_h n_h$ channels, we will lump the two terms together as one 3rd order rate of the form $K_3(1/2(n_e n_h n_e + n_e n_h n_h))$ in the analyses and models to follow. In pure (intrinsic) insulators, the approximation

$n_e = n_h$ can be made when there is negligible charge separation. This is the case in the laser experiments to be discussed as well as for electron excitation in materials with similar carrier mobilities. In addition, strong interband excitation such as produced by high energy charged particles or a laser pulse tuned above the band gap effectively produces $n_e \approx n_h$ even in doped or impure insulators during the time interval before significant charge separation or trapping can occur. We can approximately equate the generalized excitation density n(=absorbed photon density in PDR experiment) with the free carrier density of either sign,

$$n \approx n_e \approx \mathrm{n}_h. \tag{10.19}$$

Accordingly, the Auger quenching term becomes K_3n^3 and the bimolecular pairing term becomes Bn^2. This remains valid only if the gradient of carrier concentration is small enough that carriers with different mobilities will not become significantly separated spatially on the time scale in which the rate equation is applied. In the data and analyses discussed in this chapter, the relevant time scale is set by hot carrier thermalization and capture at the few picoseconds to ten picosecond range. The approximate free-carrier single rate equation that can be used for the analysis of laser-excited *photon density response* experiments in materials with low or moderate mobilities is

$$\frac{dn}{dt} = G - An - Bn^2 - K_3n^3 \tag{10.20}$$

When the photon density response measurements have been analyzed for semiconductors, [8] it was found necessary to restore an ambipolar diffusion term and use the equation

$$\frac{dn}{dt} = G + D_a\nabla^2 n - An - Bn^2 - K_3n^3 \tag{10.21}$$

where charge separation by different diffusion rates can still usually be disregarded in the analysis of PDR experiments. The case wherein charge separation by different diffusion rates cannot be neglected is when one carrier (usually the hole in alkali halides) is self-trapped and there is a strong gradient such as around an electron track. We will examine that case in Sects. 10.8 and 10.9 on local light yield in electron tracks. Equations (10.20) and (10.21) are approximations useful for analyzing PDR experiments, with no electron tracks.

Proceeding for now from the simplified (10.20), we write the expression for light yield analogous to the discussion of 2nd order quenching earlier in this section:

$$LY \propto \frac{\int\limits_V \int\limits_0^{\tau_{therm}} Bn^2 d^3\mathbf{r}dt}{\int\limits_V \int\limits_0^{\tau_{therm}} (An + Bn^2 + K_3n^3) d^3\mathbf{r}dt} \tag{10.22}$$

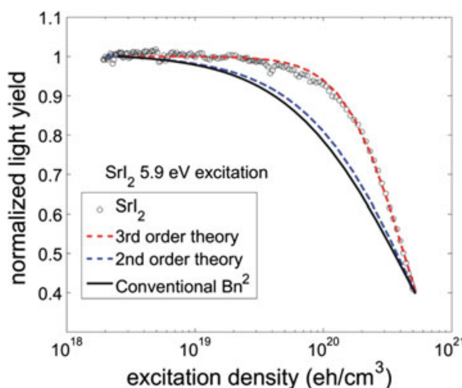

Fig. 10.14 SrI_2 photon density response data (*open points*) are compared to the 2nd order quenching model of (10.18) shown in *blue dashed line*, the conventional model of simultaneous bimolecular (Bn^2) and 3rd order quenching (10.22) and the hot-electron 3rd order model to be discussed. Only the 3rd order model for hot electrons can fit the data [42]

This is written as a proportionality because it determines the fraction of free carriers that pair as generalized excitons via the Bn^2 term in competition with other fates of deep trapping or Auger recombination. Putting aside the 3rd order term for the moment, we note that Murray and Meyer considered only the 1st and 2nd order terms without the indicated time integrals in (10.22) and then divided out the common factor of Bn^2, obtaining

$$LY = \left(\frac{A}{Bn} + 1\right)^{-1} \tag{10.23}$$

for the trend of rising light yield with excitation density. They later remarked on the ultimate decreasing light yield expected at very high excitation density, which we include by restoring the Auger term and writing an expression in all 3 orders, similar to (10.22). This qualitatively predicts a hump in light yield versus excitation density n:

$$LY = \left(\frac{A}{Bn} + 1 + \frac{K_1 n}{B}\right)^{-1} \tag{10.24}$$

It is worth noting that in going from the conventional light yield expression in (10.22) to the simplified trend expressed in (10.23) and (10.24), a step was taken that does not strictly apply to pulsed excitation such as in scintillator operation. Dividing out the Bn^2 rate term can only be done mathematically in a “continuous excitation” experiment where the excited population is continuously resupplied. Then the light yield is proportional simply to the ratio of radiative rate to total rate of depleting the excited population, as represented in (10.23) and (10.24). (We also note that J. B. Birks [41] made a similar continuous excitation assumption in deducing the “Birks term” as it has been called by various workers in the scintillator field.) But

the real application of scintillators, the measurements of electron energy response, and the photon density response laser experiment all detect the integrated light yield after pulsed excitation. This requires doing the time integrations shown explicitly in (10.18) and (10.22), before forming the ratio. The "continuous excitation model" can be convenient for discussing qualitative trends, but for fitting quantitative data the integrals must be done first and then the ratio formed to predict light yield.

For large carrier density n, where both photon density response and electron energy response experiments generally show a roll-off of light yield due to NLQ, (10.24) predicts an inverse first power dependence ($1/n$) of Light Yield versus n. Figure 10.14 plots the prediction of (10.22) including proper integration, labeled as the "conventional Bn^2 model", in comparison to measured photon density response of SrI_2. The plot of the 2nd order quenching model represented by (10.18) is also shown, and neither can fit the data because they fall off too slowly.

The failure of (10.22) to fit the roll-off slope in a 3rd order quenching material is one of the several experimental results leading us to conclude that the first, second, and third order kinetic terms do not all compete on the same time scale in materials like SrI_2 and the alkali iodides, where hot carriers persist during a significant part of the time for NLQ. The very fact of finding pure 3rd order quenching in photon density response for SrI_2 and CsI already led us to invoke hot electrons as the physical phenomenon holding off exciton formation and other electron capture channels for a finite time in iodides. The hot electron thermalization time is approximately inversely proportional to optical phonon period (10.9) and can be as long as 7 ps in CsI [2]. We can find no other way of explaining the pair of experimental findings that quenching is 3rd order in the iodides having low ω_{LO}, while it is pure 2nd order in oxides with high ω_{LO}.

The logical extension of this explanation is that not all of the rate terms in (10.21) and (10.22) can be competing in the same time range. Electron capture on traps or dopants (An) or on holes (Bn^2) is strongly suppressed until the electrons have thermalized. This is illustrated by calculations of electron temperature and of the paired fraction of electrons and holes versus time, comparing CsI and YAP in Fig. 10.15.

The calculation method employs Monte Carlo simulation with phonon scattering rates calculated by methods similar to Wang et al. [2, 33] and Vasile'v et al. [32, 43] The electron is captured by a hole when it scatters by phonon emission to a bound state in the electron-hole potential that is at least 3 kT below the ionization limit [44]. Notice that the time axes for the YAP and CsI plots are a factor of 10 different. It is seen that electron-hole pairing in CsI is prevented until electron thermalization is nearly complete on a scale of about 3 ps, and then capture proceeds rapidly after that delay. The same happens in the simulations for YAP, except about 30 times faster. Cooling and capture in YAP is substantially subpicosecond, i.e. around 100 fs. In order to match the experimental finding of pure 3rd order quenching in CsI, nonlinear quenching should be mostly complete in 3 ps or less. We have labeled the time intervals in which free-carrier kinetics would apply and in which exciton kinetics would apply, for both materials in Fig. 10.15.

An experimental observation relevant to this topic comes from picosecond infrared absorption spectroscopy of pure and Tl-doped CsI at room temperature, shown in

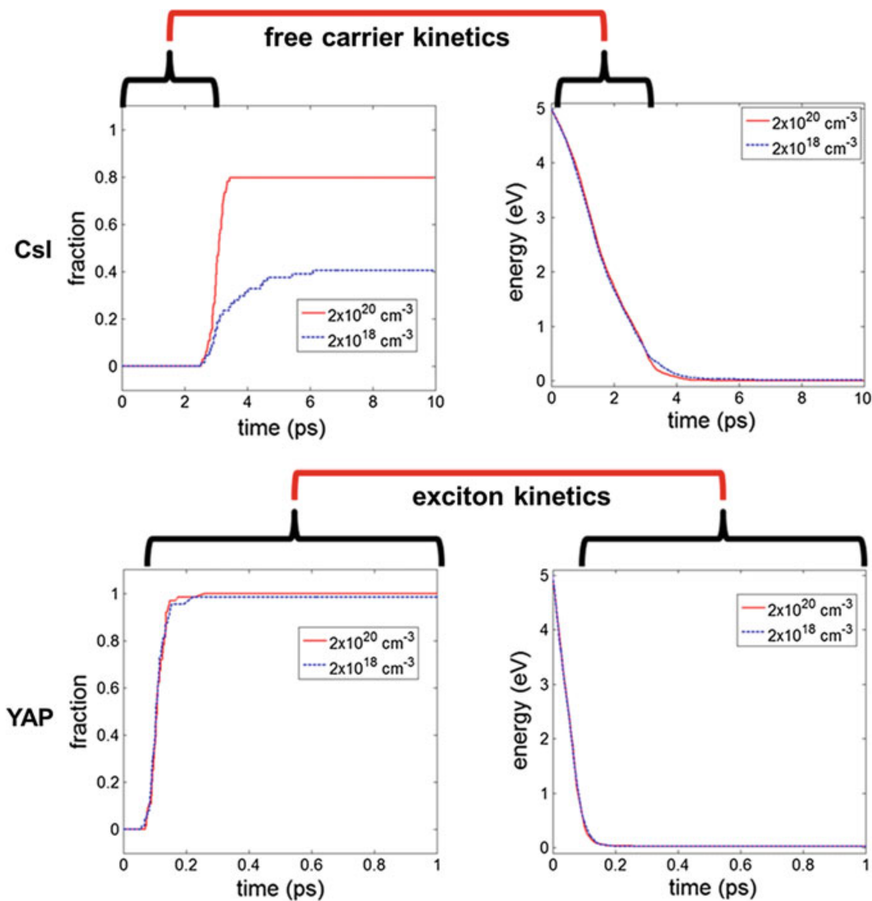

Fig. 10.15 Monte Carlo simulations of the thermalization of hot electrons and capture on holes in CsI and YAP calculated by Li et al. [44]. The method is similar to that employed by Wang et al. [2, 33] and Vasil'ev et al. [32, 43] including calculation of phonon emission rate. The electron is captured when it scatters to a bound state in the electron hole potential that is at least 3 kT below the ionization limit. Results are shown for initial excitation densities of $2 \times 10^{20} \text{cm}^{-3}$ (*red*) and $2 \times 10^{18} \text{cm}^{-3}$ (*blue*) [42, 45]

Fig. 10.16 [42, 45]. The left and right panels are for different kinetic energies shared by the electron and hole, $2h\nu - E_{gap} = 0.1$ eV and 3.06 eV respectively. The initial spike of absorption nearly coincident with the excitation pulse has a very broad spectrum and may be attributed to free carrier absorption. It can be seen that when the initial excitation is 3.06 eV above the band gap, the free carrier spike is larger relative to the more slowly developing self-trapped exciton absorption. It is relatively smaller for excitation just slightly above the band gap. The rapid drop in free carrier absorption could be due to shallow capture of electrons in high Rydberg states around holes, transferring oscillator strength dominantly to the deep infrared spectrum out

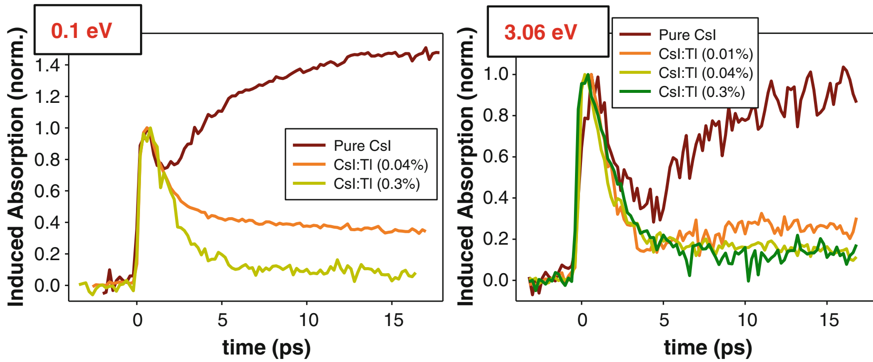

Fig. 10.16 Picosecond infrared absorption spectroscopy of pure and Tl-doped CsI at room temperature. The *left* and *right panels* are for different kinetic energies shared by the electron and hole, $2h\nu - E_g ap = 0.1$ eV and 3.06 eV respectively [42, 45]

of our experimental spectral range, and to self trapping of holes which could transfer hole oscillator strength to the ultraviolet. The re-growth of absorption having a spectrum previously attributed to self-trapped excitons in CsI at room temperature [31] could represent relaxation of self-trapped excitons to their metastable radiative state. The time for electron capture on self-trapped holes is roughly consistent with the calculated electron-hole capture rate for CsI in Fig. 10.15, i.e. a few picoseconds.

Free-carrier Auger quenching rather than exciton-exciton dipole quenching should apply in the initial time period when (the hot) carriers are free. When the carriers are thermalized and captured on spatially separated traps, their contribution to Auger quenching should effectively terminate. This would be the likely case in CsI:Tl, because holes tend to self-trap right where they are in the host lattice, while electrons trap mainly on Tl^+ dopant ions present at 0.1 % levels. The main point is that electrons and holes do not generally trap at the same location in scintillators like CsI:Tl, so trapping in a doped crystal can effectively terminate Auger recombination. When the electrons are captured on self-trapped holes and form self-trapped excitons, the dominant quenching term from that sub-population should be 2nd order dipole-dipole quenching. However, since by this time their concentration has been reduced by both diffusion and Auger quenching, they represent only a fraction of the initial electron population. Thus, their contribution to quenching can be small compared to the free-carrier contribution in the earlier, denser conditions. The measured iodides other than NaI show this exact photon density response. NaI is the exception that proves the rule. Its higher ω_{LO} relative to most other iodide scintillators leads to more rapid thermalization.

In Fig. 10.14, we saw that the conventional Bn^2 model with all rate terms competing from $t = 0$ onward cannot fit the roll-off of light yield at high carrier density n. Now let us see if the slope of the roll-off of photon density response in SrI_2 and other iodides can be properly fit when we take the thermalization time dependence of each kinetic order into account in the free-carrier rate (10.1a) and

(10.1b) and the expression for light yield (10.22). Use of explicitly calculated rate "constants" dependent on time via electron temperature is being pursued in current Monte Carlo simulations of these processes [45]. For a preliminary analysis of the photon density response data that at least takes electron thermalization into account, we have assumed a step-wise time dependence in each kinetic order of the free-carrier rate equation as follows [28]:

$$\frac{dn}{dt} = -An\Theta(t - \tau_{th}) - Bn^2\Theta(t - \tau_{th}) - K_3n^3\Theta(\tau_{th} - t) \tag{10.25}$$

where $\Theta(\mathrm{t} - \tau_{th})$ is the Heaviside step function turning on after τ_{th}, and $\Theta(\tau_{th} - t)$ turns off after τ_{th}.

In this way, we assert that the coupling rates into exciton formation (Bn^2) and carrier trapping (An) cannot turn on until it becomes possible to trap electrons on holes or on dopants, i.e. until the electron has thermalized to within the trapping potential depth. Li et al. are working to calculate the thermalization time as a function of electron energies excited in the photon density response experiments. However for the time being, we assume that the trapping and bimolecular exciton formation channels turn on after a hot electron thermalization time approximated as 6 ps in iodide crystals. This is chosen as representative of the 7 ps maximum thermalization time in CsI [2, 33] and the 6 ps capture time of electrons on Tl^+ in CsI:Tl(0.3 %) [31]. The free-carrier Auger recombination is similarly modeled as turning off when the carriers thermalize and trap on spatially separated sites as in CsI:Tl and similar activated scintillators.

Based on the time-step rate in (10.25), we can proceed to write the expression for light yield taking hot electron thermalization into account. The integration of (10.25) has been done numerically for fitting, but is not directly expressible in analytic form. However, the following expression separating the terms of (10.7) acting on different time scales into a product of probabilities of survival from each successive stage yields data fits that are practically indistinguishable from the numerical integration of (10.25). It has the advantage of being conceptually easy to dissect into three physical stages:

$$LY \approx \left(1 - \frac{\int_0^{\tau_{therm}} \int_V K_3 n(\vec{r}, t) dt d^3r}{\int_V n(\vec{r}, t = 0) d^3r}\right) \frac{\int_{\tau_{therm}}^{\infty} \int_V (S_1 n + Bn(\vec{r}, t)^2 dt d^3r}{\int_{\tau_{therm}}^{\infty} \int_V (K_1 n + S_1 n + Bn^2) dt d^3r} \times \left[\frac{\int_{\tau_{therm}}^{\infty} \int_V R_1 N(\vec{r}, t) dt d^3r}{\int_{\tau_{therm}}^{\infty} \int_V (K_{1,exc} N + R_1 N + K_2 N^2) dt d^3r}\right] \tag{10.26}$$

A crucial feature of 10.26 to note is that the 3rd order quenching process is limited to the left-hand bracket governing hot carrier quenching and determining the survival fraction that passes on to the middle bracket of processes such as capture of thermalized carriers on shallow and deep traps (K_1n) and on holes (Bn^2). The left-hand bracket as a multiplier imposes a steep slope on the roll-off of light yield at high

n, in agreement with the PDR experiments. The time integrals in the middle term run formally from τ_{th} out to ∞, but the rates within are all sufficiently fast that the trapping and exciton formation can be virtually complete in tens of picoseconds. The survivors of the middle bracket are excitons, passed on to the right-hand bracket as the exciton density N. The quadratic nature of electron-hole recombination is represented in the exciton formation (middle bracket), but the only radiative rate in the entire multiplied string of brackets is that of generalized (free or trapped) exciton radiative decay R_1N in the right-hand bracket.

In materials (most iodides) where the experimental photon density response is pure 3rd order, the exciton fraction on the right has such a small K_2N^2 quenching rate due to low density of N resulting after diffusion and Auger quenching of the free-carrier progenitors, that it reduces to a constant fraction $R_1/(K_1 + R_1)$. In NaI, this term apparently contributes some 2nd order dependence because of the relatively short thermalization time of NaI compared to heavier iodide scintillators. To numerically evaluate (10.26), we solve (10.20) for (r, ζ, z, t), where $n(r, \zeta, z, t = 0)$ was specified for the z-scan method in (10.8).

If the thermalization time is long (e.g. 7 ps), the left-hand bracket has time to significantly diminish the carrier concentration by Auger quenching before excitons can form. After thermalization of carriers, the competing linear rates of deep trapping and of shallow trapping as separated electrons and holes compete with the formation of excitons capable of dipole-dipole annihilation. In doped crystals, the S_1n shallow capture rate (energy storage rate) may be especially competitive since the dopants can be present at percent concentrations, i.e. higher than the highest hole concentration. Experiments searching for excitation density-dependent lifetime quenching on activators [7, 22] have shown instead that the quenching occurs only among the intrinsic host excitons. If that is found to be a widespread result, it means that the S_1n rate of charge storage is a protection from NLQ. This is the way it is incorporated in (10.22) and (10.26), and examples following from it will be discussed in Sect. 10.7.

After the free carriers survive Auger quenching, capture on deep traps, capture on shallow storage traps including activators, and finally formation of excitons, the resulting concentration N of host excitons susceptible to dipole quenching is apparently small enough to discourage 2nd order quenching in most iodides. This is concluded directly from the PDR experiments showing very little 2nd order quenching in most iodides other than NaI. In the case of negligible 2nd order quenching, the right-hand bracket becomes a constant fraction and (10.26) constitutes the "3rd order theory" that successfully fits the photon density response of SrI_2 in Fig. 10.14, where the conventional Bn^2 model and the 2nd order theory both failed. The same was found true for CsI:Tl excited at 6.1 eV in Fig. 10.10.

Even in the oxides exhibiting experimental 2nd order quenching, (10.26) serves formally as the applicable light yield. It is a general light yield expression encompassing the phenomena leading to both 2nd and 3rd order quenching behavior. To see this, allow τ_{th} to become negligibly short. Then the left bracket tends toward unity. The carriers immediately begin trapping and forming excitons as described by the second bracket, which contains no terms of NLQ rate. The only nonlinear quenching rate is K_2N^2 in the right hand term, which is just the same as the 2nd order exci-

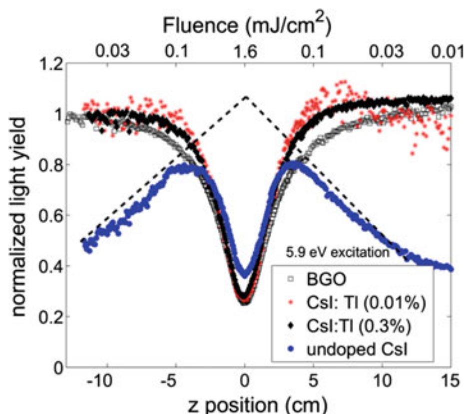

Fig. 10.17 Superposition of z scans for CsI:Tl(0.3 %), CsI:Tl(0.01 %, undoped CsI, and BGO measured on the same day with 5.9 eV photon energy, same beam profile, and same external beam power [28]

ton quenching model presented in Sects. 10.4.1 and 10.16. Physical examples of the important roles of the rates Bn^2, $K_1 n$, and $S_1 n$ in the middle bracket will be illustrated using the data presented in the next Section.

10.5 Wings, Humps, Charge Separation, and Energy Storage

There are additional parameter dependences that can be seen in photon density response data, but it was necessary to introduce the analysis methods, particularly (10.26), before going farther. With the analysis methods in hand, we now consider the raw data (z scan) form of PDR results for CsI in Fig. 10.17. The data for undoped CsI exhibits pronounced "wings" of rising light yield versus fluence going toward $z = 0$, until the nonlinear quenching dip finally takes over at the high fluence values close to $z = 0$. Two samples of CsI:Tl with increasing concentration of Tl^+ activator are also shown. The rising wings become progressively flatter with increasing Tl concentration. Recall that at this 5.9-eV excitation energy, the quenching kinetics in CsI are mixed 2nd and 3rd order. As a standard of 2nd order quenching, data for BGO are superimposed.

When the data for undoped CsI and several levels of Tl doping are re-plotted in the photon density response format in Fig. 10.18, the rising wings and central dip appear instead as a "hump" reminiscent of the well-known hump in electron energy response of halide scintillators measured by Compton coincidence (e.g. SLYNCI) and K-dip measurements, illustrated in Fig. 10.3 of Sect. 10.2. They are indeed related but not identical, as we shall see.

As shown in Fig. 10.18, the hump is pronounced in undoped CsI and becomes progressively smaller with Tl doping, almost disappearing in CsI:Tl(0.3 %). The solid line plotted through each set of data points in Fig. 10.18 is a fit using (10.26), where all parameters except S_1 are held constant for the whole family of curves. The constant parameters $K_3 = 6.6 \times 10^{-29}\,\text{cm}^6\,\text{s}^{-1}$, $K_2 = 1.7 \times 10^{-15}\,\text{t}^{-1/2}\,\text{cm}^3\,\text{s}^{-1/2}$, and $R_1 = 7.1 \times 10^8\,\text{s}^{-1}$. are based on measurements reviewed in this chapter and the radiative lifetime of Tl in CsI. The data were fit with the mixed order model for $\eta_{eh} = 0.65$ determined for 5.9 eV laser excitation of CsI. The shallow trapping rate constant S_1 (energy storage rate) was the only variable fitting parameter used to fit the individual curves for different Tl doping levels. The dominant energy storage electron trap in CsI:Tl is known to be Tl^+ itself, acting to trap an electron as Tl^0 [31]. Since S_1 is thus identified with the rate of electron trapping on Tl^+, the value of S_1 in undoped CsI should be zero, as is the case for the fitting curve in Fig. 10.18. The values of S_1 needed to fit the data for the three concentrations of Tl in the remaining data sets of Fig. 10.18 are $S_1 = 1.43 \times 10^9\,\text{s}^{-1}$ for 0.01 % Tl, $S_1 = 5.0 \times 10^9\,\text{s}^{-1}$ for 0.04 % Tl, and $S_1 = 43.5 \times 10^9\,\text{s}^{-1}$ for 0.3 % Tl. The ratios $S_1(0.04\,\%)/S_1(0.01\,\%) = 3.5$, and $S_1(0.3\,\%)/S_1(0.01\,\%) = 30.4$ are close to the concentration ratios 0.04 %/0.01 % and 0.3 %/0.01 %. The comparison suggests that the S_1 rate constant is indeed roughly proportional to Tl^+ concentration.

The reason for suppression of the hump can be seen on examination of the middle bracket in (10.26). The middle ratio is the one that causes the rising trend, due to the bimolecular exciton formation rate Bn^2 competing with the total depletion rate of n in the denominator, including the linear rate of deep trapping. As noted earlier, this is just the ratio discussed by Murray and Meyer [5] as governing the yield of excitons in NaI.

While the middle bracket of (10.26) creates the rising trend versus carrier density in photon density response, the falling trend comes from the more dominant of the left bracket or the right bracket containing the 3rd and 2nd order quenching rates respectively. That dominance depends particularly on τ_{th} and Bn^2. If the electron thermalization time is long as in iodides, the time integration interval in the left-hand bracket is long enough to substantially deplete the carriers at high density, and the light yield should fall according to 3rd order quenching. If the thermalization time is extremely short compared to the total duration of NLQ, then the left bracket becomes unimportant and the right bracket dictates a dominant 2nd order fall-off. This is expected to be the case for oxides. In CsI excited very near the band edge by 5.9-eV laser photons, we have seen that both left and right brackets exert their effects at high density, so mixed kinetic order was found

We have compared the rising exciton yield (proportional to light yield) dictated by the middle bracket of (10.26) with the *Murray-Meyer* model of exciton formation. It also bears similarity to the model based on Onsager radius as used by Payne et al. Both the *Murray-Meyer* and *Payne-Onsager* mechanisms are functions only of excitation density, not of relative carrier mobility and gradients driving diffusion to charge separation. As discussed in Sect. 10.2.5, the laser PDR measurement has only small carrier density gradients relative to electron tracks, so a model depending only on excitation density such as Murray–Meyer/Payne–Onsager should be applicable. The

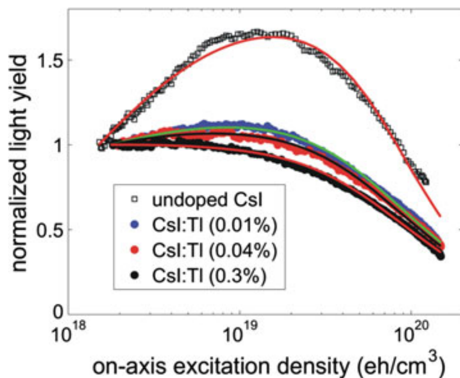

Fig. 10.18 PDR of undoped CsI and CsI:Tl with 0.01, 0.04, and 0.3 % Tl (weight %). The laser photon energy was 5.9 eV. The *solid lines* are fits to (10.26), changing only the values of S_1

successful use of (10.26) to fit the family of CsI and CsI:Tl data in Fig. 10.18 seems proof of that. The role of the energy storage or S_1 trapping rate is clear on examination of (10.26). When the linear $S_1 n$ rate becomes comparable to the quadratic Bn^2 rate (over the experimental range of n), the middle bracket begins to resemble a ratio of two linear terms and the hump flattens to a constant, as seen in Fig. 10.18. It is also observed in our photon density response experiments that increasing the laser pulse energy (therefore n_0) enhances the hump.

Because of the visual similarity of the hump in photon density response and electron energy response experiments, and the success of the *Murray-Meyer/Payne-Onsager* (*MM/PO*) model in fitting the former, it is tempting to conclude that the *MM/PO* model explains the hump in both experiments.

However, note that the hump in photon density response goes flat for 0.3 % Tl. It is mostly flat for 0.04 %, and by interpolating, one can project that the hump in photon density response should be mostly flat for CsI:Tl(0.1 %). The electron energy response for CsI:Tl(0.1 %), shown in Fig. 10.19, exhibits a substantial hump, in contrast.

The electron energy response in Fig. 10.19 has a considerably more pronounced hump than PDR for CsI:Tl in Fig. 10.18. Since the electron energy response of light yield is an integral over all excitation densities in the electron track starting from a given initial energy, it should be expected that the integration would have smoothed out a hump expressed versus excitation density, if anything. This is a very understandable disagreement in the two experimental results. The electron energy response measures light yield when there are electron tracks; photon density response is measured without electron tracks, i.e. without large radial gradients emphasizing diffusion effects. In [13, 22], we described how thermalized diffusion of carriers with widely different mobilities in the strong radial gradient around an electron track leads to charge separation, which we referred to in the earlier works as an Independent Fraction of carriers driven by the different electron and hole diffusion rates to trap at spatially separated sites rather than form excitons. To produce light from spatially separated shallow traps, the carriers need to de-trap and migrate back together

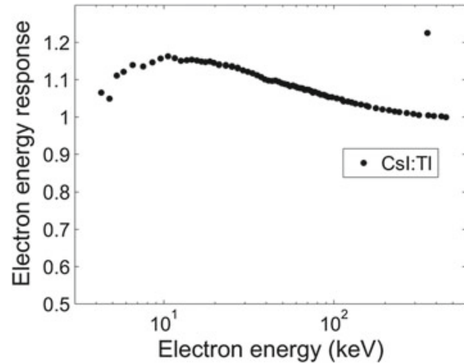

Fig. 10.19 Electron energy response curve for CsI:Tl from the SLYNCI experiment

through a field of possible deep traps represented in the earlier work as producing a *quenched fraction* k_1 of the Independent Fraction (IF). This depends on local carrier density because the density gradient controlling IF and the collective electric field that encourages recombination upon de-trapping depends on carrier density. The formation of the hump in this model requires an inequality of electron and hole mobilities, a strong gradient of density, *and* a linear quenched fraction k_1 due to deep traps. Without all 3 of those factors, the charge separation mechanism forming a hump disappears.

In contrast, the *MM/PO* model continues to predict a hump whether there is a mobility difference and a gradient or not. The *MM/PO* contribution to a hump requires only that the free-carrier fraction η_{eh} be significant and that the S_1 storage rate be small compared to Bn^2. An S_1 storage rate that flattens the *MM/PO* hump will not flatten the charge separation hump.

Comparing the CsI:Tl photon density response in Fig. 10.18 and the electron energy response in Fig. 10.19, we conclude that the hump in laser *photon density response* (PDR) is due almost entirely to the MM/PO mechanism dependent on excitation density and linear deep trapping, whereas the hump in electron energy response of CsI:Tl is due mainly to the charge separation mechanism. The latter depends on unequal electron and hole mobilities, the strong gradient of the electron track, and also on linear deep trapping. That is why a hump persists in SLYNCI electron energy response of CsI:Tl even though the Tl concentration has been shown (Fig. 10.18) to be sufficient to flatten the *MM/PO* contribution to the hump.

10.6 Tabulation of Results from Photon Density Response

Table 10.1 presents a summary of parameters extracted from photon density response measured in two oxide and three iodide scintillator materials using 6.1 eV excitation. The electronic band gap E_g for free carrier production at room temperature, the corresponding energy $h\nu - E_g$ in excess of the band gap shared by the initial electron and hole, the observed kinetic order of NLQ, and the free-carrier fraction

Table 10.1 For two oxide and four iodide scintillator materials measured so far, Table 10.1 lists band gap E_g at room temperature, initial energy of the 6.1 eV laser excitation in excess of E_g, the order of NLQ deduced from fitting photon density response, corresponding free carrier fraction η_{eh}, the measured quenched fraction $QF(n_0)$ at an excitation density of $n_0 = 1 \times 10^{20}$ e − h/cm^3, and the rate parameters $K_2(t)$ and K_3 for 2nd and 3rd order quenching

Crystal	E_g (eV)	$h\nu - E_g$ (eV)	Order of NLQ	η_{eh}	QF(n_0)	K_2 (10^{-15} $t^{-1/2}$ cm^{3}s$^{-1/2}$)	K_3 (10^{-29} cm^{6}s^{-1})	α (10^5 cm^{-1})	ω_{LO} (10^{13} s^{-1})	τ_{th} (ps)
BGO	4.2[a]	1.9	2	0	0.593	0.01	NA	5.6[b]	15.3[c]	≤0.5
$CdWO_4$	4.8[d]	1.3	2	0	0.52	0.0029	NA	9.6[e]	17.3[f]	≤0.5
SrI_2	5.5[g]	0.6	3	1	0.24	NA	0.73	4	2.6[h]	∼4
CsI:Tl	5.9[i]	0.2	3	1	0.41	NA	6.6	2.7[j]	1.79[k]	7[l]
NaI:Tl	5.8[m]	0.3	mixed	0.65	0.33	2.3	3.2	4[n]	3.47[k]	2[l]
CsI	5.9[i]	0.2	3	1	0.37	NA	4.5	2.7[j]	1.79[k]	7[l]

Also listed are the approximate absorption coefficient at 6.1 eV, the highest zone center longitudinal optical phonon frequency ω_{LO}, and the calculated or estimated electron thermalization time, τ_{th}.starting from E_g above the CBM

References are attached to numbers from the literature as superscript letters: [a][46], [b][46], [c][47], [d][48, 49], [e][50], [f][51], [g][52], [h][53], [i][34, 54, 55], [j][22], [k][56], [l][2], [m][34, 57, 58], [n][34]

$\eta_{eh} = n/(n + N)$ are listed. The total nonlinear quenched fraction $QF(n_0)$ at a fixed excitation density $n_0 = 1 \times 10^{20}$e-h/cm^3 and the rate parameters $K_2(t)$ and K_3 for 2nd and 3rd order quenching are listed. The best measured value (or estimate, otherwise) of optical absorption coefficient α at 6.1 eV is tabulated,along with the highest zone-center longitudinal optical phonon frequency ω_{LO} and the calculated electron thermalization time τ_{th} starting from an energy E_{gap} above the conduction band minimum. References to values from the literature are noted by superscript letters.

The kinetic order and η_{eh} are direct from fitting, whereas the conversion to excitation density n_0 for specifying $QF(n_0)$ requires knowledge of absorption coefficient at 6.1 eV. Extraction of the nonlinear rate constants requires model assumptions described in Sect. 10.4. The insulators we have studied that exhibit 2nd order quenching also exhibit self-trapping of excitons, so the analysis is given in terms of an immobile excited species yielding time-dependent $K_2(t)$ [8] listed in units 10^{-15} t$^{-1/2}$ cm^3 s$^{-1/2}$. The materials exhibiting 3rd order free-carrier quenching kinetics have mobile electrons during the quenching (even though holes self-trap in most of the halides). Thus the 3rd order materials can be approximately treated as maintaining a uniform distribution of interacting species during the quenching. The rate constant K_3 in such a case is time-independent. NA means that a population quenching by the corresponding kinetic order was not produced significantly by 6.1 eV photons.

Figure 10.20 lists and plots Auger rate constants K_3 (cm^6 s^{-1}) measured by fitting PDR in iodide insulators and CdTe, along with published Auger rate constants in narrow-gap and wide-gap semiconductors measured by reflectivity [32] and photoluminescence [54, 59], respectively. The semiconductors form a sloping line expressing

Crystal	K_3 ($cm^6 s^{-1}$) $\times 10^{-29}$	Reference	E_g(eV)	ω_{LO} (s^{-1}) $\times 10^{13}$
InSb	1200	[72]	0.17	3.7
GaSb	7	[72]	0.7	4.3
GaAs	0.7	[73]	1.43	5
CdTe	0.5	PDR	1.44	3.1
$In_{0.15}Ga_{0.85}N$	0.2	[74]	2.64	14
$In_{0.09}Ga_{0.91}N$	0.14	[74]	2.83	14
SrI_2	0.7	PDR	5.5	2.6
NaI:Tl	3.2	PDR	5.7	3.47
CsI:Tl	6.6	PDR	5.8	1.79
CsI	4.5	PDR	5.8	1.79

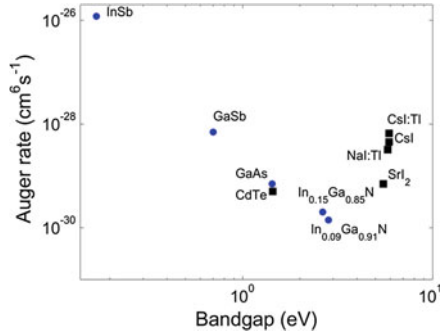

Fig. 10.20 Auger recombination rate K3 ($cm^6\ s^{-1}$) plotted versus bandgap (eV) [28]

a general "band gap rule" of decreasing Auger rate versus increasing band gap. The alkali iodide rate constants measured in this work are about 2 decades above the trend line and SrI_2 is about 1 decade above.

The basic reason for a band-gap dependence of Auger rate constants is that the energy given to the spectator electron or hole by e–h recombination increases with band gap. The corresponding final-state wavevector of the spectator particle increases accordingly, soon exceeding the range of wavevector $\boldsymbol{k}$ in the initial state and thus progressively closes down the possibility of satisfying $\boldsymbol{k}$ conservation. Our measured K_3 for CdTe falls in line with the other semiconductors, but K_3 for the iodides with larger band gap lies considerably above the trend extrapolated from the semiconductors.

There are at least two interpretations for the Auger rate constants found in alkali iodides from PDR measurements being higher than predicted by the band-gap rule extrapolated from semiconductors: (1) The hole in alkali halides [56] (and alkaline earth halides [56] including SrI_2 [59] is self-trapped. This localization to one lattice site removes the wave-vector conservation rule that otherwise severely limits possible final states of the Auger transition as band gap increases. If at least one of the interacting carriers is localized (e.g. self-trapped), the initial state already contains a spread of k components, so the Auger rate should not be so restricted. If we feel confident to press details of the data, we can point out that the Auger rate constant of SrI_2 is about 6 times smaller than the average of CsI and NaI. Since we have seen that SrI_2 quenches only by Auger recombination, the fact that it has a smaller Auger rate constant than alkali iodides seems to be yet another reason why SrI_2 has better proportionality and light yield. As a possible cause for the difference, one wonders if possibly the hole is not as completely localized in SrI_2 as in the alkali iodides. (2) The electron is hot during the free carrier phase when nonlinear quenching is assumed to occur. The carriers excited by laser in the photon density experiments remain out of equilibrium with the lattice, possessing up to 300 meV excess kinetic energy (i.e. up to 2300 K electron temperature) in alkali iodides and up to 1.6 eV in SrI_2 during the Auger recombination observed in the 6.1 eV PDR experiments [28]. It is known that lattice temperature accelerates Auger recombination particularly in

wide-gap materials, for the reason discussed just above. At high lattice temperature, phonons can provide the needed momentum in indirect Auger events, as is well known. Similarly, excess electron temperature should also increase the probability of conserving momentum for large energy transfers in Auger recombination. Although moderately hot electrons do not possess mean momenta as large as phonons, neither do hot carriers as sources of momentum imply a 4th participant (phonon) as required in indirect Auger processes. Both reasons support plausibility of the enhanced Auger rates observed in iodide crystals by the PDR experiment.

Yet another alternate interpretation could be that the premise of (10.25) and the surrounding discussion is wrong, i.e. that the free-carrier Auger (3rd order) quenching continues well beyond the time limit imposed by carrier cooling and trapping. Then a smaller K_3 rate constant would be deduced from the photon density response. But we would have to look elsewhere than hot electron thermalization to resolve the observed 3rd order/2nd order dichotomy of iodides vs oxides and to account for changing kinetic order upon tuning photon energy about 300 meV above the band gap in iodides. We have not found an alternative explanation for the latter observations

10.7 Calculating Local Light Yield Versus Excitation Density in Electron Tracks

The fitting of photon density response data to the general light yield expression in (10.26) based on the rate (10.1a), (10.1b) and (10.2) was shown to be reasonably successful in accounting for many of the parameter dependences and consequent curve shapes of laser-excited PDR in Sects. 10.4, 10.5 and 10.6. Now we want to see if such rate equations will also be capable of predicting the nonlinearities and consequent nonproportionality of scintillators excited by high energy electrons. Carrier diffusion takes on greater importance in electron tracks because of the strength and spatial complexity of the radial gradients of carrier density. Diffusion was already formally included in the rate equations (10.1a), (10.1b) and (10.2). We neglected the diffusion terms temporarily when analyzing laser photon density response of insulators, but now we should restore diffusion to the rate equations and carry it forward into light yield when modeling electron track excitation.

To get a conceptual physical feel for what influences scintillator performance, we will describe certain trends of light yield or proportionality that are linked to different aspects of the interaction of diffusion and nonlinear rate terms in the rate equations. The concepts of “rescue” from NLQ by temporary charge separation and by ambipolar diffusion out of the densest excitation zone are examples. The rate equations and the light yield (10.26) based upon them will be evaluated for an assumed cylindrical Gaussian electron track. The result is a plot we call Local Light Yield, Y_L, versus excitation density $n_0(x)$ where x is length along the primary track. The excitation density n_0 is specified on the axis of the electron track at the evaluated local position along the length of the track. Section 10.9 will detail the process of convolving this local light yield plot, $Y_L(n_0)$, with an excitation distribution function

$F(n_0, E_i)$ which can be obtained from Monte Carlo simulations (e.g. Geant4) [60]. The result of the convolution is a calculated curve of electron energy response versus initial electron energy E_i, to be compared to experimental electron energy response.

10.7.1 Dilution of e–h Density in the Track Core by Ambipolar Diffusion

References [13, 61, 62] developed a local light yield model based on the premise that by diluting excitation density and in some cases separating charges in the track core, diffusion of electrons and holes can affect the NLQ. It was found that the dominant diffusion effects manifest themselves differently in different classes of materials. We will illustrate in turn two competitions in which diffusion can preserve some excitations from the NLQ that would otherwise occur, thus preserving those excitations to have a chance at emitting light. The first competition is simple dilution of carrier pair density by ambipolar diffusion of electron and hole pairs to diminish the amount of dipole-dipole quenching that would otherwise occur in the dense track core if carriers and excitons were static. The essence of the track-dilution effect of ambipolar diffusion on NLQ is illustrated for the exciton rate equation (10.2) applied to an assumed cylindrical electron track in Fig. 10.21. To reiterate, it is simply a competition in whether excitons will more quickly reduce their concentration *N* by the quenching itself (a loss of the exciton *number*) or by diffusion to larger radius causing reduction of exciton *density* and thus of quenching rate, but not necessarily a reduction of exciton number.

The above consideration of ambipolar diffusion competing with NLQ suggests that one should look for correlations between experimental measures of energy-dependent quenching or nonproportionality and parameters related to carrier diffusion. A complete and reliable set of carrier mobilities is not yet available for the whole range of insulators employed as scintillators. Not only are they insulators, with attendant difficulty of establishing contacts and with defect traps producing space charge, but many of the interesting ones are also hygroscopic and difficult to measure. Therefore investigators have looked instead for correlations between nonproportionality and "stand-in" parameters or experimental quantities that are related to mobility and for which values do exist over a wide range of scintillators. We will briefly review three such surveys and the conclusions they reached.

Figure 10.22 shows a plot of an empirical proportionality measurement 1-σ_{NP} tabulated by Setyawan et al. [4] for oxide, halide, and ZnSe:Te scintillators. The experimental quantity σ_{NP} was defined by Dorenbos [11], as reviewed in Sects. 10.2, 10.6. The quantity plotted on the horizontal axis of Fig. 10.22 is the ratio of effective masses (chosen always to be greater than unity), $m_r = \max\left(m_h^*/m_e^*, m_e^*/m_h^*\right)$, from band structure calculations that were performed by Setyawan et al. [63]. They noted that the mainly oxide scintillators follow a trend versus the effective mass ratio m_r. The empirical function $1 - \sigma_{NP} = 0.33e^{m_r/2.8} + 0.77$ shown in the black solid line was superimposed as a guide for the eye. Setyawan et al also noted that a

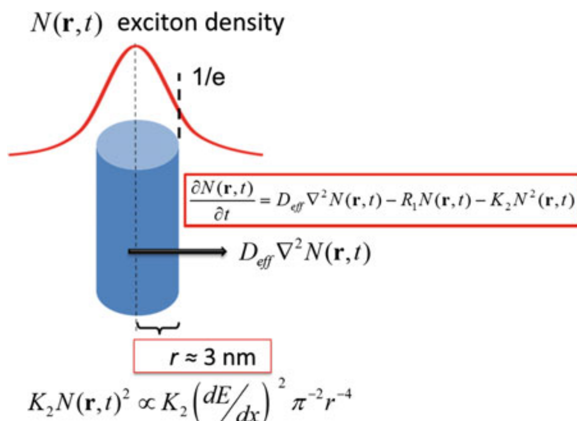

Fig. 10.21 Schematic statement of the competition between loss of luminescence due to nonlinear (e.g. 2nd order) quenching in an electron track, and ambipolar diffusion out of the densely populated quenching zone, which preserves population at lower density for possible later luminescence

group of mainly halide materials in the upper right are outliers, dramatically outside the empirical trend. We have added the red outline to highlight the outliers, with exclusion of ZnSe:Te. We showed in [13] that ZnSe:Te joins the oxides as part of an oxide and semiconductor trend in a physical model based on Fig. 10.21 when a modeled ambipolar diffusion coefficient is the independent variable rather than simply the effective mass ratio.

To look for a physical mechanism behind the trend such as seen in Fig. 10.22, [13, 61, 62] ran numerical simulations of ambipolar diffusion competing with exciton dipole-dipole quenching. The result shown as the solid red curve in Fig. 10.23 plots simply the fraction of excitations surviving NLQ (1-QF) versus ambipolar diffusion coefficient D_{eff}. The fraction (1-QF) of excitons surviving 2nd order quenching at a fixed rate constant K_2 was evaluated for on-axis excitation density of 10^{20} e-h/cm^3, characteristic of the approach to the end of an electron track. The values of D_{eff} were based on the calculated band effective masses in the oxides and ZnSe, with D_{eff} computed according to a model describing ambipolar diffusion as a sum of two carrier populations described in [13]: *excitons*, which scatter more weakly as neutral particles, and *carriers undergoing ambipolar diffusion* with stronger Coulombic scattering,. D_{eff} in alkali halides is dominated by low hopping mobility of the self-trapped holes. The D_{eff} so modeled scale with calculated effective band masses in a reasonable way and so represent a physical hypothesis that can be tested against the relative change of observed nonproportional light yield from material to material. The points plotted for various materials are experimental values of the same quantity 1-σ_{NP} tabulated by Setyawan et al. [63]. We added approximate 1-σ_{NP} values for two semiconductor detector materials where charge collection *vs* γ-ray energy was substituted for light yield. The red solid line is the fraction of excitations that sur-

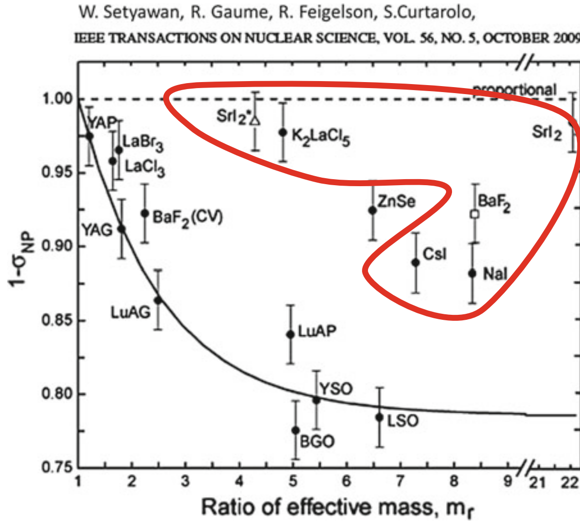

Fig. 10.22 An empirical measure of proportionality, $1 - \sigma_{NP}$, from gamma energy response (10.6) was plotted versus effective mass ratio $m_r = \max\left(m_h^*/m_e^*, m_e^*/m_h^*\right)$ by Setyawan et al. [63]. They plotted an empirical trend line through the mainly oxide points at *lower left*. We have added a *red line* encircling the halide outlier points, which Setyawan et al. also noted. Reprinted with permission [63]

vive dipole-dipole quenching simply by virtue of how far radially they can diffuse (depending on D_{eff}) in a set time, competing with a set rate constant of 2nd order quenching. If one looks just at band effective masses transcribed into a single plausible diffusion parameter D_{eff}, there emerges a consistent trend shared by the oxides and semiconductors. The conceptual conclusion of the empirical trend observed is that when D_{eff} is sufficient to get out of the track core faster than dipole-dipole quenching can occur, the excitations survive to have a chance at emitting light (oxide scintillators) or being collected as charge (the semiconductors). A semiconductor that emits light (ZnSe:Te) obeys the same trend.

There is a much more complete data set of refractive index measurements (n_r) across the scintillator materials than there is of carrier mobilities. If the refractive index is reported at a standard wavelength, e.g. sodium D-line, then the refractive index bears a qualitative inverse relationship with the band gap, based simply on the Lorentz oscillator model of dispersion. On the other hand, simple $\mathbf{k} \cdot \mathbf{p}$ theory predicts a qualitative inverse relationship between band curvature (inverse effective mass) and band gap. On this basis, we can expect that refractive index bears a qualitative proportionality to mobility ($\mu \propto n_{ref}$) when viewed across a broad range of materials. Semiconductors have higher visible index and higher carrier mobilities than insulators. Wide-gap insulators have rather flat bands and low carrier mobilities along with lower visible index in general.

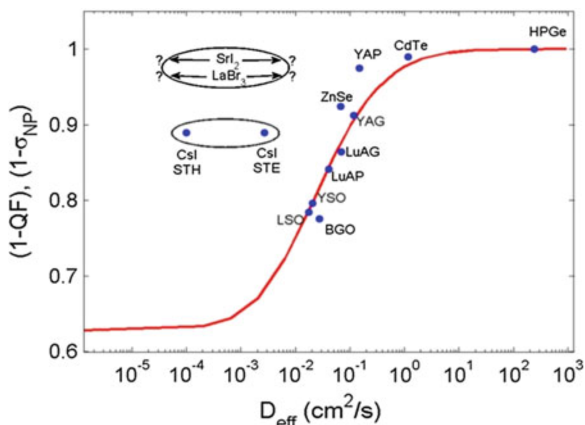

Fig. 10.23 The *solid red curve* plots results of survival against the model of NLQ illustrated in Fig. 10.21 evaluated for $r_0 = 3\,\text{nm}$, $t_{NLQ} = 10\,\text{ps}$, $n_{0excited} = 10^{20}\text{e} - \text{h/cm}^3$ as a function of ambipolar diffusion coefficient D_{eff}. Reprinted with permission [13]. The points plot empirical $1-\sigma_{NP}$ measures of energy dependent light yield (or collected charge in CdTe and Ge) versus D_{eff} computed for each material from band effective mass

Khodyuk and *Dorenbos* plotted a measure of nonproportionality, derived from photon energy response, versus refractive index within various families of 33 scintillator materials [18]. There was a consistent correlation. Higher refractive index, also implying higher carrier mobility, was found to correlate generally with better proportionality. Alkali halides obeyed their own trend line, with a slope different from the trend of oxides vs index. In that sense, the phenomenon of halides as outliers to the oxide trend was found in the survey of [18] as well.

Yet a fourth survey finding a general qualitative correlation between higher carrier mobility and better proportionality is that of Singh [64].

But the occurrence of significant outliers in both of Figs. (10.22 and 10.23) begs attention. Two observations are apparent:

(1) Experimental values of the parameter $(1 - \sigma_{NP})$ vary in agreement with the solid line prediction of simple competition between NLQ and radial diffusion in the oxide scintillators and semiconductor materials plotted. This suggests that thermalized ambipolar diffusion is an adequate treatment of diffusion-dependent light yield in oxide scintillators.
(2) On the other hand, many of the halide materials depart drastically from the model prediction versus D_{eff}. Ambipolar D_{eff} is very low in alkali halides because of self-trapping of holes and excitons. Thus severe NLQ leading to small (1-QF) and small $(1 - \sigma_{NP})$ should be expected, according to the plotted red line. But the experimental $(1 - \sigma_{NP})$ is not correspondingly bad for the halide scintillators that comprise the outliers. We will show in the following discussion that the ambipolar diffusion *versus* NLQ model is inadequate for an accurate description of the halides, for two important reasons: (a) Metal halides often exhibit hole

self-trapping [56]. Electrons and holes will tend to be separated by their very different diffusion rates in the track gradient, so treatment by ambipolar diffusion is not adequate. (b) Metal iodides and even bromides and chlorides have substantially lower optical phonon frequencies than oxides and fluorides. Therefore hot electrons thermalize more slowly in the iodides and heavier halides generally. Trapping probability (including that of electrons on holes) is very small until the electrons thermalize. See Sect. 10.4.2. Furthermore electron transport is faster and the diffusion range larger during the hot-electron phase. We shall see that the result of factors (a) and (b) together is that charge separation is a dominant effect in the halides and especially iodides, but not the oxides. It is therefore understandable that the heavier halides will follow a different trend with effective mass ratio or modeled ambipolar diffusion coefficient than do the oxides and fluorides.

10.7.2 Effects of Charge Separation

The charge separation caused by diffusion of electrons and holes at different rates can vary in characteristic ways depending on the material, as illustrated in Fig. 10.24 for a case typical of alkali halides. The holes are self-trapped in alkali halides. Based on hopping rates, they can be assumed to stay near their places of initial formation for the tens of picoseconds time scale important for NLQ. Recent experiments [28] and calculations [35, 65] agree on a hole distribution radius of about 3 nm in alkali halide electron tracks, which is represented schematically as a cylinder of fixed radius versus excitation density in Fig. 10.24. The funnel shaped contour represents the electron radial distribution at each value of hole and electron density after diffusion of electrons at lattice temperature occurs until there are no further changes [22]. The funnel shape results from the *collective* Coulombic attraction increasing as the number of holes near the axis increases. At the left end, representing low density of carriers early in an electron track, the electric field attracting electrons to the holes is not sufficient to restrain the electrons from diffusing widely and creating charge separation at equilibrium, roughly analogous to the space charge layer in a p-n junction [22, 35]. At the right end, representing high carrier densities near the track end, collective Coulomb attraction strongly limits the charge separation of the electron and hole distributions, i.e. a much thinner space charge layer in the cylindrical geometry. The detailed results and analysis supporting this description were given in [13, 22].

In the numerical modeling of [22, 61] that first led to the funnel track depiction of electron distribution, the electrons were modeled as diffusing outward from the $\sim$3 nm cylinder of initial electron-hole pair production and approaching the equilibrium diffusion profile from the inside outward. Shortly we shall discuss the fact that hot electrons produced in electron tracks in iodide and other heavier halide scintillators travel outward considerably farther than the $\sim$10 nm radius of the equilibrium funnel track shown (for CsI numerical simulations at $n_0 = 2 \times 10^{18}\,\mathrm{eh/cm^3}$) on the left end of Fig. 10.24. In such a case (e.g. CsI), the far-flung electrons will

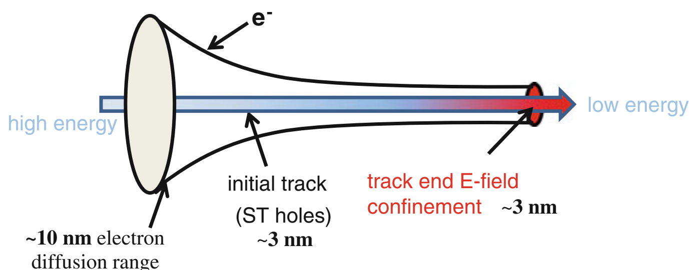

Fig. 10.24 Illustration of the electron distribution radius established by thermalized diffusion to electrostatic equilibrium when the holes self-trap near the track core. The electron track radius shrinks as carrier density increases going from left to right from (schematic) beginning to the end of the track

diffuse backward toward the self-trapped holes on the track axis after thermalization to establish the equilibrium diffusion profile as depicted in Fig. 10.24. This collective recapture of far-flung electrons during thermalized diffusion of electrons in the electric potential of a "line charge" of self-trapped holes near the axis occurs over a distance much larger than the single-hole Onsager radius, as discussed shortly.

Wang et al. calculated distributions of hot electrons resulting at the end of electron thermalization around tracks in CsI and several other scintillators [2]. Such hot electrons start the diffusion with energy up to one band gap above the conduction band minimum, and so their diffusion range during the thermalization period is not strongly restrained by the Coulomb attraction to the holes, which were presumed to remain near the axis. The radial electron distribution established during the hot electron diffusion phase thus does not have the funnel shape of Fig. 10.24, but more of a constant radius that can be much larger than the hole radius. In CsI, for example,the most probable radius of stopped hot electrons upon first reaching thermalization with the lattice temperature in CsI was found to be about 60 nm in CsI [2]. The tail of the distribution extends out to 250 nm in CsI. Wang et al. [2] called "stopped electrons"those whose last phonon-mediated energy loss brought them within kT of the conduction band minimum. Such electrons are thermalized to lattice temperature, but not permanently stopped. What happens to them, *vis a vis* the hole distribution, during recombination by either thermalized band diffusion or de-trapping and hopping transportdepends on the cylinder of self-trapped hole charge near the axis in alkali halides, for example?

10.7.3 Recombination in the Field of a Cylinder of Self-Trapped Holes

A cylinder of charge viewed from outside, or simply a "line charge", has a much longer range of interaction than a single point charge. The radial electric field of a

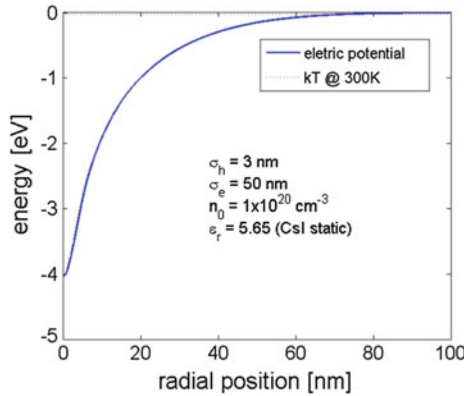

Fig. 10.25 Electrostatic potential of a Gaussian cylinder of holes and electrons, where the self-trapped hole distribution has a 1/e radius of 3 nm and the electron distribution has a 1/e radius of 50 nm. There are equal numbers of electrons and holes, and the hole density on-axis is $1 \times 10^{20} \mathrm{cm}^{-3}$

cylinder charge of infinite length falls off radially as 1/r and its potential is logarithmic in r. There is no distance from which an electron could escape such a positive line charge, but of course electron tracks are not infinite lengths of straight cylinders and there is screening by the electrons inside the radius considered. A cylinder charge of finite length L has potential

$$V(r) = \frac{\lambda}{4\pi\varepsilon_0} \ln\left[\frac{L + (L^2 + r^2)^{1/2}}{r}\right]_{\infty}^{r} \tag{10.27}$$

There is a finite escape radius, but it is substantially larger than the Onsager radius of a point charge (single hole), as we shall illustrate in Fig. 10.25. The Onsager radius of a single electron in the field of a single hole is found by equating the potential function to –kT and solving for the radius, which is, e.g., 9.9 nm at room temperature in CsI with $\varepsilon = 5.65$. We have calculated the potential for $n = 10^{20}$ self-trapped holes/cm^3 on axis of a 3 nm radius Gaussian cylindersurrounded by an equal total number (linear density λ) of electrons contained in a 50 nm radius Gaussian cylinder (chosen to simulate a distribution of hot electrons in a track). The potential function is plotted in Fig. 10.25 along with a horizontal dashed line at –kT. The intersection fixes the cylindrical Onsager radius of the collective holes in this cylinder segment as $\sim$70 nm at room temperature, including the shielding effect of the electron distribution. The conclusion is that most of the hot electrons at their point of equilibration with the lattice temperature still lie within the Coulombic collection range of the line charge of self-trapped holes in this example of an alkali halide. They are not "stopped" unless captured in a deep trap. If free or in a shallow trap, the thermally equilibrated electrons should diffuse back toward the equilibrium diffusion distribution depicted in Fig. 10.24 unless deeply trapped or recombined during the process.

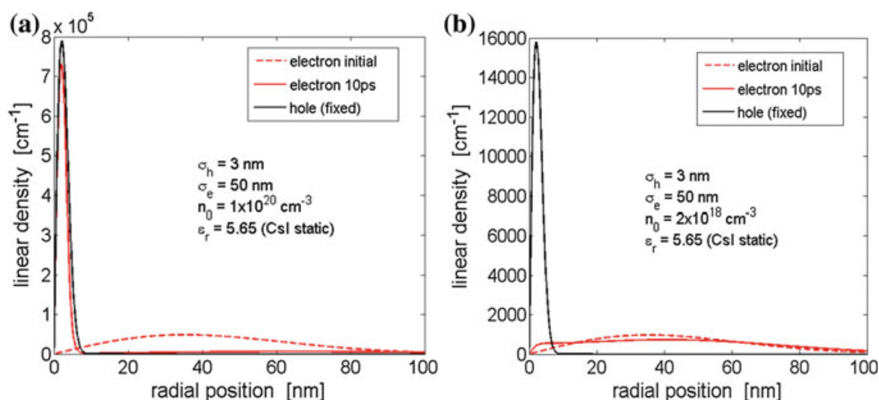

Fig. 10.26 Self-trapped holes are distributed in a Gaussian cylinder of radius 3 nm, and on-axis density at **a** 1×10^{20}eh/cm^3 and **b** 2×10^{18}eh/cm^3 shown by the *black solid line* in each figure. Electrons are distributed initially with a 1/e radius of 50 nm, shown by the *dashed line* with a peak at 32 nm in the $rn(r)$ azimuthally integrated radial density per unit track length ("linear density"). The electron distribution after thermalized diffusion and dipole-dipole quenching for 10 ps is shown in each case by the *red solid line*

To illustrate this, we conducted the following simulations of the diffusion of electrons in the field of a cylindrical core of self-trapped holes of Gaussian radius 3 nm. The electrons are started at specified Gaussian initial distributions labeled in the figures, and their subsequent diffusion in the electric field of the charge cylinder of holes is calculated. In Fig. 10.26, the quantity $rn(r)$ giving linear density (cm^{-1}) is plotted, where $n(r)$ is the radial hole or electron density as identified in the legend. The material parameters for this simulation are those of CsI as discussed in [22]. The self-trapped holes are stationary in the 3 nm Gaussian cylinder distribution appropriate for STH. In Fig. 10.26a, the on-axis excitation density is 10^{20} eh/cm^3, representative of densities near the end of an electron track. The initial electron distribution tested is a Gaussian $n(r)$ with significant population extending out to about $r = 100$ nm as shown by the dashed curve. The peak of $rn(r)$ is around 30 nm. This is roughly representative of the distribution of "stopped" or thermalized hot electrons in CsI found in the KMC simulations by Wang et al. After diffusing as thermalized conduction electrons for 10 ps, the final electron distribution is shown by the solid red curve. Figure 10.26a shows that the thermalized electrons have diffused backward from large radial distances under electric field attraction to rejoin the holes in their 3 nm cylindrical distribution. The simulation included 2nd order quenching as well as diffusion, so the area under the final electron distribution is smaller than the initial hole distribution.

Figure 10.26b shows the corresponding scenario when the on-axis excitation density is only 2×10^{18}eh/cm^3, representative of the high energy part of an electron track. The electrons are started from the same large radius, but now after 10 ps of

diffusion, they remain close to the starting distribution extending out to 100 nm. Only a few have been pulled in to form a small bump overlapping the holes.

The rate of dipole-dipole or Auger NLQ is strongly attenuated by the *charge separation* evident at the left end of Fig. 10.24. Electrons and holes must be present at the same location for either of these quenching processes to occur. Radiative emission of scintillation light is also attenuated by such charge separation. However, radiative emission can occur on a much later time scale, still within the useful scintillation pulse width, as trapped electrons and holes recombine by hopping migration in the mutually attractive space-charge field. This hopping migration occurs gradually and at much lower average population of overlapped electrons and holes which would be subject to NLQ, so the delayed recombination has much less competition from the NLQ channels. In fact, experiments have indicated negligible lifetime shortening by NLQ in the excited activator population [22, 24]. Toward the right side of the track illustrated in Fig. 10.24, the electrons and holes overlap strongly and are subject to higher rates of both NLQ and radiative recombination. But Auger recombination goes as the 3rd power of overlapped electron-hole density, whereas binary recombination to form excitons and emit light goes only as 2nd order in n, so quenching wins at the highest densities. Roughly in the middle of the trajectory, the carriers are confined together well enough to benefit from radiative recombination, but not so closely as to be dominated by Auger quenching. One then sees conceptually how the "halide hump" of light yield in electron energy response can arise when holes are self-trapped near the track axis. (Recall in Sect. 10.4.2 that thermalization during quenching complicates this picture a bit, but leaves the bottom line basically correct).

10.7.4 Effect of Charge Separation During Thermalized Diffusion on Light Yield

Effects of charge separation on light yield have been modeled in terms of the ratio of thermalized electron and hole mobilities, μ_e/μ_h and the fraction of free electrons captured on deep traps, k_1. If, as in alkali halides, the electron mobility is much greater than the hole mobility, the electrons will outrun the holes in the radial concentration gradient of the modeled cylindrical track, trapping separately as independent carriers in preference to pairing as excitons, up to the time of eventual de-trapping and recombination on activators or defects. The excitations that are captured as excitons on an activator will emit promptly. In contrast, the excitations that are captured as separated electrons and holes on different activators or defects must recombine more slowly by de-trapping mechanisms. During that process, the fraction of independently trapped carriers (*IF*) will be exposed to deep trapping, particularly by charged defects having a large cross section for independent charge carriers. *IF* in general changes along the track length due to changing electric field effects that accompany the changing excitation density. Values of IF in CsI:Tl were numerically simulated in

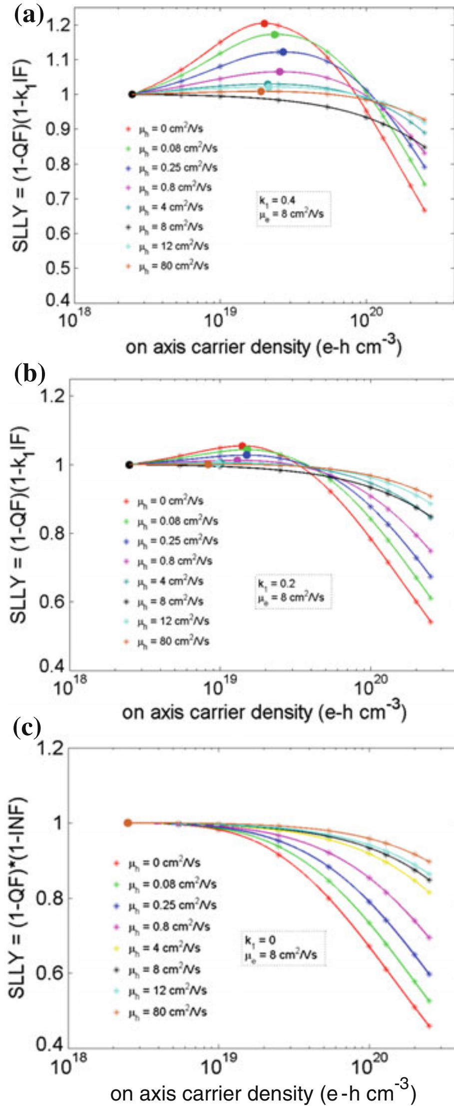

Fig. 10.27 Simulated local light yield, SLLY $= Y_L(n_0) = (1 - QF)(1 - \mathrm{k}_1 IF)$ versus on-axis excitation density n_0 is plotted for different hole mobilities as listed. The electron mobility is fixed at 8 cm^2/Vs. The linear quenched fraction k_1 is 0.4 in (**a**), 0.2 in (**b**), and 0 in (**c**)

[13, 22, 61]. The trapping hazard is represented by the multiplier of fraction IF, called the linear quenched free-carrier fraction k_1 [22]. The survival fraction is thus $(1 - k_1 IF)$. Plotting $(1 - k_1 IF)$ versus on-axis excitation density n_0 for several different mobilities μ_h relative to fixed μ_e shows a rising trend versus n_0.

In some ways analogous to the product of "Birks and Onsager" terms in the model described by Payne et al. [9, 16], the product $(1 - QF)(1 - k_1 IF)$ approximates the overall probability of an electron-hole pair surviving nonlinear quenching (QF) in the track core, followed by the probability of being driven to independent status by unequal diffusion and yet surviving deep trapping to recombine radiatively. Figure 10.27a–c plots the simulated local light yield in the model of [13, 22, 61] for a series of hole mobilities μ_h while holding $\mu_e = 8\,\text{cm}^2/\text{Vs}$. Without a significant mismatch of μ_e and μ_h, there is no hump. But also without some linear quenching k_1, there is no hump either.

10.7.5 Effect on Light Yield of Charge Separation Due to Hot Electron Diffusion

The dramatic difference between the hot-electron thermalization range and the restricted radial distribution of self-trapped holes produces even greater charge separation than in the thermalized model (Fig. 10.27) above. The charge separation achieved during the hot electron phase can be large even at high carrier densities near the track end because the diffusion of hot electrons is less sensitive to electric field attraction toward the track core of self-trapped holes. In halide crystals with slow electron thermalization and hole self-trapping, this wide radial dispersal of some hot electrons will occur first during thermalization, and should be followed by return of thermalized electrons toward the equilibrium diffusion distribution (funnel-shaped track) illustrated in Fig. 10.24. In crystals with fast carrier thermalization such as oxides, the thermalized electrons and holes diffuse outward from the initial track more or less together, with mobility ratios (related to effective mass ratios) determining the amount of charge separation, which will be smaller than in crystals with hole self-trapping.

Basically, all the effects of charge separation discussed earlier, i.e. protection from prompt NLQ and observation of a halide hump in electron energy response, can be expected to be magnified in cases where a large radial range of hot electrons exists together with hole self-trapping. This clearly applies in iodides and bromides where the anion is heavy enough to ensure a low optical phonon frequency that in turn dictates slow thermalization. Conversely, oxides and fluorides have high ω_{LO}, and thus fast thermalization ($\sim$0.5 ps or less) [2], meaning they should be well described by the model of thermalized band-edge diffusion [22] discussed in Sect. 10.7.1. We suggest that this is a large part of the reason why the oxides fit the thermalized diffusion trend line in Figs. 10.22 and 10.23 so well, whereas the halides appear as outliers. We further suggest that it is the reason fluorides behave more like oxides in the shape of electron energy response curves and light yield. Empirically, chloride compounds seem to behave more like the iodides and bromides than like the oxides and fluorides, which seems plausible given that the chlorine mass is about double the oxygen and fluorine mass.

Kirkin, Mikhailin, and Vasil'ev show that the thermalization rate in crystals with a unit cell basis larger than 2 atoms will be accelerated by phonon emission and absorption involving the multiple LO-phonon modes, so that more complex crystal structures should have faster hot-electron thermalization [32]. Kozorezov et al. also discussed the role of hot electron diffusion in scintillators, paying additional attention to a bottleneck in dissipation of generated phonons [66].

It remains to explain the quite different proportionality and light yield found among different members just within the iodide family. Alkali and alkaline earth iodides have similar values for many of the parameters considered to control proportionality and light yield. NaI:Tl and SrI_2:Eu comprise a case in point. Most of the multivalent halides with excellent performance like SrI_2:Eu have complex unit cells (e.g. 24-atom basis in SrI_2) and corresponding dense and flat conduction bands. Others in the group of high-performance scintillators like $LaBr_3$:Ce and $LaCl_3$:Ce contain lanthanum in the host which contributes a dense and flat set of 4f conduction bands about 3.5 eV above the cbm. A common element in the favorable materials is having a lot of flat conduction bands in the phonon-cooling range of energy, whereas the simple binary alkali halides have sparser bands more similar to free electron dispersion over significant ranges. The band structures of NaI and SrI_2 in the energy range of phonon cooling of hot electrons from $E_{cbm} + E_{gap}$ to E_{cbm} are compared in the top panels of Fig. (10.28). It appears visually that hot electrons have higher group velocity on average in NaI than in SrI_2. Following up on this suggestion, Li et al. calculated the distribution of group velocities from first-principles band structure over the hot-electron range from E_{cbm} up to $E_{cbm} + E_{gap}$. The results confirm that the averaged hot electron speed in SrI_2 over the energy range from E_{cbm} to $E_{cbm} + E_{gap}$ is about 5 times smaller than in NaI [71].

To the extent that both NaI and SrI_2 are iodides and should thus have similar thermalization times, the hot electron group velocity is a reason coming from electronic structure of the host crystal for finding smaller hot electron range in SrI_2 than in NaI. The effect on charge separation, and consequently host structure dependence of the linear quenched fraction k_1, is illustrated schematically in Fig. 10.28c. For an assumed equivalent background of deep traps and similar thermalization times, SrI_2 with smaller radial distribution of hot electrons (based on smaller v_g) has a shorter path for thermal diffusion through the deep traps on the way back to eventual recombination with self-trapped holes in the track core. Therefore it has a smaller linear quenched free-carrier fraction k_1. Just as in the thermalized model discussed above, small k_1 leads to higher light yield ($LY \leq 1 - k_1$) and flatter electron energy response curve.

10.8 Calculating Electron Energy Response

In the experimental characterization of energy-resolving scintillator performance, the ratio of total light emission to the initial energy of the electron being stopped, often called "electron response", can be measured by several experimental methods including Compton coincidence and K-dip spectroscopy. These were introduced and

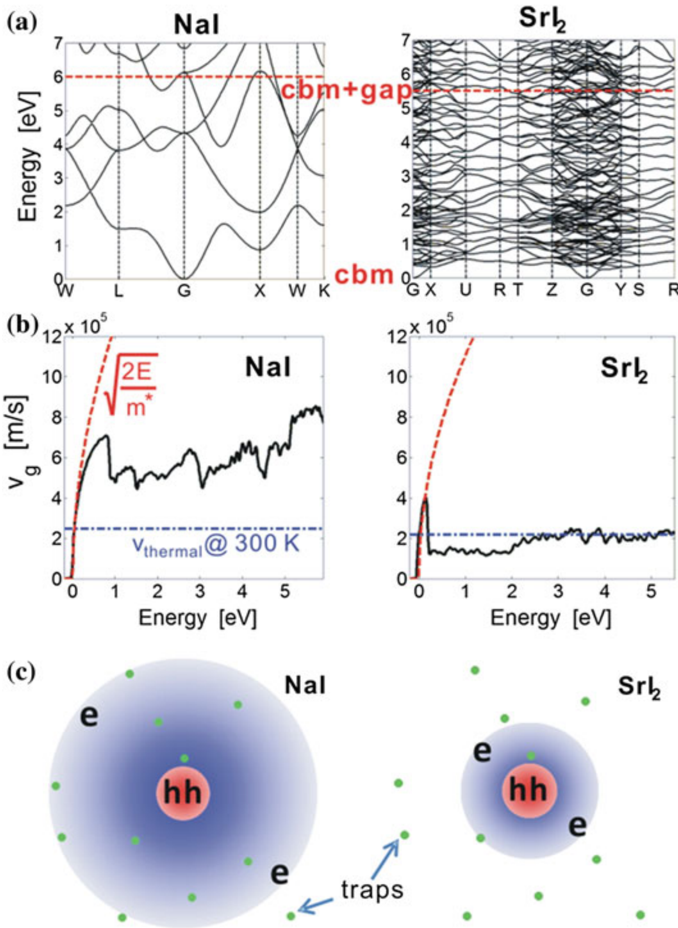

Fig. 10.28 Comparison in NaI and SrI_2 of **a** conduction band structure, **b** group velocity distribution *versus* energy, and **c** schematic representation of electron track cross sections in halides with *self-trapped holes* at the core, and thermalization range of hot electrons represented by the larger radial distributions. On a longer time scale, the electrons will diffuse back toward the holes through a distribution of traps (shown as *dots*), determining the linear quenched fraction k_1. Reprinted with permission [71]

illustrated in Sect. 10.2. Electron energy response such as measured in the high-throughput SLYNCI experiment, [1] correlates light yield $Y_e(E_i)$ with total stopping of a Compton electron of initial energy E_i. K-dip spectroscopy[2] yields data to lower electron energy by correlating $Y_e(E_i)$ with the kinetic energy of K-shell photo-electrons excited by tunable synchrotron radiation. The scintillator is said to exhibit intrinsic nonproportionality of response if $Y_e(E_i)$ varies with E_i. Because of the non-porportionality, its energy resolution will be degraded by fluctuations in the energy deposition process [3].

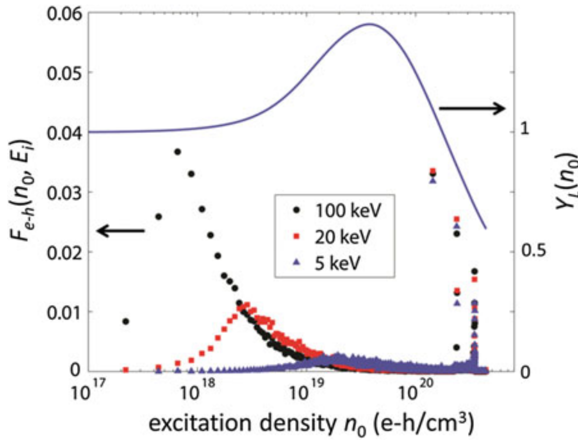

Fig. 10.29 Plotted points (*left axis*) are distributions $F_{e-h}(n_0, E_i)$ of on-axis e–h density n_0 for 100, 20, and 5 keV electron tracks in NaI. *Solid blue curve* (*right axis*) is local light yield $Y_L(n_0)$ for NaI modeled with $k_1 = 0.47$, 3rd order kinetics with $K_3 = 3 \times 10^{-30}\text{cm}^6\,\text{s}^{-1}$, and other parameters in Table 10.2. Reprinted with permission [27]

The previous section dealt with modeling local light yield $Y_L(n_0)$ versus initial excitation density n_0, as a function of measured rate constants, diffusion coefficients, and free carrier fraction depending on thermalization rate. One must convert from $Y_L(n_0)$ to electron energy response $Y_e(E_i)$ in order to quantitatively compare the modeled local light yield to experiments done with electron or gamma ray excitation. The lower curves plotted as points in Fig. 10.29 are the results of Monte Carlo simulations of the electron energy deposition using Geant4. [60] at each n_0 in NaI:Tl at three different E_i of 100, 20, and 5 keV. The low-energy Penelope electromagnetic models were used with a 100 eV threshold. The quantity plotted is $F_{e-h}(n_0, E_i)$, the fraction of all e-h excitations created in a bin around n_0 by stopping of an electron of initial energy E_i. The plot is the average of 2000 simulations at the lowest E_i and 200 at the highest E_i. Note that both $Y_L(n_0)$ and $F_{e-h}(n_0, E_i)$ are functions of n_0. The convolution integral

$$Y_e(E_i) = \int_0^{n_0 max} F_{e-h}(n_0, E_i) Y_L(n_0) \mathrm{d}n_0 \qquad (10.28)$$

yields the predicted electron energy response for direct comparison to Compton coincidence or K-dip experimental light yield as a function of initial particle energy, $Y_e(E_i)$.

The parameters used to calculate local light yield curves for NaI:Tl and SrI_2:Eu are listed in Table 10.2. The column labeled "measured NaI:Tl" gives values from the literature as referenced. It can be seen that the "used" and "measured" columns for NaI:Tl are the same except for slight differences in β and E_{gap}. The column "method

Table 10.2 Tabulated parameters for NaI:Tl and SrI_2:Eu.

	Used NaI:Tl	Measured NaI:Tl	Method NaI:	References	Used SrI_2:Eu
$\boldsymbol{k_1}$	0.47	0.47	$LY \leq 1 - k_1$	[67]	0.04
$\boldsymbol{K_2(t)}$**(exc.)** ($cm^3\ t^{-1/2}\ s^{-1/2}$)	NA	0.7×10^{-15}	PDR 5.9 eV	[28]	NA
$\boldsymbol{K_3}$**(e-h)** ($cm^6\ s^{-1}$)	3×10^{-30}	3×10^{-30}	PDR 6.1 eV	[28]	1×10^{-30}
$\boldsymbol{\alpha}$ (cm^{-1})	4×10^5	4×10^5	thin film	[34]	4×10^5
$\boldsymbol{r_{NLQ}}$ (nm)	3	3	PDR, K-dip	[28]	3
$\boldsymbol{\mu_e}$ (cm^2/Vs)	10	10	photocond.	[69]	10
$\boldsymbol{\mu_h}$ (cm^2/Vs)	10^{-4}	10^{-4}	STH hop 295 K	[70]	10^{-4}
$\boldsymbol{\beta}$	2.5	2–3		[11]	2.3
$\boldsymbol{E_{gap}}$ (eV)	5.8	5.9		[28]	5.5

NaI:Tl" gives short phrases to indicate the experimental method from which the parameter value came.

There are two ways of getting the linear quenched fraction k_1 from measurements: (1) Calculate it from a model based on concentration of deep traps and their cross sections, as well as the range of diffusion through a given set of traps depending on thermalization time and velocity of hot electrons. (2) Empirically measure an upper limit for k_1 directly from total light yield without a microscopic model. The latter method is used to get k_1 in the present calculations. The total light yield as a fraction of excitations cannot exceed $(1-k_1)$, i.e. $Y_T/Y_{max} \leq 1-k_1$, where Y_T is the experimental total light yield and Y_{max} is the theoretical limit determined by βE_{gap}. In NaI:Tl, $Y_T = 38,000$ photons/MeV gives $k_1 \leq 0.47$, taken here as $k_1 \approx 0.47$. The calculations assumed 0.1 % Tl doping in NaI. For comparison, CsI:Tl has $k_1 \approx 0.2$ from published $Y_T = 54{,}000$ ph/MeV, $K_3 = 2 \times 10^{-30}\,cm^6 s^{-1}$ from z-scan, and $\alpha = 2.7 \times 10^5\,cm^{-1}$, $\mu_e = 8\,cm^2/Vs$, $\mu_h = 10^{-4}\,cm^2/Vs$, and $\beta = 2.5$. The total light yield in SrI_2:Eu is so high (80,000 ph/MeV) that it is very close to the theoretical limit obtained by dividing the initial electron energy by the average energy to create one electron-hole pair, usually represented by βE_{gap} with $\beta \approx 2.5$. Accordingly, k_1 must be quite small in SrI_2, estimated here as $k_1 \approx 0.04$.

Solving (4) with the full set of F_{e-h} distributions and the parameters in Table 10.2 gives the calculated electron energy response $Y_e(E_i)$ for NaI:Tl shown with black circular points in Fig. 10.30a. Experimental SLYNCI Compton coincidence and K-dip $Y_e(E_i)$ for NaI:Tl are also plotted in Fig. 10.30b. The Compton coincidence curves are the well-known set measured on many different NaI:Tl samples, giving the spread in energy response experimental curves.

Similarly, we compare the calculated $Y_e(E_i)$ for SrI_2:Eu with both SLYNCI [15] and K-dip [17] in Fig. 10.30b. Due primarily to the hygroscopicity of SrI_2:Eu, some of its physical parameters used in the diffusion and quenching model have not yet been measured. The important K_3 and k_1 parameters and the track radius $r_0 \approx 2.8$ nm have been deduced from measurements in SrI_2:Eu, and the other parameters have been assigned NaI values. The comparison of SrI_2:Eu calculations to experiment

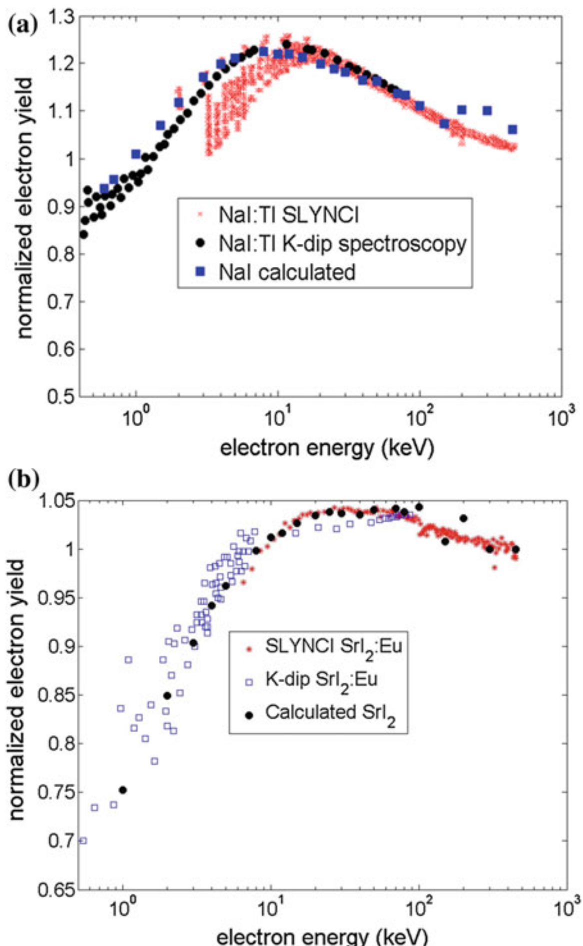

Fig. 10.30 Calculated electron energy response, $Y_e(E_i)$, for NaI:Tl **a** and SrI_2:Eu **b** compared to data from SLYNCI and K-dip. Calculated and experimental data are normalized at 70 keV

thus amounts to a test of the importance of K_3 and k_1 in determining its electron response relative to NaI. Self-trapped holes have been predicted in SrI_2:Eu, [59] so the assumption of immobile holes is made. The small value of $k_1 \approx 0.04$ dictated by light yield close to the theoretical limit in SrI_2:Eu limits the magnitude of the "hump" in electron response, which improves proportionality. This is in contrast to NaI:Tl which has a large k_1, therefore a large hump in electron response and lower light yield.

10.9 Toward a Design Rule: General Trends in Scintillator Proportionality and Light Yield Versus a Few Material Parameters

From the foregoing discussion, it should be possible to look at branch points between basic types of behavior of scintillator materials according to the value (high or low) of a few key parameters. In the following exercise, we will consider four such parameter choices in sequence as a "decision tree" to see if indeed it can predict general characteristics of proportionality and light yield based on a small number of parameters that are measureable apart from the scintillator proportionality measurement itself. If it can be confirmed, it is the beginning of a design rule for scintillator discovery and engineering.

The first parameter to be considered, therefore in some sense the most fundamental, is the (highest) LO phonon frequency. The corresponding branch point is diagrammed in Fig. 10.31, with experimental plots of PDR illustrating physical consequences of branching to high and low values of ω_{LO}. Low ω_{LO} in the right branch means that the carriers thermalize slowly relative to the time in which the main part of NLQ occurs. The basis for this conclusion is the experimental observation of *pure* third order quenching kinetics in the PDF data for CsI and SrI_2. Identifying 3rd order quenching with free-carrier Auger recombination, we conclude that in materials of the right branch, free carriers are too hot during the NLQ phase to become bound in exciton or trap states. Since the time for electron thermalization by LO phonons in iodide crystals has been calculated [2, 32, 33, 42] to be on the order of a few picoseconds, the above line of reasoning indicates that the main NLQ is complete within a few picoseconds. This conclusion is consistent with previous time-resolved data directly [27] and indirectly [31] related to NLQ in CsI. The bottom line for the decision is that free carriers dominate the NLQ process in the right branch of Fig. 10.31 corresponding to low ω_{LO}. Most iodides qualify as low ω_{LO}, although we saw in the PDR data of Fig. 10.11 that the light mass of sodium in NaI puts it in a category of mixed kinetic order, with free carriers and excitons apparently coexisting during nonlinear quenching. Heavy metal bromides and chlorides have not yet been run in the laser PDR experiments because of their larger bandgaps, but we tentatively lump them in the right branch based on ω_{LO} as the class of "heavier halides", especially when the halide is paired with a heavy metal. As a graphic illustration with real data, Fig. 10.31 includes PDR of SrI_2 as a paradigm of the materials classified in the right branch.

The left branch is for high ω_{LO}, characteristic of oxides and fluorides. High ω_{LO} causes rapid carrier thermalization. The PDR experiments on the oxides (BGO and $CdWO_4$) that have been measured exhibited pure 2nd order quenching, consistent with dipole-dipole annihilation. This indicates that excitons in some electronic state had formed before the main part of NLQ. BGO is shown as the example of a PDR curve characterizing materials in the left branch. The PDR comparison in the bottom center of Fig. 10.31 emphasizes the point that both proportionality and light yield are already affected in an important way by this first material branch point, controlled

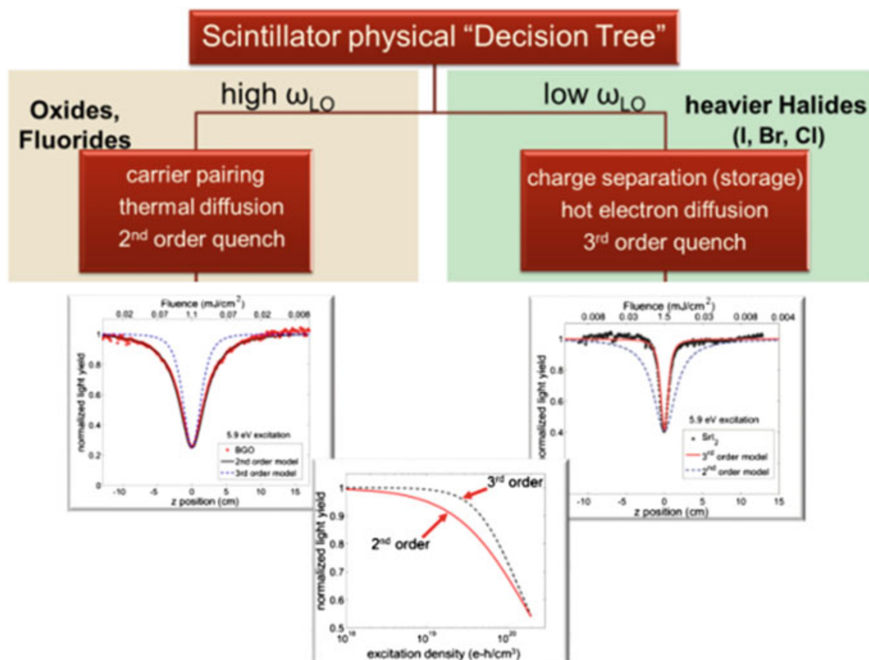

Fig. 10.31 Top level branching between exciton and thermalized ambipolar diffusing pairs on the *left* and hot free carriers on the *right*, according to high or low LO phonon frequency [42]

by the value of ω_{LO}. The winner in both proportionality and light yield at this point is the right branch simply because of the flatter and more advantageous 3rd order PDR curve. Indeed, the known scintillators with combined highest light yield and best proportionality, such as SrI_2:Eu, BaBrI:Eu, and $LaBr_3$:Ce should fall in the right branch, according to ω_{LO}. So do some more modestly-performing scintillators like NaI:Tl, CsI:Tl, but we have not yet considered the second-level branching.

Materials classified in the left branch have carriers that are thermalized (at least within one LO phonon energy of kT), and possibly paired as some bound state of electron and hole, before the main part of NLQ. Then it is reasonable to describe effects of diffusion around electron tracks in terms of ambipolar diffusion (coefficient D_{eff}) of thermalized carriers. This becomes the second-level branching parameter on the left side of Fig. 10.32 according to large or small D_{eff}. Large D_{eff} includes semiconductors used for luminescence (such as ZnSe:Te), and those used for charge collection detectors (high purity Ge, CdTe, CZT) which we include in the present survey by letting energy-dependent charge collection (Q) stand in for energy-dependent light yield (LY). YAP:Ce is also in the branch of large D_{eff} because the near equality of electron and hole effective mass (Setyawan et al. mass ratio $m_r = 1.2$ [12]) yields large D_{eff} relative to other oxide crystals [13]. Large D_{eff} allows carriers to escape the NLQ zone in the track core and thus gives a relatively flat electron energy response

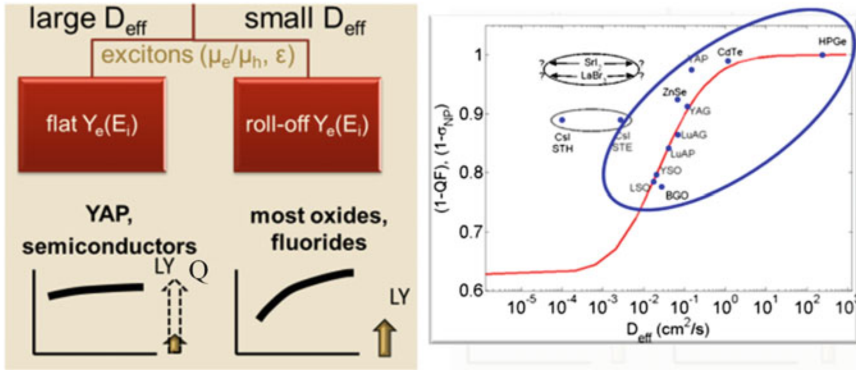

Fig. 10.32 Second level branching of thermalized carrier pairs and excitons according to large or small effective diffusion coefficient D_{eff}, correlating with schemiatic [42]

curve which is illustrated schematically at the lower left. Because of diffusing to low excitation density, the electron-hole radiative recombination suffers relative to defect trapping and so the light yield (LY) of semiconductor scintillator detectors, and YAP:Ce as well, is modest to low. Charge collection (Q) in semiconductors can be promoted by applied electric field and low defect concentration. Diffusion, albeit in different directions for electrons and holes in an applied electric field, is a good thing for charge collection. Characteristic schematic predictions of Q and LY in this class are indicated by the bar chart at lower left of Fig. 10.32.

The second-level right branch toward small D_{eff} in Fig. 10.32 applies to most oxides other than YAP:Ce, where higher hole mass begins to weigh on the ambipolar diffusion coefficient. Calculated band effective masses were used indirectly to represent or estimate D_{eff} or its stand-in, m_h/m_e, in [13] and [12]. Refractive index at the visible scintillation wavelength anticorrelates generally with band gap of the host, which in turn correlates with effective masses at both band edges. This was used in [18] to organize scintillators by refractive index in a way that amounts approximately to a stand-in for effective mass and therefore for carrier diffusion coefficients. In all three forms of experimental surveys of the nonproportionality (∼roll-off of electron energy response) among oxide scintillators, the trend was confirmed that lower effective diffusion coefficient implies greater nonproportionality, as a broad trend. [12, 13, 18]

The second level branching parameter on the right hand side shown in Figs. 10.33 and 10.34 should, for symmetry, be the diffusion coefficient for hot electrons, "hot D_e." We want to put it quantitatively in those terms in future work, combining quantitative thermalization rate and hot-electron group velocity as a function of energy to calculate hot $D_e(T_e, t)$ over the time and electron temperature interval of NLQ. For the time being, we have represented the hot electron diffusion coefficient as proportional to the square root of the calculated group velocity over the range of phonon cooling of hot electrons, and simply use hot electron group velocity v_g as

the second-level branching parameter on the right side in Fig. 10.34 [71]. Most of the halide scintillators that would be on the right side of the top-level branch also have self-trapped holes. Therefore hot electron diffusion implies wide separation of charges and further implies that de-trapping and diffusion over a relatively long time will be involved to recover radiative recombination of the initially separated hot electrons and self-trapped holes. If hot-electron v_g is large, as in NaI and CsI, the electrons returning toward the track core of self-trapped holes for radiative recombination have a long path through a minefield of defect traps (F centers, impurities, extended defects) that can prevent useful scintillation light. We could expect that the linear quenched fraction k_1 may be substantial in such cases. This is represented by the schematic hump in the generic electron energy response curve depicted at the lower right of Fig. 10.33. If the value of v_g and hot electron diffusion range is small, as in crystals with complex unit cell like SrI_2 and/or having flat La 4f lower conduction bands like $LaBr_3$, the hot electrons do not go out as far radially and so have a shorter path through the traps toward recombination. The generic predicted response is therefore flatter and higher light yield, both attributable to smaller k_1 due to smaller diffusion path. Notice that materials in this latter classification, including, e.g. SrI_2:Eu, BaBrI:Eu, and $LaBr_3$:Ce, get positive recommendations for good proportionality and light yield at *both* levels of branch points in Fig. 10.34: At the first branching, free carrier dominance in this group leads to pure 3rd order quenching, which has inherently a flatter shape over most of the photon density response. This implies flatter electron energy response and higher light yield. Then at the second-level branch point, small hot-electron diffusion range (small v_g) implies smaller linear quenched fraction k_1 and this means flatter electron energy response and higher light yield yet again. The left second-level branch under the right top-level branch is dou-

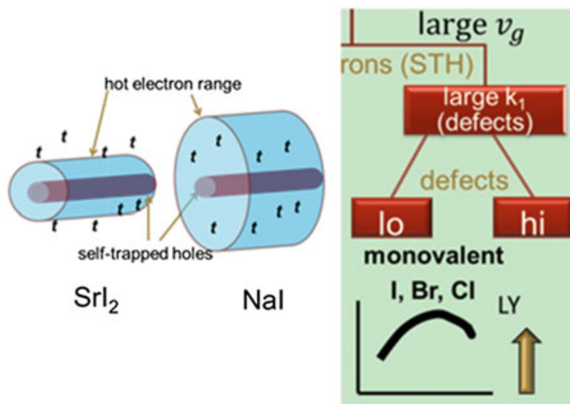

Fig. 10.33 Second level branching on the right side according to hot electron group velocity v_g, standing in for hot electron diffusion coefficient. Existence of self-trapped holes in most halides and concentration of defects also play roles as discussed [42]

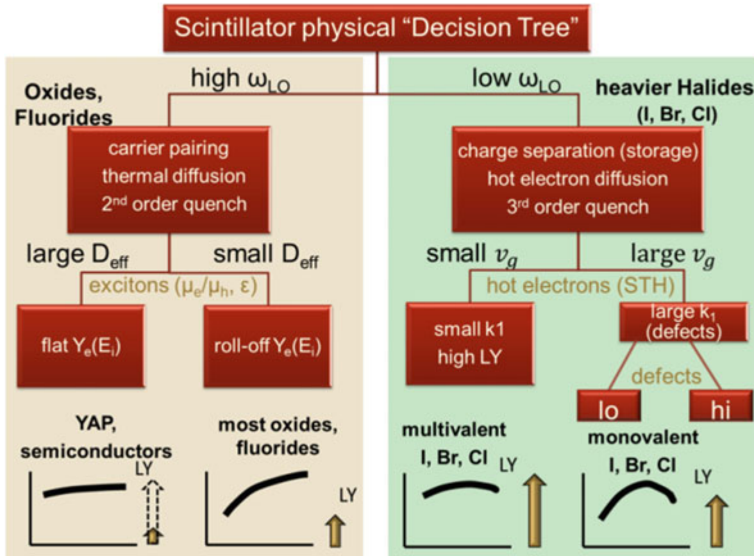

Fig. 10.34 Assembly of all the branching points considered for this decision tree comprising the start of a design rule for proportionality and light yield of oxide scintillators and semiconductors [71]

bly blessed and comprises a sweet spot in material parameter space for scintillator proportionality and light yield.

Acknowledgments This research was supported by the National Nuclear Security Administration, Office of Nonproliferation Research and Development (NA-22) of the U.S. Department of Energy under Contracts DE-NA0001012 and DE-AC02-05CH11231. The authors wish to thank Jai Singh, Bill Moses, Andrey Vasil'ev, Vitali Nagirnyi, Steve Payne, Daniel Aberg, Babak Sadigh, Sebastien Kerisit, and Fei Gao for helpful discussions. We thank Jaimie Grim for manuscript editing. Partial support was also provided by the US Department of Homeland Security, Domestic Nuclear Detection Office, under National Science Foundation contract ECCS-1348361of the Academic Research Initiative (ARI) program. This support does not constitute an express or implied endorsement on the part of the Government.

References

1. A.N. Vasil'ev, in *Proceedings of the 8th International Conference on Inorganic Scintillators and their Use in Scientific and Industrial Applications*, 2006, pp. 1–6
2. Z. Wang, Y. Xie, L.W. Campbell, F. Gao, S. Kerisit, J. Appl. Phys. **112**, 014906 (2012)
3. M. Moszyński, J. Zalipska, M. Balcerzyk, M. Kapusta, W. Mengesha, J.D. Valentine, Nucl. Instrum. Methods Phys. Res. Sect. A. Accel. Spectrom. Detect. Assoc. Equip. **484**, 259 (2002)
4. M. Moszynski, MRS Proc. **1038**, 1038 (2011)
5. R. Murray, A. Meyer, Phys. Rev. **122**, 815 (1961)

6. S.A. Payne, W.W. Moses, S. Sheets, L. Ahle, N.J. Cherepy, B. Sturm, S. Dazeley, G. Bizarri, C. Woon-Seng, IEEE Trans. Nucl. Sci **58**, 3392 (2011)
7. M. Kirm, V. Nagirnyi, E. Feldbach, M. De Grazia, B. Carré, H. Merdji, S. Guizard, G. Geoffroy, J. Gaudin, N. Fedorov, P. Martin, A. Vasil'ev, A. Belsky, Phys. Rev. B **79**, 233103 (2009)
8. A.N. Vasil'ev, IEEE Trans. Nucl. Sci. **55**, 1054 (2008)
9. S.A. Payne, N.J. Cherepy, G. Hull, J.D. Valentine, W.W. Moses, W.-S. Choong, IEEE Trans. Nucl. Sci. **56**, 2506 (2009)
10. M. Moszynski, J. Zalipska, M. Balcerzyk, M. Kapusta, W. Mengesha, J.D. Valentine, Nucl. Instrum. Meth. A **484**, 259 (2002)
11. P. Dorenbos, Nucl. Inst. Meth. Phys. Res. A **468**, 208 (2002)
12. W. Setyawan, R.M. Gaume, S. Lam, R.S. Feigelson, S. Curtarolo, ACS Comb. Sci. **13**, 382 (2011)
13. Q. Li, J.Q. Grim, R.T. Williams, G.A. Bizarri, W.W. Moses, J. Appl. Phys. **109**, 123716 (2011)
14. B.D. Rooney, J.D. Valentine, IEEE Trans. Nucl. Sci. **43**, 1271 (1996)
15. G. Hull, W.-S. Choong, W.W. Moses, G. Bizarri, J.D. Valentine, S.A. Payne, N.J. Cherepy, B.W. Reutter, IEEE Trans. Nucl. Sci. **56**, 331 (2009)
16. S.A. Payne, W.W. Moses, S. Sheets, L. Ahle, N.J. Cherepy, B. Sturm, S. Dazeley, G. Bizarri, W.-S. Choong, IEEE Trans. Nucl. Sci. **58**, 3392 (2011)
17. I. V Khodyuk, P. A. Rodnyi, and P. Dorenbos, J. Appl. Phys. **107**, 113513 (2010).
18. I. V Khodyuk and P. Dorenbos, IEEE Trans. Nucl. Sci. **59**, 3320 (2012).
19. M. Nikl, J.A. Mares, M. Dusek, P. Lecoq, I. Dafinei, E. Auffray, G.P. Pazzi, P. Fabeni, J. Jindra, Z. Skoda, J. Phys. Condens. Matter **7**, 6355 (1995)
20. V. Nagirnyi, S. Dolgov, R. Grigonis, M. Kirm, L.L. Nagorn, F. Savikhin, V. Sirutkaitis, S. Vielhauer, A. Vasil'ev, IEEE Trans. Nucl. Sci. **57**, 1182 (2010)
21. R. Laasner, N. Fedorov, R. Grigonis, S. Guizard, M. Kirm, V. Makhov, S. Markov, V. Nagirnyi, V. Sirutkaitis, A. Vasil'ev, S. Vielhauer, I.A. Tupitsyna, J. Phys. Condens. Matter?: an Institute of Phys. J. **25**, 245901 (2013)
22. R.T. Williams, J.Q. Grim, Q. Li, K.B. Ucer, W.W. Moses, Phys. Status Solidi (b) **248**, 426 (2011)
23. J.Q. Grim, Q. Li, K.B. Ucer, R.T. Williams, W.W. Moses, Nucl. Instrum. Methods Phys. Res. Sect. A. Accel. Spectrom. Detect. Assoc. Equip. **652**, 284 (2011)
24. V. Nagirnyi, in *Presented at the 12th International Conference on Inorganic Scintillators and Their Applications*, Shanghai (2013)
25. M. Sheik-Bahae, A.A. Said, E.W. Van Stryland, Opt. Lett. **14**, 955 (1989)
26. M. Sheik-Bahae, A.A. Said, T.-H. Wei, D.J. Hagan, E.W. Van Stryland, IEEE J. Quantum Electron. **26**, 760 (1990)
27. J.Q. Grim, Q. Li, K.B. Ucer, R.T. Williams, G.A. Bizarri, W.W. Moses, Mater. Res. Soc. Commun. Res. Lett. **2**, 139 (2012)
28. J.Q. Grim, K.B. Ucer, A. Burger, P. Bhattacharya, E. Tupitsyn, E. Rowe, V.M. Buliga, L. Trefilova, A. Gektin, G.A. Bizarri, W.W. Moses, R.T. Williams, Phys. Rev. B **87**, 125117 (2013)
29. K. Edamatsu, M. Sumita, S. Hirota, M. Hirai, Phys. Rev. B **47**, 6747 (1993)
30. R.M. Van Ginhoven, J.E. Jaffe, S. Kerisit, K.M. Rosso, IEEE Trans. Nucl. Sci. **57**, 2303 (2010)
31. R.T. Williams, K.B. Ucer, J.Q. Grim, K.C. Lipke, L.M. Trefilova, W.W. Moses, IEEE Trans. Nucl. Sci. **57**, 1187 (2010)
32. R. Kirkin, V.V Mikhailin, A.N. Vasil'ev. IEEE Trans. Nucl. Sci. **59**, 2057 (2012)
33. Z. Wang, Y. Xie, B.D. Cannon, L.W. Campbell, F. Gao, S. Kerisit, J. Appl. Phys. **110**, 64903 (2011)
34. W. Martienssen, J. Phys. Chem. Solids **2**, 257 (1957)
35. G.A. Bizarri, W.W. Moses, J. Singh, A.N. Vasil'ev, R.T. Williams, J. Appl. Phys. **105**, 44507 (2009)
36. F. Gao, Y. Xie, Z. Wang, S.N. Kerist, L.W. Campbell, R.M. Van Ginhoven, M.P. Prange, in *International Conference on Defects in Insulating Materials (ICDIM 2012)* (2012)
37. J. Q. Grim, K. B. Ucer, A. Burger, G. A. Bizarri, and R. T. Williams, To Be Published (n.d.).

38. H. Nishimura, M. Sakata, T. Tsujimoto, M. Nakayama, Phys. Rev. B **51**, 2167 (1995)
39. L.B. Rubin, O.V Braginskaya, M.L. Isakova, N.A. Efremov, V.Z. Paschenko. J. Lumin. **29**, 399 (1984)
40. T.R. Waite, Phys. Rev. **107**, 463 (1957)
41. J.B. Birks, *The Theory and Practice of Scintillation Counting* (Pergamon Press, London, 1964), p. 662
42. R.T. Williams, J.Q. Grim, Q. Li, K.B. Ucer, G.A. Bizarri, S. Kerisit, F. Gao, P. Bhattacharya, E. Tupitsyn, E. Rowe, V.M. Buliga, A. Burger, *Proceedings of SPIE*, 2013, Vol. 8852, pp. 88520J-1
43. A. Vasil'ev, A. Gektin, in *SCINT2013*, Shanghai, China, 2013
44. Q. Li, J.Q. Grim, N.A.W. Holzwarth, R.T. Williams, in *SCINT2013*, 2013
45. K.B. Ucer, G.A. Bizarri, A. Burger, A. Gektin, L. Trefilova, R.T. Williams, Phys. Rev. B **89**, 165112 (2014)
46. F. Antonangeli, N. Zema, M. Piacentini, U.M. Grassano, Phys. Rev. B **37**, 9036 (1988)
47. M. Couzi, J.R. Vignalou, G. Boulon, Solid State Commun. **20**, 461 (1976)
48. Y. Abraham, N.A.W. Holzwarth, R.T. Williams, Phys. Rev. B **62**, 1733 (2000)
49. V. N. Kolobanov, I. A. Kamenskikh, V. V Mikhailin, I. N. Shpinkov, D. A. Spassky, B. I. Zadneprovsky, L. I. Potkin, G. Zimmerer, Nucl. Instrum. Meth. A **486**, 496 (2002).
50. M. Fujita, M. Itoh, T. Katagiri, D. Iri, M. Kitaura, V.B. Mikhailik, Phys. Rev. B **77**, 155118 (2008)
51. J. Gabrusenoks, A. Veispals, A. von Czarnowski, K.-H. Meiwes-Broer, Electrochim. Acta **46**, 2229 (2001)
52. D.J. Singh, Appl. Phys. Lett. **92**, 201908 (2008)
53. Y. Cui, R. Hawrami, E. Tupitysn, P. Bhattacharya, M. Groza, M. Bryant, V. Buliga, A. Burger, N.J. Cherepy, S.A. Payne, Solid State Commun. **151**, 541 (2011)
54. D. Fröhlich, B. Staginnus, Y. Onodera, Phys. Status Solidi (b) **40**, 547 (1970)
55. K. Teegarden, G. Baldini, Phys. Rev. **155**, 896 (1967)
56. K.S. Song, R.T. Williams, *Self-Trapped Excitons, Second* (Springer, Heidelberg, 1996)
57. J.E. Eby, K.J. Teegarden, D.B. Dutton, Phys. Rev. **116**, 1099 (1959)
58. P. A. Rodnyi, in (CRC Press LLC, 1997), p. 79.
59. P. Erhart, A. Schleife, B. Sadigh, D. Aberg, arXiv:1311.350v1 [cond-mat.mtrl-sci] (2013).
60. S. Agostinelli and others, Nucl. Instrum. Meth. A **506**, 250 (2003).
61. J.Q. Grim, Q. Li, K.B. Ucer, A. Burger, G.A. Bizarri, W.W. Moses, R.T. Williams, Phys. Status Solidi (a) **209**, 2421 (2012)
62. Q. Li, J.Q. Grim, R.T. Williams, G.A. Bizarri, W.W. Moses, Nucl. Instrum. Meth. A **652**, 288 (2011)
63. W. Setyawan, R.M. Gaume, R.S. Feigelson, S. Curtarolo, IEEE Trans. Nucl. Sci. **56**, 2989 (2009)
64. J. Singh, J. Appl. Phys. **110**, 024503 (2011)
65. F. Gao, Y. Xie, S. Kerisit, L.W. Campbell, W.J. Weber, Nucl. Instrum. Methods Phys. Res. Sect. A. Accel. Spectrom. Detect. Assoc. Equip. **652**, 564 (2011)
66. A. Kozorezov, J.K. Wigmore, A. Owens, J. Appl. Phys. **112**, 53709 (2012)
67. http://www.detectors.saint-gobain.com/(n.d.)
68. J.Q. Grim, K.B. Ucer, R.T. Williams, A. Burger, P. Bhattacharya, E. Tupitsyn, G.A. Bizarri, W.W. Moses, in (Presented at SORMA West, Oakland, May 16 (2012)
69. B.P. Aduev, E.D. Aluker, G.M. Belokurov, V.N. Shvayko, Phys. Status Solidi (b) **208**, 137 (1998)
70. H.B. Dietrich, R.B. Murray, J. Lumin. **5**, 155 (1972)
71. Q. Li, J.Q. Grim, K.B. Ucer, A. Burger, G.A. Bizarri, W.W. Moses, R.T. Williams, Phys. Status Solidi RRL **6**, 346 (2012)
72. S. Marchetti, M. Martinelli, R. Simili, J. Phys. Condens. Matter **14**, 3653 (2002)
73. U. Strauss, W.W. Rühle, K. Köhler, Appl. Phys. Lett. **62**, 55 (1993)
74. Y.C. Shen, G.O. Mueller, S. Watanabe, N.F. Gardner, A. Munkholm, M.R. Krames, Appl. Phys. Lett. **91**, 141101 (2007)